2018

AN EXPERIMENTAL AND COMPUTATIONAL STUDY OF FUEL SPRAY INTERACTION: FUNDAMENTALS AND ENGINE APPLICATIONS

Le Zhao
Michigan Technological University, lez@mtu.edu

AN EXPERIMENTAL AND COMPUTATIONAL STUDY OF FUEL SPRAY INTERACTION: FUNDAMENTALS AND ENGINE APPLICATIONS

By

Le Zhao

A DISSERTATION

Submitted in partial fulfillment of the requirements for the degree of

DOCTOR OF PHILOSOPHY

In Mechanical Engineering - Engineering Mechanics

MICHIGAN TECHNOLOGICAL UNIVERSITY

2018

This dissertation has been approved in partial fulfillment of the requirements for the Degree of DOCTOR OF PHILOSOPHY in Mechanical Engineering - Engineering Mechanics.

Department of Mechanical Engineering - Engineering Mechanics

Dissertation Advisor:	*Dr. Seong-Young Lee*
Committee Member:	*Dr. Jeffrey D. Naber*
Committee Member:	*Dr. Raymond Shaw*
Committee Member:	*Dr. Chang-Kyoung Choi*
Department Chair:	*Dr. William W. Predebon*

Table of Contents

LIST OF FIGURES

LIST OF TABLES

PREFACE

The materials in this dissertation (Chapter 2 on the part of literature review, Chapter 4 on the part of CFD simulation description, Chapters 6, 7, and 8 on the results and discussion of droplet-wall impingement, the evaporation sub-model applications, the spray-wall impingement, and the multiple spray-to-spray collision) come from 8 of my publications in SAE World Congress. I have included the permission to use the published materials in the Appendix. 7 publications have my name as the first author, I was responsible for the part of experiments (Rate of injection, backlight, Mie, Schlieren, heat flux) and data analysis, and running most CFD simulations and analyzing the simulation results. Furthermore, I made the final plots and wrote the manuscript. My co-authors at both MTU and participating institutions have helped in setting up the experiments, analyzing the experimental data, and performed some of simulation support, as well as incorporation of comments on grammar and theory. I was the second author for one publication in Chapter 6 on the validation and application of evaporation sub-model, where I wrote the part of numerical results, plotted some of figures, and reviewed the manuscript for further comments and editing.

ACKNOWLEDGEMENT

I would like to express my deepest gratitude to my research advisor Dr. Seong-Young Lee, for all of your support and guidance while pursuing my graduate education. In particular, thanks Dr. Lee for offering me the opportunity to pursue my Ph.D. in Michigan Technological University, thanks Dr. Lee for participating in daily based discussions with his patience and always gave the valuable advices on the research. As well, my scientific confidence has been established due to the great help from Dr. Lee with his respect to my ideas; my connections with many experts in the relevant field are also built because of the opportunities created by Dr. Lee, which gives me more chances to present my work outside and helps me grow up in the academic society. All of the above make that my four year Ph.D. study became a fruitful, memorable and joyful journey.

I would also like to acknowledge my committee members, Dr. Naber, Dr. Shaw, and Dr. Choi, for taking time to serve on my committee and be involved in my graduate education. Thanks Dr. Naber for supporting and guiding my research work during the projects reports and discussions. Thanks Dr. Naber for the kind help on my future career. Thanks Dr. Shaw and Dr. Choi for reading the thesis and providing the valuable feedbacks, which makes my final dissertation successful.

I would like to express my acknowledgement to my colleagues and friends, especially Xiucheng Zhu, Dr. Abdul Moiz, Zhihao Zhao, Nitisha Ahuja, Meng Tang, Sthaya Potham, I appreciate all the help and assistance you provided on my research work and personal life. We had a lot fun by many interesting discussions on spray combustion and other subjects. It was also a nice experience to closely work with my fellow colleagues Dr. Khanh Cung, and Dr. Anqi Zhang. I would also like to thank every member such as Henry Schmitt, Bill Atkinson, Tyler Menucci in Alternative Energy Research Center (AERB) for your support through the years.

I have done two co-ops during my Ph.D., one is in Argonne National Laboratory, and another is in ANSYS Inc. I would like to thank Dr. Sibendu Som, Dr. Janardhan Kodavasal, Dr. Roberto Torelli, and Dr. Muhsin Ameen from ANL and Dr. Ellen Meeks, Dr. Yue

Wang, and Dr. Long Liang from ANSYS Inc. for all the support and help to extend my knowledge, especially in high-performance computing.

I also thank the friendly and creative atmosphere created by many friends in MEEM department, such as Xin Wang, Jiajun Song, Simon Wang, Luting Wang, Roger Yang, Justin Zhang, Shangyan Zou, Chong Cao, Jianyang Lyu, and Xin He.

The people that I am missing most are my families at this moment, who always love and support me. Thank you for everything you have done for me. Finally I would like to acknowledge Xuebin Yang, being with you brings me so many fun and happiness, your support has been instrumental in my success.

I would like to thank all the people who have helped me!

ABBREVIATIONS

IC	Internal combustion
AMR	Adaptive mesh refinement
ASOI	After start of injection/impingement
CFD	Computational fluid dynamics
CFL	Courant-Friedrichs-Lewy
CHF	Critical heat flux
CI	Compression ignition
CV	Combustion vessel
DAQ	Data acquisition system
DI	Direct injection
DME	Dimethyl ether
DNS	Direct numerical simulation
DOM	Disappearance of mist
DWI	Direct Water Injection
EOI	End of injection

GDI	Gasoline direct injection
GHG	Greenhouse gases
HRIC	High-resolution interface capturing
IC	Internal combustion
IIR	Infinite impulse response
KH-RT	Kelvin Helmholtz- Rayleigh Taylor
LIF	Laser induced fluorescence
MAC	Marker-and-cell
ND	Neutral density
NTC	No time counter
OpenFOAM	Open source field operation and manipulation
PDA	Phase doppler anemometry
PDF	Probability density functions
PFI	Port fuel injection
PLIC	Piecewise-linear interface calculation
PCCI	Premixed Charge Compression Ignition

RANS	Reynolds averaged Navier-Stokes
RCCI	Reactivity Controlled Compression Ignition
RIM	Refractive index matching
ROI	Rate of injection
SAT	Saturation
SI	Spark ignited
SMD	Sauter mean diameter
TAI	Time after impingement
UDF	User define function
UHC	Unburned hydrocarbon
ULSD	Ultra-low sulfur diesel
VOF	Volume of fluid
WIES	Wall-impinged expanding spray

NOMENCLATURE

R_a	Average surface roughness
$A_{b,s}$	Axial arc
$C_{b,s}$	Axial corrugation ratio
Z_s	Axial free spray liquid penetration
H_s	Axial impinged spray height
R_s	Axial impinged spray radius
$R_{b,s}$	Axial impinged spray radius in bottom view
$R_{s,w}$	Axial impinged spray radius on wall
$A_{b,f}$	Radial arc
$C_{b,f}$	Radial corrugation ratio
Z_f	Radial free spray liquid penetration
H_f	Radial impinged spray height
R_f	Radial impinged spray radius
$R_{b,f}$	Radial impinged spray radius in bottom view
$R_{f,w}$	Radial impinged spray radius on wall

δ_{bl}	Boundary layer thickness
Ca	Capillary number
U_{cl}	Contact line velocity
ρ	Density
D	Diffusivity
u	Dimensionless impact velocity
β	Dimensionless roughness parameter
θ	Dynamic contact angle
μ	Dynamic viscosity
g	Gas phase
U_0	Impact velocity
f	Impinging frequency
D_0	Incident droplet diameter
h_0	Initial wall-film thickness
ν	Kinematic viscosity
h	Latent heat

l	Liquid phase
m	Mass
Y	Mass fraction
n	Normal
Oh	Ohnesorge number
p	Pressure
r_{cl}	Radius of the wetted area
Re	Reynolds number
c	Specific heat
d	Spreading diameter
Δ	Spreading factor
κ	Surface curvature
σ	Surface tension
T	Temperature
k	Thermal conductivity
V	Total volume of the control volume

$\boldsymbol{n_{w,i}}$	Unit vectors normal to the wall
$\boldsymbol{t_{w,i}}$	Unit vectors tangential to the wall
$\boldsymbol{v}$	Vapor phase
$\boldsymbol{U}$	Velocity vector
$\boldsymbol{\lambda}$	Viscosity length
$\boldsymbol{\alpha}$	Void fraction
$\boldsymbol{We}$	Weber number

ABSTRACT

An efficient spray injection results in better vaporization and air-fuel mixing, leading to combustion stability and reduction of emissions in the internal combustion (IC) engines. The impingement of liquid fuels on chamber wall or piston surface in IC engines is a common phenomenon and fuel film formed in the spray-piston or cylinder wall impingement plays a critical role in engine performance and emissions. Therefore, the study of the spray impingement on the chamber wall or position surface is necessary.

To understand the spray-wall interaction, a single droplet impingement on a solid surface with different conditions was first examined. The droplet-wall interaction outcomes, in particular focusing on the splashing criteria, were inspected and post-impingement characterizations including spreading factor, height ratio, contact line velocity, and dynamic contact angle was further analyzed based on the experimental data. The non-evaporation volume of fluid (VOF) model based on Eulerian approach was used to characterize single droplet impinging on the wall and provide a better understanding of the dynamic impact process. In addition, the study of droplet-to-droplet collision and multi-droplet impingement on a solid surface are performed, which is essential to aid in the spray-wall impingement investigation. As well, due to the evaporation drawing more attention during the engine combustion process, an evaporation VOF sub-model was developed and applied to multi-droplet impingement on a hot surface to qualitatively and quantitatively analyze the vaporizing process as droplets impacting onto the hot surface.

After that, the non-vaporizing and vaporizing spray characteristics of spray-wall impingement at various operating conditions relevant to diesel engines were undertaken, with spray characterized using schlieren and Mie scattering diagnostics, as well as Refractive Index Matching (RIM) technique. Free and impinged spray structures and deposited wall-film formation and evaporation were qualitatively analyzed, spray properties and wall-film properties were quantified, and surface temperature and heat flux were measured. An Eulerian-Lagrangian modeling approach was employed to characterize the spray-wall interactions by means of a Reynolds-Averaged Navier-Stokes (RANS)

formulation. The local spray characteristics in the vicinity of the wall and the local spray morphology near the impingement location were studied. Furthermore, multiple spray-to-spray collision derived from droplet-to-droplet collision, considering as one of the advanced injection strategies to enhance the engine performance, was studied at various gasoline engine conditions to explore the effect of colliding spray on spray related phenomena like atomization, vaporization, and mixing. Spray characteristics were obtained by the schlieren diagnostics and the experimental validated Computational Fluid Dynamic (CFD) simulations were based on Eulerian-Lagrangian approach to understand the mechanism behind the collisions of sprays and characterize the different types of multiple spray-to-spray collision.

In summary, on the strength of the study of droplet-wall impingement and droplet-to-droplet collision at non-evaporation and evaporation states, the main objective of this dissertation is to enhance the understanding of spray-wall impingement and multiple spray-to-spray collision under diesel or gasoline engine conditions from both experiments and CFD simulations, therefore providing feedbacks to the ultimate task in future development and application of a more reliable and effective fuel injection system.

CHAPTER 1 INTRODUCTION

1.1 Motivation

Although the future of renewable energies appear to be rich and the research on them is thriving due to its sustainability, the limitations of various renewable energies exist. For instance, the safety issue has to be considered when using nuclear energy and the time/place selection has to be taken into account. Therefore, to meet the global energy requirement in the near future, the fossil fuels oil, gas, and coal will still be the main sources for the global energy supply. The dominant consumption of fossil fuels is combustion that is one of the major driving forces to make progress on the society, since it is easy to utilize and create the high power intensity and is applied into many sectors like transportation, power generation, etc. Today more than one billion vehicles are driven on all over the word and vehicle ownership is expected to double worldwide in the next decade [1] and total oil consumption was 37% of all the energy consumed in the United States in 2016 [2]. Internal combustion (IC) engines associated with motorized vehicles, a notable invention with a profound impact on human life, are one of the key partakers of combustion. In spite of the wide use and the promoted combustion efficiency of IC engines, it still shows the significant impact on the environment.

Both diesel and gasoline engines have been occupying the majority of the IC engine sector [3, 4]. The emissions from both engines include nitrogen oxides (NO_x), particulate matter (PM), carbon monoxide (CO), and greenhouse gases (GHG), mainly carbon dioxide (CO_2) [5]. According to various reports, the exhaust emissions from engines have undesirable effects on human health and deteriorating environment is also directly related to exhaust emissions from engines [6-11]. Federal government regulations have strictly controlled environmental pollutions from IC engines. As well, progressive and increasing restrictive European emission standards have been implemented on all conventional motor vehicles [12, 13]. These regulations have pressed researchers and the automobile industry to explore and improve the conventional IC engines as well as develop a cleaner and more efficient combustion process.

Many combustion technologies have been developed in the past few decades, for example, the development of partially premixed compression ignition (PPCI), homogenous charge compression ignition (HCCI), gasoline compression ignition (GCI), and low-temperature combustion (LTC). The main challenge during such research and development of IC engines is to optimize the engine combustion system to improve power output, enhance fuel efficiency, and reduce pollutant emissions concurrently. Optimized combustion is a result of careful matching of air-fuel mixture and accuracy in the injection process. Therefore, research in the area of traditional fuel injection systems needs to be done to fully understand the process of fuel injection and the cause of the emissions. During the injection, especially in direct-injection spark-ignition (DISI) gasoline engines and small-bore diesel engines, fuel impingement on engine piston head or cylinder wall caused by the high injection pressure or low ambient temperature inevitably occurs and it has substantial effects on air–fuel mixing, combustion and emissions processes inside the combustion chamber.

1.2 Overview

In this dissertation we focus on the spray-wall impingement under engine operating conditions, and in particular, its development process during spray impinging on a solid surface. Two primary coupled physical processes, including impinged spray development and wall film formation, are involved as spray impinging on the wall. A spray itself is comprised of a large number of droplet with different size and velocity as the liquid fuel is injected and the spray after impingement on wall results from different droplets rebounding, splashing, and deflecting. This impinged spray may strengthen the vaporization of the spray due to an increase of the total spray surface area caused by the shattered droplets. As well, a better dispersion of the impinged spray is led by the gas jet vortex in the vicinity of the impinged wall. As the wall film may cause deviations of the required air-fuel ratio, this thin film attributed by the fuel deposition on the wall may create some negative influences as this thin film, for example, the soot formation might be enhanced and the unburnt hydrocarbons might be increased [14, 15].

Additionally, multiple spray-to-spray collision is another viable way to achieve the efficient, smart and economic injection system in order to overcome the pitfalls in the conventional injection systems. The reason for this is that multiple spray-to-spray collision helps the droplets break-up to achieve an improved atomization during combustion process. The effective atomization and vaporization lead to low emissions formation, high fuel efficiency, and reduction in spray-wall interaction [16-19]. However, there are challenges in studying multiple spray-to-spray collision process since it causes complex flow structure geometry and spray characteristics variation which depends on engine load variation, as well as considering optimization of controlling parameters.

In summary, considering the more rigorous regulation on exhaust emissions and the wide use of the IC engines in both light and heavy duty vehicles, the current research mainly consists of spray-wall impingement and a viable option of spray injection, multiple spray-to-spray collision at diesel or gasoline engine conditions to obtain a comprehensive understanding of their effects on the engine performance. However, first, due to the complexity of the practical fuel injection systems, it is difficult to attain the detailed local information of the spray impingement such as droplet mass, number, size and velocity distributions at the near wall region from the experiments. Second, because of the Lagrangian particle concept (a particle representing a number of droplets in simulations), the spray-wall interaction model under Eulerian-Lagrangian approach is always developed based on the individual droplet. Therefore, the individual droplet's impingement on wall and the droplet-to-droplet collision have been extensively studied to assist in a profound perception on the spray-wall impingement and multiple spray-to-spray collision.

In the current thesis, the encouraging experimental observations of applying optical diagnostics technology to study droplet/spray-wall impingement and droplet-to-droplet/spray-to-spray collision are extensively used, but it is sometimes hard to obtain detailed information of spray impingement through experiment in either the optical engines or the combustion vessel. For example, as mentioned above, the local detailed information such as droplet mass, number, and velocity distributions near the wall is difficult to measure experimentally. Therefore, computational modelling is an ideal tool to offer a

promising alternative owing to the fact that it is usually inexpensive compared with experiments and more detailed information such as spray impingement characteristics are available from the simulation results.

1.3 Goals and objectives

This research consists of four main goals which are achieved through several objectives. The first goal is to improve the perception of a single droplet-wall impingement characteristics under various ambient and surface conditions using both experimental backlight imaging and CFD simulation. This includes the droplet-wall interaction outcomes (in particular focusing on the splashing criteria and spreading regime) and post-impingement characterizations (including spreading factor, height ratio, contact line velocity, and dynamic contact angle). Achievement of this goal contributes to the improvement of splashing criteria based on the present experiments, understanding of the droplet spreading mechanism, and the complement of detailed knowledge on the dynamic contact angle measurement by testing various liquid fuels.

The second goal is the development of an evaporation sub-model based on the existing Volume of fluid (VOF) model. VOF model which belongs to the class of Eulerian approach is physics based and requires no modeling or parameter tuning model. However, it lacks of an evaporation model to address the vaporization during phase change. Further, the new concepts of liquid and vapor void fractions are introduced in the evaporation sub-model to differentiate the vapor fuel and surrounding gas phases. This developed evaporation sub-model is validated with the available experimental results, then applied into multi-droplet impingement on a hot surface to qualitatively and quantitatively analyze the vaporizing process during the impingement process.

The third goal is to obtain an understanding of non-vaporizing and vaporizing spray characteristics of spray-wall impingement at different fuel injection and ambient states at conditions relevant to diesel engines. An optically accessible combustion vessel with different optical diagnostics (Schlieren, Mie scattering, and simultaneous schlieren and Mie scattering imaging, as well as Refractive Index Matching (RIM) technique) is used to

visualize the spray impingement from three perspective views (front, side, and bottom). The spray characteristics comprises of the liquid penetration, spray dispersion angle, spray impingement mechanism, impinged spray properties, the wall film formation and characteristics, as well as surface temperature and heat flux measurements. This goal succeeds in characterizing the spray-wall impingement through the global key parameters and supports validation and development of spray-wall interaction model through Eulerian-Lagrangian based simulations. The simulations are used to investigate spray-wall impingement, liquid film formation, and post-impingement processes, in particular, the local spray characteristics in the vicinity of the wall with a particular focus on Sauter Mean Diameter (SMD) and Reynolds and Weber numbers (*Re* and *We*) and the local spray morphology near the impingement location, as related to the diesel engines, which is difficult to accomplish in experiments.

The final goal focuses on a novel designed injector with multiple spray-to-spray collision at the different gasoline engine conditions, consisting of experimental and simulation work to study the effect of colliding spray on overall spray related phenomena like atomization, vaporization, and mixing, etc. The experimental work utilizes the constant volume combustion vessel lab with optical diagnostics of schlieren to visualize the spray structure and measure the liquid and vapor penetrations, vapor fraction, and spray angle. The experimental validated simulations are based on Eulerian-Lagrangian approach to understand the mechanism behind the collisions of droplets and how they affect the overall spray growth, as well as numerically characterize different types of multiple spray-to-spray collision by calculating the post collision angle, bend angle, and droplet mass, number, and size distributions. The purpose of this goal is to investigate the collision process and spray behaviors of multiple spray-to-spray collision injector at gasoline engine conditions, supporting in the practical applications of the research in novel injector design.

These goals will be achieved through a series of objectives as follows,

- **Droplet related studies:**

1. Incorporate optical diagnostics to visualize and quantify the macroscopic droplet structure and characteristics.

2. Develop image processing programs to measure the droplet characteristics, including droplet spreading factor, height ratio, contact line velocity, and dynamic contact angle, and heat flux.

3. Characterize a single droplet impinging on the wall over a wide range of conditions, including different liquid fuels, different *We,* and smooth, roughened, isothermal and heated surfaces.

4. Validate the VOF simulation results with experimental data and further analyze velocity flow field and pressure coefficient.

5. Develop and validate the evaporation VOF sub-model and apply it into multi-droplet impingement on a hot surface. The temporal evolution of liquid and vapor void fractions, droplet spreading factor, droplet levitation, surface temperature, and liquid droplet mass fraction are obtained.

- **Spray related studies:**

1. Incorporate optical diagnostics to visualize and quantify the macroscopic spray structure and characteristics.

2. Develop image processing programs to measure the macroscopic spray characteristics, including spray liquid and vapor penetrations, vapor fraction, spray dispersion angle, impinged spray radius and height, expansion ratio, corrugation ratios, global and local film mass, global and local film thickness, global and local film area.

3. Characterize diesel and gasoline sprays over a wide range of conditions in combustion vessel, which is related to the normal diesel or gasoline engine

operating conditions, including ambient temperature, ambient density, and fuel injection pressure.

4. Validate the Eulerian-Lagrangian simulation results with spray-wall impingement experimental spray structure, liquid penetration, spray dispersion angle, and impinged spray properties, as well as the film properties. Further analyze local spray characteristics near the wall and the local spray morphology near the impingement location.

5. Validate the Eulerian-Lagrangian simulation results with multiple spray-to-spray collision experimental spray structure, liquid and vapor penetrations, post collision and bend angles, and vapor fraction. Further analyze different types of multiple spray-to-spray collision with droplet mass, number, and size distributions, and velocity flow field distributions.

6. Produce the combustion experiments for spray-wall impingement and multiple spray-to-spray collision under engine conditions.

1.4 Thesis organization

With the focus of study on droplet/spray-wall impingement and droplets/sprays collision, this thesis is organized in ten chapters. The current chapter, Chapter 1, introduces the background of the present research, and illuminates the motivation and objectives of this work.

In Chapter 2, a literature review is provided, with discussions on the fundamental mechanism as a single droplet impingement on an unheated and hot surfaces, post-impingement characterization, processes of droplet-to-droplet collision and multi-droplet impingement, the experimental work and numerical model development reviews of spray-wall impingement, and the model application of spray impinging on the wall, in conjunction with the study on multiple spray-to-spray collision.

Chapter 3 discusses the experimental apparatuses, test setup with optical diagnostics, and detailed methodologies for data analysis for each work (droplet/spray-wall impingement and droplets/sprays collision). First, the descriptions of the high- and low-pressure fuel injection systems, the specific injector nozzles used for the different purpose of study, and the rate of injection systems are provided. Second, the start-of-art combustion vessel associated with the above systems is introduced. Last, the optical diagnostics with image/data analysis for each work are presented.

Chapter 4 explains the detailed numerical theories to model the targeted droplet/spray-wall impingement and droplets/sprays collision. The content of this chapter is as follows: the introduction of the overall concept including Eulerian and Eulerian-Lagrangian methods, which are two main approaches used in this thesis, and how the Eulerian and Eulerian-Lagrangian methods function and are linked for each work. Then, the summary of computational platform utilized in the research. Next, the detailed description of the Eulerian based VOF method and the development of the evaporation sub-model. Followed by the detailed explanation of the spray models in the basis of Eulerian-Lagrangian approach. Finally, the other simulation configurations including the general computational domain and the mesh refinement method.

Chapter 5 shows the main contributions obtained from the research

Chapter 6 starts the experiment and application of the theories to test and model of droplet-wall impingement at different conditions and droplet-to-droplet collision, as well as multi-droplet impingement on a hot surface. This chapter presents the improved splash criteria, the post-impingement characteristics including spreading factor, height ratio, contact angle, and contact line velocity, and the validation of the non-evaporation VOF simulation results based on the wide range of experimental data, the developed evaporation sub-model, and the application the sub-model into the multi-droplet impingement on the hot surface.

Chapter 7 reports the experimental and numerical study on the spray-wall impingement at different ambient/injection conditions to characterize the global and local free and impinged spray behaviors from various perspective views, and the qualitative analysis film

formation and quantitative analysis on film properties, as well as the heat flux analysis when the spray impacts onto a heated surface with various temperatures and operating conditions.

Chapter 8 gives the experimental and simulation work on the multiple spray-to-spray collision to study the collision process and examines the practical applications of the research in novel injector design.

In Chapter 9, the main conclusions and findings of this study are summarized, and recommendations are made for future studies.

Appendix in Chapter 10 includes the data and image processing programs and the simulation model constants for different simulations and Reference list is in Chapter 11.

CHAPTER 2 LITERATURE REVIEW

Fuel injection with spray technology is widely used in industrial and research sectors [20]. In IC engines, efficient spray injection leads to improved vaporization and air-fuel mixing, resulting in combustion stability and reduction of emissions [16]. During the fuel injection, the fuel spray impingement onto the interposed surfaces is a very common phenomenon occurring in either a direct or an indirect equipped IC engine; it causes a fundamental issue affecting the preparation of air-fuel mixture prior to the combustion, further, affecting engine performance and emissions [21]. Therefore, the study of the spray impingement on the chamber wall or piston surface is essential and needs to be fully understood. In addition, the various advanced injection strategies have to be considered as another orientation to enhance the engine performance. Multiple spray-to-spray collision is one of the approaches, which yields improved spray characteristics and vaporization before fuel impacting on the wall [22]. The spray-wall impingement and the spray-to-spray collision phenomena is known to require a detailed record of droplet size, number, and velocity near the impinged surface, of either primary or secondary droplets. It is also associated with the liquid fuel properties, surface morphology, and geometry of the fuel injection system [21]. However, due to the complexity of the practical fuel injection systems, the current physical models to depict the spray impingement have been inferred based on the fundamental studies with the simplified flow geometries. Specifically, the individual droplet impingement on the substrate or the impingement between droplets have been extensively used to describe the spray impact behavior and predict the interaction outcomes, although a summation of individual droplet characteristics may not exactly be applicable to a spray.

This chapter presents a literature review relevant to the research undertaken for this thesis. Review is included on studies of droplet-wall impingement, droplet-to-droplet collision, spray-wall interaction, and multiple spray-to-spray collision. The purpose of this review is to achieve an understanding of the impinging dynamic processes from the droplet-wall interaction and multi-droplet collision, to further aid in studying the spray-wall impingement and multiple spray-to-spray collision, and to set the stage for the scope and application of the current work with respect to the existing research.

2.1 Interaction between a single droplet and a solid surface

2.1.1 Droplet-wall impingement mechanism overview

To understand the underlying mechanism of spray-wall interaction, it is essential to focus on the fundamental physics of individual droplet impact on the wall under various conditions.

The fluid dynamic phenomena when a single droplet impacts on a solid surface depends upon many parameters, such as fuel properties (surface tension, viscosity, wettability, and density) and operating conditions (wall temperature and surrounding gas temperature and pressure) [23]. Therefore, the understanding of a droplet impingement process is crucial to achieve a deeper insight into the influence of the above mentioned factors on spray-wall interaction. The impingement characteristics of a liquid droplet on a solid surface (dry, wetted, isothermal, or hot) include stick, spread, rebound, splash, and break-up [24] as seen in Figure 2.1. The study of droplet interaction with a dry or wetted solid surface has been done by many researchers; they found that all these impingement processes are strong functions of the droplet impact energy [24, 25]. When the impact energy is very low, the droplet sticks to the wall, while as impact energy increases, the liquid film spreads and rebounds until all the energy is dissipated. Further increasing the impact energy, the droplet disintegrates within the first instant after impingement; the splash occurs when the droplet interacts with the surface by leaving some liquid on the surface (contributing to the wall-film formation) and splashing back the remaining part. This remaining part comprises of droplets that have different sizes and velocities with respect to the one that originally impinged on the wall [21, 24, 25].

The mechanism of droplet deposition-splash is more complex compared with other interaction outcomes, and it depends on the combination of the boundary conditions such as droplet velocity, impact angle, and surface topography. Therefore, the splash criterions are summarized based on the experimental work of the droplet impinging on the dry or wetted surface. These criteria are usually based on non-dimensional parameters, characterizing the relative magnitude of the forces acting on the droplet. The most common

parameters are Reynolds number ($Re = \rho D_0 U_0/\mu$), Weber number ($We = \rho D_0 U_0^2/\sigma$), Ohnesorge number ($Oh = We^{0.5}Re$), and Capillary number ($Ca = We/Re$) (ρ, σ, and μ are the density, surface tension and dynamic viscosity, respectively, D_0 is the initial droplet diameter, U_0, being the impact velocity). Note that the parameters of *Re, We, Oh, and Ca* are calculated from the normal velocity component of the impinging droplet.

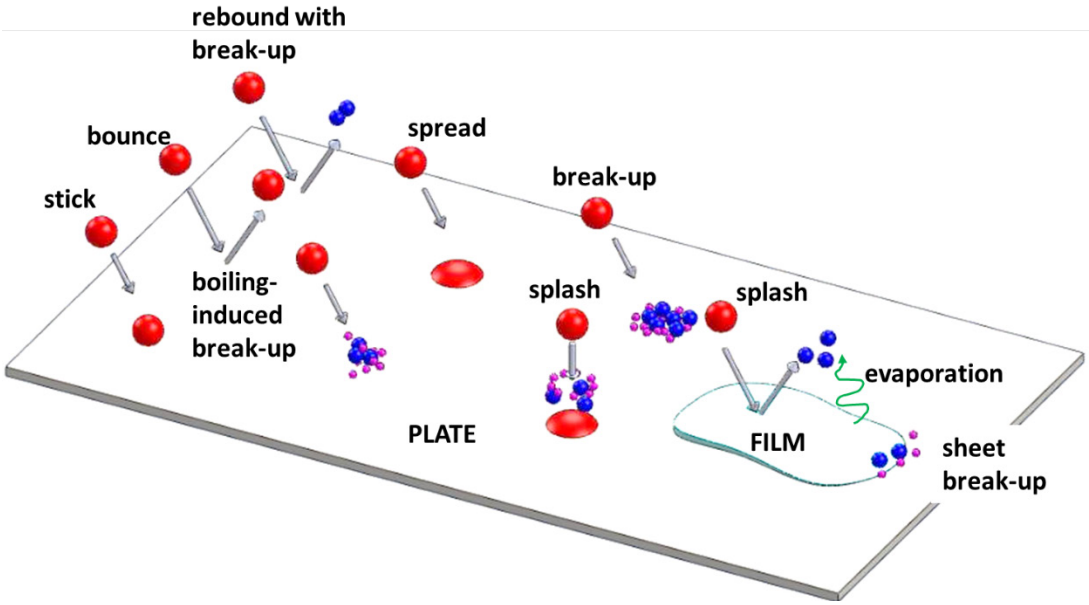

Figure 2.1: A schematic of the drop impinging on a solid surface (dry/wetted/isothermal/hot surface).

Stow et al. [26] conducted one of the earliest experimental studies to understand the droplet-wall interaction phenomena and its dependence on the *Re* and *We* of liquid fuel and surface roughness, by studying water droplets impinging on a roughened aluminum surface. They postulated a splashing threshold $K = We^{0.5}Re^{0.25}$, in which the value of *K* is highly dependent on the surface roughness [27], although further studies by Yarin and Weiss [28] and Mundo at al. [29] showed that the surface roughness had less effect on the splashing criteria. Yarin and Weiss [28] studied the single train of droplets falling on a solid substrate with a thin film at a known impinging frequency (*f*). They proposed a splash mechanism and found a splashing threshold as a function of impact parameters of a droplet: *Ca* and non-dimensional viscosity length ($\lambda = \left(\frac{\nu}{f}\right)^{0.5} \sigma/(\rho\nu^2)$), as shown in Equation (2.1)

(v is kinematic viscosity), where the dimensionless impact velocity (u) is introduced. They found that splashing threshold does not depend on droplet diameter and is slightly effected by mean surface roughness. They also concluded that the splashing threshold at u = 17 to 18 corresponds to developed crown instability, strong enough to produce a group of secondary droplets.

$$Ca\lambda^{\frac{3}{4}} = Constant = u = \frac{U_0}{\left(\frac{\sigma}{\rho}\right)^{\frac{1}{4}}\left(\frac{\nu}{\rho}\right)^{\frac{1}{8}} f^{\frac{3}{8}}} > 17\sim18 \tag{2.1}$$

Nevertheless, this criterion does not hold true for many cases, as the derived splashing threshold provides an explanation only for the corona splash but not for the prompt splash mechanism. Corona splash arises from the instabilities in the rim of the crown [28] and prompt splash arises at the contact line in the beginning of the spreading phase [30]. In addition, this correlation posed under an assumption of no interaction of droplets with the solid dry surface but rather with a thin liquid film; therefore, it may not be applied for droplet impingement directly on a dry surface.

Another major study in terms of the deposition-splashing process of a droplet impinging on a flat surface was done by Mundo et al. [29]. They formulated an empirical model for deposition and splashing regimes, using the train of monodispersed droplets by varying liquid properties, droplet diameter, and impingement angle. A deposition-splashing criterion as a function of *Oh* and *Re* of the impinging droplet was derived as $K = OhRe^{1.25}$ = 57.7. This splashing threshold was based upon the energy conservation of the impinging droplet, in which the pre-impact kinetic energy and surface energy of the droplet were conserved into the surface energy of droplet spreading and viscous dissipation. Further, the spreading factor and dynamic contact angle were considered as constant properties for any given liquid and solid in the deposition-splashing process. However, in the current study, both the spreading factor and contact angle vary with the impinging droplet *We* during the droplet impinging on the plate.

2.1.2 Detailed study of droplet impingement on a solid surface

2.1.2.1 Droplet impingement on a solid surface at the isothermal condition

Although most experimental study of droplet impinging on an isothermal surface described above has been studied for a long time, the computational study began long after. Foote [31] simulated liquid droplet behavior by using a new technique. The computing method is based on an extension of the Marker-and-Cell (MAC) method, and considers the effects of surface tension. He reviewed the theory related to the droplet oscillation problem and discussed the predicted characteristics of the large amplitude oscillation. His numerical prediction for small amplitude oscillations agreed well with the theory. Trapaga and Szekely [32] developed a mathematical representation and simulated the spreading of droplets impacting onto a solid substrate at the isothermal condition by using VOF method. They found that the spreading times were of the order of microseconds when droplet sizes in the 100 μm range and droplet velocities in the 100 m/s range. Fukai et al. [33] numerically studied the deformation of a spherical liquid droplet impinging on a flat surface by using two liquids water and liquid tin. In their work, surface tension during the spreading process was considered. They solved a set of finite element equations built on a theoretical model to accurately simulate the large deformations and characterize the spreading process. The effects of impact velocity, droplet diameter, surface tension, and material properties on the fluid dynamics of the deforming droplet were studied. The results showed that the numerical simulations successfully predict the occurrence of droplet recoiling and mass accumulation around the splat periphery. Bussmann et al. [34] developed a 3-D model based on VOF method to study a water droplet impact onto asymmetric surface. During the numerical work, surface tension is modeled as a volume force acting on fluid near the surface and contact angles are applied as a boundary condition at the contact line. They compared the simulation results with the experimental photographs and the good agreement was shown. A 3-D numerical investigation of a droplet impinging normally onto a wall film was presented by Nikolopoulos et al. [35]. The finite volume solution of the Navier–Stokes equations was coupled with VOF method and an adaptive local grid refinement technique for tracking more accurately the liquid–

gas interface was utilized. Their results were comparable with the available experimental data for the lamella temporal development. They also found the correlations between *We* and diameter and number of secondary droplets formed after droplet interacting with the surface.

2.1.2.2 Droplet impingement on a hot solid surface

Surface temperature introduces further complexity to the analysis of droplet-surface impingement phenomena due to the droplet evaporation and heat transfer between solid-liquid and solid-surrounding gas. In general, four different heat transfer regimes as depicted Figure 2.2 in (top) are identified when a droplet deposited on a hot surface [36-38].

I) When the wall temperature is lower than the droplet saturation temperature ($T_w < T_{Sat}$), the droplet evaporation is primarily driven by the vapor diffusion and the heat transfer occurs by the conduction and free convection. This regime is known as the natural convection.

II) When the wall temperature is larger than the droplet saturation temperature, but below the critical heat flux temperature ($T_{Sat} < T_w < T_{CHF}$), the droplet evaporation mainly driven by the heat transfer from the hot surface to the droplet falls into nucleate boiling regime. The vapor bubbles form near the hot surface in this regime and the buoyancy moves the vapor bubbles towards to the liquid-surrounding gas interface. The vaporization removes the heat, and the droplet reaches the maximum evaporation rate and heat reaches a maximum value at T_{CHF} [39].

III) When the wall temperature is above the critical heat flux temperature but below the Leidenfrost temperature ($T_{CHF} < T_w < T_{Leidenfrost}$), the droplet evaporation enters the transition boiling regime. An insulating vapor layer forms at the solid-liquid interface with the increase of the vaporization rate. The heat flux reduces to a local minimum value when the Leidenfrost temperature achieves [40].

IV) When the wall temperature is larger than the Leidenfrost temperature ($T_w > T_{Leidenfrost}$), the film boiling regime occurs. In this regime, a thin vapor film forms and prevents the physical contact between droplet and the wall. The heat transfer is dominated by conduction initially but radiation starts to take a significant role at higher temperature. Afterwards, the heat flux to the droplet slightly decreases.

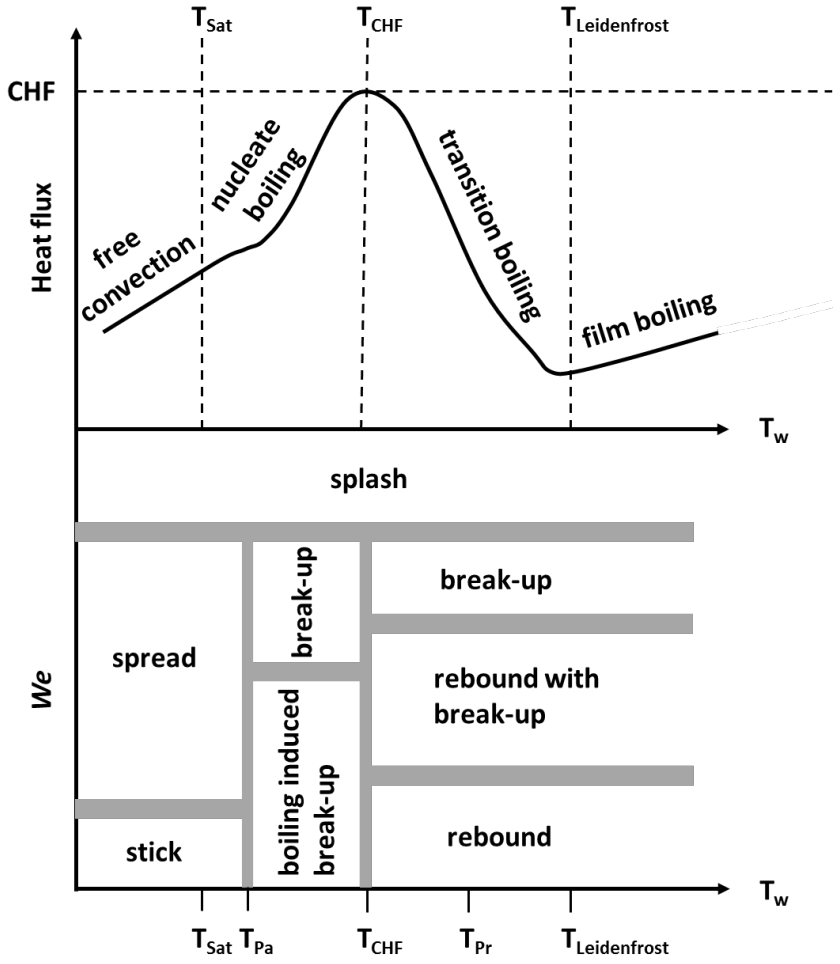

Figure 2.2: General boiling curve and associated boiling regimes (top); the impingement regimes and transition conditions when a droplet impinges on a hot surface (bottom). T_{Pa} is the pure adhesion temperature, below which adhesion happens at low impact energy, and T_{Pr} is the pure rebound temperature, above which bounce happens at low impact energy.

Furthermore, the impingement outcomes become complicated when a single droplet impacts onto a heated surface. The various phenomena as observed at the cold impingement must be re-considered within each boiling regime. Figure 2.1 covers a relatively complete impingement outcomes at various surface conditions. Bai and Gosman [24] proposed a general representation of the interaction outcomes from the available experimental work, which provides a good qualitative description of the heat induced phenomena, as shown in Figure 2.2 (bottom). In this qualitative map, the impingement regimes are described along with the transition regions (shaded regions) in a 2-D space based on *We* and the surface temperature.

Additionally, Nguyen and Avedisian [41] numerically studied the film evaporation of a liquid droplet on a horizontal surface by two principal cases. One case is that the horizontal surface is maintained at a constant temperature, another is that the surface is insulated while the ambience is hot. They found that the total droplet evaporation time decreased with the increase in temperature of isothermal wall or increase of ambient temperature in the insulated surface case. Besides, the droplet significantly moved away from the surface when it evaporates. Pasandideh-Fard et al. [42] experimentally and numerically studied tin droplets impacting on a flat stainless steel plate. The stainless steel surface temperature was varied from 25 to 240°C. The droplet impingement process was recorded by photographs during the experiment, the evolution of droplet spreading diameter and contact angle were measured from the images. The measured contact angle was used as one of the boundary conditions for the numerical model. Their numerical work was based on a modified SOLA-VOF method coupled with the Navier-Stokes and energy equations to model tin droplet deformation and the heat transfer between the droplet and the substrate. The simulated correctly predicted the droplet impacting process by comparing the droplet impingement images with the experimental results. Harvie et al. [43] simulated an axisymmetric volatile liquid droplet impinging on a hot solid surface in the film boiling regime by using VOF method coupled with a 1-D algorithm. The model solved heat transfer within the solid, liquid and gas phases, and a kinetic theory treatment was applied to describe the non-equilibrium conditions at the vapor layer boundaries. The model was

validated with the documented actual droplet impacts. Nikolopoulas et al. [44] did a numerical investigation of the evaporation of n-heptane and water droplets impingement upon a hot surface. Three different surface temperatures were employed to cover flow regimes below and above Leidenfrost temperature. VOF method was used to simulate flow hydrodynamics and vapor phase and an evaporation model was used to calculate mass transfer during phase change. They found that the simulated results matched well with the published experimental data with respect to the impingement outcome and the droplet shape during the impingement process. The simulations also provided the additional information such as the droplet evaporation rate and the temperature and vapor concentration fields. Mahulkar et al. [45] used VOF method with geometric reconstruction scheme to build the regime maps of hydrocarbon droplet impingement on a heated wall. The simulation results aided in constructing the regime maps for single-component droplets with a diameter of 50 and 100 μm and the built regime maps were validated by comparing with these in literature. They concluded that the impingement outcomes of stick, splash, rebound and breakup are well predicted with CFD simulations for single and multi-component liquids with different size. They also derived the improved correlations based on energy balances for regime transitions and post-impingement behavior of droplet-wall interaction.

2.1.3 Post-impingement characterization

In addition to the study on droplet-wall interaction outcomes and droplet deposition splashing criterion, post-impingement parameters which define liquid-solid interaction such as surface wettability also govern the wall-film formation and dynamics. After the droplet impinges on a flat plate, wall surface wettability is a significant factor in deciding the complete impact and deformation process. The surface wettability has an influence on the maximum wetting wall-film area and determines whether the impinged droplets in a spray undergoes coalescence to form a continuous film on the wall or not. Therefore, it is important to qualitatively and quantitively study the factors that affect surface wettability. One of the factors that characterizes the surface wettability is the liquid solid contact angle formed at the solid-liquid-surrounding gas three-phase contact line [46]. The contact angle

formed between the liquid-gas and liquid-solid interface dramatically depends on the flow at three-phase contact line and the corresponding stresses acting on it. The final shape of the deposited droplet is determined by equilibrium contact angle and the maximum spreading of the droplet is significantly influenced by dynamic contact angle [47]. The contact angle formed at a moving contact line is called the dynamic contact angle which is usually required as a boundary condition for modeling in capillary hydrodynamics, including certain stages of the drop impact problem [48]. Dynamic contact angle is appreciably related to the contact line velocity. However, the static equilibrium contact angle as per the Young's equation [49] is only a function of surface tension at liquid-gas-solid interfaces. To account for dynamic contact angle variations during droplet impingement, advancing, receding and equilibrium are differentiated by the motion at the three-phase contact line, therefore, corresponding to the occurrence of dynamic advancing and receding and the static equilibrium contact angles. On the strength of the experiment, there are various dynamic contact angle models implemented in CFD codes to help predict the underlying physical mechanisms of droplet-wall interaction [50].

Further, the flow at three-phase contact line and the contact angle at the moving contact line influence the spreading rate [51]. The dynamic of spreading is considerably characterized into four regions by the impinging droplet *We* and *Oh,* as reported by Schiaffino et al.[52]. The spreading regime map is shown in Figure 5.3. *We* measures the driving force for droplet spreading and *Oh* scales the force to resist the spreading. Four regions are described as: inviscid-impact driven (at low *Oh*, high *We*); inviscid-capillarity driven (at low *Oh*, low *We*); highly viscous-capillarity driven (at high *Oh*, low *We*); highly viscous-impact driven (at high *Oh*, high *We*).

2.2 Droplet-to-droplet collision

2.2.1 Droplet-to-droplet collision mechanism overview

Although the single droplet impacting on a solid surface provides an understanding of the fundamental mechanisms, interactions occur between drops with different diameters, impact velocities and directions are quite different in terms of the impingement outcomes

of splash and rebound observed at the impact of single droplet. As well, to construct a spray, droplet-to-droplet collision is essential part.

Experimental and theoretical studies have been implemented to explore the underlying mechanisms of droplets collision. The earliest dealings [53] with the collision process were with small rain droplets bouncing upon collision and the phenomenon of collision between small droplets with a larger pool of water. These studies helped researchers understand the mechanisms about the raindrop development. Droplet collisions were also performed to illustrate that the collision angle and *We* influence on coalescence [54-56]. Qian and Law [57] found that there are four outcomes of droplets collision: 1) "bounce" which means two droplets bounce back after hitting each other; 2) "coalescence" which shows that two droplets combine together when they encounter; 3) "reflexive separation" which refers to two droplets impinging close to head-on collision and then flatten and stretch into a long chain; and 4) "stretching separation" which states that a series of small droplets form when the two droplets collide in the shape of liquid-chain, see Figure 2.3. In general, there are three controlling parameters which significantly influence the above-mentioned four outcomes, as shown in Figure 2.4. They are *We*, which is defined as the ratio of the kinetic energy on impact to the surface energy; Impact parameter is the dimensionless distance as $2B/(D_1 + D_2)$, B is perpendicular distance between the path of a drop and the center of the field created by the other drop, D_1 and D_2 are droplet diameters [57, 58]; and droplet diameter ratio.

Bouncing can be explained as when two drops collide, a gas film between them is formed, and the pressure increases inside this gap. If the collisional kinetic energy [59] is not enough to overcome this pressure force to remove the gap film, two drops do not coalesce but bounce back from each other. When *We* is low or impact parameter is not large enough, then the collision kinetic energy is lower; the two drops will touch each other and combine into a single larger drop. This is referred to as coalescence. Furthermore, the reflexive separation happens under medium *We* and low impact parameter with the surplus collision kinetic energy, in which the two drops engage in a near head-on collision, flatten, and then

retract to form a long cylinder-like water globule. The two drops impinge and then stretch into a long chain of adjacent drops, which is called stretching separation.

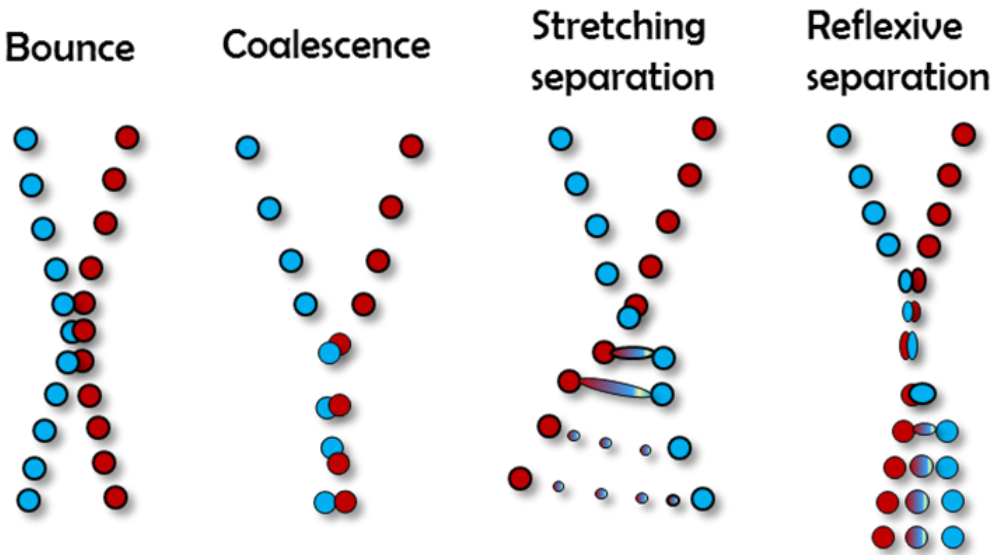

Figure 2.3: Four different classifications of collision model.

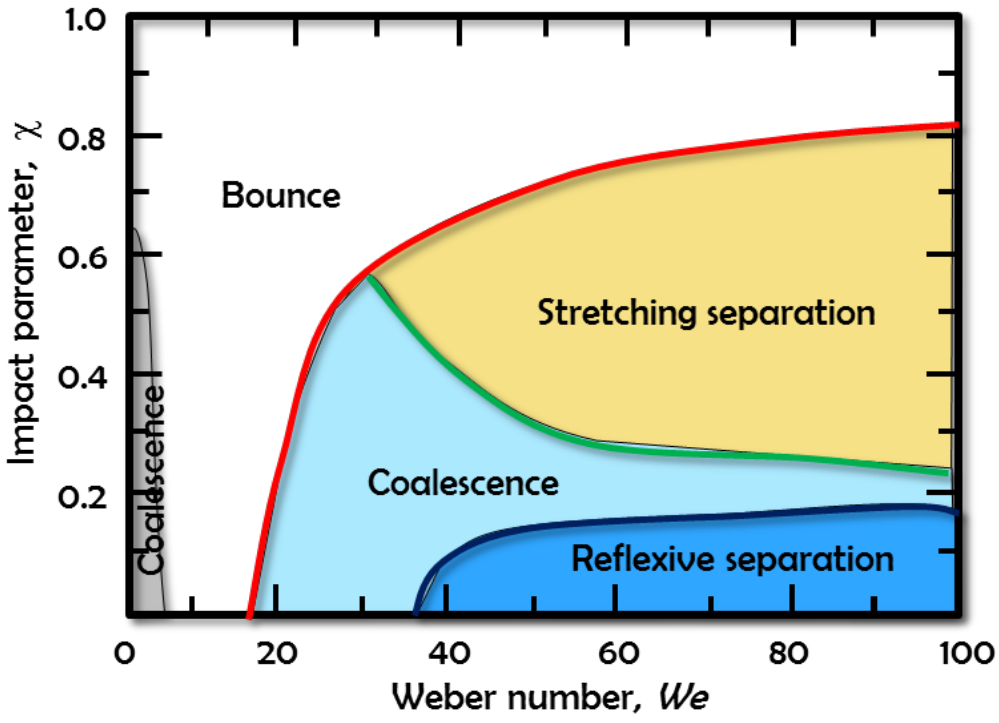

Figure 2.4: Different classifications of collision model with Impact parameter and *We* contour.

2.2.2 Detailed study of droplet-to-droplet collision

Ashgriz and Givi [60] conducted an experimental study on the collision dynamics of two burning and non-burning n-haxane fuel droplets. The effect of the high temperature combustion environment like IC engine condition on the dynamics of the collision was accessed. Their results indicated that the collision type moves toward higher energy collision when *We* increases, while various types of collision occurred for the same *We*. They also found that with the range of *We* studied, the collision type of bouncing, grazing, or coalescence depends on the local value of the impact parameter for the non-burning droplets. However, only coalescence was observed in the same *We* range for the burning droplets. Subsequently, Jiang et al. [61] experimentally investigated the collision dynamics of the equal-sized water and normal-alkane droplets with the 150 μm radius range. They observed that the behavior of hydrocarbon droplets is considerably more complex than that of water droplets at the same conditions. For instance, permanent coalescence always happened in water droplets, but the collision outcome is non-monotonic for the hydrocarbon droplets at head-on collisions. As the droplet *We* increases, the collision led to coalescence, bouncing, and coalescence with separation. The similar conclusion was also drawn at off-center collisions.

A numerical study of binary droplets collision by level set method has been conducted by Pan and Suga [62]. The incompressible Navier-Stokes equations coupled with the convective equation of the level set function to capture the interface between the liquid and the gas phases was solved. The simulation results agreed with the available experiments by Ashgriz and Poo [63] for the water droplets collision consequences. The simulations results on hydrocarbon droplets were compared with the time-resolved images of the collision processes obtained by Qian and Law [57]. Based on the detailed time-resolved dynamic simulation results, the mechanism of satellite droplet formation for head-on and stretching separation collisions was also studied. It was concluded that the main reason for satellite droplet formation in head on collisions was end pinching, whereas the twisting and stretching were the dominating factors in off-axis collisions. Li and Fritsching [64] numerically carried out the binary droplet collisions using VOF method along with ghost

cell method to simulate bouncing and retarded coalescence in head-on collisions. Five regimes of binary droplet collision including coalescence with minor deformation, bouncing, coalescence with major deformation, reflexive separation, and stretching separation were covered by the simulations. The achievable experimental data was used to validate the simulation results, and the detailed analysis of inter droplet pressure was accessed. Saroka et al. [65] presented the 3-D numerical simulations of drop collisions in an inert environment using VOF method. The equal size of three different liquid fuel (water, mercury and tetradecane) droplets with head-on collisions was studied. The droplet diameter was varied from 5 mm to 200 mm. The results revealed that tetradecane droplets did not lead to the separation for the range of *We*s but a separation criterion was found at for mercury and water droplets with the lower critical *We*.

2.3 Multi-droplet impingement

Despite the fact that single droplet impingement and droplet-to-droplet collision are the fundamental aspect of spray impingement and are widely researched, the results of these studies cannot be directly extrapolated to reach an accurate understanding of spray impingement on a solid surface and multiple spray-to-spray interaction. Multi-droplet impingement comprised of droplets-surface impact and droplets-to-droplets interaction is essential to be studied. The single and mono-sized droplet train impingement on surfaces subject to the constant heat flux conditions were studied by Soriano et al. [66] to obtain the experimental characterization. In the experiment, Laser Induced Fluorescence (LIF) technique with a focus on the droplets impingement region was applied to characterize the film morphology by measuring film thickness and film wetted area. The surface temperature at the liquid-solid interface was also measured by Infrared thermography. The effects of the droplet frequency, fluid flow rate, and droplets temperature on the surface temperature were examined. The results showed that the higher heat flux was caused by multiple droplets with higher fluid flow rate. Lewis et al. [67] compared the impingement heat transfer of a droplet train and the free surface jets on a heated and wetted surface using the VOF method in OpenFOAM. They concluded that droplet train showed the noticeable temporal variations compared with the impinging jets, which was because the nature of

continuous droplet impacts affected the impingement region and an unsteady cooling and heating of the fluid near the wall was increased. On the contrary, the film and the corresponding free surface are nearly steady with small perturbations for the jet.

2.4 Spray-wall impingement at engine operating conditions

2.4.1 Experimental work on non-reacting spray-wall impingement

With the increase in efforts towards development of cleaner technologies, advanced fuel injections strategies are being implemented in IC engines [68, 69]. Spray-wall interaction governs the fuel-oxidizer mixture formation in both port fuel injection (PFI) as well as direct injection (DI) equipped engines. Spray impingement on wall has a huge effect on engine emissions and performance. In PFI Spark Ignited (SI) engines, some of the fuel does not vaporize completely in the port and is deposited on the walls of the combustion chamber, where it can escape combustion. This behavior that occurs predominantly under cold-start and warm-up conditions is generally referred to as wall-wetting [70]. Therefore, wall-wetting is a concern for PFI engines. As well, in DI engines, formation of a wall film on the piston surface is highly probable, causing higher emissions during cold start [27, 71-73]. Fuel-wall wetting has been shown to significantly affect the mixture formation and combustion for low temperature combustion concepts such as Premixed Charge Compression Ignition and Reactivity Controlled Compression Ignition (PCCI/RCCI) [74] engines with poor efficiency and increased pollutant emissions. Therefore, spray-wall interactions and fuel film formation and evaporation have been shown to play an important role in engine combustion processes.

The techniques for measuring details of spray-wall interaction and the resultant droplet sizes and wall-film characteristics have been carried out since the inception of the engines. However, with engine studies limited to the visualization access and unclear boundary conditions, much of the work on spray-wall interaction took support from atmospheric or constant volume chamber measurements. One of the early work from Akop et al. [75, 76] performed a series of studies on fuel impingement on a plate under atmospheric pressure conditions. In ref. [75], they performed the high-speed shadowgraphy and a mass

measurement scale was used to weight the impingement fuel mass to begin the experimental campaign. Later the influence of plate angle and area was explored with a mass measurement scale which was used to weigh the film. Subsequently, high speed images were also taken capturing the entire injection event [76]. Further studies have been performed to measure *We* and SMD of the impinging droplets using empirical relations and combining with film mass measurements [77]. A correlation with ambient pressure variation was later derived and *We* correlations were subsequently revisited [78]. Since the spray impinging on the wall causes surface cooling, the temperature of the wall can be taken as an index to measure how much the temperature drops down along with getting an estimate of the film spread. This can be done with an infrared camera. One such study was performed in a recent work by Schulz et al. [79] where along with measuring the film area and temperature on the plate, a Phase Doppler Anemometry (PDA) system was used to measure the droplet size combined with high speed shadowgraphy to visualize the spray development.

Montanaro et al. [80] experimentally studied the effects of wall temperature and injection pressure on atomization and vaporization of impinging spray on a heated surface by using a single-hole gasoline direct injection (GDI) injector in a quiescent vessel. They used Mie-scattering and schlieren diagnostics to simultaneously predict the liquid and vapor of spray and measured the liquid and vapor width penetration and thickness growth after spray impinging on the wall. In ref. [80], the liquid width is defined as the maximum radial elongation of an intact liquid core coming from the nozzle and flowing along the surface of the wall. The maximum height of the liquid on the plate is defined as liquid thickness. The liquid core is surrounded by an area composed of fuel vapor mixed with liquid ligaments, where the vapor phase is considered and the vapor width and vapor thickness are defined as the similar way with liquid width and thickness. The authors found that the liquid and vapor width penetrations increase proportionally with respect to the increasing of the wall temperature at the fixed injection pressure, and the liquid and vapor thicknesses increase with time but no proportional correlation with the wall temperature; they also concluded that at the fixed wall temperature of 573 K, the effect of the injection pressure

highlighted a linear increasing of the liquid and vapor width vs. time and showed a proportional increasing with respect to the increasing of injection pressure, and the liquid and vapor thicknesses were directly proportional to the injection pressure with a conduct tending to a saturation at longer time. Yu et al. [81, 82] carried out an experimental work on spray-wall impingement evaluating several injection strategies, by using different fuels including n-butanol, diesel, dimethyl ether (DME) and gasoline. Their results indicated that the impingement spray radius and wall film formation are significantly affected by impingement momentum and air entrainment when varying the injection pressure or impingement distance, whereas the viscosity and surface tension have a great impact on the impingement spray height.

2.4.2 Experimental work on reacting spray-wall impingement

Some researchers also studied the spray combustion after the liquid fuel impingement on the wall. Li et al. [83] studied the effects of spray-wall interaction on diesel combustion and soot formation in a constant volume combustion vessel. A two-dimensional piston cavity was used to generate the impinging spray flame. The distance from the single-hole nozzle (hole diameter is 133 μm) tip to the impinging point is 30 mm and 13.5^{o} angle between the injector axis and the flat wall. Three different injection pressures from 100 MPa to 200 MPa were employed. In their experiment, the color luminosity were adopted to analyze the flame structure and combustion process. Soot emission and temperature distribution were calculated based on the two-color pyrometry. They concluded that the soot mass caused by impinging spray flame was higher than that from the free spray flame. The higher soot concentration was found in the head vortex region while it was observed close to the flame tip at the free spray flame. The soot level from impinging and free spray flames was not obvious when the injection pressure was increased up to 200 MPa. The same group continued studying the spray-wall impingement to characterize the diesel combustion behaviors in a constant-volume vessel [84]. The same injector was installed perpendicularly to the flat wall and the same injection pressures were applied. Mie scattering was applied to observe the spray formation and OH* chemiluminescence and natural color luminosity were adopted to analyze the combustion process. Their results

showed that the diesel combustion deteriorated caused by the spray-wall impingement, while combustion was enhanced as long as an appropriate impinging distance between the injector tip and the flat wall was selected. They also found that the soot formation decreases with the increase of injection pressure, and the combustion is not linearly improved as the injection pressure raises. To achieve optical access to the combustion chamber and the fuel injection event, Borthwich and Farrell [85] modified a single cylinder diesel engine from a multi-cylinder commercial service engine. The effects of chamber gas density, chamber temperature, injection pressure, engine RPM, and injection duration on spray penetration, spreading angle, and velocity, as well as combustion characteristics were studied. The results showed that at the fixed volume chamber, as the gas density or the chamber temperature increases, the spray liquid penetration, spreading angle, and spray velocity reduce; as the fuel injection pressure increases, the spray penetration decreases but the spreading angle and penetration velocity increase; the change of fuel injection duration showed insignificant effect on the spray properties; and the spray impinging on the wall occurred at lower chamber densities and engine speeds.

2.4.3 Experimental work on spray-wall film formation

To investigate the wall-film formation, laser based technique is one of the quantified film thickness measurements. For instance, laser reflection method was used by Saito et al. [86] to explore the behavior of adhered fuel film on a wall during a small size DI diesel or gasoline engine development. They observed that more than 50% injected fuel mass was adhered to the plate. They found that the film thickness of the adhered fuel was found to be 10 μm to 50 μm; and the fuel film area on the wall is strongly affected by the wall temperature. Senda et al. [87] investigated the effects of wall films arising from spray-wall interactions in the SI engine port fuel injection where a 355 nm LIF technique was employed to measure the film thickness of a spray impinging on a glass plate in a constant volume combustion vessel. In their experiments, iso-octane mixed with biacetyl was injected against the impinged surface at the ambient pressure and temperature. The results showed that ratio of the adhered fuel to the total injected fuel is about 40% at 10 ms after the end of injection and this ratio does not change with the injection duration. Later, LIF

technique was employed by Lindgren et al. [88] in an open atmospheric condition along with a photomultiplier tube to detect light from Mie scattering of droplets in an effort to obtain a wall film thickness measuring device. Due to the highly turbulent nature of the engine in-cylinder flow field, efforts were made to replicate this and check if the cross flows have an effect on the spray-wall interaction. One such study was performed by Panao et al. [89] using Argon-Ion laser combined with a schlieren setup. The physics of impingement was sought and thickness of vapor layer (on a plate) was obtained. The use of PDA to measure spray droplet sizes has been long in use in various applications of sprays. It has been used by Lindgren et al. [27] to investigate the effect of wall characteristics on a gasoline spray after impingement from a wall. Argon-Ion laser was used for LIF to measure the film thickness and high-speed image for spray visualization was obtained coupled with PDA measurements for post-impingement droplet distribution measurements. Cheng et al. [90] studied the effects of the injection duration, impingement distance and impingement angle on the fuel film thickness, fuel film length and fuel film area. The film thickness on the wall was also measured by using LIF technique and iso-octane mixed with 3-pentanone was injected against the impinged wall. Their results showed that the film area and the film thickness increase as the injection duration enlarges and the impingement distance reduces. The impingement angle reduction results in the increase of film area but the thinner film thickness.

Some other non-intrusive diagnostics were also used for the film property measurement. Ko et al. [91] studied the diesel fuel spray impingement on a vertical flat wall in a high-pressure chamber by full field optical imaging technique. They found that the ratio of adhered fuel to total injected quantity is more than 40% in cases of wall distances of 30, 50, and 70 mm; the film thickness was measured in the range of 10 ~ 30 μm. These results are very similar to Saito et al. [86] and Senda et al. [87]'s findings. In addition, the adhered fuel ratio decreases significantly as wall distance becomes shorter; the film thickness also becomes thinner. The total internal reflection method using a roughened Plexiglas surface was used by Mathews et al. [92] to analyze the film thickness. The film thickness was observed in a similar range of 16 ~ 42 μm.

Unlike the laser based techniques that are usually expensive and complex in signal calibrations, there is a non-intrusive simple optical technique called the Refractive Index Matching (RIM). In current study, RIM is used to characterize the film formation after the n-heptane spray impingement on a roughened surface. RIM method was first provided in details by Drake et al. [72] to quantitative time and space resolved measurements of fuel film mass on a roughened quartz piston window of an optically-accessible DI engine. Yang et al. [93] measured diesel film thickness by spray impingement in a chamber at low temperature diesel combustion conditions using RIM technique. They concluded that the ambient temperature shows a dominating effect on the fuel film volume and the fuel film thickness, the effect of ambient density is secondary, and the nozzle diameter is found no significant influence on film properties. Moreover, the film radius increase as the ambient temperature reduces and the fuel film is circular in shape with a constant thickness in the inner zone. Maligne et al. [94] also used the RIM technique to characterize the fuel film thickness during spray impingement in a high pressure high temperature chamber. They used a mixture of fuels instead of a single component fuel as a calibration fluid (10% dodecane (heavier compound) and 90% isooctane (volatile) by volume) to calibrate the film thickness, which can obtain the calibration results of thin film. They also qualitatively compared the RIM fuel film images with those taken by LIF method. The results indicated that the RIM images were consistent with the LIF images with respect to film structure. The results also showed that the fuel film thickness highly depends on the ambient temperature, but is insignificantly affected by the ambient density, which is consistent with the findings from ref. [93]. The injection pressure and the injection duration were found to have an important effect. Zheng et al. [95] used the same fuel mixture as Maligne et al. [94] to measure the film properties based on RIM method. They also did a numerical study on spray behavior and film characteristics analysis. The simulation results agree generally with the experimental observations in terms of spray and fuel film shape and the film thickness. However, the predicted film mass is greater than the RIM results possibly due to the large surface roughness. One of the shortcomings using mixture for film thickness calibration is that the film thickness might be underestimated since the volatile fuel may dissolve into the heavier compound. Therefore, the present work used two different ranges

of mixture to finalize the calibration and find out the calibration curve based on variation of scattered light intensity and the film thickness.

2.4.4 Numerical spray-wall interaction model development

The experimental studies mentioned above laid the foundations of droplet-wall and spray-wall interaction study. A number of numerical models for the dynamics and vaporization of the liquid wall film in IC engines were then developed to help further understand the wall-film formation and characteristics, as well as predict the engine performance [96].

Naber and Reitz [97] firstly developed a relevant model used in multidimensional engine simulations, where they proposed three different outcomes of a droplet impingement on the wall, depending on the incident droplet *We*. The three outcomes are stick (drops adhere to the wall), reflect (drops rebound) and jet (drops slide along the wall); however, this model does not consider all the possible outcomes of droplet-wall interaction such as splash. Splashing is an important factor since it affects the atomization and vaporization in the vicinity of the wall, and the wall-film formation [98]. Additionally, the surface conditions (wet/dry surface and surface roughness) can widely contribute in varying the results of a droplet/spray-wall interaction. Bai and Gosman [24] predicted the outcomes of spray impinging on both wet and dry walls through gasoline spray droplet impingement simulations. Their model covered all of impingement regimes and they found that these processes are strong function of the incident droplet *We*. The calculated wall spray characteristics also showed favorable agreement with the experimental results. Stanton et al. [71] developed a fuel film model in KIVA-II code and showed the same impingement regimes for a droplet impinging on a thin liquid film. Their criterion showed that when a low impact energy droplet ($We < 5$) impinges on a thin liquid film, it tends to stick. As the impact energy increases, $5 < We < 10$, the air layer between drop and surface causes low energy loss, and droplet tends to rebound. Further increase in impact energy ($10 < We < 18^2 D_0 (\frac{\rho}{\sigma})^{1/2} \nu^{1/4} f^{3/4}$, where D_0 is droplet diameter, ρ, σ, ν and f are the drop density, surface tension, kinematic viscosity, and frequency) droplet tends to spread and droplet with higher impact energy ($We > 18^2 D_0 (\frac{\rho}{\sigma})^{1/2} \nu^{1/4} f^{3/4}$) splashes and produces secondary

droplets. The impingement regime developed by Stanton et al. [71] is widely used in many multidimensional engine models.

O'Rourke and Amsden [96, 99] proposed a most complete film particle tracking method and developed the spray-wall interaction model for the transport of vapor mass, momentum, and energy in the turbulent boundary layers above the film in KIVA-3V code. The spray-wall interaction model, especially for splashing regime and secondary droplet distributions, was derived and extrapolated based on the previous experimental work from Mundo et al. [29] and Yarin and Weiss [28]. The splash criteria in O'Rourke and Amsden model is shown in Equation (2.2), the droplet splashes after impinging on the wall when $E^2 > 3330$, where E is a splash Mach number based on the impact velocity and the capillary wave speed. In Equation (2.2), a boundary layer thickness δ_{bl} was introduced and replace of initial film thickness (h_0) when h_0 goes to 0.

$$E^2 = \frac{\rho_l U_0^2 D}{\sigma} \frac{1}{\min\left(\frac{h_0}{D_0}, 1\right) + \frac{\delta_{bl}}{D_0}} > 57.7^2 \tag{2.2}$$

where ρ_l is the liquid droplet density, σ is surface tension, U_0 is the impact velocity, D_0 is incident droplet diameter, h_0 is initial wall-film thickness, δ_{bl} is the boundary layer thickness as shown in $\delta_{bl} = \frac{D_0}{\sqrt{Re}}$, Re is the incident droplet Re.

O'Rourke and Amsden implemented their model to study droplets impinging on the cylinder walls to start the inception of the fuel film in an ad-hoc manner. Thorough validation of these droplet and film models are lacking due to the lack of high-fidelity experimental data.

After O'Rourke and Amsden's work, Han et al. [98, 100] extended and improved the impingement regimes splash criterion for both dry and wet surface including the surface

roughness effect. The authors provided a new splash threshold in consideration of the experimental and numerical studies from [28, 29, 71, 99] in Equation (2.3) as follows:

$$H_{cr} = \left(1 + 0.1Re^{0.5} \min\left(\frac{h_0}{D_0}, 0.5\right)\right)(1500 + \frac{650}{\beta^{0.42}}) \quad (2.3)$$

where Re is the incident droplet Re number, h_0 is initial wall-film thickness, β is dimensionless roughness parameter with respect to the incident droplet diameter.

When$WeRe^{0.5} > H_{cr}$, droplet impinging on wall tends to splash. Other regimes in Han et al. [98] follow the similar transition criteria for a wetted wall by Stanton et al.[71]. However, the splash threshold was mentioned in Han et al. [98] to be valid on the relatively smooth surfaces at which the initial film thickness should be much larger compared with the surface roughness.

Most recently, Ma et al. [101] numerically studied spray/wall impingement based on droplet impact phenomenon. They summarized the previous experimental work from many researchers [102-105] based on incident *Re* and *Oh*. They found a splash criterion line of $OhRe = 17$ for those experimental data. Despite this, there still showed un-sharp criterion for droplet splash at high *Re* region (more than 4000) and a clear splash criterion shown in low and medium *Re* range. In the current study, we will describe more details on the splash criterion by Ma et al. [101] in Chapter 6.

2.4.5 Application of numerical models to spray-wall interaction

The spray-wall interaction models have been extensively applied in accurately simulating engine combustion processes by many researchers. Multi-dimensional modelling of thin liquid film and spray-wall interaction arising from impinging sprays was conducted by Stanton et al. [71, 106]. They assumed a 2-D film flowing on a 3-D surface and the wall-film interaction within the stick, rebound, spread, and splash regimes. This was achieved by solving the momentum, energy and continuity equations for the 2-D film. Their results displayed a good agreement with the experimental data for film height, spreading radius and the amount of fuel that adhered on the surface. The model also predicted the drop size

and the velocity trends correctly over majority of injection periods. Montorsi et al. [107] studied diesel spray impinging on the cylinder wall in the case of split injection, using simulations on STAR-CD, KIVA-3V framework to verify their results with experimental data. They concluded that the spray-wall interactions are sensitive to the ambient pressure and wall temperature and therefore influence the heat-release rate and emission formation. In their subsequent work [108], they found that the heat transfer rate is strongly affected by film thickness, the wall film thickness is directly influenced by the wall temperature variation in non-evaporating cases during the entire injection duration. As well, in evaporating cases, the film thickness is affected by the wall temperature only during the first injection period, whereas the second injection has no effect on the film thickness. Habchi et al. [109] employed an Eulerian-Lagrangian method until the spray hits the piston wall to study the effect of piston temperature on mixture preparation under stratified charge operating conditions in a DI gasoline engine. As the droplets interact with the wall and form a film, this liquid film mass is tracked in a Volume of Fluid (VOF) framework. The main film formation affecting physical mechanisms depends on the impingement wall conditions on a dry surface.

Zhang et al. [110] developed a new sub-model for spray-wall interaction under engine conditions. This sub-model was improved by changing the momentum source term during spray impingement and avoided the excessive prediction of the momentum that is predicted by the O'Rourke and Amsden model [99]. With the application of their sub-model, the combustion and the film/wall heat flux characteristics were reproduced reasonably. The evaporation rate of fuel film is faster than the one O'Rourke and Amsden model predicts. Zhao et al. [69] [111] did both experimental and numerical studies of high pressure fuel spray impinging on a flat plate. The experimental work was carried out in a constant volume combustion vessel to characterize the properties of free and post-impingement sprays on a multi-hole diesel injector. The numerical study was based on a RANS methodology with the spray-wall interaction model from O'Rourke and Amsden [99] to investigate the global and local spray behaviors near the wall with a special focus on SMD and *Re* and *We*. In this study, the authors found that the droplet distribution information

near the wall is primarily driven by the droplet sizes and most of the mass in the same region is characterized by very low velocities. However, the current models are still not accurate enough to characterize the impinged height from the spray impingement. There have been attempts to depict the physics and develop a better spray-wall interaction model for diesel engine conditions.

In engine-spray applications, multi-component fuel droplet interaction with wall and film formation were performed using probability density function in the Eulerian-Lagrangian framework to capture the vaporization trends by Lippert et al. [112]. It was found that during cold start in diesel engine applications, varying spray impingement angle results in more secondary atomization (splashing) of the film after spray hits the film and enhances vaporization. Micro-scale analysis with a single droplet's normal impingement on a wetted-wall was performed to observe and correlate with the empirical 'splashing' equation results as done by Cole et al. [113]. They reported that the crown formation after droplet splash ejects the liquid and the subsequent crater collapse lacks the energy to overcome surface tension and ejects a droplet. As the film is thickened, the crown lacks the energy to eject fluid, but the subsequent fountain created by the collapse ejects the liquid. Such micro-scale studies were implemented in macroscale model of spray-wall interaction using the Eulerian-Lagrangian model. When the representative parcel hits the wall, the behavior is replicated based on the results of the microscale study. Low *We* cause the particles to stick, while high ones cause them to splash with more outbound reflected mass.

2.5 Multiple spray-to-spray collision

Collision processes take a notable role in the spray-to-spray interactions. Collision between two cylindrical liquid jets is one of the acknowledged configurations for atomizers used in many propulsion, energy-conversion, material processing, and chemical engineering systems [18, 114]. Multiple spray-to-spray collision is an efficient method for atomization and mixing. The impinged streams form a sheet after collision and the resultant sheet destabilizes, breaks, and disintegrates into a spray of droplets under the influence of

surface-tension, viscous, inertial, and aerodynamic forces. Thus, this process eventually leads to fragmentation of the injected liquid into ligaments and droplets [22].

Some work has been conducted in the past with a novel spray mechanism for the introduction of fuel into engines. This novel mechanism concerns colliding type sprays, with sprays emerging from a multi-hole nozzle, whose geometrical arrangement allows the sprays to collide with each other after exiting the nozzle orifice. A high-fidelity numerical framework has been developed and implemented to study the dynamics of the liquid sheets formed by two impinging jets by Chen et al. [19]. The work employs a three-dimensional VOF method with adaptive mesh refinement (AMR) based on Octree meshes. Detailed flow physics is explored and compared with experimental data over a wide range of *Re* and *We*. The temporal evolution and spatial development of the injected liquid, including the jet impingement, sheet formation and rupture, and atomization into ligaments and droplets, were examined in detail.

Various patterns of liquid sheet and rim formed by impinging jets were obtained by Chen et al. [115]. Detail flow-field was studied based on existing theoretical prediction. New insights were obtained to the flow-field near the stagnation point. It was shown that the impact wave is caused by the interfacial shear stress which forms the surface waves on the two sides of liquid sheet. The interaction of waves on the two sides forces the liquid sheet to resonate at natural frequency. The ratio of wavelength and jet diameter is independent to jet velocity, liquid viscosity and surface tension.

Ghasemi et. al. [116] studied the effect of incidence angle and nozzle separation distance on the collision of two merging sprays. They concluded that increasing nozzle separation distance leads to an increase in penetration length and SMD, however, reducing the spray cone angle results in reduction of spray tip penetration and SMD. Tsuru et al. [117] carried simulation and experimental work on NO_x reduction effects for a Direct Water Injection (DWI) system using a novel diesel droplet collision model which takes care of outcomes from the immiscible droplet collision. This model was a Lagrangian particle tracking based approach. They concluded that the water distribution and spray penetration length are

affected by the angles between the spray propagation; and spray propagation is in-turn affected by the air-entrainment. Ko et al. [58], worked on developing the O'Rourke and Amsden's model [99] by adding conservation equations between before and after collision. They validated the models and concluded that the velocities of droplets have a great degree of dependence on the impinging angle, and the droplet sizes depend on the impingement distance.

The above sections mentioned VOF and Lagrangian methods separately, however, there has been work done by combining VOF with Lagrangian methods to study spray characteristics of impinging jets. Bravo et al. [118] employed a novel VOF method coupled to a stochastic Lagrangian spray model to simulate the atomization process. This employs a sense of coupling of VOF and Lagrangian particle approach. They also studied mean stream wise velocity and volume fraction statistics which show the structure of the high-speed jet. And, the turbulent kinetic energy and volume fraction intensity profiles characterize the interfacial mixing processes. Besides, they compared with Reitz spray theory and available measurements of the near nozzle flow field and showed that the simulation captures the correct dispersion characteristics.

CHAPTER 3 EXPERIMENTAL FACILIT, TEST SETUP, AND MEHTODLOGY

3.1 Introduction

High-pressure and low-pressure spray and combustion experiments use two different fuel injections systems due to the difference of fuel properties. In this chapter, the fuel injection system for diesel and gasoline experiments including the fuel delivery system, injector driver, and specific injectors are firstly described. The rate of injection measurement is then introduced to meter fuel mass flow rate of injectors. Subsequently, an overview of combustion vessel (CV) is given and various optical diagnostics are explained to study the detailed diesel and gasoline spray and combustion process. Finally, image processing for qualitatively analyzing and quantitatively measuring the spray and combustion characteristics are discussed.

3.2 Fuel injection system overview

In current study, fuel injectors are electronically controlled solenoid activated injectors designed by Bosch. The injectors are driven by a custom driver developed by MTU. The driver is designed to generate a current profile simulating injector operating conditions.

3.2.1 High pressure fuel delivery system

The high-pressure fuel injection system used in the current study is capable of producing output fuel pressures from 41.4 MPa (6,000 psi) to 414 MPa (60,000 psi) which is higher than the upper limit in current production technology diesel engines and injectors. Figure 3.1 shows a photograph of the diesel fuel delivery system used in spray-wall impingement tests. Fuel is drawn from the tank into the air operated pump (Hydraulics International 5L-SD-600-N) by passing an accumulator. This air operated pump is used to boost fuel pressures to the desired output pressure and the output fuel pressure is controlled by regulation of the inlet air pressure. The high-pressure fuel is stored in another accumulator before releasing the high-pressure fuel line to the injector. The two accumulators used in

the fuel injection system have a 100 mL volume each to sustain a relative static injection pressure during the injection event; the pressure drop due to injection is approximately less than 1%. The injection pressure is measured using a Kistler 5010 piezo-electric dynamic pressure transducer coupled with a Kistler 5010B charge amplifier and a low pass filter with cutoff frequency of 60 kHz, which enables monitoring of the fuel pressure to verify that injection will occur at the desired pressure conditions.

Although only high-pressure fuel injection system was utilized during the spray-wall impingement test, the current system as shown in Figure 1 also works for low-pressure fuel delivery conditions such as gasoline spray and combustion tests. If the low pressure of 2.76 MPa (400 psi) to 82.7 MPa (12,000 psi) is desired, it switches to low-pressure line passing through a regulator. It would be always preferable to have regulator engaged before boost pump starts to work. The upper limit for low-pressure line is 82.7 MPa (12,000 psi).

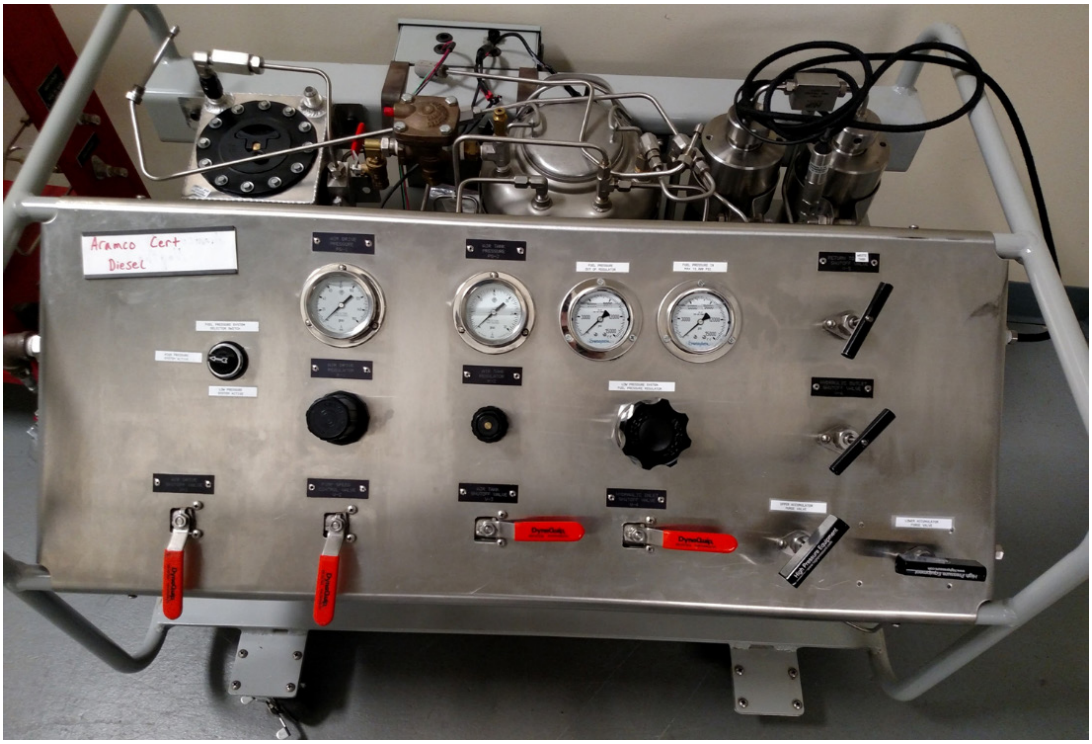

Figure 3.1: Fuel pressurization and delivery system.

3.2.2 Low pressure fuel delivery system

Before the fuel delivery system as discussed in Chapter 3.2.1, a low-pressure fuel system based on gasoline engine requirements was built in-house and utilized for multiple spray-to-spray collision tests.

Figure 3.2 shows a photograph of the low-pressure fuel delivery system which allows to control the fuel pressure up to 20 MPa (2900 psi). The fuel system is a high-pressure bladder type accumulator, which on one side is pressurized with nitrogen and with fuel on the other side. Fuel is drawn from the storage tank by connecting a suction pump with the nitrogen side of the bladder, then the suction pump is isolated by closing the vent valve and the bladder is pressurized with nitrogen to achieve the desired injection pressure [119].

Figure 3.2: Low pressure fuel delivery system.

3.2.3 Solenoid injector

The fuel injectors used in this study are electronically controlled solenoid activated injectors. For any tests, the injector is always placed in one of the windows on CV. The solenoid diesel injector comprises of the fuel supply line, the main needle, the fuel return line, the control needle, and the solenoid. When the high-pressure fuel enter the injector, pressure is equal throughout the injector. The solenoid is then energized, the control plunger is pulled upwards, which causes a small amount of fuel released from the fuel return line and a pressure differential is created, allowing the main needle to come off its seat. Finally, the fuel is injected into the chamber and the injector current is turned off. The control needle re-seats and the pressure above the main needle increases and pushes the nozzle closed. GDI injector works in a similar fashion. The only difference is that solenoid directly controls needle without any hydraulic actuation comparing to diesel injectors.

Figure 3.3 shows the solenoid injector used in the current study. Bosch 0445120042 diesel injector (left) was used in the spray-wall impingement test and Bosch 0261500 GDI injector (right) was used for the multiple spray-to-spray collision study.

Figure 3.3: Diesel (left) and GDI (right) injectors used in current study.

3.2.3.1 Off-center nozzle

In the spray-wall impingement test, a custom made single-hole nozzle is assembled with the diesel injector. As shown in Figure 3.4, the nozzle is characterized by a 200 μm diameter, a K factor of 0, an included angle of 120°, and the orifice orientation relative to the injector axis is 60°.

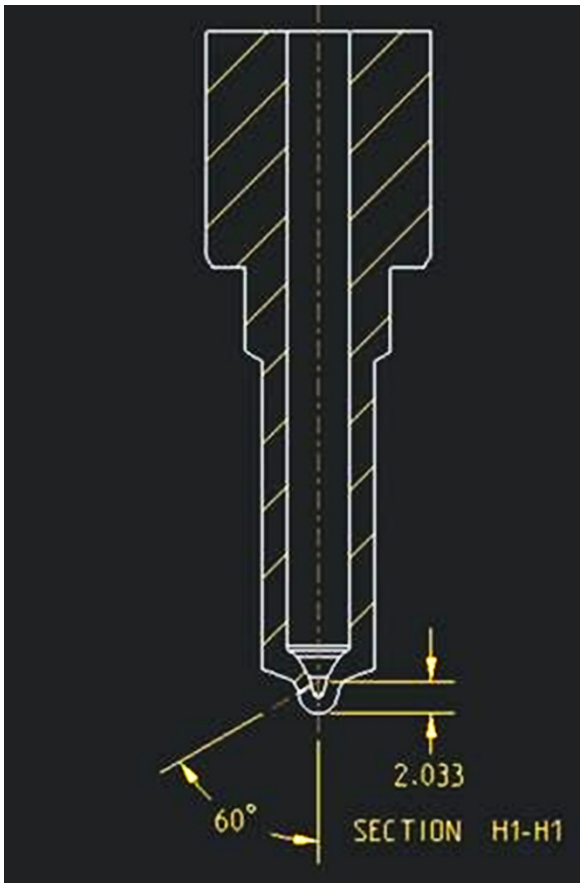

Figure 3.4: Schematic of single-hole nozzle used for spray-wall impingement test.

3.2.3.2. Colliding spray nozzle

In the multiple spray-to-spray collision study at the gasoline and diesel engine-like conditions, various colliding spray nozzles including 2-hole and 4-hole nozzles are used for the spray and combustion tests. The schematic of 4-hole colliding spray nozzles is shown in Figure 3.5. The colliding spray nozzles have the multiple inwardly opening nozzles which is different with the conventional outwardly opening nozzles. In the current work, 2-hole and 4-hole colliding spray nozzles have the nozzle diameter are 239 μm and 324 μm, respectively. The collision angle "Φ" which is defined as the angle between any two injecting sprays is 90º. The post collision angle (also known as the spray dispersion angle in the traditional outwardly opening nozzles) "θ" illustrates the angle of fuel spray after collision.

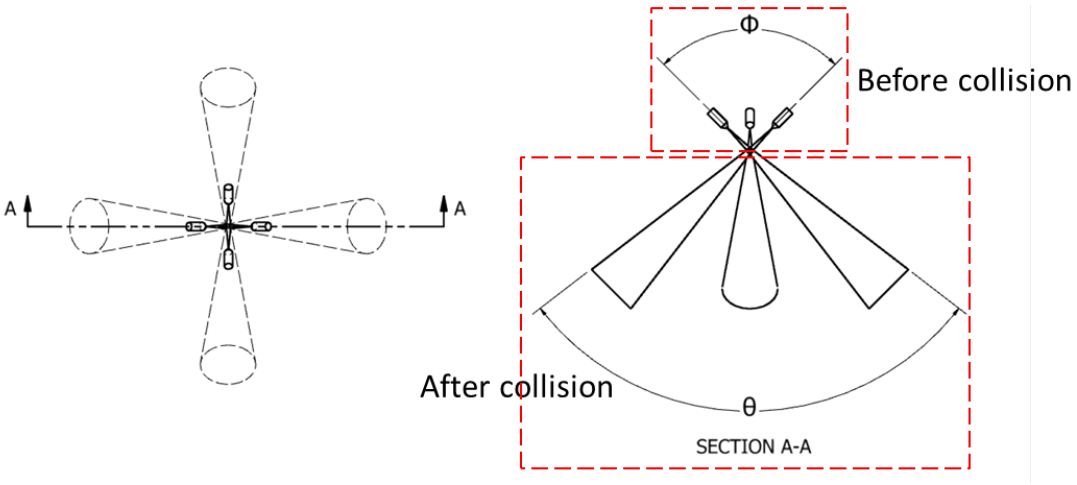

Figure 3.5: Schematic of 4-hole colliding spray nozzles.

3.3 Rate of injection measurement

3.3.1 Carbon Zapp mass flow rate measurement

The GDI injectors used in multiple spray-to-spray collision study were tested in a flow bench to measure the total injected mass at the given operating conditions. This flow bench is produced by Carbon Zapp GRU.4R model as shown in Figure 3.6. The bench can test 4 injectors simultaneously up to 850 bar rail pressure. It utilizes dynamic electronic mass measurement with an accuracy of 0.2% full scale (FS) and a repeatability of 0.05% [120].

In current study, 2-hole and 4-hole colliding spray injectors were tested at various operating conditions in this bench. The bench measured total volume of injected fuel over 1000 injections under given test conditions. Total injected mass is finally calculated based on total injected volume. The rate of injection (ROI) profile, as one of inputs in CFD simulations, is generated through CMT website [121] based on the measured injected mass combined with the operating conditions such as ambient pressure, injection pressure, injection duration, and nozzle diameter.

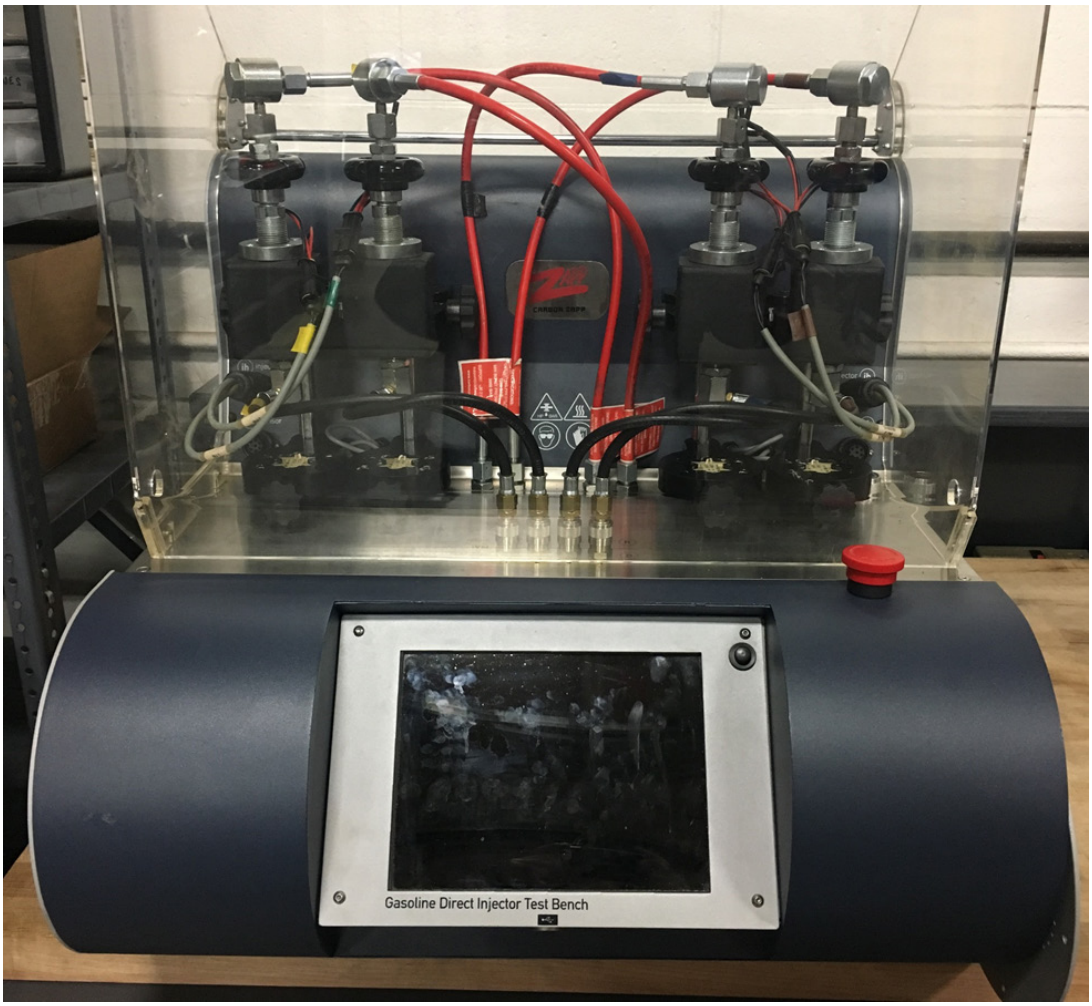

Figure 3.6: GRU.4R model.

3.3.2 Bosch ROI meter

In the spray-wall impingement study, Bosch ROI meter is adopted to obtain the injection rate shape by measuring the pressure wave generated when the injector injects fuel [122].

Figure 3.7 shows the rig setup of the Bosch type rate of injection meter. The meter comprises of rate tube, ROI fixture, a BP66-1A11CEN151 regulator, and NI cDAQ-9178 and NI 9223 card. The injector is mounted in the ROI fixture and the injector tip is positioned at the beginning of the rate tube. A Kistler 5010 piezo-electric dynamic pressure transducer is also held by the ROI fixture and is used to record the pressure waves. The length of the rate tube is approximately 29.25 m and outer diameter of 9.52 mm (0.375

inch) with a wall thickness of 0.51 mm (0.02 inch). The inside diameter of the rate tube determines the magnitude of the pressure waves while the length of the rate tube influences the attenuation efficiency of the meter. A regulator is located at the end of the meter tube to adjust the back pressure on the enclosed volumes so that typical injection pressures can be used when testing an injector.

The mass flow rate for incompressible fluid is defined in Equation (3.1) derived from continuity equation.

$$\dot{m} = \frac{dm}{dt} = \rho * A * V \tag{3.1}$$

where ρ is the liquid fluid density, A is cross section area of fixture where spray occurs, and V is fluid flow speed.

The bridge that links fluid flow speed and measured pressure wave is the pressure-velocity equation valid for a pressure wave in transient flow.

$$P = a * \rho * V \tag{3.2}$$

where P is the pressure of fluid and a is the speed of sound in fluid.

Thus substituting Equation (3.2) into Equation (3.1) and rearranging terms, the governing equation is derived as:

$$\frac{dm}{dt} = \frac{A}{a} * P \tag{3.3}$$

For the data acquisition system with 10k Hz sampling rate, integration of eq. 3 in a discrete form results in,

$$m = \frac{A}{a} * P * \Delta t|_{SOI}^{EOI} \tag{3.4}$$

where *EOI* and *SOI* represent end of injection and start of injection, respectively.

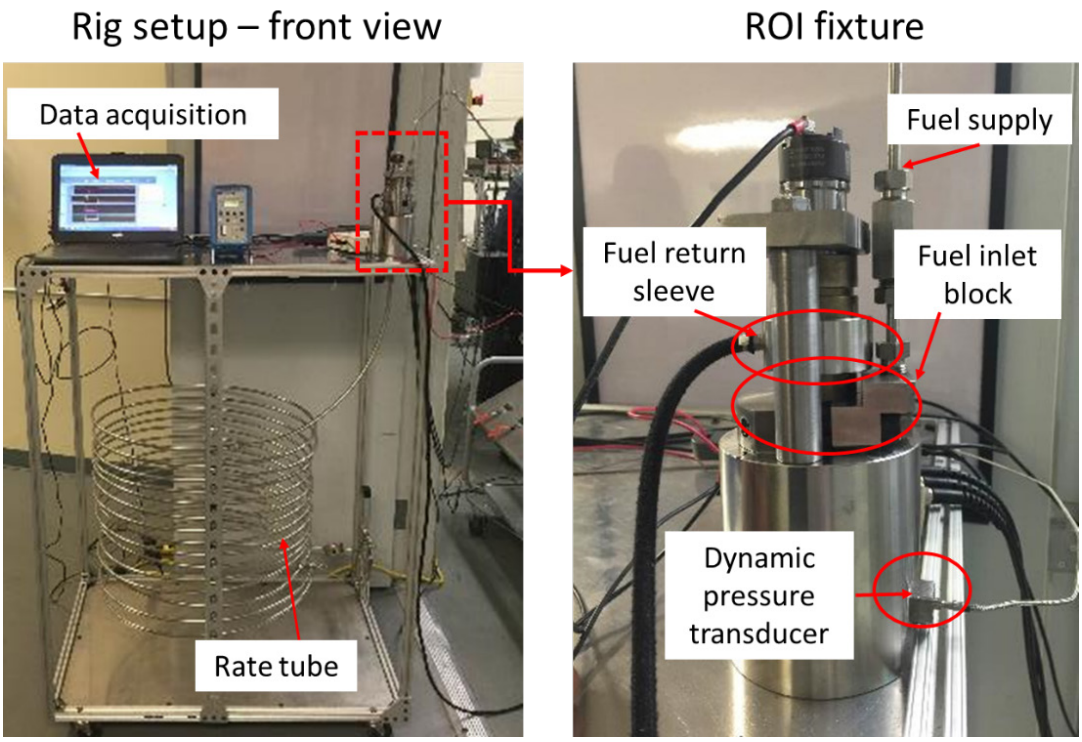

Figure 3.7: Rate of injection rig setup.

Pressure wave measurements are repeated 120 times for each test condition and the data is later processed to obtain the ROI profile. Figure 3.8 shows an example of ROI profile. The procedures taken to get the averaged ROI are: a). Piezo-electric transducer measures pressure wave with a calibration of 36 pc/bar; b). Charge is amplified and outputs as 30 bar/volt through a Kistler model 5010B charge amplifier; c). Data is quantized using a 16-bit NI-9223 card at 1 MHz sample rate; d). A 3rd order infinite impulse response (IIR) butterworth low pass filter with a cutoff frequency of 10 kHz is used and 80 out of 120 least drifted from zero bar reference injections are selected; e). Offset each of 80 selected pressure profiles with their respective mean value before the start of injection; f). Speed of sound is obtained by averaged division of the length the tube and time between the start of injection and second start of pressure rise; g). 80 pressure profiles are averaged and then used to calculate ROI profile.

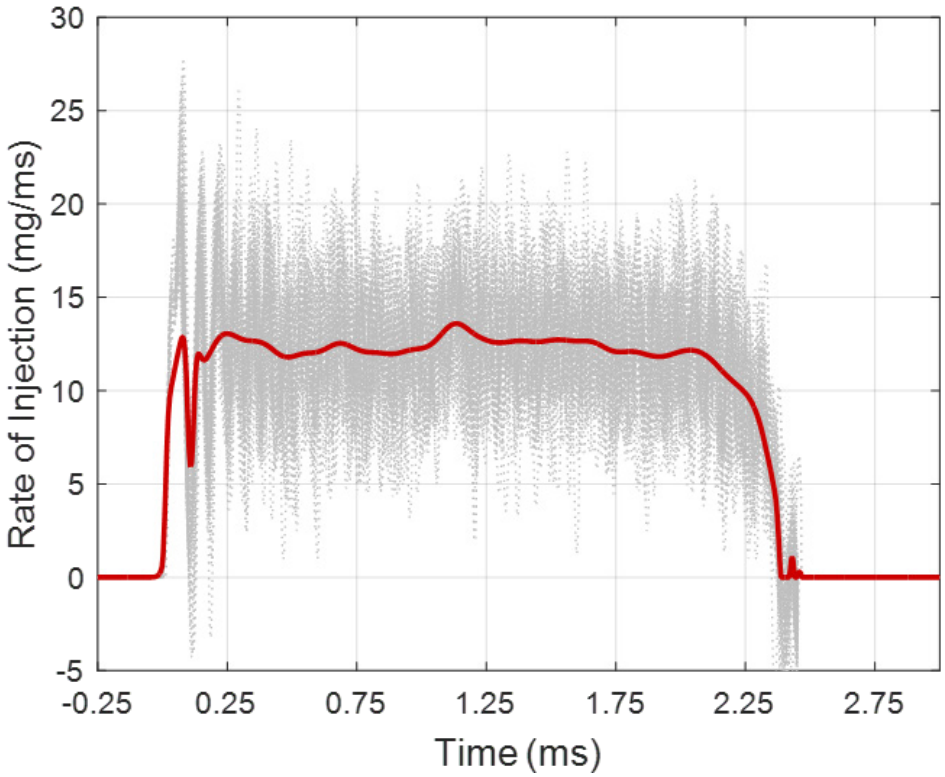

Figure 3.8: Sample mass flow rate result.

3.4 Combustion vessel overview

An experimental study for testing spray impingement on a flat plate and multiple spray-to-spray collision is carried out in an optically accessible constant volume combustion chamber as shown in Figure 3.9. This vessel is a 1.1 L constant volume combustion chamber. The chamber is cubical with an interior of ~100 mm per side. On each of the six faces of the cube are ports. In three of these ports windows were installed providing unobstructed orthogonal optical access to the combustion chamber. Optical windows provide access for high-speed imaging to study spray development. The top face port houses the spark plug assembly and two fans in order to create turbulence inside the vessel. A face port houses the injector assembly. On the eight vertices of the combustion chamber there are instruments located with actuator access ports. In four of these ports are an intake and two exhaust ports and a dynamic pressure transducer. The latter is a Kistler 5010 piezo-

electric dynamic pressure transducer that is coupled to a Kistler 5044a charge amplifier to measure the CV pressure [69, 123, 124].

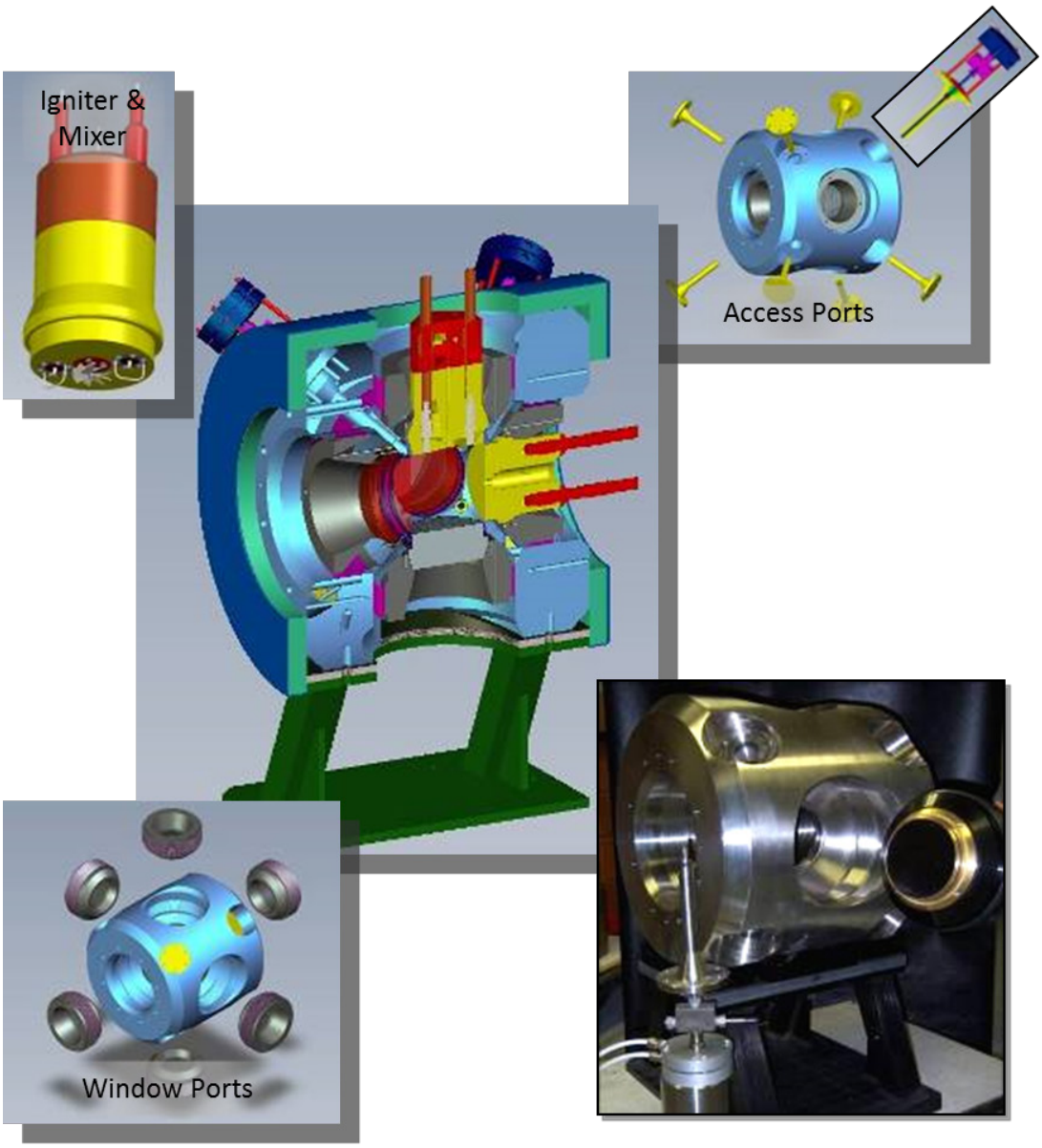

Figure 3.9: The optically accessible constant volume CV.

This chamber is capable of bearing high temperatures and pressures through a process of pre-burn. Two types of the ambient mixture were prepared such that the ambient temperature below 453 K is to use N_2 and the ambient temperature above 453 K using pre-burn. A high-pressure and high-temperature ambient environment, replicating the

thermodynamic condition of internal engine, is attained by combusting a pre-calculated composition of premixed hydrocarbon mixture. This pre-burn mixture is introduced at pre-calculated initial pressure and then ignited by a spark while the burned products are continuously mixed by a rotating fan inside CV. The burned products of combustion are the target species which would be otherwise present in the diesel engine at this temperature and pressure. This pre-burn increases the chamber temperature and pressure until target thermodynamic condition is reached; at this point the fuel is injected.

A sample of pressure profile in CV due to pre-burn and spray combustion is shown in Figure 3.10. The chamber is filled with premixed combustion mixture (H_2, C_2H_2, O_2, and N_2) at a set pressure labelled as "Fill pressure" to achieve a proper temperature and pressure of the ambient species in the chamber. Mixture is then ignited with a spark to combust a lean/dilute mixture and produce a high temperature and pressure atmosphere. As the pressure peak is reached, it decreases based upon fill pressure and the pre-burn combustion products cool down. Once the experimental conditions are reached, fuel injection event is triggered, auto-ignition and combustion processes follow to occur.

In Table 3.1, the O_2 content remaining after pre-burn combustion is shown along with other species composition including both reactions and products. Non-reacting vaporizing spray condition (0% O_2) and combustion conditions (15% and 19% O_2) are highlighted as the ambient composition of interests in the current study. A detailed description of the combustion chamber and other details about negligible effect of the resultant post pre-burn combustion gases on diesel spray ignition can be found in ref.[124, 125].

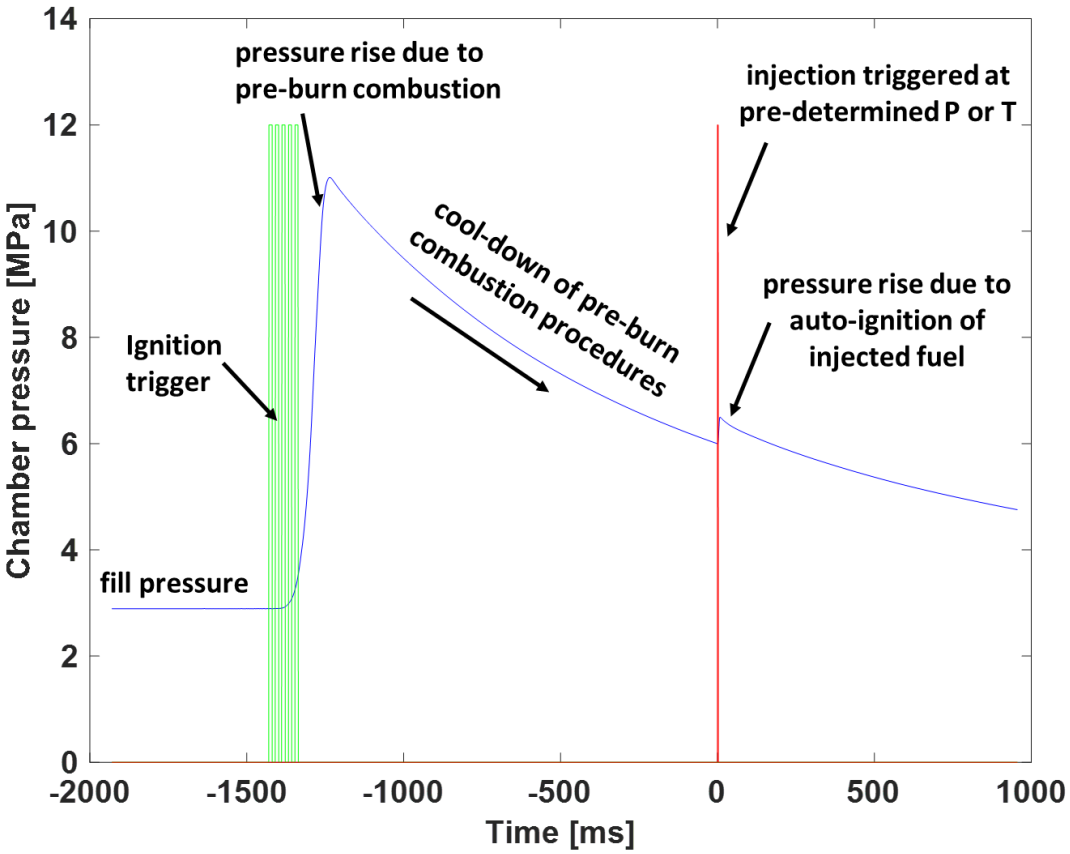

Figure 3.10: The ignition- pre-burn and injection-spray-combustion events.

Table 3.1: Composition of reactants and products from pre-burn combustion

Products					**Reactants**			
When diesel injected					**Prior to pre-burn**			
O_2	N_2	CO_2	H_2O	MW	rC_2H_2	rH_2	rO_2	rN_2
19	71.27	6.15	3.58	29.4	3.02	0.5	26.46	70.02
15	75.15	6.23	3.62	29.24	3.06	0.5	22.63	73.82
0	89.71	6.52	3.77	28.68	3.2	0.5	8.25	88.05

3.5 Optical diagnostics with image processing

Optical diagnostics is used to characterize spray and combustion behaviors. Two main optical based diagnostics used in the present work are Schlieren/shadowgraph imaging and Mie scattering. Shadowgraph diagnostics provides information on the vapor phase of

sprays as this diagnostic detects density gradients by collecting the collimated light which passed through the region of interest, and Mie scattering is used to quantify the liquid phase of the spray based on scattering principles. In this section, the different optical diagnostics with their setup in CV are introduced, the corresponding sample images are provided, and the images processing process is also discussed. The detailed experimental setup with the specific test settings and conditions for each test will be employed in the later sections.

3.5.1 Backlight for droplet-wall impingement

For the measurements of a single droplet impingement on a flat surface, the experimental setup as shown in Figure 3.11 consists of a drop generator, a high-speed camera with appropriate lens systems and high-intensity light source. Single droplet is generated by a precision syringe pump with the volume flow rate of 0.2 mL/min, it is detached from the tip of the needle when the droplet weight overcomes the capillary force. The droplet with an initial diameter (D_0) is released and accelerates by gravity before it impinges on the surface and reaches an impact velocity (U_0). The initial droplet diameter varies with different fuels and the impact velocity changes from 0.72 to 3.0 m/s as the droplet release height varies between 26 and 456 mm in this work. Two different flat plates were used, smooth and roughened, to study the effect of roughness on the droplet-wall interaction dynamics. The roughened surface has an average roughness of 16 μm and peak-to-peak roughness of 80 μm, which is similar with a conventional piston surface [93]. An analog mode LED lamp focused by an iris was passed through a plano-convex lens to generate a collimated cylindrical light. Photron Fastcam SA 1.1 high-speed camera along with a 200 mm Nikon Nikkor lens and f-stop 4 was placed on the opposite direction of the LED to capture the process of droplet impinging on the plate. The image acquisition frequency was varied between 9,000 and 12,000 fps, the exposure time is set to a range of 5.6 to 111 μs varying with the liquid fuel and duration of droplet impingement process. Furthermore, to understand the effect of surface temperature on the dynamic process of the droplet-wall interaction, the smooth flat plate was heated-up using heater controller. In the present work, the roughened surface is the BK-7 window while the smooth, heated surface is the heat-treated stainless steel.

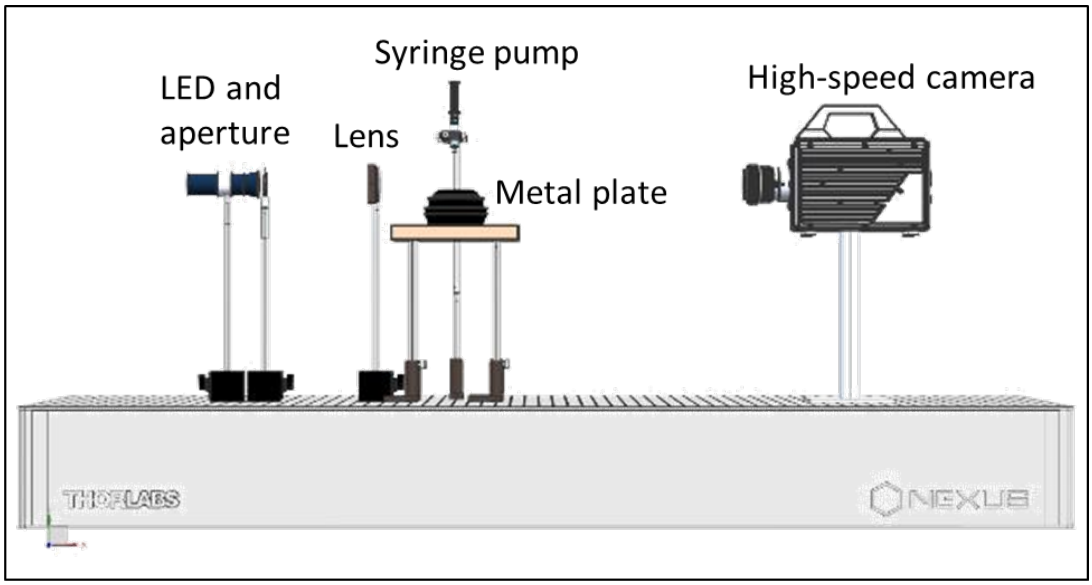

Figure 3.11: Experimental setup for single droplet-wall impingement.

3.5.1.1 Image processing

Figure 3.12 (top) shows the schematic of a single droplet placed at a certain location over the impinged plate with an initial velocity and Figure 3.12 (bottom) provides the schematic after the droplet impinging on the surface. The various global parameters such as the initial droplet diameter (D_0), the impact velocity (U_0), spreading diameter (d), spreading factor (Δ), contact line velocity (U_{cl}), height ratio (h/ D_0) and dynamic contact angle (θ), are described to characterize the process of droplet impacting on the surface.

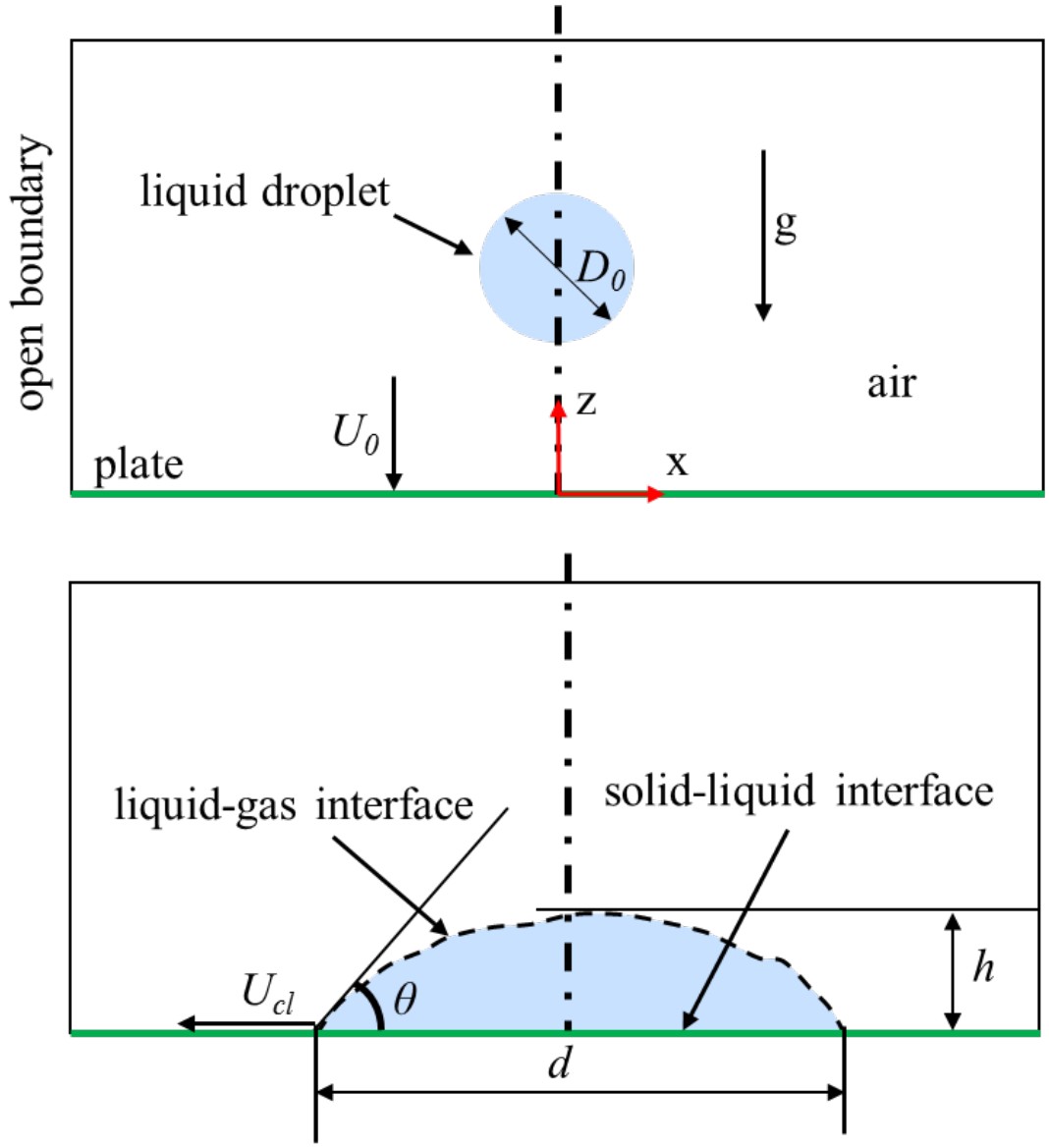

Figure 3.12: Schematic of droplet impingement on the flat surface.

Spreading diameter (d) is the distance between the left and right visible three-phase contact points. The three-phase contact points are defined as the points where all three phases meet, i.e. solid, liquid, and gas. Spreading factor (Δ) is the ratio of spreading diameter (d) to initial droplet diameter (D_0). Impinged height is defined as the maximum height in the perpendicular direction with respect to the impinged surface and impinged height ratio (h/D_0) is the ratio of impinged height to initial droplet diameter (D_0). The contact line velocity (U_{cl}) is the rate of change of spreading diameter (d) with respect to the time. The angle

formed between the liquid gas interface and solid-liquid interface at the three-phase contact point is defined as contact angle. The dynamic contact angle (θ) can be defined as the contact angle observed at this moving contact line during the droplet impingement process. In general, three stages are observed during a droplet impinging on the surface based on contact line velocity: advancing, receding and equilibrium. In the present work, if the $U_{cl} > 0$, the dynamic contact angle is advancing contact angle; if $U_{cl} < 0$, the dynamic contact angle is receding contact angle; and if $U_{cl} = 0$, the droplet becomes stable which corresponds to the equilibrium contact angle. The averaged contact angle at each phase is calculated by taking the mean of the instantaneous contact angles of respective phases.

To analyze the droplet impinging on a flat surface, an in-house MATLAB code was developed to process the images. The procedure of image processing is shown Figure 3.13. In Figure 3.13 (top), first, the background was subtracted to remove the unnecessary object other than the droplet based on the original image. Then, the image was converted into a binary image based on a threshold which is a constant value chosen by applying Otsu's method [126] to aid in accurately predicting the droplet boundary. The possible deformation of an impacting droplet due to drag force was measured by determining the difference between horizontal and vertical diameters. We found this difference to be less than ±1 % for all measurements, showing that the drag force does not have a substantial influence on droplet size. Therefore, the image of the droplet is approximated as a circle, on the basis of the area of this circle, the initial diameter of the droplet is extracted. A sensitive analysis for the threshold value was done on a sample case by increasing and decreasing default threshold by 20 % and the initial droplet diameter shows only ±2 % for different threshold values. The processing of post-impingement images is shown in Figure 3.13 (bottom). The boundary points are separated into two interfaces: solid-liquid interface (blue) and liquid-gas interface (red). The spreading diameter (d) is calculated as the distance between leftmost and rightmost visible three-phase contact points. The spread factor (Δ), ratio of spreading diameter and initial droplet diameter is then calculated at each time step. Similarly, the height of the impinged droplet is measured as a distance from the

topmost point of the droplet to the flat surface and the impinged height ratio (h/ D_0) is found. The contact line velocity (U_{cl}) follows the same way to be obtained.

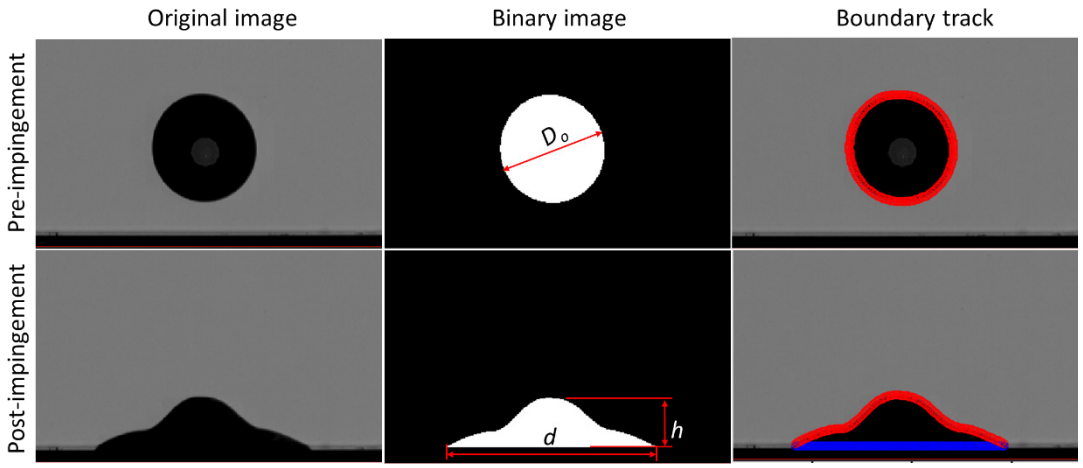

Figure 3.13: Image processing procedure for single droplet-wall impingement.

The dynamic contact angle (θ) is processed as an angle between the tangent to drop profile at the moving contact line and horizontal solid-liquid interface. The boundary points corresponding to the liquid-gas interface are considered, as shown in Figure 3.13. Only the pixels, very near to the three-phase contact point on the liquid vapor interface, are considered to curve-fit a line. This curve fitted line is used as a tangent to the droplet from the three-phase contact point as shown in Figure 3.14 (right). The contact angle is finally obtained from the slope of the curve fitted line. The dynamic contact angle is extracted from each image by averaging the visible left and right contact angles as shown in Figure 3.14. Besides, the reference scale in the experiment was determined by measuring the number of pixels corresponding to a known length and the known length was oriented normal to the camera's line-of-sight.

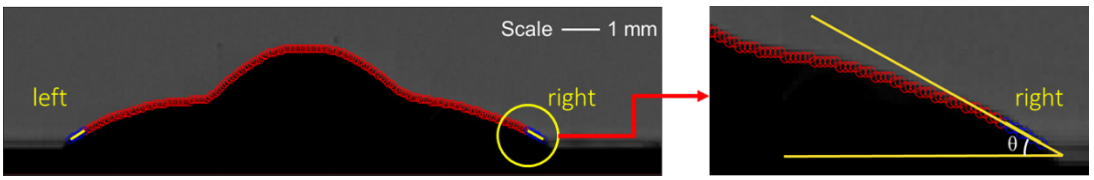

Figure 3.14: Contact angle measurement technique.

3.5.2 Spray visualization for spray-wall impingement test

Optical diagnostics is used to characterize spray and combustion behaviors. Two main optical based diagnostics used in the present work are schlieren/shadowgraph imaging and Mie scattering. The schlieren/shadowgraph diagnostics is based on density gradients to visualize vapor phase fuel spray behavior, which is enabled by changing in refractive indices. A high intensity pulsed LED with a pin-hole aperture is applied as the light source. One schlieren mirror is used to generate a collimated beam which is directed passing through the optical vessel and it is placed where its focal point coincides with the light source. Another schlieren mirror collects the beam and makes it converge on a negative bi-convex focusing lens where it is finally captured by a high-speed camera. Unlike schlieren imaging system, the LED which is used for Mie scattering imaging is located in front of the side optical access of the combustion chamber [127]. Furthermore, to capture both liquid and vapor for the same single spray event, a hybrid imaging system was performed as a combination of both Mie scattering and schlieren along the same line of sight of the schlieren setup. A continuously on/off sequence of two LEDs was setup to provide light source for Mie and schlieren imaging that are captured frame by frame in the camera. In this way, consecutive Mie and schlieren images are available to represent liquid and vapor, respectively, for the same spray event.

Three views, namely side, front, and bottom views in Figure 3.15 were obtained to visualize the entire process of diesel spray impinging on the plate and capture the diesel spray characteristics at different operating conditions. The optical setup of simultaneous Mie scattering and schlieren was applied for the spray-wall interaction test. The side view images were obtained from hybrid Mie scattering and schlieren imaging techniques [123] by using camera #1 and the front view images were attained from Mie scattering by positioning camera #2 in front of the injector window. For the side view, a Photron Fastcam SA 1.1 high-speed camera was used to acquire the liquid/vapor spray at 36,000 fps with an exposure time of 27.11 μs. The camera used a Nikon Nikkor 85 mm lens with f-stop 1.4. For the front view, a Photron Fastcam-APX RS high-speed camera with a 52-mm lens and

f-stop 1.8 was employed to capture the liquid spray at 36,000 fps with an exposure time of 27.77 µs.

With the help of a 45° mirror located directly below the transparent impinged window, the bottom view images were captured from Mie scattering by repositioning camera #1 beneath camera #2 and pointing it at the 45° mirror. The same Photron Fastcam SA 1.1 high-speed camera with 85 mm lens and f-stop 1.4 was used to obtain the liquid fuel spray at 25,000 fps. The exposure time was set to 16.57 µs.

Regarding the n-heptane setup, only front and side views were used to visualize the spray. Mie scattering and schlieren were used for the front view and the side view respectively. Unlike what was done with the camera setting of diesel spray, Photron Fastcam SA 1.1 high-speed camera was firstly used in side view at 50,000 fps with an exposure time of 20 µs, using a Nikon Nikkor 85 mm lens with f-stop of 4.0. After the side view spray was recorded, the same camera with the same lens and a different f-stop of 1.4 was then applied in front view to capture the liquid spray at 50,000 fps with an exposure time of 3 µs.

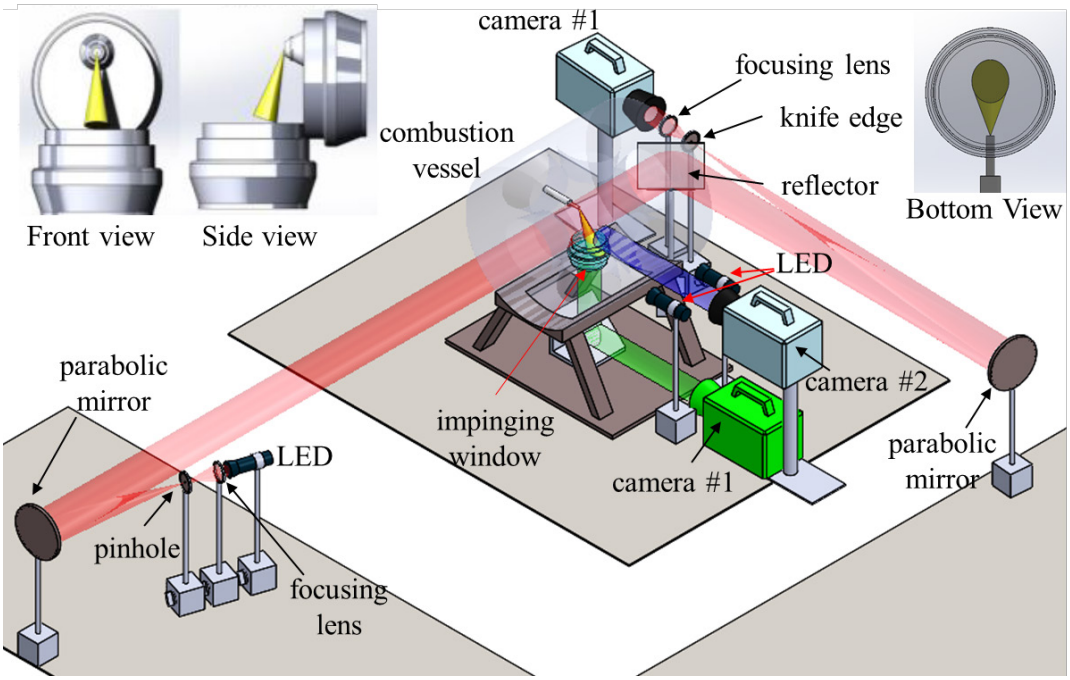

Figure 3.15: Experimental optical setup for spray-wall impingement test.

Figure 3.16 (left and middle) shows the installation of metal and quartz windows inside CV, the sample images are taken from front view. Figure 3.16 (right) provides a picture of temperature controlled heated window surface, which includes six heaters, seven thermocouples, and three heat flux probes.

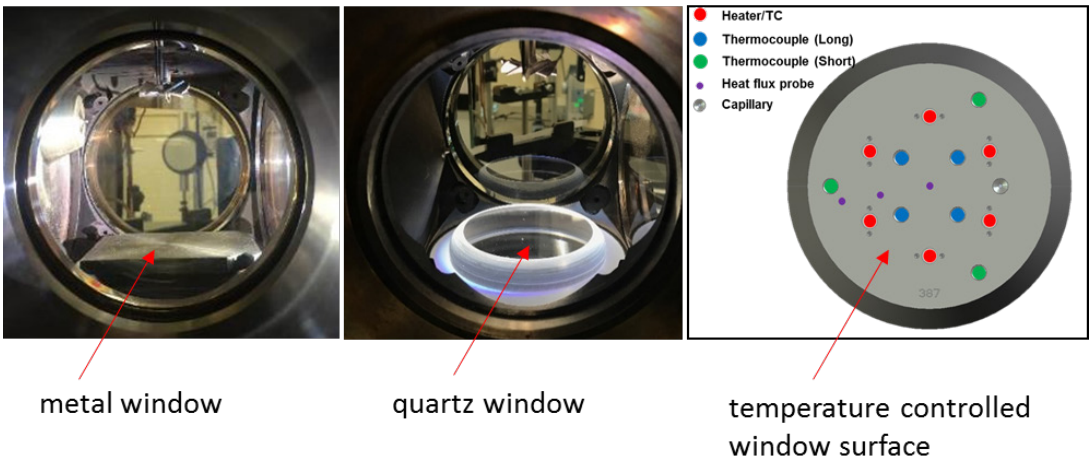

Figure 3.16: Metal, quartz, and heated window installation in CV.

3.5.2.1 Image processing analysis

Figure 3.17 shows the schematic of a liquid spray impinging on the wall in front (top), side (middle) and bottom (bottom) views. The schematic representation describes several global parameters such as free spray liquid penetration (Z), impinged spray radius (R), impinged spray radius on the wall (R_w), and impinged spray height (H) to characterize the free and impinged spray. These global parameters were measured by processing the images obtained experimentally through Mie scattering and schlieren imaging techniques.

In front and side views of Figure 3.17, the free spray liquid penetration (Z_f or Z_s) is defined as the distance between the nozzle tip and the spray leading edge that represents the maximum extension of the spray in the vessel at any given time. The impinged spray properties were extracted from the *side* view schlieren images which provided a sharper boundary visualization than the Mie scattering images. In Figure 3.17 (middle), impinged spray radius (R_s) characterizes the maximum axial spray spread distance with respect to

injector axis after the liquid fuel impinges on the wall. The impinged spray radius on wall ($R_{s,w}$) is the distance between the injector axis and the farthest point of the spray in the axial direction, which always maintains a contact with the impinged wall. The impinged spray height (H_s) is considered as the maximum height in the perpendicular direction with respect to the impinged wall, which is caused by impingement regimes of splash, rebound or the free spray flowing over the thin film. In Figure 3.17 (bottom), a schematic view of the Mie scattering output is provided to visualize the bottom view spray images. In particular, the radial ($R_{b,f}$) and axial ($R_{b,s}$) radii are defined as the distance between the impinging point and the wall-impinged expanding spray (WIES) radial and axial fronts, respectively. The ratio between $R_{b,f}$ and $R_{b,s}$ is defined as the expansion ratio. The radial and axial corrugation ratios ($C_{b,f}$ and $C_{b,s}$), i.e., the ratio of the actual impinged spray front length over the corresponding smooth elliptic arc length, are also measured in the bottom view. The corrugation ratio is therefore a measure of the extent of the corrugation or wrinkling effect of an impinged spray front.

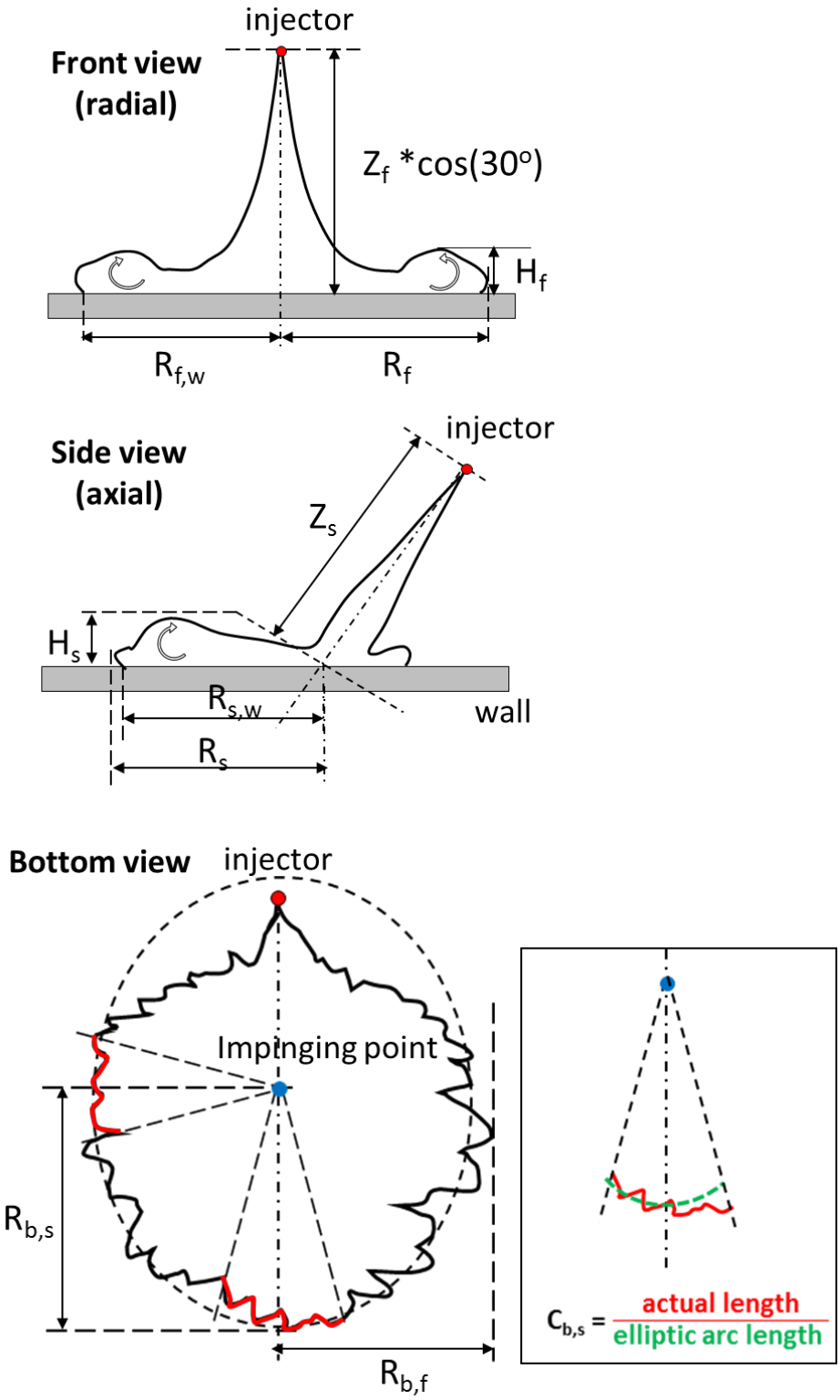

Figure 3.17: Schematic of a liquid spray in front (top), side (middle) and bottom (bottom) views.

To analyze the free spray and impinged spray characteristics, the sequence of images captured for one injection were converted into binary images, and the built-in morphological tools in MATLAB were applied for extraction of the above mentioned global parameters. Figure 3.18 shows sample image processing from front view (Mie scattering). Figure 3.18 (top) and (bottom) give the spray penetration and spray angle, as well as impinged properties processing procedure, respectively.

Firstly, the raw image was converted into a binary image based on a threshold which is a constant value chosen by applying Otsu's method [128]. Since the image consists of light object on a dark background, the threshold separates pixel points into two main modes with intensity values to extract the spray. If any point for which intensity is larger than threshold x 255 is considered as an object point and others as background points [129]. As shown in Figure 3.19, a sensitive analysis to the threshold on a sample case is done by increasing and decreasing threshold by 20% and the free-spray penetration shows insensitive for different threshold values. Then, the largest connected area based on the selected threshold was considered for exact contouring of the boundary of the spray. After this, the spray penetration and impinged properties were determined by measuring the extreme points of each modified image. The spray angle (θ) in this study is measured by estimating the angle formed by 60% of spray length from injector tip. Left and right edges of spray are identified from the spray boundary points in each image. A linear fit is calculated for these left and right edges. These linear fit lines are used to calculate the spray angle.

In our initial study of spray-wall impingement, a 7-hole diesel injector is used. To analyze the single jet impinging the plate, masks were created to block other extra plumes. Then the rest of procedures for image processing to analyze the spray characteristics are the same with those from the single-hole injector as described in the above.

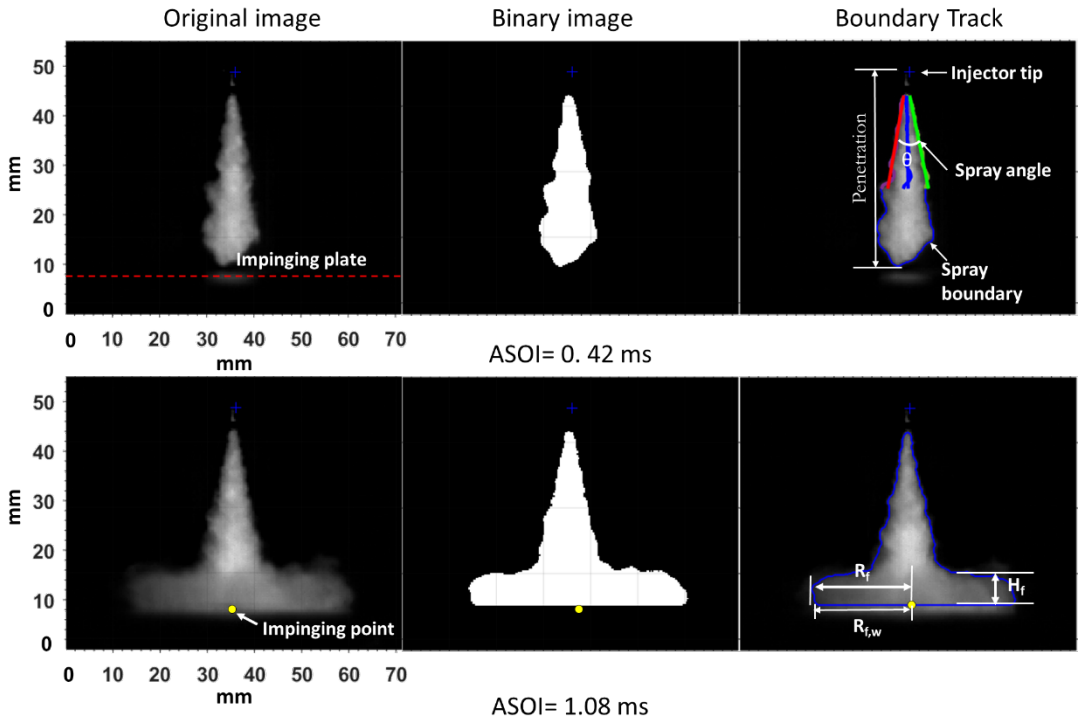

Figure 3.18: Image processing from Mie scattering images, liquid penetration and spray angle (top) and radial impinged properties (bottom) (Sample image is from injection pressure of 180 MPa and ambient density of 22.8 kg/m^3).

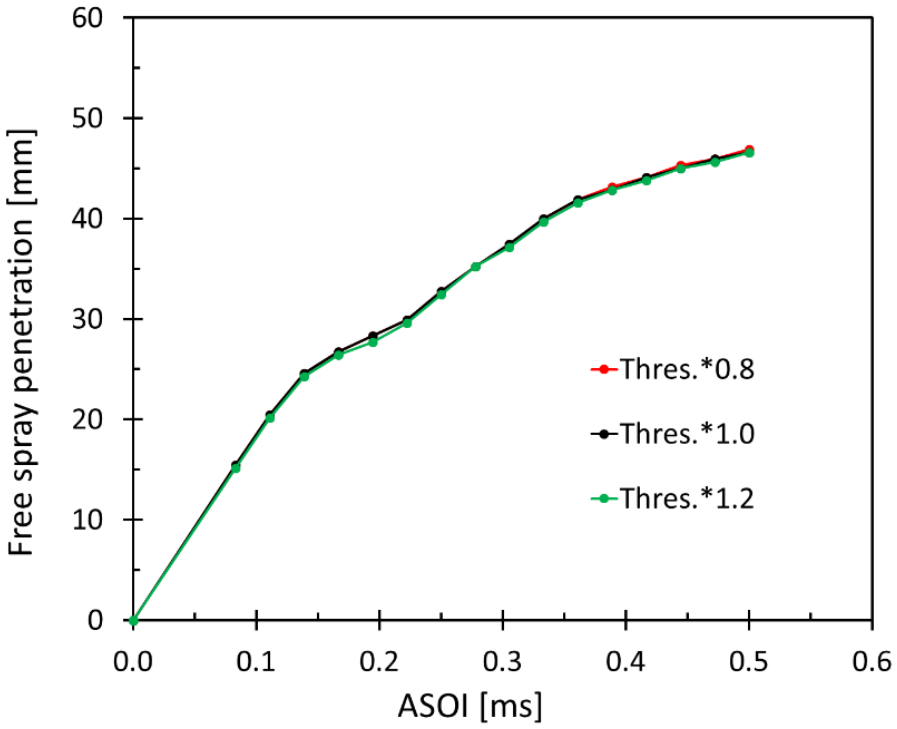

Figure 3.19: The sensitivity of liquid penetration to thresholds.

The imaging analysis of the bottom view images shows slight difference with that of front and side views. As shown in Figure 3.20, a 'centroid' method was used to identify the impinging point based on a number of the pixels near the impinging location. The boundary of the WIES front was traced by the same method used in the front and side view images. Due to the highly wrinkling of the WIES front as it propagates on the surface of the wall, an additional procedure was taken for estimating the averaged radial and axial radii over the arc sector. The final central angle of arc was found to be 30° based on the sensitivity analysis. This angle leads to the minimum variation of the radius over the entire impinged spray lifetime [130]. The radial or axial arc ($A_{b,f}$ or $A_{b,s}$) is the length of the leading edge of the detection sector, which is also used for the corrugation ratio calculation.

The reference scale used in the current study, was determined experimentally by measuring the number of pixels corresponding to a known length. The known length was oriented normal to the camera's line-of-sight and an angle between the wall on which the injector is mounted and the plumes was considered during the data processing.

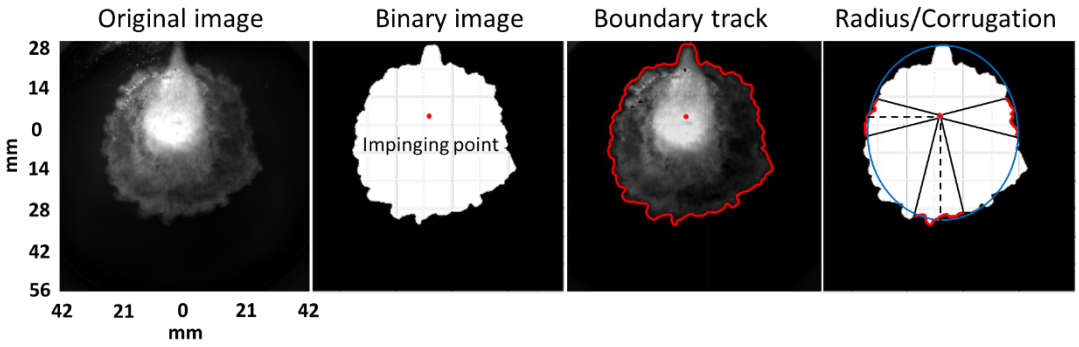

Figure 3.20: Bottom view image processing.

3.5.3 Refractive index matching technique

3.5.3.1 Calibration procedure and image processing

In the current work, Refractive Index Matching (RIM) technique was used to calibrate and measure the liquid fuel film thickness. RIM technique developed by Drake et al. [72] is an optical method to measure the spatial and temporal distribution of liquid film thickness, which is applied to characterize the fuel impingement on the plate. RIM method utilizes the similar refractive indexes between the impinging plate (glass/quartz in the present study) and liquid fuel, as the incident light illuminating the plate, it is scattered from the roughened interface due to the difference in index of refraction between surface and air. This scattering is modified by the presence of the liquid that closely matches the index of refraction of the plate. The refractive index of n-dodecane is 1.42 and the refractive index of n-heptane is 1.39, which is close to the refractive index of the impinged plate, 1.46. The fundamental mechanism of the RIM technique is schematically shown in Figure 3.21. The relation between the fuel film thickness and the variation of intensity from the scattered light is extracted after RIM technique is applied.

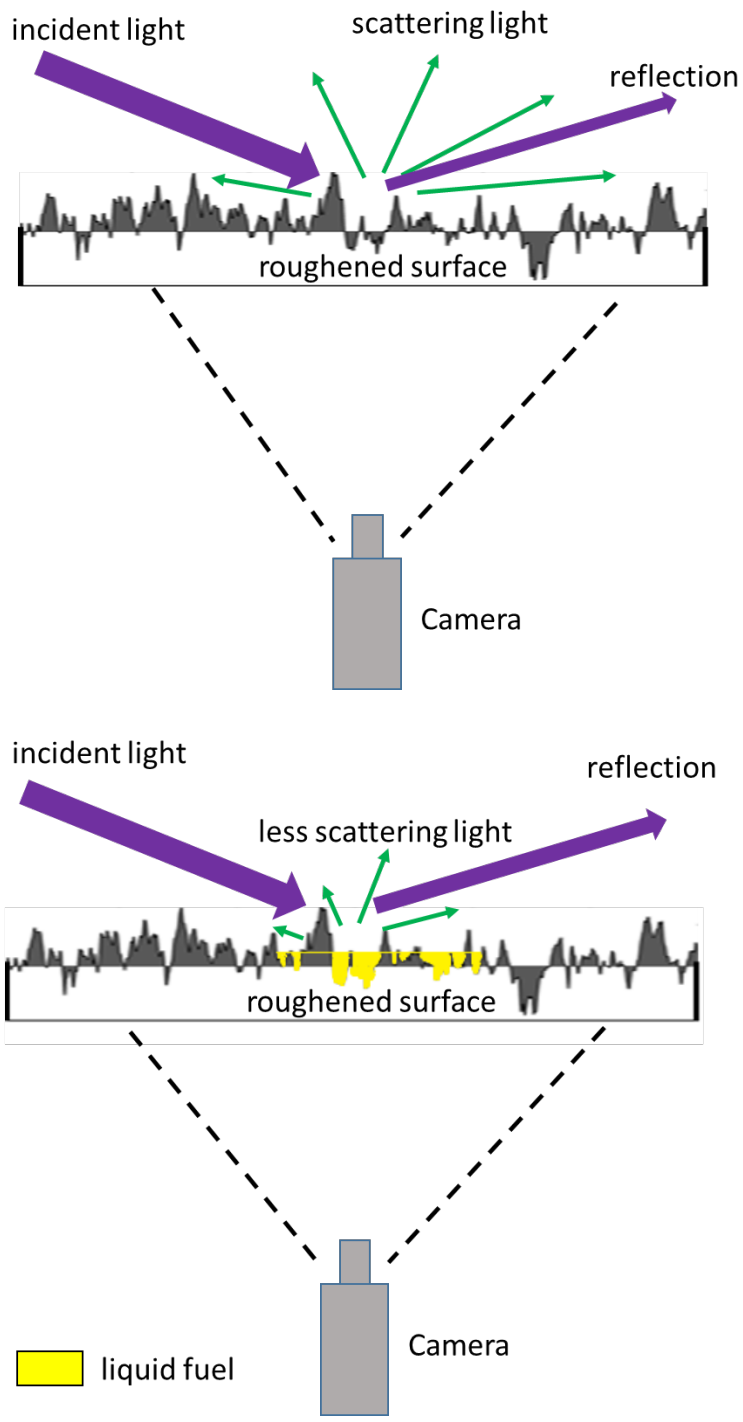

Figure 3.21: RIM technique applied at a roughened surface without (top) and with (bottom) liquid covering the surface.

Figure 3.22 gives the experimental setup of liquid fuel film thickness calibration and measurement on a single-hole injector. Two perspectives, including the side view and front view, are provided in Figure 3.22. A single-hole injector with nozzle diameter of 200 μm was mounted on a face port of the chamber and the nozzle orifice orientation with respect to injector axis is 60°. The distance between the injector tip and the impinged roughened surface is 33.65 mm. This roughened surface is a roughened glass with 0.25 in (6.35 mm) thickness imposed on top of the transparent sapphire window. The impinged surface roughness profile is given in Figure 3.23, the averaged roughness and the maximum (peak-to-peak) roughness of the impinged plate are 16 μm and 80 μm, respectively, which is similar with a conventional piston surface [93]. A LED was used to provide the light from the side window with a tilt angle about 10°. A Photron Fastcam SA 1.1 high-speed camera was applied to capture the film images at 10,000 fps and an exposure time of 99.33 μs with the help of a 45° mirror located directly below the impinged plate. The camera lens is a Nikon Nikkor 85 mm lens with f-stop 1.4. The bottom view of the spray is finally captured.

Note that a high precision syringe was used during calibration of the liquid film thickness, instead of single-hole injector. In addition, a very thin n-dodecane film is deposited between the roughened glass and bottom transparent window to avoid the movement of the roughened plate because of the high-pressure injection impact.

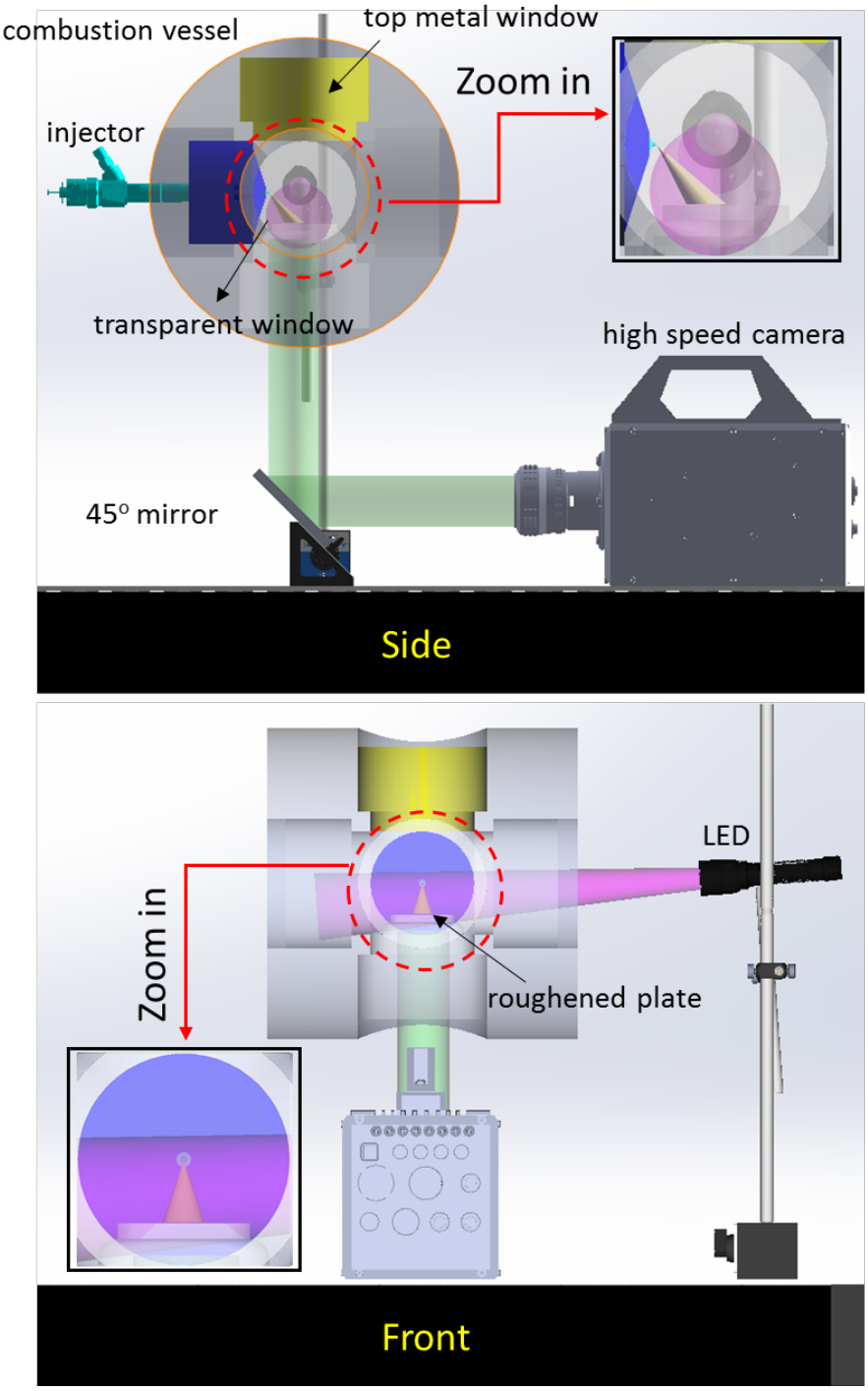

Figure 3.22: Side (top) and front (bottom) views of experiment setup.

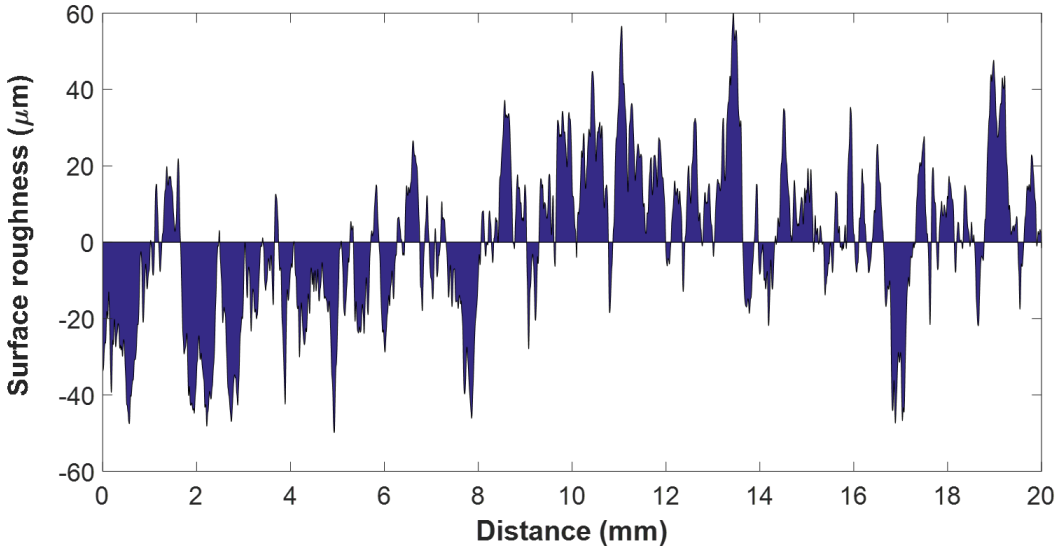

Figure 3.23: Surface roughness profile.

A liquid mixture of n-dodecane (low volatile fuel) and n-heptane (high volatile fuel) [94] with various volume fractions was employed for liquid film thickness calibration. The percentage of n-dodecane in the mixture was volume basis and varied, one is 5% and another is 10%, to get a wider range of data points to correlate with the transmissivity variations and further obtain an accurate calibration curve. A high precision syringe dispensing a minimum volume of 0.05 mm^3 replaced the injector for depositing the liquid film in calibration. The total volume of the mixture that was injected on the roughened plate was varied from 1.0 µL to 2.5 µL with an increment of 0.5 µL. The vessel was cooled down to 323 K to avoid the evaporation of n-dodecane. Initially, 100 images are captured before injecting fuel on the surface and averaged based on intensity, which is considered as background image (I_{dry}). A known volume of mixture consisting of n-heptane and n-dodecane is deposited on the roughened surface.

Variation in transmitted scattered light intensity due to presence of fuel mixture is calculated by Equation (3.5):

$$\Delta T(x,y) = 1 - \frac{I_{wet}(x,y)}{I_{dry}(x,y)} \tag{3.5}$$

where ΔT is transmissivity variation, I_{dry} is the intensity of the scattered light in the background image at the location of (x, y) and I_{wet} is the intensity with the fuel deposited on the surface.

The transmissivity variation $\Delta T(x, y)$ can be cast as a function of film thickness, $h(x, y)$ by Equation (3.6):

$$\Delta T(x, y) = f[h(x, y)] \tag{3.6}$$

Since the maximum film area is obtained just before the n-heptane is completely evaporated, the volume of remaining fluid is known, therefore, the film thickness is equal to the ratio of the known volume of the remaining fluid and the maximum film area. The above procedure was repeated for a range of fluid volume to establish a final calibration relation between transmissivity variation and film thickness.

Before the droplet is deposited on the wall, the surface is dry and the intensity remains at the maximum level as noted in the manuscript I_{dry}. As long as the droplet impinges on the wall, the intensity decreases rapidly as shown in Figure 3.24. Then it experiences two stages and increases towards its initial level. In the first period, the increase of intensity is relatively rapid within a few seconds. During the second period, the increase of intensity is slower and it takes longer time to return to its original value (I_{dry}) (not shown in the figure). Since the droplet mixture contains two different fuel, one is high volatile fuel (n-heptane) and another one is heavy compound (n-dodecane), thus the first stage corresponds to the rapid evaporation of the high volatile fuel while the second stage corresponds to the evaporation of n-dodecane. The calibration point is chosen at the joint of these two stages and the intensity shows obvious difference at this point, which indicates the complete evaporation of n-heptane and the maximum area. Second, in current work, the vessel temperature is set to 323 K to get the calibration results. The reason why the vessel temperature cannot be set to 423 K for the calibration process is that the relative small volume (below 2.5 μL) of droplet fully evaporates before reaching the maximum area when the vessel is set to 423 K, it is due to the very low vapor pressures of n-heptane and n-dodecane.

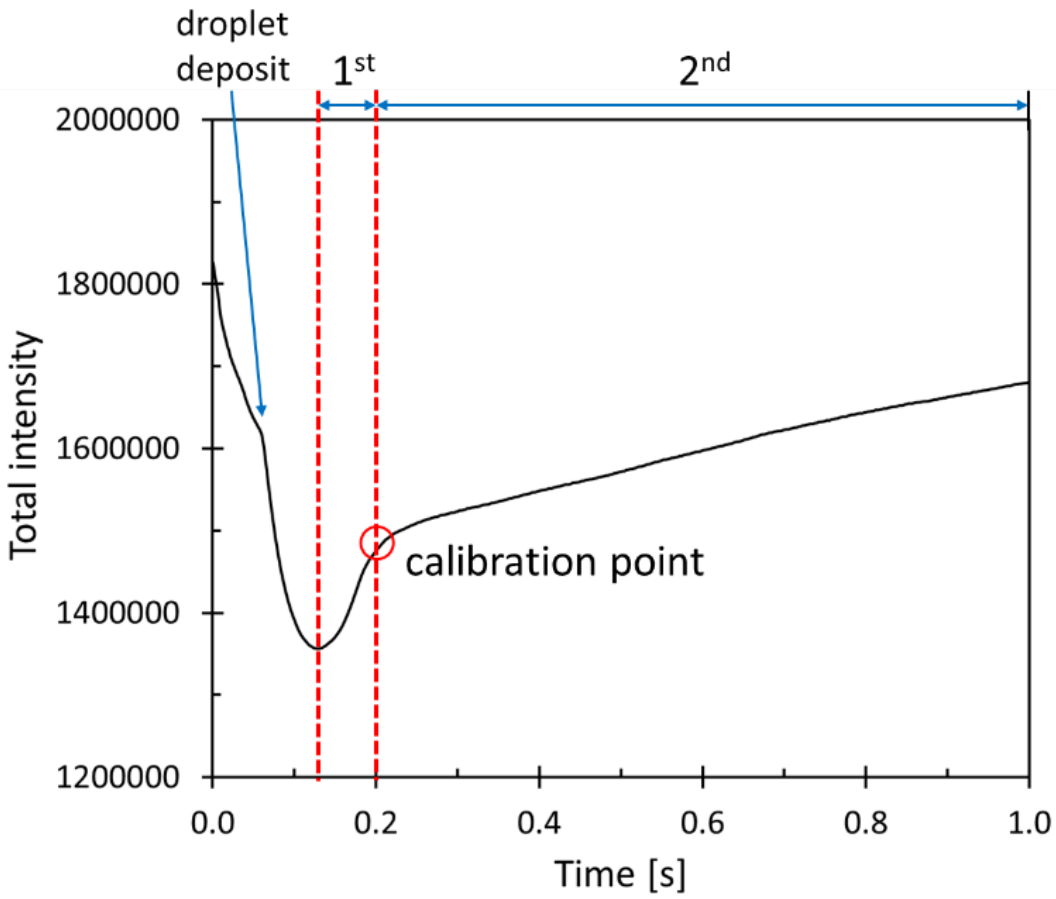

Figure 3.24: Evolution of total intensity pre- and post-impingement.

The experimental images were post-processed using an in-house MATLAB code by following procedures. First, a great number of background images (100 images for the current study) were averaged to get the intensity of the scattered light I_{dry}. The fuel mixture with various volumes (known) was then dropped onto a roughened surface in the testing site. The test images were cropped to only view the area around the film, I_{wet} is obtained after averaging the intensity from this area. As n-heptane is high volatile fuel and evaporated rapidly, it is assumed that n-heptane was completely evaporated after a short time and only n-dodecane was remained on the surface. The calibration point is considered just before the n-dodecane starts to evaporate at which the film area was considered as the maximum area. The maximum area was measured by binarizing the image and its corresponding transmissivity variation was also calculated. The threshold value to determine this deposit area in the binary image was found using Otsu's method [126] and

the number of pixels above the threshold was counted to obtain the size of area. A sensitive analysis to the threshold on a sample case is done by increasing and decreasing the default threshold obtained from Otsu's method by 20% and the detected film area shows insensitive for different threshold values. Then, the largest connected area based on the selected threshold was considered for exact contouring of the boundary of the spray.

Figure 3.25 shows the local transmissivity variation ΔT at the calibration point with different known volumes and two various mixtures. As known for the total volume and the percentage of n-dodecane, the averaged thickness of the entire film can be calculated, which corresponds to a fixed area-averaged transmissivity value. Finally, the calibration relation between liquid film thickness and averaged transmissivity variation along with the curve fit to the data were found as shown in Figure 3.26. It is important to note that the RIM technique in the current work may lose sensitivity when film thickness is above 1.5 μm and below 0.45 μm and the corresponding ΔT is above 0.7 and below 0.3. Therefore, during the calculation of film mass discussed in Equation (3.3) below, pixels with film thickness > 1.5 μm were assigned the calculated film mass based on film thickness = 1.5 μm with ΔT = 0.7 and pixels with film thickness < 0.45 μm were given the film mass to be 0 mg by default.

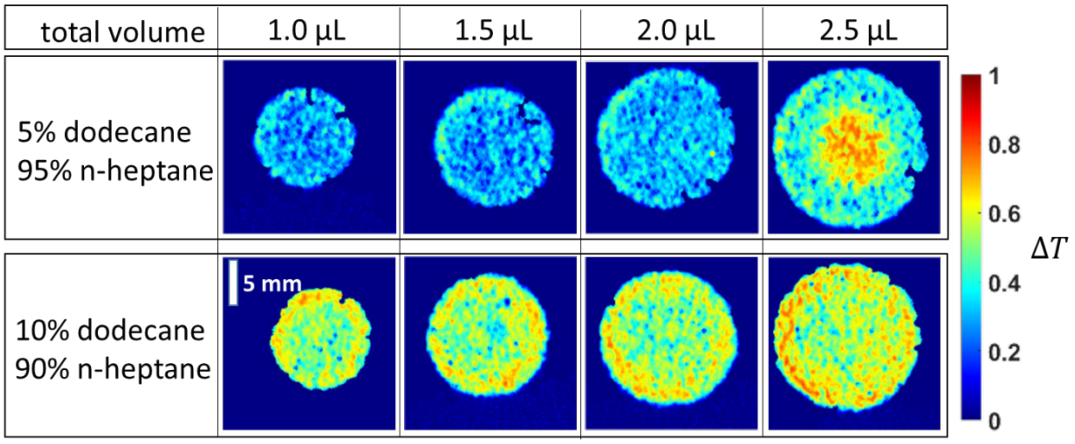

Figure 3.25: The transmissivity variation of the calibration points with different percentage mixture.

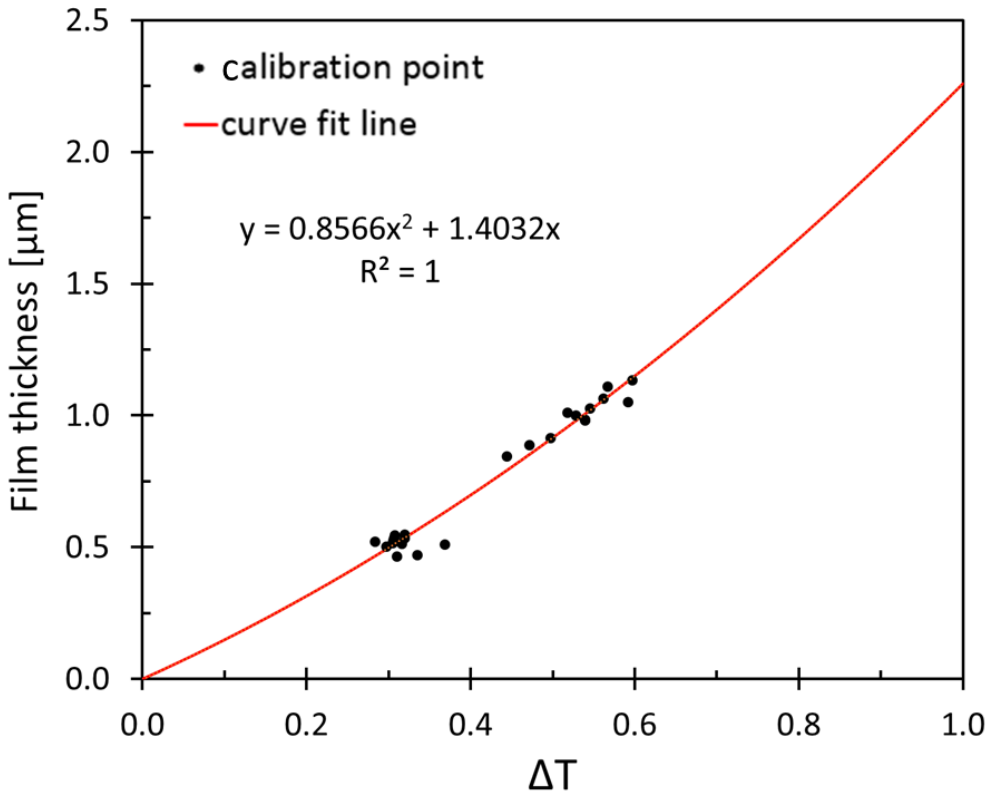

Figure 3.26: Relationship between transmissivity and film thickness.

3.5.3.2 Film thickness measurement in spray-wall interaction test

During spray-wall impingement test, n-heptane as the liquid fuel was injected on the roughened flat surface at various ambient and injection conditions. The film characteristics such as local film thickness, the averaged film thickness, film mass and film occupied area can be found based on the above calibration result. The local film thickness was obtained directly from the calibration relation between the transmissivity variation and film thickness. In current study, the local film thickness is calculated along the axial and radial directions as shown in Figure 3.27 with respect to the impinging point, which is also the original point and obtained by using the 'Centroid' based on a number of the pixels near the impinging location. A square region (2.25 x 2.25 mm^2) located in the central upper region around the impinging point as shown in Figure 3.27 (blue box) was selected to

calculate the averaged film thickness [94]. The averaged film thickness is calculated by taking the mean of the instantaneous images of respective region.

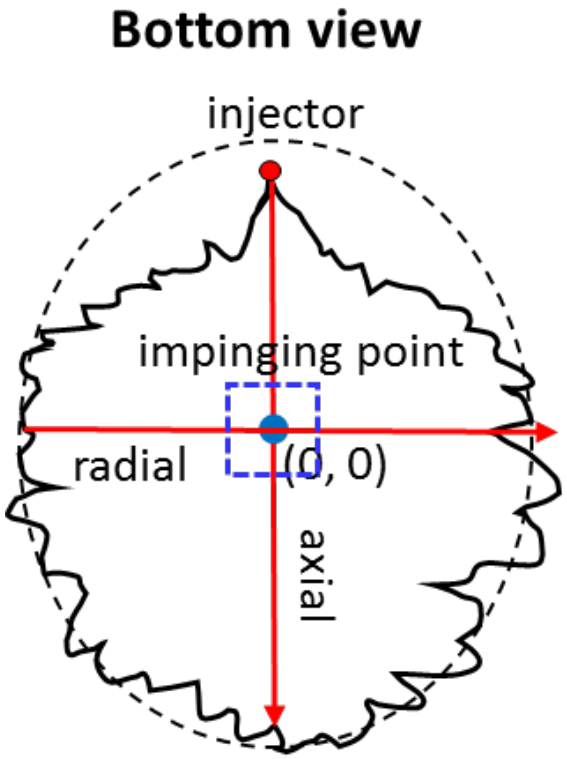

Figure 3.27: Schematic of local and averaged film thickness measurement.

3.5.3.3 Film area measurement in spray-wall interaction test

The film area is measured based on the boundary of the film image, which is post-processed using an in-house MATLAB code by following steps. The sample experimental image in Figure 3.28 is used to show the image processing procedures. First, the raw film image is converted to binary image, based on Otsu's method with the default threshold, the boundary of the binary image is obtained. The threshold value to determine this deposit area in the binary image is found using Otsu's method. A sensitive analysis to the threshold on a sample case is done by increasing and decreasing the default threshold by 20% and the detected film area shows insensitive for different threshold values. Then, the largest connected area based on the selected threshold is considered for exact contouring of the boundary of the spray.

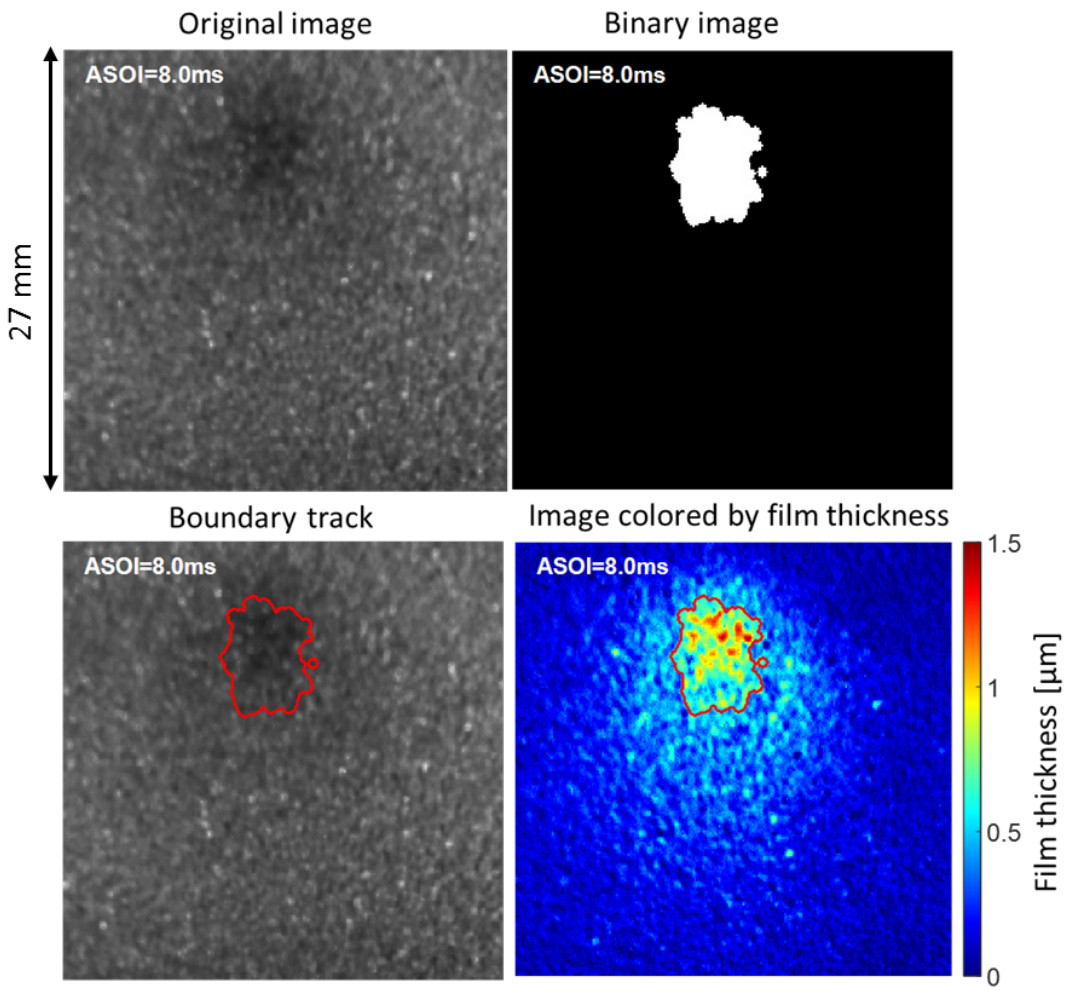

Figure 3.28: Image processing procedure for film area measurement.

During the image processing, the film area is detected by using the fixed threshold after sensitivity analysis. However, when the program extracts the biggest blob area from the binary image of film area, it fills the 'holes' inside the binary area. The points which corresponds to the lower threshold but resides in the biggest blob area are still counted as part of the film area. Therefore, this way may lead to overestimation of film area and film mass.

3.5.3.4 Film mass calculation in spray-wall interaction test

While the temporal evolution of film mass is calculated based on the calibrated film thickness and measured film area in the entire film zone, as shown in Equation (3.7):

$$m_{film}(t) = \rho_{fuel} A_{film}(t) \left(\frac{1}{n}\sum_{i=1}^{n} h(x_i, y_i, t)\right) \quad (3.7)$$

where ρ_{fuel} is the liquid fuel density at the ambient temperature; $A_{film}(t)$ is fuel film area of the entire film region at the certain time; $h(x_i, y_i, t)$ is the film thickness at location (x, y) at the given time.

3.5.4 Spray visualization for multiple spray-to-spray collision

The experimental study for multiple jet-to-jet impinging spray was also conducted in CV to characterize the efficiency of the spray-to-spray collision processes using a simple geometry of multi-hole interacting jet nozzles, see Figure 3.5. The multi-hole IJ nozzle assembly is mounted on one side of the vessel orthogonal to windows to develop gasoline spray. A Z-type schlieren diagnostic is utilized by passing the collimated light through the sample region of interest, and collecting the shadows of the light using an imaging device as seen in Figure 3.29. For the multiple jet-to-jet impinging spray, the spray penetration (including both liquid and vapor penetrations) and post collision angle follow the same procedure as discussed in Chapter 3.5.2.1.

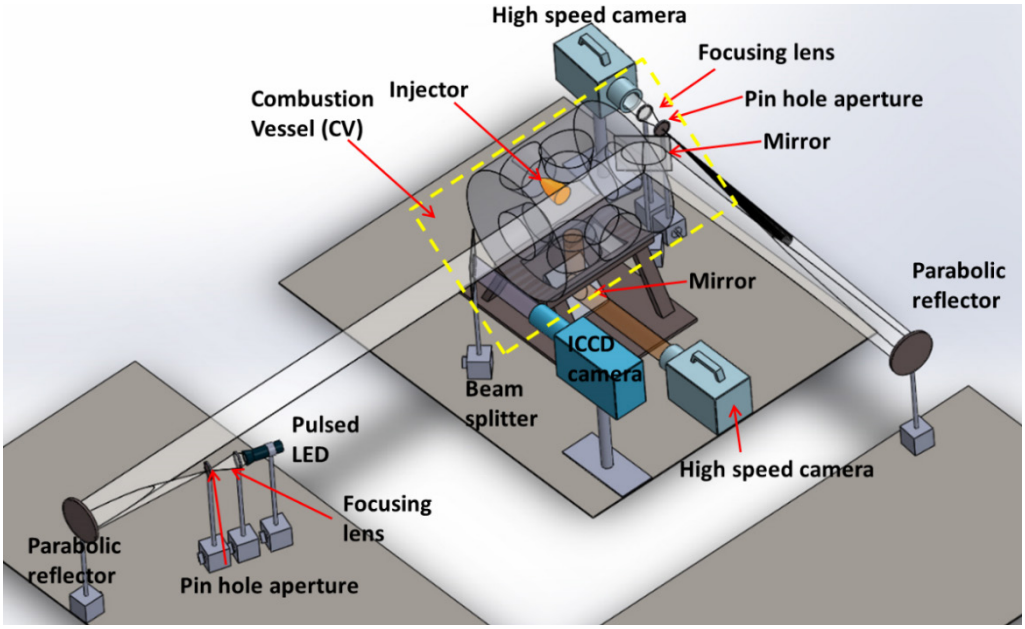

Figure 3.29: Optical setup for schlieren imaging.

3.5.5 Flame luminosity

Combustion luminosity of diesel flame both for spray-wall impingement and multiple jet-to-jet impinging spray tests is captured in the same line of sight of shadowgraph setup as shown in Figure 3.29. The only difference of flame luminosity with shadowgraph is that a neutral density (ND) filter is couple with the camera to reduce the image intensity spectrally along with using a low shutter time since the luminosity was bright enough to saturate the image for diesel imaging (sooty flame). The better diesel flame structure can be finally captured. A sample raw image of diesel spray impingement on wall is shown in Figure 3.30.

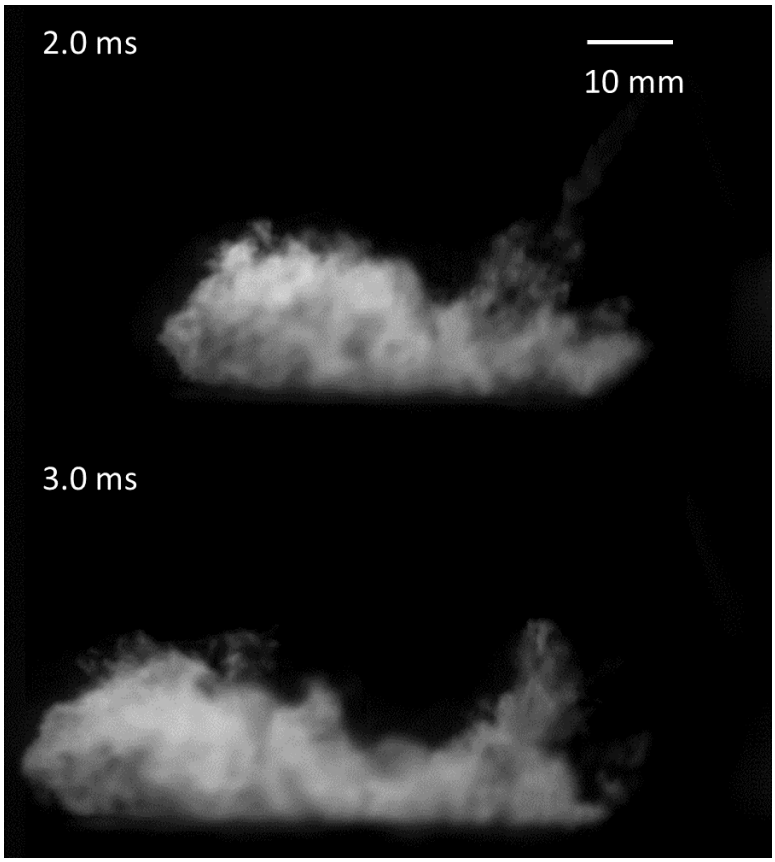

Figure 3.30: Sample combustion images from diesel spray-wall impingement test (19% O_2, injection pressure of 150 MPa, ambient density of 22.8 kg/m^3).

3.5.6 Others optical diagnostics

Laser diagnostics work by the interaction of electromagnetic radiation with sprays and combustion flames and measure temperature, velocity, and constituent concentrations by using scattering, absorption, or emission techniques [55]. There are various laser diagnostics including planar laser-induced fluorescence (PLIF) which is widely used for flow visualization and quantitative measurements, laser induced incandescence (LII) which is for visualizing soot, and laser induced exciplex fluorescence (LIEF) for characterizing fuel-air mixing formation and evaporation phenomenon. Figure 3.31 shows optical arrangement for carrying various tests in CV lab. This configuration allows to do simultaneous imaging of laser test (PLIF, LII), and Schlieren and Mie imaging (or Hybrid).

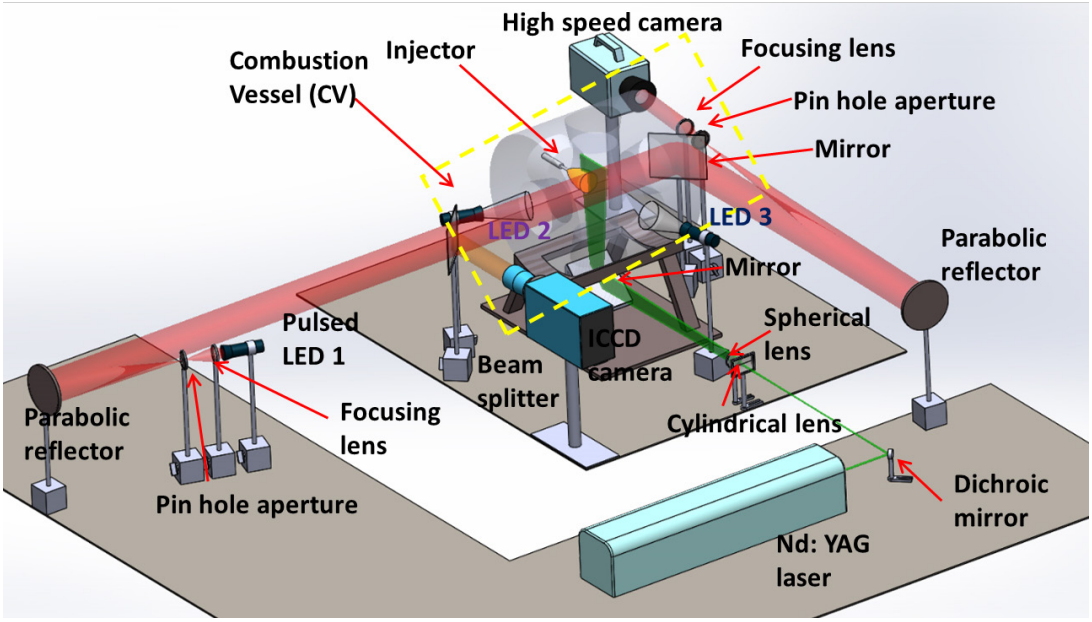

Figure 3.31: Optical arrangement for carrying various tests.

3.6 Heat flux measurement

Three heat flux probes are linearly deployed on the heated impinging plate with 0.5 inch distance of each other. The heat flux probe is a 3-wire heat flux probe that consists of a 0.060 inch probe and two welded junctions. The surface junction is a platinum junction between an independent positive lead and a common negative lead. The embedded junction

shares the common negative lead and is paired with another independent positive lead. The 3-wire probe provides the ability to measure surface, embedded, and differential temperatures. One probe essentially is two "J" type thermocouples (TCs), one is installed at the surface of the plate and the other is at 2 mm directly under the surface thermocouple. The small size of the junction provides the fast time response that can satisfy the data acquisition requirement within injection duration of 2 ms. The voltage signal from the heat flux probes will be sent to a national instrument PXI DAQ system (two PXI 6251 cards and two SCB-68a blocks with CJC built in).

Figure 3.32 (top) shows the schematic of the 3-wire heat flux probe. Figure 3.32 (bottom) shows the testing locations of the three heat flux probes (Location A, B, and C). This sample image is taken from bottom view during a spray impinging on a sapphire window for a better illustration. The red arrow indicates that the spray comes from the top direction. Location A is always set at the center of the impinging plate; other two locations B and C are linearly positioned on the heated plate. The distance between any adjacent locations is 0.5 in. By rotating the heated impinging plate 90^{o} and 180 ^{o}, the three heat flux probes can reach total 7 different locations to examine the heat flux when spray impinges on the heated surface.

The data is obtained from all three heat flux sensors (total 6 J-type TCs) by using a National Instrument DAQ and LabView program. The following equation is used to obtain heat flux from the temperature data obtained.

$$q'' = -k_{ss}\frac{dT}{dy} \tag{3.9}$$

where q'' is the heat flux (W/m^2), k_{ss} is the thermal conductivity of the stainless steel 44.5 W/m-K. dT is the change in temperature between the embedded thermocouple and surface thermocouple and dy is the linear distance between the two thermocouples which is 2 mm.

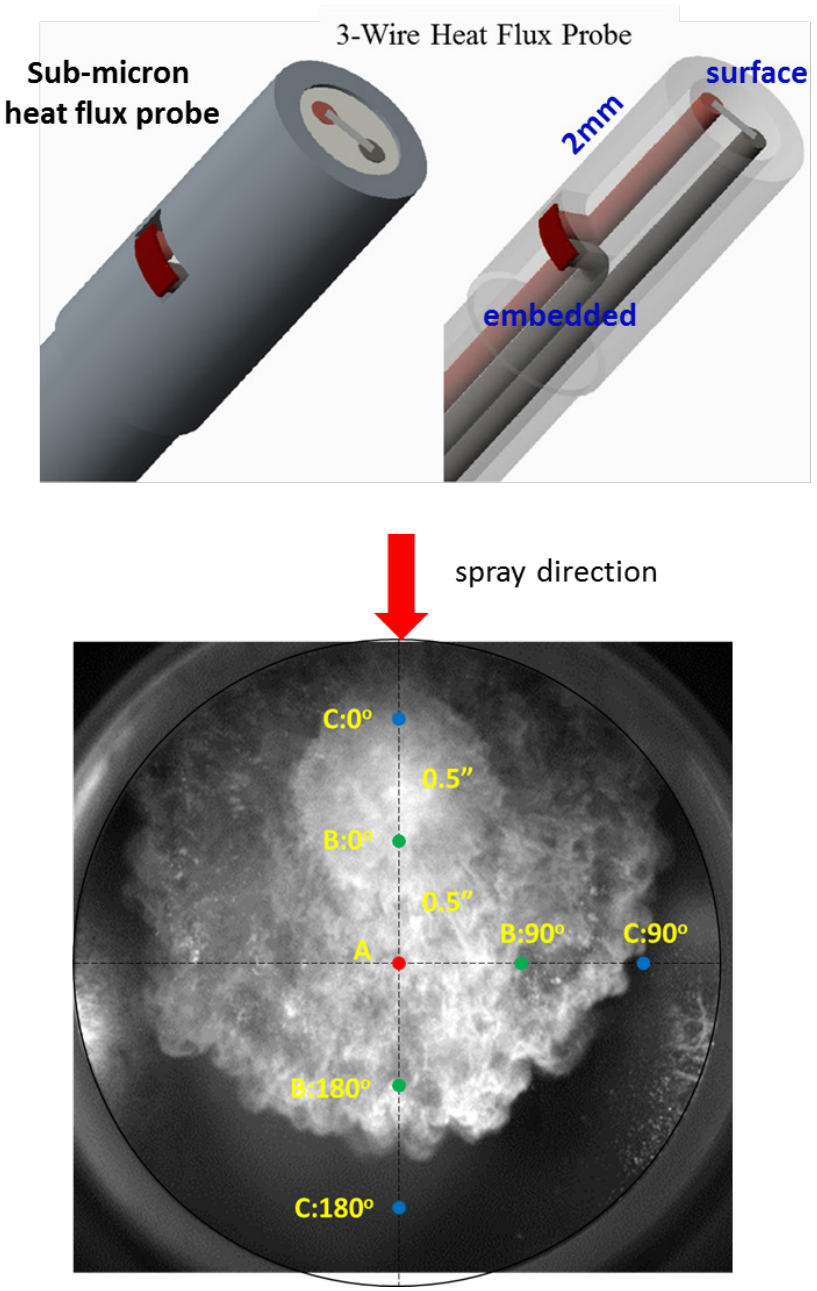

Figure 3.32: Experimental details of the heat flux measurement.

Due to the noise shown in the original signal during the fuel injection, median filter and fast Fourier transform (FFT) are applied to the original temperature profile. Median filter is applied for the portions before and after the injection. FFT is applied for the portion during the injection because of the unreasonable noise from the injection trigger signal; it starts when the injection is triggered. Finally, the smooth signal based on the above two

filters at each portion is obtained and combined to generate the final data. Figure 3.33 shows the temperature profile processing flow. Time after impingement (TAI) is presented for the evolution of heat flux. The detailed information of median filter and FFT, such as cutoff frequency of FFT and the order of median filter, can be found in Chapter 10 Appendices.

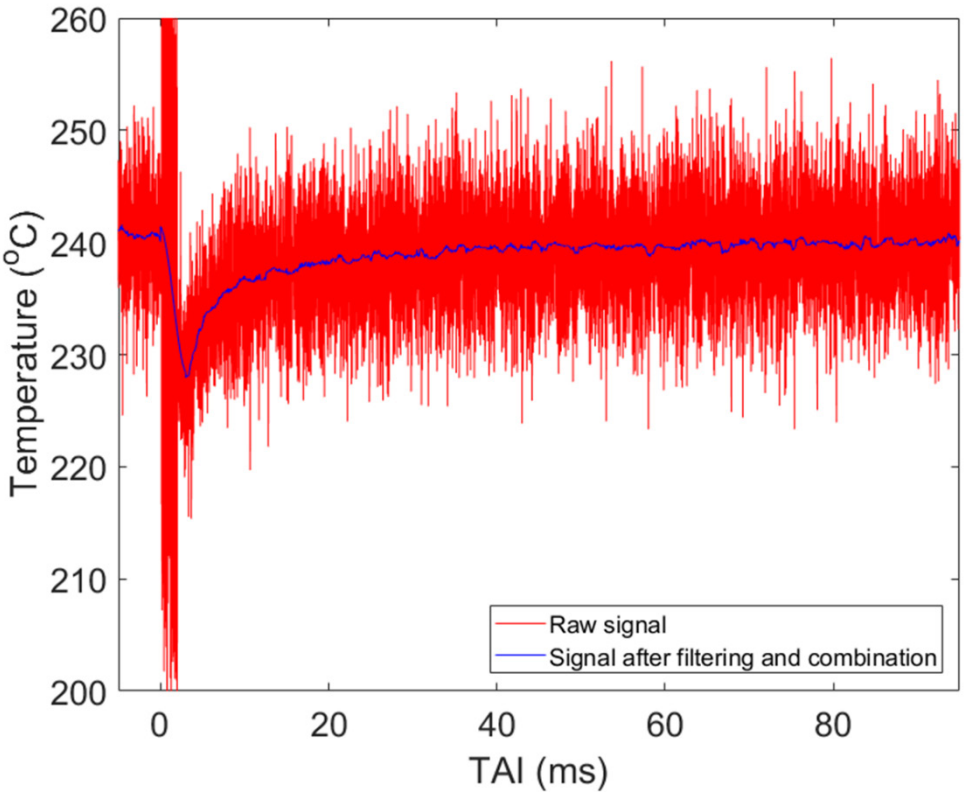

Figure 3.33: Data processing flow of the heat flux data.

CHAPTER 4 NUMERICAL SIMULATION DETAILS

4.1 Introduction

Spray including both non-reacting and reacting process is extensively used in many industrial and transportation areas, for instance, IC engines, liquid rocket engines, furnaces, etc. A deep understanding and accurate prediction of the spray behaviors are important to reach a cleaner and more efficient spray for a better environment and human beings. There are many phenomena and processes involved in the spray and the strong link between them is essential. In normal spray simulations, the turbulence, dispersion, mixing, and combustion require to be considered for the gas phase; whereas the atomization and evaporation have to be modeled for the liquid phase. This two-phase flow is usually coupled with momentum, mass, and heat transfer. Based on the numerical treatment of each phase, there are different approaches to handle the two-phase flow filed: Eulerian-Eulerian, Eulerian, and Eulerian-Lagrangian approaches.

Eulerian-Eulerian method states two fluids and transport equations for continuum properties associated with both fluids are solved. The volume fraction of each phase is weighted with respect to the terms in the transport equations. Each phase and the interaction between any two phases at any location in the space have to be solved, which causes the large costs of Eulerian-Eulerian models. However, only one set of governing equations need to be resolved for all phases in Eulerian approach, which is a tremendous cost-saving compared with Eulerian-Eulerian method. VOF method is one of the most widely used Eulerian approaches. As part of this work, droplet impingement on a solid surface and droplet-to-droplet collision under non-evaporation conditions are simulated by the existing VOF model. A VOF modeling technique that can accurately capture evaporation of droplets impinging on a solid surface is yet to be developed. In particular, modeling evaporation in such complex contact line (encountered in liquid-gas-solid systems) geometries requires an accurate VOF methodology for volume-tracking three-phase systems in 3-D. Therefore, the development, implementation, and validation of a VOF modeling approach including vaporization integrated into CFD codes to provide accurate

and predictive simulation of droplet/spray-wall interactions are performed in the current work. This is accomplished by development and inclusion of an evaporation sub-model in existing VOF modeling framework and it is validated through extensive experimentation of the droplet-wall impingement and droplets collision, spread and vaporization dynamics.

Furthermore, the Eulerian-Lagrangian method is most frequently used in spray and combustion modeling. The dispersed (liquid) phase is solved in Lagrangian method while the continuum (gas) phase by transport equations. The spray-wall impingement and multiple spray-to-spray collision are studied by Eulerian-Lagrangian approach in the present work. When comparing the Eulerian and Eulerian-Lagrangian methods, the main advantage of Eulerian method is that the phase interface can be captured and reconstructed, as well as it is physics basis and requires no physical models or parameter tuning. However, it always calls for a high computational expense and only few properties can be validated with experiment and tracked out. The advantage of Eulerian-Lagrangian method is that it allows to accurately address many physical processes, such as collision, atomization, break-up, heat transfer and so on, with less computational efforts. This makes Eulerian-Lagrangian method more practically applicable. For instance, compared with a single droplet impacting on the wall by VOF model, the VOF based simulation of spray-wall impingement, involving a large number of droplets with different sizes and velocities interacting with the wall, might be impracticable for the engineering application. In addition, the simulation results from Eulerian-Lagrangian approach also provide accurate boundary conditions in terms of droplet sizes, droplet temperature, and flow-field information for the Eulerian based VOF calculations. Besides, it is to be noted that the spray models based on Eulerian-Lagrangian method need to be fine-tuned to achieve better results by validating with the experimental data or VOF simulation results.

In a word, as part of the thesis work shown by the flowchart in Figure 4.1, droplet impingement on a solid surface and droplet-to-droplet collision were simulated by VOF method and evaporation sub-model was implemented based on the existing VOF model. On one hand, VOF calculations capture important details of spray impact dynamics onto an unheated or a heated solid surfaces under non-evaporating and evaporating conditions.

For example, the contact line formed by the impacting droplets in the droplet-wall impingement case is irregular and needs to be captured by a VOF methodology that is capable of robustly reconstructing liquid-gas-solid interfaces. The information obtained from VOF simulation can be used to improve the spray-wall interaction models in the liquid spray Eulerian-Lagrangian method based CFD simulations. As well, the validated evaporation sub-model in terms of droplet relevant simulations can be further extended to study the spray-wall impingement and sprays collision in the VOF context. Moreover, with the inclusion of the results of the VOF analysis on droplet/spray-wall impingement and droplets/sprays collision, accurate predictive simulations of sprays and their impingement or collision can be eventually performed with less need of extensive parameter tuning. On the other hand, for example, the information of local spray characteristics of the impinged or collided spray needs to be extracted at any point in time in order to provide the initial conditions for VOF calculations. The initialization of VOF calculations is done with quantities that can be determined statistically (SMD, *We* and *Re* distributions) and/or locally for both liquid (droplet size, temperature, velocity, etc.) and gas (gas velocity, temperature, pressure, etc.) phases.

In this chapter, the brief overview of the computational work is first introduced as the above. Then, the computational platform is described. Followed by the general Eulerian based VOF method and the implementation of the evaporation sub-model into the existing VOF model. The Eulerian-Lagrangian method and the physical spray models is presented in the next section. Finally, the overall simulation configuration is mentioned.

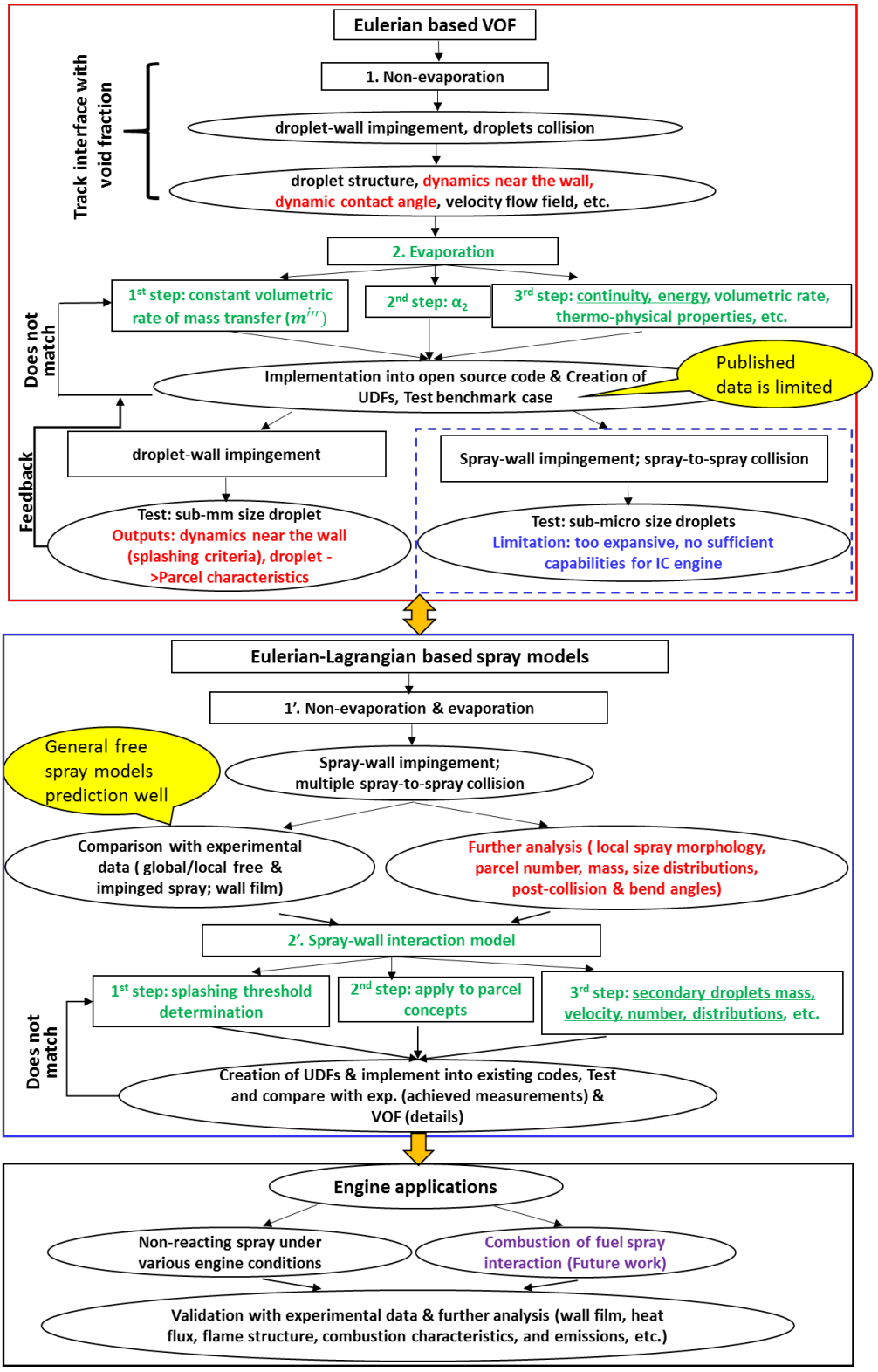

Figure 4.1: Schematic of the CFD work methodology.

4.2 Computational platform

It is important for a successful spray simulation that a well-established computational platform can be offered to integrate all necessary model components efficiently. The typical modern CFD software shows capability to build such a program since it can address millions of lines of code and call for enormous amount of knowledge. The principle of CFD is to use a numerical method to solve differential equations including the mass, energy, species, and momentum. The CFD simulation results can predict details of flow, heat and mass transfer, combustion and other process details, thus the CFD become a powerful tool for optimization and quantitative design. The current numerical study mainly focuses on the spray physical modeling, rather than the CFD code development from scratch, therefore, a couple of existing CFD codes have been applied in the current work and the secondary developments have been performed based on these existing codes. The commercial CFD software CONVERGE® and ANSYS Forte®, and an open source CFD package OpenFOAM® were used in the research of this thesis.

The open source CFD code such as OpenFOAM® attracts the attention in the past decade, attributing to its accessibility and transparency. The open source code has many validated models available and the development of these code is primarily driven by the active user community. However, the insufficiently source code documentation and the reading and understanding issue of the code usually happen, the accuracy and stability of the open source code may not be guaranteed. Hence, users need to be more patient and careful when using such code. CONVERGE® and ANSYS Forte® are commercial CFD software owned by Convergent Science Inc. and ANSYS Inc., respectively. Both of them have been widely used by academic research and industrial applications to solve many sorts of practical problems such as spray and combustion characteristics of IC engines. A second-order spatial discretization was used to resolve the flow field, while time-dependent quantities were described with a first-order accuracy using a Courant–Friedrichs–Lewy (CFL) based time-step. There are many required and similar models available which can be directly applied to solve a certain problem in both software.

In the thesis, OpenFOAM® is used at the initial stage and the simulation results are presented in Chapter 5. The main purpose of using OpenFOAM® is to carry out part of droplet impingement and droplet-to-droplet collision simulation work based on the VOF method and develop the evaporation VOF sub-model to simulate the droplet impingement on a hot surface. However, limitations of using OpenFOAM® exist, for instance, VOF method implemented in OpenFOAM simulates only incompressible immiscible flows. CONVERGE® is then selected to simulation the droplet impingement on a solid surface by comparing with the experimental data. The evaporation VOF sub-model is also applied into CONVERGE framework to further study the evaporation and heat transfer process when a droplet impacting onto a hot surface. Further, most spray simulations with respect to Eulerian-Lagrangian method, for example, the analysis of free and impinged spray properties based on the spray-wall impingement and multiple jet-to-jet impinging spray, are obtained by CONVERGE®, the simulation results from CONVERGE® are presented in Chapters 5, 6, and 7. Furthermore, ANSYS Forte® is used to achieve a better validation and understanding of spray wall-film study due to its novel spray wall-film model. Use of ANSYS Forte® to carry out the wall film properties is presented in Chapter 6.

Although the different CFD codes are used in the current study, the general concepts behind the solver, in particular, the Eulerian based VOF method and Eulerian-Lagrangian method used for spray simulations are almost same at these codes. The detailed VOF method and spray models are introduced in the following sections.

4.3 Eulerian based VOF method

4.3.1 Non-evaporation governing equations

The conservation laws of mass and momentum are used to describe the fluid motion of isothermal, single phase flows. Multiphase flows involving two or more phases require additional equations to describe each of the additional phases and the relation between phase properties. These additional equations are transport equations of void fraction variables and are solved to capture the interface. They are solved simultaneously with the conservation equations of mass and momentum. The conservation of mass is expressed as

continuity equation. The momentum equation is obtained by balancing the total forces acting on a fluid element with gravity forces, viscous forces, surface tension and body forces.

The mass conservation and momentum equation for compressible flows are expressed as follows,

$$\frac{\partial \rho}{\partial t} + \nabla \cdot (\rho \boldsymbol{U}) = 0 \tag{4.1}$$

$$\frac{\partial (\rho \boldsymbol{U})}{\partial t} + \nabla \cdot (\rho \boldsymbol{U} \otimes \boldsymbol{U}) = -\nabla p + \nabla \cdot \left[2\mu S - \frac{2\mu (\nabla \cdot \boldsymbol{U}) I}{3} \right] + f_{st} + f_g \tag{4.2}$$

where I is identity matrix, p is pressure, μ is dynamic viscosity, f_{st} is surface tension force and f_g is gravity force.

$$S = 0.5[\nabla \cdot \boldsymbol{U} + (\nabla \cdot \boldsymbol{U})^T] \tag{4.3}$$

The continuity and momentum equations for incompressible flows are obtained by considering the changes in density of an infinitesimally small element as negligible or zero as follows [131, 132]:

$$\nabla \cdot (\boldsymbol{U}) = 0 \tag{4.4}$$

$$\rho \left(\frac{\partial U}{\partial t} + \boldsymbol{U} \cdot \nabla \boldsymbol{U} \right) = -\nabla p + \nabla \cdot [\mu (\nabla \cdot \boldsymbol{U} + (\nabla \cdot \boldsymbol{U})^T)] + f_{st} + f_g \tag{4.5}$$

In VOF, an interface capturing method, and the location of interface is known based on the value of a scalar function called, void fraction. It is represented by α,

$$\alpha = \frac{V_g}{V} \tag{4.6}$$

where V_g is the volume of gas phase and V is the total volume of the control volume.

Void fraction α is 1 in liquid phase, 0 in gas phase and between these two values (0 and 1) at interface. Its value is defined at the center of the cell. Mass of each phase is conserved

when the transport equation of its phase fraction is satisfied. Transport equation of void fraction α is given by

$$\frac{\partial \alpha}{\partial t} + \boldsymbol{U} \cdot \nabla \alpha = 0 \tag{4.7}$$

Interface separating the phases is a numerical discontinuity in fluid properties. VOF method of modeling multiphase flows neglects the discontinuity and involves obtaining a mixture representation of two or more phases. Transport properties and velocity of the mixture phase are obtained by volume averaging the properties of individual phases.

$$\rho = \rho_g \alpha + (1 - \alpha)\rho_l \tag{4.8}$$

$$\mu = \mu_g \alpha + (1 - \alpha)\mu_l \tag{4.9}$$

$$\boldsymbol{U} = \boldsymbol{U_g} \alpha + (1 - \alpha)\boldsymbol{U_l} \tag{4.10}$$

where ρ_g is the density of gas phase and ρ_l is the density of liquid phase; μ_g is the viscosity of gas phase and μ_l is the viscosity of liquid phase; $\boldsymbol{U_g}$ is the viscosity of gas phase and $\boldsymbol{U_l}$ is the viscosity of liquid phase.

4.3.2 Governing equations with evaporation

Phase change in VOF is modeled using source terms in continuity, momentum and phase fraction equations along with the transport equation of temperature. In the current work, multiphase flows with three phases are considered: liquid, its vapor phase, and surrounding gas. Vapor and surrounding gas are modeled as continuum phases without interface separation between them. This continuum phase is referred to as gaseous phase. Vapor diffuses in gas, however both vapor and gas are insoluble in liquid phase. The bulk or advection based velocities of both gas and vapor phases are identical. Two void fraction variables are used to describe the presence of three phases: liquid void fraction (α_1) and vapor void fraction (α_2). When α_1 = 1, representing only liquid fuel phase, and When α_2 = 1, standing for only vapor fuel phase. The detailed information of liquid and vapor void fractions is shown in Equations (4.11) and (4.12) and Figure 4.2.

$$\alpha_1 = \begin{cases} 0 & \text{In surrounding air or vapor fuel phase} \\ 0 < \alpha_1 < 1 & \text{At liquid interface} \\ 1 & \text{In liquid fuel phase} \end{cases} \tag{4.11}$$

$$\alpha_2 = \begin{cases} 0 & \text{In liquid or surrounding air phase} \\ 0 < \alpha_2 < 1 & \text{vapor fuel and surrounding air mixed} \\ 1 & \text{In vapor fuel phase} \end{cases} \tag{4.12}$$

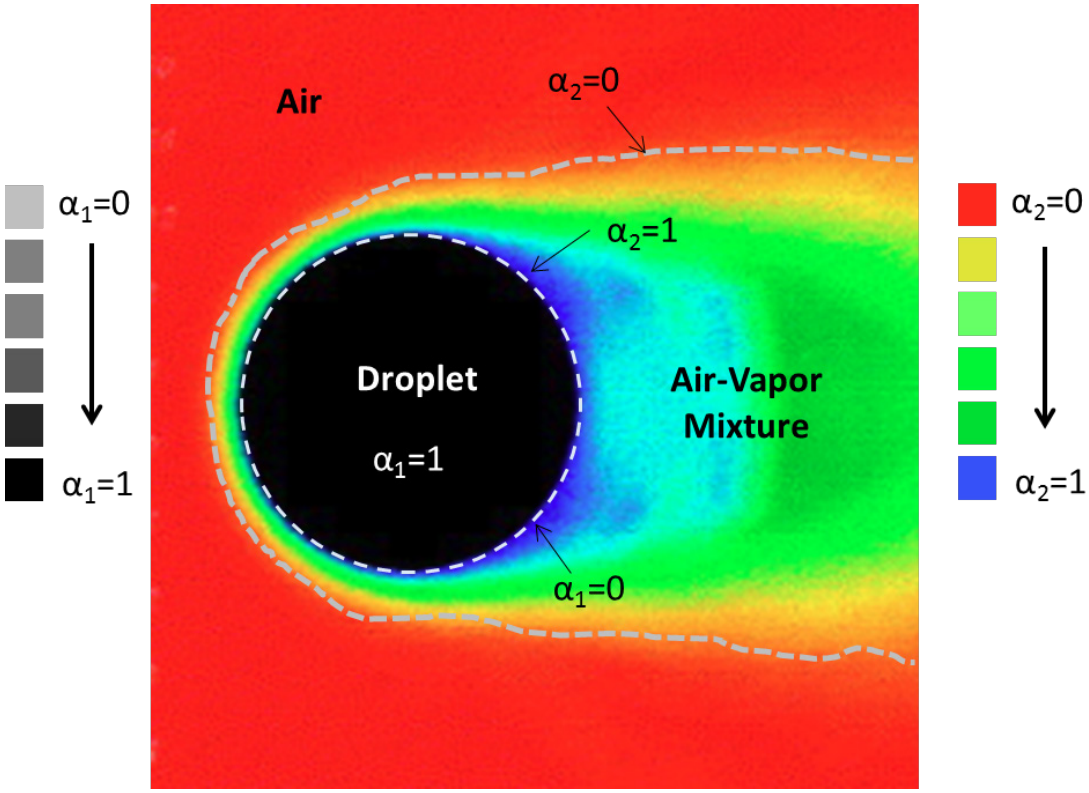

Figure 4.2: Schematic of liquid and vapor void fractions in the computational domain.

Transport properties like density *(ρ)*, thermal conductivity *(k)* of individual phases are volume averaged to obtain properties of single mixture phase.

$$\rho = \alpha_1\rho_l + \alpha_2\rho_v + (1 - \alpha_1 - \alpha_2)\rho_g \tag{4.13}$$

$$k = \alpha_1 k_l + \alpha_2 k_v + (1 - \alpha_1 - \alpha_2)k_g \tag{4.14}$$

where ρ_l is the liquid fuel density, ρ_v is the vapor fuel density, and ρ_g is the surrounding gas density; k_l is the liquid fuel conductivity, k_v is the vapor fuel conductivity, and k_g is the surrounding air/gas conductivity.

Specific heat (c_p) at constant pressure is obtained by mass averaging the specific heats of individual phases.

$$c_p = \rho_l\alpha_1 c_{p,l} + \rho_v\alpha_2 c_{p,v} + \rho_g(1 - \alpha_1 - \alpha_2)c_{p,g} \tag{4.15}$$

where $c_{p,l}$ is the liquid fuel specific heat, $c_{p,v}$ is the vapor fuel specific heat, and $c_{p,g}$ is the surrounding gas specific heat.

Velocity is modeled as,

$$\boldsymbol{U} = \boldsymbol{U}_l\alpha_1 + \boldsymbol{U}_{gp}\alpha_2 + \boldsymbol{U}_{gp}(1 - \alpha_1 - \alpha_2) \tag{4.16}$$

Or simply as

$$\boldsymbol{U} = \boldsymbol{U}_l\alpha_1 + (1 - \alpha_1)\boldsymbol{U}_{gp} \tag{4.17}$$

where $\boldsymbol{U}_{gp}$ is velocity of gaseous phase (including vapor and surrounding gas).

Mass transfer during the phase change in incompressible flows is modeled as addition or removal of liquid or vapor volume, which modifies the continuity equation as,

$$\boldsymbol{\nabla} \cdot (\boldsymbol{U}) = -\dot{m}'''\left(\frac{1}{\rho_l} - \frac{1}{\rho_v}\right) \tag{4.18}$$

where $\dot{m}'''$ is the volumetric rate of mass transfer [133] from liquid phase to vapor phase due to the temperature and mass fraction gradient and is calculated as follows,

$$\dot{m}''' = \frac{D_{vg} * \rho_{gp}}{1 - Y_v} \nabla Y_v \cdot \nabla \alpha_1 - \frac{k}{h_v} * \nabla T \cdot \nabla \alpha_1 \tag{4.19}$$

where D_{vg} is diffusivity of vapor in gas and ρ_{gp} is density of gaseous phase (including vapor and surrounding gas).

Mass fraction of vapor phase (Y_v), is calculated using vapor phase volume fraction, density of vapor and gaseous phases as follows,

$$Y_v = \frac{\alpha_2}{1 - \alpha_1} \frac{\rho_v}{\rho_{gp}} \tag{4.20}$$

The momentum equation as shown in Equation (4.5), obtained by balancing the total forces acting on a fluid element with gravity forces, viscous forces, surface tension and body forces, is not affected by the evaporation sub-model. Therefore, no source terms are added to momentum equation as their effect is already introduced in continuity equation.

The interface between liquid and gaseous phases is assumed to be at saturation state during phase change. Mass fraction of vapor at interface [133] is given by,

$$Y_{v,\,sat} = \frac{P_{v,\ sat}}{P} * \frac{M_v}{M_{gp,\,sat}} \tag{4.21}$$

where $P_{v,\ sat}$ is saturated vapor pressure, P is static pressure, M_v is molecular weight of vapor, M_g is molecular weight of gas/air and $M_{gp,\,sat}$ is molecular weight of gaseous phase.

$$M_{gp,\,sat} = \frac{P_{v,\ sat} * M_v + (P - P_{v,sat}) * M_g}{P} \tag{4.22}$$

Saturated vapor pressure is calculated using the Wagner equation [133] given by,

$$P_{v,\ sat} = \frac{P_c * T_c}{T} * \left[a * \left(1 - \frac{T}{T_c}\right) + b * \left(1 - \frac{T}{T_c}\right)^{1.5} + c * \left(1 - \frac{T}{T_c}\right)^{3} + d * \left(1 - \frac{T}{T_c}\right)^{6} \right] \tag{4.23}$$

where T_c is critical temperature and P_c is critical pressure.

Energy equation is introduced to model the effect of heat transfer. The source term in the energy equation is the heat transferred due to mass transfer during evaporation.

$$\frac{\partial(\rho c_p T)}{\partial t} + \boldsymbol{\nabla} \cdot \left(\rho \boldsymbol{U} c_p T\right) = \boldsymbol{\nabla} \cdot (k \boldsymbol{\nabla} T) + h_v \, \dot{m}''' \tag{4.24}$$

The temperature at the interface is constrained to saturation temperature and surface superheat is not considered.

Transport equations of liquid and vapor volume fractions have source terms to simulate reduction of mass from liquid and addition of mass to vapor phase during evaporation. If $\dot{m}'''$ represents the volumetric rate of mass transfer from liquid to vapor and an artificial interface compression flux term is introduced, the liquid phase fraction transport equation can be represented as Equation (4.25) and the vapor phase fraction transport equation can be represented as Equation (4.26),

$$\frac{\partial \alpha_1}{\partial t} + \boldsymbol{\nabla} \cdot (\boldsymbol{U} \alpha_1) \; + \boldsymbol{\nabla} \cdot \left((1 - \alpha_1) \boldsymbol{U}_r \, \alpha_1\right) = \alpha_1 (\boldsymbol{\nabla} \cdot \boldsymbol{U}) - \dot{m}''' \left(\frac{1}{\rho_l} - \alpha_1 \left(\frac{1}{\rho_l} - \frac{1}{\rho_v}\right)\right) \tag{4.25}$$

$$\frac{\partial \alpha_2}{\partial t} + \boldsymbol{\nabla} \cdot (\boldsymbol{U} \alpha_2) - \boldsymbol{\nabla} \cdot (\alpha_2 \boldsymbol{U}_r \, \alpha_1) = \boldsymbol{\nabla} \cdot \left(D_{vg} \boldsymbol{\nabla} \alpha_2\right) + \alpha_1 (\boldsymbol{\nabla} \cdot \boldsymbol{U}) +$$

$$\dot{m}''' \left(\frac{1}{\rho_v} + \alpha_1 \left(\frac{1}{\rho_l} - \frac{1}{\rho_v}\right)\right) \tag{4.26}$$

Although this evaporation sub-model is developed for the incompressible flows as described in the above equation, it is found to be also compatible for the compressible flows as the error due to the incompressible assumption is much less than 10% [134]. Significant improvements in the simulation results will be achieved by considering the evaporation and clarifying the vapor fuel and surrounding gas phases quantitatively.

The overall algorithm used to solver the evaporation problem is described. Initially available fields are ($\mathbf{U}^0$, T^0, α^0) at t = 0 and a pseudo time-step projection is performed to

yield a divergence free initial velocity field. The following time cycle is performed: for all t^n [n = 1 → (N) maximum time step]

1. Compute $\dot{m}'''$ using T^{n-1} and thermo-physical properties.
2. Advect α (α_1 and α_2): α^{n-1}->α^n using $\dot{m}'''$ as the source.
3. Update thermo-physical properties at all computational cells.
4. Predict velocity by excluding the pressure field: $\mathbf{U}^*$ => (convection + viscous + surface tension + gravity)
5. Compute pressure field by projecting $\mathbf{U}^*$ into divergence free space except near the interface
6. Correct the velocity field to compute $\mathbf{U}^n$ from $\mathbf{U}^*$ by adding contribution of ∇p.
7. Repeat steps (3) to (5) until convergence in $\mathbf{U}^n$.
8. Compute T^n by solving the conservation of energy.

4.4 Eulerian-Lagrangian based spray models

The Lagrangian description of the liquid spray was modeled through the Discrete Droplet Modeling approach by Dukowitz [135] which consists of a fully interacting combination of Eulerian gas phase and Lagrangian liquid particle calculations. This approach is known to present consistent advantages in terms of both avoidance of numerical diffusion and computational affordability. In the current study, the liquid fuel spray is modeled as dispersed phase in Lagrangian framework and the surrounding air is modeled as continuous phase in Eulerian framework. Navier-stokes equations are solved for continuum phase. The effect of dispersed phase on continuous phase is modeled by the implementation of source terms in Navier-Stokes equations as discussed in Chapter 4.2.1. For the dispersed phase, particle position is given by vector X_d and its motion is given by,

$$\frac{dX_d}{dt} = U_d \tag{4.27}$$

Sum of all forces acting on a droplet is given by force F_i and is considered as the sum of gravity and drag forces [132].

$$\sum F_i = m_d * \frac{dU_d}{dt} \tag{4.28}$$

where m_d is the mass of each droplet.

In addition, various spray models are available within the two commercial codes used in the thesis to model spray, liquid drop dynamics, turbulence, and combustion. The blob injection model developed by Reitz [136] was employed to model the primary atomization of the liquid parcels . For the secondary breakup, the Kelvin Helmholtz – Rayleigh Taylor (KH-RT) model as implemented by Patterson and Reitz [137] was used. This model combines in a competing manner the development of the Kelvin-Helmholtz instabilities [136] arising on a jet surface with the theoretical consideration of Taylor [138], who investigated the stability of liquid-gas interfaces when accelerated in a normal direction with respect to the plan that contains them. The droplet collision was modeled with the No Time Counter method [139] combined with the Post Collision Outcomes, [140] which include both the stretching and reflecting separations together with grazing collision and coalescence outcomes. The evaporation of the liquid and the consequent droplet radius rate of change were described through the Frossling correlation [141]. The momentum exchange between the two phases was described with the dynamic drag model. In the implementation proposed by Liu et al. [142], the model accounts for the distortion of drops due to the interaction with the flow, considered as a spring-mass system. This theory, known as Taylor's analogy, condenses the effect of the drop distortion in the calculation of a coefficient known as droplet distortion parameter and ranging between 0 and 1. This parameter is then used to linearly scale the calculation of the drag coefficient of a distorting drop between the lower limit of a rigid sphere and the upper limit of a disk, which represent the two opposite conditions of minimum and maximum distortion acting on a droplet.

4.4.1 Spray-wall interaction model

In the current work, spray-wall impingement was studied based on two spray-wall interaction models. To address the global impinged spray properties at the initial stage of the spray-wall impingement study, the spray-wall interaction model by O'Rourke and Amsden [99] was used. To further analyze the film formation and quantitative the film properties including film thickness, mass, and wetted area, the spray-wall film model by Han et al. [98] was applied.

In Chapter 2.4.2, the spray-wall impingement models from O'Rourke and Amsden and Han et al. are briefly discussed. The theory of O'Rourke and Amsden's model [99] accounts for rebounding, sticking and splashing of the liquid droplets under conditions of both dry and wet wall. The model evaluates the property of the droplets at the moment of the impact on the wall and, on the basis of the droplet *We* and the thickness of the wall film (if already present) modifies the droplet size and velocity. Very low Weber (*We*) numbers (less than 5, in this study) are typical of rebounding droplets. Higher values of *We* correspond to droplets that can either partially or completely splash, or become part of the wall film. The splashing occurs if the parameter E^2 exceeds a fixed critical value, according to Equation (2.2).

In addition to a splash criteria, splash results in a number of secondary droplets from the impingement location. The expressions for the secondary droplets mass, size distribution, and velocity distribution need to be derived. In the basis of the experimental results of the total mass of secondary droplets from Yarin and Weiss [28], the following expression is developed to show the ratio of the total mass (m_s) of secondary droplets to the incident droplet mass (m_0),

$$\frac{m_s}{m_0} = \begin{cases} 1.8 \cdot 10^{-4}\left(E^2 - E_{crit}^2\right) for\ E_{crit}^2 < E^2 < 7500 \\ 0.75\ for\ 7500 < E^2 \end{cases} \tag{4.29}$$

Both Mundo et al. [29] and Yarin and Weiss [28] reported the secondary droplets size distributions are reported, the probability density functions (PDFs) of secondary droplet radius divided by incident drop radius are given and the results are consistent with a

Nukiyama-Tanasawa [143] size distribution. Secondary droplet velocity distributions were developed based on the jet model hypothesis by Naber and Reitz [97] and experimental results from Mundo et al. [29] The averaged normal and tangential velocities of secondary droplets were scaled with incident droplet normal and tangential velocities, respectively. Whereas, the widths of the normal and tangential velocity distributions of secondary droplet were scaled approximately with incident droplet normal velocity [96, 99].

Han et al. [98] extended and improved the impingement regimes splash criterion for both dry and wet surface including the surface roughness effect after O'Rourke and Amsden's work. The wall impingement model determines the outcome of the collision between the droplet and the wall when an airborne spray droplet hits a wall surface, depending on the *Re* and *We* of the incident droplet and the surface condition. Four impingement regimes are considered, including stick, rebound, spread and splash. The regime transition criteria for a wetted wall as used in ref. [71] are employed in ANSYS Forte®:

1. Stick: $We \leq 5$
2. Rebound: $5 < We \leq 10$
3. Spread: $We > 10$ and $WeRe^{0.5} < H_{cr}$
4. Splash: $WeRe^{0.5} \geq H_{cr}$

The splash threshold H_{cr} is proposed by Han et al. [98] as shown in Equation (2.3). Splash results in the rebounding of many smaller secondary droplets from the impinging location. The correlation for the secondary droplets mass fraction from Han et al. [98] is given as,

$$\frac{m_s}{m_0} = 0.75(1 - \exp(-10^{-7}(H - H_{cr})^{1.5}) \tag{4.30}$$

where $H = WeRe^{0.5}$.

In Han et al.'s model, the size distributions of the secondary droplets are also modeled using a Nukiyama-Tanasawa [143] size distribution. The secondary droplets velocity distributions follow the general idea of O'Rourke and Amsden [96, 99] and the flying angle of droplet along the azimuthal direction on the impinged surface is also based on the jet

analogy [97]. The difference to derive the secondary droplet velocity distributions with O'Rourke and Amsden [99] is that a function was introduced to model the tangential velocity magnitude distribution along the azimuthal direction to obtain the realistic spray shapes. The detailed process and description on secondary droplets size and velocity distributions can be found to ref. [98].

4.5 Turbulence model

Turbulence is a non-linear fluid motion of irregular in space and chaotic in time, this movement exhibits a very complex flow state; its complexity mainly presents randomness, rotation and statistic of the turbulent flow. The basis of turbulence is Navier-Stokes equations. Since Navier-stokes equations deal with different scale of turbulence, turbulent numerical simulation method is divided into three types: Direction Numerical Simulations (DNS), RANS and Large Eddy Simulations (LES) [144]. RANS and LES models which are two commonly used turbulence models will be introduced below.

RANS simulation is also known as statistical theory of turbulence. It averages the unsteady Navier-stokes equations of time and solved the time-averaged amount. There are two different RANS models. One is Standard k-ε model which solves turbulent kinetic energy and dissipation rate equations. Turbulent kinetic energy transport equation is derived through a precise equation, but the dissipation rate equation is obtained by physical reasoning and simulating the similar prototype equation. The standard k-ε model assumes that the flow is fully turbulent and viscosity of molecule can be ignored. Therefore, the standard k-ε model is only suitable for fully turbulent flow simulation [145]. Another RANS model is Re-Normalization Group (RNG) k-ε model which is derived by using a mathematical method of renormalization group on instantaneous Navier-stokes equations, developed from $k-\varepsilon$ model by Yakhot and Orszag [146] using a statistical technique called renormalization. It uses wall functions to model flow nearby wall thereby eliminating the need for a fine mesh near walls.

In the current study, the turbulence closure was ensured using the Standard k- ε model [147]: the round-jet correction theory [79] was exploited to properly address momentum transport and dissipation in the gas phase.

In addition, the main idea of LES is briefly introduced since LES overcomes some of the limitations of the RANS approach by directly simulating larger eddies which are on the order of the size of the mesh and are influenced by the flow field. It becomes one of the major trends to deal with the complex turbulence. In the context of LES, the large eddy is influenced significantly by the flow field but small scale vortices can be considered to be isotropic. Thus, the calculations of large and small eddy can be addressed separately, as well as use unified model to calculate the small eddy. Under this thinking, large eddy simulation is conducted through a filtering process. First, filtering out the vortex which is smaller than a certain size from the flow field and only considering large eddy [148, 149]. Then, get the solution of small vortices by solving additional equation. Usually the scale is taken for filtering is grid scale. LES is more efficient and more accurate than solving RANS equations, as well as less consumption of system resources. There are sub-models divided into two classes: zero-equation and one-equation. For zero-equation models, no additional transport equations are solved. For one-equation models, an additional transport equation is added for sub-grid kinetic energy. The sub-models in the zero equation models including upwind LES, smagorinsky model, dynamic smagorinsky model; and the one equation models contains one equation viscosity model, dynamic structure model, consistent dynamic structure model [132].

4.6 Combustion model

Combustion plays an essential role in the internal combustion engine working process. There are a variety of combustion models like SAGE model, Representative Interaction Flamelet (RIF) model, SHELL and Characteristic Time Combustion (CTC) model, and Extended Coherent Flamelet Model 3 Zone (ECFM3Z) model. The theory of the models is presented below.

SAGE model [150], which is the combustion model used in the current study, allows using detailed chemical kinetics in combustion simulations with a set of CHEMKIN formatted input files. SAGE calculates the reaction rates for each elementary reaction based on Arrhenius type correlation while the CFD code solves the transport equations. The governing equations for mass and energy conservation can be solved for a given computational cell and at each computational time-step; and the species are updated appropriately. With an accurate reaction mechanism, SAGE can be applied for modeling any combustion regimes like ignition, premixed and mixing-controlled in gasoline and diesel combustion scenarios. Note that SAGE is commonly used with a multi-zone solver, which solves the cells with similar thermodynamic conditions in groups and saves run-time.

RIF model is based on the laminar flamelet idea from Peters [151, 152]. Later, a stable term of the Favre-averaged mixture fraction and a varying term of mixture fraction variance were considered for calculation of species mass fraction by Pitsch et al. [153]. As part of the RIF model, mass fraction of the species is found as a function of mixture fraction. Then to calculate back the mass fraction in each cell, a β-PDF distribution of the mixture fraction is used. RIF model can handle detailed chemistry, but the procedure of solving the combustion chemistry is based on the transformation from mixture fraction space to real 3D space. As explained in the SAGE model description above, detailed chemistry is handled based on Arrhenius rate equations combined with transport equations in the SAGE detailed chemistry solver.

SHELL and CTC models are two individual combustion models. SHELL model is used to predict the auto-ignition in diesel engines based on a set of eight reactions [154]. CTC model [155] on the other hand assumes that seven species are involved in the combustion process: fuel (C_nH_{2m}), O_2, N_2, CO_2, H_2O, CO, and H_2.In the CTC model, the species are solved by a set of atom balances, equilibrium constant equations and water-gas shift reaction using a Newton-Raphson solver technique. Thus, by using the SHELL and CTC models together, the SHELL model solves for the computational cells which are in the ignition stage and the CTC model solves the cells which are in the combustion process.

ECFM3Z model originates from the Extended Coherent Flame Model of Colin et al. [155]. The ECFM model has been successfully used in premixed fuel combustion environment of gasoline engines [156-158]. This is modified to model combustion in perfectly or partially mixed mixtures. As part of the ECFM3Z model, a 'Conditioning averaging technique' allows for accurate calculation of local flame properties in burnt and burning mixtures. The ECFM3Z model is for a diesel like application unlike the gasoline application of the older ECFM model. This calls for an inclusion of a 'mixing state' for diesel like combustion to account for the unmixed combustion. Thus, the ECFM model is applied to 3 zones, a pure fuel zone (injected fuel), a pure air plus possible residual gases zone (burnt fuel and re-circulating air or EGR) and a mixed zone. Using the ECFM3Z model for diesel combustion scenario requires the predictability of auto-ignition together with premixed and diffusion flame construction. Auto-ignition is modeled using either a simplified cetane number based correlation or using an outside input from CHEMKIN which models for different auto-ignition times based on varying ambient conditions.

4.7 Other simulation configurations

In general, the computational domain used in the current simulations was a cylinder with a certain dimension which represented the constant volume CV domain. The different size of injectors for different purpose of simulations were mounted in one of the chamber walls. The orthogonal hex volume mesh elements were generated as the base mesh size in all simulations. Both CONVERGE® and ANSYS Forte® adopt a Cartesian cut-cell approach to mesh generation, which is done at run time. A user-supplied base mesh size represents the size of the largest cells in the domain, and there is the ability to perform AMR based on local gradients in fields such as temperature, velocity, and species in CONVERGE®. The similar concept to automatically generate the mesh can be found in ANSYS Forte®. As well, the fixed embedding at various levels over the base mesh size in specific regions of interest during certain portions of the simulation, such as at the nozzle exit during injection or near the impinged surface region is used to increase the resolution. Fine mesh is obtained from the base mesh as in Equation (4.31).

$$fine\ mesh = \frac{based\ mesh}{2^{embed\ level}} \tag{4.31}$$

In addition, spray models and model constants for each application study are summarized in Chapter 10 Appendices.

CHAPTER 5 MAIN RESEARCH CONTRIBUTIONS

Generally, this dissertation covers the different scenarios of interaction during fuel spray injection, such as droplet-wall impingement, droplet-to-droplet collision, spray-wall impingement, and multiple spray-to-spray collision. The fundamental mechanism and dynamic process of spray impinging/colliding are studied to get a sound understanding of their overall behaviors. The current research makes contributions in the following ways:

First, based on the literature review, it is known that many empirical correlations and assumptions were introduced during studying droplet impingement on a solid substrate due to the complexity of physics of droplet-wall interaction and the lack of the detailed experimental data. Therefore, the conclusions such as the splashing criterion summarized from the previous work are flimsy when evaluating it with respect to the experimental data in this work. In the current study, the experimental work with a wide range of operating conditions is provided to examine the droplet impingement regimes including splashing and deposition. The evolution of the dynamic process of droplet-wall interaction is also explored. Few droplet-wall impingement experiments took into account the liquid fuels such as water, diesel, n-dodecane, and n-heptane, which are extensively used in the fuel injection process under engine operating conditions. In the current experimental work, the aforementioned liquid fuels and the various surface conditions including smooth, roughened, unheated, and heated surfaces are tested to obtain a new splashing correlation. In addition, the evolution of the dynamic process of a specific liquid droplet-wall interaction with the measurement of key parameters such as spreading factor and dynamic contact angle is discovered. Contact angle is often determined experimentally and is required as a boundary condition for modeling problems, including certain stages of the drop impingement problem. In particular, it provides the crucial information on the development of dynamic contact angle model under DNS or VOF methodology.

Second, since the VOF model is a physics based model and requires no parameter tuning, it is often applied to study droplet-wall impingement or droplet-to-droplet collision under non-evaporation conditions. For such non-evaporation problems, only liquid and

surrounding gas phases exist. The existing VOF model does not address the phase change if evaporation occurs in these problems. Therefore, an evaporation sub-model is developed and implemented into the OpenFOAM® and commercial code. This sub-model is broadly based on the existing VOF model but a few significant enhancements with respect to the volume of conservation and the velocity of interface are employed. Under the evaporation conditions, three phases (liquid fuel, vapor fuel, and surrounding gas phases) are present. In order to distinguish the vapor fuel and surrounding gas phases, the additional variables of liquid and vapor void fractions (α_1 and α_2) are introduced. This evaporation sub-model is tested with the past studies and used to investigate the dynamic process of multi-droplet impingement on wall. The important details of droplet impact dynamics onto a solid surface under non-evaporating and evaporating conditions are captured and the information obtained from VOF simulation can be used to improve the spray-wall interaction models used in the Eulerian-Lagrangian based liquid spray simulations. In addition, this evaporation sub-model can be further applied to study the spray relevant behaviors under engine operating conditions, in which the mixing of fuel-air is important for quality of combustion in IC engines.

Third, the experimental spray-wall impingement work contributes to the exploration of the dynamic impinging process at various diesel engine operating conditions. This gives insight into the nature of primary and secondary vaporization formation when spray impinging on the wall. Primary vaporization occurs before the spray impingement, whereas secondary vaporization occurs after the spray impingement. The vapor fuel mixing process with ambient gas is qualitatively described by the mechanism of spray-wall interaction. The post-impingement dynamics is quantitatively illustrated by the measured key parameters such as the temporal impinged spray radius, impinged spray height, and impinged spray expansion ratio. The wall film formation process and characteristics that directly influence the pollutant emissions during IC engine combustion process are also investigated. The evaporation process of wall film is examined through the natural spray-wall film images and global and local film properties. These targeted experimentations of the spray-wall interaction under conditions matching the thermodynamic charge state and

surface temperatures to those of engines support development and validation of the spray-wall interaction models. An Eulerian-Lagrangian with RANS approach was employed to characterize spray-wall impingement, liquid film formation, and post-impingement processes. In particular, the local spray morphology near the impingement location, as related to the diesel engines. As well, the information of local spray characteristics of the impinged or collided spray is extracted at any point in time to provide the necessary conditions for DNS or VOF simulations.

Other than the above, the contribution of multiple spray-to-spray collision under gasoline engine conditions is to investigate vaporization mechanism as a function of the impingement location and the collision breakup process of the multiple colliding sprays. The inception of collision process and spray behaviors of the different types of multiple spray-to-spray collision injectors also assists in practical application of designing of such novel injectors.

CHAPTER 6 DROPLET-WALL IMPINGEMENT AND DROPLETS COLLISION[1]

This chapter presents results from experiments and simulations for droplet-wall interaction and droplets collision. The first section discusses the experimental and numerical study of a single droplet impinging on wall at iso-thermal condition. The next section presents the results obtained from droplet to droplet collision at the ambient conditions through the numerical method. The final section summarizes the multi-droplet impinging on a high temperature flat surface.

6.1 Droplet-wall impingement

6.1.1 Experimental results

The test conditions of a single droplet impingement on the flat surface are listed in Table 6.1. Four different fuels were used for droplet-wall impingement test and their detailed properties are listed in Table 6.2; the range of the essential dimensionless parameters of impact *We* and *Re* are also given.

---

[1]Reprinted with permission from SAE papers 2017-01-0852 ©2017 SAE International and 2018-01-0289©2018 SAE International. The materials in this chapter were published in the following papers:

- Zhao, L., Ahuja, N., Zhu, X., Zhao, Z. et al., "Splashing Criterion and Topological Features of a Single Droplet Impinging on the Flat Plate," SAE Technical Paper 2018-01-0289, 2018.
- Potham, S., Zhao, L., and Lee, S., "Numerical Study on Evaporation of Spherical Droplets Impinging on the Wall Using Volume of Fluid (VOF) Model," SAE Technical Paper 2017-01-0852, 2017, https://doi.org/10.4271/2017-01-0852.

Table 6.1: Test conditions for single droplet-wall impingement

Parameter	**Values**
Ambient temperature (°C)	25
Ambient pressure (atm)	1
Fuel	diesel, water, n-dodecane, n-heptane
Height between needle and impinged surface (mm)	26 - 456
Impact velocity U_0 (m/s)	0.72- 3.0
Surface temperature (°C)	25; 130 (heated surface)
Average surface roughness R_a (μm)	1.6 (smooth); 16 (roughened)

Table 6.2: Liquid properties

Parameter	**diesel**	**water**	**n-dodecane**	**n-heptane**
ρ (kg/m^3)	848	1000	750	684
σ (N/m)	0.024	0.070	0.023	0.019
v (cSt)	2.6	1.0	1.97	0.38
D_0 (mm)	2.87	3.6	2.86	2.6
We	52 - 925	26 - 458	43 - 833	45 - 836
Re	789 - 3300	2562-10718	1037- 4339	4941- 20669

Figure 6.1 shows a sequence of droplet shape evolution at various time instants for diesel and water with the dynamic impingement process of a liquid droplet onto a smooth surface. The initial droplet-impinged surface distance of 52 mm was chosen as the baseline non-splashing condition and therefore the corresponding impact *We* for diesel is 104 and impact *We* for water is 53. For splashing condition, the initial droplet-impinged surface distance of 286 mm was chosen. The corresponding impact *We* for diesel is 569 and impact *We* for water is 289. Since the initial droplet-surface height is a large value compared with the droplet size, the initial location of droplets is not shown in Figure 6.1, and instead, the center of droplets to the plate are set to the same distance of 4 mm for all conditions to show the pre-impingement phenomena. In addition, due to the different exposure time applied for different fuels, there is an obvious difference of the visualization of liquid

droplet with background images. Besides, the time stamps are selected with respect to the time when droplet just impacts on the plate (i.e., t = 0 ms when droplet interacting with the plate). The time stamps along with each image illustrate slightly variances in water and diesel fuels as a result of the particular events occurring at the different time, especially after droplet impinging on the surface.

A series of *non-splashing* events for droplet impinging on a smooth plate with the baseline test condition is observed in Figure 6.1 (top). From left to right, there are (a) pre-impingement, (b) impingement, (c) post-impingement, (d) maximum spreading, and (e) receding. In Figure 6.1 (top) (a), the initial water droplet size (D_0 = 3.6 mm) is larger than diesel droplet (D_0 = 2.87 mm); In Figure 6.1 (top) (b), as stated in Image processing section, the droplet size shows no substantial change before impinging on the surface due to the insignificant influence of the drag force on it; After impingement, it can be clearly seen in Figure 6.1 (top) (c) that droplets start spreading radially with the current view, the diesel droplet spreads more rapidly compared with water droplet at 1.8 ms due to the larger surface tension of water (see Table 6.2); In Figure 6.1 (top) (d), the water droplet reaches its maximum spreading factor of 2.4 around 6.0 ms and diesel droplet achieves its maximum spreading factor of 3.1 around 11.0 ms; In short period after spreading as shown in Figure 6.1 (top) (e), the water droplet begins receding under the effect of capillary force, however, it is difficult to observe the receding in diesel droplet due to higher viscosity and lower surface tension of diesel fuel. Afterwards, the droplets tend to be stable which corresponds to the equilibrium stage (not shown here). The quantitative comparison of spreading for non-splashing case will be discussed in the following sections.

Similarly, Figure 6.1 (bottom) shows a series of *splashing* events for droplet impinging on a smooth plate with the baseline test condition. From left to right, there are (a) pre-impingement, (b) impingement, (c) splashing, (d) further splashing, and (e) primary deposited equilibrium. In Figure 6.1 (bottom) (a) and (b), the initial droplet size of diesel (D_0 = 2.87 mm) and water (D_0 = 3.6 mm) are the same as mentioned in the non-splashing case; After interacting with the plate, in Figure 6.1 (bottom) (c) droplets spread radially and splash at 1.0 ms, the stronger splashing is observed in diesel droplet in comparison to

water due to higher surface tension of water. Based on Yarin and Weiss [28] and O'Rourke and Amsden [96, 99], the splash threshold corresponds to the formation of a kinematic discontinuity. The velocity discontinuity, located at the boundary between fluid moving outward from the splash location and slower moving fluid on the surface, leads to fluid to be ejected away from the surface. The secondary droplets are then generated; In Figure 6.1 (bottom) (d), the diesel and water droplets further splash into a number of secondary droplets, because of smaller surface tension in diesel case, more satellite droplets are formed in diesel case. On the other hand, oscillation is observed in water case due to the higher surface tension of water; Around 40 ms after droplets impinging on the plate, as shown in Figure 6.1 (bottom) (e), both diesel and water droplets tend to achieve the equilibrium stage while the spreading diameter in diesel is longer than that in water case.

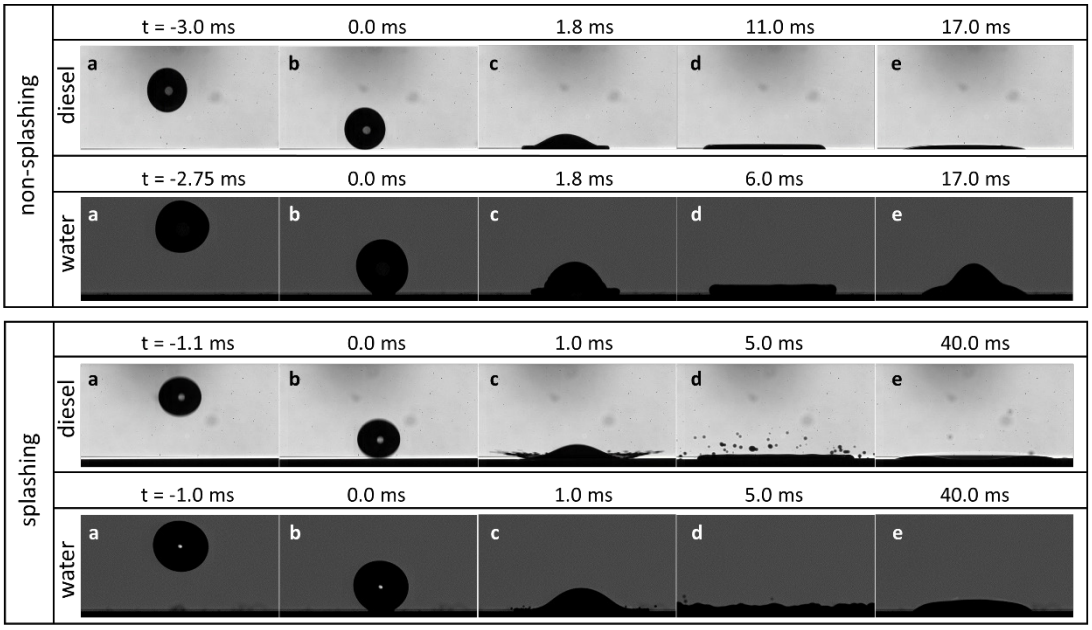

Figure 6.1: A sequential visualization of droplet-wall impingement experiment for diesel and water: non-splashing (top); splashing (bottom).

6.1.1.1 Splashing Criteria

As discussed in Introduction section, the splashing threshold of $Ca\lambda^{\frac{3}{4}} = u > 17 \sim 18$ is found by Yarin and Weiss [28], who studied a single train droplets falling on a solid

substrate with a thin film at a known impinging frequency (*f*). Figure 6.2 (top) provides the correlation between Capillary number (*Ca*) and non-dimensional diffusion length (λ), the black solid line represents the splashing criteria line obtained from Yarin and Weiss [28]. The data points shown in Figure 6.2 (top) represent our experimental results at various conditions (including variation of liquid viscosity, surface tension, smooth and roughened surfaces, heated plate), where the red points denote the splashing events while the blue points signify the non-splashing events. Overall, our experimental results follow the same trend in predicting the non-splashing phenomena with the literature for water, diesel, and n-dodecane, but not for n-heptane. The data points from non-splashing cases with n-heptane fuel are observed to shift towards the splashing region. On the other hand, the data points representing splashing characteristics from other fuels cross the Yarin and Weiss's splashing criteria line (solid black line). As stated in previous, Yarin and Weiss's criterion may not work for many cases since the derived splashing threshold provides an explanation only for corona splash but not for prompt splash mechanism. Moreover, this correlation posed under an assumption of no interaction of droplet with the solid dry surface instead of a thin liquid film; therefore, it may not be applied for droplet impingement directly on a dry surface. Therefore, the best fit for the current experimental data is found to be between a dash line showing $Ca\lambda^{\frac{3}{4}} = 12$ and a round dot line exhibiting $Ca\lambda^{\frac{3}{4}} = 10$ in Figure 6.2 (top). It should be noted that the frequency (*f*) in the current work is assumed to be U_0/D_0 [106], λ can be further derived as $\lambda = \frac{Re^{1.5}}{We}$. As well, $Ca = \frac{We}{Re}$, $Oh = \frac{We^{0.5}}{Re}$. Therefore, the correlation based *Ca* and λ is also noticed as the relation in terms of *Oh* and *Re*.

We have also discussed another splashing criteria based on *Oh* and *Re* in Chapter 2.4.4, which was presented by Ma et al. [101] by summarizing a larger number of researchers' experimental data at various test conditions shown in Figure 6.2 (bottom). The black dash line stands for the splashing correlation of $OhRe = 17$ from Ma et al. [101], the rest of four dash lines exhibit the correlations of $OhRe^{1.25} = 124.3$, $OhRe^{1.25} = 126.7$, $OhRe^{1.17} = 63$, and $OhRe^{1.29} = 197.9$ from Geppert et al. [159], Cossali et al. [160],Vander Wal et al. [103], and Bernard et al. [161], respectively. Most of blue symbols from our experiment are below these critical lines while most of red data points are above it. However, one of the

exceptions occurs again in n-heptane case, rather than following the splashing criteria line of *OhRe* = 17, n-heptane data points resides at *OhRe* of 26. It is also observed that splashing on the roughened plate happens slightly below the *OhRe* = 17 because the probability of prompt splash increases as the amplitude of roughness increases [30].

Although a great number of experimental studies done on the droplet-wall interaction, due to the complexity of physics of droplet-wall interaction and the limitations of the experimental data, the splashing criteria is necessary to be studied and improved. The best correlation in terms of the current experimental data and test conditions is found as follows:

$$OhRe^{0.886} = 6.7 \tag{6.1}$$

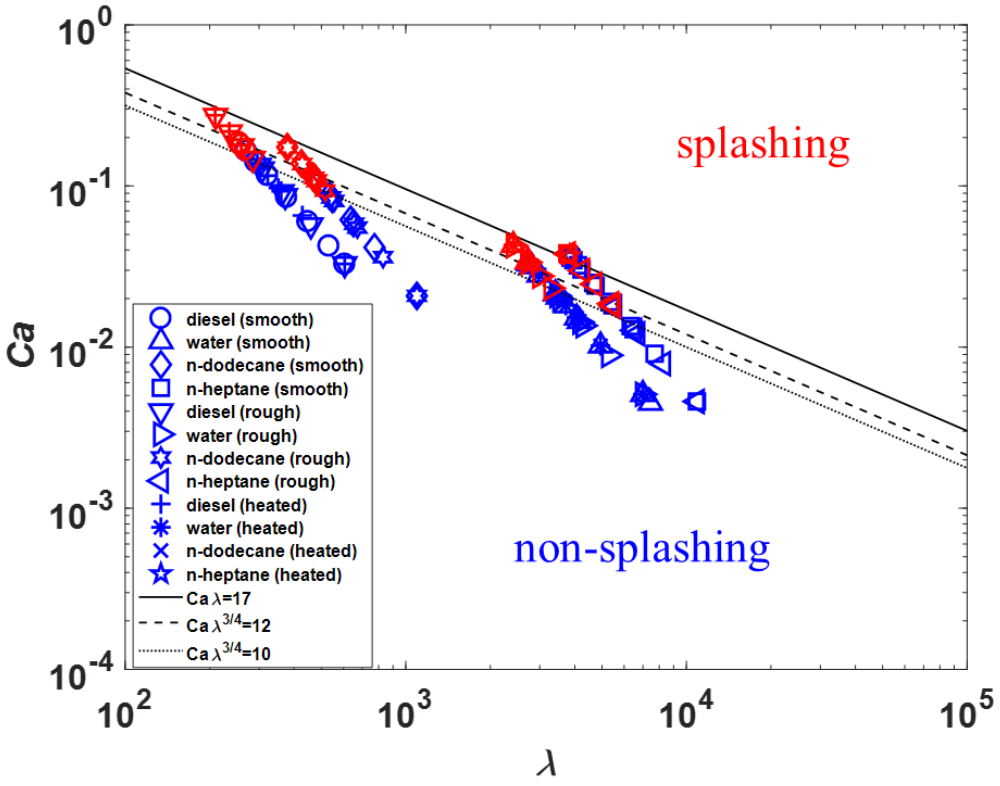

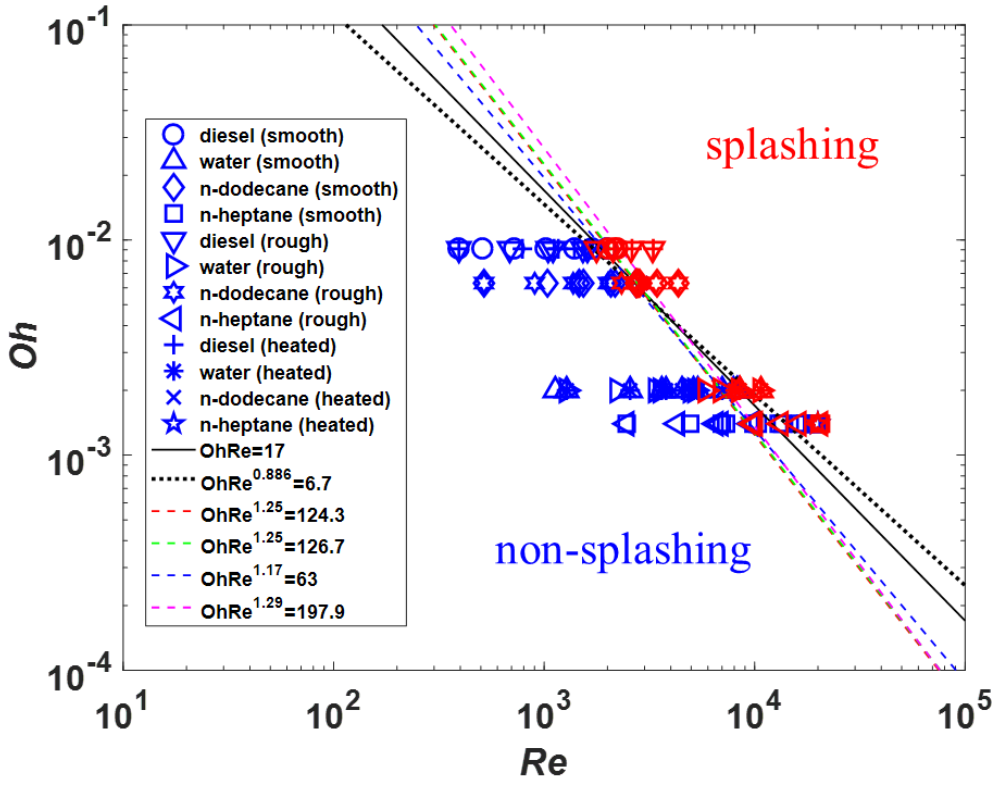

Figure 6.2: Splashing criteria for various test conditions: *Ca* vs. λ (top); *Oh* vs. *Re* (bottom).

To further understand and examine the splashing correlation, for instance, the splashing threshold from Yarin and Weiss [28] determined by *Ca* and λ is discussed. As the formulas below, *Ca* represents the relative effect of viscous forces versus surface tension acting across an interface between a liquid and a gas; λ is known as the non-dimensional viscosity length.

$$Ca = \rho U_0 \nu/\sigma = We/Re \tag{6.2}$$

$$\lambda = \left(\frac{\nu}{f}\right)^{0.5} \sigma/(\rho \nu^2) \tag{6.3}$$

As the black dash line (splashing criteria line) shown in Figure 6.3, at any splashing conditions, assuming the liquid density ρ, impact velocity U_0, and the droplet initial diameter D_0 are constants, Equations (6.2) and (6.3) become:

$$Ca \sim \nu/\sigma \tag{6.4}$$

$$\lambda \sim \sigma/\nu^{1.5} \tag{6.5}$$

At the same viscosity ν, Ca decreases and λ increases as the surface tension σ increases. This means that to ensure the splashing occurring, a relative longer viscosity length is needed to overcome the surface tension force, namely, a larger surface tension holds the droplet break-up until a certain viscosity length reaches and vice versa. Note that viscosity is resistant to flow motion while the surface tension is the force of attraction acting between the liquid molecules.

Similarly, at the same surface tension σ, Ca increases and λ decreases as the viscosity ν increases. This indicates that a relative shorter viscosity length ensures the splashing occurrence, viz., a higher viscosity results in a shorter viscosity length after droplet spreading on the wall, leading to the break-up of droplet and vice versa.

Moreover, the experimental data points as shown in Figure 6.2 have been looked into, it is interesting to point out that the data points are regularly seated in the figure with certain slopes, for example, and four sets of data are observed from Figure 6.2 (top) in terms of four different tested liquid fuels. Diesel and n-dodecane with similar liquid properties are shown in the left two sets but water and n-heptane are shown in the right two sets of Figure 6.2 (top). In addition, Diesel and n-dodecane have relatively higher viscosity and lower surface tension than water and n-heptane. To describe and extend this phenomenon by a general way, as the red and blue lines shown in Figure 6.3, with any given liquid fuel, the liquid properties remain unchanged at a given condition, Equations (6.2) and (6.3) become:

$$Ca = C_1 U_0 \tag{6.6}$$

$$\lambda = C_2 D_0^{0.5}/U_0^{0.5} \tag{6.7}$$

where $C_1 = \rho\nu/\sigma$ and $C_2 = \sigma/(\rho\nu^{1.5})$ are constants.

In Figure 6.3 (top), as the impact velocity U_0 increases and the droplet initial diameter D_0 remains the same, Ca increases and λ decreases, causing higher chance of splashing occurrence and vice versa.

When the droplet initial diameter D_0 increases, Ca remains the same but λ increases. Therefore, the dash line consisted by data points shifts toward the right as D_0 increases due to the change of λ as displayed in Figure 6.3 (bottom). However, the slope of the line based on the data sets shows insignificant change with D_0. It was also found that this slope shows no substantial change when the same size droplets with different liquid fuels were considered, as the experimental data points shown in Figure 6.2.

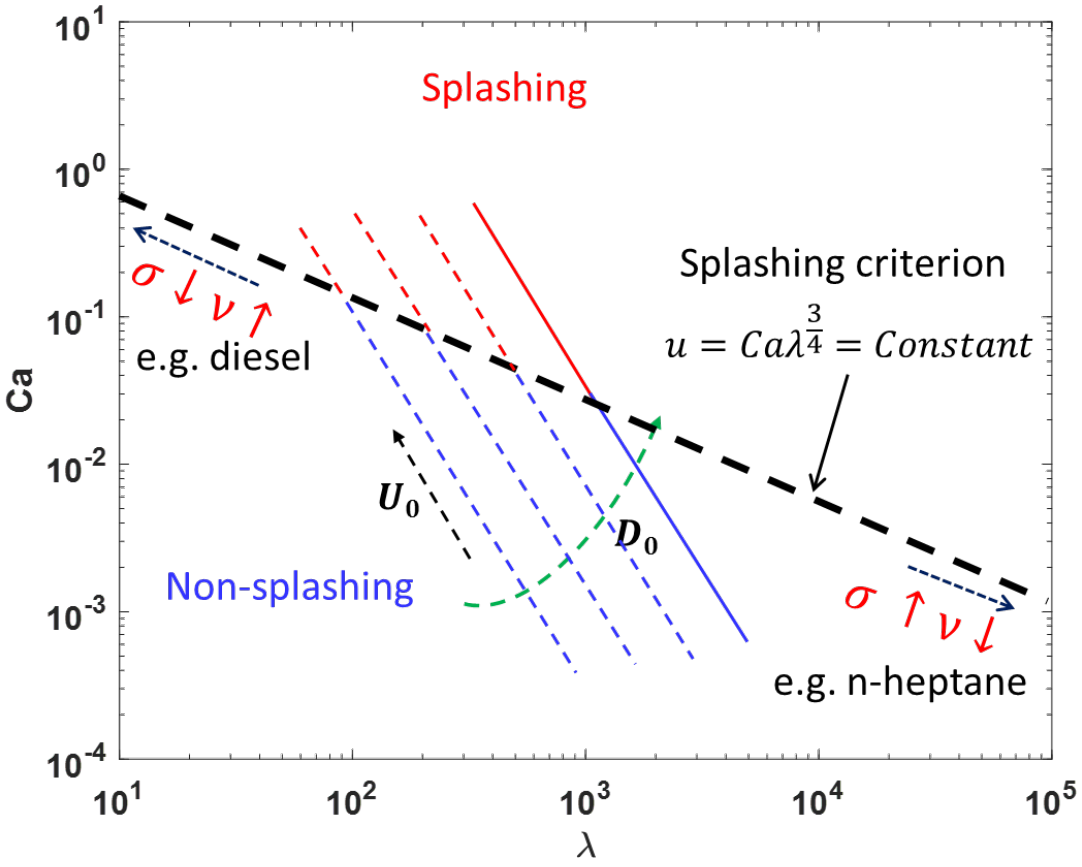

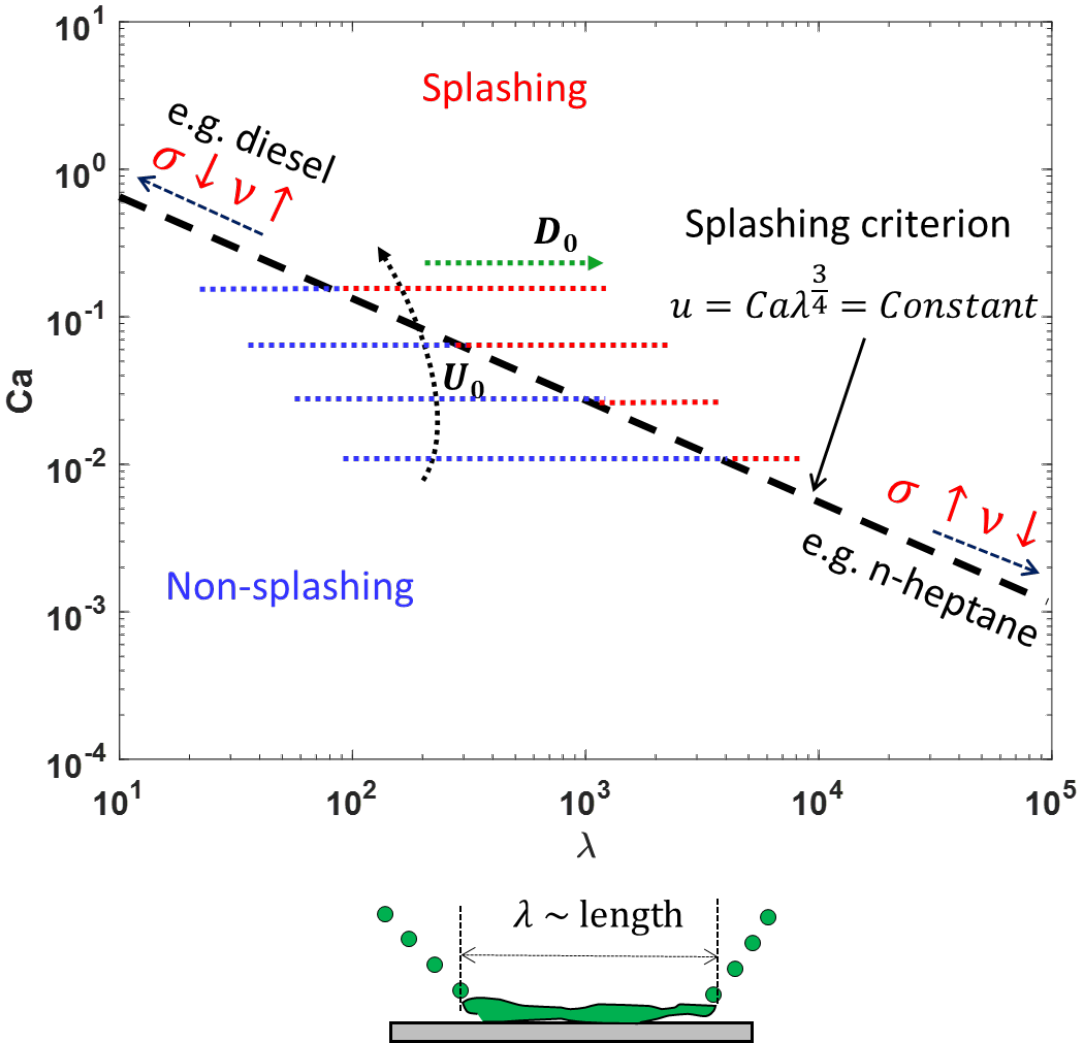

Figure 6.3: Schematic of splashing criteria: red and blue dash line (D_0 = constant) (top); red and blue dot line (U_0 = constant) (bottom);

In consideration of the above analysis, the cross point of the splashing criteria line and the data sets with different liquid fuels and droplet initial diameter differentiates the non-splashing (blue) and splashing (red) characteristics. Since the current experiment tested sub-mm based droplets which shows the larger magnitude compared with typical droplets found in high pressure sprays, thus, the correlations and the concepts are summarized from Figure 6.3 might be proposed and extended to the actual sub-μm based droplets splashing study. Other than the liquid properties and droplet size, from another point of view, only the spherical droplets are considered in the present work but the droplet shape before or

after impingement and further splashing is possible changed into an unregual shape. This behavior is also necessary to be taken into account for the universal spalshing correlation development, which can be supproted by Eulerian based VOF simulations.

As discussed in Chapter 2.1.3, according to Schiaffino et al. [52], the spreading process after droplet impact can be classified into four regimes characterized by impact *We* as a driving force and *Oh* as a resisting force as shown in Figure 6.4. In region I, at low *Oh* and high *We*, the spreading is driven by dynamic impact pressure and resisted primarily by inertia, and viscous effect is relatively weak. The data points shown in Figure 6.4 represent our experimental results at various conditions (including variation of liquid viscosity, surface tension, smooth and roughened surfaces, heated plate), it is observed that all experimental data points fall in region I as the range of *We* is 26 to 925 and the range of *Oh* is 0.0014 to 0.009. Therefore, it can be concluded that the droplet-wall interaction results at the conditions described in this work are inviscid-impact driven. In this region, from the high-speed images (as shown in Figure 6.1), in the final stage of spreading, the contact line advance slows after the main part of the spreading is over. Additionally, other three regimes are inviscid-capillarity driven (at low *Oh*, low *We*); highly viscous-capillarity driven (at high *Oh*, low *We*); highly viscous-impact driven (at high *Oh*, high *We*), respectively.

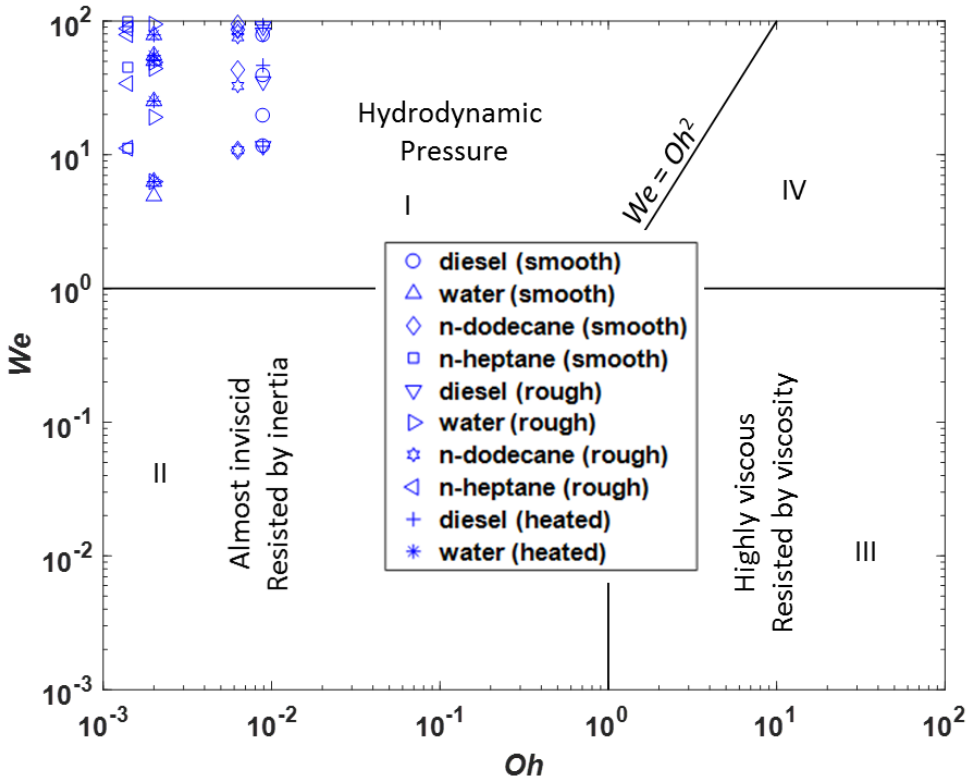

Figure 6.4: Regime map of spreading.

6.1.1.2 Post-impingement evolution

In this section, initially, the effect of impact *We* (or initial droplet-plate height) on the temporal evolution of spreading and dynamic contact angle for diesel and water will be presented and followed by the temperature effect on the post-impingement process. Then, the roughness effect based on the impinged plate on the dynamic process of droplet-wall interaction are presented.

6.1.1.2.1 Impact *We* effect

The results of the effect of impact *We* on spreading factor, height ratio, contact line velocity, and contact angle for a single droplet impinging on an unheated smooth surface are presented in this section. Due to a larger number of test conditions, diesel and water are chosen as the reference fuels, three non-splashing conditions for each fuel are selected to

be shown here. In terms of the heights between initial location of droplet and the impinged plate, these three conditions are 26 mm, 52 mm, and 104 mm, the corresponding impact *We* is 52, 104, 207 for diesel; 26, 53, 105 for water, respectively. Nevertheless, the relevant results from the remaining different impact *We* conditions are summarized in Table 6.3 and Table 6.4. In addition, the experimental results at each condition are averaged from five runs and after start of impingement (ASOI) time is presented for the post-impingement evolution.

Figure 6.5 shows the spreading factor (top) and height ratio (bottom) for diesel fuel at various impact *We* conditions. During the initial stage of the impingement, the droplet reaches the plate and starts expanding outward with respect to the impinging point under the impact pressure. In general, the spreading factor increases as the impact *We* increases while the height ratio decreases with the impact *We*, which is caused by the relatively higher impact velocity at the higher impact *We* case driving the droplet to move outward. In sequence, the droplet achieves the maximum spreading factors obtained are 3.4, 3.1, and 2.8 around 8 ms, 11 ms, and 24 ms as the impact *We* reduces. The flattened droplet (see Figure 6.1 (top)) then starts to recede under the capillary force and the spreading factor slightly decreases due to this recoiling. There is no oscillation observed due to the high viscosity of diesel, and finally, spreading factor and height ratio remain unchanged when the droplet becomes stable.

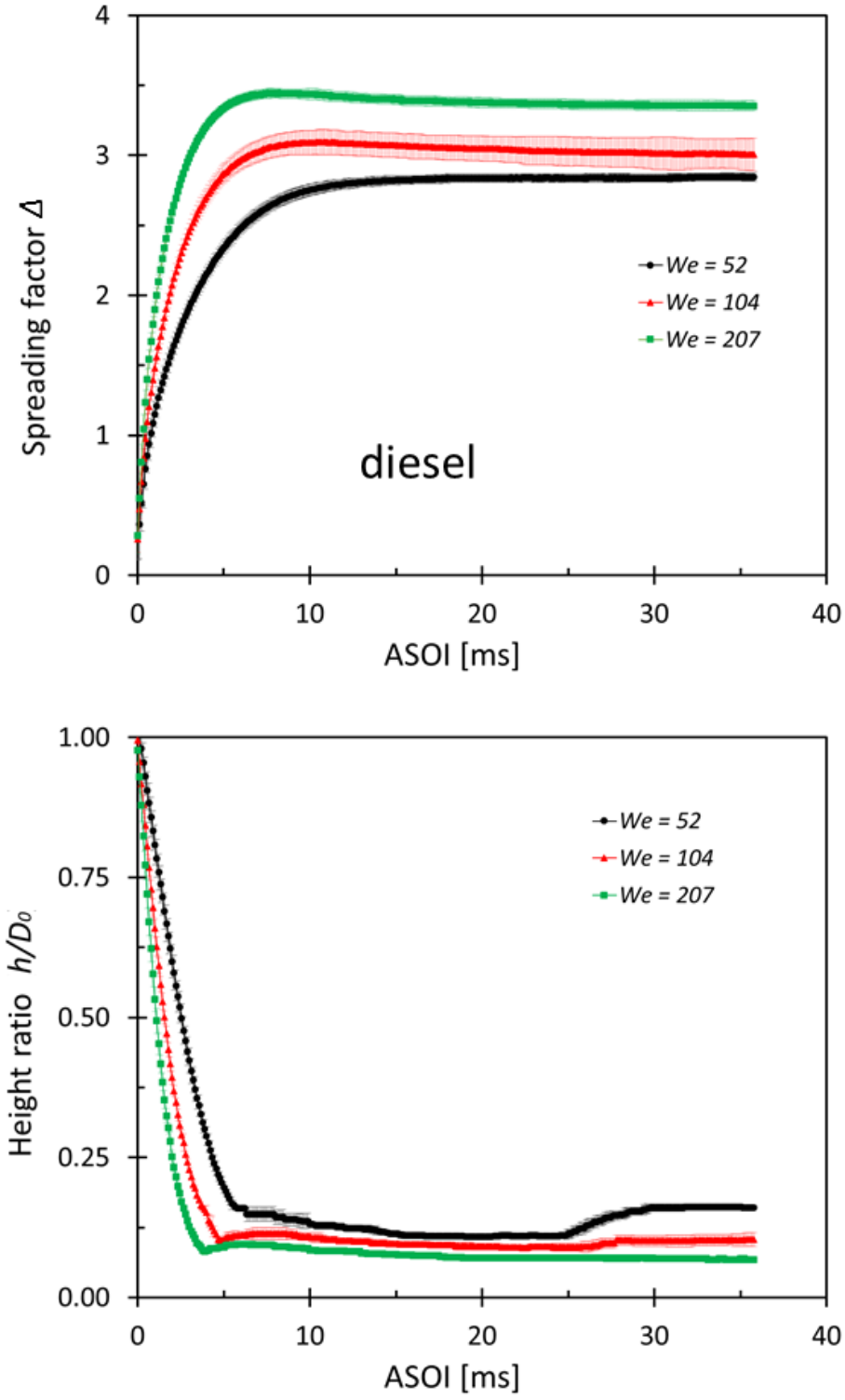

Figure 6.5: Spreading factor (top) and height ratio (bottom) for diesel at various impact *We* (for non-splashing conditions).

The results of the contact line velocity and dynamic contact angle for diesel droplet impinging on a smooth surface with different impact *We* are presented in Figure 6.6. The impact *We* has an insignificant effect on the contact line velocity and contact angle. In Figure 6.6 (top), initially, a spike on the contact line velocity at each condition is detected when the droplet impinges on the plate. Then, an almost exponential reduction of its magnitude with time is shown before the contact line velocity drops close to 0 m/s, this stage is known as the advancing phase. Next, at the impact *We* of 52 and 104 cases, it is difficult to observe the negative contact line velocity, however, at the impact *We* of 207, the contact line velocity starts to fluctuate around 0 m/s during the stage of time interval between 6.5 ms and 7.5 ms, the corresponding contact angle in Figure 6.6 (bottom) decreases from the advancing contact angle to the receding contact angle in this stage. At later stage of the impact *We* of 207 case, after 10 ms, the contact line velocity exhibits negative values with the substantially smaller magnitude compared with the advancing phase, at which the droplet recedes. After 30 ms, the contact line velocity approaches to 0 m/s and the equilibrium stage occurs. Despite all this, the receding and equilibrium stages are unapparent to be distinguished in the diesel case.

In Figure 6.6 (bottom), the similar behavior as described in Figure 6.6 (top) is shown in the temporal evolution of dynamic contact angle. The dynamic contact angle is approximately 150° when the liquid droplet just interacts with the plate. Subsequently, the contact angle reduces rapidly to around 100°, and decreases during the rest of the advancing phase. The receding phase initiates when the dynamic contact angle drops to 30° around 10 ms and slowly decreases till 30 ms. After 30 ms, the contact line velocity comes to be 0 m/s and the contact angle becomes stable, which indicates the start of equilibrium stage. Again, in diesel case, the receding phase is not obvious to be observed, this is also evidenced by the high-speed images as shown in Figure 6.1 (top) (e).

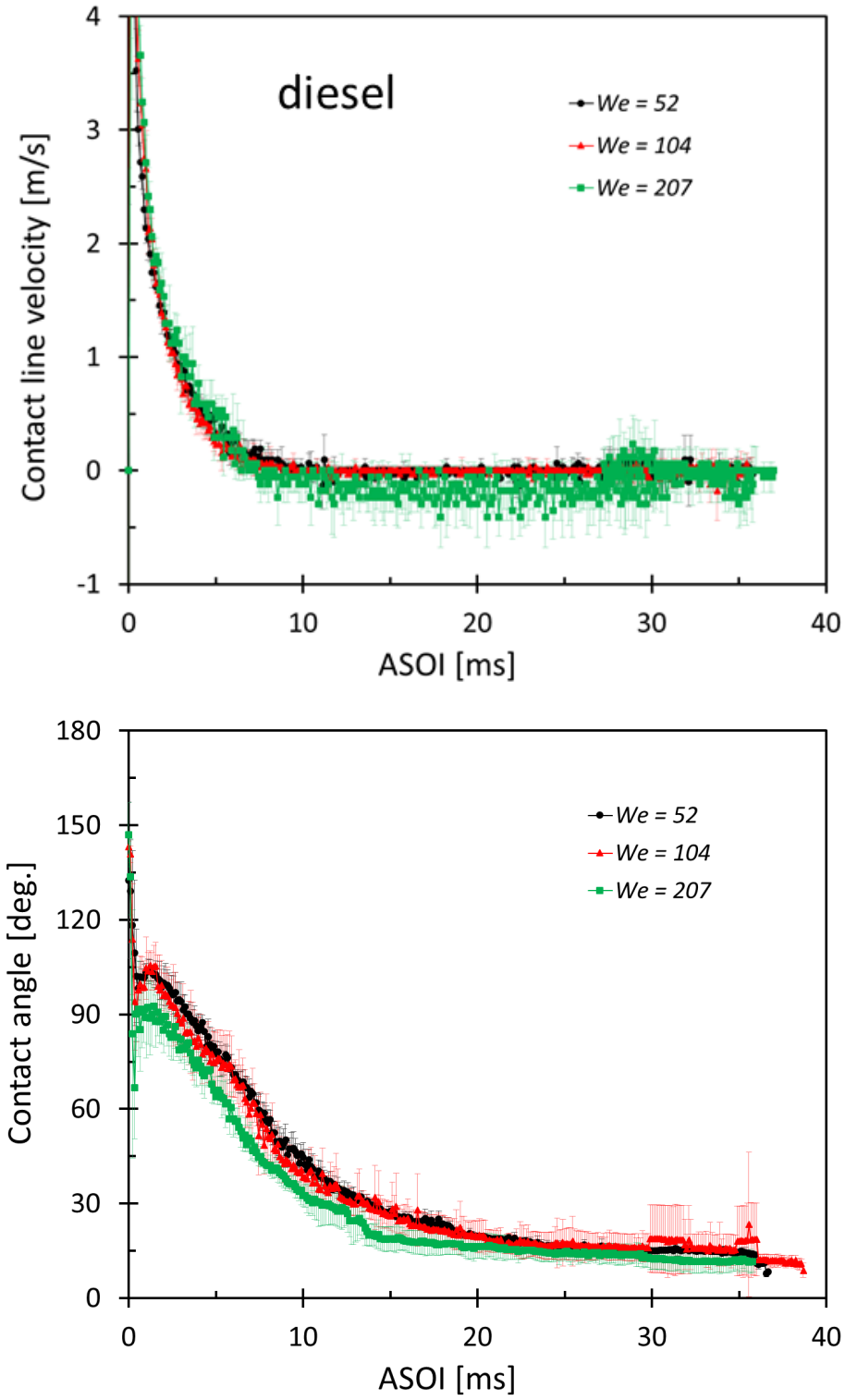

Figure 6.6: Contact line velocity (top) and contact angle (bottom) for diesel at various impact *We* (for non-splashing conditions).

Figure 6.7 shows the spreading factor (top) and height ratio (bottom) for water at the various impact *We* conditions. The similar observation with diesel in the beginning of the impingement is shown here that the droplet impacts on the plate and spreads outward under the impact pressure. The spreading factor increases as the impact *We* increases while the height ratio decreases with the impact *We*, due to the relatively higher impact momentum at the higher impact *We*. The droplet reaches the maximum spreading factors obtained of 3.25, 2.4, and 2.0 around 5.5 ms, 6.0 ms, and 6.2 ms as the impact *We* reduces. Unlike diesel, the flattened droplet then starts to show an obvious recoiling under the capillary force and reshaping perpendicularly (see Figure 6.1 (top)). Additionally, as a result of higher surface tension and lower viscosity of water, an obvious decrease of spreading factor and increase of height ratio are observed in Figure 6.7. Around 22 to 25 ms with different impact *We*, the spreading factor tends to be stable while the height ratio shows small fluctuations because of slight oscillation occurred in water case. The height ratio at the impact *We* of 105 turns out to be stable after 30 ms.

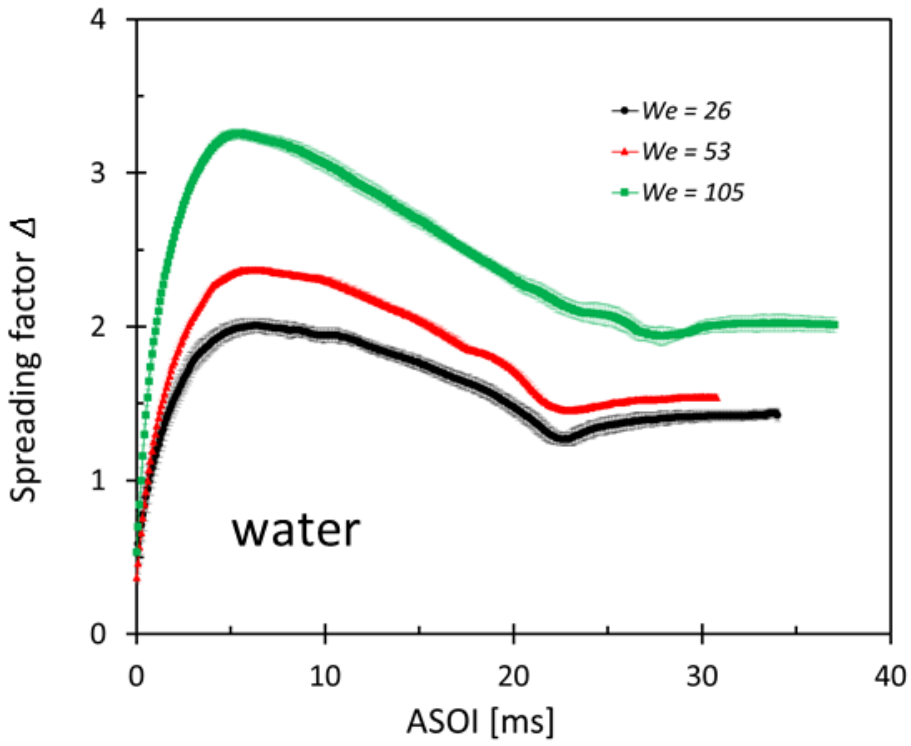

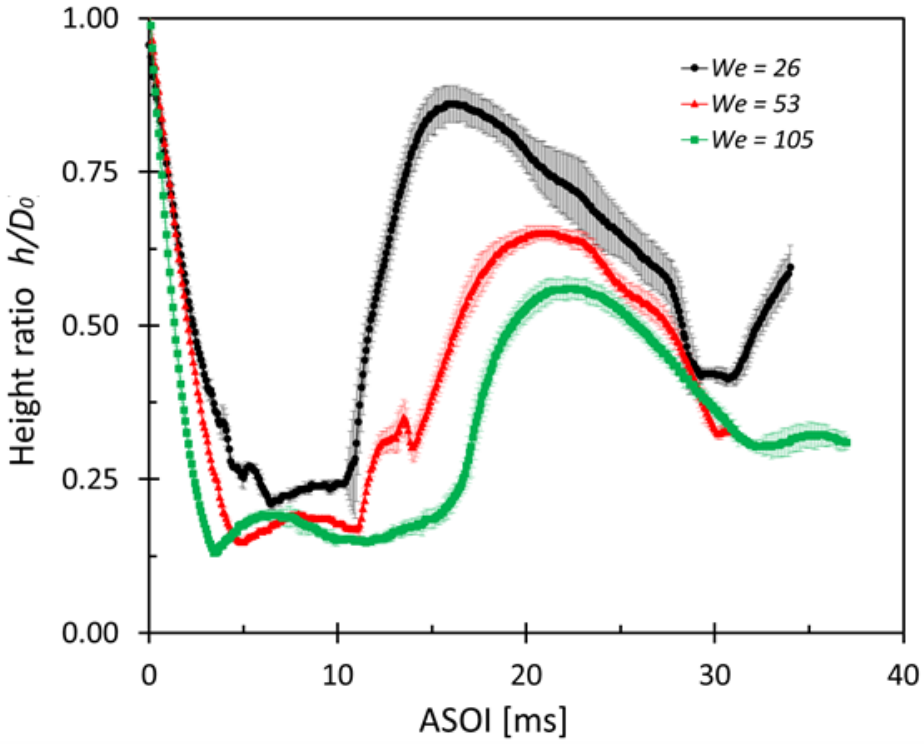

Figure 6.7: Spreading factor (top) and height ratio (bottom) for water at various impact *We* (for non-splashing conditions).

Figure 6.8 shows the results of the contact line velocity and dynamic contact angle for water droplet impinging on a smooth surface with different impact *We*. The impact *We* has an insignificant effect on the contact line velocity while the contact angle slightly decreases as the impact *We* raises. When the droplet impinges on the plate, a spike on the initial contact line velocity at each condition is observed in Figure 6.8 (top). Followed by a dramatic reduction of its magnitude with time before the contact line velocity drops close to 0 m/s. After advancing phase, the contact line velocity starts to fluctuate around 0 m/s at 5.0 ms, the receding phase occurs. The equilibrium phase is presented afterwards. In Figure 6.8 (bottom), the dynamic contact angle is approximately 150° when the liquid droplet just interacts with the plate. Subsequently, the contact angle reduces rapidly below 60°, and increases during the rest of the advancing phase. The receding phase initiates around 5 ms and the contact angle in this stage decreases till approximately 20 ms, then

raises again by the oscillation of water droplet, as the similar observation in height ratio. After 30 ms, the equilibrium stage starts.

Table 6.3 and Table 6.4 summarized the results of the maximum spreading factor, averaged advancing, receding, and equilibrium contact angles for both diesel and water at non-splashing conditions with all various impact *We*. The maximum spreading factor both in diesel and water cases increases with the impact *We* due to the higher impact velocity and momentum at the higher impact *We* which drives the droplet moves outward. The averaged advancing contact angle from diesel case ranges from 55° to 76° which shows insignificant difference as displayed in Figure 6.6, the averaged advancing contact angle based on different conditions is around 68°. Furthermore, in diesel case, the receding and equilibrium contact angles at various impact *We* change at a small scale. The averaged receding contact angle is 20° that is around 3° larger than the averaged equilibrium contact angle of 17°. At water case, the range of averaged advancing contact angle is from 53° to 93° and the averaged advancing contact angle in terms of all various conditions is about 75°. Unlike diesel case, the receding contact angle is quite smaller compared with the equilibrium contact angle at each condition. As well, the receding and equilibrium contact angles at each condition show clear differences, they decrease with the impact *We*. The averaged receding contact angle is 30° and the averaged equilibrium contact angle is around 55°.

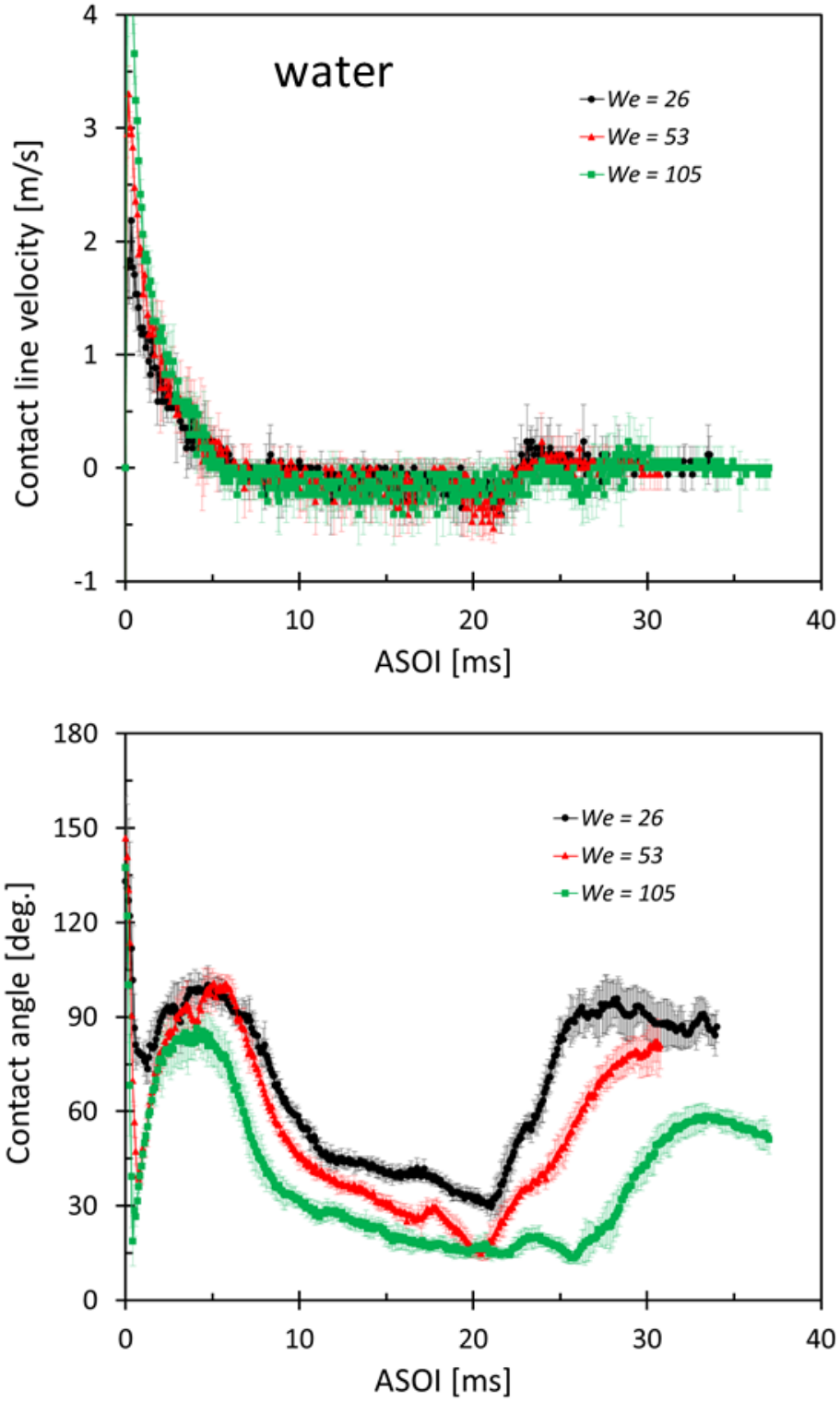

Figure 6.8: Contact line velocity (top) and contact angle (bottom) for water at various impact *We* (for non-splashing conditions).

Table 6.3: Post-impingement properties for diesel at various impact *We*

Case #	Height (mm)	*We*	Max. Δ	θ_{adv} (°)	θ_{rec} (°)	θ_{eq} (°)
1	26	52	2.9	55	15	15
2	52	104	3.1	76	22	19
3	57	113	3.2	70	23	20
4	104	207	3.5	74	20	12
5	114	226	4.5	67	20	16

Table 6.4: Post-impingement properties for water at various impact *We*

Case #	Height (mm)	*We*	Max. Δ	θ_{adv} (°)	θ_{rec} (°)	θ_{eq} (°)
1	26	26	2.0	93	45	88
2	52	53	2.4	83	36	61
3	57	57	3.1	79	33	53
4	104	105	3.3	73	25	52
5	114	115	3.3	69	25	42
6	195	196	3.7	53	18	36

6.1.1.2.2 Surface temperature effect

The baseline condition of initial droplet-plate height of 52 mm with two different surface temperatures (25°C and 130°C) is selected for diesel to assist the study of surface temperature effect on the post-impingement process. The results of the surface temperature effect on the dynamic process of droplet impingement are repeatable for other conditions, which is not shown in this article.

A 3-wire heat flux probe was installed in the metal plate to measure surface, embedded, and differential temperatures. This probe consists of two "J" type thermocouples, one of which was installed at the plate surface and another was at 2 mm directly under the surface thermocouple. Figure 6.9 gives the controlled surface temperature profile of the heated plate during droplet impingement. It is observed that the surface temperature is about 4°C lower than the expected temperature of 130°C due to the heat transfer between the plate surface and surrounding air. The temperature remains 126°C before the droplet impinges on the plate at ASOI of 0 ms. The surface temperature then decreases suddenly to 119.5°C because of the temperature difference between the relatively cold droplet (initially 25°C)

and hot surface. Later, slow increase in temperature is caused by the movement of droplets towards heated plate and exposure to the high temperature.

The sequential images to compare the diesel droplet (D_0 = 2.87 mm) impinging on an unheated surface with it impacting on a hot surface shown in Figure 6.10. The first five images show the similar events as described in Figure 6.1: from left to right, there are pre-impingement, impingement, and post-impingement, maximum spreading, receding, respectively. It is seen that the maximum spreading factor at 130°C is 4 which is slight larger than that of 3 at 25°C. Also, droplet reaches its maximum spreading factor after impinging on the hot surface around 9 ms and it is 2 ms earlier than it hitting on the unheated surface. The additional image shown in Figure 6.10 is the last image at 37.0 ms. At 130°C, the diesel droplet appears to recede more horizontally and the perpendicular height with respect to the surface is larger compared with it at 25°C.

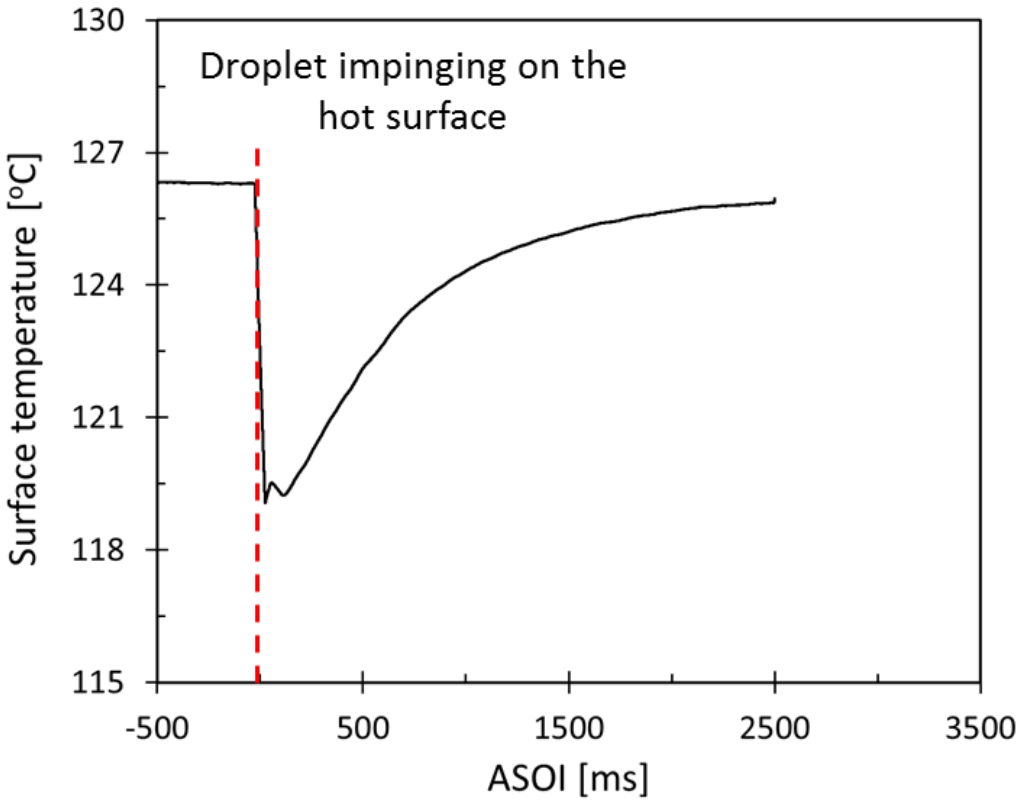

Figure 6.9: Controlled surface temperature profile of heated plate.

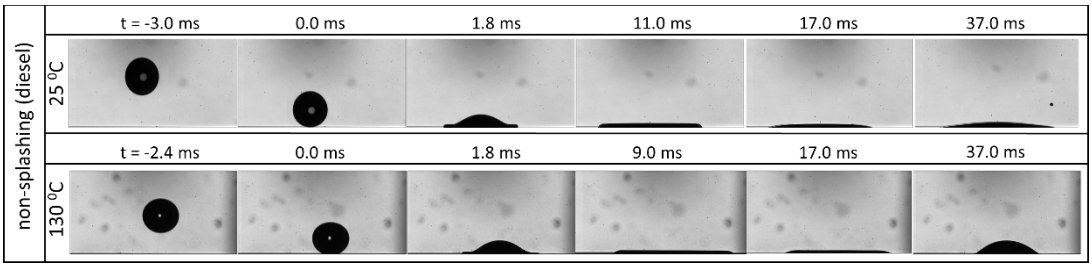

Figure 6.10: A sequential visualization of surface temperature effect on diesel droplet-wall impingement: 25°C (top); 130°C (bottom).

Figure 6.11 shows the spreading factor (top) and height ratio (bottom) for diesel droplet impinging on the unheated and heated surface. At 25°C, the similar droplet-wall interaction behavior is displayed as the previous section described. After reaching the maximum spreading diameter and the relatively minimum height, the receding phase is unobvious to visualize from both high-speed images and quantitative results, which turns out the almost stable spreading factor and height ratio as shown in Figure 6.11 (T = 25°C). However, at 130°C, droplet continues to spread after impact till a thin flake appears at the end of the advancing phase while height ratio shows little change during this stage. After droplet reaches its maximum spreading diameter around 9 ms, the receding phase begins. During the receding phase, diesel droplet appears to oscillate slightly and attempts to reshape, the vertical elongation is observed. Correspondingly, the spreading factor continues decreasing and the height ratio shows a sudden rising at 23 ms and dropping around 35 ms at this stage. Since it takes a long time (>> 40 ms) for droplet to be stable and reach the equilibrium phase, hence, the equilibrium phase with higher surface temperature condition is not shown in Figure 6.11 and Figure 6.12.

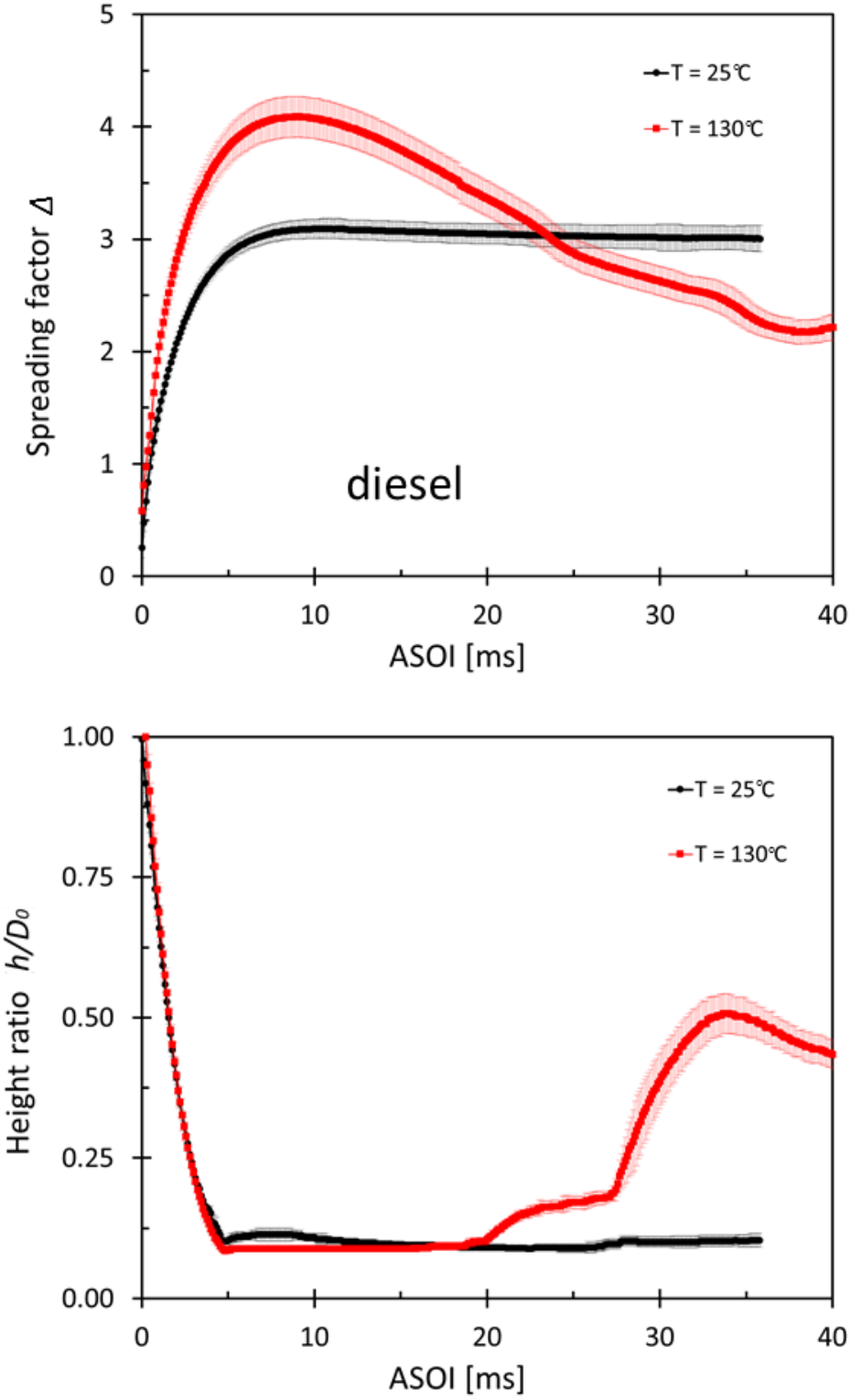

Figure 6.11: Surface temperature effect on spreading factor (top) and height ratio (bottom) for diesel at the same impact *We* (for non-splashing conditions).

Figure 6.12 provides the surface temperature effect on the contact line velocity and dynamic contact angle for diesel droplet. The contact line velocity and contact angle at 130°C overall follows the similar trend with those at 25°C. In Figure 6.12 (top), however, at the surface temperature of 130°C, after the advancing phase (before the contact line velocity $U_{cl} \leq 0$ m/s), the contact line velocity fluctuates around 0 m/s during the time interval between 8 and 10 ms, the receding phase starts afterwards and it is clearly seen that the negative contact line velocity with considerably smaller magnitude than that in the advancing phase occurs. During the same stage, the contact angle in Figure 6.12 (bottom) changes from dynamic advancing angle to receding contact angle. Moreover, in Figure 6.12 (bottom), the contact angle is about 150° as soon as the droplet contacts with the plate at both surface temperature conditions. The contact angle then reduces substantially to around 30° at 130°C. The averaged advancing contact angle is 76° at 25°C and 40° for 130°C case, the averaged receding contact angle is similar in both conditions, about 22°. As pointed in previous, the receding phase and equilibrium phase are not clear to be notable in diesel case at 25°C. However, the receding is apparently shown as the droplet impacts on the hot surface as explained in Figure 6.10.

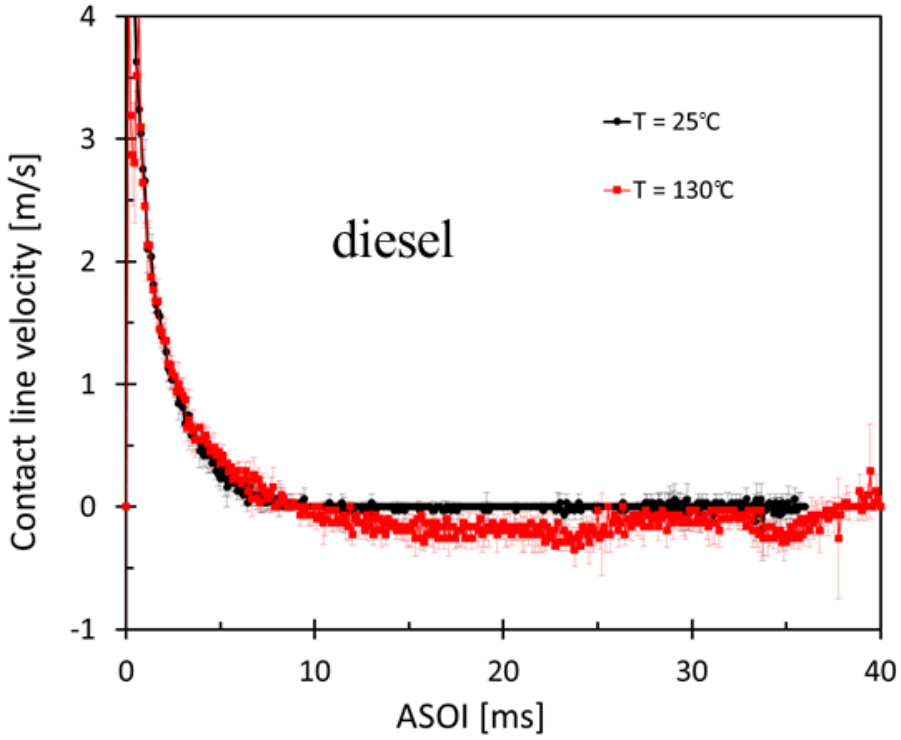

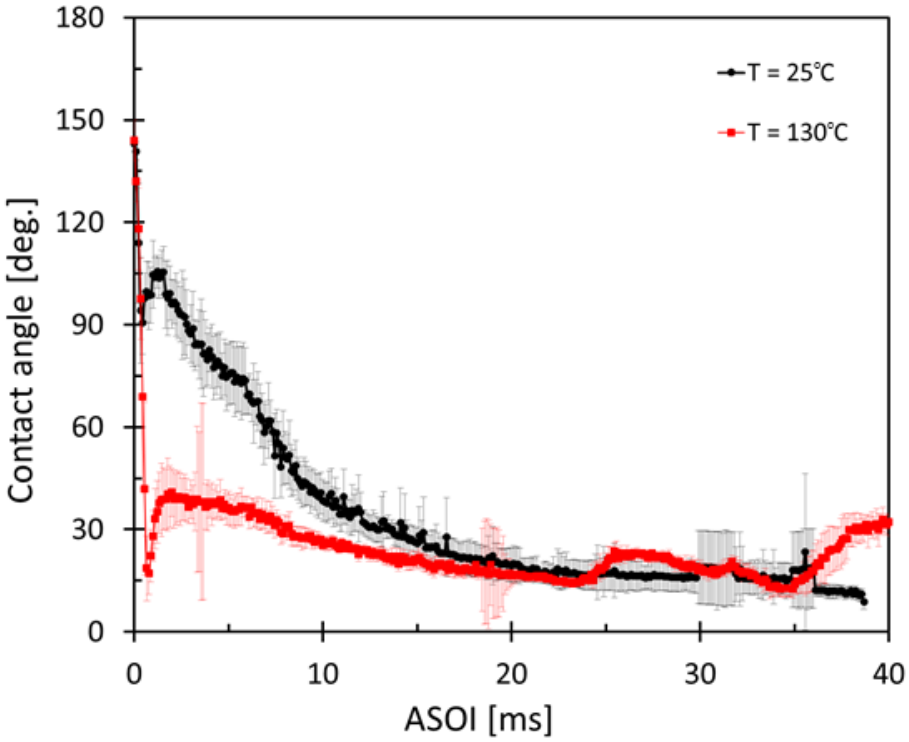

Figure 6.12: Surface temperature effect on contact line velocity (top) and contact angle (bottom) for diesel at the same impact *We* (for non-splashing conditions).

6.1.1.2.3 Surface roughness effect

The effect of impinged surface roughness on the dynamic process of droplet-wall impingement are presented in this section. The roughness profile of roughened surface is provided in Figure 3.23, the mean roughness of the surface is 16 μm and the peak-to-peak roughness is 80 μm, while the average roughness of the smooth surface is only 1.6 μm. As well, it should be noted that a splashing case with initial height of 189 mm (impact *We* of 358) for both smooth plate and roughened plate is selected to study the roughness effect since the larger amplitude of the roughness will increase the perturbations and also increase the probability of a prompt splash [162].

Figure 6.13 shows a series images from the selected *splashing* condition for diesel droplet (D_0 = 2.87 mm) impinging on a smooth (top) and roughened (bottom) plates. Due to the different exposure time applied for the current condition, compared with the images shown

in Figure 6.10, an obvious difference of the visualization of liquid droplet with background images is observed. Considering the roughened surface as the reference, from left to right, there are pre-impingement, impingement, start of splashing, further splashing, and maximum spreading, and slight receding. After droplet interacting with the roughened plate around 0.6 ms, splashing starts and smaller secondary droplets are created while the same phenomenon is not shown in smooth plate case. As the droplet spreads radially in the current view, around 1.4 ms, the splashing is also visible in smooth plate and secondary droplets are observed in both smooth and roughened conditions. During droplet hitting on a relatively smooth surface with a higher impact velocity, the splashing mainly depends on the surrounding air near the drop while the roughness of the surface is the dominating factor for splashing when the droplet impinges on a roughened surface. The droplets then reach the maximum spreading factor at 5.0 ms at both conditions. Afterwards, the mild receding can be observed.

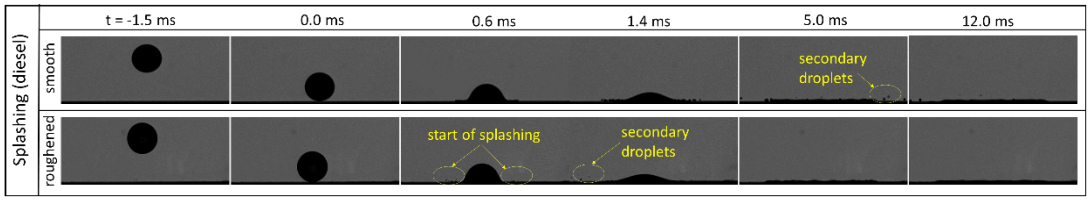

Figure 6.13: A sequential visualization of the diesel droplet impinging on a smooth plate (top) and roughened plate (bottom).

Figure 6.14 shows the effect of surface roughness on the spreading factor of a diesel droplet as functions of time from impact. In the first stage of the spreading from 0 to 3 ms, due to the earlier splashing occurred when the droplet hitting on the roughened plate, the secondary droplets generate earlier and the dissipated energy increases, therefore, the spreading diameter and spreading factor at the smooth plate case are always larger than those at the roughened plate condition. The spreading factor is comparable after 3 ms and reaches its maximum value around 5 ms in both conditions. After that, the spreading factor slightly decreases, the receding phase begins but it is inconspicuous due to higher viscosity of diesel fuel.

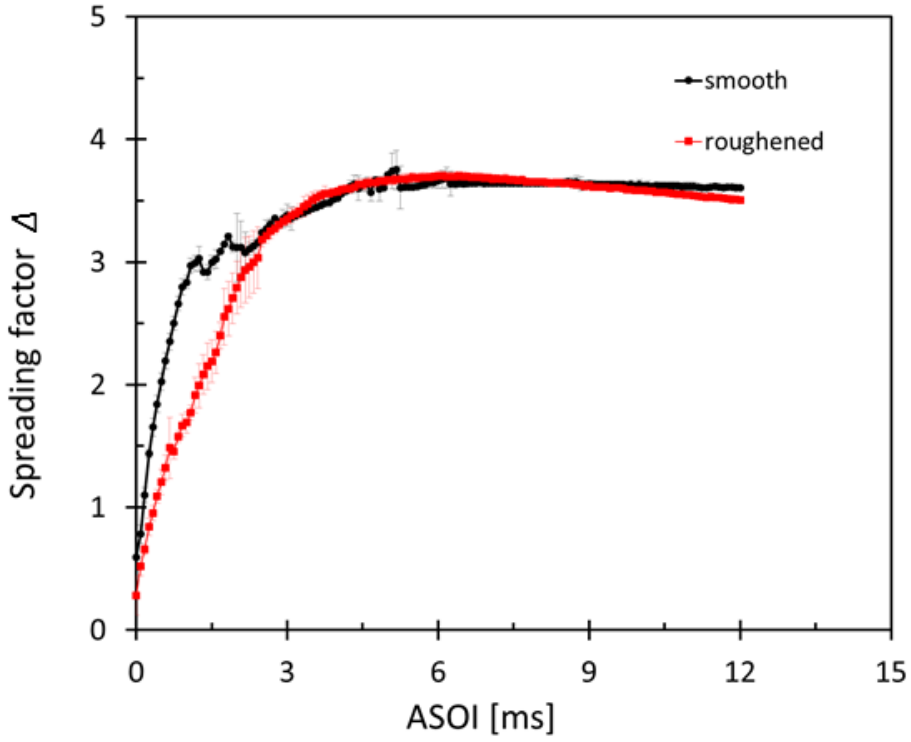

Figure 6.14: Surface roughness effect on spreading factor (for splashing conditions).

6.1.2 Numerical details

The droplet-wall interaction process is implemented with the VOF method in CONVERGE software [132]. High-resolution interface capturing (HRIC) is activated for the current set of simulation to reconstruct the interface details. Since the air density and viscosity are much smaller than those of diesel fuel, the flow in the air have no significant effect on the flow in the droplet, air flow works only around the droplet. Therefore, it is not necessary to provide a very large computational domain to represent an infinite domain. A 3-D computational domain (18 x 18 x 8 mm^3) was chosen to simulation the entire process of a single droplet impingement on a flat plate, the fuel droplet is initially positioned at a certain distance above the substrate with an initial velocity. The droplet travels downward toward the substrate under the influence the gravity force and reaches the substrate at an impact velocity. The liquid phase is fuel and the gas phase is the surrounding air under atmospheric pressure. Open boundary conditions are used at the top and side to simulate an infinite domain. A no-slip condition is used for the impinged wall at the bottom.

Furthermore, a specify contact angle θ of fluid at the wall is used as a boundary condition. Then based on this value, the surface normal at the live cell next to the wall is as follows [132]:

$$n_i = n_{w,i}\cos(\theta) + t_{w,i}\sin(\theta) \tag{6.8}$$

where $n_{w,i}$ and $t_{w,i}$ are the unit vectors normal and tangential to the wall, respectively.

Based on the studies by Šikalo et al. [48] and Roisman et al. [51], the contact line velocity in the current work is simply approximated as the time derivative of the radius of the wetted area (r_{cl}) in Equation (6.9),

$$U_{cl} = dr_{cl}/dt \tag{6.9}$$

After the contact line velocity is found, the dot product of the velocity vector with the unit free surface normal provides the direction of contact line movement to define if the advancing or receding occurs.

Single diesel droplet impinging on the plate is selected for numerical study which serves for high-pressure diesel spray-wall interaction study. The initial droplet-surface height is 52 mm and incident drop diameter is 2.87 mm. To reduce the computational time, the initial perpendicular distance between droplet and the solid surface is set to 4 mm with the same diameter and velocity as in the experiment. The relevant parameters and liquid properties for which computations have been performed are found in Table 6.1 and Table 6.2. Constant contact angle was assumed between the liquid and the solid substrate with a value of θ = 13°, following the experimentally measured equilibrium contact angle. The simulation was performed with a base mesh size of 1.0 mm, and with two levels of AMR based on void fraction. Further, three levels of fixed embedding were included along with the droplet traveling path and four level of fixed embedding was imposed near the impinged surface. Thus, the minimum cell size in the entire domain was 62.5 µm. Figure 6.15 shows the mesh generation in the vertical cross section with the diesel droplet at 1.0 ms. Grid convergence study will be discussed in Simulation results section.

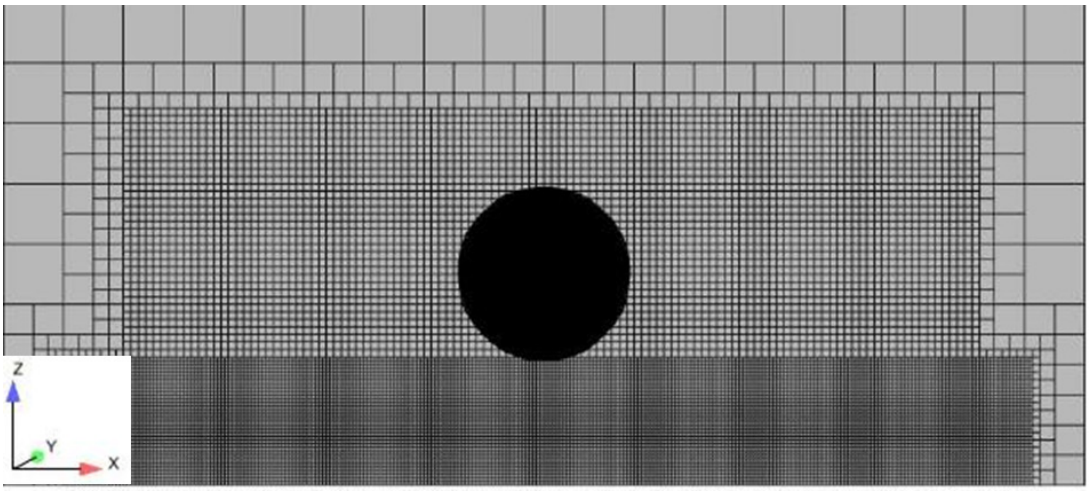

Figure 6.15: Mesh generation with the numerical 3-D diesel droplet (iso-surface at α = 0.5) at 1.0 ms.

6.1.3 Simulation results

In this section, the simulation results are presented. Firstly, a brief mesh dependency study will be presented together with results for validating the global behavior of the model. Then, detailed predictions for the temporal evolution of the relevant phenomena are presented.

As stated in the previous section, the diesel droplet (D_0 = 2.87 mm) with the initial droplet-surface height of 52 mm (impact *We* of 104) is selected as the baseline condition for numerical study. The mesh convergence study was performed for two minimum mesh sizes. Simulations with minimum mesh sizes of 62.5 µm were performed using three and four levels of embedding refinement for the droplet travelling path and near impinged surface regions, respectively. In additional, the embedding on the impinged surface is set to four times thicker in 62.5 µm case than that in 125 µm case, which has a significant effect on the droplet shape after impinging on the plate. In terms of cell count, the 62.5 µm case resulted in a peak cell count of ~2.3 million while 125 µm case resulted in a peak cell count of ~1.3 million, which requires at least twice more computationally demanding in 62.5 µm case. Based on the grid convergence, computational demand, and droplet shape considerations, 62.5 µm case mesh size was selected as the reference minimum mesh size for the current study.

The spreading factor and height ratio with the two meshes are plotted respectively in Figure 6.16 and validated by experimental results. The simulation results with finer mesh (62.5 μm) overall match well with experimental data compared with the coarse mesh case. The spreading factor and height ratio show a stronger agreement with experimental results in the early spreading process before ASOI of 5 ms. As the spreading factor increases with time, the discrepancy between numerical and experimental results is observed, which might be by reason of handle of contact angle in the simulation. At the maximum spreading diameter, the difference between the experimental and numerical spreading factor is 3.0 %. Afterwards, the simulation results in the receding stage around ASOI of 10 ms are quite comparable with experimental data. Further, due to the computational demanding of numerical study, the experiments also show a longer spreading stage than the simulation.

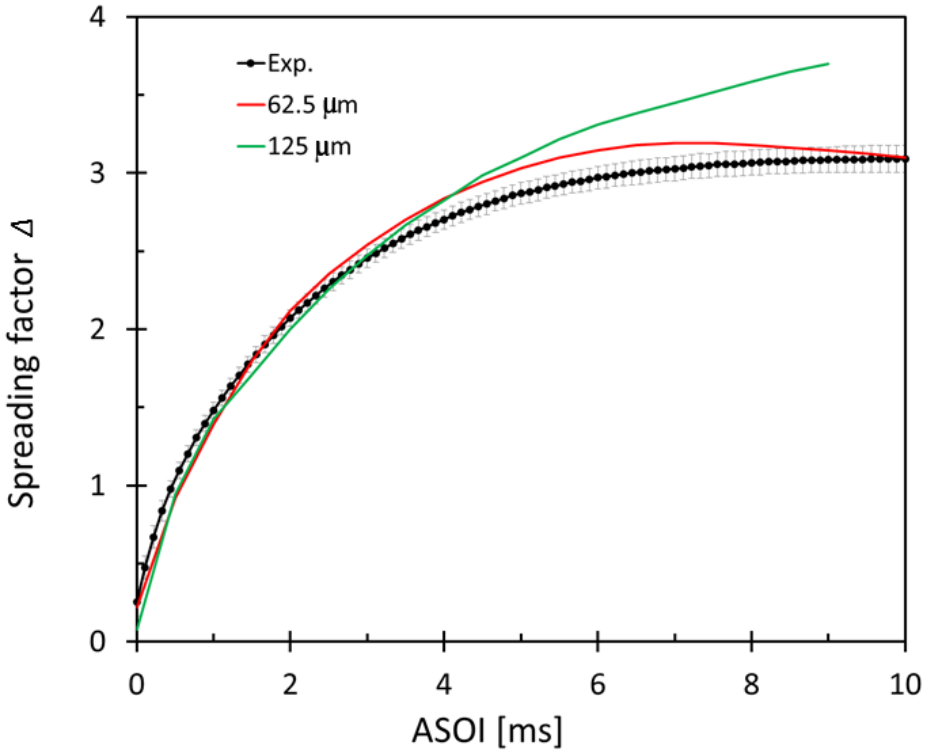

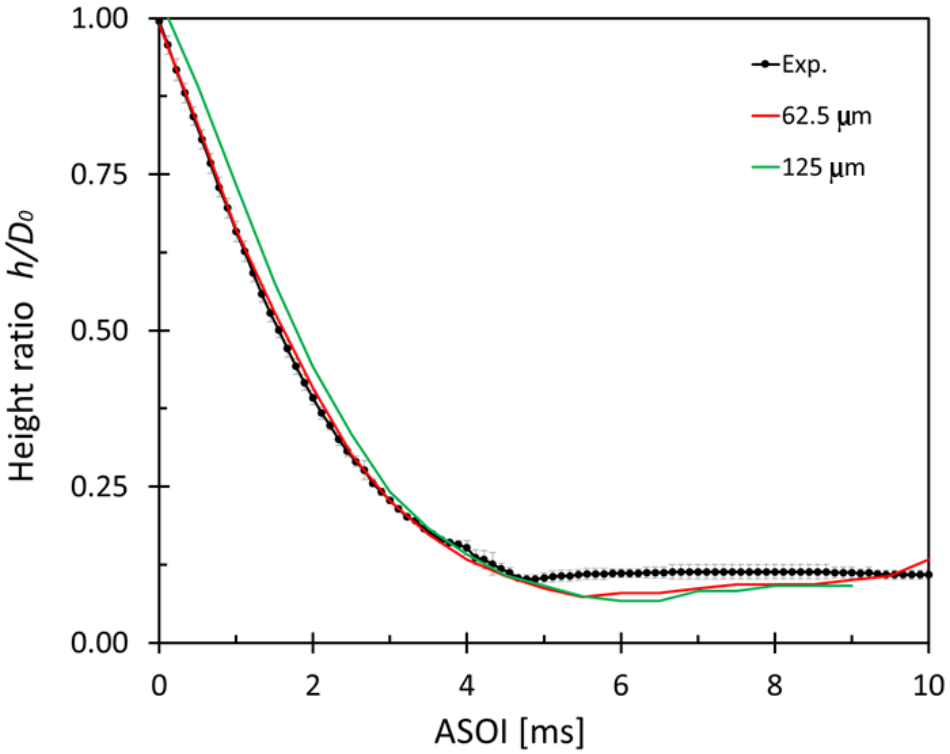

Figure 6.16: Comparison of spreading factor and height ratio between experiment and simulation results.

For comparative purposes between the experimental data and the numerical simulation results, Figure 6.17 indicates a sequence of high-speed images and the corresponding numerical simulations (iso-surface of droplet in black with $\alpha = 0.5$) during the droplet impinging on the surface. The simulation results generally show a good agreement with the experimental data in terms of the droplet shape, impinging time, spreading process. At ASOI of 8 ms, the numerical spreading diameter and the droplet structure shows difference with the experimental result, which might be due to the influence of surface tension. When the maximum spreading diameter is reached, the flattened droplet then starts to recede under the capillary force and finally tends to be relatively stable (not shown here).

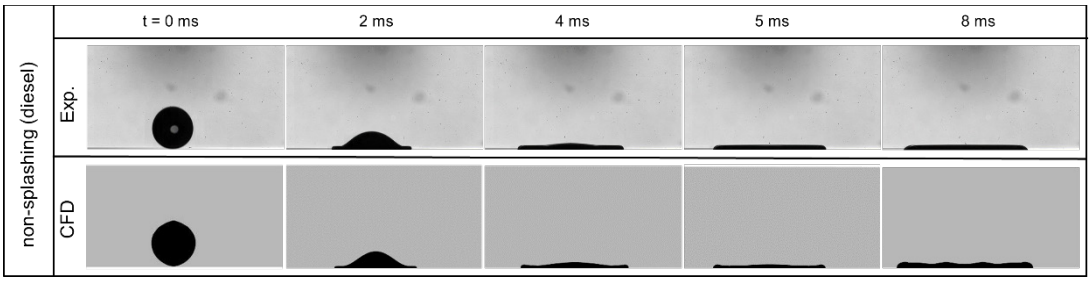

Figure 6.17: A sequence of high-speed images (top) and the corresponding numerical simulations (bottom) (3-D iso-surface of droplet in black with α = 0.5).

Moreover, pressure coefficient (C_p) and the induced flow field around the droplet during droplet-wall interaction are presented Figure 6.18. The pressure coefficient (C_p) is defined as [50],

$$C_p = \frac{P - P_\infty}{\frac{1}{2}\rho_{liq} U_0^2} \tag{6.10}$$

where P is the pressure of the computational domain, P_∞ is the pressure on the far field, ρ_{liq} is the liquid fuel density, and U_0 is the impact velocity.

Figure 6.18 shows C_p (top) and velocity vectors (bottom) on a vertical plane through the center of the droplet. The same scale with respect to the initial droplet size as that in Figure 6.17 is applied into Figure 6.18. From Figure 6.18, at the initial stage of droplet impinging on the surface, pressure increases up to 1.6 times of droplet initial kinetic energy because a dimple is formed based on droplet impact [162]. In this stage, the velocity magnitude is around 1.2 times of initial impact velocity near impinged surface region. The vortex on the top of the droplet is observed. At the remaining spreading stage from ASOI of 2 ms, C_p is 0.1 times lower compared with that in the initial spreading phase and it reaches its maximum value on the leading edge of spreading. The velocity magnitude in this stage is also lower than that at the initial spreading phase and it is about 0.6 times of impact velocity. The vortex is visible on the droplet rim in both left and right with the current cross section view, which also changes the direction when the receding phase initiates. It appears that the vortex motion is associated with the motion of leading edge of the spreading droplet, where the size of vortex is proportional to the contact line velocity. This relation can be

identified by the fact that the variation observed in the vortex magnitude is similar to that of contact line velocity during the spreading process as shown in Figure 6.6.

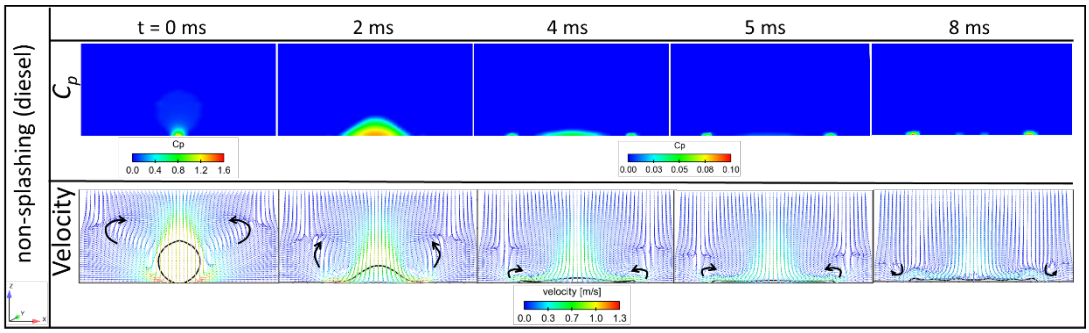

Figure 6.18: Pressure coefficient C_p (top) and induced flow field profiles shown by velocity vector (bottom) on a vertical plane through the center of droplet. The first C_p contour legend applies to the first picture,while the second legend applies to the rest four pictures.

6.1.4 Summary

In this section, a detailed analysis of the dynamic process of the single droplet impinging on a flat plate with various conditions has been performed. The current experimental work was carried out at the room temperature and pressure and water, diesel, dodecane, and n-heptane were considered as the test fuels and injected at various *We* numbers. The droplet impingement regimes including deposition-splash criteria is studied and a new correlation in terms of the current experimental data is developed. As well, the study on the evolution of the dynamic process of droplet-wall interaction is one of the unique contributions to expand the database of relevant studies, such as aiding the development of dynamic contact angle model under DNS or VOF methodology. For numerical study, the volume of fluid (VOF) method was used to characterize the single fuel droplet impinging on the plate and provide a better understanding of the dynamic impingement process in the CONVERGE^{TM} framework. The main findings under the conditions studied in this work are as follows:

(1) In experiment, considering the impingement outcomes, the splashing and non-splashing criterions were summarized based on the earlier research and applied to

evaluate the current experimental data. With the droplet impacting on the smooth, roughened, and heated plates, the experimental results generally show good agreement in predicting the splashing and non-splashing phenomena with the published droplet-wall interaction models. Further, a new correlation in terms of *Oh* and *Re* based on our experimental data to indicate the droplet splashing was proposed: $OhRe^{0.886} = 6.7$.

(2) The effects of the impact *We* and different wall conditions on the time evolution of droplet spreading factor, height ratio, the dynamic contact angle, and the contact line velocity were studied. The dynamic contact angle, contact line velocity, and spread factor vary with the impact *We*. The maximum spreading factor both in diesel and water cases increases with the impact *We*. The averaged advancing contact angle for diesel based on different conditions is around 68°. Furthermore, in diesel case, the receding and equilibrium contact angles at various impact *We* change at a small scale. At water case, the averaged advancing contact angle in terms of all various conditions is about 75°. The receding contact angle is quite smaller compared with the equilibrium contact angle at each condition. As well, the receding and equilibrium contact angles at each condition show clear differences, they decrease with the impact *We*.

(3) At higher surface temperature of 130°C, the maximum spreading factor is larger than that at 25°C. After droplet reaches its maximum spreading diameter, the clear receding phase begins at 130°C. During the receding phase, diesel droplet appears to oscillate slightly and attempts to reshape, the vertical elongation is observed.

(4) As the droplet impinges on a relatively smooth surface with a higher impact velocity, the splashing mainly depends on the surrounding air near the drop while the roughness of the surface is the dominating factor for splashing when the droplet impinging on a roughened surface. After droplet spreads on the plate, the splashing is shown and secondary droplets are observed in both smooth and roughened plate conditions. However, the splashing occurs earlier at the roughened surface. After spreading factor

reaches its maximum value, the receding phase starts but it is inconspicuous in both smooth and roughened surface due to higher viscosity of diesel fuel.

(5) In simulations, the diesel droplet with the initial droplet-surface height of 52 mm is selected for numerical study. A good agreement is observed between the temporal evolution of the experimental spreading factor and height ratio. Further, the pressure coefficient C_p and the velocity magnitude are much larger at the initial stage of spreading. The vortex is visible on the top of droplet rim during the initial spreading phase and it is also visible around the droplet rim on both left and right with the cross-section view, which also changes the direction when the receding phase initiates.

6.2 Droplet-to-droplet collision

Two equally sized water droplets with diameter of 800 µm, relative velocity of 1.9 m/s and *We* of 40 and *Re* of 1520 undergoing a head-on collision in a three-dimensional domain are studied. The domain with size of 5 mm x 3 mm x 3 mm is filled with air at standard atmospheric pressure and temperature. The uniform mesh size of 16 µm is used for the entire domain. The physical properties of both the phases are listed in Table 6.5.

Table 6.5: Thermo-physical properties of phases

Phase	**σ (N/m)**	**ρ (kg/m^3)**	**ν (cSt)**
air	-	1.2	14.8
water	0.072	1000	1

Figure 6.19 shows a sequence of two water droplets collision evolution at various time by comparing the simulation results (bottom) with the attainable experimental results (top) by Ashgriz and Poo [63] The simulation results generally show a good agreement with the experimental data in terms of droplet shape, collision time, and further collision outcomes.

Furthermore, the coalescence is initially visualized as the two droplets collide each other and the new droplet elongates at the horizontal direction, then the direction of elongation

is changed into perpendicular direction and the reflexive separation can be further observed. Finally, the reflexive separation with a satellite droplet formation occurs.

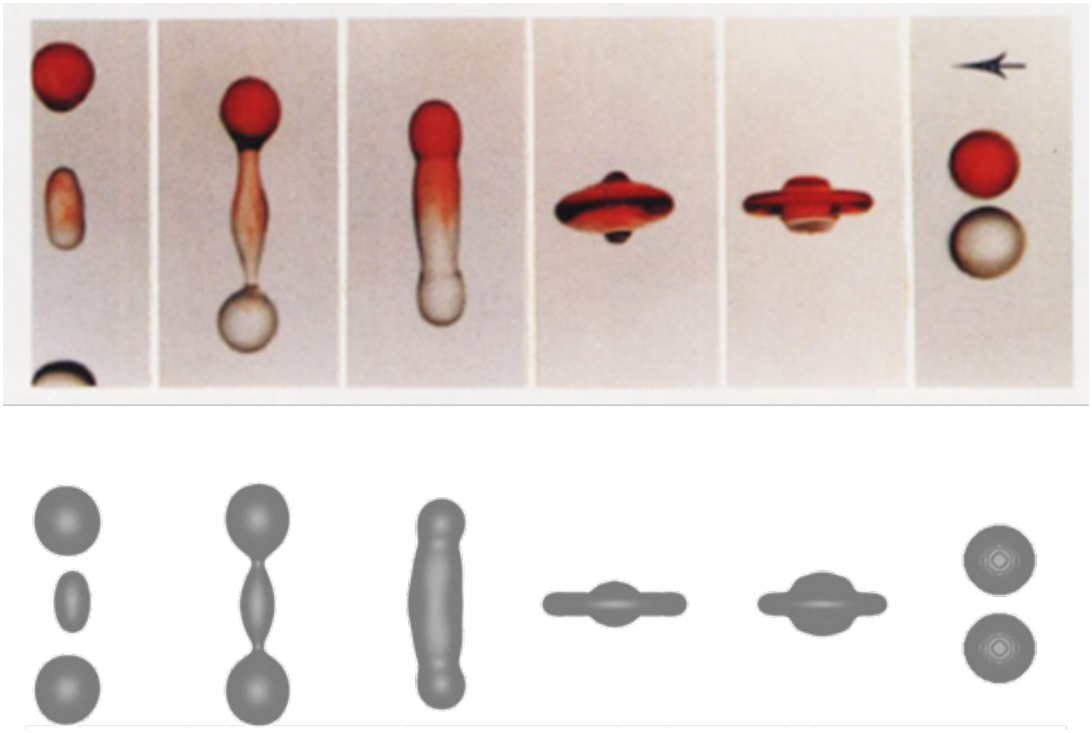

Figure 6.19: Head-on collision of two water droplets at *We* = 40, droplet diameter ratio = 1, impact parameter = 0: published experimental results (top); current simulation results (bottom).

6.3 Multi-droplet impingement on a hot surface

6.3.1 Evaporation sub-model validation

To validate the evaporation sub-model, a water droplet in the cross-stream of hot air is simulated in a three-dimensional domain (10 mm x 4 mm x 4 mm) as shown in Figure 6.20 and compared with the published results [133]. In this domain, the left face is modelled as an inlet and right face as outlet. The lateral faces are modeled as walls with free slip condition. The air with temperature of 363 K and velocity of 15 m/s is uniformly across the inlet. The water droplet diameter is 2.1 mm and initial temperature is 343 K.

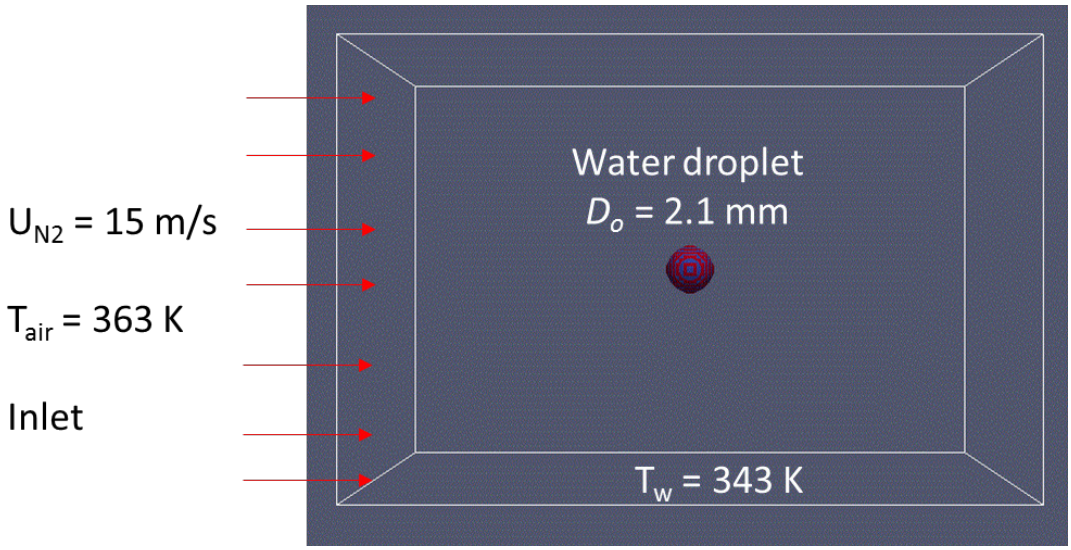

Figure 6.20: Computational domain.

The phase change phenomenon with heat transfer from surrounding hot air to droplet and the mass transfer of droplet from liquid phase to vapor phase is affected by droplet thermophysical properties, and temperature and vapor distributions around the droplet. The vapor distribution with the tangential velocity vectors in the domain is presented in Figure 6.21. The droplet deforms from the sphere to ellipsoid at the compared time while it recovers to the spherical shape afterwards, attributing to the cohesive force on the droplet surface. As well, at the surface of droplet, the highest vapor concentration is observed, followed by the region near the vortices behind the droplet due to the low velocity of surrounding air and the insufficient mixing between the vaporized droplet and surrounding air.

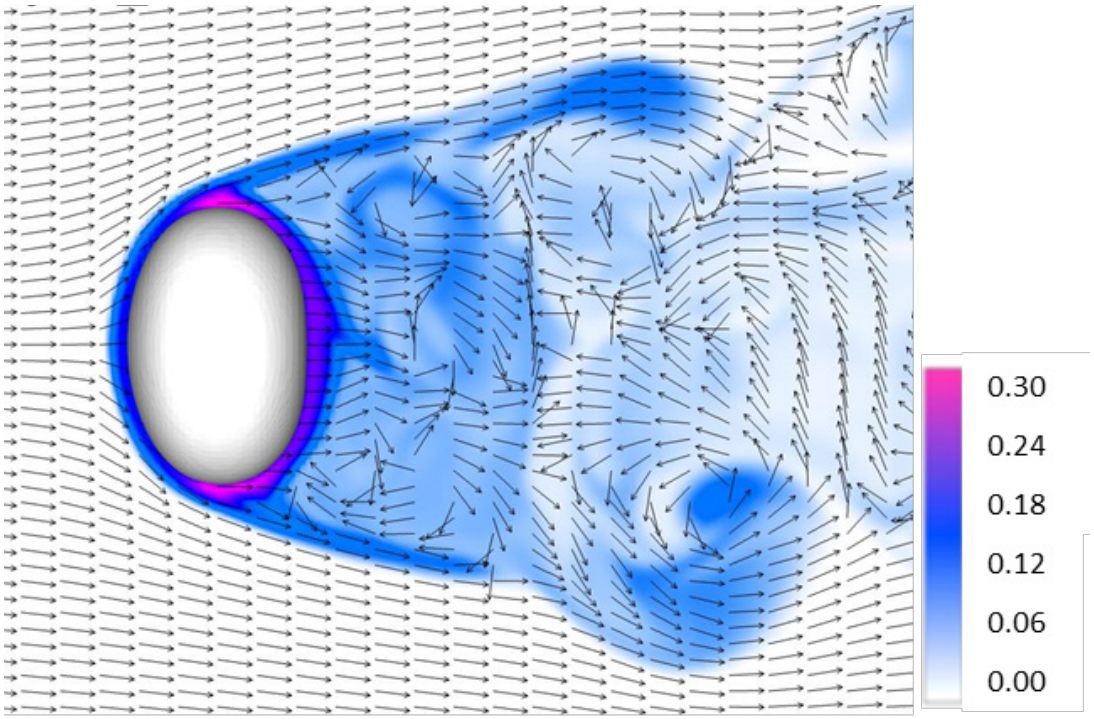

Figure 6.21: Vapor fraction distribution around the droplet at 12 ms.

The temperature distribution with the tangential velocity vectors in the domain is shown in Figure 6.22. The temperature distribution inside the droplet is homogenous and the droplet resides in the lower temperature zone compared with the surrounding air. In addition, the low temperature field corresponds to the high vapor concentration region at which the vapor shows inadequate mixing with air. Overall, the simulation based on the evaporation sub-model is in agreement with the results by Schlottke and Weigand [133].

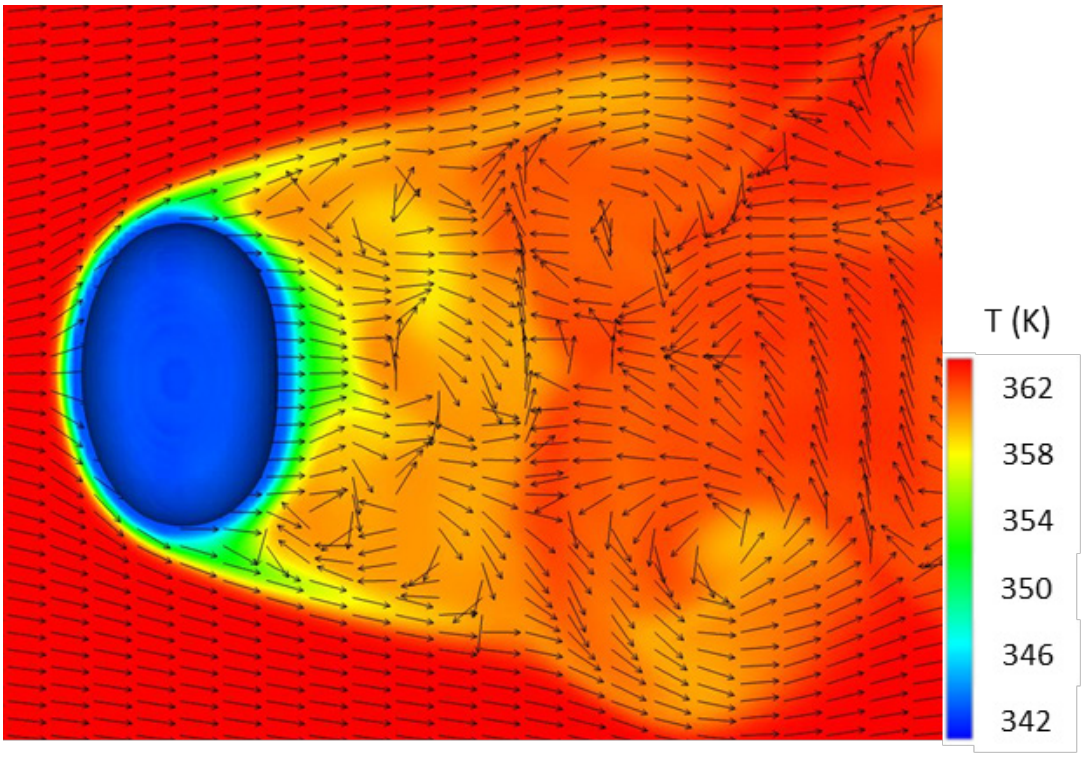

Figure 6.22: Temperature distribution around the droplet at 12 ms.

6.3.2 Numerical details

After the evaporation sub-model validation, the evaporation of spherical droplets impinging on a hot surface and the effects of droplet number and surface temperature on evaporation are studied by three cases.

The arrangement of multiple n-heptane droplets and the simulation conditions are shown in Figure 6.23 and Table 6.6, respectively. The droplets are indicated by blue colored circles and the hot wall is indicated by a grey rectangle. The total liquid mass remained same in all cases, therefore, the droplet size varies at each case and multiple droplets always have equal size. The initial distance between any two droplets in Case 2 and Case 3 is equal to the radius of this set of droplet. The initial distance between each droplet center and wall is the same for all three cases. The droplets fall with an initial velocity of 0.8 m/s. The initial temperature and pressure of the domain including the droplet is 298 K and 1 atm. The surface temperature is maintained at 483 K, which is above the Leidenfrost

temperature of n-heptane (473 K). Hence, the evaporation of the droplets is in film boiling regime referred to Figure 2.2. The contact angle between the droplet and the hot surface is set to 120^{o} [44].

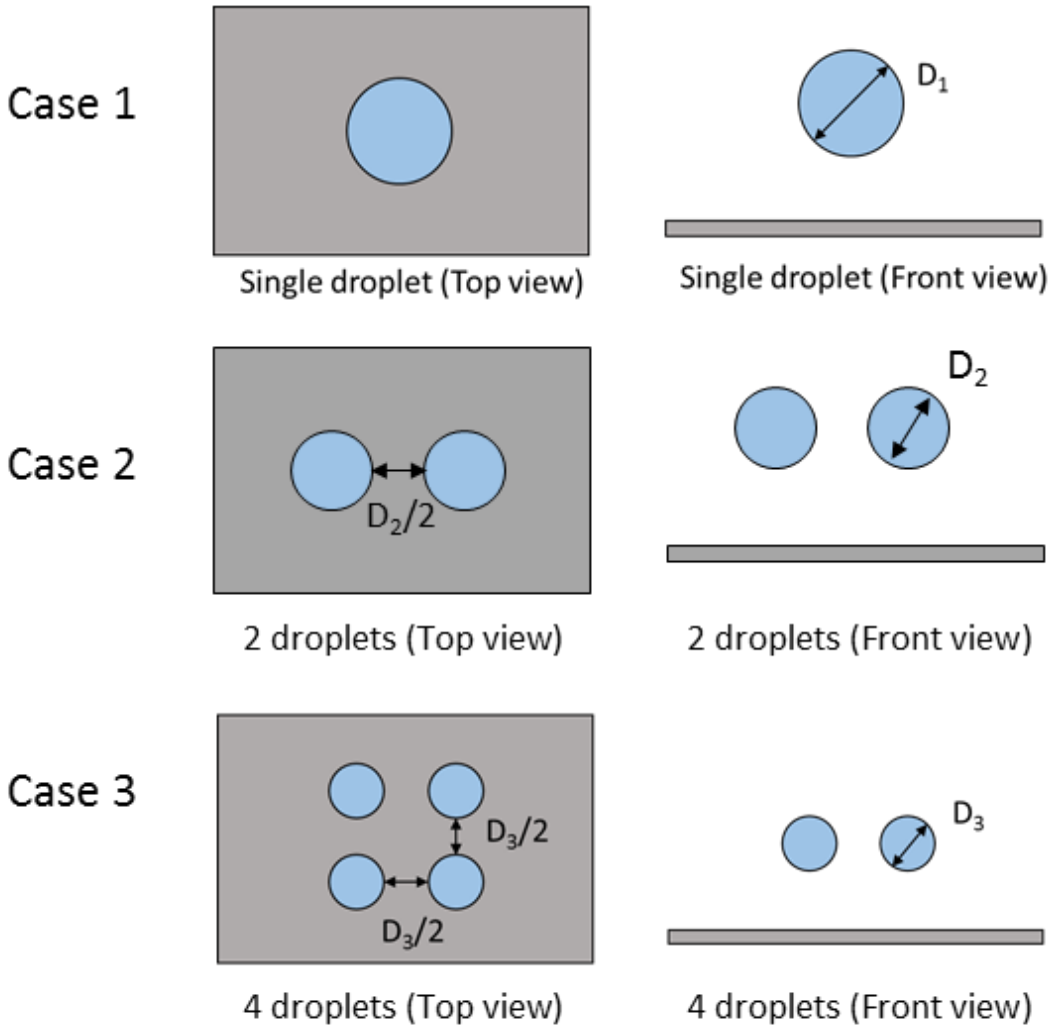

Figure 6.23: Droplet arrangement of three cases.

Table 6.6: Simulation parameters of three cases

	Case 1	**Case 2**	**Case 3**
Fuel	n-heptane	n-heptane	n-heptane
Number of droplets	1	2	4
D_0 (mm)	1.50	1.19	0.94
V_0 (m/s)	0.8	0.8	0.8
We	41	33	26
Re	3750	2975	2360

The computational domain used in this study is three-dimensional domain (8 mm x 5 mm x 5 mm) with air inside at atmospheric pressure and temperature of 298 K. A non-uniform mesh with the maximum size of 200 µm and minimum size of 50 µm in x, z directions and maximum size of 613 µm and minimum size of 7.5 µm in y direction is generated. A finer mesh is used in the center of the domain and near the hot surface region where. The heat conduction to the droplet is maximum in this zone and droplet shape after impact is also dependent upon grid resolution in this region. Figure 6.24 shows the mesh generation of Case 1 and a similar grid distributions is used in Case 2 and Case 3.

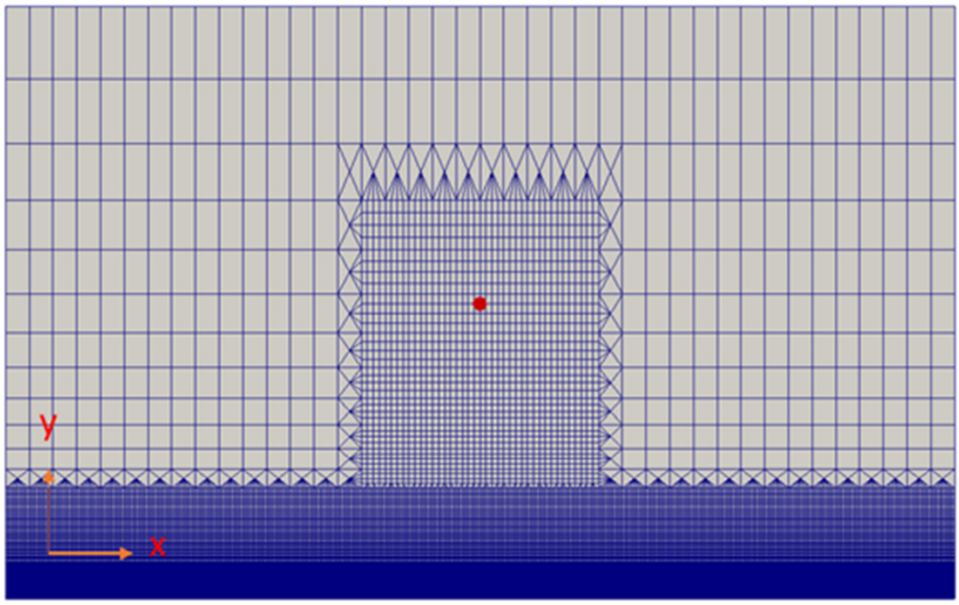

Figure 6.24: Numerical grid distribution in Case 1.

6.3.3 Simulation results

This section presents the results of the simulations in three cases. As all the cases correspond to film boiling regime, a vapor film can be observed between the droplet and the wall. This vapor layer prevents the droplets from getting into physical contact with the wall. Heat flux to the droplet from wall is by conduction through the vapor film.

Figure 6.25 presents the temporal variation of droplet shape and vapor formation for Case 1, Case 2, and Case 3. A cut section view of plane at z = 0 is presented for Case 1 and Case 2. A diagonal plane cutting the centers of droplets is used in Case 3. In Figure 6.25, the white color stands for the liquid fuel phase and the color with the legend represents the vapor phase of fuel. Overall, it can be observed that in all three cases, the droplet shape and vapor volume fraction follow the similar trend. Also, the droplet shape and vapor volume fraction distribution of single droplet case match well with the results of Nikolopoulos et al.[15]. As the droplet approaches the hot wall around 3 ms, a portion of the liquid droplet vaporizes and forms a thin film. This film prevents the physical contact between droplet and the wall. Droplet continues to spread after impact till a thin neck region appears at the end of the spread droplet. Then, it starts to recede and rebound from the surface after 9 ms. During the rebound phase, droplet appears to oscillate in shape from vertical elongation in the beginning to near spherical shape in the later stages. The temperature is higher closer to the wall and reduces nearby the droplet. Additionally, from Case 2 and Case 3 of multi-droplet, it can be seen that droplets start to merge together after 3 ms when they impinge on the wall, and there is more vapor in the center of the domain at 5 ms which might be caused by the pressure difference during multi-droplet impinging on wall and spread out to a larger region on the wall compared with single droplet. Finally, the multi-droplet merges to form a single droplet starting from 8 ms and rebound away from the plate.

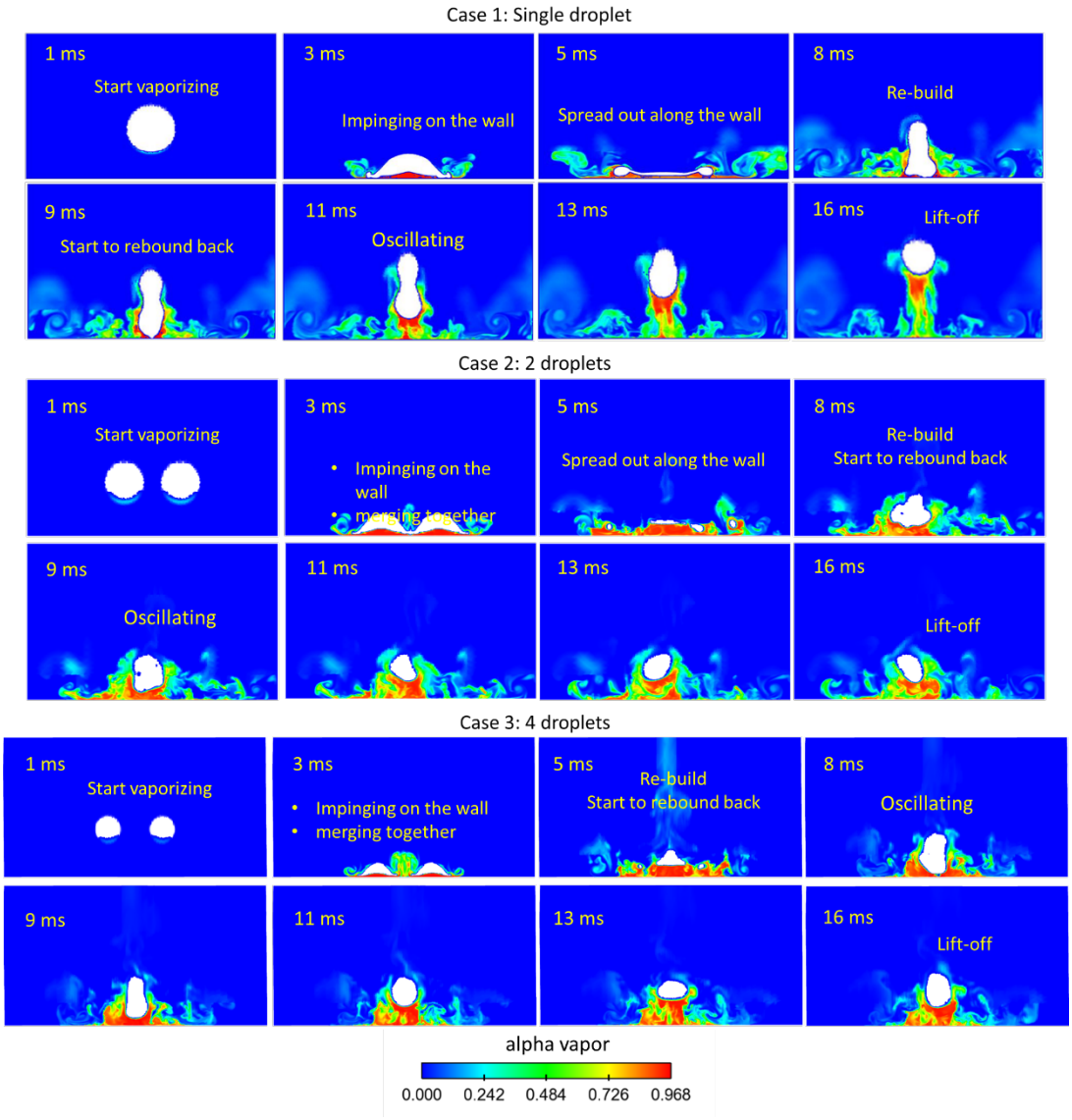

Figure 6.25: Temporal evolution of liquid and vapor volume fractions.

Droplets impinging on a hot wall surface above Leidenfrost temperature levitate above the surface due to vapor film forming between the droplet and surface. In the current study, droplet levitation is calculated as the minimum of the vertical distances between the surfaces of the droplets to the hot surface. Droplet levitation has an effect on the surface temperature and vapor distributions around the droplet, and thus the evaporation rate.

Figure 6.26 shows the variation of droplet levitation in three cases over time. Initial droplet lift is different in each case due to the differences in droplet diameter. Droplet lift approaches its minimum value in each case at about 2.5 ms when it comes closer to the surface. As the droplet spreads and continues to evaporate, its levitation increases due to the distribution of vapor below the droplet. When the droplet reaches its maximum extent along the surface, droplet levitation decreases again as it tries to overcome the force exerted by the vapor. The fluctuation of droplet levitation is observed until a steady state between the vapor mass below the droplet and the droplet mass is achieved. During the receding stage, the levitation decreases to some extent initially and then increases. When the droplets rebound from the surface, droplet levitation in Case 1 (single droplet) is higher compared to those in multiple droplets. In a similar trend, droplet lift is expected to be higher in Case 2 (2 droplets) compared to that in Case 3 (4 droplets), however, the opposite trend is shown. Since droplets are arranged in two rows in z direction in Case 3, each droplet has two neighboring droplets opposing its spreading, which results in the merged droplet rising earlier. The droplet levitation becomes similar in Case 2 and Case 3 after 14 ms.

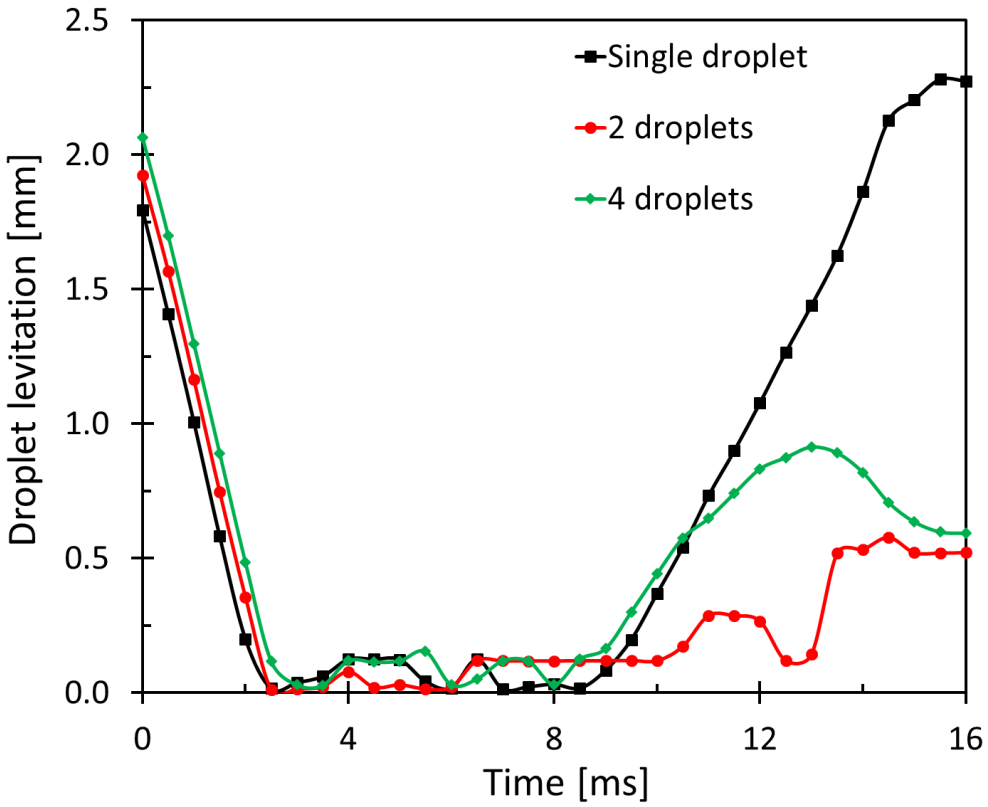

Figure 6.26: Droplet lift-off height from the wall.

The average surface temperature of a droplet is an important parameter associated to phase change of droplet. Surface superheat is neglected in this study. Theoretically, the average surface temperature of droplets with infinitesimally thin surface, undergoing phase change, must be saturation temperature. The saturation temperature of n-heptane is 371 K at atmospheric conditions and hence the droplet starts evaporation when the droplet surface reaches saturation temperature. Nevertheless, VOF simulations cause an interface smeared across few cells with finite thickness excluding the effect of grid resolution. Therefore, average surface temperature might be different with saturation temperature even with droplet phase change. Figure 6.27 presents the results of average surface temperature in all the cases.

It can be observed that initially the droplets are at a room temperature of 298 K. The surface temperature increases steadily to saturation temperature at about 2.5 ms. Increase in

temperature is due to the movement of droplets towards heated wall and exposure to its high temperature. The temperature of the surface drops considerably decreases after 8 ms in Case 1 (single droplet), because the droplet lift above the wall starts to increase at the same time as seen in Figure 6.25 and Figure 6.26. As the droplet moves away from the hot surface into the colder domain and the temperature gradient exists in the computational domain, its surface temperature decreases. The decrease in surface temperature is less pronounced in Case 2 (2 droplets) and Case 3 (4 droplets). The surface temperature in Case 3 is lower than that in Case 2 beyond 7.5 ms which is due to less levitation occurred in Case 2 compared with that in Case 3 as shown in Figure 6.25 and Figure 6.26.

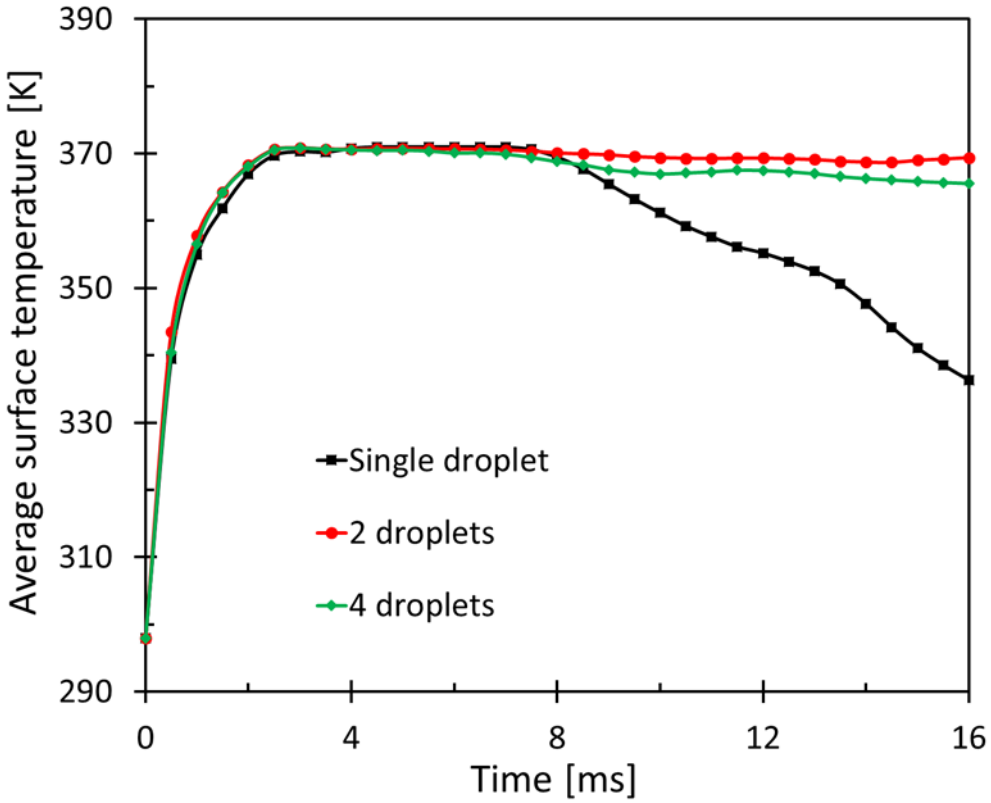

Figure 6.27: Temporal variation of average surface temperature.

The liquid mass fraction inside the domain is normalized with the initial mass fraction and is plotted as a percentage over time in Figure 6.28. Initially, droplets are at room temperature and the liquid mass fraction is at 100%. The total liquid mass at the beginning

of the simulation is the same in three cases. Liquid mass fraction decreases slightly at the beginning of the simulation due to mass diffusion from droplet surface to the surrounding air. During this period, the temperature of the droplets increases to saturation temperature. Then, there is a sudden decrease in liquid mass fraction due to the onset of evaporation caused by temperature and mass diffusion gradient. The evaporation rate in Case 3 (4 droplets) is the highest, then Case 2 (2 droplets), finally Case 1 (single droplet). This is because of larger surface area in Case 3 compared to Case 2 and Case 1. Larger surface area facilitates more heat transfer and hence higher evaporation rate. The evaporation rate significantly reduces after the droplets rebound from the wall. In Case 2 and Case 3, merging of multiple droplets at about 4.5 ms leads to reduction in surface area. This leads to decrease in evaporation rate in Cases 2 and Case 3 compared with Case 1. Higher droplet levitation and less spread lead to less evaporation and higher liquid mass fraction in Case 3 compared to Case 2. Liquid mass fraction after 5 ms achieve to the lowest in single droplet case due to higher droplet spread which resulted in more evaporation. A very high droplet levitation ensures that evaporation is negligible in single droplet case after 10 ms, where as a low evaporation rate causes sustained decrease in liquid mass fraction in Cases 2. This leads to liquid mass fraction becoming almost equal in Cases 1 and Cases 2 after 15 ms. Cumulative heat transfer to the droplet can be calculated based on the liquid mass evaporated and the latent heat of vaporization. It turns out that maximum heat transfer takes place in Case 1 and minimum in Case 3. However, the heat transfer in Case 2 continues to increase even beyond 9 ms and becomes almost the same to that of Case 1.

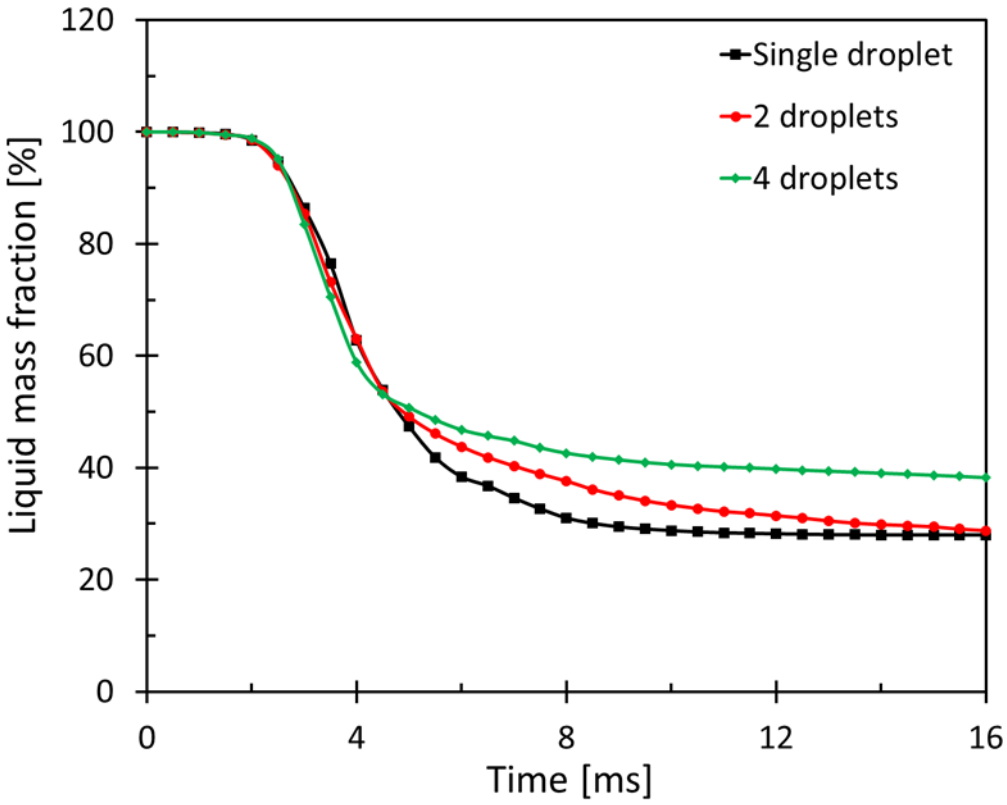

Figure 6.28: Time dependency of liquid mass fraction.

6.3.4 Summary

In current section, an evaporation sub-model was successfully implemented into the existing solver with VOF model in OpenFOAM framework. The newly developed solver was validated with the published results and mesh dependency study was carried out to give an idea of optimum mesh resolution. The current work then concentrated on numerical study on the evaporation of spherical droplets impinging on the wall and investigated the effect of droplet number and arrangement on evaporation in film boiling regime. Three cases including Case 1 (single droplet), Case 2 (2 droplets) and Case 3 (4 droplets) were examined for droplet lift and spread, surface temperature, heat transfer, and evaporation rate. The main conclusions on evaporation of spherical droplets impinging on the wall are summarized as follows:

(1). The simulations successfully predict the droplet levitation characteristic of evaporation above Leidenfrost point.

(2). Droplet spread in Case 2 and Case 3 is influenced by the presence of multi-droplets and their relative positions. Droplet spread decreases as droplet number increases in a direction and take less time to recede.

(3). Droplet levitation from the wall approached zero as the droplet impinges on the wall and oscillates as the droplets spread and recede on the surface. Maximum lift-off reduces as droplet number increase in a direction. Additionally, droplet number in a perpendicular direction leads to reduction in droplet spread and increase in lift-off.

(4). Droplet average surface temperature is directly influenced by its lift-off from the heated wall. Higher lift-off results in lower average temperature. The temperature increases from 298 K to saturation temperature as the droplet approaches wall.

(5). Droplet evaporation rate is higher in Case 3 as it has larger surface area compared with Case 2 and Case 1. But after the impact, droplets merge together and the spread and surface area are smaller in multi-droplets cases and hence the evaporation rate decreases.

CHAPTER 7 SPRAY-WALL IMPINGEMENT UNDER DIESEL ENGINE CONDITIONS[2]

This chapter presents results from experiments and simulations for spray-wall impingement under various diesel engine conditions. The first section discusses the experimental and numerical study of spray-wall impingement with a 7-hole diesel injector. The second section presents the results obtained from spray-wall impingement with a single-hole diesel injector. The next section provides the experimental and simulation results of spray-wall film characteristics. The final section gives the heat flux measurement results when a single-hole diesel spray impinging on a high temperature flat surface.

7.1 Spray-wall impingement with 7-hole diesel injector

The test condition for spray wall interaction is listed in Table 7.1. The 7-hole diesel nozzle was tested in the current work. The nozzle is characterized by a 139 μm diameter, a K factor of 1.5 and an included angle of 148°. The ultra-low sulfur diesel (ULSD) is used as the fuel and its detailed properties listed in Table 7.2.

[2]Reprinted with permission from SAE papers 2017-01-0854 ©2017 SAE International, 2018-01-0276©2018 SAE International, and 2018-01-0312©2018 SAE International. The materials in this chapter were published in the following papers:

- Zhao, L., Torelli, R., Zhu, X., Scarcelli, R. et al., "An Experimental and Numerical Study of Diesel Spray Impingement on a Flat Plate," SAE Int. J. Fuels Lubr. 10(2):407-422, 2017, https://doi.org/10.4271/2017-01-0854.
- Zhao, L., Torelli, R., Zhu, X., Naber, J. et al., "Evaluation of Diesel Spray-wall Interaction and Morphology around Impingement Location," SAE Technical Paper 2018-01-0276, 2018.
- Zhao, L., Zhao, Z., Zhu, X., Ahuja, N. et al., "High Pressure Impinging Spray Film Formation Characteristics," SAE Technical Paper 2018-01-0312, 2018.

Table 7.1: Test conditions for 7-hole diesel spray-wall impingement test

Parameter	**Values**
Ambient gas temperature (K)	423 K
Ambient gas density	Varied
Ambient gas composition	100% N_2 (non-vapor)
Ambient gas velocity (m/s)	~0
Nominal nozzle outlet diameter (μm)	139
Nozzle K factor	1.5
Number of holes	7 (multi-hole)
Orifice orientation relative to injector axis	74° (included angle: 148°)
Fuel injection pressure (MPa)	150
Fuel	ULSD
Fuel temperature at nozzle (K)	423
Energizing injection time (ms)	2.0
Distance between injector tip to impinging surface (mm)	65

Table 7.2: Fuel (ULSD) properties

Parameter	**Values**
Density (kg/m^3)	848
Distillation	Initial boiling point: 344 K
	10%: 418 K
	50%: 514 K
	90%: 599 K
	Final boiling point: 656 K
Viscosity (cSt)	2.6
Carbon (wt %)	86.8
Hydrogen (wt %)	13.2
Sulfur	8
Cetane Index	47.2
Net heating content (MJ/kg)	42.83

Bosch ROI meter is adopted to obtain the injection rate shape [122]. ROI profiles for the energizing injection time of 1 ms, 2 ms, and 4 ms at the injection pressure of 150 MPa are shown in Figure 7.1. The corresponding injection durations are approximately 1.6 ms, 2.9 ms and 4.8 ms. Figure 7.1 shows that the ROI profile is repeatable for different injection durations. ROI profile at energizing injection time of 2 ms was selected as the baseline condition for experimental and numerical evaluations. The total injected mass measured at ambient temperature is 114.5 mg, subsequently, this ROI measurement was scaled based on fuel temperature for the CV tests and then used in simulations.

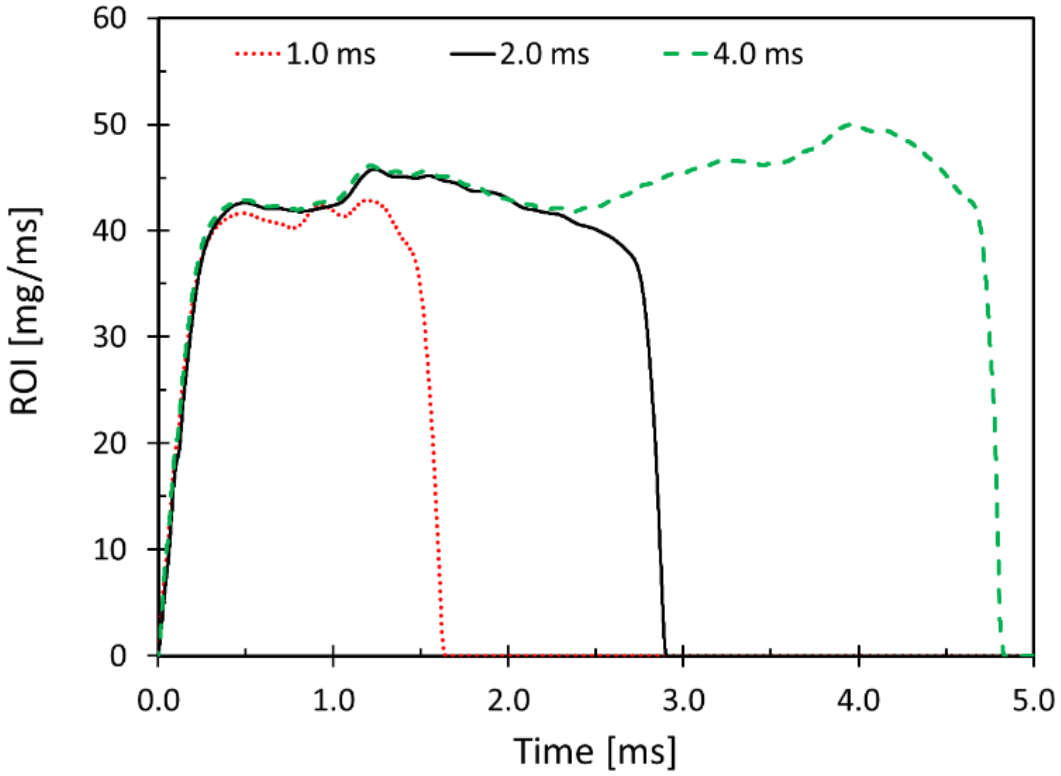

Figure 7.1: Rate of injection profiles for injection pressure of 150 MPa and 1-2-4 ms energizing injection time.

7.1.1 Experimental results

The detailed schematic of spray-wall impingement is shown in Figure 7.2. Droplets induced by spray injection are distributed near the plate where these droplets show higher velocity and momentum than those relatively farther from the plate. As a result, the lower momentum droplets are lifted higher from the plate surface and their height parallel to the plate becomes larger. The spray layer away from the plate stays quiescent while the spray near the plate is preceded by the larger size droplets. Due to this phenomenon, leading edge parallel to the plate generates wake, called wall jet vortex and increases surrounding air entrainment. Main jet region resides inside non-impinged part and their velocities, momentum and densities are quite large. Mixing flow region stays outside of spray surrounding the main flow region where turbulence is generated between spray and surrounding gas such that these droplets rebound above due to the loss of momentum

between surrounding and droplets. Wall jet vortex is observed near the area for impinging jet. Droplet distribution around the region is complicated by the mixing of oncoming low-momentum droplets farther from the plate and relatively high-momentum droplets near the plate. Therefore, there exists a secondary region for high probability of collisions between the large and small droplets.

Figure 7.2 also defines the free spray and radial impinged spray properties in side view; similar concepts are applied in front view with axial impinged spray properties. The front view with radial impinged spray properties and the side view with axial spray properties are presented in Figure 7.3. As mentioned in previous section, spray penetration is the distance between the injector tip and the end point of spray that represents the maximum presence of spray in chamber. The impinged spray radius is the maximum spread distance using the point of spray impinging on wall as the reference. The impinged spray on wall is defined similarly to the impinged spray radius, but, unlike the latter, impinged spray on wall is the spread distance along the plate/wall and is shorter than the impinged spray radius. The impinged height is the height formed by the spray in the orthogonal direction with respect to the impinged plate.

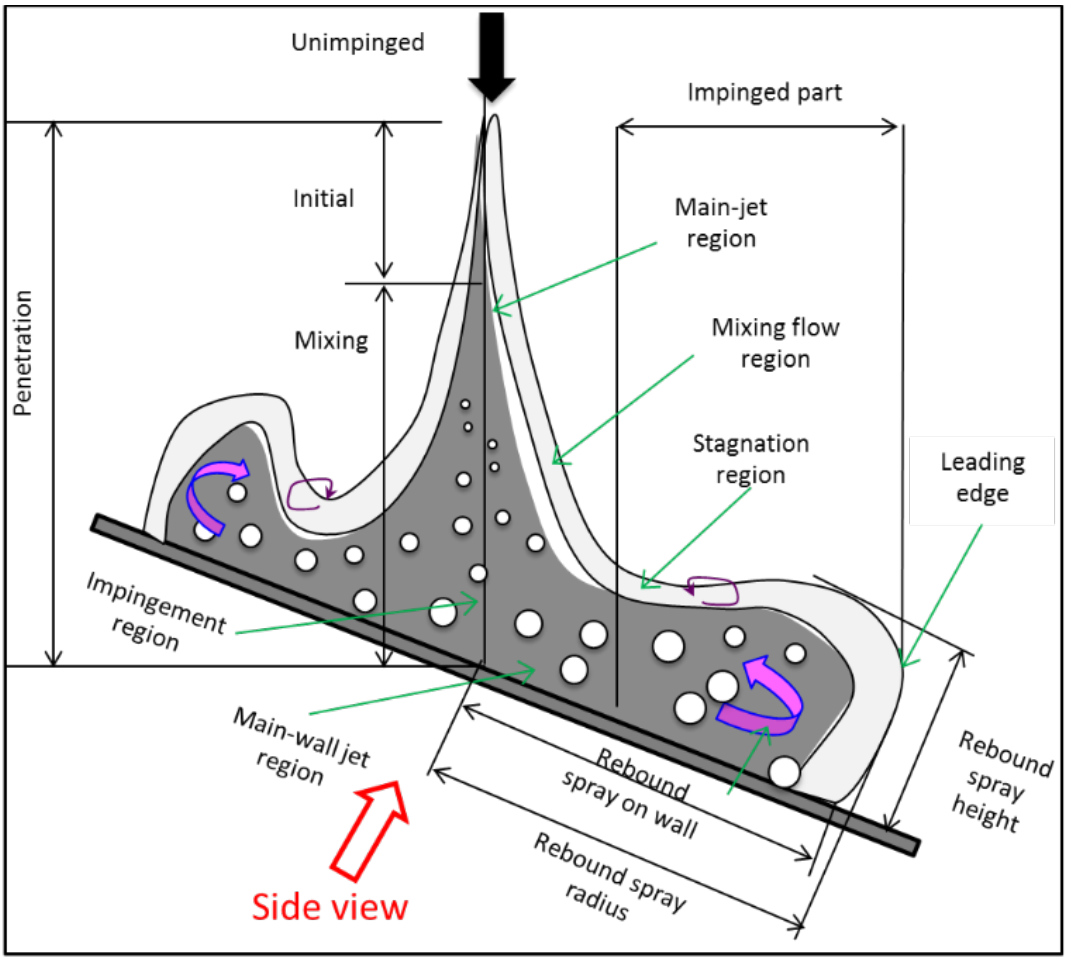

Figure 7.2: Schematic of spray-wall interaction with nomenclature.

Figure 7.3 shows sequential images of the Mie scattering of spray impinging on the plate with front and side views. From the front view shown in Figure 7.3 (top), the 7-hole injector can be seen and the single plume which impinges on the plate is the focus for the current study. This plume looks slightly skewed since the adjustment of nozzle orientation was done manually, and hence could not be placed exactly aligned with the vertical axis. Additionally, there is an angle of 16° between the wall on which the injector is mounted and the plumes, clearly visible from side view of Figure 7.3 (bottom). This was accounted for in reporting liquid penetration measurements. As expected, it can be observed that the rebound spray spreads radially and axially once the spray hits on the wall. Care has been

taken for the image analysis to avoid the adjacent plume interference, particularly in the side view spray analysis.

Figure 7.4 shows the results of free spray and rebound spray properties (averaged from three runs). The liquid penetration is shown in secondary y-axis and it can be seen that the spray impinges the wall at after start of injection (ASOI) of 1.3 ms and the maximum penetration is about 65 mm. Note: terminologies used in the legends refer to Figure 7.2. Other rebound properties are shown in primary y-axis and start from 1.3 ms which is after spray impinging the plate. The rebound radii have larger penetrations than the rebound spray on wall. This phenomenon occurs for both the axial and radial direction as shown in Figure 7.3. However, the axial rebound properties, including rebound radius and rebound on wall, are slightly higher than those in radial direction, and the rebound height in axial direction is slightly lower than the one in the radial direction.

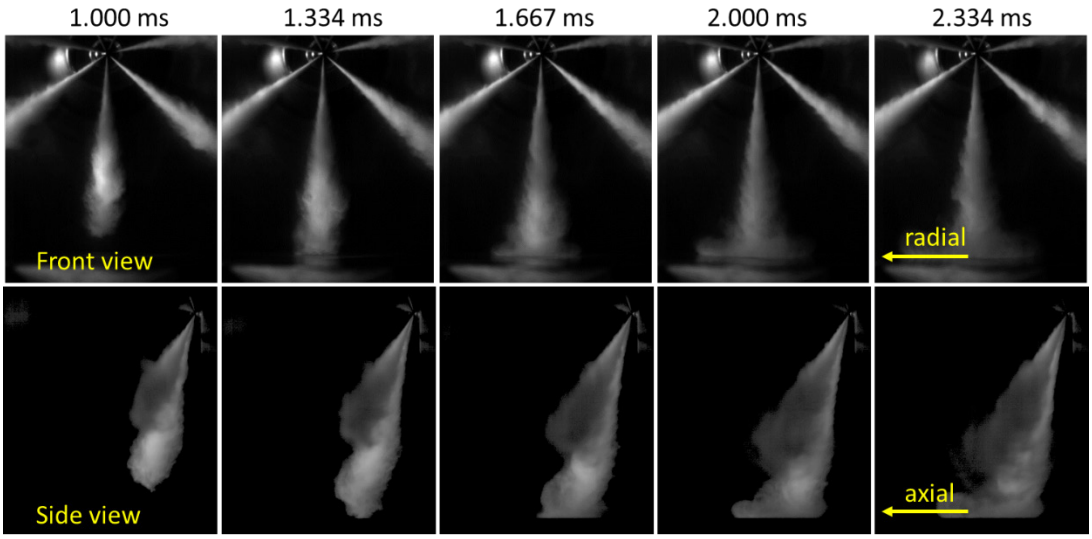

Figure 7.3: A sequential visualization of spray-wall impingement experiment from front and side views.

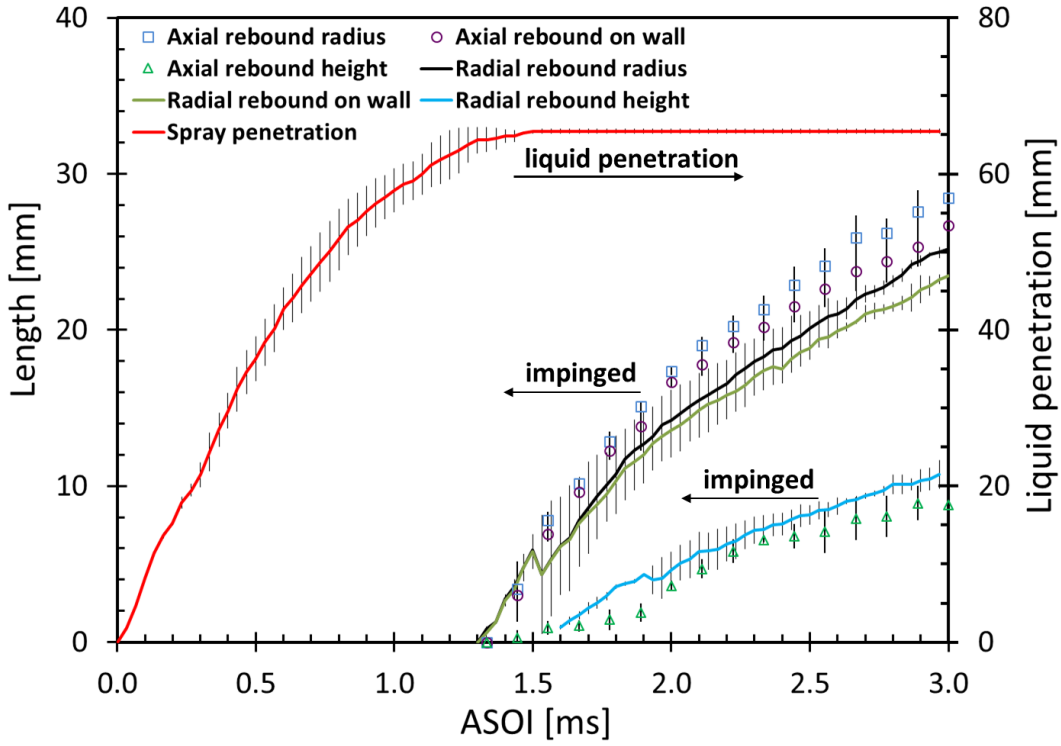

Figure 7.4: Spray penetration and impinged spray properties.

7.1.2 CFD model validation

7.1.2.1 Details on mesh strategy

The constant volume vessel was modeled with a cubic domain whose edge size was equal to 130 mm. All the simulated cases were characterized by a Cartesian grid with a base mesh size of 4 mm. For the reference case, four levels of refinement were adopted by means of fixed embedded regions in the near nozzle areas and AMR based on velocity, temperature, and species gradients. This allowed to achieve a minimum size of 0.25 mm in those areas where the interaction between the liquid and the gaseous phases occurred. These choices resulted in the peak cell count growing from an initial value of 220,000 to approximately 1.8 million, over the 3.0 ms simulation time.

The first part of the numerical study focused on mitigating the dependency of the results on the orientation between each spray plume injection direction and the grid elements. This activity had to account also for the geometrical constraint given by the orientation of one

of the seven plumes (the one used for the result comparisons) with respect to the impinged wall. The preliminary studies show that the choice to align one of the seven plumes with one of the main direction of the grid elements might lead to a high variability of the computed liquid penetration. In particular, due to the number of nozzles (seven), only one of the plumes resulted in being perfectly aligned with the grid elements, leading to the under-estimation of its liquid penetration with respect to the other six plumes (see Orifice 1 in Figure 7.5). This under-estimation is related to the different diffusion of the momentum source term that, in turn, provided lower gas velocities in those cells where the liquid droplets were located. This resulted in higher relative velocities, which corresponded to higher drag acting on the liquid and hence leading to the overall lower liquid penetration. In order to overcome this source of variability, the grid structure was rotated by ~6.43° around the injector axis with respect to the CFD domain and the plume injection directions. The identified angle was the result of the misalignment maximization between the main directions of the grid elements and the injection direction of the closest plume. As shown in Figure 7.6, the mesh-induced variability was successfully reduced leading to a similar liquid penetration for all the plumes. The rotated mesh (results shown in Figure 7.6) is used for all the simulation studies reported in the next sections.

A note on the liquid penetration plots needs to be provided for clarity: the liquid penetration is defined at any given time-step as the distance of that parcel representing the 98% threshold of the cumulated mass distribution of all the parcels present in the domain at that given time-step, and ordered according to their distance from the orifice from which they have been introduced.

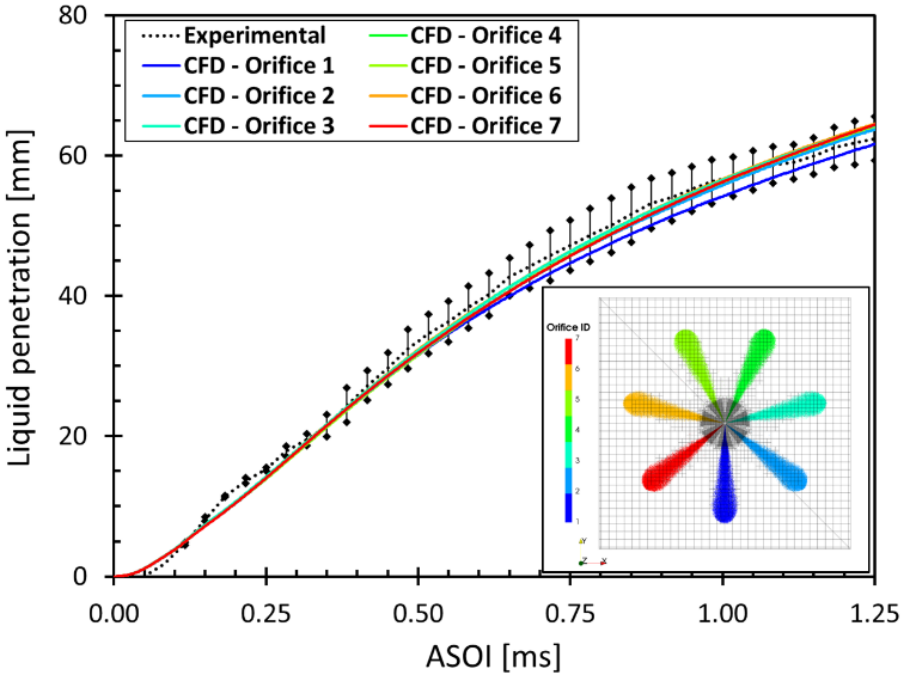

Figure 7.5: Liquid penetration comparison: grid elements aligned with one of the plumes (i.e., Orifice 1).

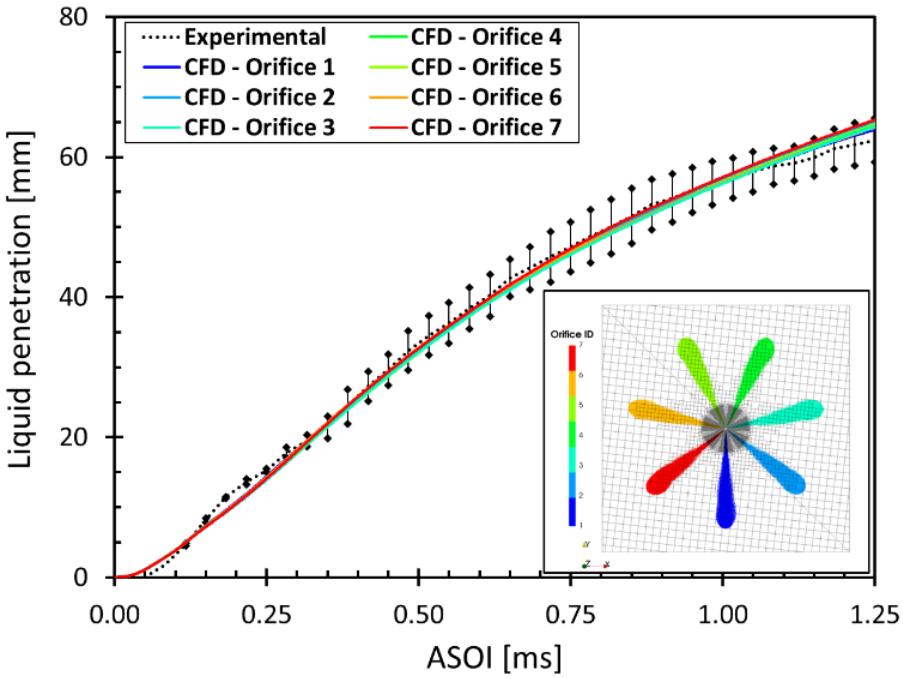

Figure 7.6: Liquid penetration comparison: grid elements rotated to ensure all the orifices are misaligned with the mesh.

7.1.2.2 Grid convergence study

This subsection presents grid convergence studies using the rotated mesh. For brevity only the results obtained for Orifice 1 are shown for liquid penetration.

The grid convergence study was performed for three minimum mesh sizes. In addition to the 0.25 mm reference case, two more cases were simulated. Simulations with minimum mesh sizes of 0.5 mm and 0.125 mm were performed using respectively three and five levels of refinement for both AMR and near-nozzle embedded regions.

Figure 7.7 shows that the 0.25 mm min. mesh size results are close to the most refined mesh of 0.125 mm, while the 0.5 mm case tends to under-estimate the liquid penetration.

In terms of cell count, the 0.125 mm case resulted in a peak cell count of ~2.1 million at 1.5 ms, which made it at least three times more computationally demanding compared to the 0.25 mm case. On the basis of the grid convergence and computational demand considerations, 0.25 mm mesh size was selected as the reference minimum mesh size for the remaining part of the study.

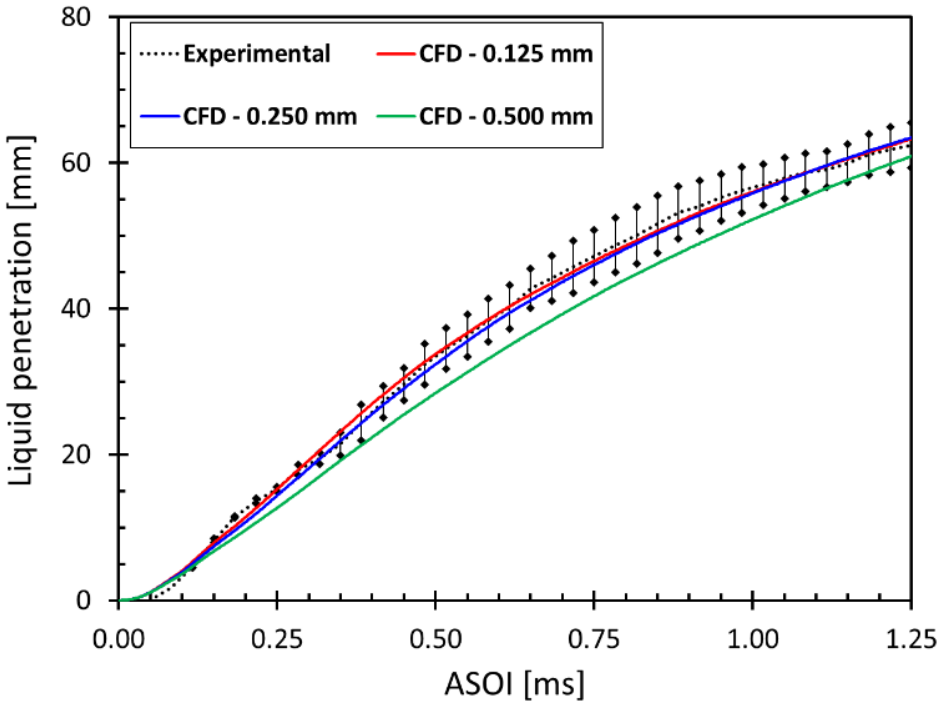

Figure 7.7: Grid convergence study is performed by plotting liquid penetration for Orifice 1 with different minimum mesh sizes vs. experimental data.

This section presents the comparison between the experimental measurements described in the previous subsection and the numerical simulation of the reference case described in the "Simulation Methodology" section. In order to provide a consistent comparison between experimental and numerical results, a series of post-processing tools was developed in the MATLAB™ framework [163].

In particular, all the quantities reported from experiments in Figure 7.4 were also calculated for the CFD simulations with a definition similar to the one used for the CFD liquid penetration, i.e., axial and radial spray lengths were identified with 98% mass threshold (based on the mass on the impinged plate). It should be noted that the parcel subset considered for the comparison is made of all those parcels that at some point during the simulation interacted with the wall (i.e., the parcels in the free spray are not considered in the post-processing of the CFD results, see red-colored spray in Figure 7.8).

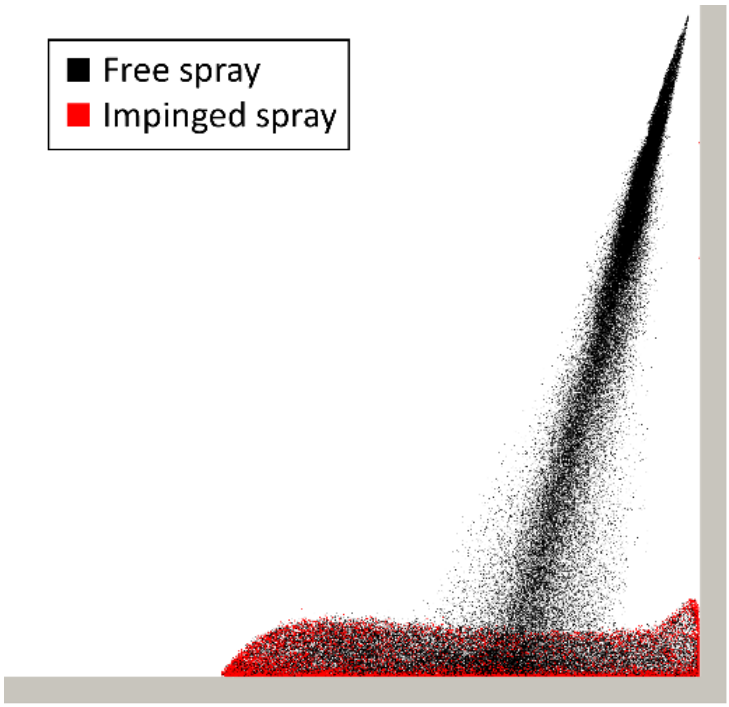

Figure 7.8: Orifice 1 plume at 2.5 ms: in red the parcel subset considered for the spray-wall interaction analysis.

7.1.2.3 Assessment of spray-wall interaction model

After carrying out the preliminary study and validation of the CFD spray model against the experimental liquid penetration, this section focuses on further assessment of the spray-wall interaction model against the spray impingement data. Since the liquid penetration from simulations matched well with experiments (cf. Figure 7.6), the prediction of the spray-wall impact time would be consistent with the experimental one. This allowed us to perform an unbiased evaluation of the spray-wall interaction process from simulations.

The plots in Figure 7.9 and Figure 7.10 show that the O'Rourke and Amsden model was able to capture the general behavior of the rebounded spray. In particular, the best agreement was found in terms of axial penetration of the rebounded/splashed liquid for both the bulk spray radius (cf. Figure 7.9, top) and the wall radius (Figure 7.9, middle for which only the wall film parcels were considered for the analysis). A disagreement was observed for the spray spreading in the orthogonal direction to the wall. One possible

reason that explains the lower prediction of the spreading could be connected with the under-prediction of the momentum of the splashed droplets traveling against the original direction of the free spray. This might be possibly due to the spray-wall interaction model under-estimating either the amount of splashed mass, or the droplet velocities. In any case, further investigation is needed in order to correctly asses the nature of the spray height under-prediction, and will be certainly addressed in future works.

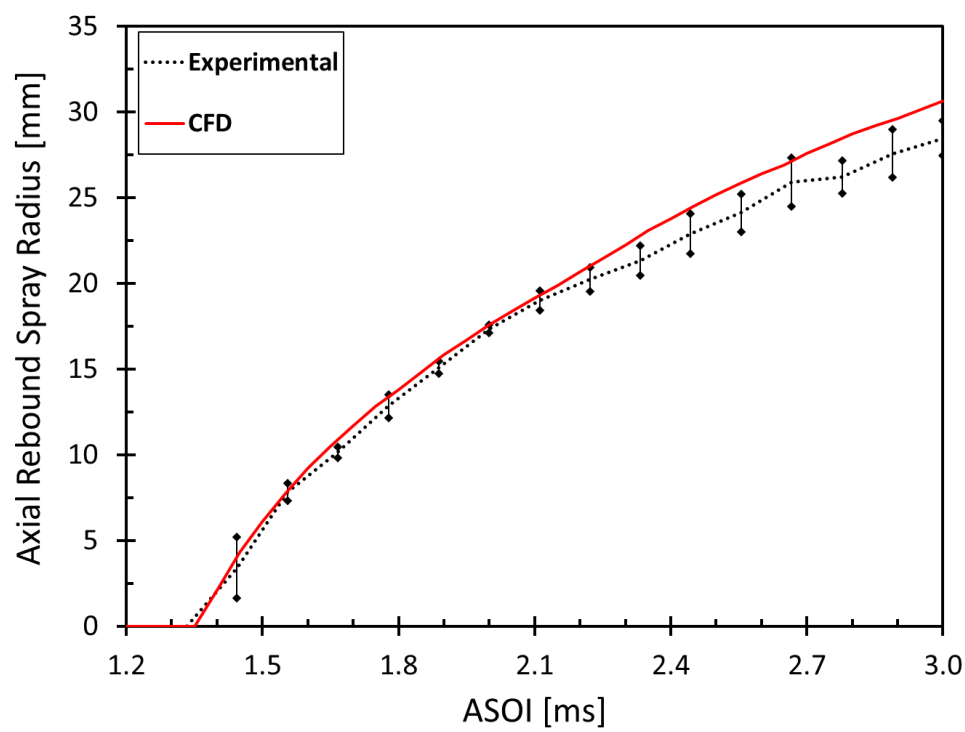

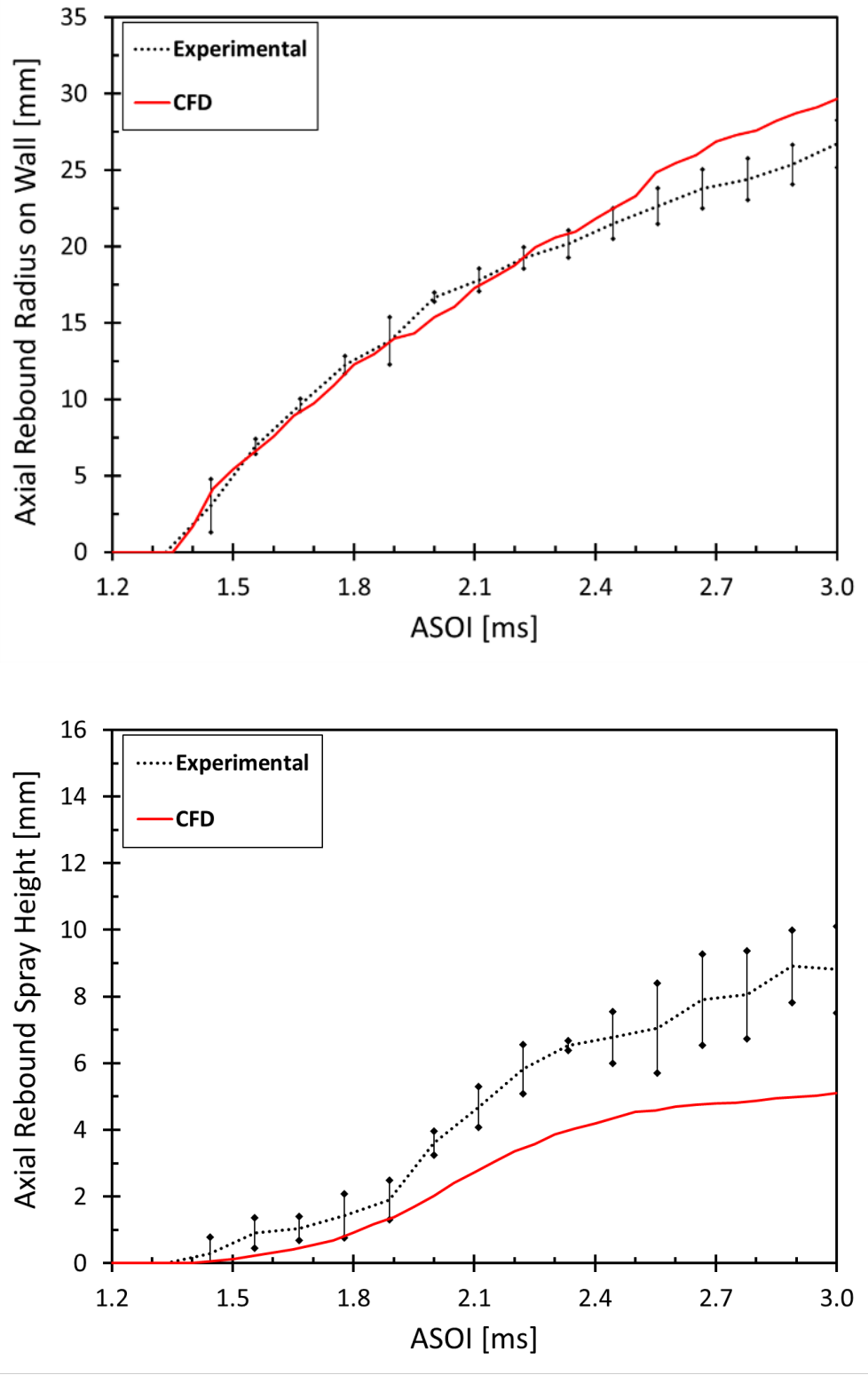

Figure 7.9: Maximum rebound radius (top), rebound on wall (middle), and spray height (bottom) vs time in the axial direction.

Similar conclusions can be drawn from the analysis of the radial profiles. Figure 7.10 shows that the model is able to capture the radial expansion of the spray, but tends to over-predict the spray penetration. Figure 7.10 (top) shows that the simulation predicts the distribution of the rebounded liquid to be symmetrical with respect to the injection direction, i.e., the two branches of the reflected free spray are very close to each other for the whole time range.

Figure 7.10 (middle) shows a good agreement of the radial rebound in the vicinity of the wall against the corresponding experimental measurement. At the same time some differences were found between the predictions of the two sides. This is possibly due to the asymmetric arrangement of the grid elements with respect to the direction of the spray which, in turn, does not allow for a perfectly symmetric representation of the numerical problem. In the authors' opinion, this error is much less important than the one introduced by the wrong prediction of the spray penetration obtained with the aligned mesh (cf. Figure 7.5). Indeed, a wrong prediction of the spray penetration is correlated with a wrong prediction of the interaction of the liquid and gas phases. This in turn affects the computation of the velocities of both liquid and gas anywhere the two phases interact, including the vicinity of the wall.

Similar to what was found for the axial profiles, the radial height of the rebounded spray in Figure 7.10 (bottom) is underestimated with respect to the experiments. The experimental measurements showed that the spray is not symmetrical due to a small offset of the orifice angular position with respect to the perpendicular direction to the plate. A more precise alignment of the reference plume could make the axial rebounding more symmetrical and lower the maximum spray height from experiments. We believe that, together with the higher momentum dissipation in the orthogonal direction previously pointed out, this represents an additional explanation for the mismatch between experiments and simulations.

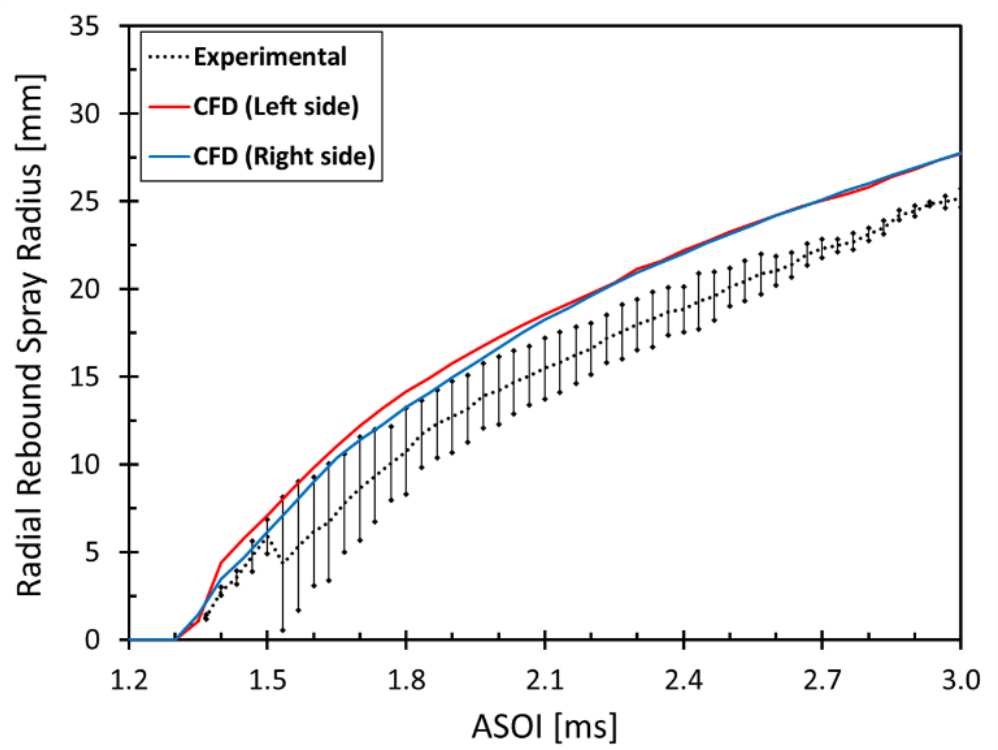

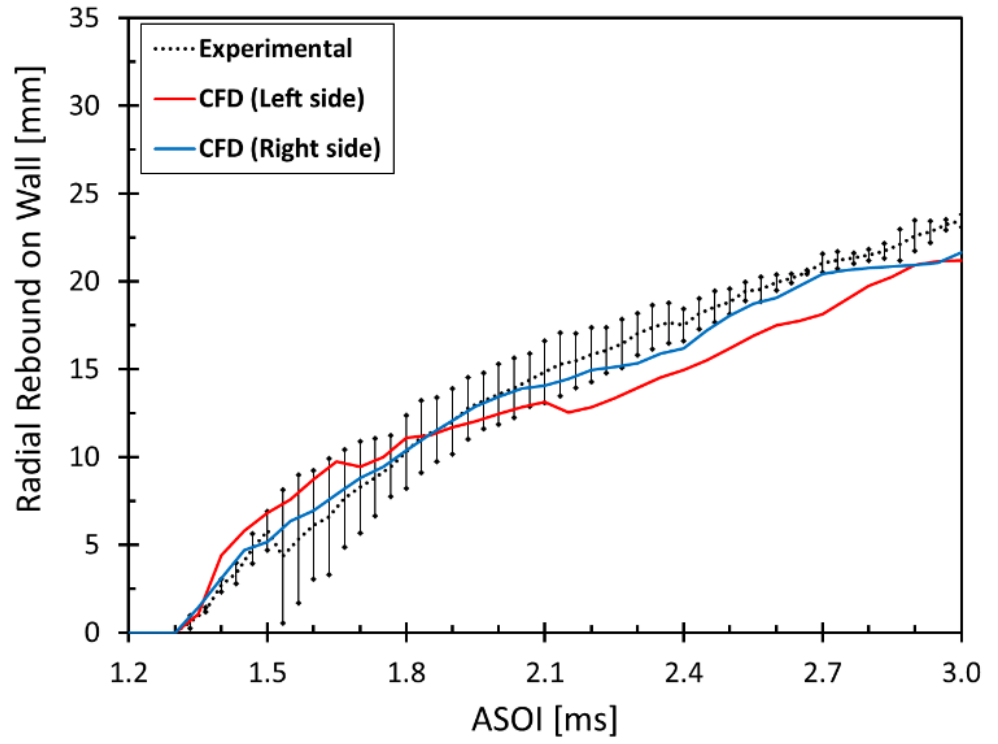

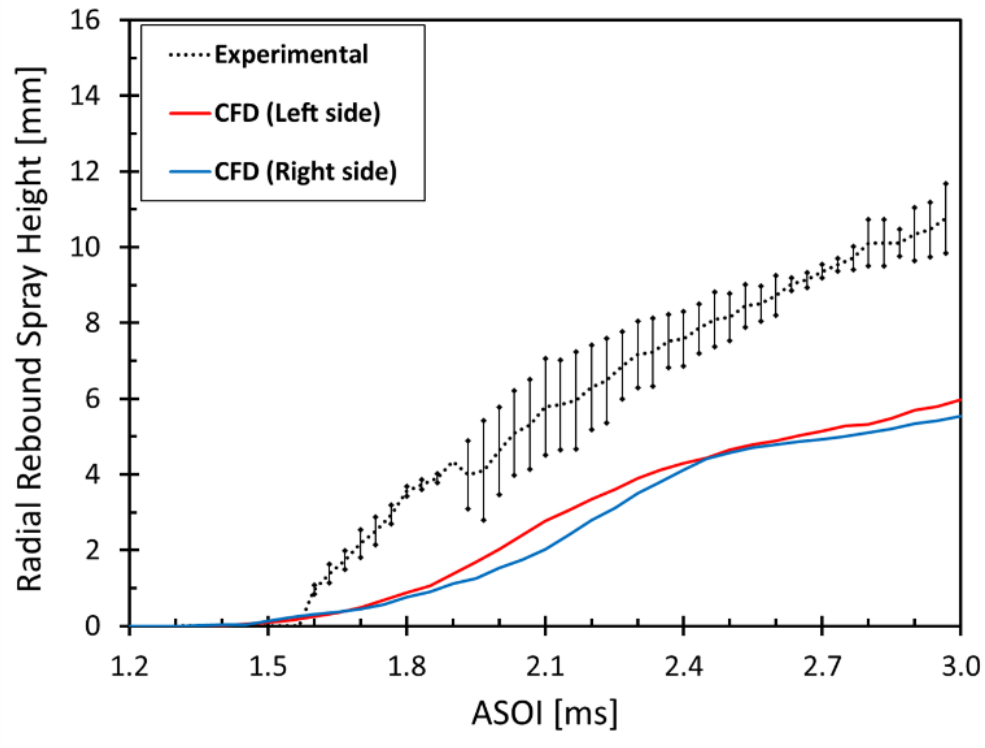

Figure 7.10: Maximum rebound radius (top), rebound on wall (middle), and spray height (bottom) vs time in the two radial directions.

The sequence of qualitative plots in Figure 7.11 shows that the CFD model was able to capture qualitatively the overall free-spray shape. On the other hand, the simulations were not able to replicate the shape of the rebounded liquid in the late stages of the injection event. Indeed for the simulated spray, the leading edge tends to stay attached to the wall, while the experiments show some recirculation that begins tangential to the wall and then deviates upwards resulting in larger thickness of the rebounded spray in experiments compared to the simulations. Some of the timestamps provided for the CFD analysis were not perfectly synchronized with the experiments, but were considered to be close enough for the general purpose of this analysis.

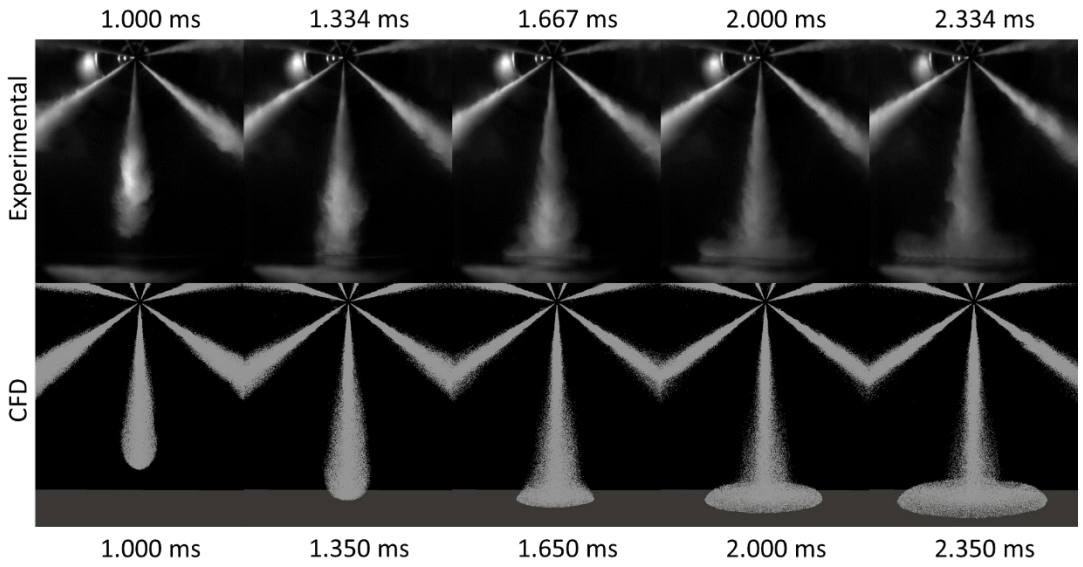

Figure 7.11: Qualitative comparison of liquid spray between experiment (top) and CFD (bottom) at different time instants.

7.1.3 Local spray characteristics of the impinging spray

This section focuses on estimating the local characteristics of the liquid phase in the vicinity of the impinged wall from simulations. A region of 1 mm thickness near the wall was used for the analysis of the global spray. SMD vs. time, and PDFs of normalized liquid mass with respect to *We* and *Re* were analyzed using post-processing tools written in MATLAB. The analysis was carried out by taking in account the following: spray parcel was (1) incorporated in the wall film, or (2) rebounded or splashed on the impinged wall, or (3) belonged to the free spray. This classification was made possible by the definition of an integer flag variable that changes its value each time a particular event occurs (e.g., the parcel becomes part of the wall-film, splashes, or rebounds).

The plot in Figure 7.12 shows the SMD vs. time. The free spray parcels were characterized by the lowest SMD, slightly lower than for the rebounded parcels, while those included in the wall film showed the highest SMD. The parcels that underwent wall film inclusion were characterized by higher *We* compared to those that rebounded. A possible explanation is that for similar velocity values, the wall film parcels are generally characterized by a

larger diameter. The parcels included in the "rebounded" subset showed a slightly higher SMD than those contained in the free spray. Assuming that after the impact, the liquid velocity could not be larger than the value before the impingement, due to low velocities and opposite direction of motion, the "rebounded" parcels were most likely involved in collision and coalescence phenomena with the incoming free spray. The collision and coalescence models regroup droplets from two different parcels into a single parcel with larger droplets. This is done in order to mimic the behavior of liquid droplets colliding in a spray.

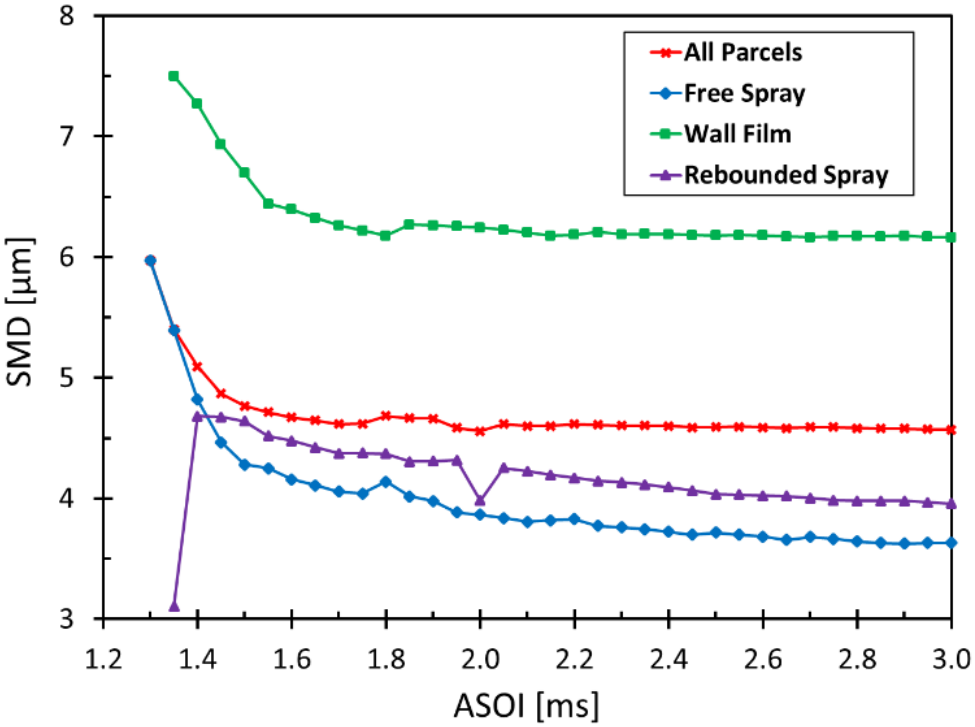

Figure 7.12: SMD vs time on varying the nature of the spray-wall interaction.

Figure 7.13 and Figure 7.14 show the time evolution of the PDFs of normalized mass with respect to *We* and *Re*. The normalized mass at a given time-step is intended as a non-dimensional total mass normalized to 100%. All the bars plotted in the graphs are therefore calculated as the ratio of the mass included in the parcels representing each bar, and the total liquid mass present in the domain at that given time-step.

A general outcome is that, due to the distance between the orifice and the wall, the fuels spray velocity is relatively low compared to the injection velocity, hence the *We* and *Re* values are quite low. Except for the *We* plot at 1.5 ms (cf. Figure 7.13, top), all the plots show a monotonic decrease in the normalized mass distribution as the *We* increases. This means that most of the mass is characterized by very low velocities. The plots also shows that at 1.5 ms (soon after impact) the mass is mostly included in the free spray, while at 2.0 and 2.5 ms, wall film mass is the dominant component. This implies that most of the mass that impinged on the wall was included and accumulated in the film. A comparison of the *We* and *Re* plots at 2.0 ms, shows that most of the liquid mass is characterized by a very low *We*, while its *Re* numbers are distributed along a wider range. This suggests that, for the analyzed parcels, due to the quadratic dependency of *We* on the liquid velocity, both *We* and *Re* numbers are mostly governed by the parcel size (linear dependency for both non-dimensional groups), hence the droplets in the wall film are bigger than those in the other two groups (free spray and rebounded liquid). This is consistent with what was already hypothesized from the analysis of the SMD plot in Figure 7.12.

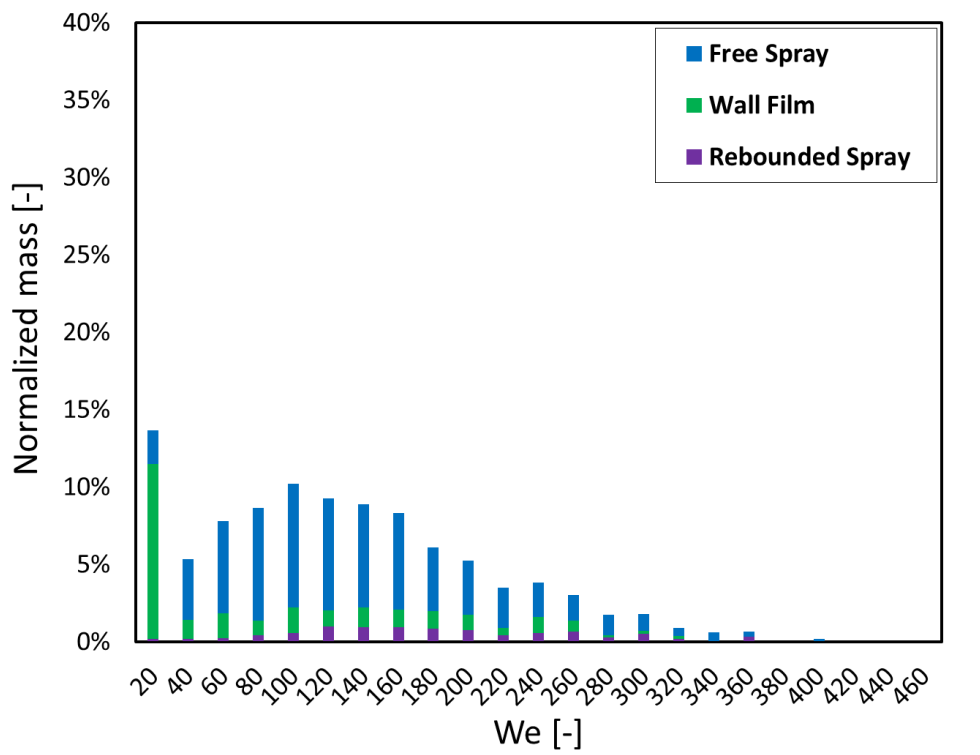

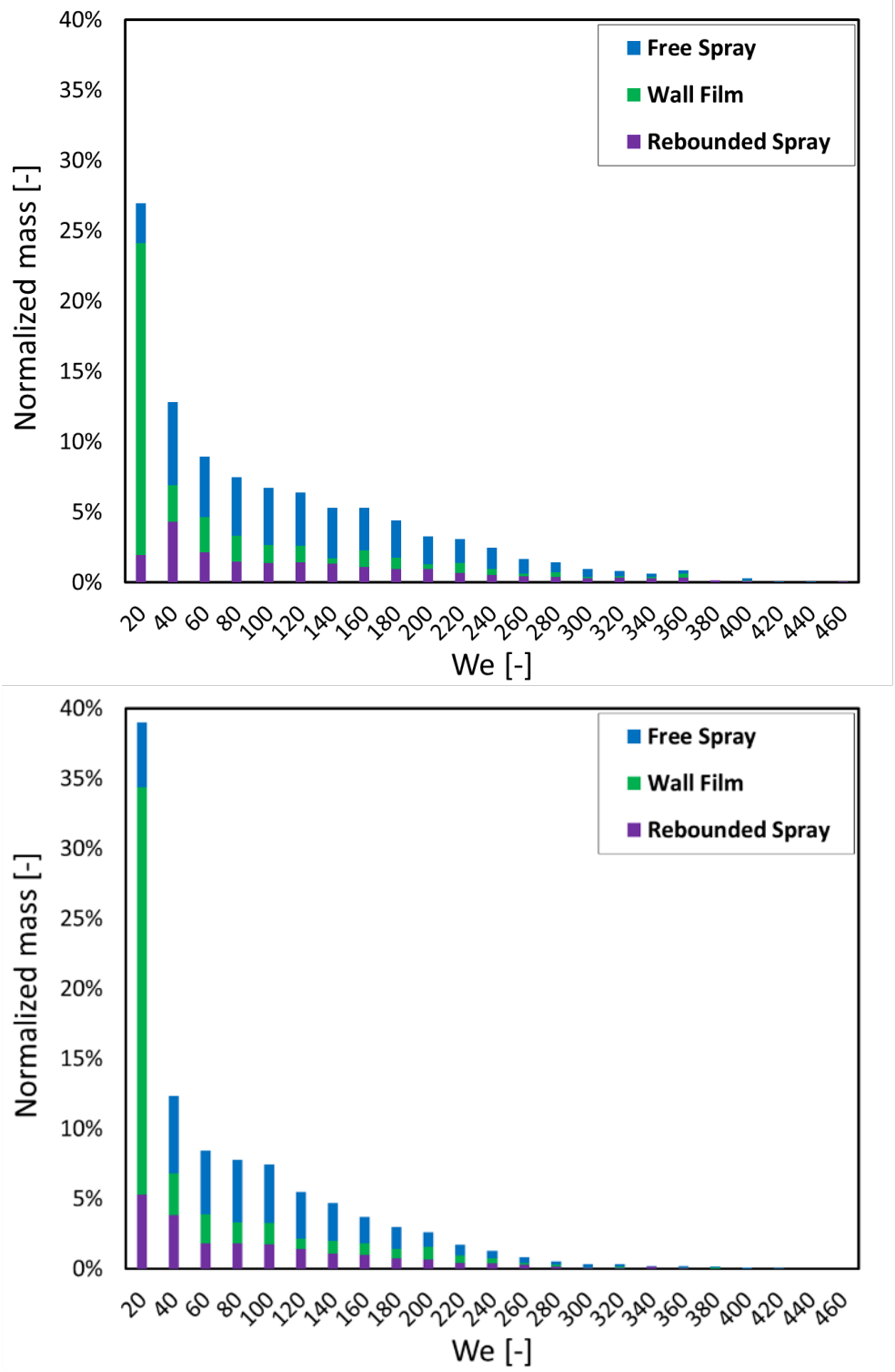

Figure 7.13: PDFs of normalized mass vs *We*: 1.5 ms (top), 2.0 ms (middle), 2.5 ms (bottom).

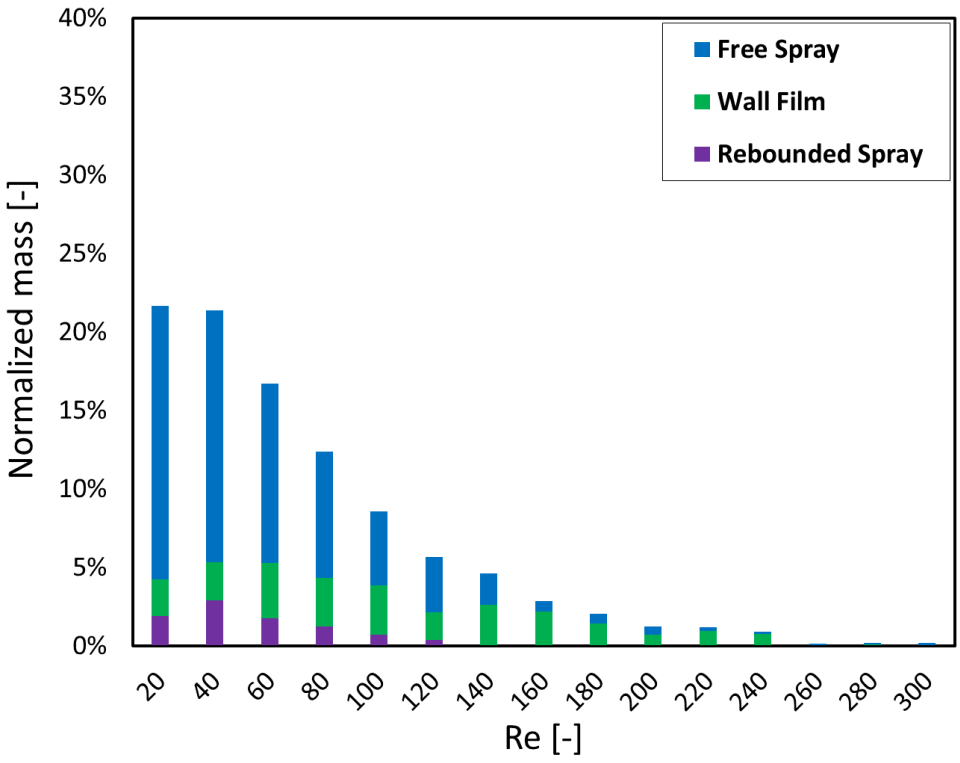

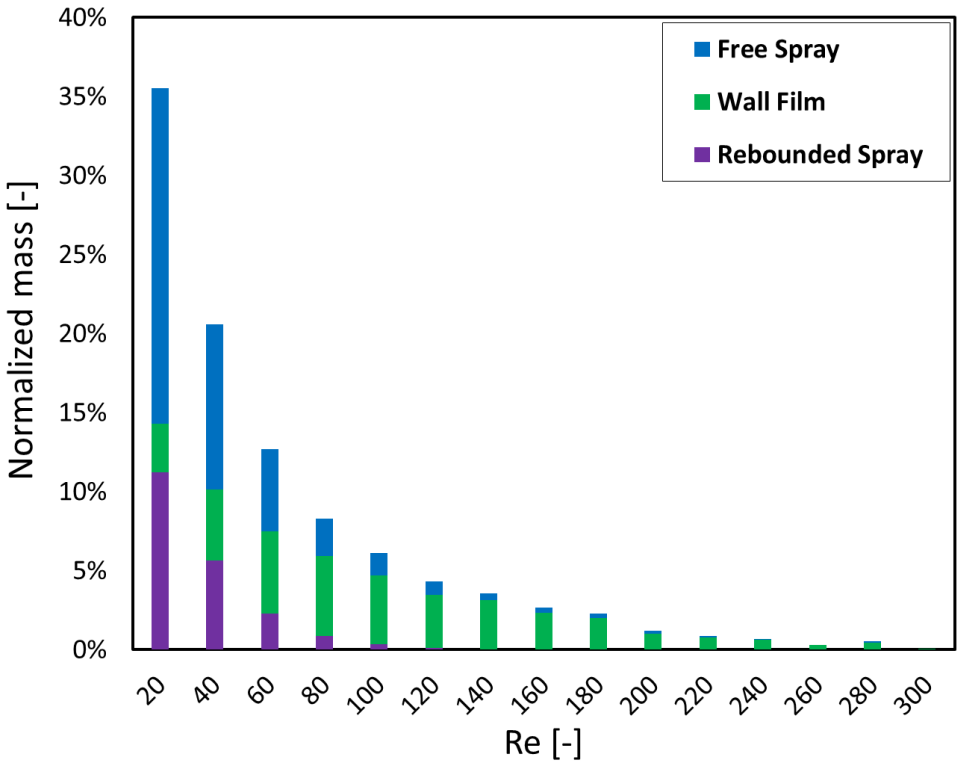

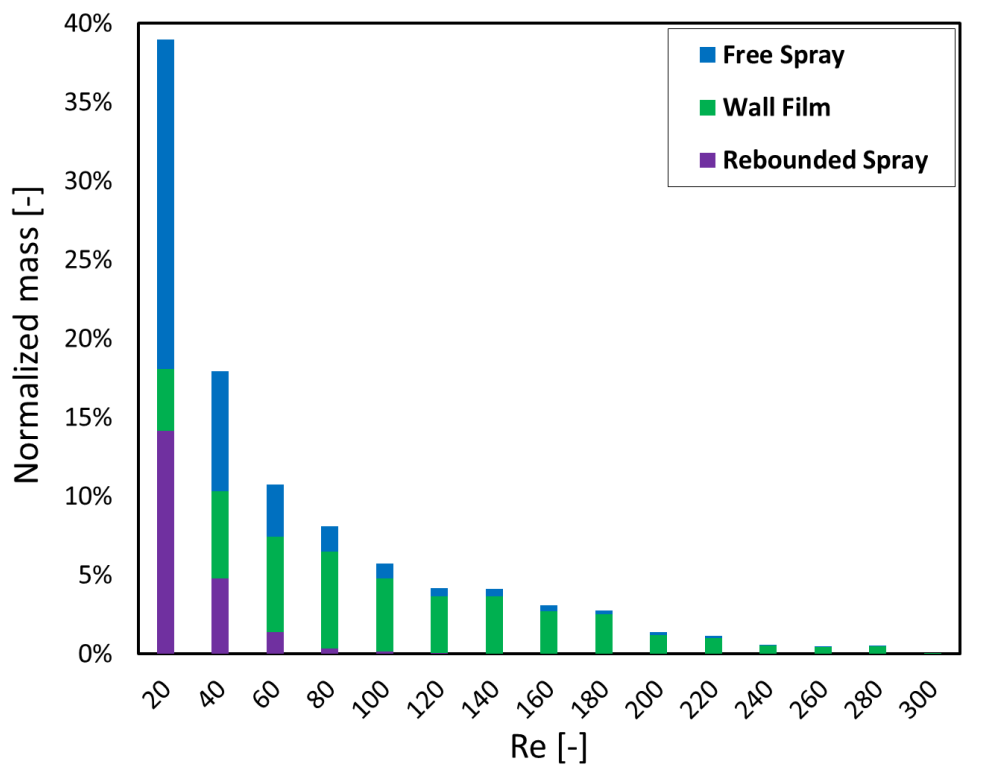

Figure 7.14: PDFs of normalized mass vs *Re*: 1.5 ms (top), 2.0 ms (middle), 2.5 ms (bottom).

7.1.4 Summary

Experimental and numerical studies of high pressure fuel spray impinging on a flat solid wall have been performed. The experimental work was performed in a constant volume CV to characterize the properties of free and rebounded portion of the spray. A RANS based methodology was used for the simulations. The general description and main conclusions in this study are summarized as follows:

(1) In experiment, diesel fuel was injected with a 7-hole production injector at a pressure of 1500 bar into ambient gas at a density of 22.8 kg/m^3 with isothermal conditions (fuel, ambient, and plate temperatures of 423 K). The simultaneous Mie scattering and schlieren optical diagnostics was carried out to depict the liquid spray development and the spray-wall interaction. An in-house Matlab code for image processing was used to extract the free and rebounded spray properties. From the experimental results, the

rebound radii have larger penetrations than the spray expanding distance on the wall for both axial and radial directions. However, the rebound radius and rebound on wall in axial direction are slightly higher (~2 mm) than those in radial direction, and the rebound height in axial direction is slightly lower (~2 mm) than that in radial direction. The experimental data was then used to support the validation of a spray-wall interaction and associated film formation modeling approach.

(2). In simulations, a preliminary study focused on the reduction of variability due to mesh alignment with the sprays and grid resolution. Thereafter, a combination of turbulence and spray break-up model constants was identified to match experimental liquid penetration data. The CFD results of the spray-wall interaction were compared to the experimental measurements in order to assess the capabilities of the O'Rourke and Amsden model in the CONVERGE CFD code. Post-processing tools were developed to compute both the global and local spray characteristics in the vicinity of the wall with a particular focus on SMD, and *Re* and *We*. The analysis was performed by considering before- and after-impingement conditions in order to take into account the influence of spray-wall impingement on the spray morphology. The simulations were able to capture many experimental trends quite well: in particular the spray rebound in the vicinity of the wall and the spreading in the axial direction were matched within their experimental confidence interval. At the same time, some discrepancies were also found in terms of over-prediction of radial spreading and under-prediction of orthogonal rebounding. This suggested that, while the spray-wall model has been able to catch the general trends, model developments are necessary to improve the quantitative predictions.

(3). Droplet distribution information near the wall provided some unique insights about the morphology of the spray in this region. In particular, PDFs of liquid mass with respect to *Re* and *We* numbers showed that these distributions in the vicinity of the wall are mainly governed by the droplet sizes and that most of the mass in that region is characterized by very low velocities. The analysis also showed how the wall-film tends

to grow with time and that bigger droplets tend to contribute to its formation more than the smaller ones.

7.2 Spray-wall impingement with single-hole diesel injector

An experimental study for testing spray impingement on a flat plate was carried out in an optically accessible constant volume CV [68, 164]. A single-hole injector with an orifice diameter of 200 µm was mounted on a face port of the chamber and the nozzle orifice orientation with respect to injector axis was equal to 60°. The smooth transparent impinging window was located at a distance of ~40 mm from the injector tip. The test conditions for the spray-wall interaction experiments are listed in Table 7.3. Diesel (ULSD) and n-heptane were selected as test fuels and their fuel properties are available in ref.[69].

Table 7.3: Test conditions for single-hole diesel spray-wall impingement test

Parameter	**Values**
Ambient gas temperature (K)	423
Ambient gas density (kg/m^3)	14.8, 22.8, 30.0
Ambient gas composition	100% N_2
Ambient gas velocity (m/s)	~0
Nominal nozzle outlet diameter (µm)	200
Nozzle K factor	0
Number of holes	Single-hole
Orifice orientation relative to injector axis	60° (included angle: 120°)
Fuel injection pressure (MPa)	120, 150, 180
Fuel	diesel / n-heptane
Fuel temperature at nozzle (K)	363
Energizing injection time (ms)	2.0
Distance between injector tip to impinging surface (mm)	40 (smooth plate)

In addition, based on Bosch ROI meter, normalized ROI profiles of diesel and n-heptane fuels for the energizing injection time of 2 ms at the injection pressure of 150 MPa are shown in Figure 7.15, the same condition was also selected as the baseline condition for

experimental and numerical evaluations. The corresponding actual injection durations for diesel and n-heptane are approximately 2.39 ms and 2.41 ms, respectively. The total injected mass measured at ambient temperature is 28.39 mg for diesel fuel and 23.37 mg for n-heptane. Further, the discharge coefficient is approximately 0.79 for diesel and 0.72 for n-heptane during the quasi-steady-state portion of the injection.

Finally, the baseline condition in this work is based on an engine operating condition typical for a diesel engine [165]: ambient density of 22.8 kg/m^3, ambient temperature of 423 K, and injection pressure of 150 MPa, injection duration of 2.39 ms. Diesel (ULSD) was chosen as reference fuel in experiment and diesel #2 is commonly used as surrogate fuel for model validation. Parametric variations around this reference point were performed: injection pressure and ambient density.

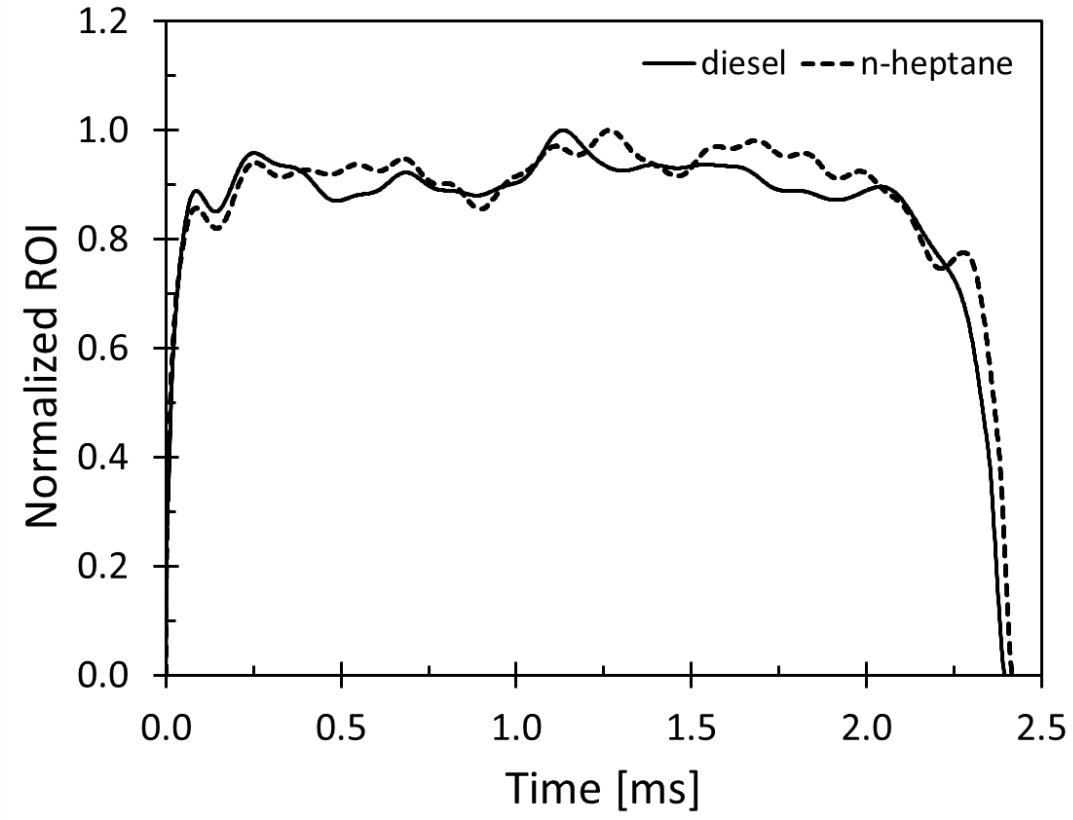

Figure 7.15: Rate of injection profiles for diesel and n-heptane fuels at injection pressure of 150 MPa and energizing injection time of 2 ms.

7.2.1 Experimental results

Figure 7.16 shows the sequential images of spray impinging on the wall with front (Mie scattering) and side (schlieren) views at baseline condition (injection pressure of 150 MPa and ambient density of 22.8 kg/m^3). A qualitative description of diesel and n-heptane sprays in a quiescent combustion chamber is given. For diesel imaging, the exposure time is longer than the one used for the n-heptane spray. This explains the visual differences between diesel and n-heptane as shown in the side views of Figure 7.16. Similarly, the time values reported above each image slightly differ between the two fuels due to different fps rates used during the tests. Figure 7.16 also highlights the series of events that characterize the two fuel sprays impinging on the smooth wall with the baseline test condition. From left to right, there are (a) pre-impingement, (b) impingement, (c) post-impingement, and (d) further spreading. Note that there is an angle of 30° between the wall where the injector is mounted and the spray plume. The angle is clearly visible from the side views and was accounted for with the liquid penetration measurements obtained from the front view images. Figure 7.16 (top) (a) and bottom (a) show that the diesel spray penetration is slightly larger than that from n-heptane spray; the diesel spray reaches the wall ~0.12 ms earlier than the n-heptane spray as shown in Figure 7.16 (b). After impingement, it can be clearly seen from both front and side views that the diesel spray starts spreading radially and axially. On the other hand, due to n-heptane's high volatility, it is difficult to observe the same behavior for n-heptane, especially when front view images (obtained with Mie scattering) are considered. The side view schlieren images provide a better contrast to highlight the vaporized spray spreading.

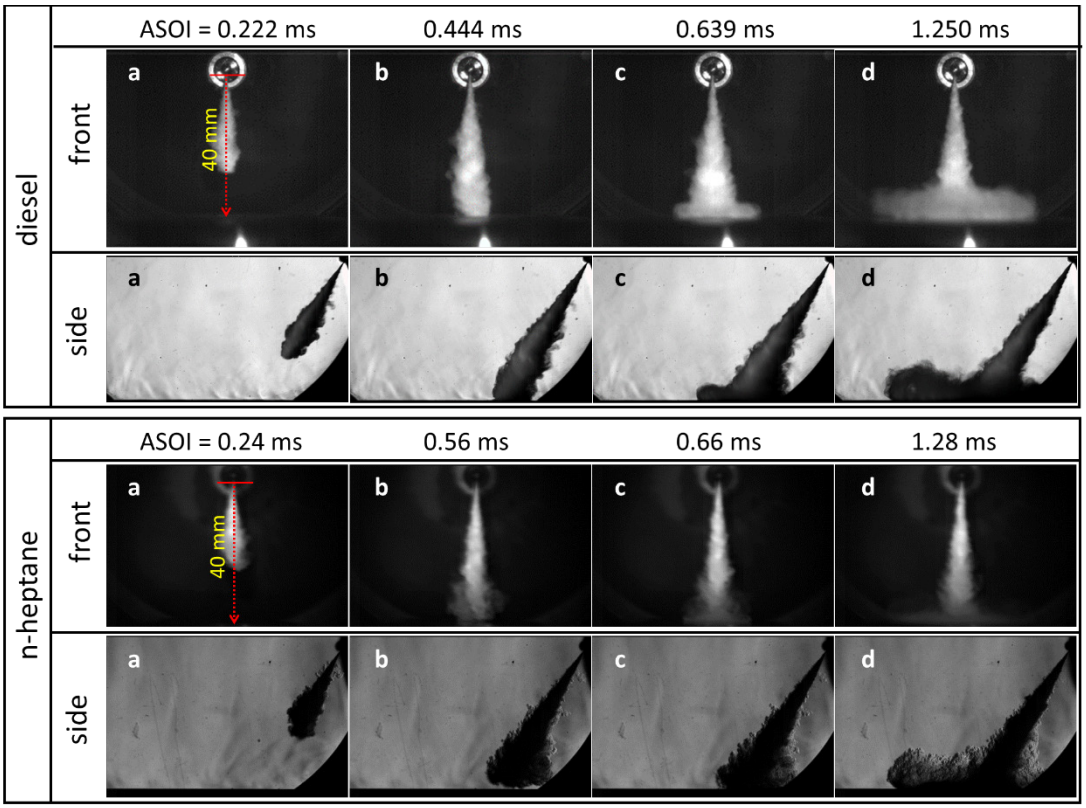

Figure 7.16: A sequential visualization of spray-wall impingement experiments from front and side views: diesel (top); n-heptane (bottom).

Figure 7.17 presents the effect of ambient density (14.8, 22.8, and 30.0 kg/m^3) on the time evolution of the liquid free spray penetration for diesel (top) and n-heptane (bottom) fuels at the injection pressure of 150 MPa. Figure 7.17 also shows the injection pressure (120, 150, and 180 MPa) effect on the liquid free spray penetration for two fuels at ambient density of 22.8 kg/m^3. It is worth mentioning that only the two lower injection pressures were investigated for n-heptane because the injection pressure of 180 MPa resulted in instabilities during the test. The free spray penetration of diesel is acquired from front and side view images, named as Z_f and Z_s, however, the free spray penetration in n-heptane case is only measured from side view schlieren images since the front view Mie scattering images are not visible enough at later times due to the evaporation of the fuel. Finally, the experimental results shown in the present work were averaged from five runs.

In general, from Figure 7.17, the free spray penetration decreases with the ambient density and increases with the injection pressure both in diesel and n-heptane sprays. The maximum liquid penetration is about 46 mm and the impinging time is around 0.44 ms for diesel case and 0.56 ms for n-heptane case under baseline conditions. The free spray penetrations from front and side views in diesel case closely agree with each other at different test conditions. Furthermore, the spray impinges on the wall earlier (~0.05 ms) at lower ambient density due to lower drag, which results in higher spray momentum and velocity; a similar behavior is observed at higher injection pressure as well. In addition to this, it is interesting to point out that the free spray penetration of diesel at the injection pressure of 150 MPa shows negligible differences compared with the one obtained when an injection pressure of 180 MPa was used. A similar observation was made for n-heptane at injection pressure of 120 and 150 MPa and with ambient densities of 22.8 and 30.0 kg/m^3. This phenomenon is explained by the fact that liquid penetration is not linearly related to the injection pressure and ambient density; as the ambient density and injection pressure increase, their effect on spray penetration is mitigated [166].

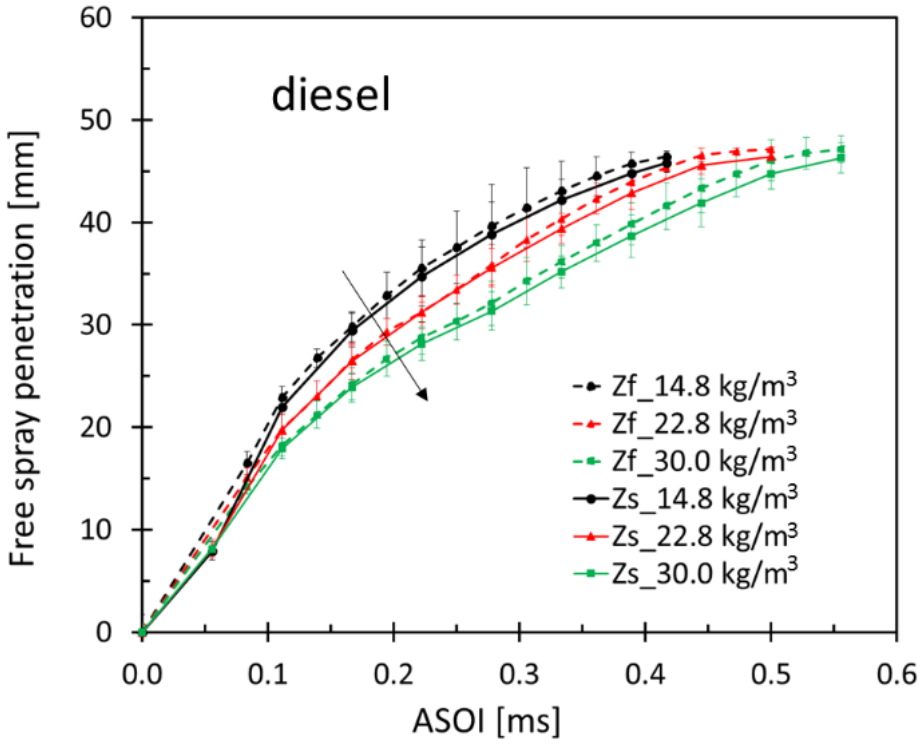

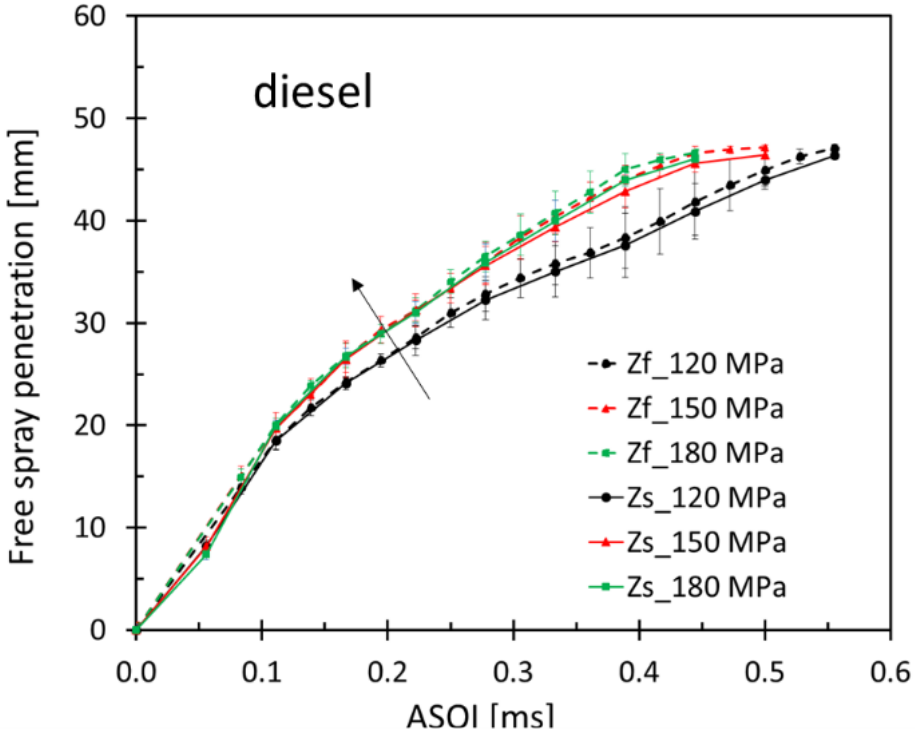

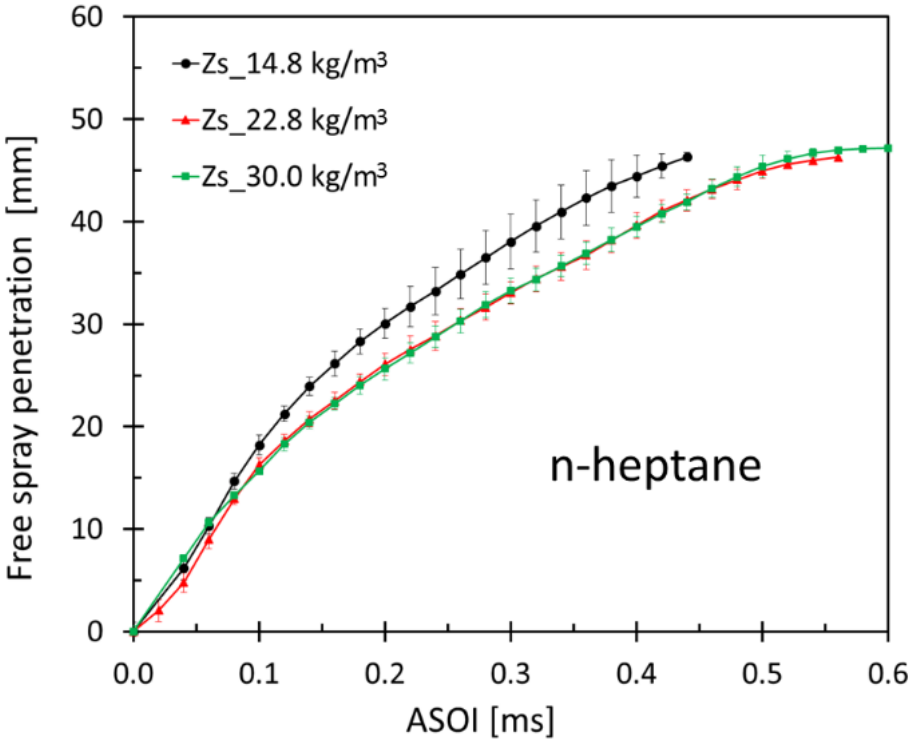

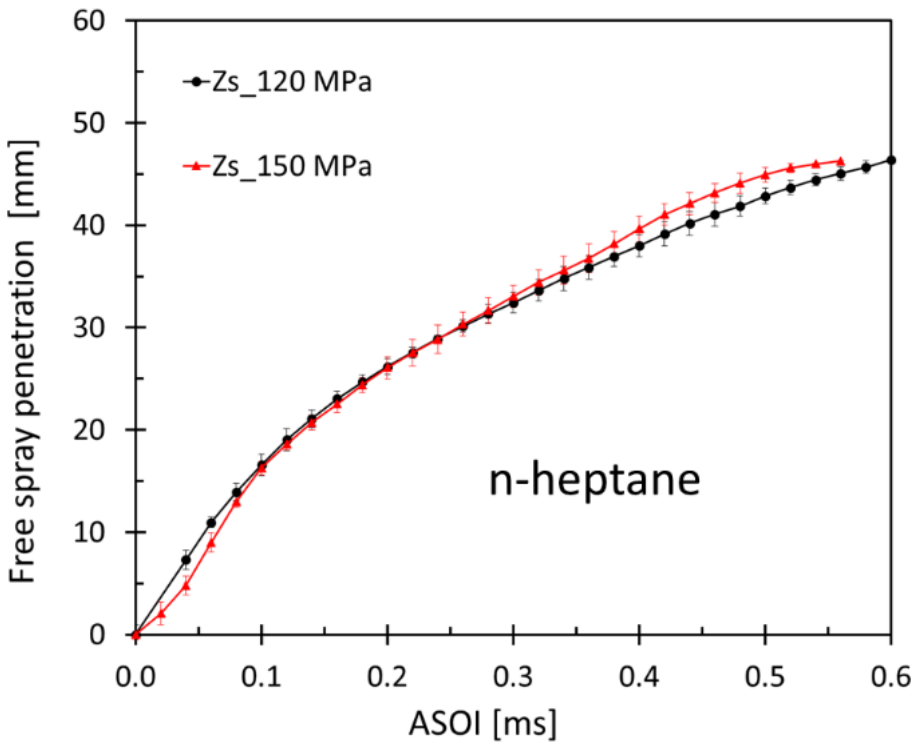

Figure 7.17: Free spray penetration for diesel (top) and n-heptane (bottom) at different ambient densities and injection pressures.

Due to the quick evaporation of n-heptane, the impinged spray boundary of n-heptane is not easily trackable, therefore only diesel fuel is accounted for when studying the effects of ambient density (top) and injection pressure (bottom) on the impinged spray features. The impinged spray properties in Figure 7.18 are from the side view schlieren images and they are measured from ASOI of 0.5 ms just after the spray impinges on the wall. The impinged spray radius, impinged spray radius on wall, and impinged spray height decrease with the ambient density and increase with the injection pressure which is caused by the enhanced spray momentum achieved near the impinging wall at lower ambient density and higher injection pressure. It is also observed in Figure 7.18 that the impinged spray radii are generally longer than the impinged spray on wall. This phenomenon occurs in both side (axial) and front (radial) views and the relevant study can be found in our previous work of 7-hole diesel spray-wall impingement [69].

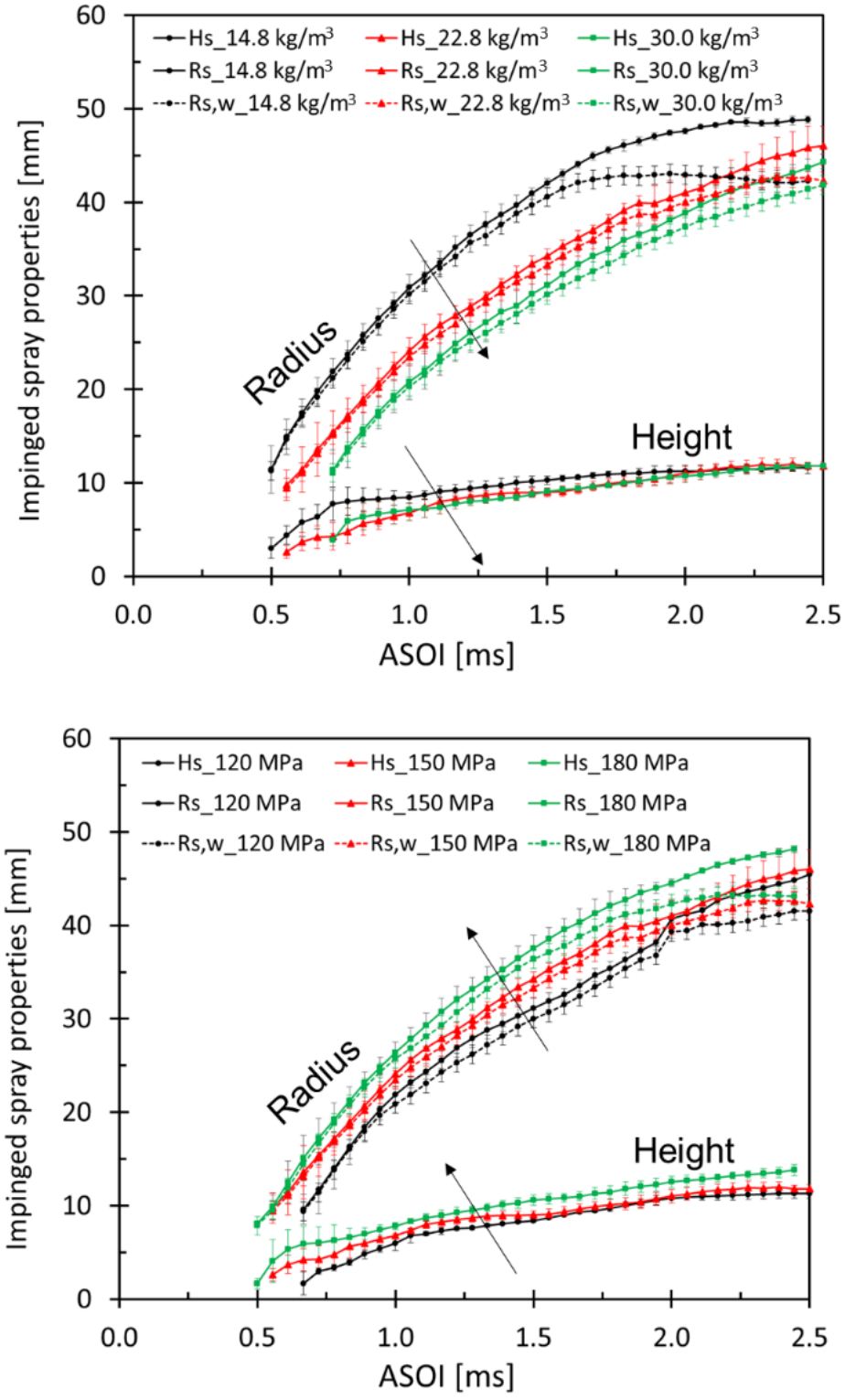

Figure 7.18: Impinged spray properties for diesel at different ambient densities (top) and injection pressures (bottom).

Figure 7.19 (top) illustrates the radial and axial radii ($R_{b,f}$ and $R_{b,s}$) from bottom view images at different ambient densities with injection pressure of 150 MPa. At any given time, both radial and axial radii decrease as the ambient density increases because the impact velocity and momentum are larger at lower ambient density condition. Furthermore, the axial radius grows faster than the radial radius under the same test conditions. The reason for this behavior is that the 30° angle between the wall where the injector is mounted and the spray plume leads to a relatively higher momentum in the axial direction compared to what happens in the radial direction, thus driving the spray to progress faster in the side views. The second figure in Figure 7.19 gives the expansion ratio of axial and radial radii at the different ambient densities. The expansion ratio raises from ~0.8 to ~1.4 for all conditions and it slightly decreases with the ambient density. The third figure in Figure 7.19 provides the length of axial and radial arcs ($A_{b,f}$ and $A_{b,s}$) from bottom view images with various ambient densities. A trend similar to the one found with the radial and axial radii is observed in this case as well. Both radial and axial arcs reduce with the ambient density at a given time and the axial arc length is always longer than the radial arc length at the same condition. The corrugation ratios ($C_{b,f}$ and $C_{b,s}$) in Figure 7.19 (bottom) are the ratios between the actual WIES front wrinkle length and the smooth elliptic arc length, and represent how much the spray leading edge is distorted by the ambient environment. The ambient density has no significant effect on the corrugation ratio, the corrugation ratio is close to 1 at all ambient densities which means that the WIES front can be approximately considered as a smooth arc.

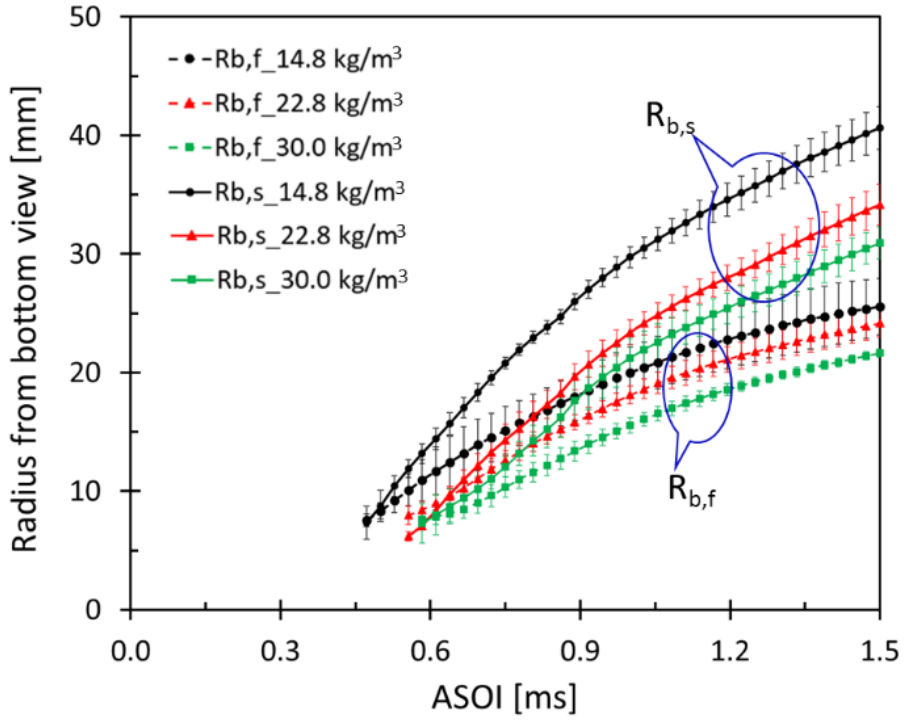

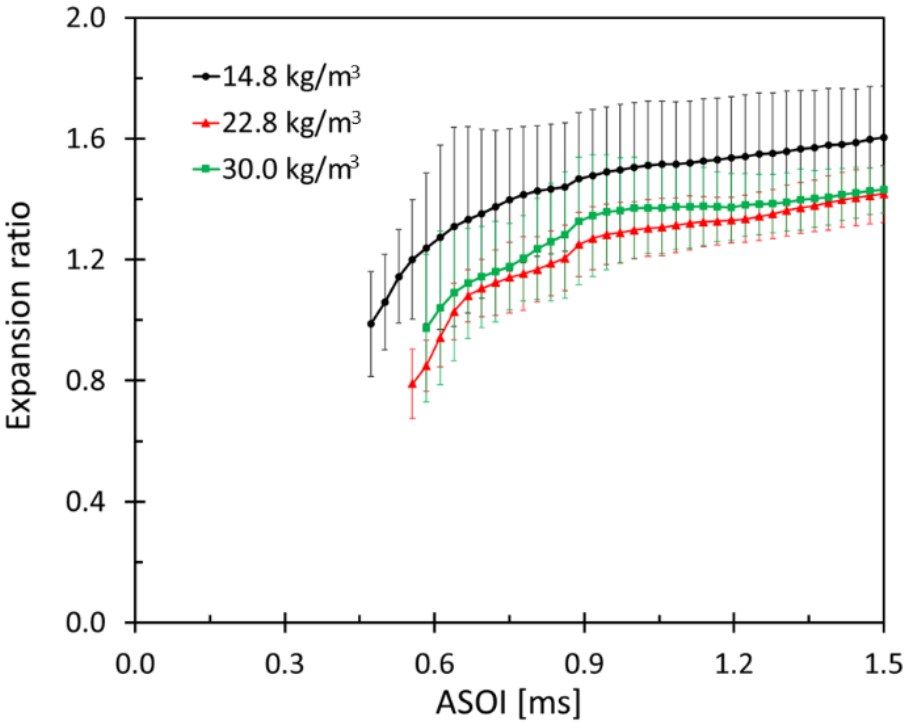

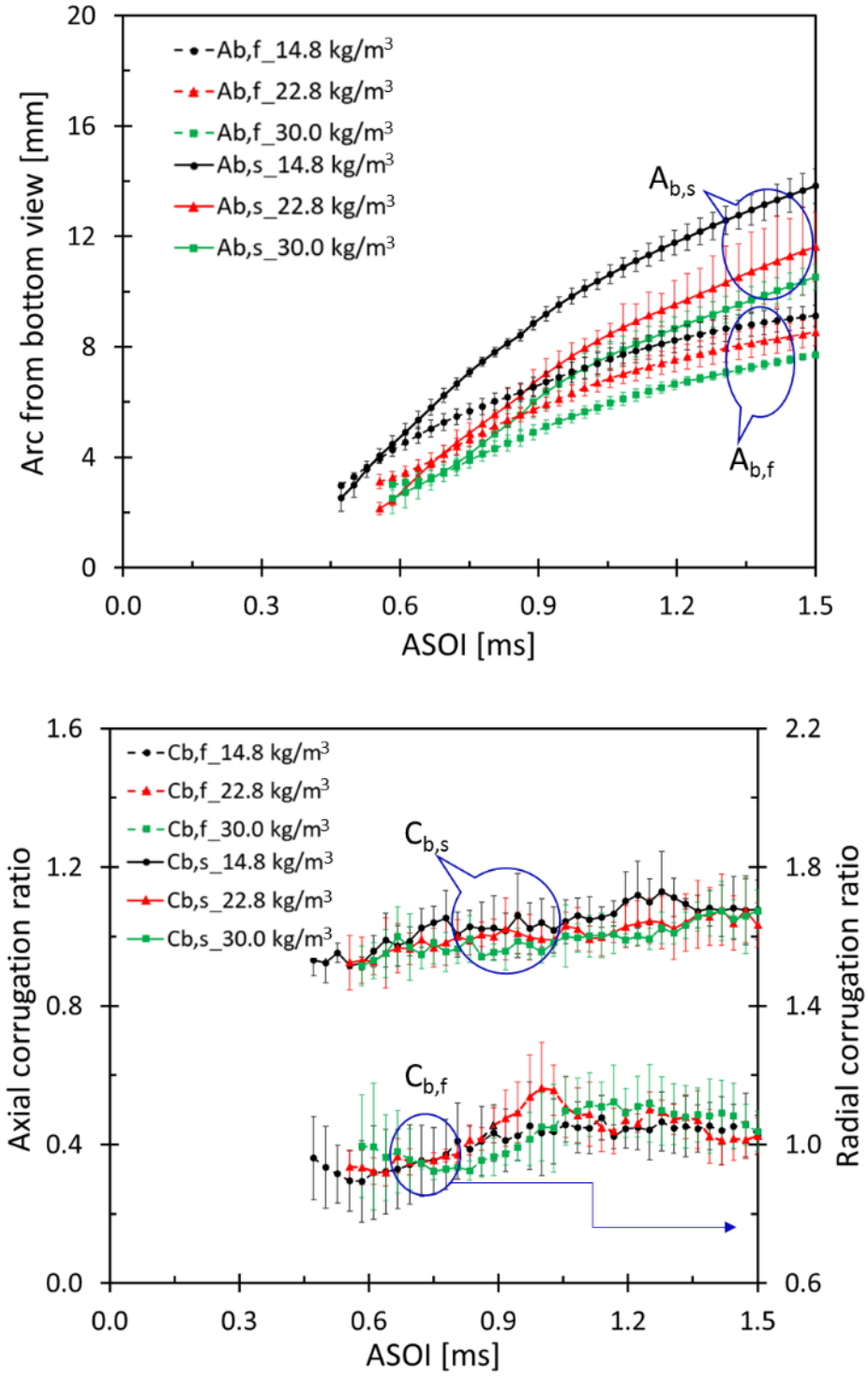

Figure 7.19: Impinged spray properties from bottom view for diesel at different ambient densities: impinged radius (top); expansion ratio (second); arc length (third); corrugation ratio (bottom).

Figure 7.20 (top) shows the radial and axial radii ($R_{b,f}$ and $R_{b,s}$) and the second figure in Figure 7.20 gives the expansion ratio from bottom view images at various injection pressures with ambient density of 22.8 kg/m^3. At any given time, the radial and axial radii increase with the injection pressure because of the higher velocity and momentum that drives the spray to move faster and further after the impingement on the wall occurs. Similarly, the axial radius propagates faster than the radial radius at the same test conditions for the same reason mentioned above. The expansion ratio shows negligible differences as the injection pressure increases. Figure 7.20 (bottom) depicts the effects of injection pressure on the length of radial and axial arcs ($A_{b,f}$ and $A_{b,s}$) and on the corrugation ratio ($C_{b,f}$ and $C_{b,s}$). The radial and axial arc lengths increase with the injection pressure at any given time and the axial arc length is always longer than the radial arc length under the same conditions. The corrugation ratio is close to 1 and does not show any substantial effect correlated with the injection pressure.

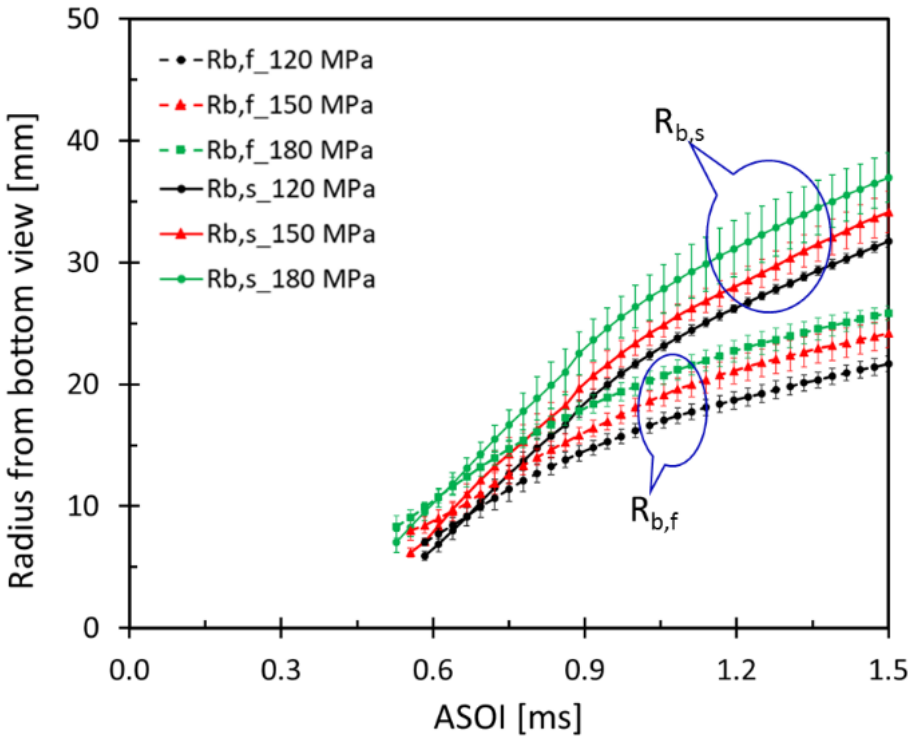

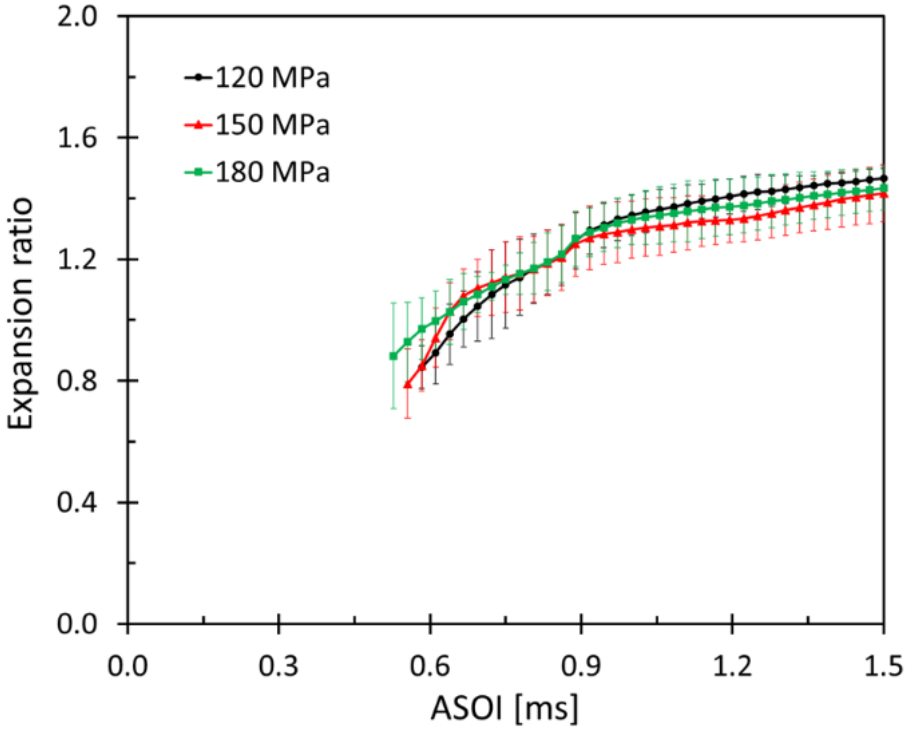

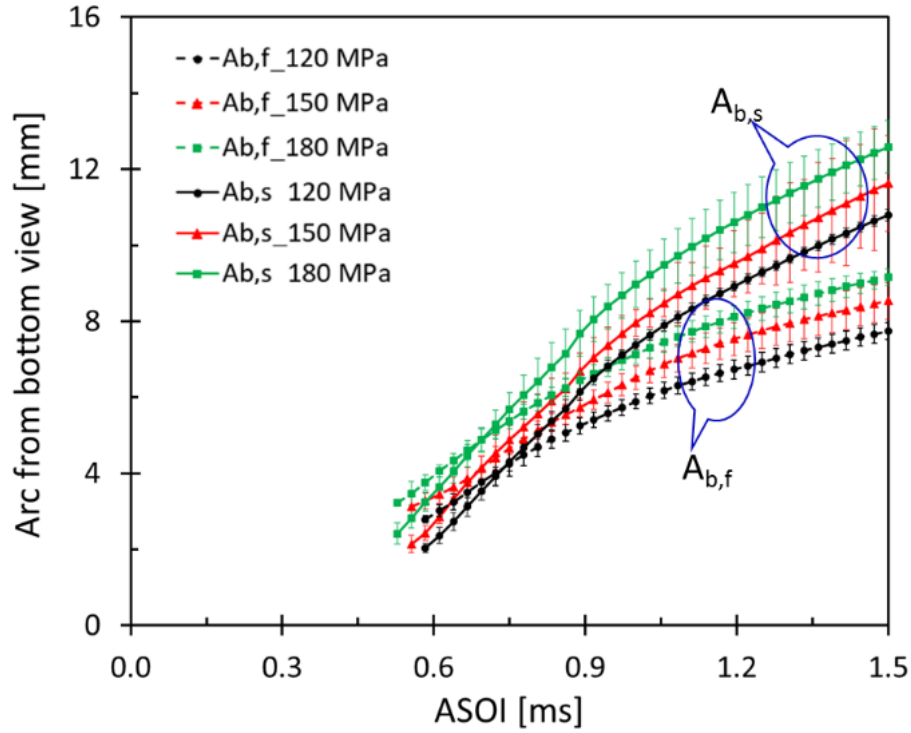

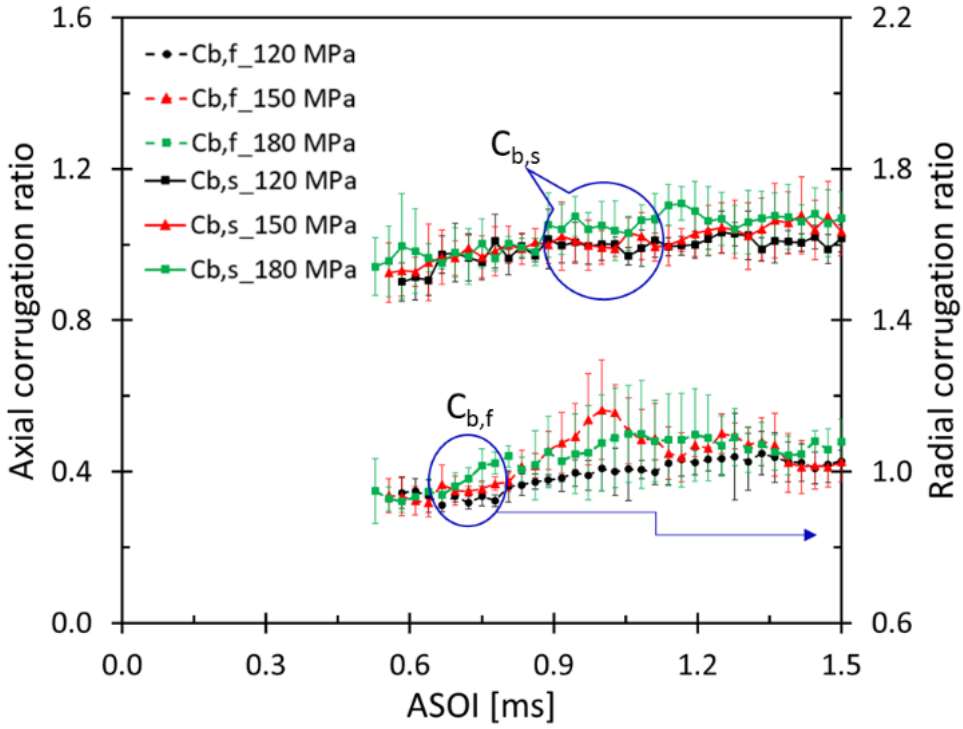

Figure 7.20: Impinged spray properties from bottom view for diesel at different injection pressures: impinged radius (top); expansion ratio (second); arc length (third); corrugation ratio (bottom).

Figure 7.21 shows the effects of the ambient density (top) and injection pressure (bottom) on the spray dispersion angle. At the early stage of the injection, dispersion angle rises to a high value, and then a relative steady angle (~23^{o}) establishes rapidly later. The large uncertainties underline the turbulent nature of the air entrainment process. From Figure 7.21 (top), the dispersion angle increases with the ambient density increase. In Figure 7.21 (bottom), however, it does not show a monotonic trend by the injection pressure. Before ASOI of 1.3 ms, dispersion angle at 120 MPa is the largest, next is the one at 180 MPa, and finally 150 MPa, implying no specific trend. After ASOI of 1.3 ms, dispersion angles from all the conditions show the very small difference. Here, the larger dispersion angle indicates the higher level of air entrainment, since the entrainment is proportional to ambient air density, orifice diameter, fuel velocity, and spray dispersion angle [22]. Spray dispersion angle is a global parameter that describes the droplet distribution. Since in fact

that the spray impingement obeys the stagnation flow model, the distribution of droplets before impacting affects their distribution after impingement.

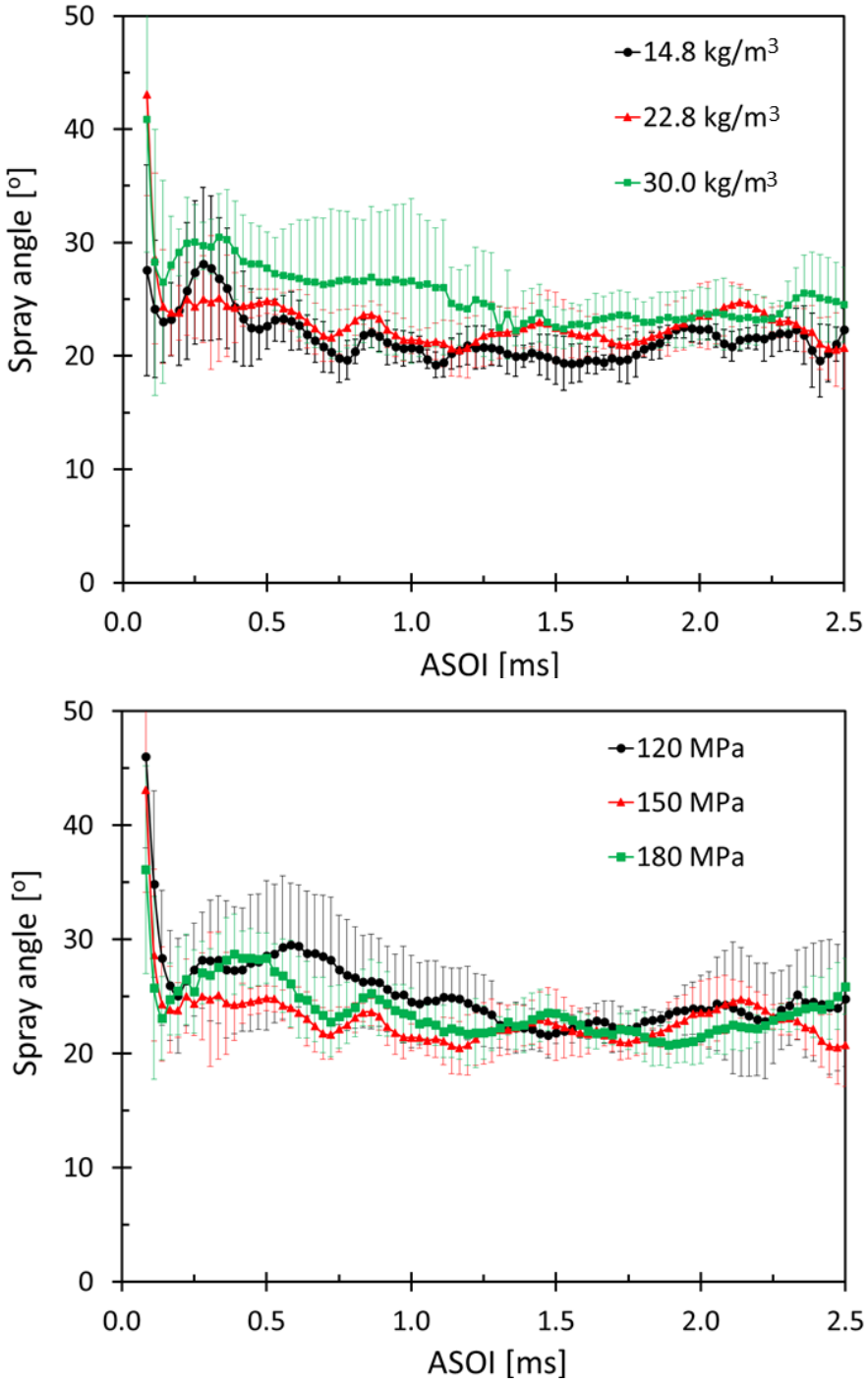

Figure 7.21: Spray dispersion angles at different ambient density with 150 MPa injection pressure (top) and different injection pressure with 22.8 kg/m^3 ambient density (bottom).

7.2.2 CFD model validation

This section briefly outlines the computational tools that were adopted for the simulations of the single-hole injector at baseline condition (i.e., 150 MPa injection pressure, 22.8 kg/m^3 ambient density, and 423 K ambient temperature), using diesel fuel. All the models and sub-models employed in this study are available in the CONVERGE software [132] and have been extensively validated in the recent years for several operating conditions, fuels, geometries, and injectors [69, 167, 168]. Consistent with our previous work of 7-hole diesel spray-wall impingement, a RANS formulation closed by the Standard *k-ε* model was used for the Eulerian-Lagrangian coupling of the liquid spray with the gaseous phase. In addition to the Standard *k-ε* formulation, the RNG *k-ε* turbulence model was also tested. No major differences were found on varying the turbulence model, therefore the results obtained with RNG *k-ε* will not be shown in this work. The gas velocity distribution in the near-wall region as well as the post-impingement spray quantities were very similar using either one of the two models. The choice to present only the Standard k-ε results was made for the sake of consistency with our previous work of 7-hole diesel spray-wall impingement [69].

The injection and break-up of the liquid parcels were modeled using the Blob Injection and KH-RT models respectively. The O'Rourke and Amsden spray-wall film model [99] was selected to account for the interaction between the liquid spray and the impinged wall. Based on empirical correlations derived from experiments, this model provides estimates of spray spreading and rebounding, and film formation resulting from the interaction of the spray with the impingement plate. More details on the model implementation are available in our previous work [69] and in the original paper by O'Rourke and Amsden [99]. The solution of the flow field at each time-step was achieved through second-order spatial discretization, while time-dependent quantities were computed with first-order accuracy using a CFL based time-step limited to a maximum value of 5.0 x 10^{-7} s. The physical properties of the modeled fuel were based on diesel #2 fuel. The current simulation set-up is consistent with the simulations of a 7-hole injector [69]. A minimum mesh size of 0.25 mm is chosen for the current work based on grid sensitivity study in ref. [69].

The focus of the numerical portion of this study was on the proper assessment of the near-impingement spray morphology to achieve a representative local characterization of the impinged spray. In our previous work, the study of 7-hole diesel spray-wall impingement was performed for all the parcels included in a 1.00 mm layer near the impinged wall. That approach provided very insightful information on the global behavior of the spray in the near-wall region. On the other hand, due to the sample volume's large extension with respect to the entire domain, the analysis included parcels that were located in very different regions of the spray and that had interacted with the wall at different times. In the current work, the analysis of the Lagrangian parcels was carried out in small subset volumes in the vicinity of the impingement point, in order to provide an improved spatial accuracy of the characterization. Therefore, cubic subsets of 1.00 mm, 0.50 mm, and 0.25 mm side were identified around the impingement location and all the parcels located within the cubes were selected for the analysis (cf. Figure 7.22).

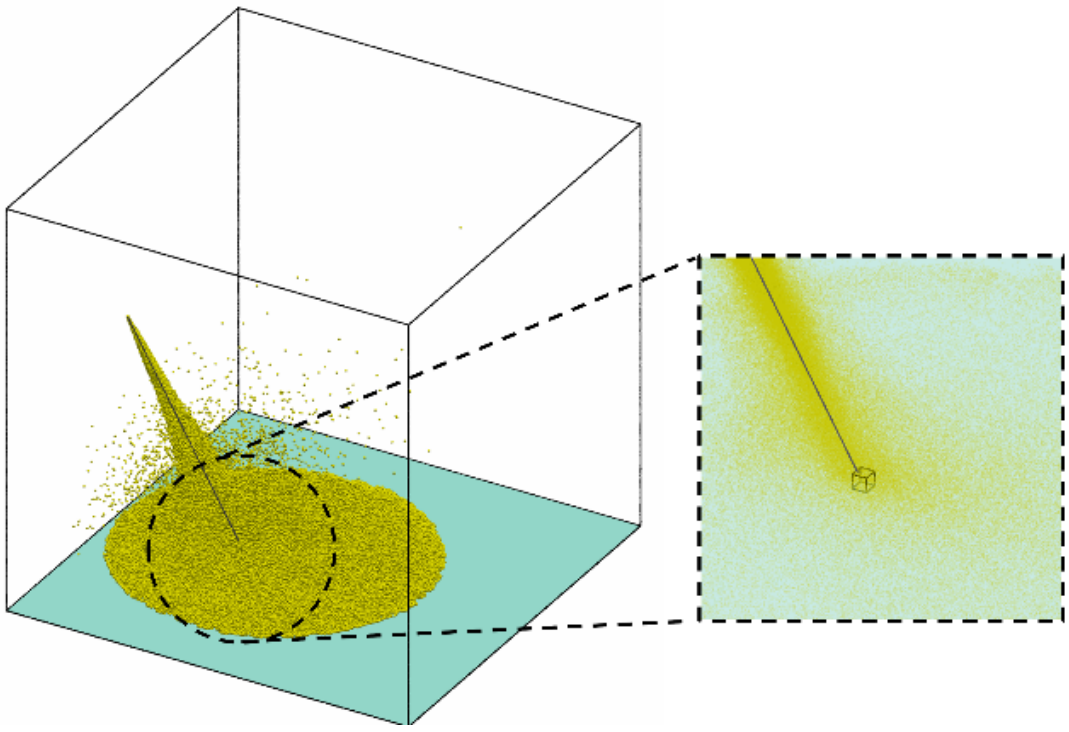

Figure 7.22: Schematic representation of the control volume near the impingement location for the spray characterization study using CFD.

Figure 7.23 shows that the model that had been previously validated under different conditions and with a different injector provided very good agreement in terms of liquid penetration (based on a 98% cumulated mass threshold). This demonstrated the robustness of the selected approach to changed conditions and provided the necessary confidence in the employed setup. It is also worth mentioning that the experimental liquid penetration was recorded only until the spray impinged on the wall, i.e., no further data were available after ~0.50 ms. Figure 7.24 shows a qualitative comparison of the spray evolution between experiments and CFD. As confirmed by the liquid penetration plot reported in Figure 7.23, the free-spray as well as the impact timing were well predicted. Some large differences were found in terms of spray-wall interaction. The three plots at 0.45, 0.65, and 1.25 ms clearly show that the recirculation observed in the experiments at the leading edge of the spray was not correctly captured by the CFD model.

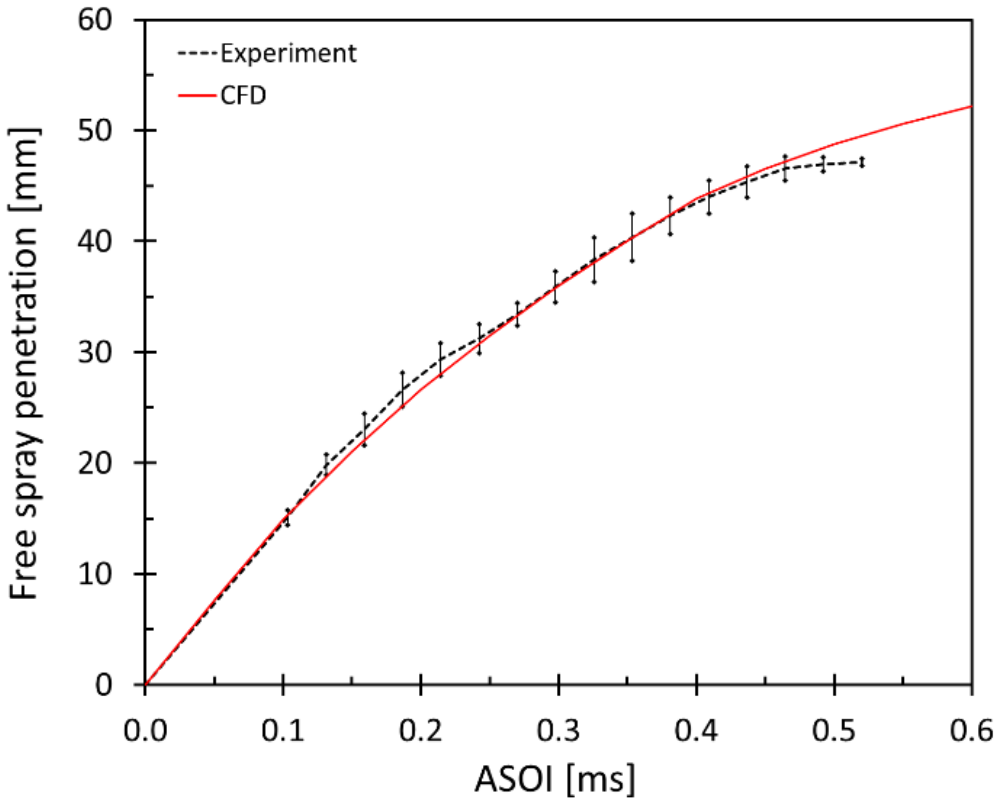

Figure 7.23: Comparison of diesel fuel liquid penetration from experiments and CFD simulations.

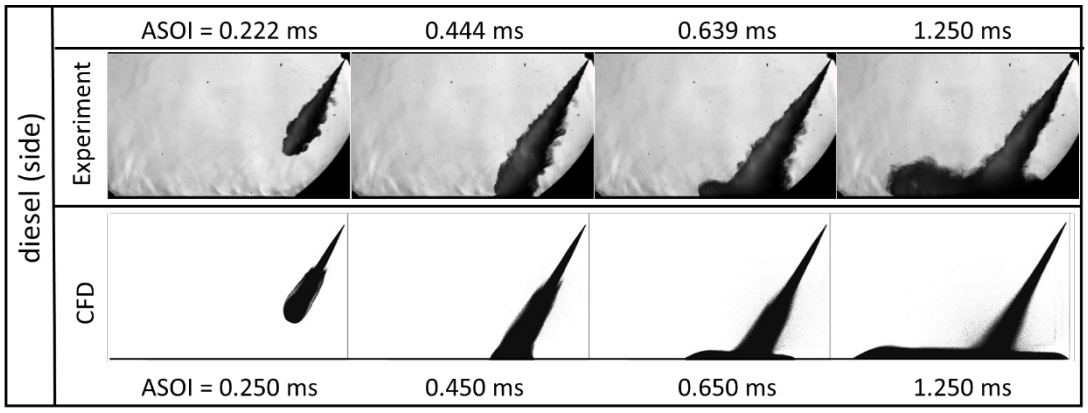

Figure 7.24: Comparison of experimental and numerical spray evolution.

The spray-wall interaction was evaluated by comparison of experimental and calculated impinged spray quantities. Figure 7.25 shows that the CFD model performed well in terms of impinged radius, especially in the radial direction where the agreement was very good. Simulations overestimated the impinged radius in the axial direction as shown in Figure 7.25 (top), and underestimated the spray height along the axial and radial directions in Figure 7.25 (third). This last result, that is qualitatively noticeable in Figure 7.24 as well, was also consistent with the findings of Naber and Reitz [97], who attributed the underestimation of the impinged spray in the wall normal direction to the use of the jet analogy, which was used to predict the velocity vectors of the rebounded and splashed parcel. Figure 7.25 (second) shows also that post-impingement, the spray is not symmetric and differs on the left and right sides. This asymmetry, which was not observed in the numerical simulations, might be ascribed to a slight angular offset of the injector with respect to the impinged wall. This is confirmed also by the experimental spray height in the radial direction, which is slightly higher for the right side.

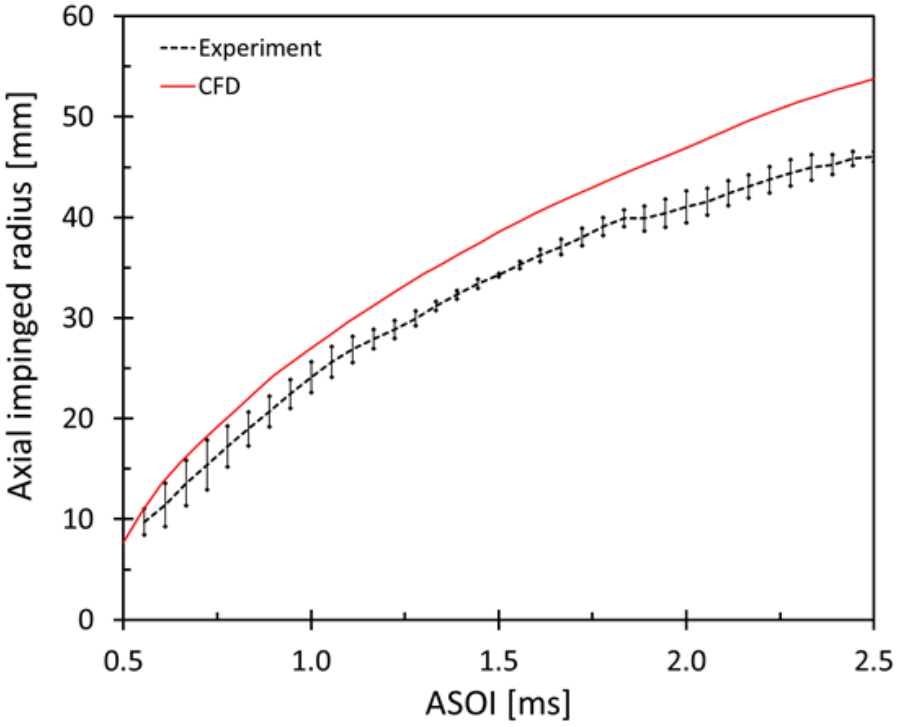

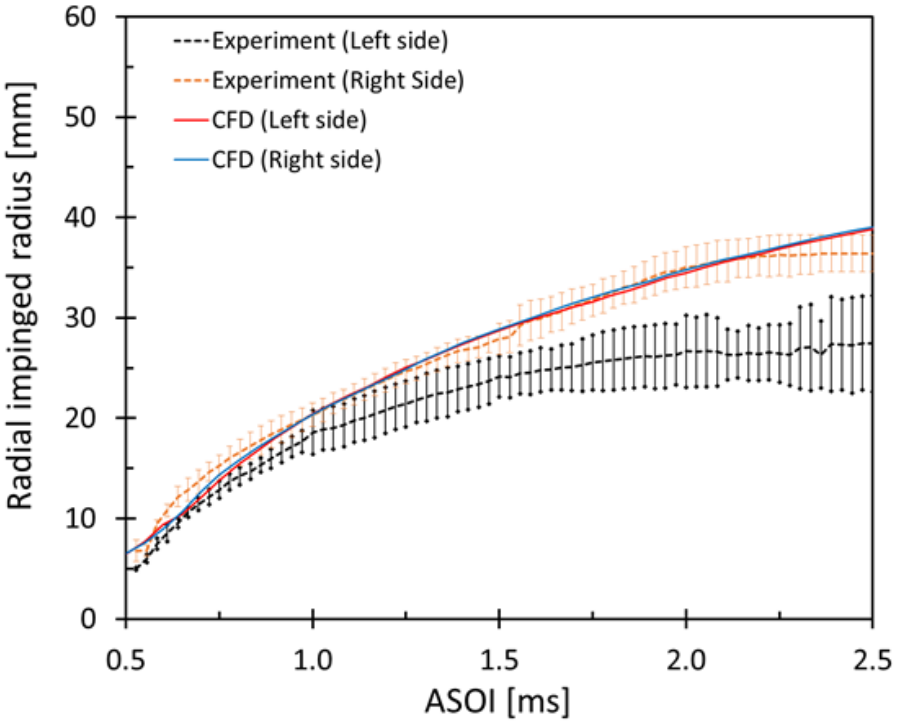

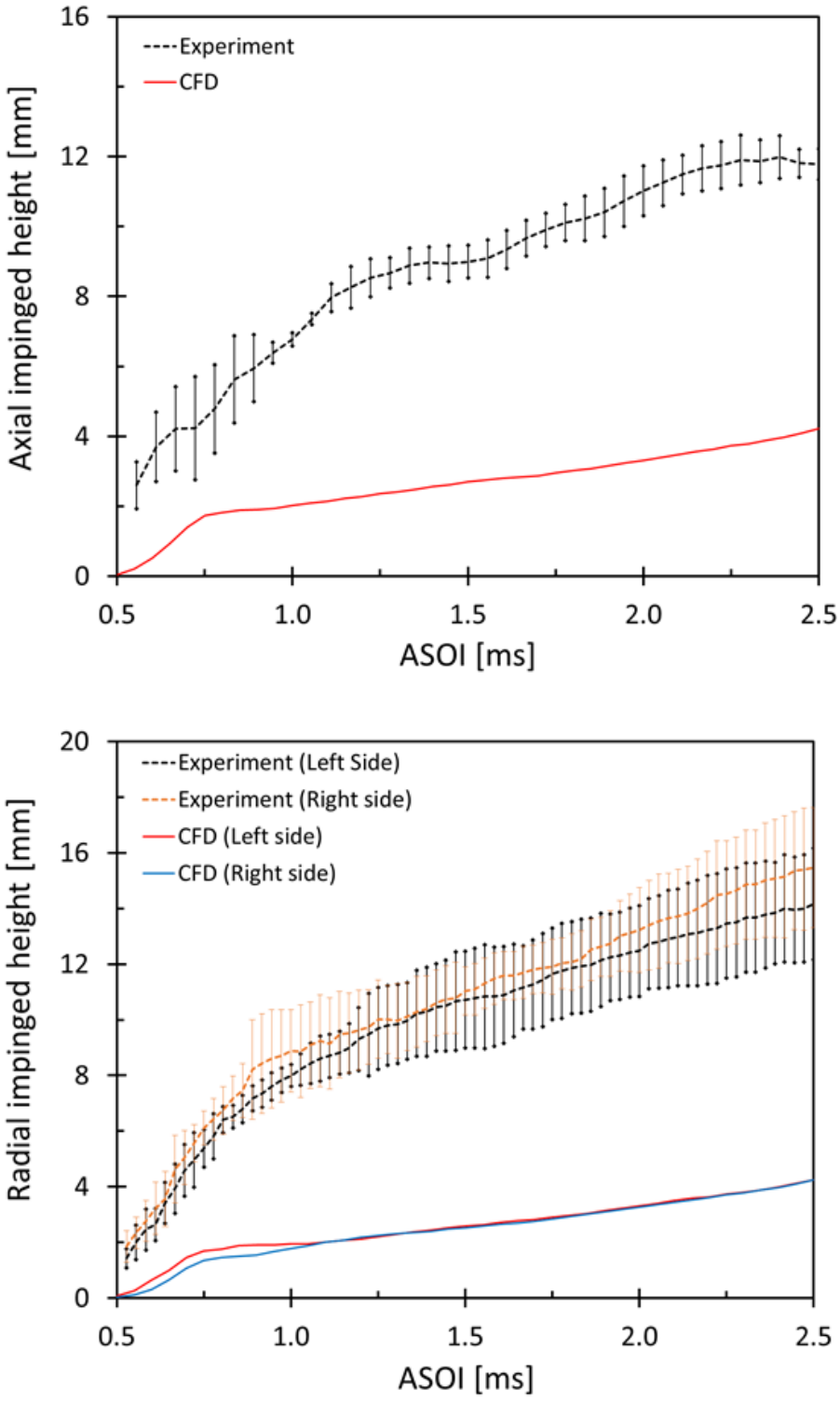

Figure 7.25: Axial impinged spray radius (top) and radial impinged spray radius (second) vs. time; Axial impinged height (third) and radial impinged height (bottom) vs. time.

7.2.3 Local spray characteristics of the impinged spray

In this section, the local characteristics of the liquid phase in a small cubic region near to the impingement location are presented. The main purpose of this analysis was to characterize the impinged spray in terms of *We* and *Re* numbers, which would eventually be used as inputs for DNS calculations of droplet-wall interaction [169]. The two-equation system, which one obtains by combining *We* and *Re* definitions, is sufficient to calculate size and droplet velocities, as the physical properties of the liquid at the given temperature are known.

As mentioned earlier, DNS will be an integral part of our future work as it will provide us with critical information about parameters that are difficult to measure in experiments. Due to very large computational demands of DNS, the size of DNS domain is at least two to three orders of magnitude smaller than the domain simulated in the present LE calculations. Therefore, to provide a more meaningful local characterization of the impinged spray, three cubic regions of 1.00, 0.50, and 0.25 mm side around the impingement location were used. The analysis was carried out by varying the number of injected parcels, in order to study the sensitivity of the results to this parameter. The results shown in Figure 7.23 and Figure 7.25 were obtained with the original value of 150k parcels. It should be noted that this is the number of parcels that are injected. Owing to break-up the number of liquid parcels in the domain can be significantly larger that this value. The value of 150k parcels proved to be sufficient for the correct estimation and statistical convergence of global quantities such as liquid penetration, and spray impinged radii and heights. On the other hand, the injected parcel number turned out to be insufficient to obtain statistical convergence of the local spray quantities in the cubic subsets, especially when the smallest cube (0.25 mm) was used. Therefore, the injected parcels were progressively doubled in number to generate four more cases with 300k, 600k, 1.2 million, and 2.4 million parcels counts. Figure 7.26 shows the different PDF of normalized mass vs. *We* at ASOI of 1.5 ms on varying the number of injected parcels. The plot with 300k parcels is not shown here for the sake of brevity. It can be clearly seen that increasing the number of injected parcels provides a

larger sample size. Similar PDFs can be drawn for *Re* distributions, but are omitted here for the sake of brevity.

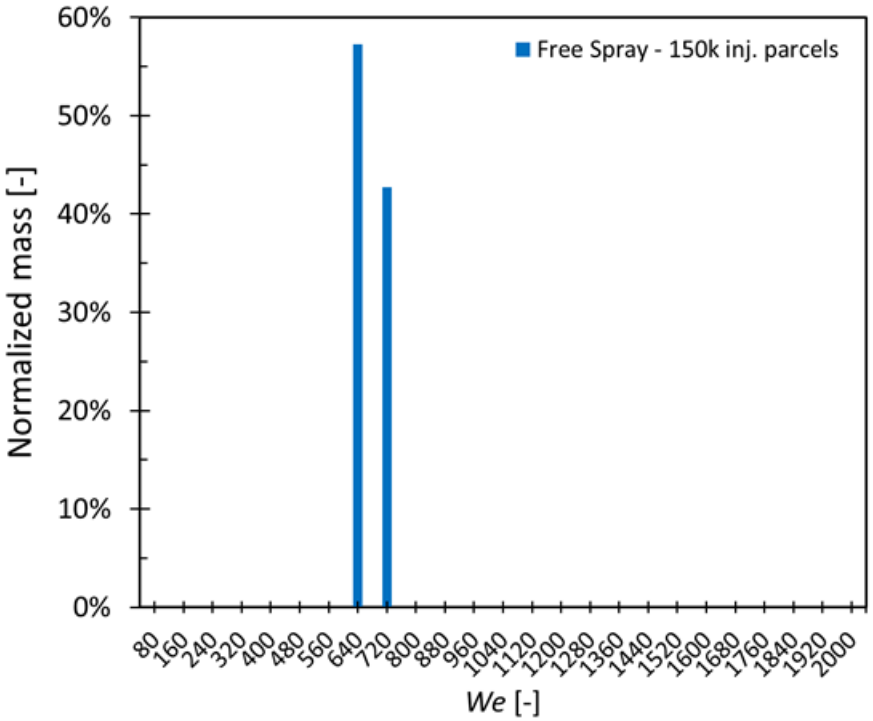

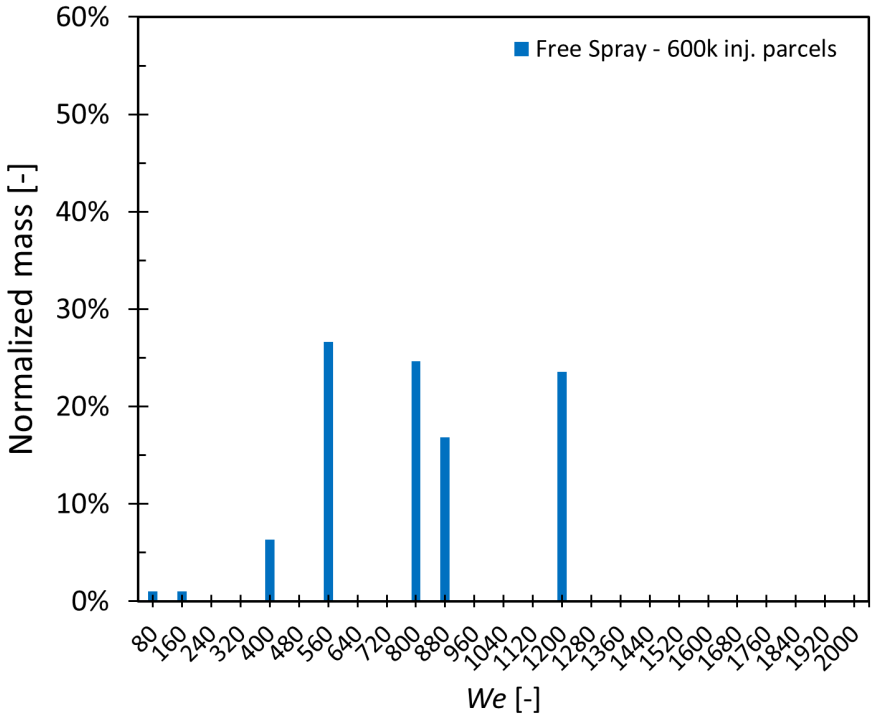

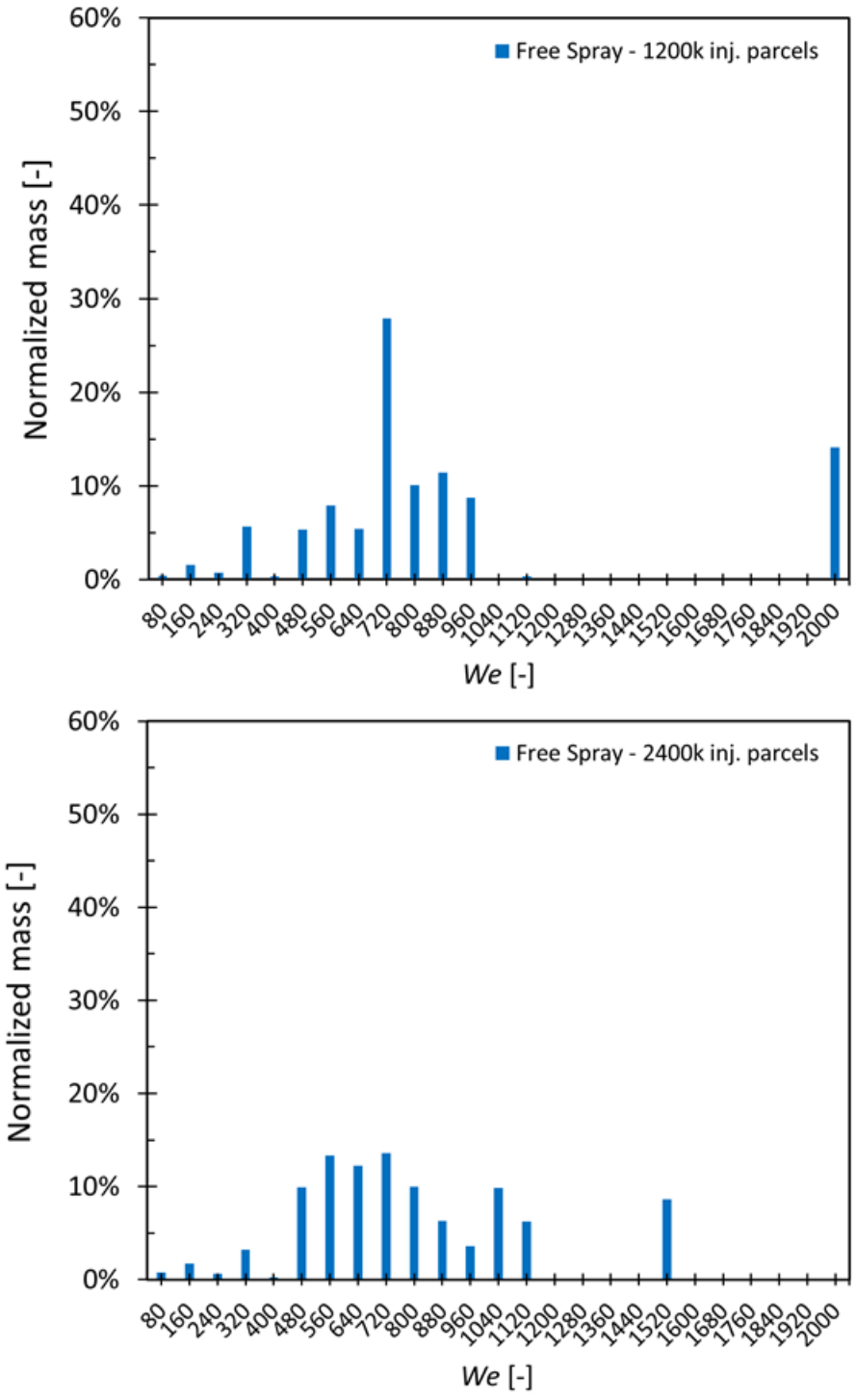

Figure 7.26: PDFs of normalized mass vs. *We* at ASOI of 1.50 ms for increasing number of injected parcels using the 0.25 mm cubic subset.

The advantage of increasing the injected parcel count is evident when the focus is placed on sample size and amount of mass included in each sample. Figure 7.27 shows the time-average of these two quantities for the 1.00 mm and 0.25 mm cubic subsets. In each of the boxes plotted in Figure 7.27, the middle line identifies the time-average, while the bottom and top lines represent the standard deviation scatter of the data. Since this analysis focused on the pre-impingement spray characteristics, the results were extracted for the free spray parcels only (i.e., those parcels that at any given time-step had not yet interacted with the wall). Furthermore, only the parent parcels (i.e., those parcels that did not undergo the KH break-up) were considered, whereas the child parcels were not included in the analysis. This was done because, as shown in Figure 7.27 (second and bottom), those parcels accounted for almost all of the free spray liquid mass included in the subsets. It is noticeable that the sample size grew linearly with the injected parcel count, therefore improving the statistical quality of each sample (cf. Figure 7.27 (top and third)). This is confirmed by Figure 7.27 (bottom), which shows that the standard deviation of the free spray parent mass (i.e., the variability of that quantity over time) decreased considerably when a large number of parcels was injected. This effect was less visible for larger cubic subset (e.g., the 1.00 mm cube, as shown in Figure 7.27 (top)).

On the other hand, increasing the number of injected parcels up to 16 times the original value caused the computational time to increase. All cases were run on 32 processors. The computational time increased from ~2 hours for the 150k case, up to ~15 hours for the 2.4 million case. The preferred value for this specific study was 2.4 million, nevertheless, in order to maintain an acceptable level of computational resources demand, a lower value (1.2 million or less) might be advisable for simulations that involve larger domains and/or multi-hole injectors.

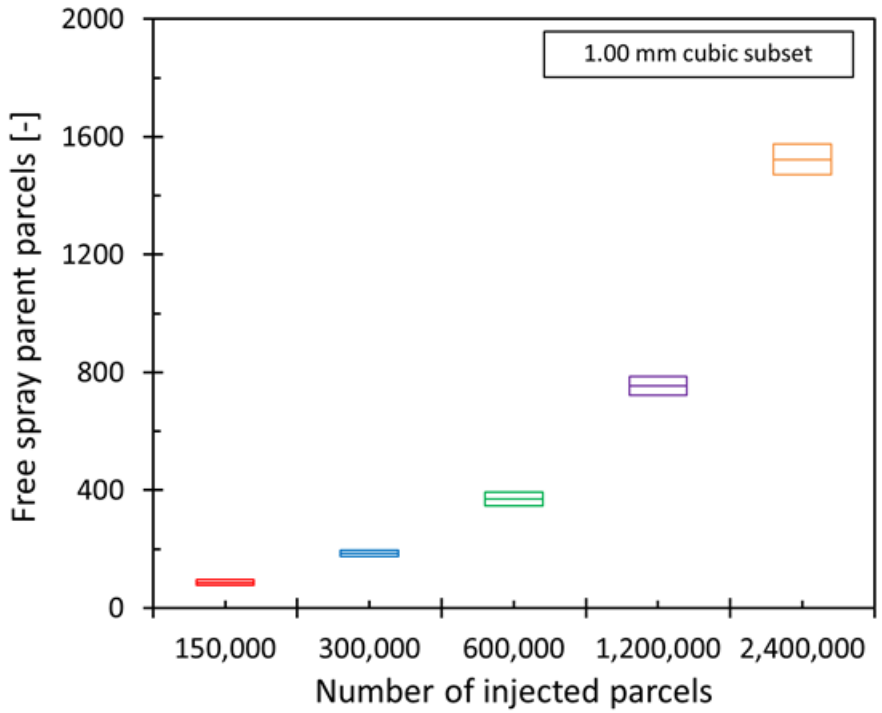

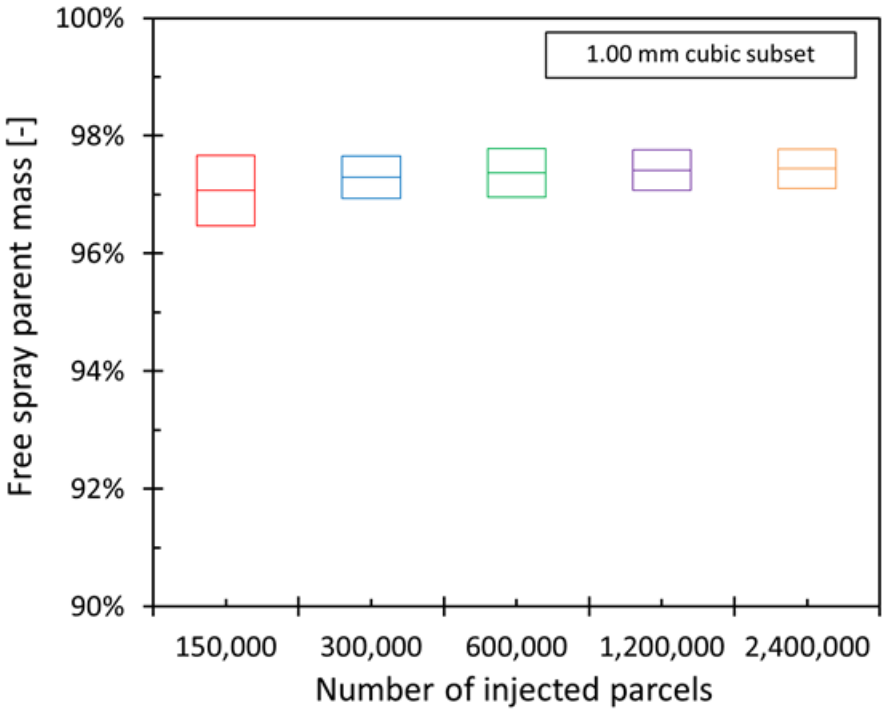

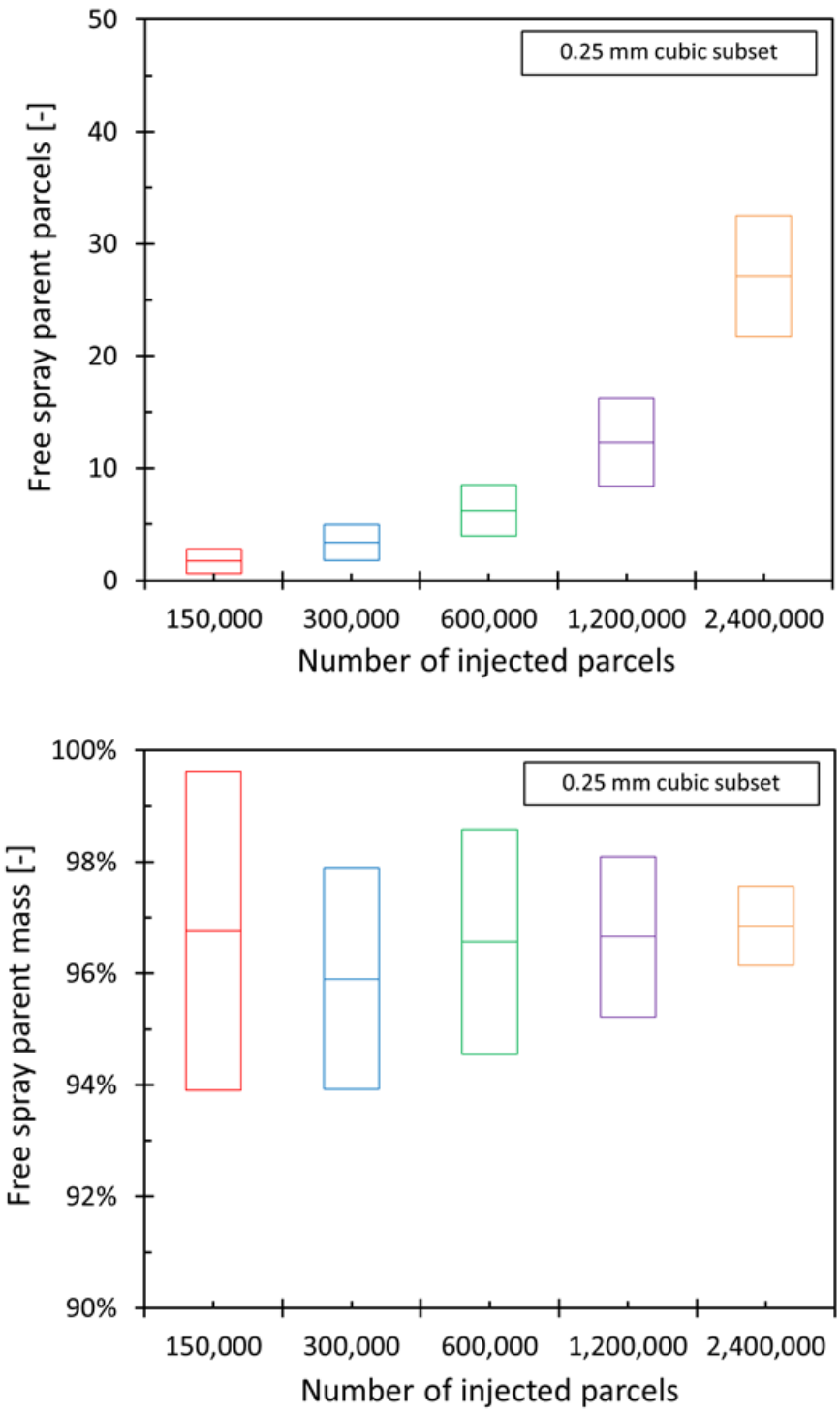

Figure 7.27: Number of free spray parent parcels and free spray parent parcel mass for the 1.00 mm (top) and Number of free spray parent parcels and free spray parent parcel mass for the 0.25 mm (bottom) cubic subsets.

Finally, Figure 7.28 shows the PDFs of normalized mass vs. *Re* for the 2.4 million parcel count case, and extracted for each of the three cubic subsets. It can be seen that for the smaller subset sizes the distribution narrowed around the peak value while the peak itself transitioned to lower *Re*. The explanation to this behavior was found to be related to two main causes:

1. In average, the parcels included in the smaller subsets were closer to the wall than those in the larger ones. Therefore, the overall velocities were lower due to longer time for which they underwent drag. This justified the shifting of peak to smaller values of *Re* (480-520 in the 1.00 mm cube to 320-400 in the 0.25 mm), as well as the disappearance of very fast parcels that were present in the 1.00 mm cube (i.e., those corresponding to *Re* larger than 1000).

The definition of the cubic subsets was such that, regardless of their sizes, the bottom face of the cubes was always centered with respect to the impingement point on the wall (cf. Figure 7.22). Therefore, the larger subsets included parcels that were further away with respect to the injection axis, compared to what happened for the smaller subsets. At any given axial location, the velocity of spray parcels is the highest on the injection axis and decreases moving away from the center [166]. This explains why the results from the 1.00 mm subset include very slow parcels (i.e., low *Re*), despite showing a higher peak and generally higher values for the right tail of the PDF.

Similar considerations were reached for the *We*-based distributions for which the results for the 0.25 mm cubic subset using 2.4 million parcels are reported in Figure 7.26 (bottom right).

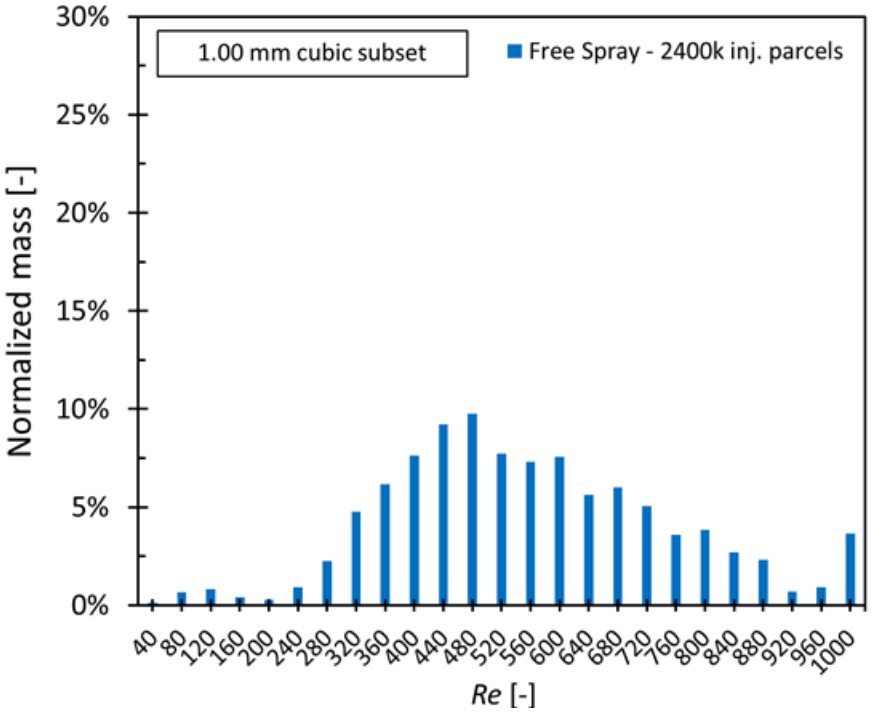

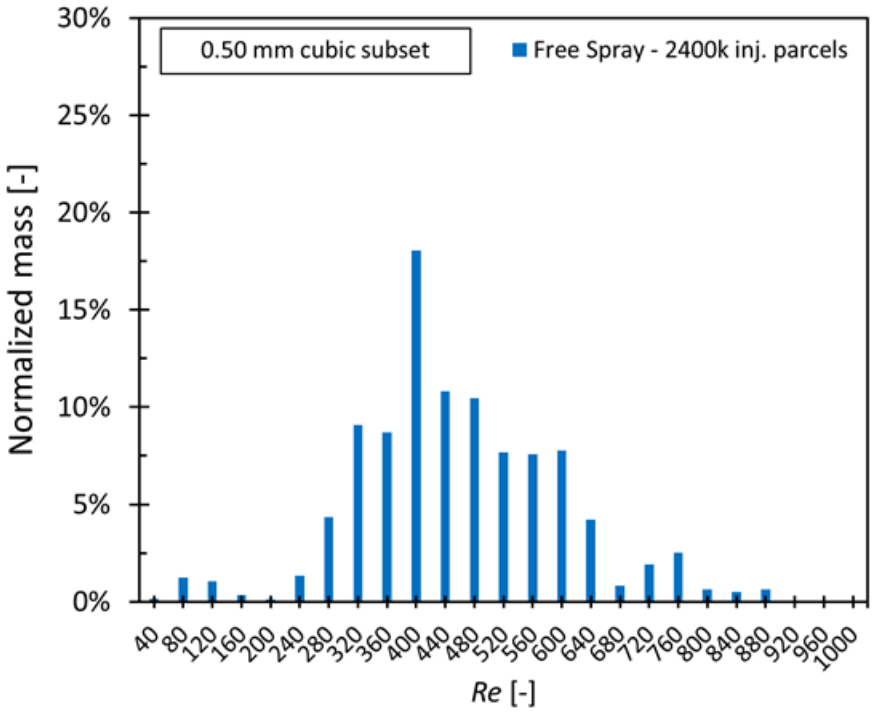

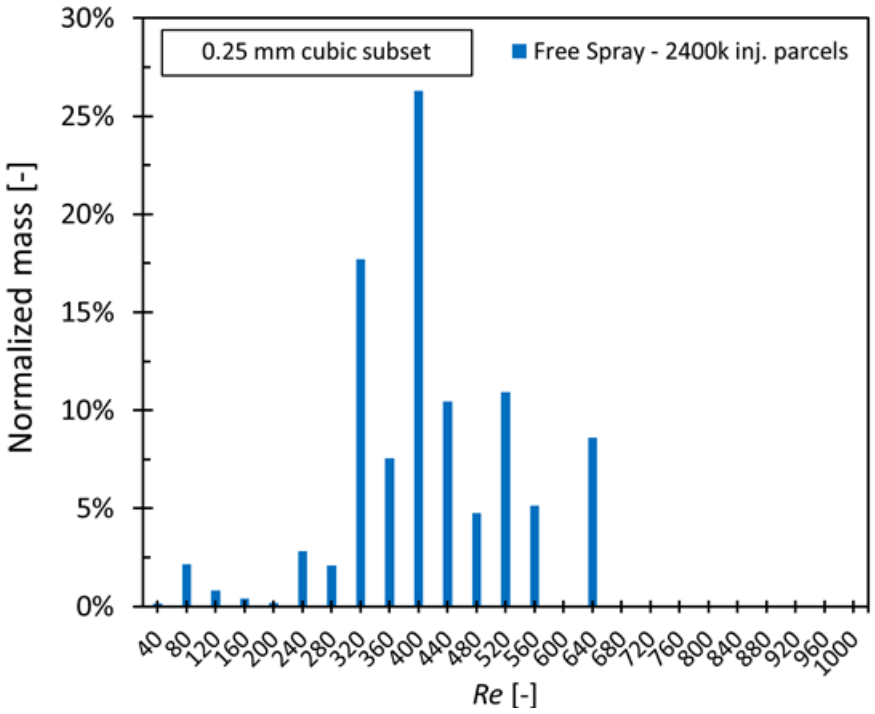

Figure 7.28: PDFs of normalized mass vs *Re* at ASOI of 1.50 ms using 2.4 million injected parcels. The cubic subset sizes are 1.00 mm (top), 0.50 mm (middle), 0.25 mm (bottom).

7.2.4 Summary

Experimental and numerical studies of high pressure fuel spray impinging on a flat plate were performed in the current study. The experimental work was carried out in a constant volume CV to characterize the properties of free and impinged portion of the spray and support validation and development of the spray-wall interaction models. A RANS based methodology was used for the simulations to study local spray quantities at different locations in the vicinity of the impingement point. The following conclusions can be drawn on the basis of the experimental and simulation efforts.

(1). In the experiments, diesel and n-heptane fuels were injected separately with a single-hole production injector. Parametric variations were performed for the different operating conditions to evaluate the effects of ambient density and injection pressure on the free and impinged spray behaviors. The free spray penetration decreased with

the ambient density and increased with the injection pressure both in diesel and n-heptane sprays. The impinged spray radii were generally longer than the impinged spray on wall. The impinged spray radius on wall and the spray height decreased with the ambient density and increased with the injection pressure. This was likely caused by the enhanced spray momentum achieved at the impinging wall at lower ambient density and higher injection pressure.

(2). Bottom view images showed that both radial and axial radii decreased as the ambient density increased at any given time-step. The expansion ratio slightly decreased with the ambient density. The ambient density had no significant effect on the corrugation ratio. Therefore, the WIES front could be almost considered as a smooth arc. On the other hand, the radial and axial radii increased with the injection pressure at any given time. The expansion ratio showed no significant variation as the injection pressure increased. The corrugation ratio did not show large variations under the different injection pressures.

(3). In simulation, global spray-related quantities such as liquid penetration and impinged radii and height from CFD simulations were found to be in good agreement with experiments. The comparison of the spray-wall interaction related quantities showed that the general trends were well predicted, especially in terms of axial and radial spray impinged on wall. On the other hand, the impinged spray height was under-predicted.

(4). The local spray morphology near the impingement location is sensitive to the physical size of the selected subset domain as well as to the number of injected parcels. In general, the pre-impingement spray morphology continuously changes along the spray axis requiring the subsets to be sampled very close to the impingement location. In addition, the spray characteristics were found to be very sensitive also to the radial distance between the selected parcels and the injection axis, suggesting that the extension of the sample should be limited to a small region around the axis, in the vicinity of the wall. On the other hand, the use of smaller subsets (as small as a cube

with a 0.25 mm side) required the number of injected parcels to be increased in order to improve the statistical significance of the selected sample. Very large numbers of injected parcels might not be a viable solution for multi-hole injectors, due to the linear increase of the parcel count with the number of holes. Nevertheless, this study demonstrated that if availability of computational resources is not a limitation, large parcel counts are fundamental for the correct assessment of local spray morphology in small sample volumes.

7.3 Spray-wall film characteristics

During spray-wall impingement test, n-heptane as the liquid fuel was injected on the roughened flat surface at various ambient and injection conditions. The ambient temperature is 423 K which is the same with the temperature of the roughened surface, and the fuel temperature is 363 K. The injection specifications and the detailed test condition for spray-wall interaction are listed in Table 7.4.

Table 7.4: Test conditions for spray-wall film measurement

Parameter	**Values**
Ambient gas temperature (K)	423
Ambient gas density (kg/m^3)	14.8, 22.8, 30.0
Ambient gas composition	100% N_2
Ambient gas velocity (m/s)	~ 0
Nominal nozzle outlet diameter (μm)	200
Nozzle K factor	0
Number of holes	Single-hole
Orifice orientation relative to injector axis	60° (included angle: 120°)
Fuel injection pressure (MPa)	120, 150
Fuel	n-heptane
Fuel temperature at nozzle (K)	363
Energizing injection time (ms)	2.0

Injected mass (mg) at 150 MPa, 22.8 kg/m^3	23.37
Average surface roughness (μm)	16
Distance between injector tip to impinging surface (mm)	33.65 (roughened plate)

7.3.1 Experimental results

Figure 7.29 shows a schematic of the entire process of spray-wall impingement. There are four stages during the spray interacting with a flat plate: start of impingement, end of injection (EOI), disappearance of mist (DOM), and film accumulation and evaporation, corresponding to t_{IMP}, t_{EOI} and t_{DOM} as the temporal time and three sample images as the spray development of first three stages. The sample images are obtained from the baseline condition (injection pressure of 150 MPa and ambient density of 22.8 kg/m^3). As shown in the first image, the spray interacts with the plate and film starts to form on the plate ASOI of 0.7 ms; the injection event ends around ASOI of 3.0 ms but a number of droplets continually impinge on the wall or float above the wall, which leads to the occurrence of mist near the impinged wall. This mist scatters the light and affects the measurement of transmissivity, further affects the accuracy of film properties prediction. Therefore, in the current study, the film thickness starts to be calculated after the mist completely disappears around ASOI of 5.0 ms. As the film evaporates, the film thickness and area decreases with the time. The quantitative analysis of film characteristics will be discussed in the following sections.

Figure 7.30 shows the sequential images of film formation at the baseline condition, which provides a visual understanding of film development and illustrates the film evaporation process after spray impinging on the flat plate. The sample images are colored by intensity to reveal the variation between the film and dry plate. Because of the inverse relationship between the intensity and film thickness, lower signal indicates higher film thickness. Also, the red boundary drawn in the figure represents the film occupied area. As mentioned in Figure 7.29, film thickness starts to be estimated when the mist completely disappears at ASOI of 5 ms. It is also observed that film thickness and film area decrease with the time due to the relatively high ambient temperature and evaporation of liquid fuel film. The

evaporation of fuel film is affected by the temperature difference between the plate and liquid film (the fuel temperature and plate temperature are initially set to 363 K and 423 K, respectively) and it is also affected by the other operating conditions such as ambient density and injection pressure.

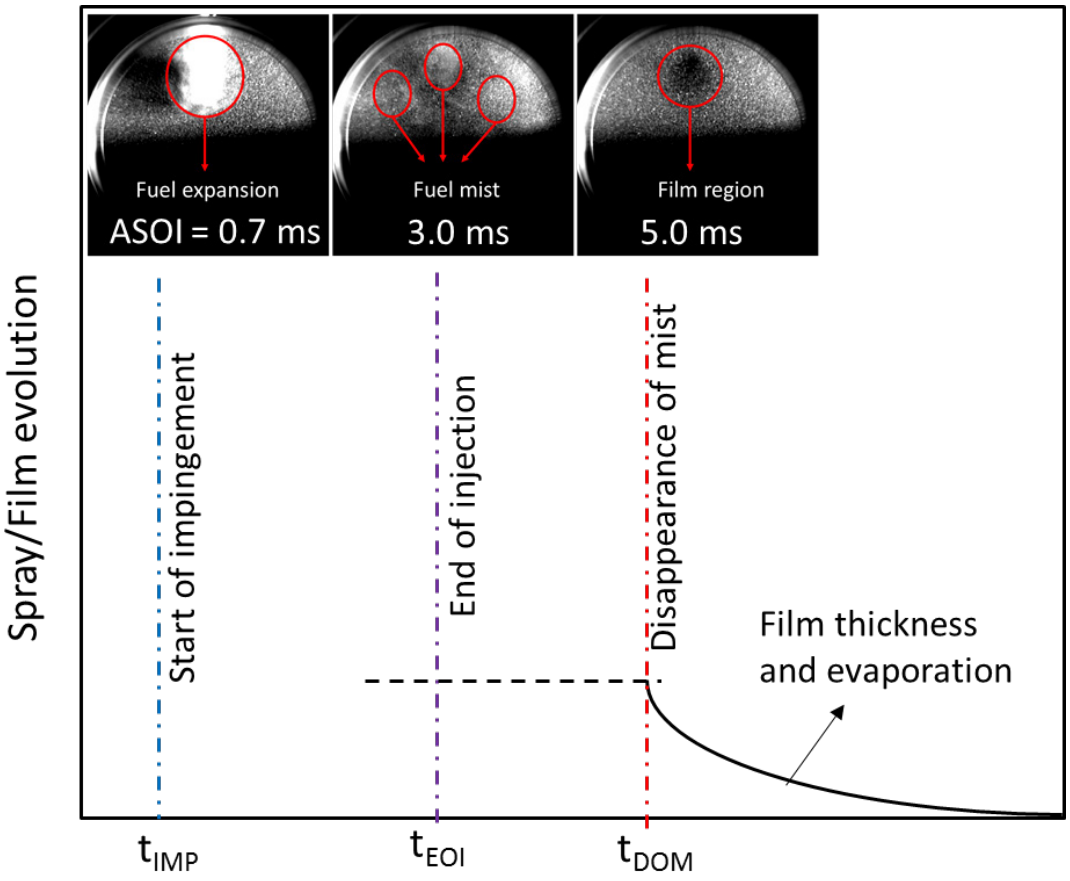

Figure 7.29: Schematic of spray/film evolution.

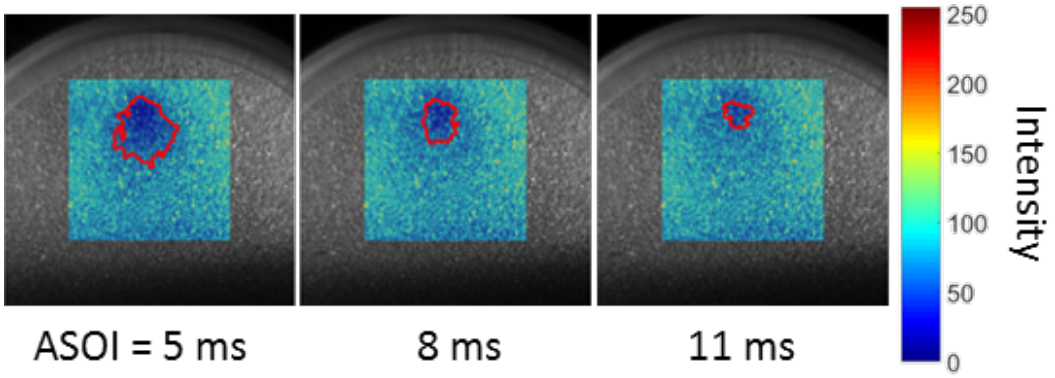

Figure 7.30: Fuel film evaporation process in CV.

Parametric variations were performed for the different operating conditions given in Table 7.4 to evaluate the effects of ambient density and injection pressure on the liquid film formation and film evaporation processes. For all experimental results shown in the following sub-sections, the temporal evolution of film properties corresponds to the averaged film characteristics as discussed in Image processing section, and these film properties are accounted at the approximately same time (~ ASOI of 5 ms) for all various conditions at which the mist is almost completely disappeared. Further, the liquid film thickness is averaged in terms of a square region in the upper central part of film deposition region as shown in Figure 3.27. While the local film thickness profiles were attained along both axial and radial directions with respect to the impinging point at ASOI of 8 ms at which the film is under development and evaporation already starts. Additionally, the experimental results presented in current work are averaged from at least three repetitions.

7.3.1.1 Ambient density effect

Figure 7.31 presents the effect of ambient density (14.8, 22.8, and 30.0 kg/m^3) on the temporal evolution of the liquid film mass (top) and film area (bottom) at the injection pressure of 150 MPa. Figure 7.32 shows the averaged film thickness variation under different ambient densities. It should be noted that the three time stamps (t_{IMP}, t_{EOI} and t_{DOM}) marked in Figure 7.31 and Figure 7.32 are only for the baseline condition (injection pressure of 150 MPa and ambient density of 22.8 kg/m^3).

In general, from Figure 7.31 and Figure 7.32, the film mass, film occupied area, and averaged film thickness decrease as the ambient density increases. At each condition, these film properties also decrease from the maximum values with the time via the film evaporation. In addition, the maximum film mass, film area, and averaged film thickness are higher at low ambient density case than the ones with high ambient density cases. Nevertheless, the difference of maximum averaged film thickness at various ambient density conditions is within 0.5 μm, this might be explained by the evidence that the average surface roughness of 16 μm is much larger than the average film thickness (below 1.5 μm). Thus, a relatively high pressure is required for all conditions to squeeze the liquid film out from the valley of the roughened surface. Conversely, the maximum variance in film area at different ambient densities occurring at ASOI of 5 ms is a comparatively larger value, 130 mm^2, for which the spray momentum reduce after spray impinging on the surface but the spray/film keeps expanding outward by inertia. For film mass, the maximum value is around 0.075 mg at ASOI of 5 ms at low ambient density which is 74% larger than the ones at high ambient density cases. As well, considering the dynamic evaporation, the rate of evaporation is much slower for the high ambient density case, because with the higher ambient density, the movement of droplets is slower and less experience with contacting high ambient temperature environment, leading to lower rate of evaporation. However, thinner film (30.0 kg/m^3) takes short time to be fully evaporated compared with thicker film (14.8 kg/m^3). Note that the complete evaporation time is not shown here due to the long timeline.

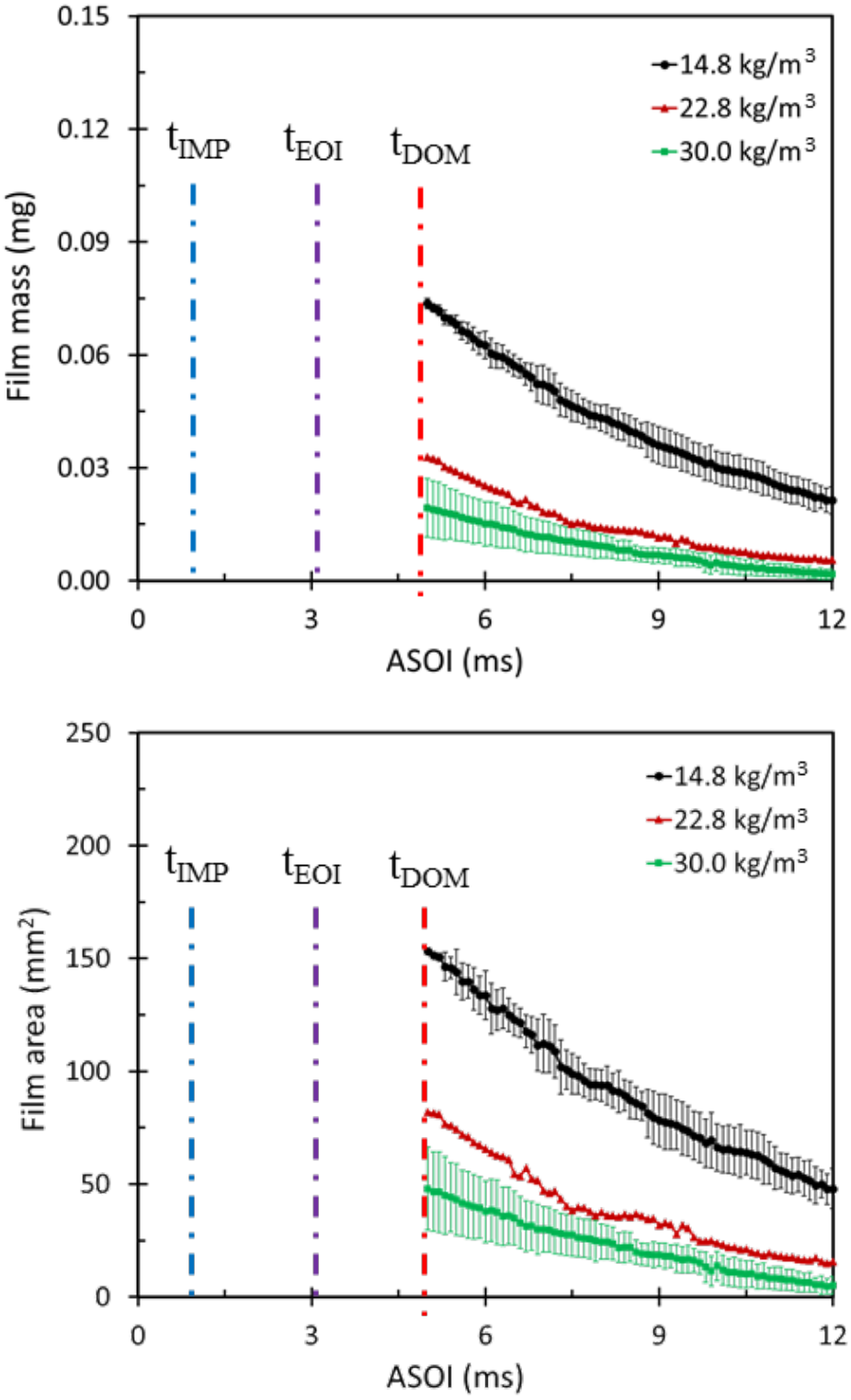

Figure 7.31: Ambient density effect on the temporal evolution of fuel film mass (top) and wetted area (bottom).

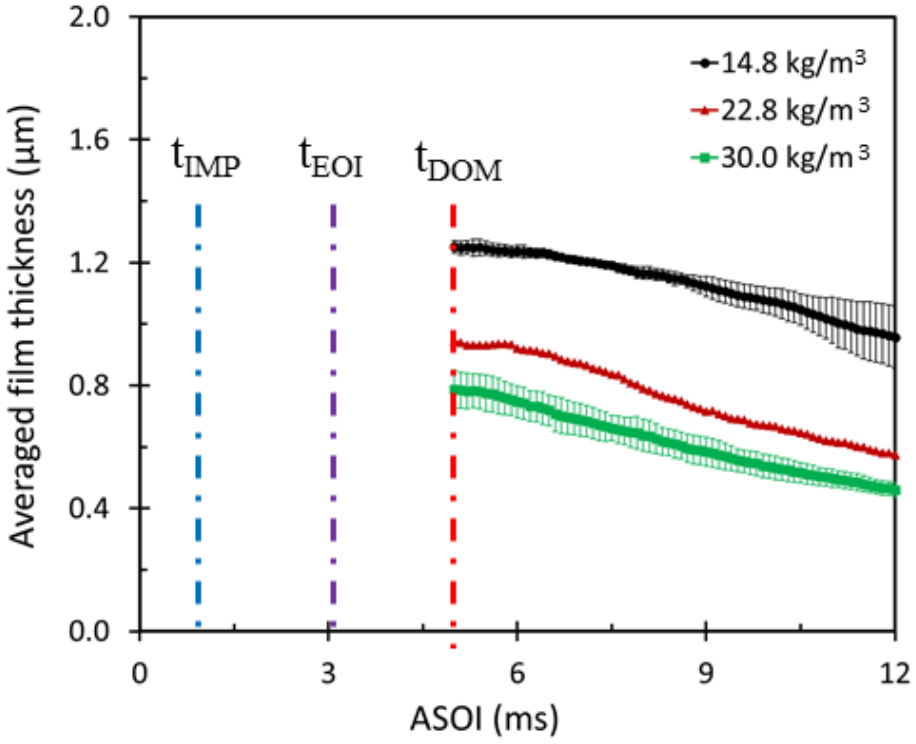

Figure 7.32: Ambient density effect on the temporal evolution of averaged film thickness (the liquid film thickness was averaged based on a square region of 2.25 x 2.25 mm^2).

Figure 7.33 shows the local film thickness along the axial (top) and radial (bottom) directions with respect to the impinging point (0, 0) at the various ambient densities and injection pressure of 150 MPa at ASOI of 8 ms. The data points for the local film thickness measurement in Figure 7.33 are taken every 0.5 mm for each condition. The smooth line is obtained after a 5^{th} order polynomial curve fitting applied to the local film thickness distribution. In both axial and radial directions, the larger local film thickness shows in the central region, near the impingement point from -2.5 mm to 2.5 mm. The local film thickness overall decreases with the increase in ambient density which follows the similar trend with the averaged film thickness as discussed and explained in the previous section. Further, in the axial direction as shown in Figure 7.33 (top), the maximum film thickness is around 1.2 µm, 0.9 µm, and 0.8 µm at ambient density of 14.8, 22.8, and 30.0 kg/m^3, respectively. The maximum film thickness at ambient density of 30.0 kg/m^3 is observed to shift near the impinging point which might be due to the lower impact momentum

happened at higher ambient density case and cause the impinging location more stable compared with the lower ambient density cases. It is also seen that in the axial direction the liquid film is thinner close to the injector side (negative sign direction). At -10 mm, the film thickness is about 0.1 μm while at 10 mm, the film thickness is around 0.3 μm for all conditions. The reason for this is that a 30° angle between the plate on which the injector is mounted and the spray plume leads to the relatively higher impact momentum in the positive axial direction to drive the spray deposit more in the positive direction and generate thicker film compared with that in the opposite direction.

Similarly, the radial film thickness reduces as the ambient density increases. However, the local film thickness in radial direction is more symmetrical with respect to the impinging point since unlike the axial direction, the spray impinging on the surface distributes uniformly in the radial direction. The maximum of local film thickness at ambient density of 30.0 kg/m^3 is closer to the impinging point by the same reason mentioned in previous.

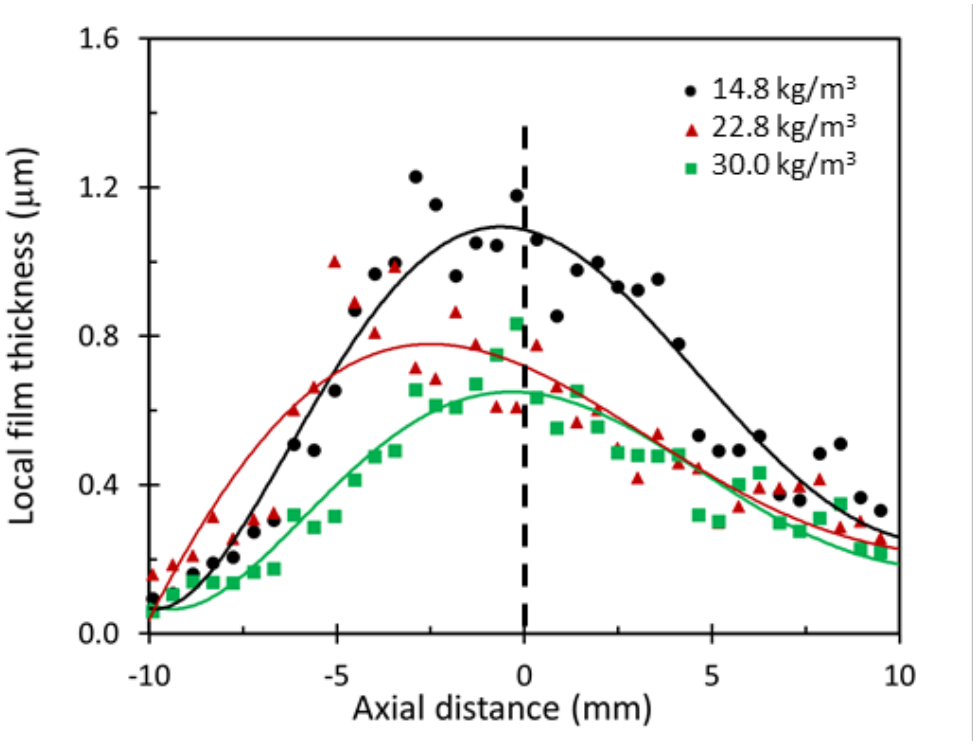

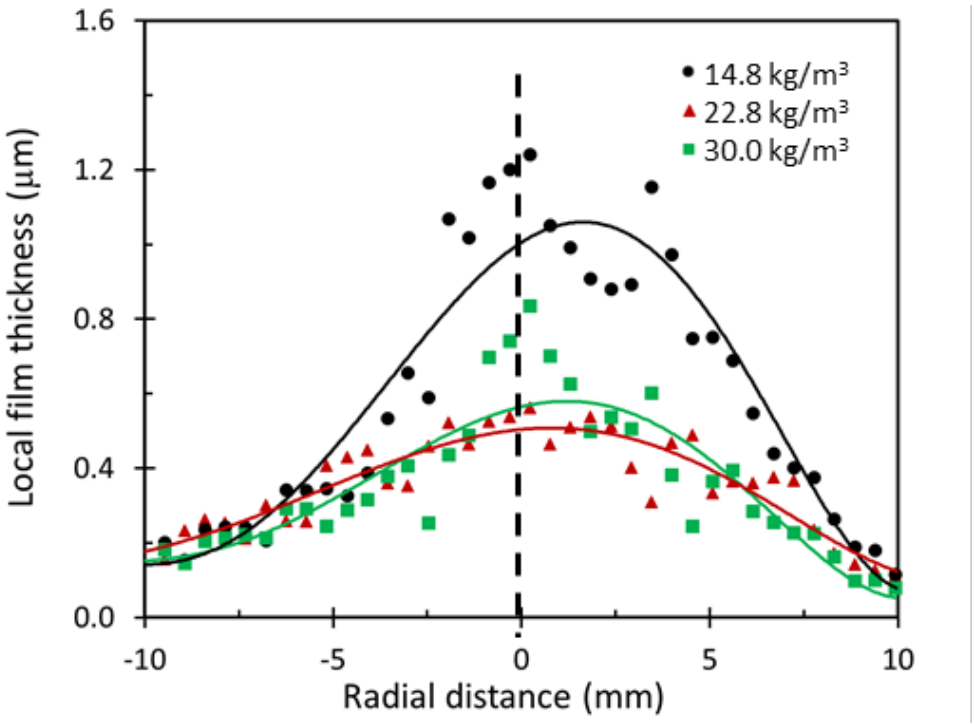

Figure 7.33: Ambient density effect on local film thickness in axial (top) and radial (bottom) directions at ASOI of 8 ms.

7.3.1.2 Injection pressure effect

Figure 7.34 shows the injection pressure (120 and 150 MPa) effect on the liquid film mass (top) and area (bottom) at ambient density of 22.8 kg/m^3. Figure 7.35 presents the averaged film thickness at the same condition with Figure 7.34. Similarly, the three different time stamps (t_{IMP}, t_{EOI} and t_{DOM}) marked in Figure 7.34 and Figure 7.35 are only for the baseline condition (injection pressure of 150 MPa and ambient density of 22.8 kg/m^3).

Generally, from Figure 7.34 and Figure 7.35, the film mass, film occupied area, and averaged film thickness apparently decrease as the injection pressure increases, also decrease from the peak values with the time at each condition. The dynamic evaporation is found that the rate of evaporation at different injection pressures is similar, while thinner film (150 MPa) evaporates faster and the thicker film (120 MPa) shows slower evaporation.

Moreover, the maximum film area is 160 mm^2 and 80 mm^2 around ASOI of 5 ms for 120 MPa and 150 MPa, respectively. When the spray impinges on the roughened surface, the impact momentum is larger at injection pressure of 150 MPa than the one at 120 MPa and thus the spray might be pushed further leading to the expansion and larger film area. However, the liquid film has to also overcome the higher force imposed and attempt to emerge against the roughened surface, which inhibits the spray/film expansion. Therefore, it may lead to the larger film area at 120 MPa than that at 150 MPa. Besides, the film thickness for 120 MPa case is around 0.26 µm larger than that at 150 MPa case at ASOI of 5 ms. This is caused by the enhanced spray momentum achieved near the impinged surface at high injection pressure and the liquid spray is impulsed farther after impingement on wall, resulting in the thinner liquid film and faster evaporation.

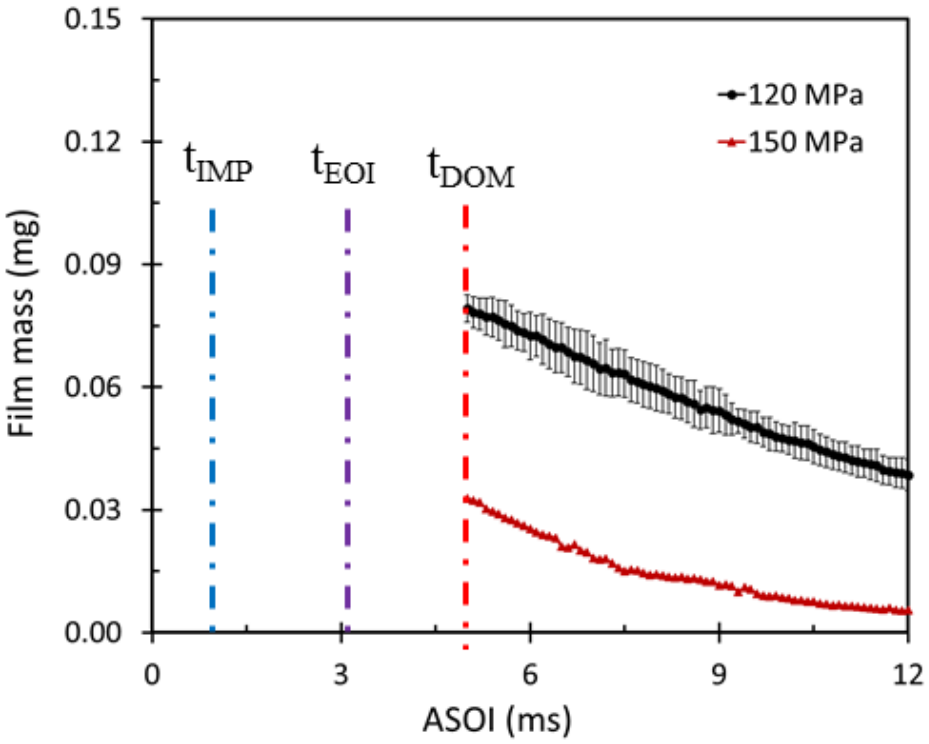

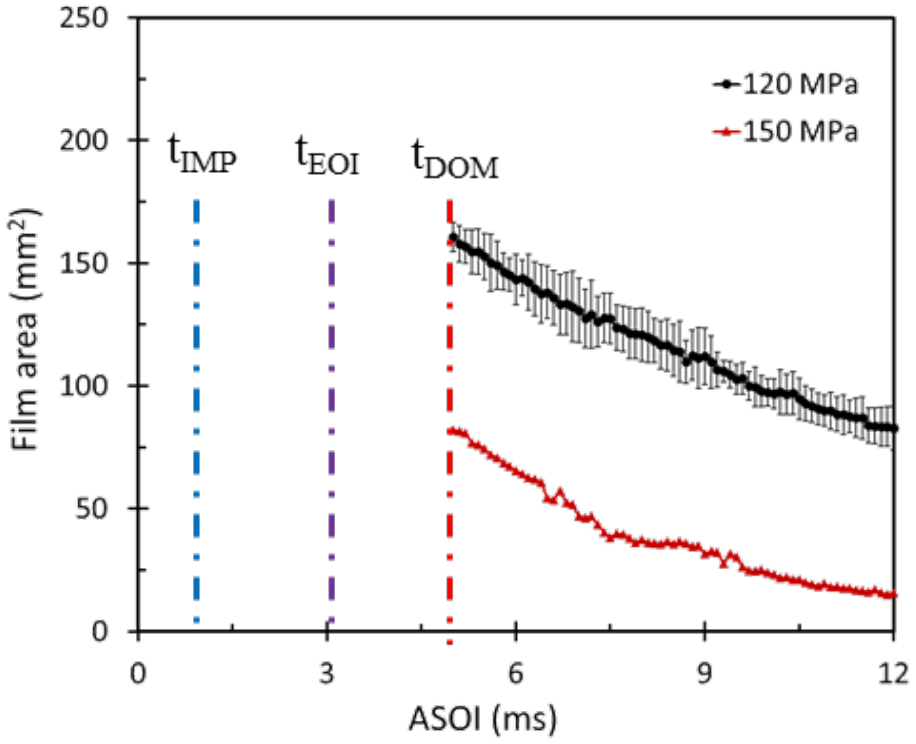

Figure 7.34: Injection pressure effect on the temporal evolution of fuel film mass (top) and wetted area (bottom).

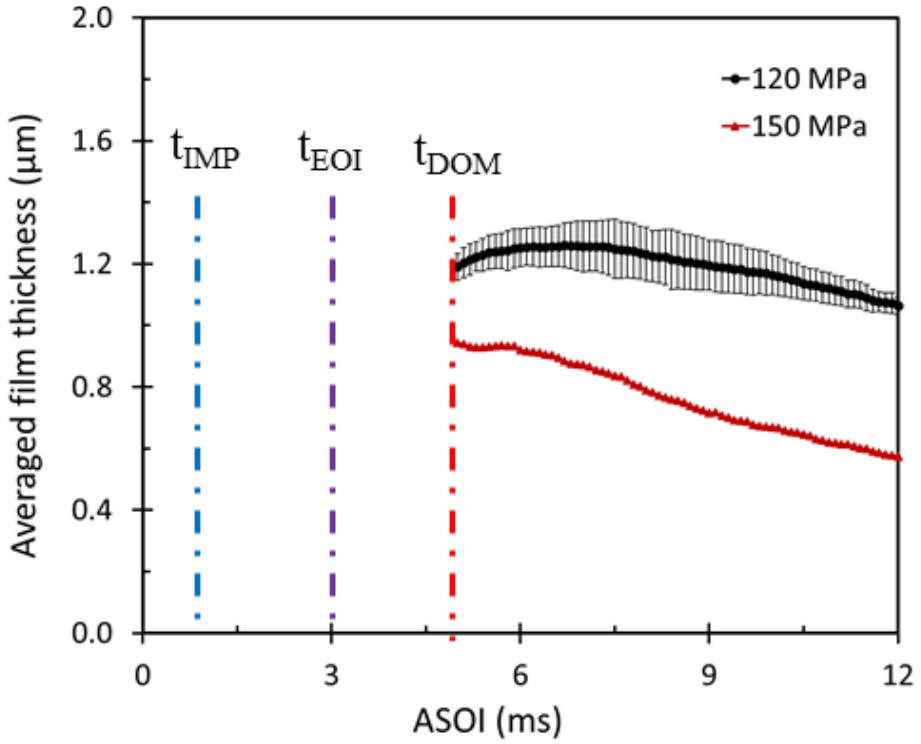

Figure 7.35: Injection pressure effect on the temporal evolution of averaged film thickness (the liquid film thickness was averaged based on a square region of 2.25 x 2.25 mm^2).

Local film thickness in the axial and radial directions is also evaluated for different injection pressures at the same ambient density of 22.8 kg/m^3 at ASOI of 8 ms as shown in Figure 7.36 (top) and (bottom). In the same way, the data points for the measured local film thickness are taken every 0.5 mm for each condition. The smooth line is attained after a 5^{th} order polynomial curve fitting applied to the local film thickness distribution. In both axial and radial directions, the local film thickness decreases in the range from -5 mm to 5 mm with the injection pressure which follows the similar trend with the averaged film thickness as discussed in the previous section. At the periphery of film area, the film thickness does not change too much even with the different injection pressures.

Additionally, in the axial direction, the maximum film thickness at 120 MPa is around 1.2 µm while shows the maximum film thickness is around 0.9 µm at 150 MPa case. The maximum film thickness at 120 MPa is observed to shift near the impinging point which

might be due to the lower impact momentum occurred at lower injection pressure case, leading to the impinging location more stable compared with the higher injection pressure case. The same phenomenon observed in the different ambient density cases is also seen in various injection pressure conditions: the liquid film is thinner on the direction closed to the injector (negative sign direction) due to a 30° angle between the wall on which the injector is mounted and the spray plume leading to the relatively higher momentum in the positive axial direction to drive the drive the spray deposit more in the positive direction and generate thicker film. Figure 7.36 (bottom) shows the local film thickness distribution in radial direction. Similarly, the radial film thickness overall reduces with the injection pressure. The maximum local film thickness in radial direction at 120 MPa is also around 1.2 µm but the maximum local film thickness at 150 MPa is only 0.4 µm.

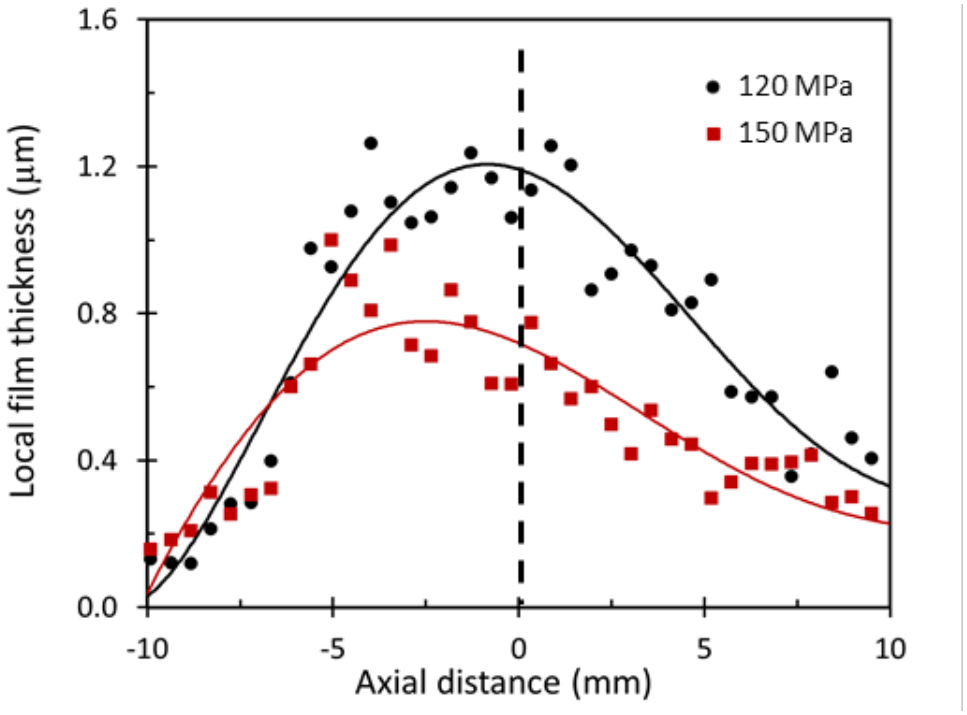

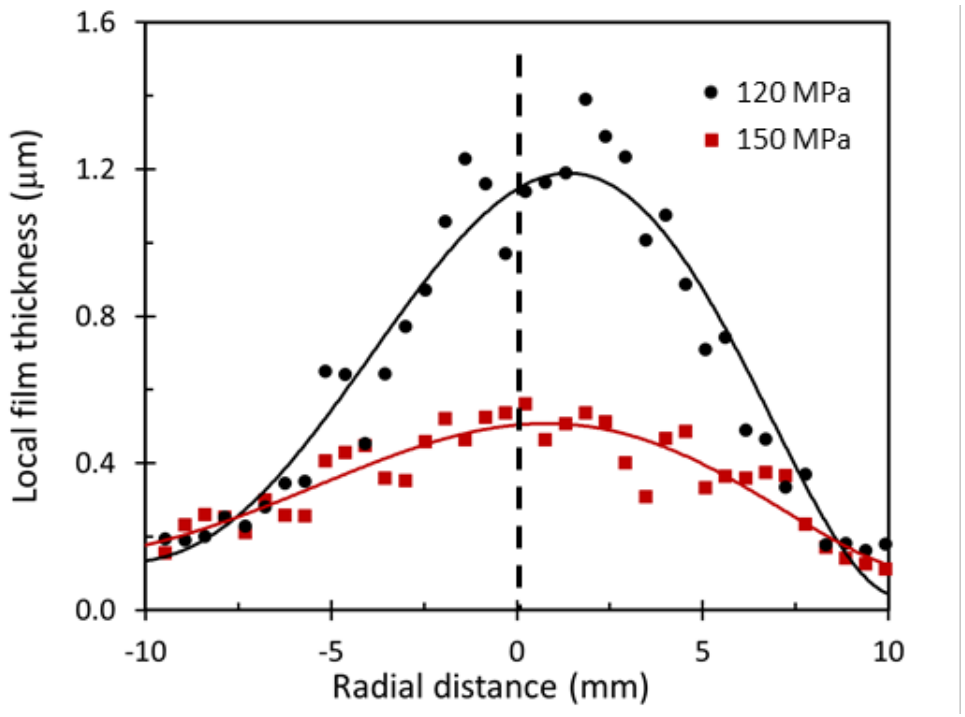

Figure 7.36: Injection pressure effect on local film thickness in axial (top) and radial (bottom) directions at ASOI of 8 ms.

7.3.2 Simulation results

The similar simulation settings, except for the spray-wall interaction model, presented during the analysis of free and impinged spray properties were applied to validate and investigate the wall-film characteristics. As discussed in Chapter 4, the spray-wall interaction model from Han et al. [98] was employed to characterize the wall-film properties. In simulation, the film mass is calculated in terms of the mass of the deposited particles in the impinged surface, however, the film area and film thickness are determined with respect to the cells and the amount of film volume within each cell.

The comparison of temporal film properties between the CFD simulation (dash line) and the experimental data (solid line) under the baseline condition (injection pressure of 150 MPa and ambient density of 22.8 kg/m^3) are shown in Figure 7.37. It can be observed that the film mass, wetted area, and film thickness show the same magnitude with experiment. In particular, the film area shows a very good agreement with that in experiment. Further,

due to the high ambient temperature and evaporation of fuel film, the film properties start decreasing with the time as long as the liquid fluid deposited on the wall and extended into the maximum area.

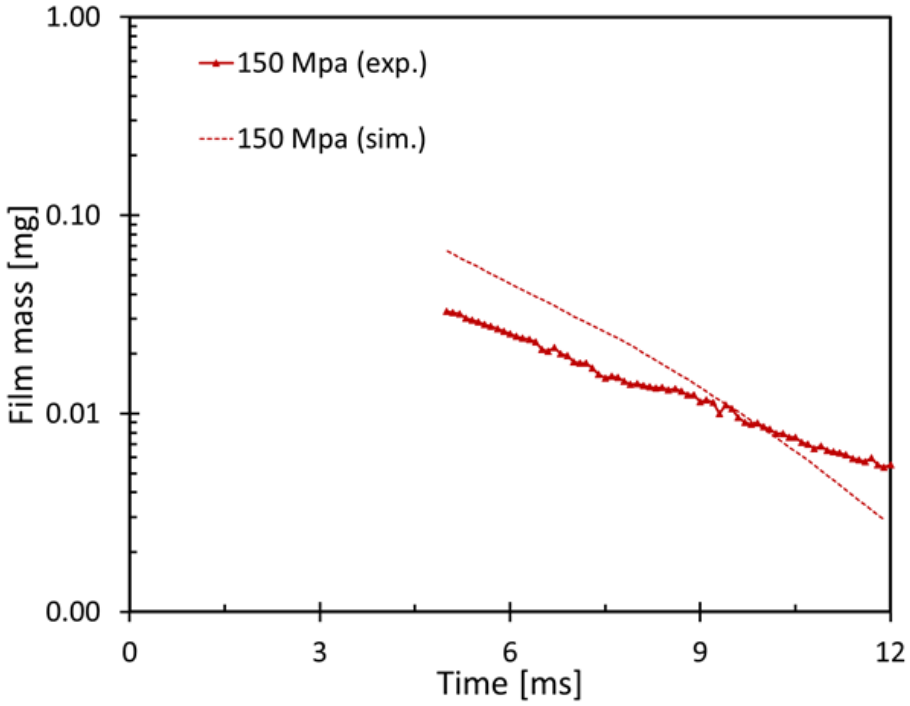

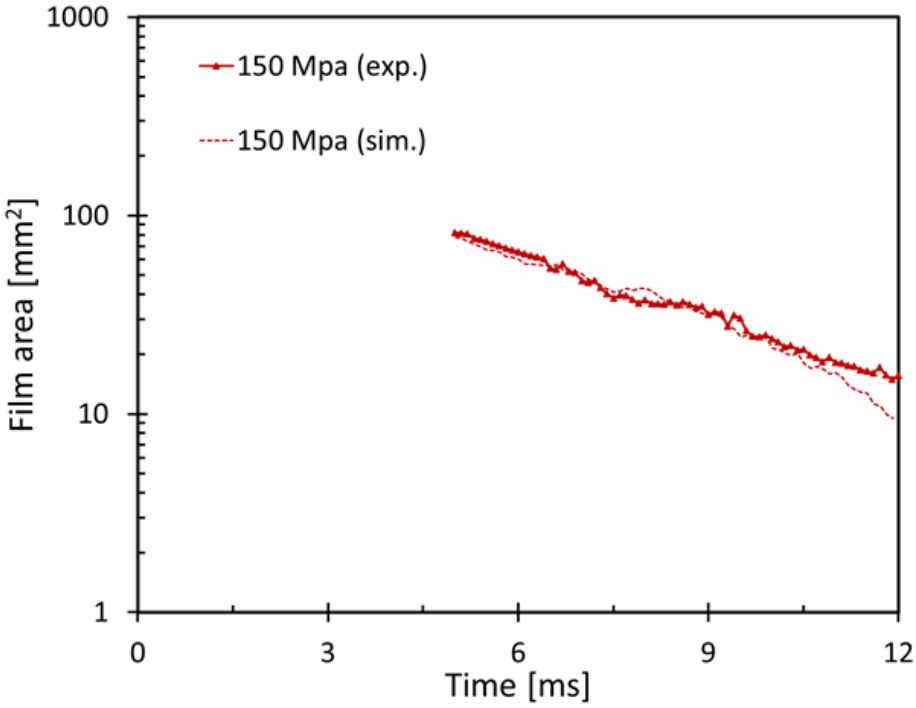

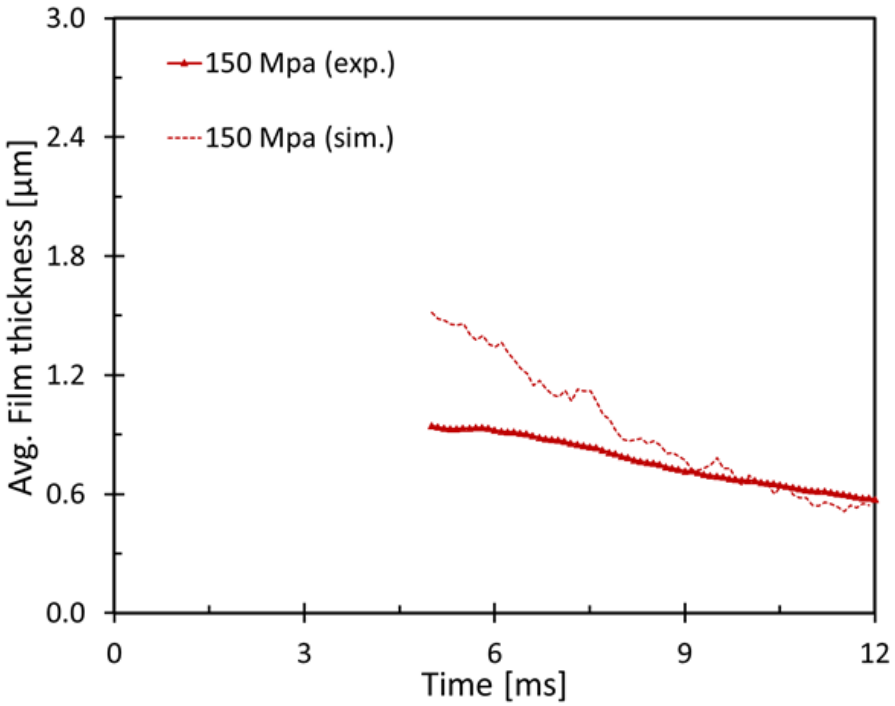

Figure 7.37: Film mass, film area, and film thickness comparison between simulation and experiment.

Figure 7.38 shows the comparison of local film thickness between experiment and simulation results at various time instants. Top images provide the experimental results. The color represents the local film thickness and the red boundary line is the one used to define the film area. Film mass is calculated based on the measured film area within this region. Beyond the boundary, the thinner film is ignored. The bottom images are from simulation. Local cell is colored by the film thickness, only cells which contain the deposited liquid film are colored. Therefore, the local film thickness distribution also stands for the film mass distribution. From Figure 7.38 (bottom), it can be observed that the magnitude of film thickness is similar with that in experiment. However, considering the film area, unlike the visualized area within the red boundary in experiment, the methodology of film area calculation in simulation is different. The actual film area is not necessarily equal to the summation of areas of all cells that have deposited film. Hence, the comparison with respect to film area is only the qualitative comparison, not quantitative analysis.

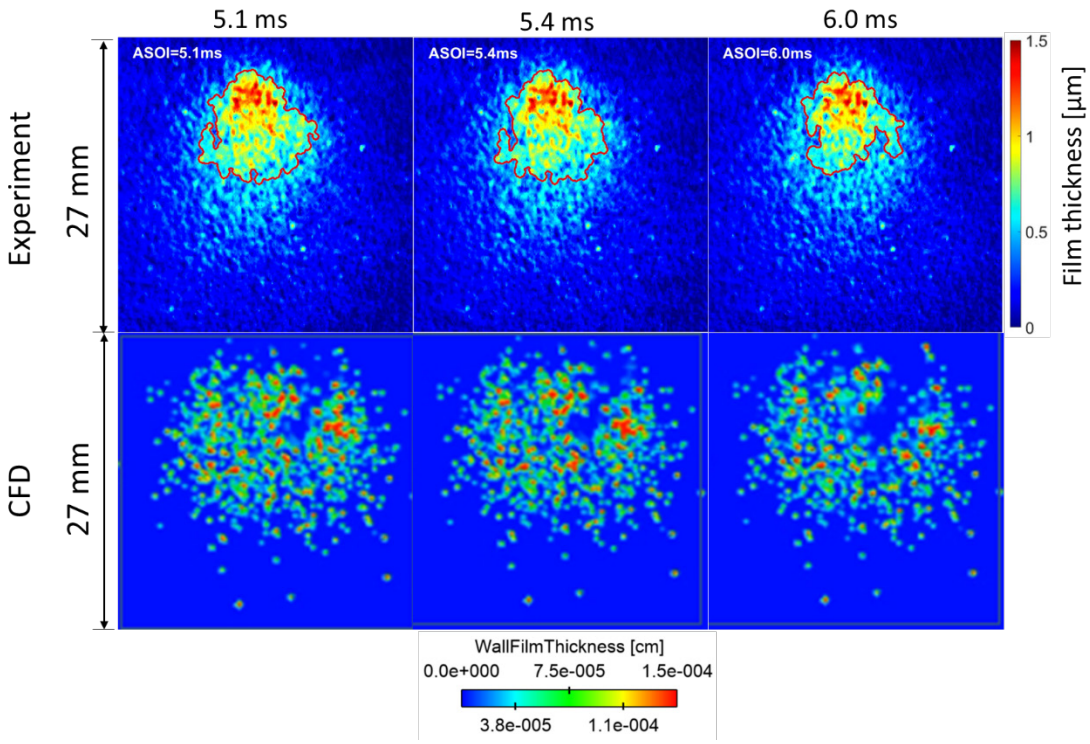

Figure 7.38: Local film thickness distribution comparison between experiment and simulation.

7.3.2.1 Injection pressure effect

Figure 7.39 shows the injection pressure (120 and 150 MPa) effect on the liquid film characteristics at ambient density of 22.8 kg/m^3 from both experiment and simulations. Due to the higher momentum at 150 MPa to enhance the breakup and evaporation of droplets, the fuel vapor mass at higher injection pressure is smaller than that at lower injection pressure. Generally, from Figure 7.39, the film mass, film occupied area, and averaged film from simulations shows a good agreement with experimental data. These properties apparently decrease as the injection pressure increases, also decrease from the peak values with the time at each condition in both experimental and simulation results. The dynamic evaporation is found that the rate of evaporation at different injection pressures is similar, while thinner film (150 MPa) evaporates faster and the thicker film (120 MPa) shows slower evaporation.

Moreover, when the spray impinges on the roughened surface, the impact momentum is larger at injection pressure of 150 MPa than the one at 120 MPa and therefore the spray might be pushed further leading to the expansion and larger film area. However, the liquid film has to also overcome the higher force imposed and attempt to emerge against the roughened surface, which inhibits the spray/film expansion. Therefore, it may lead to the larger film area at 120 MPa than that at 150 MPa. Besides, the maximum film thickness for 120 MPa case is larger than that at 150 MPa case at ASOI of 5 ms. This is caused by the enhanced spray momentum achieved near the impinged surface at high injection pressure and the liquid spray is driven farther after impingement on wall, resulting in the thinner liquid film and faster evaporation.

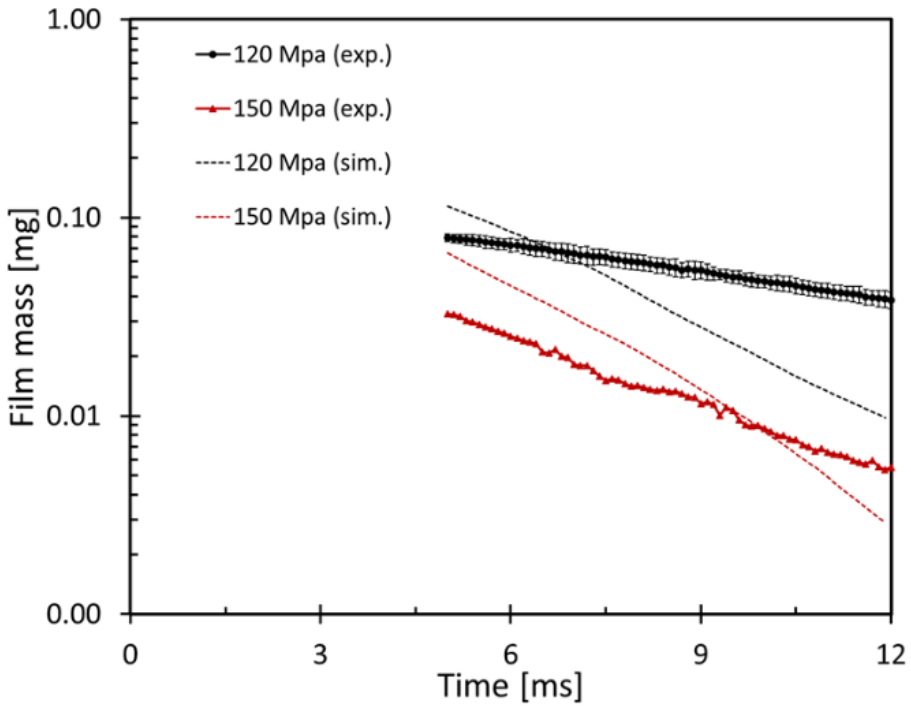

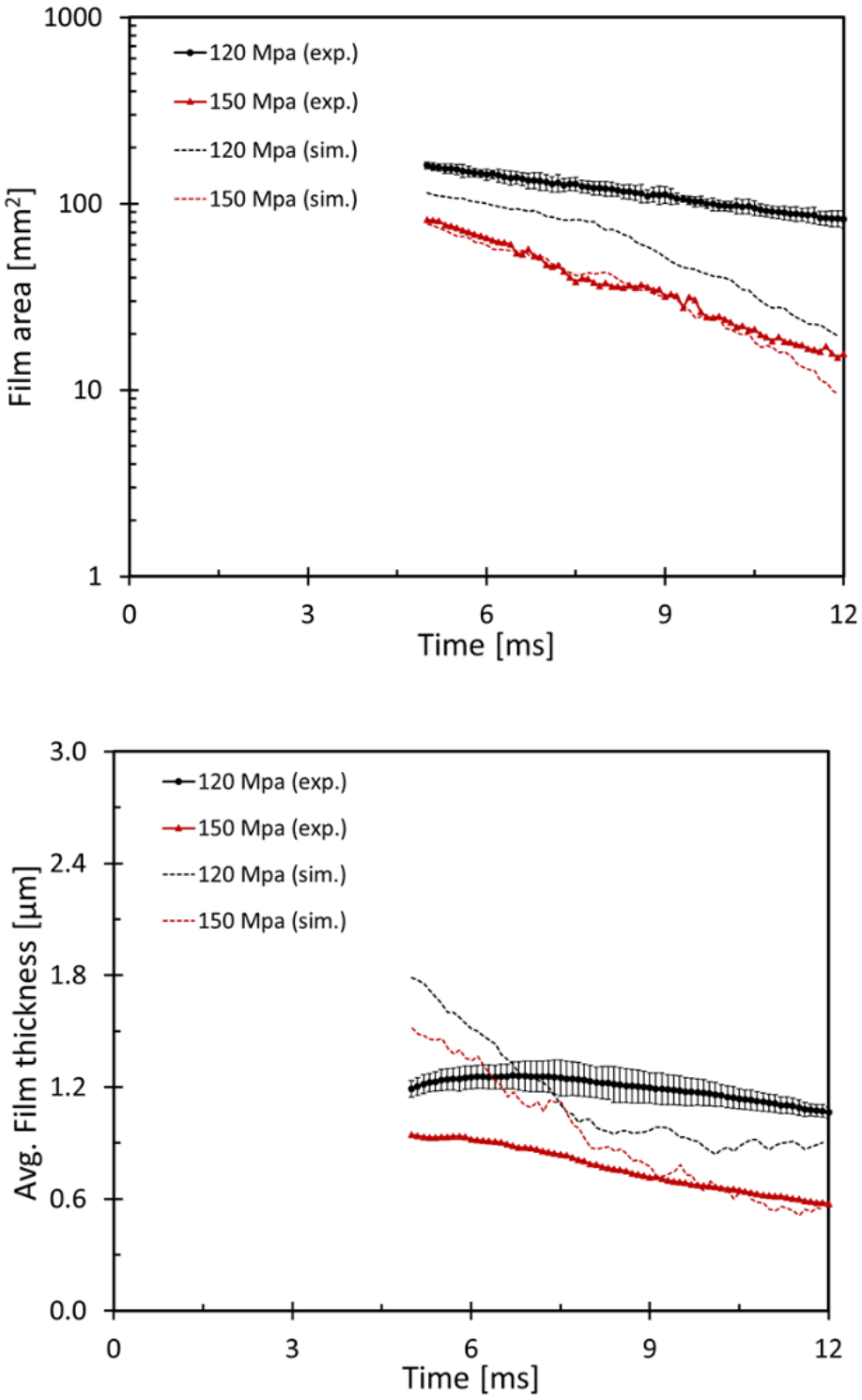

Figure 7.39: Injection pressure effect on the temporal film mass, wetted area, and film thickness.

7.3.3 Summary

The section studied the fuel film formation and the relevant film characteristics resulting from the liquid spray impinging on a flat plate in a constant volume CV by RIM technique and CFD simulations.

(1). In experiment, the liquid film thickness was calibrated with two different proportional mixtures (5% n-dodecane and 95% n-heptane; 10% n-dodecane and 90% n-heptane) pumped out from a precise syringe to achieve an accurate calibration result. The n-heptane fuel from a side-mounted single-hole diesel injector was then injected on a rough glass with the same optical setup, the distance between the injector tip and impinging plate is set to 33.65 mm. The ambient temperature and the plate temperature are set to 423 K with the fuel temperature of 363 K. The effects of various ambient density (14.8, 22.8, and 30.0 kg/m^3) and injector pressure (120 and 150 MPa) on the liquid film properties were studied. An in-house Matlab code for image processing was used to extract the spray and wall-film properties.

(2). From the experiment, the temporal evolution of film mass, area, and averaged film thickness decrease as the ambient density and injection pressure increase. The thinner film evaporates faster while the thicker film shows slower evaporation. In both axial and radial directions at various ambient densities and injection pressures, the larger local film thickness shows in the central region, near the impingement point from -2.5 mm to 2.5 mm. The local film thickness overall decreases with the ambient density and injection pressure. At -10 mm and 10 mm in the axial direction, the liquid film is always thinner on the injector side due to the relatively higher impact velocity and momentum in the positive axial direction to drive the spray deposit more in the positive direction and generate thicker film compared with that in the opposite direction. Further, the experimental work in the present study is also served as the database of spray-wall interaction model development.

(3). Simulations successfully capture the n-heptane spray structure and n-heptane film properties. The simulations are also able to capture the same trend with experimental results when varying injection pressure.

7.4 Heat flux measurement

As described in Chapter 3.6, total seven locations by three heat flux probes linearly deploying on the heated plate at different orientations (0^o, 90^o, and 180^o) are measured to obtain the heat flux during spay-wall impingement. The same test conditions as the above spray-wall impingement tests are used for heat flux measurement, for example, the single-hole diesel injector with nozzle diameter of 200 μm, the distance between the injector tip and the heated plate is 40 mm. The ambient temperature within CV is set to 150°C, while the bottom impinged plate temperature varies with 135°C (no plate heater), 150°C, 200°C, and 250°C. Diesel (ULSD) fuel temperature is set to 90°C. The effects of ambient density and injection pressure on the heat flux are studied. Table 7.5 shows the summary of heat flux test conditions. All the conditions have five runs.

The heat flux results with the heated plate of 250°C at the orientation of 0^o are reported in this Chapter, the rest of results from other locations and orientations are provided in Appendix.

Table 7.5: Test conditions for heat flux measurement

Parameter	**Values**
Ambient gas temperature	423 K (150°C)
Ambient gas density	14.8, 22.8, 30.0 kg/m^3
Ambient gas composition	100% N_2
Ambient gas velocity	~0 m/s
Nominal nozzle outlet diameter	200 μm
Nozzle K factor	0
Number of holes	Single-hole
Orifice orientation relative to injector axis	60° (included angle: 120°)
Fuel injection pressure	120, 150, 180 MPa

Fuel	diesel
Fuel temperature at nozzle	363 K (90°C)
Energizing injection time	2.0 ms
Distance between injector tip to impinging surface	40 mm (smooth plate)
Surface temperature	135°C (no plate heater), 150°C, 200°C, and 250°C
Heat flux probe location and orientation	A, B, C and 0^o, 90^o, and 180^o

7.4.1 Ambient density effect

Figure 7.40 shows the ambient density effect on the heat flux of three different locations. The injection pressure remains 150 MPa. Before fuel injection, due to the temperature difference between the surface and ambient gas, heat transfer exists and the heat flux is taken into account as shown in Figure 7.40. When the spray impinges on the heated plate, the heat flux increases to the peak value rapidly due to the relatively large temperature difference caused by the liquid fuel and the hot surface. Fuel film is deposited on the plate after the spray impingement and it starts evaporating after the end of injection, causing that the surface temperature recovers toward the initial temperature before the injection. Moreover, the surface temperature (250°C) is lower than the Leidenfrost temperature of diesel (460°C), the evaporation of the droplets when impacting on the hot surface is not in film boiling regime. There is no continuous film of vapor formed between the liquid spray and hot surface.

In addition, the heat flux at Location B is always larger than other two locations at any ambient densities at a given time. Because Location B is observed closer to the impinging point as the spray interacting with the hot surface compared with other two locations, this results in the relatively large amount of liquid film deposited near this location and the temperature difference between the liquid and surface is larger. By comparing the heat flux from Location A with that from Location C, Location A shows more heat flux at any given time. The reason for this behavior is that the 30° angle between the wall where the injector is mounted and the spray plume leads to a relatively higher momentum toward to Location A compared to that at Location C, thus causing more spray to progress in the Location A.

Furthermore, the heat flux at any fixed locations decreases with the increase of ambient density. This phenomenon is due to the fact that high ambient density causes the enhanced fuel atomization and air entrainment, resulting in more heat transfer from the ambient gas toward the liquid spray. More spray are taken away by the ambient gas flow induced by higher ambient density, instead of interacting with the hot surface, thus, the wall heat flux reduces.

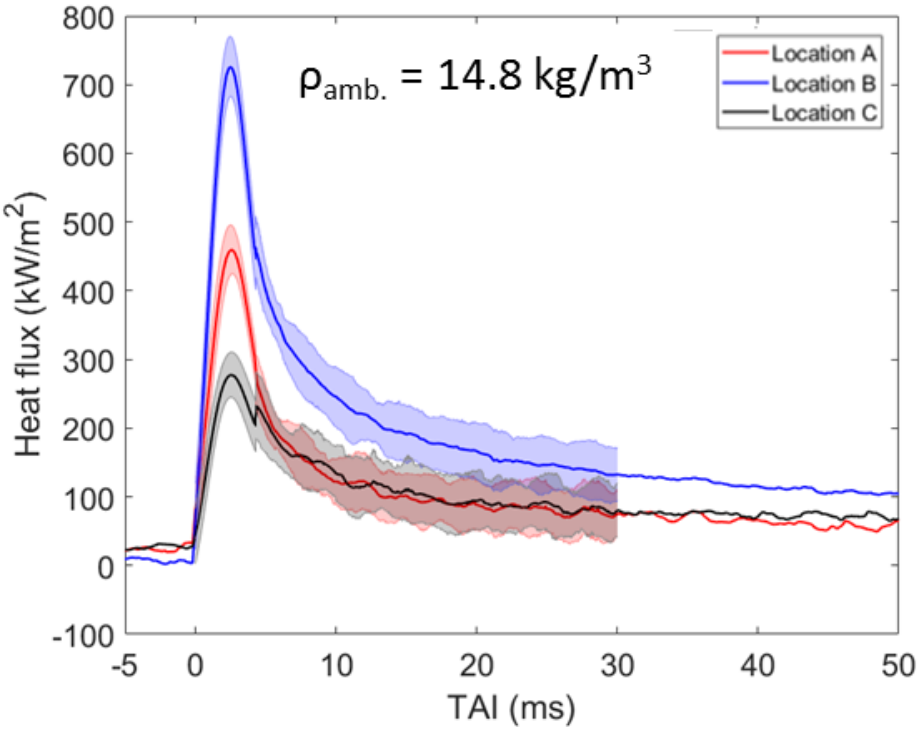

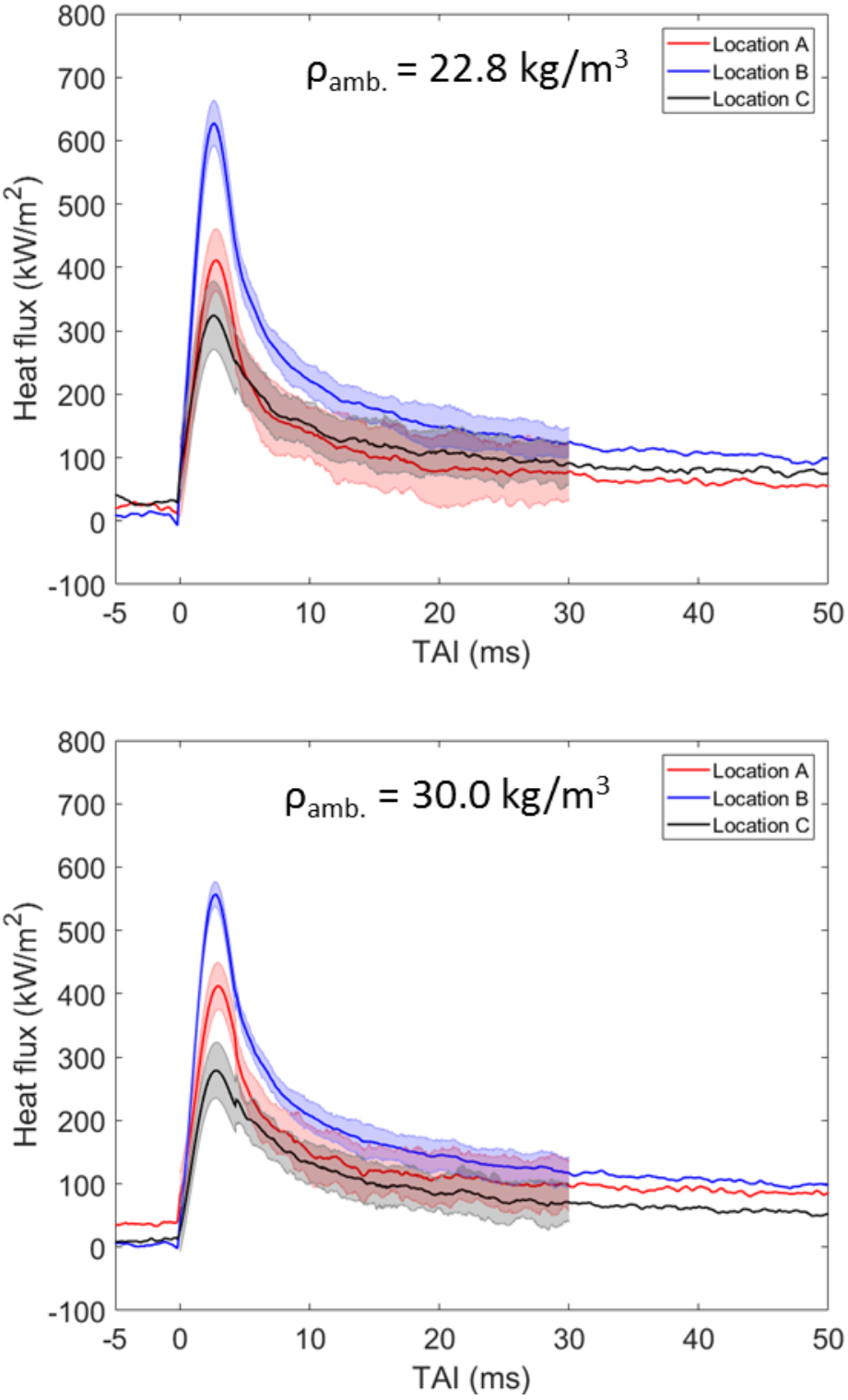

Figure 7.40: Ambient density effect on the heat flux at three different locations at 0°.

7.4.2 Injection pressure effect

Figure 7.41 shows the effect of injection pressure on the heat flux at three different locations. The ambient density during the test remains the same for all conditions, 22.8 kg/m^3. With the same injection pressure, as the same reason mentioned above, at any given time, the heat flux curve at Location B is always above ones in other two locations; the heat flux at Location A is larger than that at Location C. At any fixed location, the heat flux overall increases with the injection pressure, however, there is no a clear monotone trend of heat flux as the injection pressure increases or decreases. The heat flux at Location A shows the similar amount of value with the increase of injection pressure. At Location B and Location C, it shows the higher heat flux at injection pressure of 150 MPa.

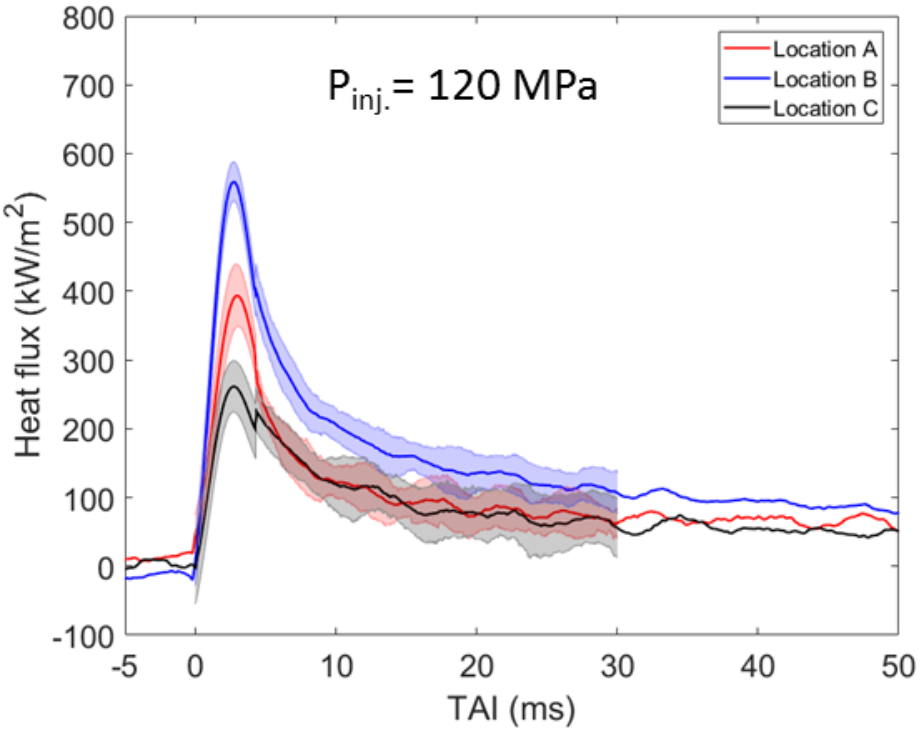

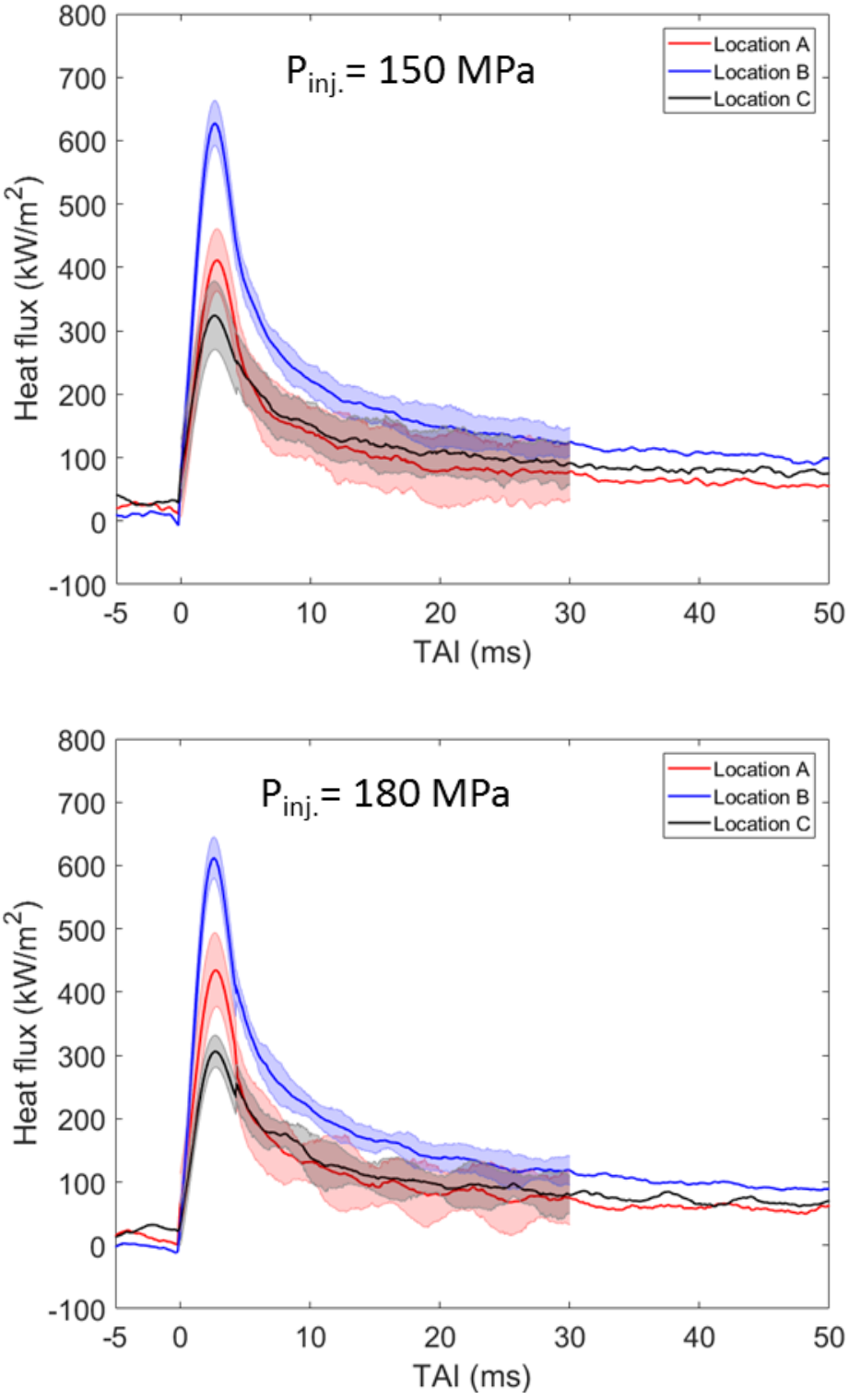

Figure 7.41: Injection pressure effect on the heat flux at three different locations at 0°.

CHAPTER 8 MULTIPLE SPRAY-TO-SPRAY COLLISION UNDER GASOLINE ENGINE CONDITIONS[3]

This chapter presents results from experiments and simulations for multiple spray-to-spray collision under gasoline engine conditions. The first section discusses the experimental and numerical study of spray-to-spray collision with a 2-hole injector. The next section presents the simulation results obtained from spray-to-spray collision with a 4-hole injector.

8.1 Spray-to-spray collision with a 2-hole injector

Mounted on one side of the vessel orthogonal to the window, a 2-hole injector is assembled in-line with view. This setup facilitates visualization of the fan angle as illustrated "in-plane view" in Figure 8.1. Although penetration barely alters from different nozzle holes views, it may depend significantly on vapor fraction. However, the vapor and liquid regions can proportionately vary with the different nozzle orientation (views), yielding similar vapor fractions. In the test, both normal and in-plane views are visualized for water and gasoline. It is observed, as the chamber pressure accretes during the test, the fan and spray angles become equivalent.

[3] Reprinted with permission from SAE papers 2015-01-0948©2015 SAE International and 2016-01-0840©2016 SAE International. The materials in this chapter were published in the following papers:

- Zhao, L., Moiz, A., Naber, J., Lee, S. et al., "High-Speed Spray-to-Spray Collision Study on Two-Hole Impinging Jet Nozzles," SAE Technical Paper 2015-01-0948, 2015, https://doi.org/10.4271/2015-01-0948.
- Zhao, L., Limbu, S., Potham, S., Lee, S. et al., "Numerical Simulations for Spray Characterization of Uneven Multiple Jet-to-Jet Impingement Injectors," SAE Technical Paper 2016-01-0840, 2016, https://doi.org/10.4271/2016-01-0840.

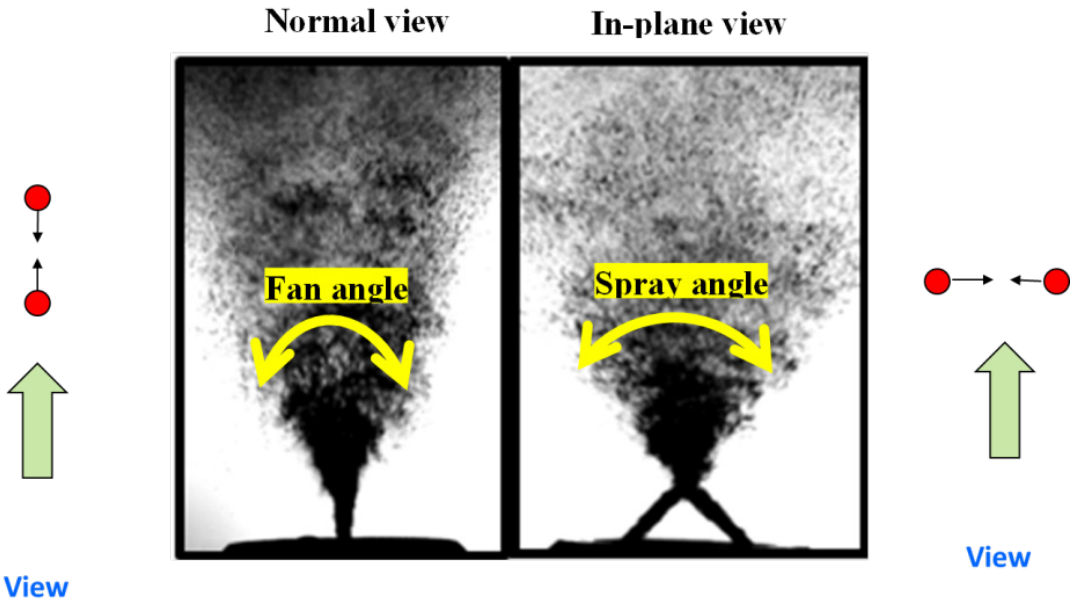

Figure 8.1: Illustration of colliding sprays.

8.1.1 Experimental results

A set of schlieren images captured by high-speed camera at different position, is presented to further explain the combustion phenomenon under condition discussed above. High-speed images show clearly the vapor (transparent spray structure) and liquid (black spray stream) and with abatement in before top dead center (BTDC), i.e., increment in the ambient temperature, a large vaporization portion can be observed. The ambient conditions are 653 K, 490 K, and 402 K for 30º, 60º and 90º BTDC, corresponding to ambient pressures of 37.4, 12.4, and 5.7 bar, respectively. The conditions as described are related to an injection in the combustion chamber of an IC engine where the piston is at 30º/60º/90º crank angle BTDC at the compression ratio of 7.5. The injection pressure is set to 172 bar. Time interval of 3 ms and gasoline are applied for all cases. Figure 8.2 displays raw images of 2-hole injector from experiments.

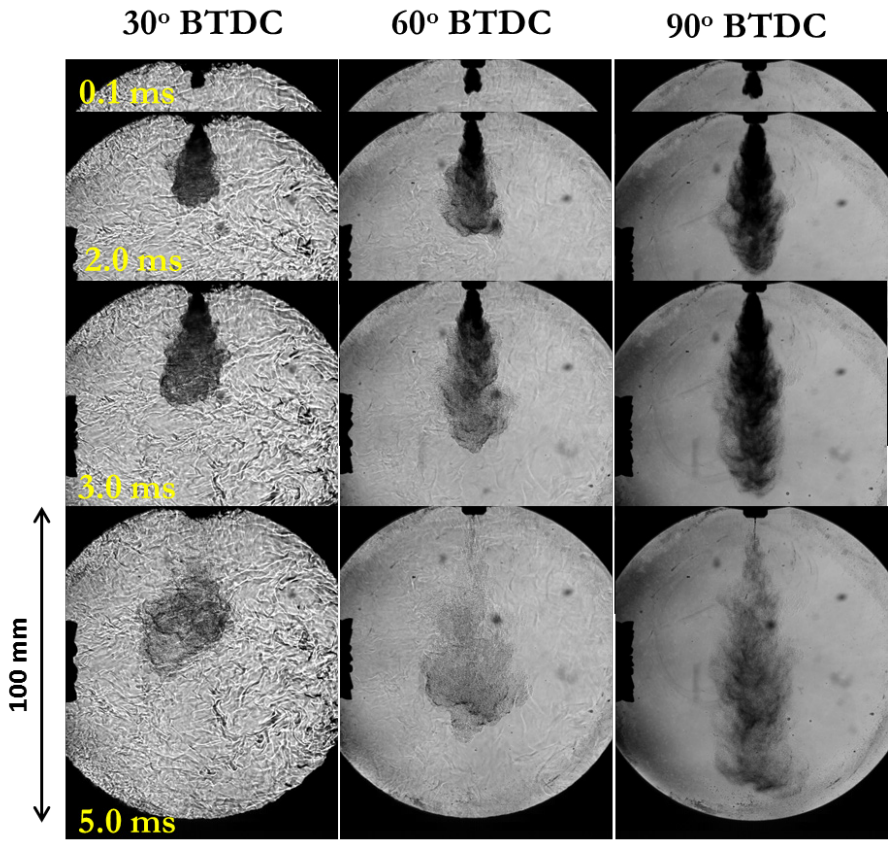

Figure 8.2: 2-hole impinging spray at ASOI of 0.1, 2.0, 3.0, and 5.0 ms.

It is noticed that the penetration length (leading spray tip) increases as the temperature and pressure conditions become less intense from 30° BTDC to 90° BTDC. It can be safely concluded that 60° BTDC is a favorable to achieve a higher degree of vaporization along with longer penetration. 30° BTDC provides better vaporization but with lesser penetration depth, whereas the 90° BTDC visual vaporization is comparatively smaller than the other two BTDC conditions.

Figure 8.3 shows the penetration lengths and vapor fractions based on spray occupied area for 2-hole injector. Based on spray occupied area, the penetration lengths and vapor fractions are recorded at different piston positions developing as time elapses. These results include the variations based on the three repeated runs for each test. Generally, vapor penetration increases with an increase in BTDC. Also, the area-based vapor fraction shows higher vaporization for the 30° BTDC compare to the other cases. Similarly the 60° BTDC

is higher than 90° BTDC case. The reason for the dipping in injection is due to the blocking of one hole during the flow at initial injection times. This blockage may arise due to the asymmetric needle motion (needle wobble). This behavior is higher in the 90° BTDC case where the back-pressure from the chamber is less.

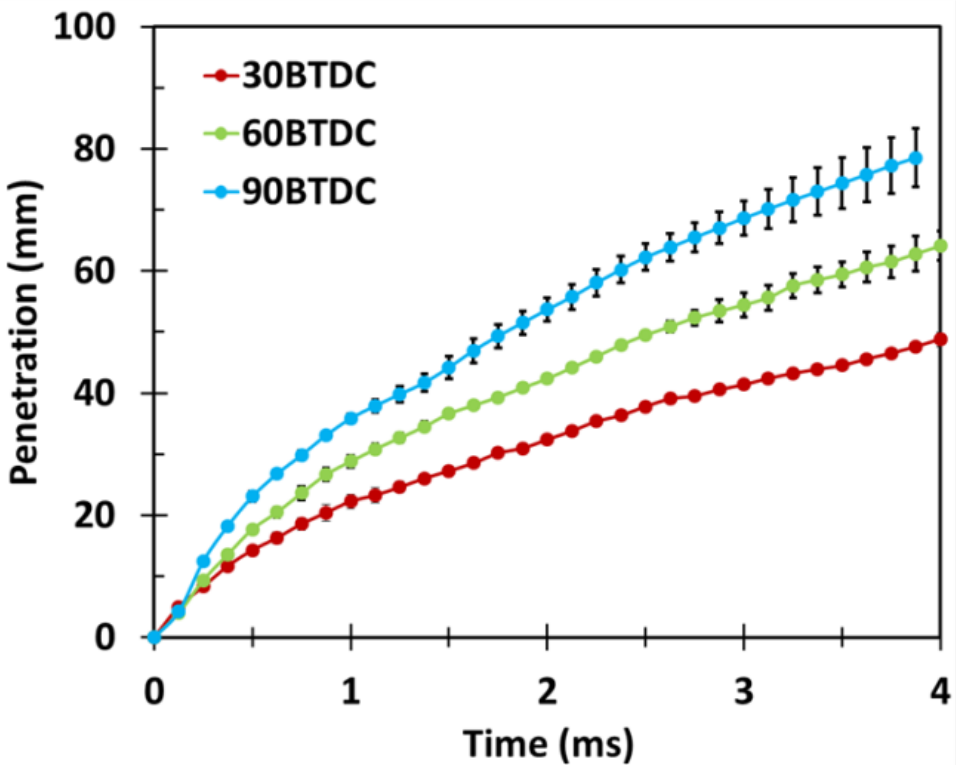

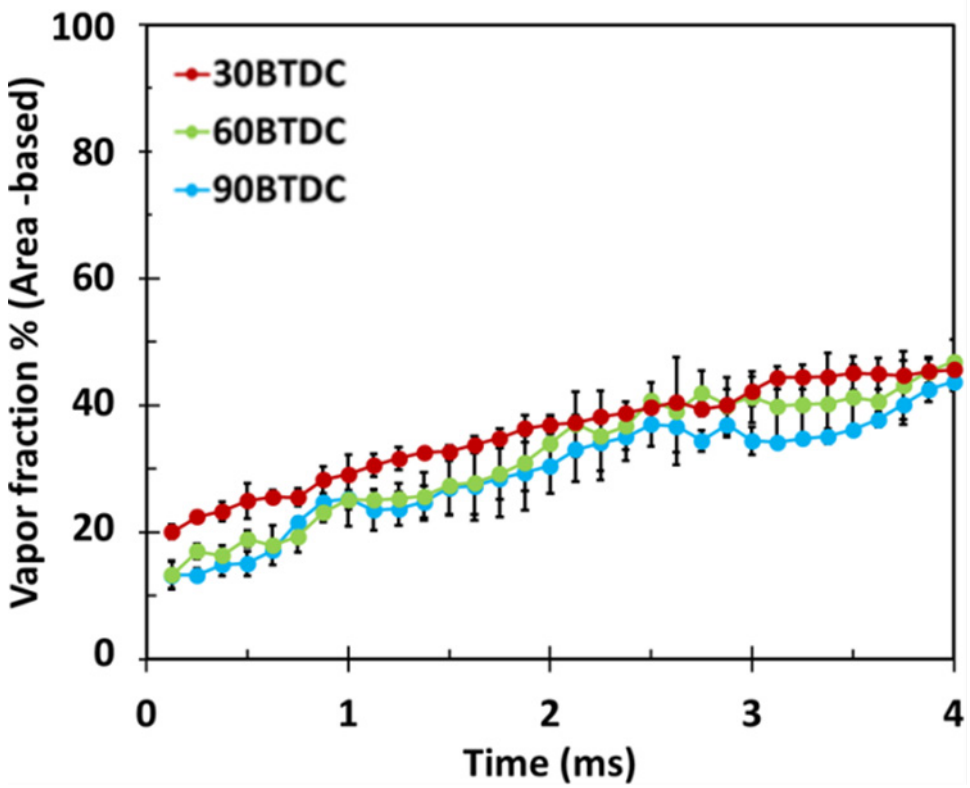

Figure 8.3: Penetration and vapor fraction of 2-hole injector.

8.1.2 Simulation results

8.1.2.1 Spray-to-spray collision with a 2-hole injector by using water

There are many valuable efforts for spray breakup and droplet collision. To investigate and gain the understanding of the collision process by multiple spray-to-spray collision, water is considered as the working liquid to exclude the effect of oil fuel on the spray behaviors. The following study focuses on the spray-to-spray collision efficiency of 2-hole interacting nozzles for three different collision angles under high pressure. The effect of collision angles on the characteristics of 2-hole colliding sprays is explored so that the efficiency for vaporization rate can be determined within three different spray cases. The simulation condition are comparable with the experimental one, injection pressure of 172 bar, chamber pressure of 5.7 bar and injection duration of 3 ms.

In the simulation, a single-hole water spray injected into an initially quiescent constant volume chamber using the Lagrangian approach is simulated to identify the breakup region firstly. According to KH-RT breakup length model for single-hole injector, the breakup length for a single-hole injector is calculated and it is around 10 mm. Figure 8.4 (top) shows SMD, which is an average size of the injected particles present in the computational domain, and penetration of single-hole spray. SMD decreases quickly near 0.3 ms, and then flattens from Figure 8.4 (top). It can be seen from SMD profile that the breakup point happened at ASOI of 0.3 ms; the corresponding penetration length is approximately 10 mm. The calculated result for breakup length matches well with the simulated result for breakup length. Furthermore, Figure 8.4 (bottom) displays 3-D image of the droplet radius distribution from nozzle exit and breakup phenomena under before (ASOI of 0.2 ms), at (ASOI of 0.3 ms), and after (ASOI of 0.4 ms) breakup point, in which the breakup point can be seen clearly to come into picture at ASOI of 0.3 ms. After that, breakup length remains invariable and reaches a steady state. Therefore, the study of single-hole water spray is considered as the reference for the prediction of the characteristics of 2-hole colliding sprays.

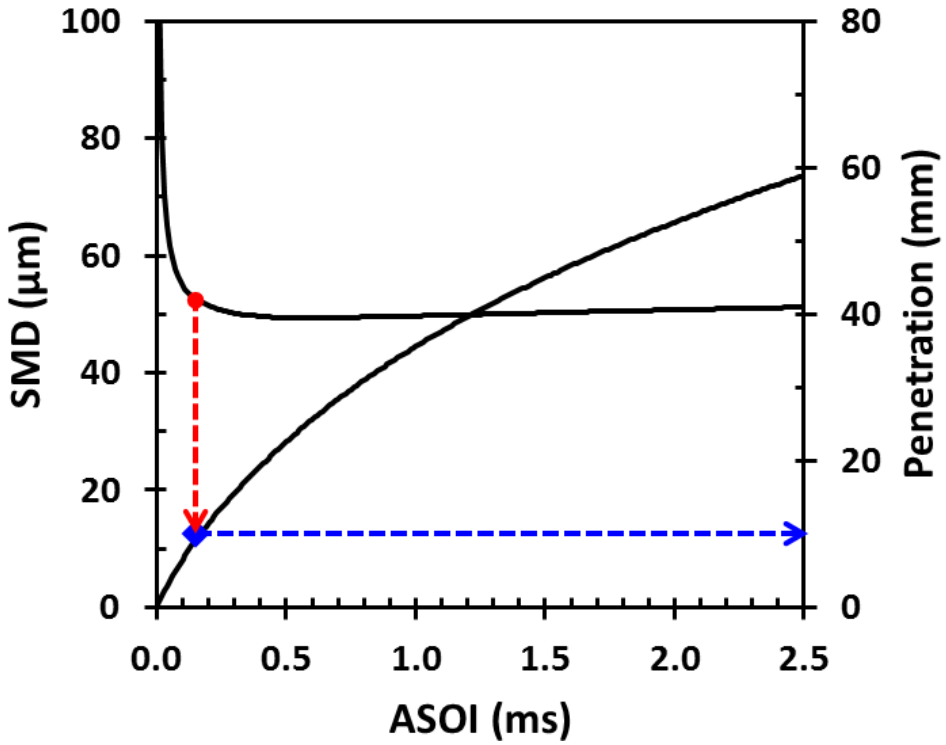

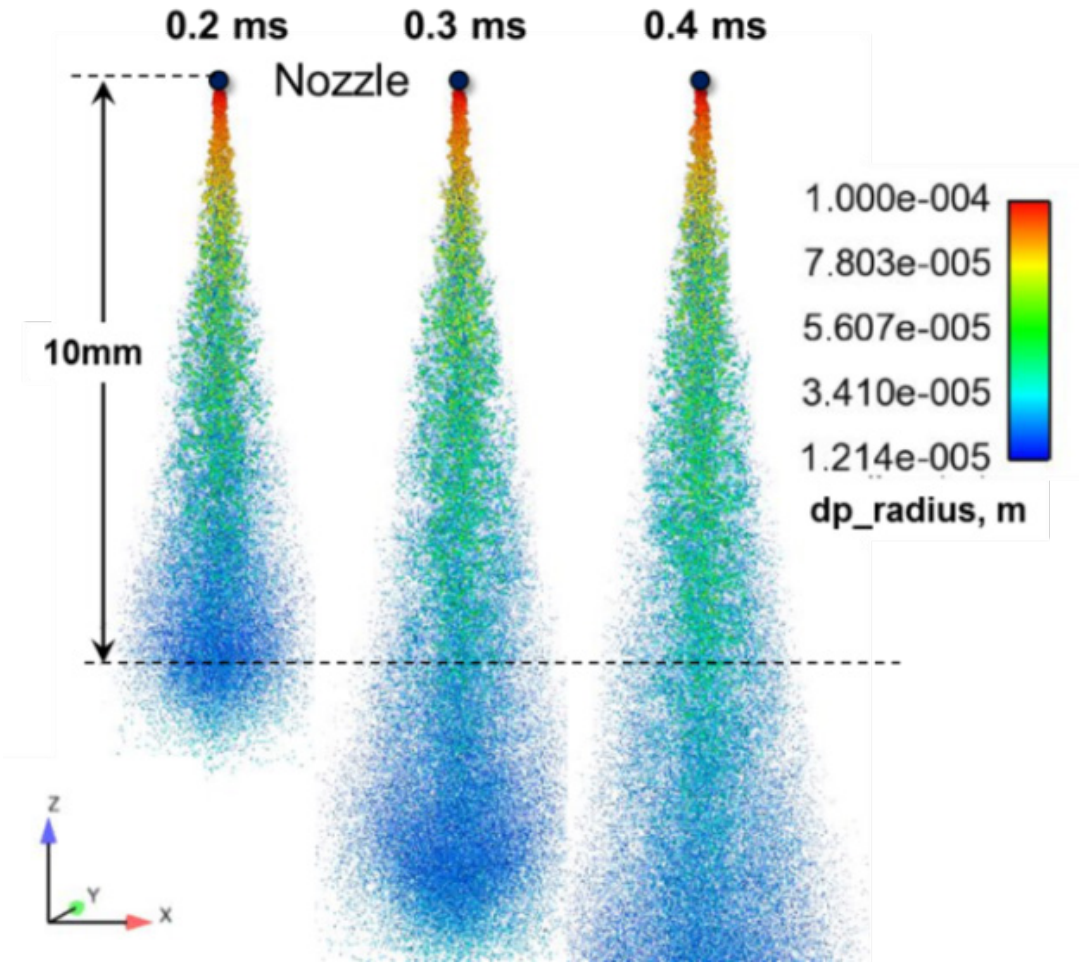

Figure 8.4: SMD and penetration for single-hole nozzle (top); distribution of droplet size (bottom).

For 2-hole nozzles, as shown in Figure 8.5, the collision angle "Φ" defines the angle between two injecting sprays, "L_n" is defined as the distance between two opposite nozzles which is not varied in simulations, "L_i" is defined as the impingement distance, the collision distance "L_C" is defined as the distance from the nozzle exit to the impingement point of two sprays, and the post collision angle "θ" illustrates the angle between two sprays after collision. Besides, three different cases, which are called Case 1, Case 2, Case 3, are considered according to different collision angles, which are defined as before (Φ = 90°, L_C = 5.3 mm), at (Φ = 44°, L_C = 10 mm) and after (Φ = 20°, L_C = 21.6 mm) collision of

two sprays, respectively. The distance between two nozzles is the same but only collision angle is changed. The information from the three Cases is listed in Table 8.1.

Table 8.1: Collision angle and collision distance for three cases

Case #	Φ	L_C
Case 1	90°	5.3 mm
Case 2	44°	10 mm
Case 3	20°	21.6 mm

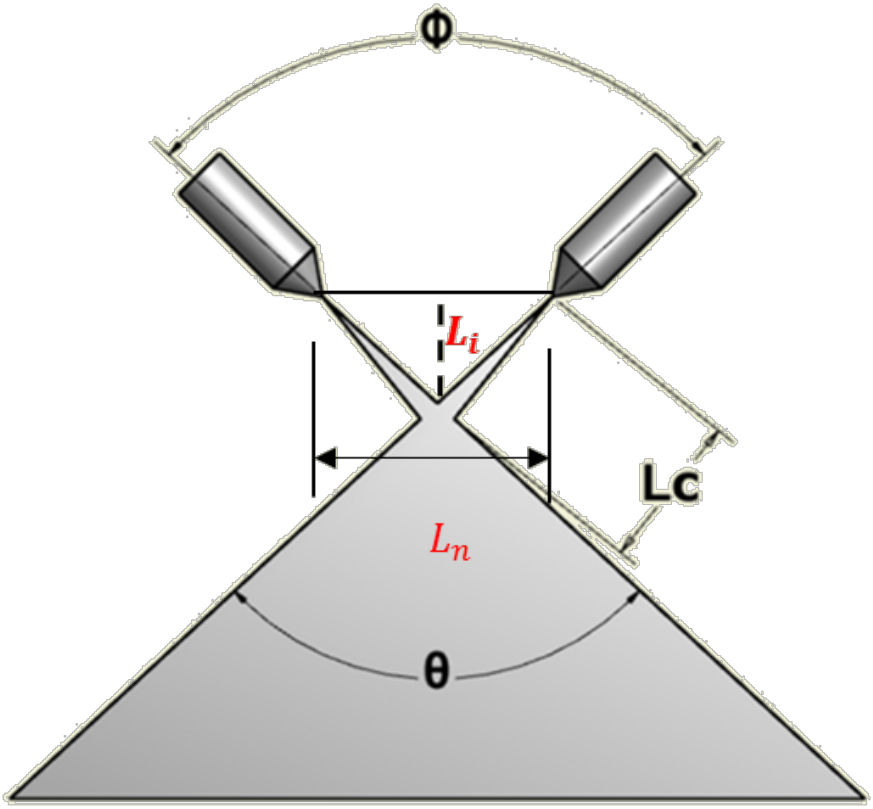

Figure 8.5: Glossary of the colliding spray with a 2-hole injector configuration.

In the following section, on one hand, the total characteristics of 2-hole colliding spray are studied; on the other hand, the local information like droplet behaviors after colliding between two sprays is analyzed. First, Figure 8.6 (top) displays the vapor penetration as the function of time under four different cases. The vapor penetration begins with a near

linear trend and takes an asymptotic shape due to the aerodynamic deceleration caused by the ambient fluid. Besides, penetration curves of Case 2 and Case 3 surpass the single spray case due to the effect of higher vaporization occurring in Case 1, leading to lower liquid length. Although, Case 2 and Case 3, have higher vaporization and lower SMD droplets than single spray case (from Figure 8.7), they tend to travel a little further than single spray (~ 10 mm) due to the impact of spray-spray collision which pushes the liquid droplets farther away. Moreover, there is considerable decline of penetrations for two-hole impinging jet nozzles when the collision angle increases from 20° to 90° (Case 3 to Case 1). The reason is that the relative velocity of collision from 20° to 90° (Case 3 to Case 1) increases, which results in a relatively high radial expansion of the spray, to shorten penetration. Finally, the simulation result when collision angle equals 90° matches in comparison with the experimental result of 90° impinging jet evident from Figure 8.6 (bottom).

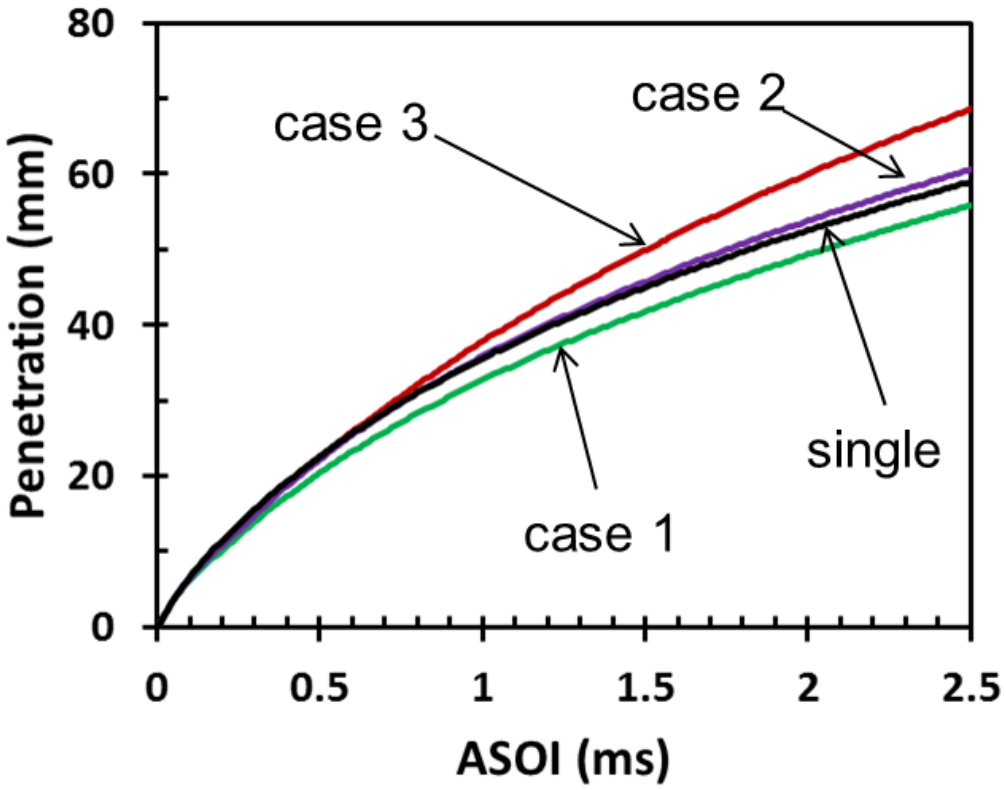

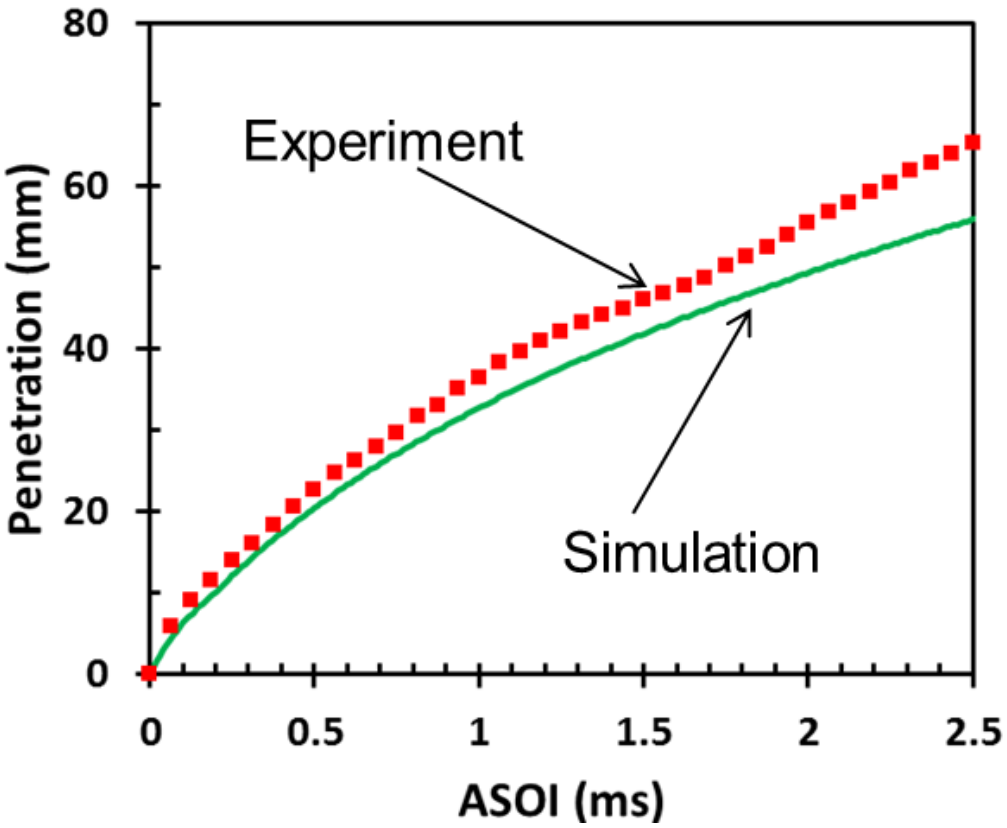

Figure 8.6: Vapor penetration for all cases (top) and validation for Case 1 (bottom).

SMD as a function of time is measured in Figure 8.7. SMD decreases rapidly at around 0.3 ms because of the breakup, and later flattens. It can be seen that SMD of single-hole nozzle spray is higher than the other three cases of two-hole impinging jet nozzles, due to no collision effect. In addition, as a result of the relative velocity increases when the collision angles rise, SMD values reduce within these three cases of two-hole nozzles from 20° to 90° (Case 3 to Case 1). On the other point, the relative velocity between two droplets is related to *We*, which is one of controlling parameters for collision between two drops. The larger *We*, the higher relative velocity; this leads to either reflexive separation or stretching separation and not bounce/ coalescence. Therefore, SMD values decrease when the collision angle increases.

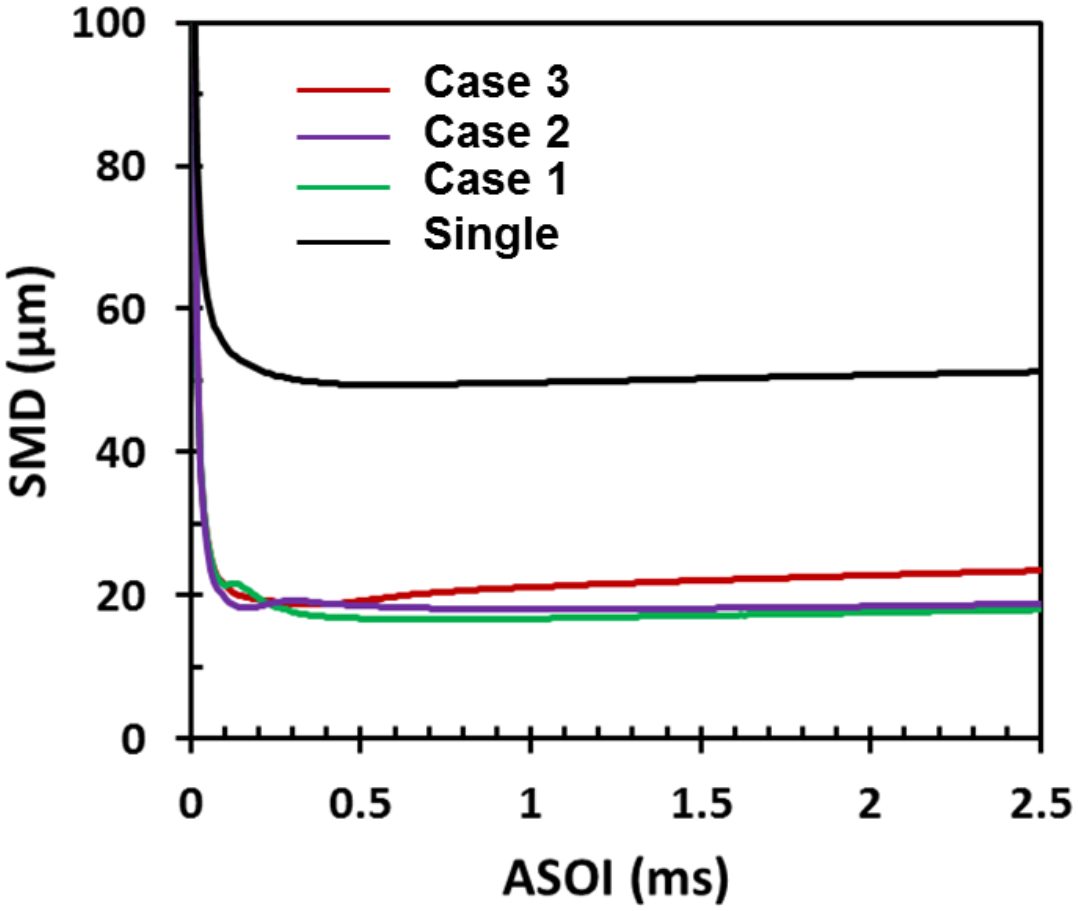

Figure 8.7: SMD for single-hole spray and 2-hole colliding spray.

Figure 8.8 compares vapor fraction for the single-hole spray and other three cases for 2-hole colliding spray. It is seen that total vapor fraction for the four cases steadily increases over time. Further, 2-hole colliding spray has higher vapor fraction than single-hole spray, because of the higher relative velocity between droplets which increases the probability of collision to create more small droplets. Also, the momentum transfer is higher in Case 1 than other cases, causing the droplet size to reduce and vaporize more. As mentioned before, Case 1 has the higher vapor fraction (at least 30% higher than single-hole spray) than other three cases for 2-hole colliding spray, implying that the vaporization rate efficiency rises as the collision angle increases. To summarize, the increase in collision angle causes more probability of collision with higher momentum exchange which atomizes the droplets to a higher degree, which leads to the resulting higher evaporation.

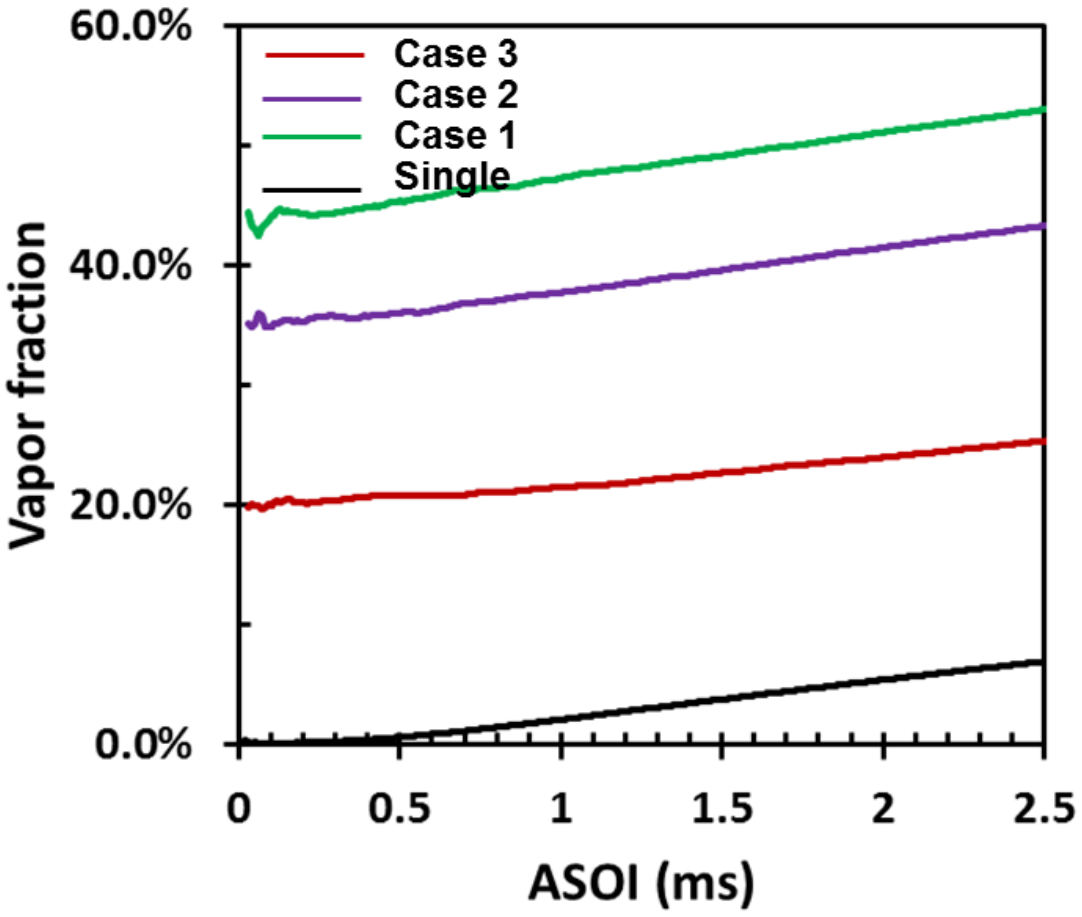

Figure 8.8: Vapor fraction for single-hole spray and 2-hole colliding spray.

Figure 8.9 presents the distribution of droplets velocity flow field of single-hole spray and other three 2-hole colliding spray at ASOI of 1.5 ms. The left column displays the in-plane view and the right column displays the perpendicular orientation with respect to the orientation of two nozzles. It can be seen that the droplet velocity is higher in the near-nozzle region and throughout the liquid core. And it is lower in the zone where the droplets interact with the surrounding gas and slowdown, since the spray-to-spray collision exists in 2-hole colliding spray. Comparatively, the droplet velocity magnitude does not change much around the colliding process due to less chance of collision in single-hole spray compared to 2-hole colliding spray. Moreover, Case 1 shows dispersed droplets after the impingement location; this dispersion decreases as the collision angle decreases. Also, the

collision angle has an effect on the spreading of the spray after collision; the higher the collision angle, the higher the spray spread will be after collision.

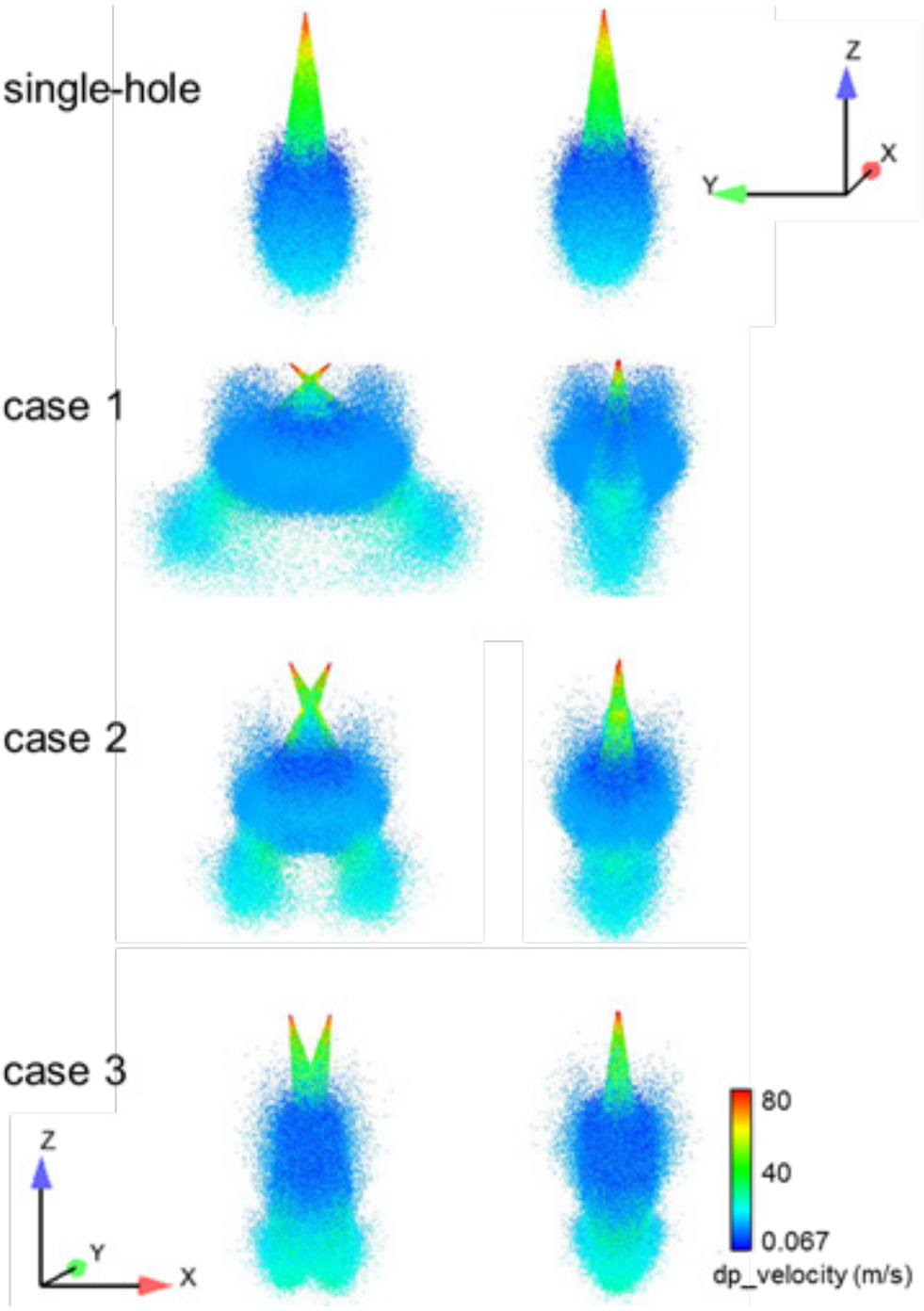

Figure 8.9: Droplets velocity for single-hole spray and 2-hole colliding spray, in-plane view (left) and normal view (right).

8.1.1.2 Spray-to-spray collision with a 2-hole injector by using gasoline model

In the inception of the work with the spray-to-spray collision under a 2-hole injector, water was used as a working fluid. In this section, however, gasoline is used as the fuel both in simulation and experimental approaches. Gasoline surrogate definition includes 70% iso-octane and 30% n-heptane by volume is used in simulation, since gasoline as a fuel is made up of multitude of components [170]. Figure 8.10 shows the comparison of the vapor penetration from the experiment and simulation. For the simulation, the boundary of 97% mass fraction of fuel was considered as the vapor extent. From Figure 8.10, it can be seen that the simulated vapor penetration is in good agreement with the experiment. There is some discrepancy in the initial start of injection times, with the simulation over-predicting the vapor penetration. This discrepancy decreases as injection is subjected to higher temperature and pressure scenarios of 60^{o} and 30^{o} BTDC. This over-prediction could be attributed to the fact that the present vapor length calculations in the models utilized by the CFD solver were developed for single component fuels. As mentioned, the present simulation work utilized a two components surrogate fuel. Also, a general observation from Figure 8.10 is that the penetration decreases as the ambient pressure and temperature increases from 90^{o} to 30^{o} BTDC.

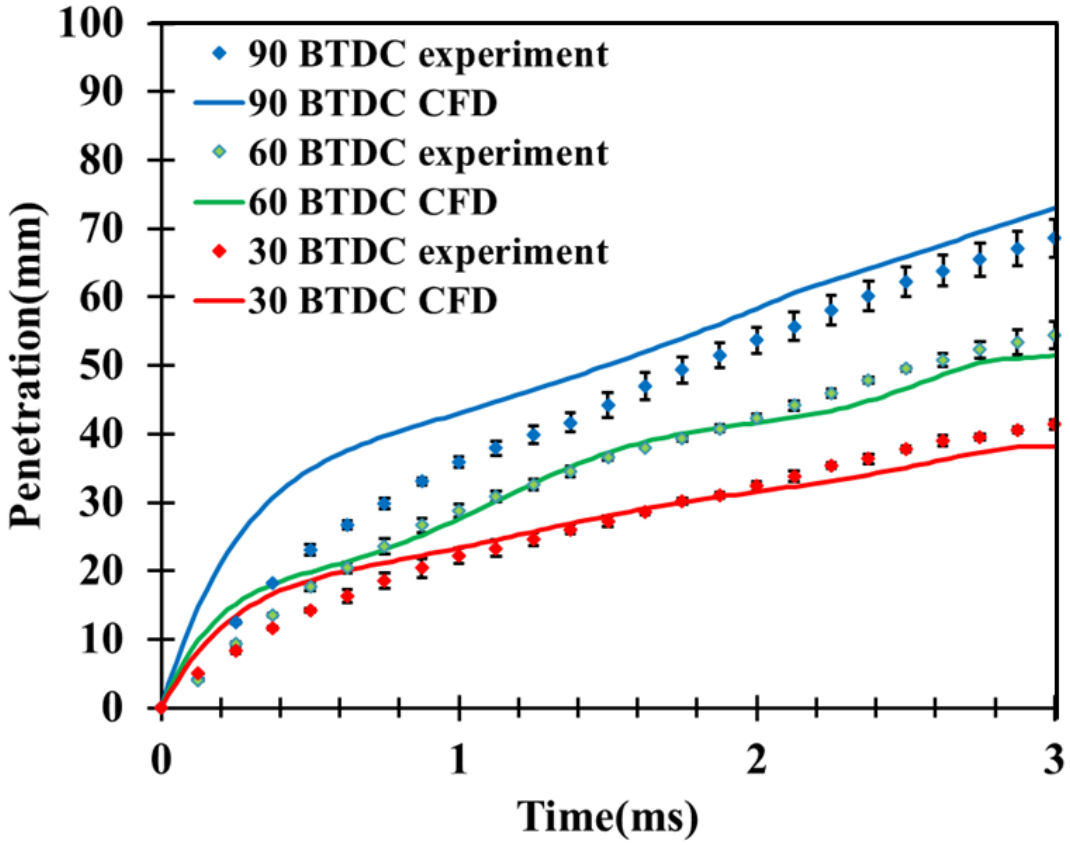

Figure 8.10: Vapor penetration comparison of experiment and CFD for the three test cases.

Figure 8.11 provides the comparison between spray structures from experiment observation and simulation for 2-hole colliding spray. Experimental (left column) and simulated (right column) spray structures for 60° BTDC condition for ASOI of 0.5 ms, 1.0 ms, 1.5 ms and 2.0 ms from top to bottom are shown at each image set. The experimental vapor lengths are marked with a red dashed line over the CFD images.

The images from simulations differentiate the droplet distribution with scattered black dots from the vapor distribution with an iso-surface of the vapor at 5 % of mass fraction of the fuel. It can be seen that the liquid portion and vapor region are visibly distinguished by using Lagrangian model, which benefits for observing the distribution of vapor phase and calculating vapor fraction as well as studying vaporization efficiency of injectors. As it clearly stated in Figure 8.11, spray structures from 2-hole colliding spray present similar

contours with experiment results, so is the simulated vapor penetration. However, compared to the water simulation results which is not shown here, the gasoline simulation shows irregular shape for spray while water simulation exhibits regular patterns, due to the fact that evaporation of gasoline tends readily compared to waters under same condition.

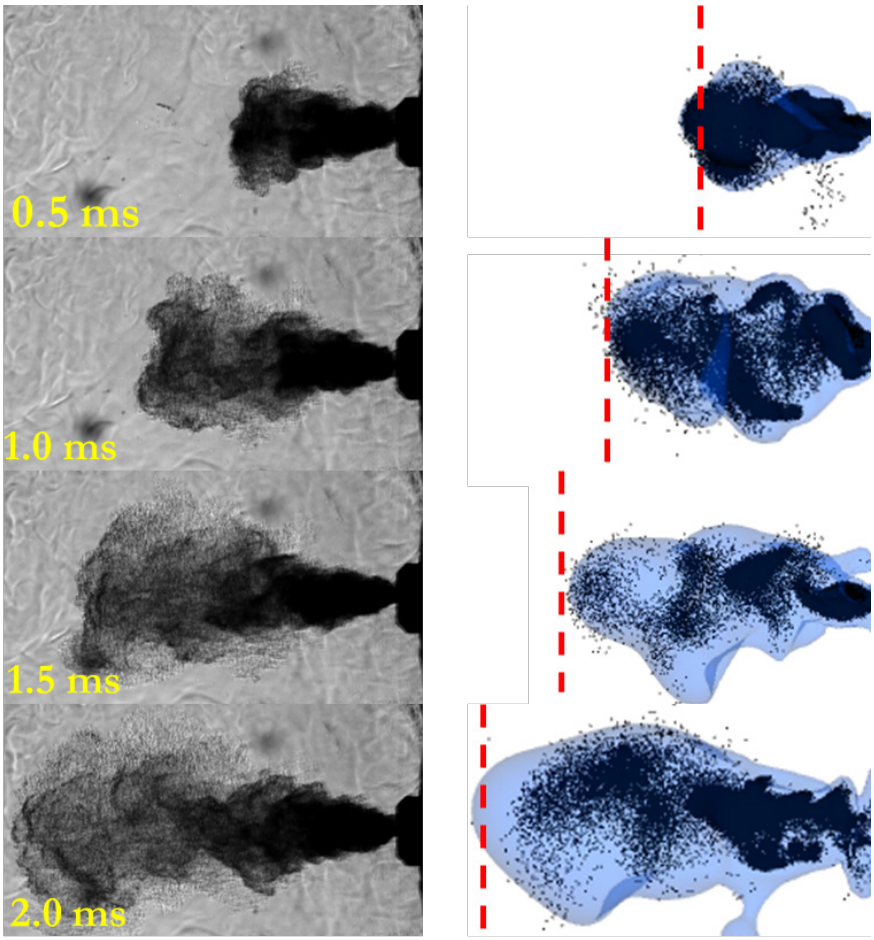

Figure 8.11: 2-hole colliding spray structure of experiment (left column) to CFD (right column) for 60^{o} BTDC condition for ASOI times of 0.5, 1.0, 1.5 and 2.0 ms.

8.1.3 Summary

The experimental and simulation work of spray-to-spray collision with a 2-hole injector is performed. Four different cases including single-hole spray, which is as the reference to

the impinging spray, and three different angles of two-hole spray, which contains pre (Case 1), at (Case 2), or post (Case 3) breakup point are investigated to gain the understanding of collision process based on multiple spray-to-spray collision. Case 1 has higher collision efficiency, shown by measuring vaporization rate and penetration length. In consideration of the vaporization, the 90° collision angle case (Case 1) is better than the other two cases. This may happen due to an increase in the relative velocity before impingement location, thus having greater momentum of collision between the sprays. SMD in Case 1 has relatively lower values than the other cases, resulting in more vaporization of these fine droplets. Moreover, since Case 1 involves higher momentum collision transfer than the other cases, the post-impingement spatial distribution of droplets of a 90°collision jet is lesser in coverage than the other cases. This may be useful in determining the best distance of a merged jet on a wall based on high-impact criteria.

Additionally, a novel colliding jet injector has been tested in a constant-volume combustion chamber under non-reaction spray conditions. The vaporization characteristics of the colliding jet injector has been studied under three conditions of prospective injection times in an engine viz., 90^{o}, 60^{o}, 30^{o} BTDC. Simulation work with new collision mesh equipped Lagrangian colliding spray model has been performed and validated with the experiments. The results from both the experiment and CFD work conclude that 60^{o} BTDC is a better injection time for the injection to take place due to higher extent of vaporized fuel delivery.

8.2 Spray-to-spray collision with uneven 4-hole injectors

Four different types of spray-to-spray collision based on the 4-hole injector are studied by using an Eulerian-Lagrangian modelling approach. In Chapter 3, Figure 3.5 shows the drawing of spray-to-spray collision with 4-hole injector. Figure 8.12 shows the hole arrangements for 4-hole series configuration. 4-hole by using blue color is a symmetric inwardly opening nozzle of the multi-hole injector. 5-1-hole, 6-2-hole, and 7-3-hole correspond to 1, 2, 3 adjacent holes blocked by using red color in 5-hole, 6-hole, and 7-hole, respectively. Four different cases are termed as Case 1, Case 2, Case 3, and Case 4 in present study. Moreover, to investigate spray structures from four different cases, two

different views which are referred to as View 1 and View 2 as in Figure 8.12 are studied. Due to the symmetric geometry of 4-hole, spray structure from View 1 is the same with the one from View 2. However, spray structures in View 1 and View 2, which are shown in Figure 4, are different in Case 2, Case 3, and Case 4.

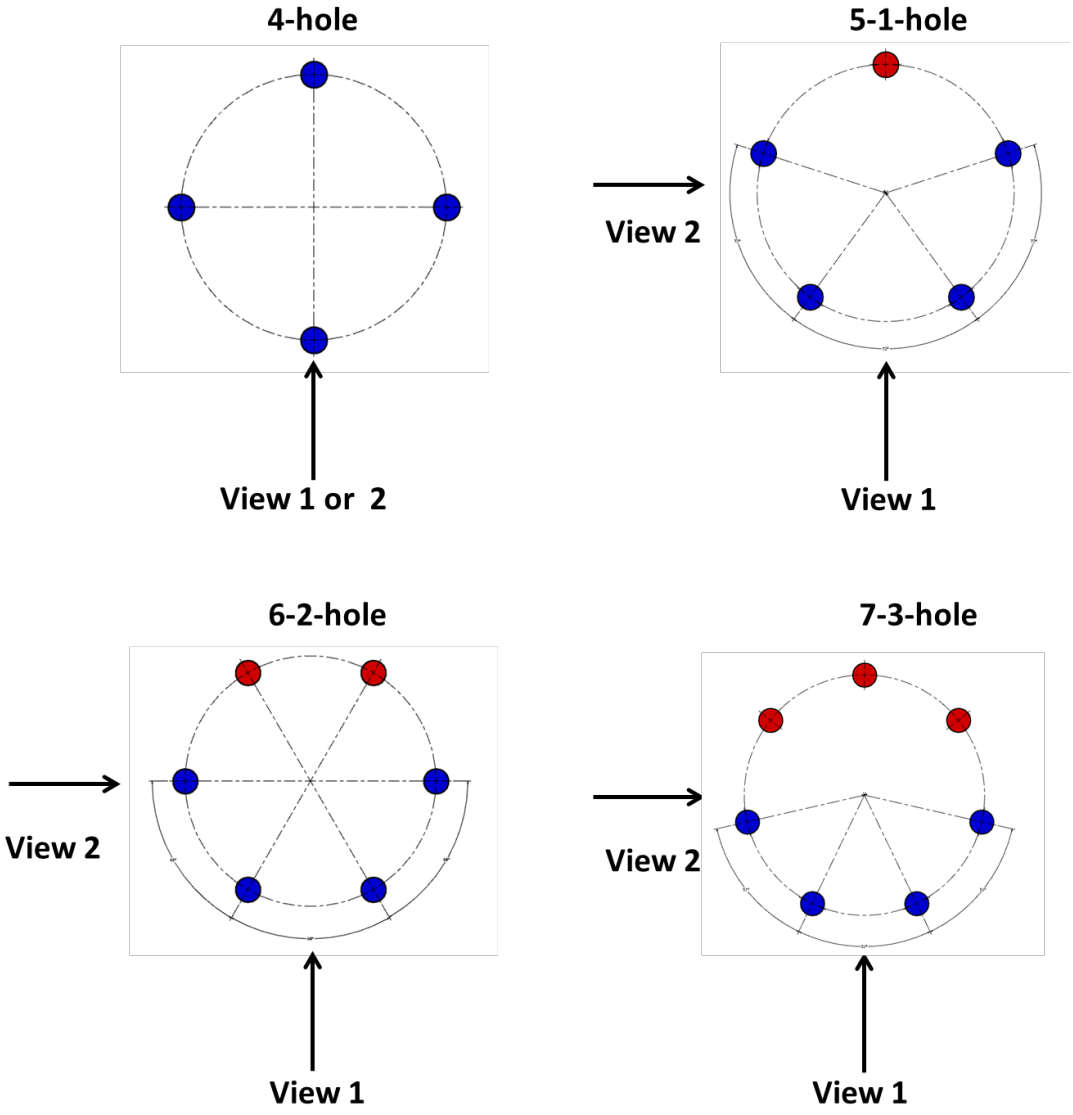

Figure 8.12: Hole arrangements for 4-hole series configuration.

Figure 8.13 exhibits definitions of different angles. The collision angle "Φ" is 90^{o} for the 4-hole series colliding sprays; the post collision angle "θ" is defined as the same way with that in 2-hole colliding spray. Figure 8.13 also shows the simple schematic of different

angles mentioned. "α" is the bend angle which is accompanied with the spray and quantifies the angular deviation of the spray from the injector axis. Post collision angle "θ" is defined as the maximum angle between two sprays after collision starting from impinging location, which is shown in View 1, as $\theta = \theta_1 + \theta_2$. Bend angle "α"is the maximum bend angle and is calculated as $\theta/2 - \theta_1$ which is shown in View 2.

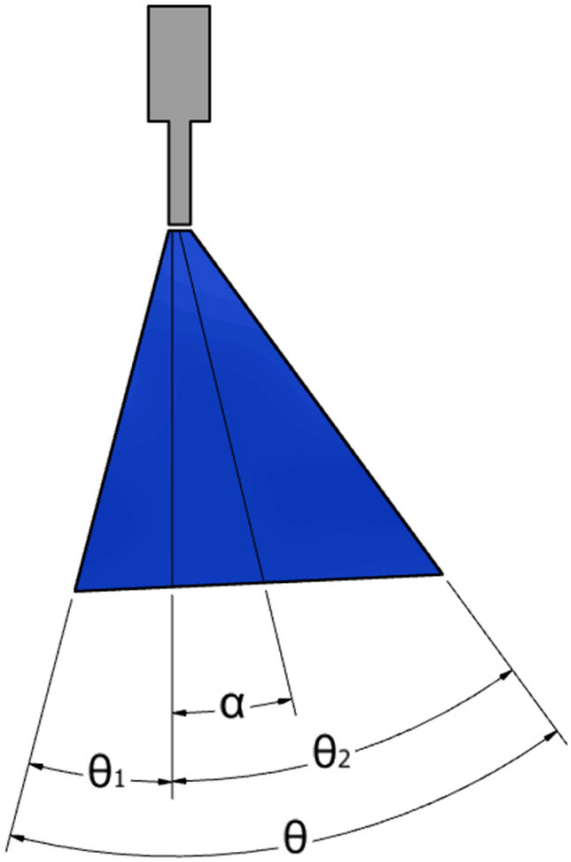

Figure 8.13: Schematic of different angles from multiple spray-to-spray collision case.

The simulation conditions are shown in Table 8.2. The total mass flow rate is same in all four cases of spray injector. The present study was done under the ambient condition, as to simulate the wide open throttle condition that the injection event occurs when the intake valve is open, and the combustion chamber is open to the atmosphere.

Table 8.2: List of the parameter for simulation

Parameter	Value
Injector type	4 / 5-1/ 6-2 / 7-3-hole
Collision angle (°)	90
Chamber pressure (bar)	1.00
Chamber temperature (K)	300
Injection temperature (K)	300
Injection pressure (bar)	100
Hole diameter (μm)	324
Injection duration (ms)	1.5
Injected mass (mg)	22.68
Fuel	iso-octane

8.2.1 Simulation results

8.2.1.1 Post collision angle and bend angle

Spray angle, formed by the angle of the outer periphery of the spray, is a very vital parameter in the application of internal combustion engines. This is because the spray angle affects the distributions of fuel in both axial and radial directions and the position and area of the spray development as well as influences the emissions and efficiency [171, 172]. For multiple spray-to-spray collision injector, spray angle is also known as post collision angle. The current work measured post collision angle in four different cases to study the change of spray structure. Bend angle is also an important parameter in the studies on spray characteristics, as it has an influence on the installation of injector and spray structure as well as spray development in the chamber.

Figure 8.14 (top) exhibits spray structure of four cases at ASOI of 1.0 ms. Spray structure is shown by particles distributions in both View 1 and View 2. As seen in View 1, the spray has a structure of a narrow-necked cone; the neck structure gradually widens and extends more but shrinks after reaching the widest width in the radial direction. In addition, it seems no big difference in spray structure among all four cases in View 1. However, it can be obviously seen in View 2 that the spray structures are different from Case 1 to Case 4 and become more steeper in Case 3 and Case 4. Also, the width of spray decreases and the

penetration of spray becomes longer as the number of blocked hole increases. The post collision angle "θ" is measured in View 1. The maximum bend angle "α" is obtained using View 2 which is after 90° rotation of View 1. Although the images presented in Figure 8.14 are indicative of spray at ASOI of 1.0 ms, spray angle is a function of time and is calculated as the average of post collision angle and bend angle at any instant of time.

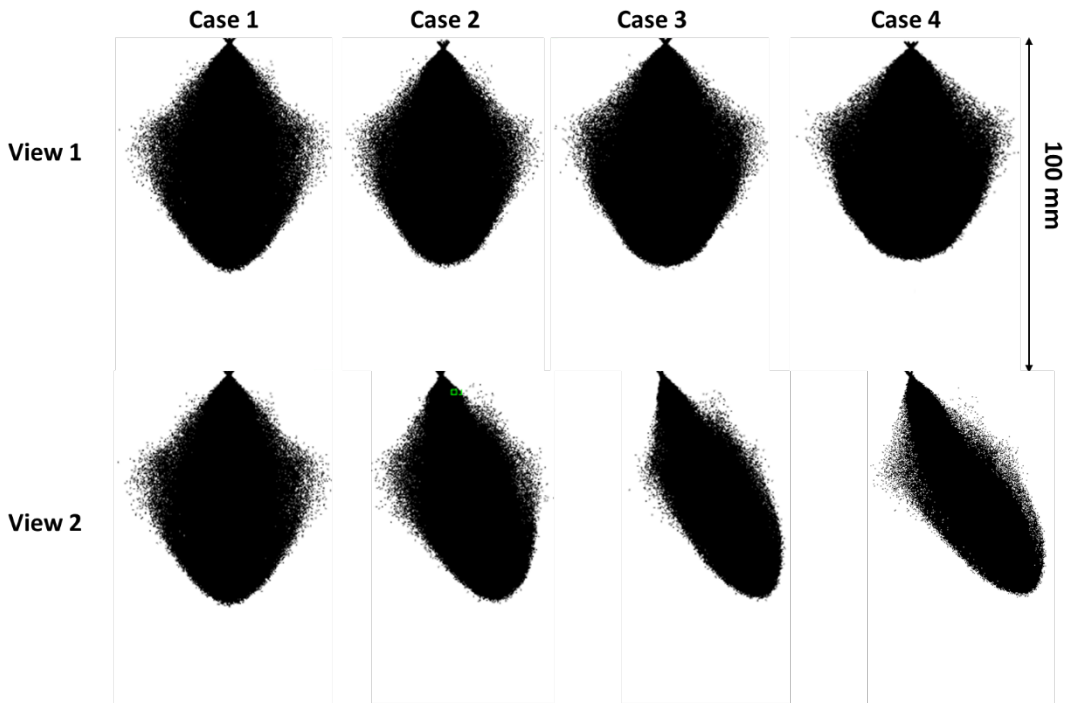

Figure 8.14: Spray structure for four different cases in both View 1 and View 2.

Table 8.3 shows the results of the post collision angle and bend angle for four cases in both View 1 and View 2. It can be seen that the maximum post collision angle in View 1 increases slightly from Case 1 to Case 4. The maximum post collision angle in View 1 for all four cases is close to 75° due to the similar spray structure in View 1 for all four cases. And, the bend angle is 0 since there is no blocked hole which leads to inclined view. However, in View 2, it is seen that the post collision angle reduces with the number of blocked hole from Case 1 to Case 4, and the bend angle increases from Case 1 to Case 4. Besides, the ratio of post collision angle and collision angle in View 1 is around 0.83. However, the maximum bend angle is shown in View 2 which increases with the number

of blocked hole from Case 1 to Case 4. Besides, the ratio of post collision angle and collision angle in View 2 is decreasing through Case 1 to Case 4 (0.83 to 0.40), as well as the ratio of bend angle and collision angle in View 2 is rising from Case 1 to Case 4 (0.00 to 0.32).

Table 8.3: Post processing results of 4-hole series cases

Hole arrangement	**Case #**	**Φ (°)**	**View 1**		**View 2**			
			θ (°)	**θ/ Φ**	**θ (°)**	**α (°)**	**θ/ Φ**	**α/ Φ**
4-hole	Case 1	90	75	0.83	75	0	0.83	0.00
5-1-hole	Case 2	90	73	0.81	62	15	0.69	0.17
6-2-hole	Case 3	90	75	0.83	49	26	0.54	0.29
7-3-hole	Case 4	90	76	0.84	36	29	0.40	0.32

Figure 8.15 (top) shows bar chart of the ratio of post collision angle and collision angle of 4-hole series at collision angle of 90° in View 1. Figure 8.15 (bottom) exhibits bar chart of the ratio between post collision angle or bend angle and collision angle of four cases in View 2. The changing of post collision angle and bend angle as described in the above can be observed. From View 1, the post collision angle shows no big difference among four cases while in View 2 the post collision angle decreases as bend angle increases from Case 1 to Case 4. To summarize, post collision angle and bend angle have an impact on the spray structure when the number of blocked hole rises.

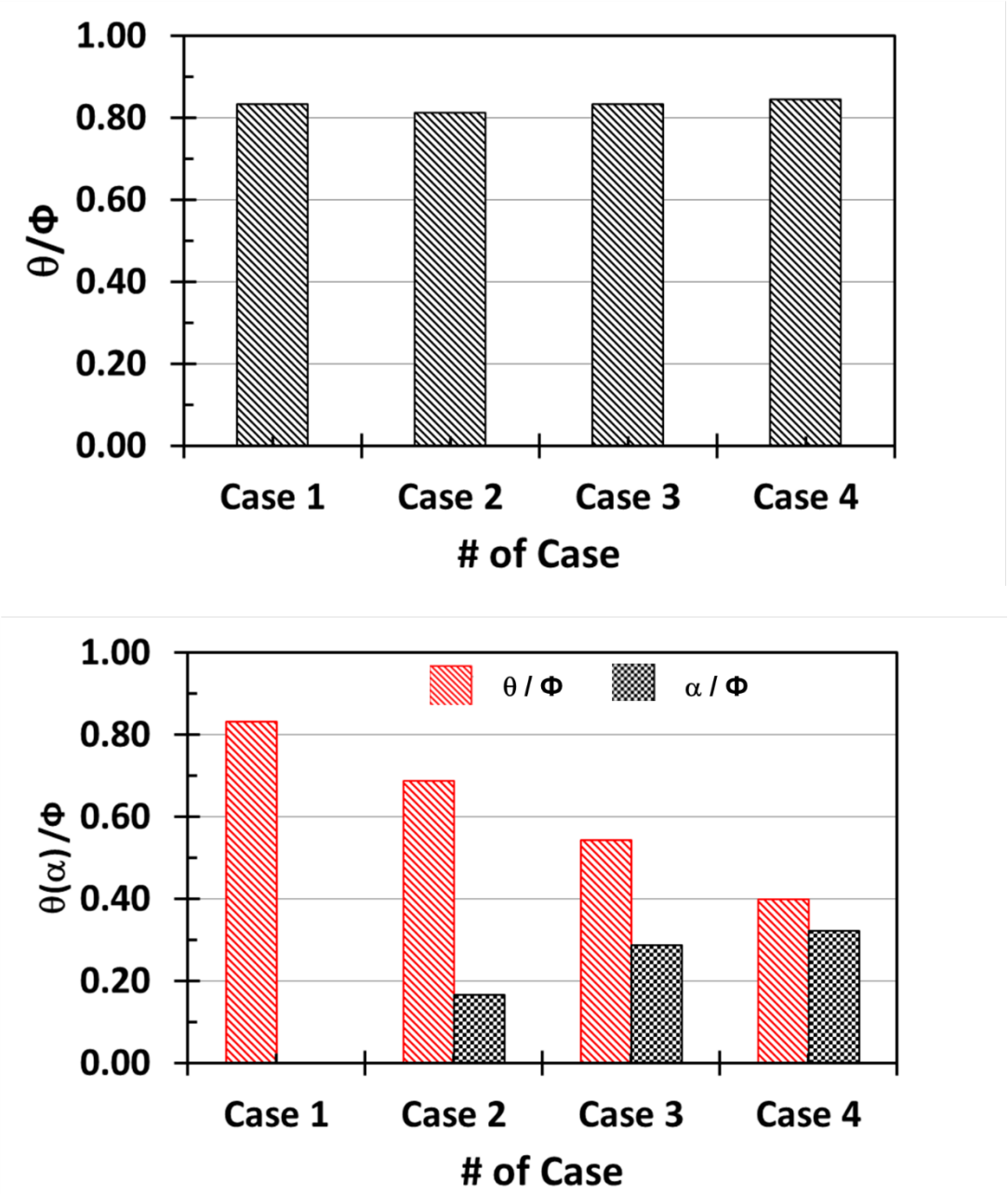

Figure 8.15: The ratio of post collision angle and collision angle of four cases in View 1 (top); The ratio of post collision angle / bend angle and collision angle of four cases in View 2 (bottom).

8.2.1.2 Spray penetration and velocity flow field

Figure 8.16 displays the spray penetration as the function of time under four different cases. The spray penetration is defined as the distance from injector tip to the point along the spray axial direction where 97% of total injection mass is present. From Figure 8.16, the spray penetration begins with a near linear trend and takes an asymptotic shape because of the aerodynamic deceleration caused by the ambient fluid. Case 1 and Case 2 shows similar penetration length and they penetrate slower than the other two cases, while Case 4 is the fastest and Case 3 is in between, which also corresponds to the spray structure shown in Figure 8.14.

The spreading angle, namely post collision angle here, is one of the main parameter influencing the spray penetration. In consideration of post collision angle and bend angle as shown in Figure 8.15, the largest post collision angle is obtained for Case 1 which has shorter penetration; and penetration increases with increasing the bend angle. These results are in accordance with the spray penetration trends in Figure 8.16. Besides, the injection pressure, the ambient pressure, physical properties of fuel and drag force also impact spray penetration. However, the influence of the injection pressure, the ambient pressure and physical properties of injected fuel on spray penetration is eliminated by maintaining the same conditions for four cases. Therefore, the drag force, which is related to the kinetic energy and the aerodynamic resistance of the ambient gas, is the one parameter to affect spray penetration. For Case 1, the velocity of spray coming out of each hole remains the same in all directions and so the influence of aerodynamic resistance becomes large in Case 1, preventing the spray from moving downstream and indicating a strong effect on spray penetration length.

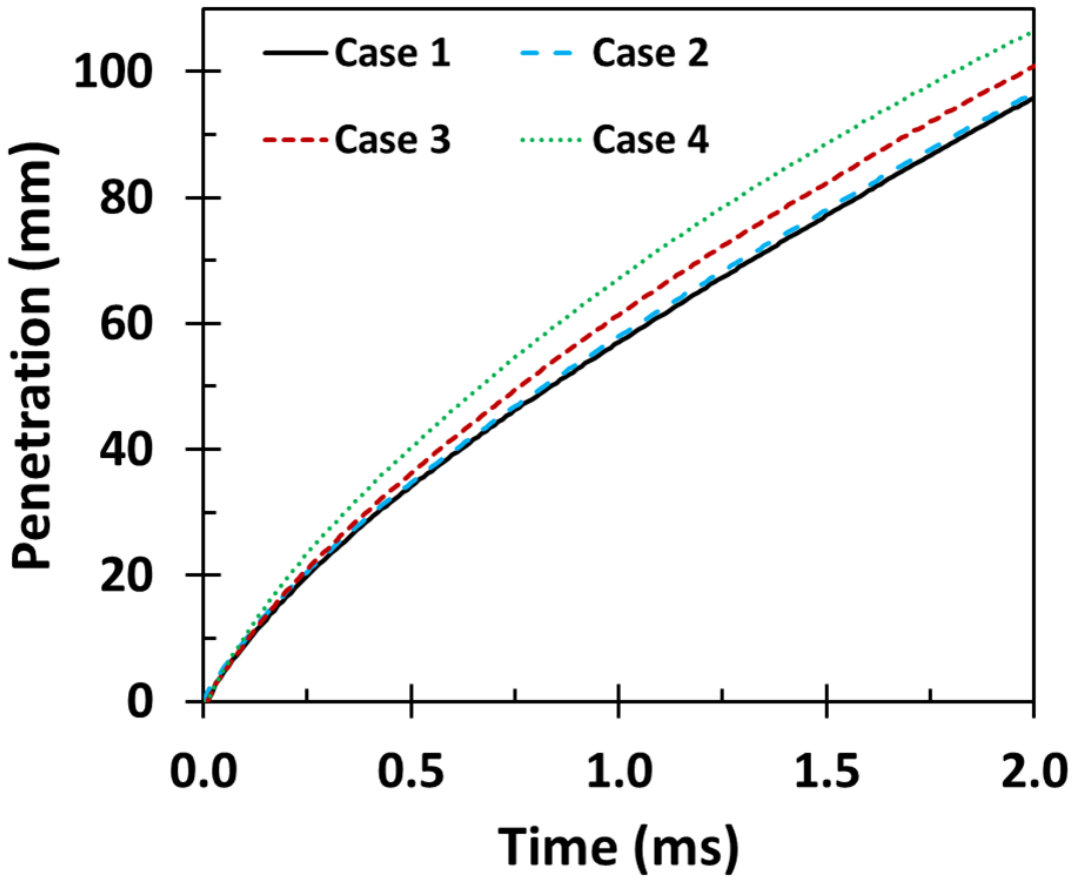

Figure 8.16: Penetration for four different cases according to time after injection.

Figure 8.17 (top) provides internal spray pressure profile and Figure 8.17 (bottom) shows the axial velocity profiles along the center line. The location of the plane in which the pressure and velocity profiles are presented is defined as one of the cut planes of View 1 and this cut plane is the exact middle plane of View 1. As seen in this figure, the trends of pressure profiles shown by dash lines are similar from Case 2 to Case 4 while Case 1 represented by solid lines provides different trend. Since air is trapped inside a small region before impinging, so pressure achieves the first peak value as seen in the beginning of plots. From impinging location to spray tip, pressure along center line decreases and is lower than the chamber pressure of 1 bar. At spray tip, stagnation pressure appears and the second peak of pressure happens. After spray tip, lower pressure is shown in the plots due to induced velocity existing. Another key reason for different spray structure in four cases is

internal spray velocity as shown in Figure 8.17 (bottom). Similarly, the similar trends of spray axial velocity show in Case 2 to Case 4 but Case 1 is different from them. According Bernoulli Equation, the axial velocity of spray is inversely proportional to internal spray pressure which can be seen in Figure 8.17 (bottom). And, recalling the spray structures for four cases in View 2, it is known that the spray of fuel through the center zone gradually weakens from Case 1 to Case 4. Thus, the internal spray pressure and velocity in Case 1 is higher than the others.

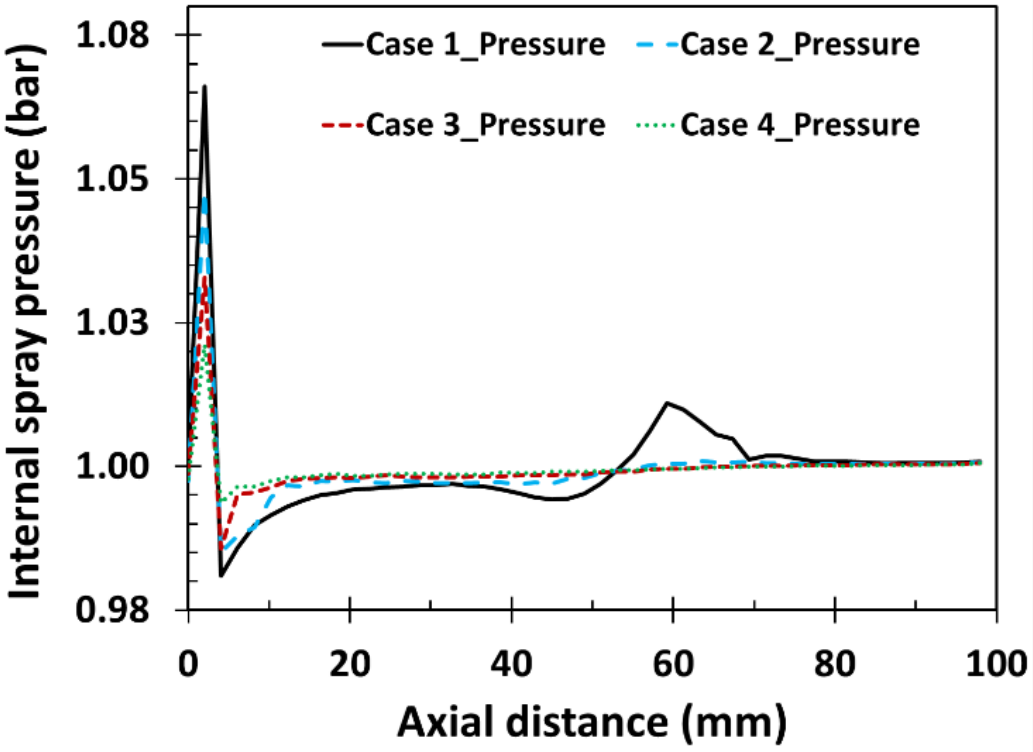

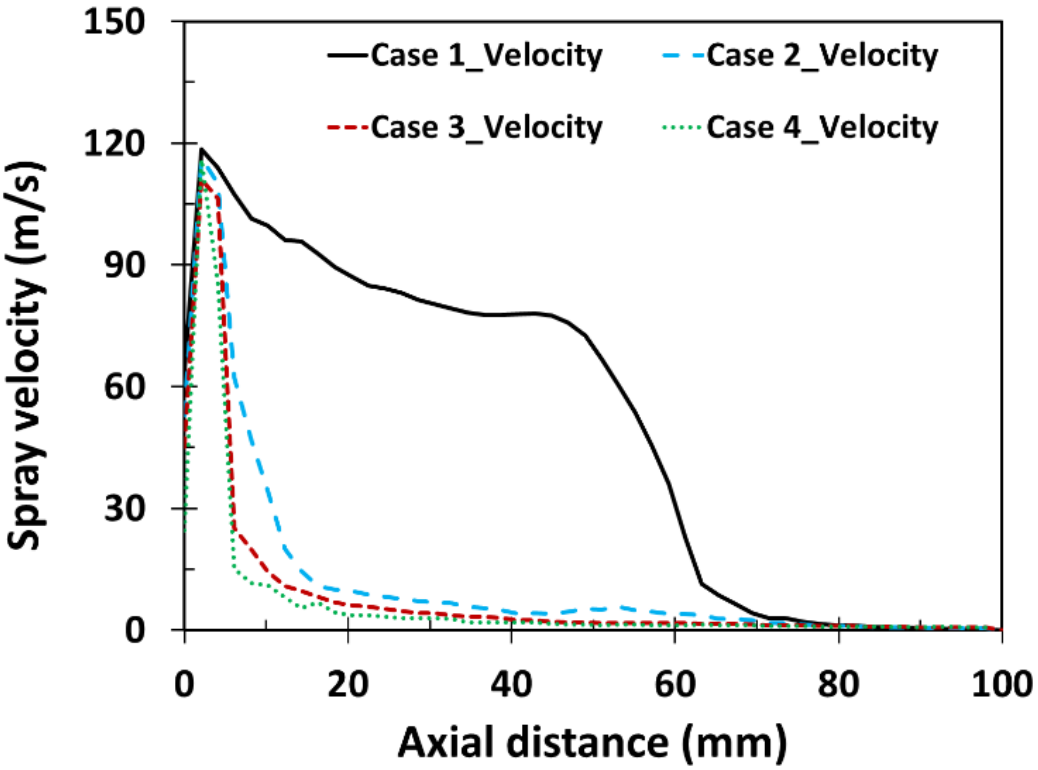

Figure 8.17: Internal spray pressure (top) and velocity (bottom) at ASOI of 1.0 ms.

Figure 8.18 describes the radial velocity of spray at axial distance of 20 mm from the nozzle exit at a given time, where the peak velocity is around 80 m/s and it shifts to the left side from Case 1 to Case 4. Even though the same injected mass exists each nozzle, the velocity vectors change in Case 2, Case 3, and Case 4 where the number of holes blocked increases, this partially leads to different spray structures in four cases as shown in Figure 8.14. Besides, the radial velocity vs. distance plot of Figure 8.18 depicts mixing of the spray with the surrounding medium. It can be seen that Case 1 covers the wider range of velocity in radial distance than other three cases which matches with spray structure shown in Figure 4, Case 2 is followed by Case 1 and the next is Case 3, finally Case 4.

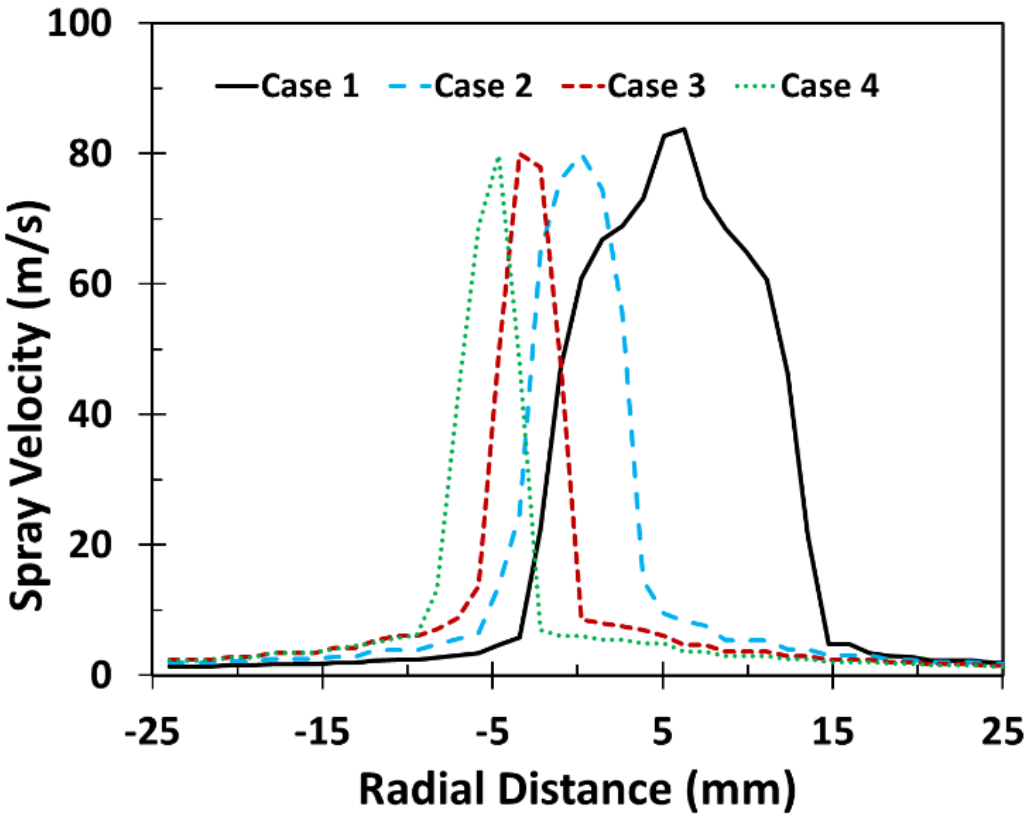

Figure 8.18: Radial velocity for four cases at axial distance of 20 mm at ASOI of 1.0 ms.

Figure 8.19 provides a vivid description of spray velocity vector of Case 1 and Case 2 in the vertical cross section of a spray at ASOI of 1.0 ms, which is to further illuminate the influence of velocity on spray structure. Overall, it is seen in both Case 1 and Case 2 that spray velocity decreases along the center line as shown in Figure 8.17 and spray velocity is larger in the spray core region than outer periphery as expressed in Figure 8.18. The reason for this phenomenon is of the influence of chamber air flow, the outside spray velocity decreases rapidly after being exposed to the air while the inside spray velocity has not been influenced by ambient air flow. Moreover, the directions of spray velocity vector are different between Case 1 and Case 2. In Case 1, the velocity vectors point out the downstream vertically but the velocity vectors of Case 2 shows tilt at a certain angle due to one blocked hole existing, which can be contributed to explain the difference of spray structure between Case 1 and others.

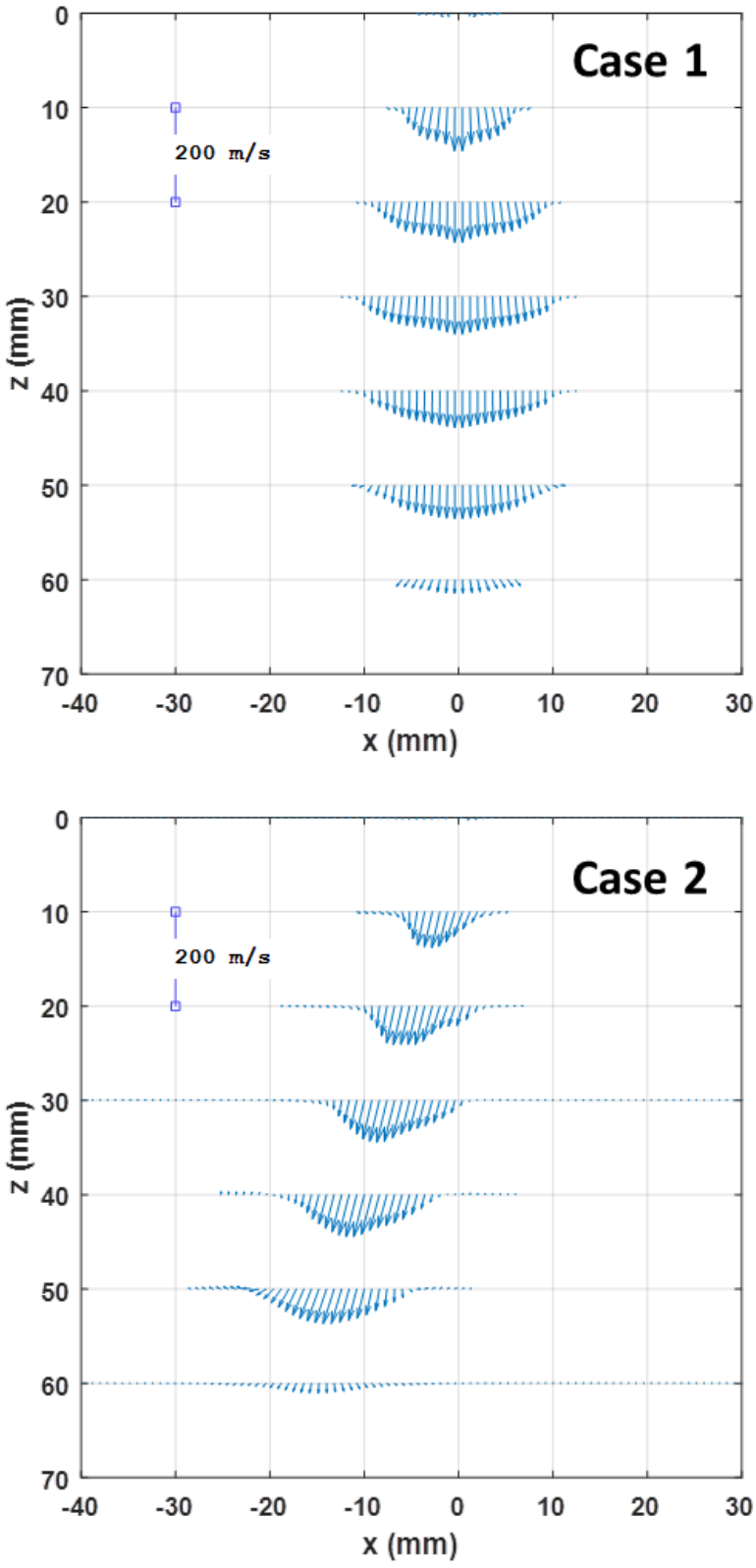

Figure 8.19: Spray velocity for Case 1 (top) and Case 2 (bottom) at ASOI of 1.0 ms.

8.2.1.3 Droplet size and droplet number distributions

Figure 8.20 shows droplet size and number distributions of Case 1 and Case 2 in the vertical cross section of a spray at ASOI of 1.0 ms under View 2. From Case 1 it is seen that most of droplets diameter is around 15 μm in the spray core region and droplets size become larger in the intermediate zone around 50 μm of droplets diameter, as well as the droplets at peripheral zone show less than 10 μm of droplets diameter. On the other hand, Case 2 has smaller droplet diameter of 20 μm in the core area, followed by larger droplet diameter of 30 μm in the intermediate zone, and droplet diameter increases above 50 μm in the periphery, as well as the outermost layer exists a small number of droplets of around 30 μm. The above can be partially attributed to the effect of spray-induced air flow. The strength of ambient air flow indicates the influence of spray dynamics on droplet size distribution.

The number density of droplets comparison between Case 1 and Case 2 in Figure 8.20 (bottom) shows a small droplet number density in core region, which is surrounded by a higher droplet number density in the intermediate zone, and droplet number density becomes small in the outer periphery. In Case 1, the drop number density is about 400 along spray axis and 800 in the center zone. It is higher than 3000 in a thin intermediate region. The outer area has less density of below 500 and the outermost layer shows a small part of droplets of 800 droplet number density. However, Case 2 gives droplet number density of 800 in the core region, lower droplet number density of 400 in the secondary intermediate region, higher droplet number density of 800 in the outer intermediate zone, and smallest droplet number density of 200 in the outermost layer.

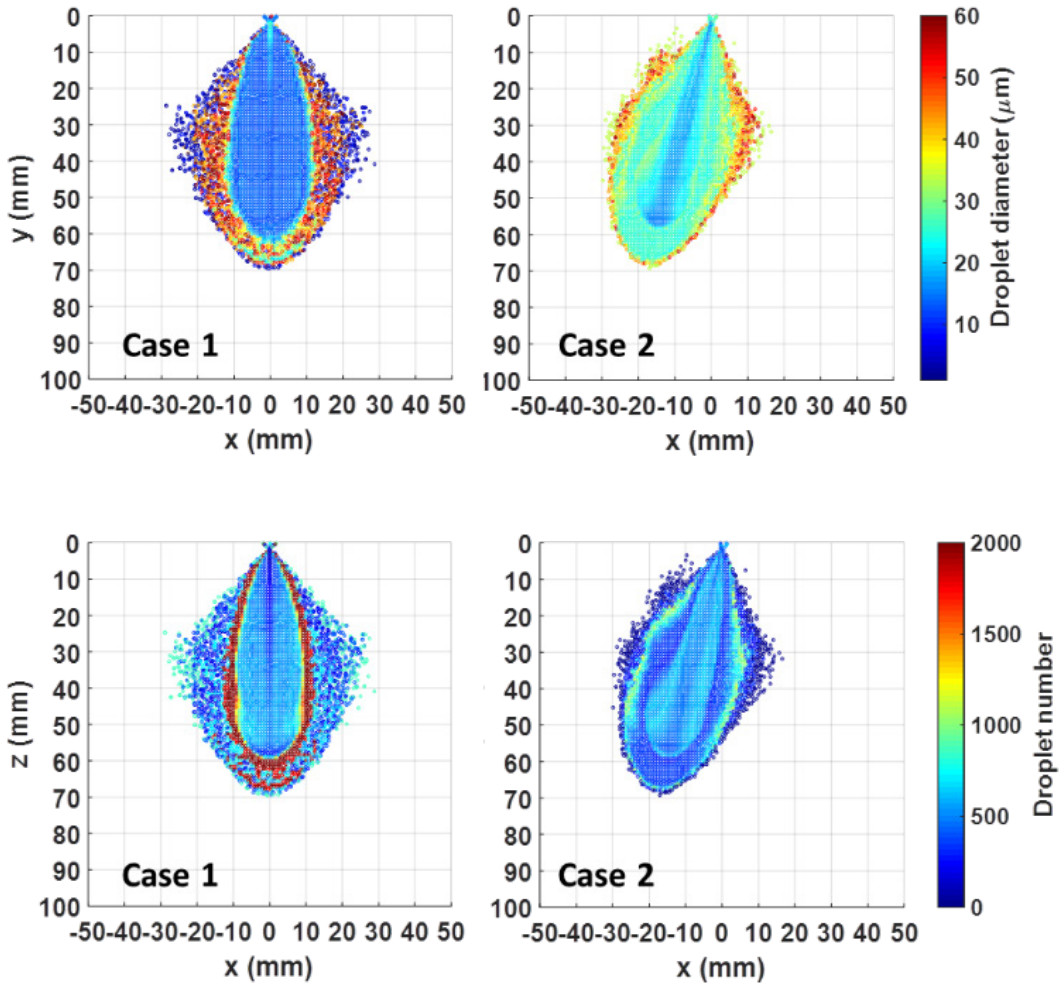

Figure 8.20: Droplets size (top) and number (bottom) distributions of Case 1 and Case 2 in the vertical cross section of a spray at ASOI of 1.0 ms.

Figure 8.21 extends to droplets size and number distributions of all four cases using Histogram. It illustrates a comparison of droplets size and number regarding the number of frequency of four different cases. It can be seen that the large scope of droplet diameter and droplet number is shown in Case 1, which is droplet diameter range from 0 to 70 µm and droplet number scope from 0 to 4000 but reduces in other three cases. Case 2 shows droplet diameter range from 10 to 60 µm and droplet number scope from 0 to 1500, Case 3 provides droplet diameter range from 10 to 50 µm and some large droplets around 90 µm

appears in the peripheral area and droplet number scope from 0 to 500, and Case 4 has droplet diameter range from 0 to 20 μm and droplet number scope from 0 to 1000.

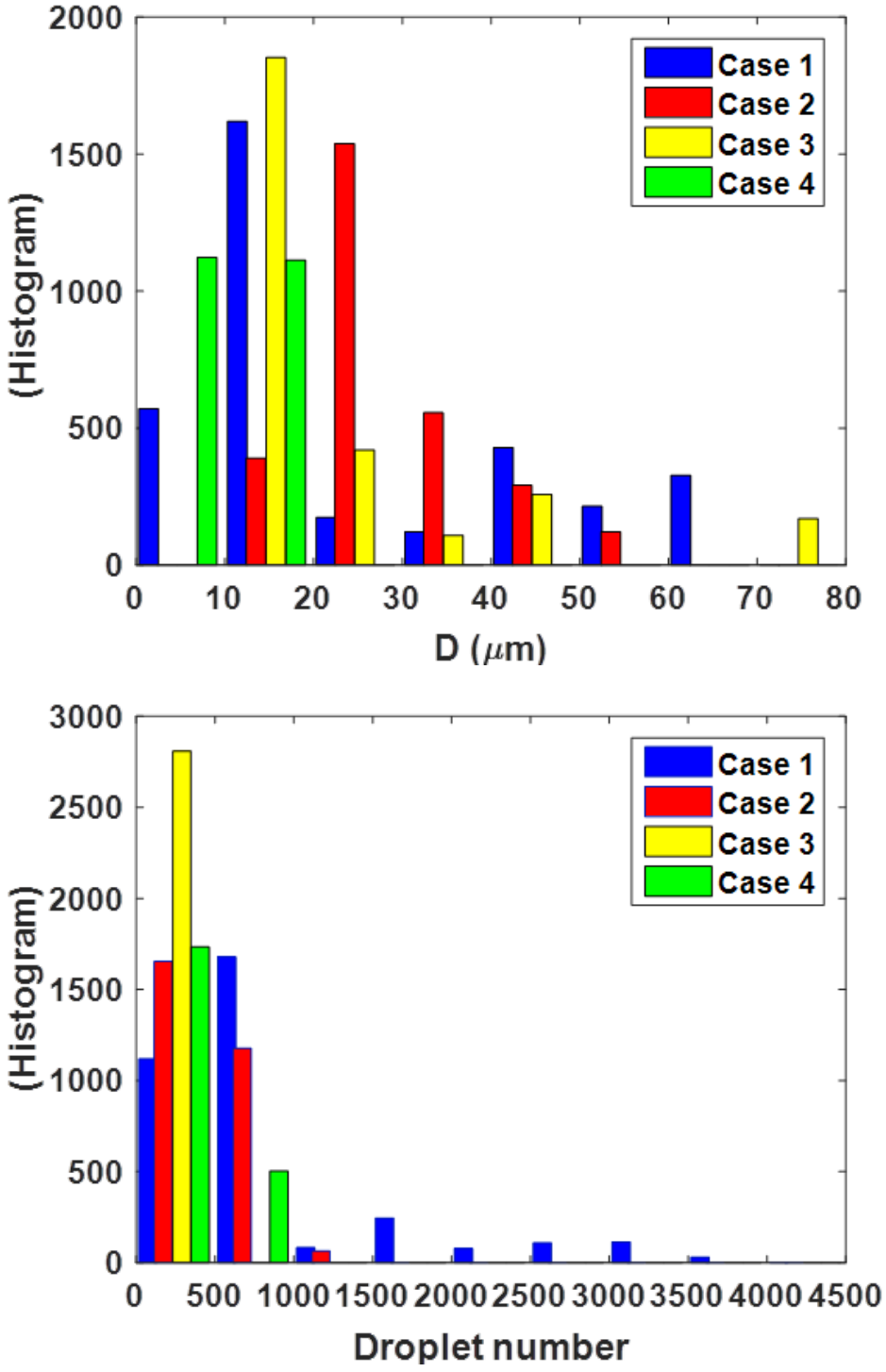

Figure 8.21: Histogram of droplet size and number of four cases at ASOI of 1.0 ms.

Figure 8.22 shows droplet size and number distributions of Case 1 and Case 2 in the horizontal cross section of a spray at axial distance of 20 mm at ASOI of 1.0 ms under View 2. In general, the droplets at center region of the spray exhibit smaller diameter than those at outer zone. A symmetrical droplet distribution can be seen from Case 1. It is also seen that most of droplets diameter is in the range from 10 to 15 μm in the spray core region and droplets size become smaller in the peripheral zone around 5 μm. However, Case 2 shows an asymmetrical droplet distribution and droplet diameter of 20 μm in the core area, followed by the mixing of larger droplet diameter of 30 μm and smaller droplet diameter of 5 μm in the periphery. The droplet number has a similar trend with droplet size as described. In Case 1, the drop number density is about 400 in the center zone and outer area has less density below 200. On the other hand, Case 2 gives droplet number density of 600 in the core region; lower droplet number density of 500 and higher droplet number density of 800 are mixing in the outer zone.

Figure 8.23 shows the PDF of droplet diameter and droplet number in the horizontal cross section of a spray at different axial distances from 10 mm to 50 mm of Case 1 at ASOI of 1.0 ms. From PDF plots of both droplet diameter and number, near nozzle tip at axial distance of 10 mm, largest mean droplet size of 40 μm can be seen and droplet size becomes smaller as axial distance increases. But, the mean droplet number density is lower at axial distance of 10 mm and increases with axial distance. Similar trends are observed but not presented here in other three cases that the larger drop size is shown in near nozzle area and droplet size decreases rapidly as axial distance increases.

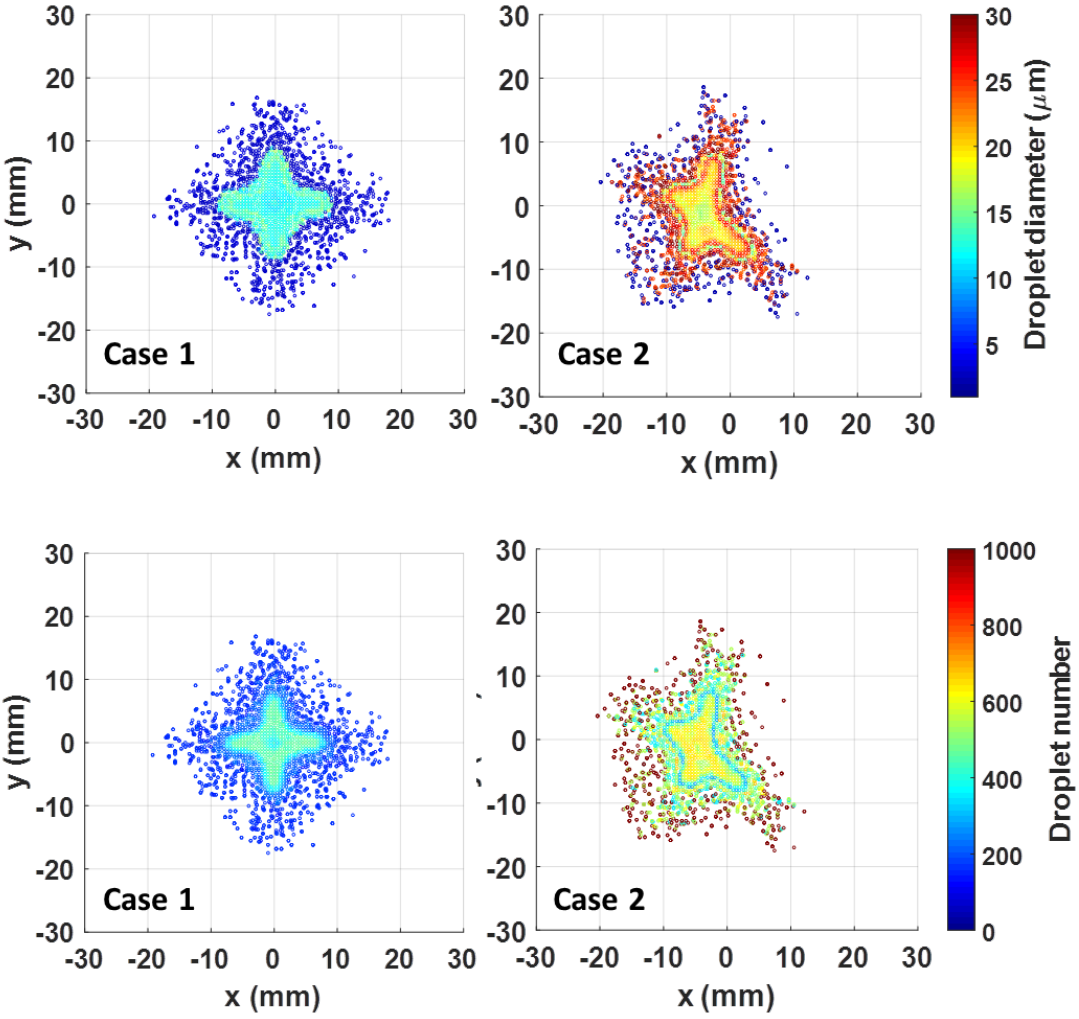

Figure 8.22: Droplets size (top) and number (bottom) distributions of Case 1 and Case 2 at axial distance = 20 mm at ASOI of 1.0 ms.

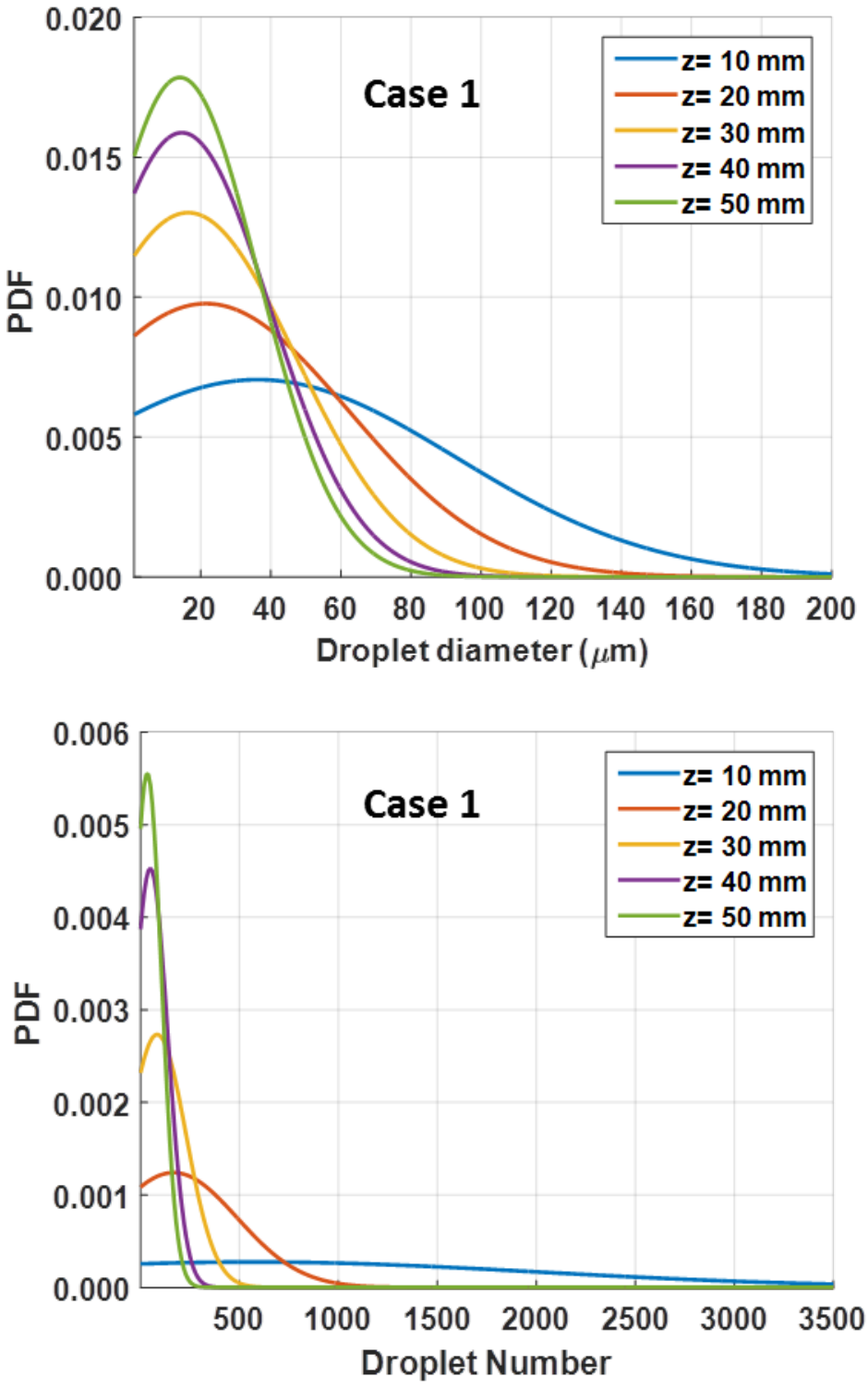

Figure 8.23: PDF of droplet size and number of Case 1 at ASOI of 1.0 ms.

8.2.2 Summary

Spray characteristics based on different types of multiple spray-to-spray collision according to injection conditions are examined, which is known as 4-hole series including Case 1 (4-hole), Case 2 (5-1-hole), Case 3 (6-2-hole), and Case 4 (7-3-hole). In particular, the spray angle, droplet diameter and number distributions as well as velocity of spray were studied on the basis of CFD simulation. The post collision angle and bend angle hardly changes in four cases in View 1, whereas the post collision angle decreases and bend angle increases from Case 1 to Case 4 in View 2. Besides, both post collision angle and bend angle have an influence the spray penetration and spray structure. The profiles of internal spray pressure and axial velocity between Case 1 and other three cases exhibit different trends and the internal spray pressure has effect on the spray structure. Also, spray velocity vector of Case 1 and Case 2 in the vertical cross section of a spray at ASOI of 1.0 ms, is provided to further illustrate the influence of velocity on spray structure. Furthermore, spray-induced ambient air flow is also studied since it has an influence on droplets size and number distributions. The droplets located outside the spray will breakup into small ones earlier than inside droplets when the spray moves downstream due to the larger relative velocity between spray and ambient air flow. As well, droplet size and number distributions in the vertical cross section of a spray at ASOI of 1.0 ms show the droplets at center region of the spray are of smaller diameter than those at outer zone. Case 1 covers the large scope of droplet diameter and droplet number, which is droplet diameter range from 0 to 70 μm and droplet number scope from 0 to 4000 but reduces in other three cases. Droplet size and number distributions in the horizontal cross section of a spray at different distances at ASOI of 1.0 ms shows that the droplets at center region of the spray are of smaller diameter than those at outer zone. And, axial distance of 10 mm provides largest mean droplet size of 40 μm and droplet size becomes smaller as axial distance increases. But, the mean droplet number density is lower at axial distance of 10 mm and increases with axial distance.

CHAPTER 9 CONCLUSIONS AND FURTURE RECOMMENDATIONS

9.1 Main conclusions

Fuel injection sprays have been well documented for a majority of the novel combustion regimes. Although a few advanced injection strategies were investigated in the past, impinged spray injection has yet to be completely understood. In the current study, the understanding on the fundamental physics of individual droplet impacting on the wall and droplets collision under various conditions has been firstly performed. This is essential and favorable to understand the underlying mechanism of spray-wall interaction at different ambient conditions. The experimental work was done in a state-of-the-art CV at Michigan Technological University with various high-speed optical diagnostics. For numerical study, VOF method was considered to characterize the single fuel droplet impinging on the wall and an evaporation sub-model was implemented into the existing VOF model to study the evaporation of spherical liquid droplets impinging on a hot surface. An Eulerian-Lagrangian modeling approach was employed to characterize the spray-gas and spray-wall interactions by means of a RANS formulation. The important findings of droplet/spray impingement studies were used to validate the current CFD model to deliver good predictions of the qualitative droplet/spray impingement phenomenon and quantitative spray characteristics. The conclusions which can be derived from the present work are summarized as follows:

9.1.1 Droplet-wall impingement and droplets collision

- The experimental results of droplet impinging on the various ambient and surface conditions agree with the splashing and non-splashing phenomena observed in the published droplet-wall interaction models. A new splashing correlation with respect to *Oh* and *Re* based on the experimental data was developed: $OhRe^{0.886} = 6.7$.

- The effects of the impact *We*, surface temperature, and surface roughness on the time evolution of droplet spreading factor, height ratio, the dynamic contact angle,

and the contact line velocity were studied. The dynamic contact angle, contact line velocity, and spread factor vary with the impact *We*. The maximum spreading factor both in diesel and water cases increases with the impact *We*. Furthermore, in diesel case, the receding and equilibrium contact angles at various impact *We* change at a small scale. In the water case, the receding contact angle is quite smaller compared with the equilibrium contact angle at each condition. At higher surface temperature, the maximum spreading factor is larger than that at lower surface temperature case. In the single-droplet impingement on wall tests, diesel droplets appear to oscillate slightly and attempt to reshape; the vertical elongation is observed during the receding phase. As the droplet impinges on a relatively roughened surface, the surface roughness is the dominating factor for splashing. The splashing occurs earlier with the roughened surface compared to the smooth surface.

- A good agreement is observed between the temporal evolution of the experimental spreading factor and height ratio and simulation results. The pressure coefficient C_p and the velocity magnitude are much larger at the initial stage of spreading. The vortex is visible on the top of droplet rim during the initial spreading phase. It is also visible around the droplet rim on both left and right with the cross-section view, which also changes the direction when the receding phase initiates.

- An evaporation sub-model was successfully implemented into the existing solver with VOF model. The newly developed solver was validated with the published results and the multi-droplet impingement on a hot surface was studied by using the evaporation sub-model. The simulations successfully predicted the droplet levitation characteristics when the surface temperature is above the Leidenfrost point. Droplet spread decreases as droplet number increases in a direction and takes less time to recede. Additionally, droplet number in a perpendicular direction leads to reduction in droplet spread and increase in lift-off. Higher lift-off results in lower average temperature.

9.1.2 Spray-wall impingement

9.1.2.1 Parametric study on free spray and impinged spray characteristics

- In the experiments, parametric variations were performed for the different operating conditions to evaluate the effects of ambient density and injection pressure on the free and impinged spray behaviors. The free spray penetration decreased with the ambient density and increased with the injection pressure both in diesel and n-heptane sprays. The impinged spray radii were generally longer than the impinged spray on wall. The impinged spray radius on wall and the spray height decreased with the ambient density and increased with the injection pressure.

- From bottom view images, both radial and axial radii decreased as the ambient density increased at any given time-step. The expansion ratio slightly decreased with the increase of ambient density. The WIES front was almost considered as a smooth arc. Additionally, the radial and axial radii increased with the injection pressure at any given time. The expansion ratio showed no significant variation as the injection pressure increased. The corrugation ratio did not show large variations under the different injection pressures.

- In simulation, the comparison of the global spray-wall interaction related quantities (including free spray penetration and impinged spray radius and height) showed that the general trends were well predicted, especially in terms of axial and radial spray impinged on wall, while impinged spray height was under-predicted.

- The physical size of the selected subset domain as well as to the number of injected parcels have a significant effect on the local spray morphology near the impingement location. The use of smaller subsets (as small as a cube with a 0.25 mm side) required the number of injected parcels to be increased to improve the statistical significance of the selected sample. Due to the linear increase of the parcel count with the number of holes, very large numbers of injected parcels might not be a viable solution for multi-hole injectors.

9.1.2.2 Spray-wall film characteristics

- In experiment, the fuel film formation and the film characteristics resulting from the liquid spray impinging on a flat plate at various ambient densities and injection pressures was studied by RIM technique. The temporal evolution of film mass, area, and averaged film thickness decrease as the ambient density and injection pressure increase. The thinner film evaporates faster while the thicker film shows slower evaporation. In both axial and radial directions, local film thickness overall decreases with the ambient density and injection pressure. However, in the central region, near the impingement point, the local film thickness is consistently larger than that in the peripheral regions.

- The simulations successfully captured the spray structure and n-heptane film properties as the injection pressure varies.

9.1.3 Multiple spray-to-spray collision

- A 2-hole novel colliding jet injector has been tested in a constant-volume combustion chamber under three non-reacting spray conditions. CFD work has been performed and validated with the experiments. The results from both the experiment and CFD work conclude that 60^0 BTDC is a better injection time for the injection to take place due to higher extent of vaporized fuel delivery.

- The further numerical simulations were performed to investigate three different angles of two-hole spray, which contains pre (90°), at (44°), or post (20°) break-up point. Higher collision efficiency occurred in the 90° case by measuring vaporization rate and penetration length.

- The simulation work to investigate spray structures based on four different multiple jet-to-jet impingement injectors were also performed to aid in the design of the impinging jet injectors. The spray angle (post collision angle and bend angle), droplet diameter and number distributions as well as velocity of spray were studied.

Both post collision angle and bend angle had an influence on the spray penetration and spray structure. Droplet size and number distributions in both the vertical and horizontal cross sections of a spray showed the droplets at center region of the spray are of smaller diameter than those at the outer zone.

9.2 Future recommendations

The remaining goals to further bridge the gap between experimental and numerical study, improve the Eulerian based evaporation VOF sub-model, and develop the Eulerian-Lagrangian based spray-wall interaction model are recommended. For future experimental and numerical study of droplet/spray impingement, the following recommendations are made:

Various test conditions with multi-train droplets, such as a sensitivity analysis of ambient condition and droplet size, as well as combustion, will be considered to further improve the correlation of deposition-splash criteria and provide the physics for spray impingement study. The splashing conditions will be studied numerically with the physics based VOF approach for predicting droplet-wall interactions. Further, the evaporation solver and the mesh dependency can be further investigated to improve the accuracy of interface representation and numerical calculation.

Further, combustion in the spray-wall test will be further researched due to its importance on IC engine process. A more accurate modeling approach based on the physics and methodology obtained from droplet impingement with fewer parameter-tuning requirements for predicting spray-wall interactions will be developed.

CHAPTER 10 APPENDICES

10.1 Copyright permission

Chapters 2, 4, 5, 6, 7

Michigan Tech

Emma Zhao <lez@mtu.edu>

RE: A kind request for permission to re-publish my papers in my dissertation

---

On Tue, Jan 16, 2018 at 1:38 PM, Emily Kroll <Emily.Kroll@sae.org> wrote:

Hello Emma,

My apologies for the delay in response.

SAE is granting you permission to include your papers listed below in your Ph.D. dissertation.

SAE 2015-01-0948 (High-speed spray-to-spray collision study on two-hole impinging jet nozzles)

SAE 2016-01-0840 (Numerical simulations for spray characterization of uneven multiple jet-to-jet impingement injectors)

SAE 2016-01-0847 (Investigation of multi-hole impinging jet high-pressure spray characteristics under gasoline engine-like conditions)

SAE 2017-01-0854 (An experiment and numerical study of diesel spray impingement on a flat plate)

SAE 2017-01-0852 (Numerical study on evaporation of spherical droplets impinging on the wall using volume of fluid model)

SAE 2018-01-0312 (High pressure impinging spray film formation characteristics)

SAE 2018-01-0289 (Splashing criterion and topological features of a single droplet impinging on the flat plate)

SAE 2018-01-0276 (Evaluation of diesel spray-wall interaction and morphology around impingement location)

Good luck with your dissertation and SAE thanks you for your past and present authoring of SAE papers.

Emily S. Kroll

Information Management Specialist

Content Management

SAE INTERNATIONAL

400 Commonwealth Drive

Warrendale, PA 15096

o +1.724.772.4077

f +1.724.776.8549

e emily.kroll@sae.org

www.sae.org

Figure 6.18

Michigan Tech

Emma Zhao <lez@mtu.edu>

FW: Permission to use Journal of Fluid Mechanics figure in PhD thesis

On Mon, Feb 19, 2018 at 5:38 AM, **Permissions Sales UK** Rights@cambridge.org wrote:

Dear Emma,

1 figure from: Ashgriz, N., & Poo, J. (1990). Coalescence and separation in binary collisions of liquid drops. *Journal of Fluid Mechanics, 221*, 183-204 © Cambridge University Press

Thank you for your request to reproduce the above material in your forthcoming PhD thesis, for non-commercial publication. Cambridge University Press are pleased to grant non-exclusive permission, free of charge, for this specific one time use, on the understanding you have checked that we do not acknowledge any other source for the material. This permission does not include the use of copyright material owned by any party other than the authors. Consent to use any such material must be sought by you from the copyright owner concerned.

Please ensure full acknowledgement appears in your work.

Should you wish to publish your work commercially in the future, please reapply to the appropriate Cambridge University Press office, depending on where your forthcoming work will be published. Further information can be found on our website at the following link:

http://www.cambridge.org/about-us/rights-permissions/permissions/

Kind regards

Permissions Sales Team
Cambridge University Press
University Printing House
Shaftesbury Road
Cambridge CB2 8BS, UK

http://www.cambridge.org/about-us/rights-permissions/permissions/

10.2 Others

10.2.1 Simulation details of spray-wall impingement under diesel engine conditions

In the simulations of spray-wall impingement under diesel engine conditions, the agreement with the experimental data was achieved by using the simulation setup shown in Table 10.1 and values for break-up and turbulent model constants shown in Table 10.2. As briefly pointed out in Chapter 4.5, the only correction that was performed involved the increase of the $C_{\varepsilon 1}$ turbulence constant to 1.535 in order to account for the round-jet effect. Note that B_1 is KH breakup model time constant, C_{RT} is RT breakup model size constant,

Table 10.1: Model summary

Modeling Parameters	CONVERGE
Method	Eulerian-Lagrangian
Turbulence model	Standard k-ε
Breakup model	Modified KH-RT
Drag-law	Dynamic drag model
Evaporation model	Frossling
Collision model	No time counter (NTC)
Collision outcomes	Post-collision (bouncing, stretching separation, reflexive separation, or coalescence)
Dimensionality and type of grid	3-D, structured with AMR
Grid size	Base grid size: 4 mm, Finer grid: 250 μm
Time step	Variable based on spray, vaporization

Table 10.2: Breakup and turbulence model setup

	Parameter	**Value**
Breakup model	B_1	7
	C_{RT}	0.1
	Breakup length	disabled
Turbulence	$C_{\varepsilon 1}$	1.535

	$C_{\varepsilon 2}$	1.9
	$C_{\varepsilon 3}$	-1
	$Pr_{t,k}$	1
	$Pr_{t,\varepsilon}$	1.3

10.2.2 Simulation details of multiple-spray-to-spray collision under gasoline engine conditions

In the simulations of multiple spray-to-spray collision under gasoline engine conditions, the agreement with the experimental data was achieved by the simulation setup shown in Table 10.3.

Table 10.3: Model summary and breakup model constant

Modeling Parameters	CONVERGE
Method	Eulerian-Lagrangian
Turbulence model	RNG k-ε model
Breakup model	KH-RT breakup length model; time constant (B_1 = 3)
Collision model	O'Rourke model
Collision outcomes	Post-collision (bouncing, stretching separation, reflexive separation, or coalescence)
Dimensionality and type of grid	3-D, structured with AMR
Grid size	Base grid size: 1 mm, Finer grid: 375 μm
Time step	Variable based on spray, vaporization

10.2.3 Image processing for droplet-wall impingement test images

```
% Droplet-wall impingement test

%%%%%%%%%%%%%%%%%%%%%%%%%%%%%%%%%%%%%%%%%%%%%%%%%%%%%%%%%%%%%%%%%%%%%%%%%%%%%%%%

clear all
```

```
close all


dir_raw = 'D:\DOE droplet impingement Dec';

YYYYMMDD = '20171226';

HHMM = '1749';

cd([dir_raw '/' YYYYMMDD '/' HHMM]) % Change the working directory to
the desired folder


%% Create movie.

writerObj = VideoWriter('Droplet_1742.avi');

writerObj.FrameRate = 20;

open(writerObj);


%% Predetermined parameters

Impinging_time =76; % frame number

Center_Location =322;% frame number

Appearing_time =50; % frame number

Ending_time = 3000; %+430+(350-142);

fontSize = 6;

frame_speed = 25000; % pixel/sec

scale = 0.0294; % mm/pixel

rho=848; % kg/m^3 Density for the fluid being impinged

mu=2.6e-6; % m^2/s Kinematic viscosity for the fluid being impinged

sigma=24e-3;% N/m surface tension of fluid being impinged

Height=52.05;% mm between nozzle to plate

Fluid = 'Diesel'; % fluid being impinged

Vg=(2*9.8*Height/1000)^0.5; %based on the gravity
```

```
% Defining Background

BackgroundfileName = [dir_raw '/' YYYYMMDD '/' HHMM '/' HHMM '0000'
num2str(Appearing_time) '.bmp'];

BackImage = imread(BackgroundfileName);

BackImage1=imcomplement(imbinarize(BackImage));

numberToExtract =1;

Background =(ExtractNLargestBlobs(BackImage1, numberToExtract));

se = strel('square',10);

Background = imopen(Background, se);

BackImage1=imcomplement(BackImage1);

Background=imcomplement(Background);

BackImage1(Background==0)=1;

numberToExtract =1;

BackImage1=imcomplement(BackImage1);

BackImage1 =(ExtractNLargestBlobs(BackImage1, numberToExtract));

BackImage1=imcomplement(BackImage1);


figure('units','normalized','outerposition',[0 0 1 1])

for i=Appearing_time:Ending_time% Read files after start of drop

    %% Read Image

if i < 10

     fullFileName = [dir_raw '/' YYYYMMDD '/' HHMM '/' HHMM '00000'
num2str(i) '.bmp'];

    elseif i < 100

     fullFileName = [dir_raw '/' YYYYMMDD '/' HHMM '/' HHMM '0000'
num2str(i) '.bmp'];

    elseif i < 1000
```

```
    fullFileName = [dir_raw '/' YYYYMMDD '/' HHMM '/' HHMM '000'
num2str(i) '.bmp'];

    elseif i < 10000

    fullFileName = [dir_raw '/' YYYYMMDD '/' HHMM '/' HHMM '00'
num2str(i) '.bmp'];

end


Original_Image = (imread(fullFileName));

time(i)=(1/frame_speed)*1000*(i -(Appearing_time)); % ms

Impingingtime(i)=(1/frame_speed)*1000*(i -(Impinging_time)); % ms


%% binaryImage conversion

if i < Impinging_time %% before impingement calculations


level=graythresh(Original_Image);

binaryImage=imcomplement(imbinarize(Original_Image,level));

se = strel('disk', 2, 0);

binaryImage=imfill(binaryImage,'holes');

binaryImage = imclose(binaryImage,se);

binaryImage=binaryImage.*Background;

numberToExtract =1;

binaryImage = ExtractNLargestBlobs(binaryImage, numberToExtract);

BinaryImage_crop = imcrop(binaryImage,[300,310,384,186]);


imshow(Original_Image);

hold on;
```

```
Vertical_Location_bottom = find(binaryImage(:,Center_Location) == 1, 1,
'last' );

Vertical_Location_top = find(binaryImage(:,Center_Location) == 1, 1,
'first' );

Cl(1,i)=(Vertical_Location_bottom+Vertical_Location_top)/2;

C=round(Cl(1,i));

Horizontal_Location_right = find(binaryImage(C,:) == 1, 1, 'last' );

Horizontal_Location_left = find(binaryImage(C,:) == 1, 1, 'first' );

Vertical_rowbottom(1,i) = Vertical_Location_bottom;

Vertical_rowtop(1,i) = Vertical_Location_bottom;

%% Calculation of velocity to verify gravity based calculation

timeDiff=(1/frame_speed); %s

U(1,i)=((Vertical_rowbottom(1,i)-Vertical_rowbottom(1,i-
1)).*scale)/(1000*timeDiff); %m/s

U(1,i)=((Cl(1,i)-Cl(1,i-1)).*scale)/(1000*timeDiff); %m/s

u1(i)=U(1,i);

tmp = abs(Vg-u1);

[idx idx] = min(tmp); %index of closest value

closest(i) = u1(idx); %closest value

U(1,i)=closest(i);



%% Diameter calculation

[L,num]=bwlabel(binaryImage,4);% labelling the area in the binary image
using for regionprops, num=1 is actually already defined in line
"numberToExtract = 1"

stats2 = regionprops(L, 'orientation','area','Extrema','centroid');%
the data of properties stored

area2=[stats2.Area]; %call for area, spray area in pixel^2

Area(i)=max(area2)*scale*scale;

Diameter(1,i)=(Area(i)*4/pi)^(0.5);
```

```
D(1,i)=((Vertical_Location_bottom-Vertical_Location_top)*scale)/1000;

D1(1,i)=((Horizontal_Location_right-
Horizontal_Location_left)*scale)/1000;

Dia(1,i)=((D(1,i)+D1(1,i))/2)*1000;

%% Reynold's No Calculation

Re(1,i)=U(1,i)*D(1,end)/mu;

%% Weber number calculation

We(1,i)=rho*(U(1,i))^2*D(1,end)/sigma;

%% Ohnesorge number calculation

Oh(1,i)=sqrt(We(1,i))/Re(1,i);

DD(1,i)=D(1,i)*1000;

else

    %% after impingement calculations


    %% binary conversion

level=graythresh(Original_Image);

binaryImage=imcomplement(imbinarize(Original_Image,0.5));

se = strel('disk', 2, 0);

binaryImage=imfill(binaryImage,'holes');

binaryImage = imclose(binaryImage,se);

binaryImage=binaryImage.*Background;

numberToExtract =1;


% boundary extraction

binaryImage = ExtractNLargestBlobs(binaryImage, numberToExtract);

boundaries = bwboundaries(binaryImage);

A = cell2mat(boundaries) ;
```

```
[r11,c11]=size(binaryImage);

Maskb=zeros(r11,c11);

for kk=1:length(A)

Maskb(A(kk,1),A(kk,2))=1;

end

[y,x] = find(Maskb);

dx = [0];

dy = [0];

x_corners = bsxfun(@plus, x, dx);

y_corners = bsxfun(@plus, y, dy);

x_corners = x_corners(:);

y_corners = y_corners(:);

%% corners extracted for calculations

imshow(Original_Image, 'InitialMagnification', 'fit')

hold on %% displaying original image


[rows,columns]=size(Maskb);

heights = zeros(1, columns);

topEdge = zeros(1, columns);

bottomEdge = zeros(1, columns);

for col = 1:columns

    thisCol = binaryImage(:,col);

    topIndex = find(thisCol, 1, 'first');

    if ~isempty(topIndex)

        topEdge(col) = topIndex; % it is not necessary since yInj is
fixed

        bottomEdge(col) = find(thisCol, 1, 'last');
```

```
        heights(col) = bottomEdge(col) - topIndex;
    end
end
BE=max(bottomEdge);
widths = zeros(1, rows);
    thisRow = Maskb(BE,:);
    topIndex = find(thisRow, 1, 'first');
    if ~isempty(topIndex)
        lE = topIndex;
        rE = find(thisRow, 1, 'last');
        SD(i)= rE - lE;
    end
leftout=find(y_corners~=BE);
Aa=cat(2,x_corners(leftout),y_corners(leftout));
bb=[lE,BE];
cc=[rE,BE];
AA=cat(1,Aa,bb,cc);
x_corners=AA(:,1);
y_corners=AA(:,2);
plot(x_corners, y_corners, 'or')
hold on


%% calculation of contact angle
lC=cat(2,x_corners,y_corners);
diff1=abs(lC(:,1)-lE);
diff=abs(lC(:,2)-BE);
distance=((diff1).^2+(diff).^2).^(0.5);
```

```
lC=cat(2,lC,distance);
lC=sortrows(lC,3);
rC=cat(2,x_corners,y_corners);
diff2=abs(rC(:,1)-rE);
diff3=abs(rC(:,2)-BE);
distancer=((diff2).^2+(diff3).^2).^(0.5);
rC=cat(2,rC,distancer);
rC=sortrows(rC,3);
if SD(i)>SD(i-1)
    nou=4;
else
    nou=10;
end
lx=lC(1:nou,1);
ly=lC(1:nou,2);
plot(lx, ly, 'ob')
hold on
rx=rC(1:nou,1);
ry=rC(1:nou,2);
plot(rx, ry, 'ob')
hold on
leftCoefficients = polyfit(ly,lx,1);
rightCoefficients = polyfit(ry,rx,1);
yleftFit = polyval(leftCoefficients, ly);
plot(yleftFit, ly,'y-', 'LineWidth', 2);hold on
yrightFit = polyval(rightCoefficients, ry);
plot(yrightFit, ry, 'y-', 'LineWidth', 2); hold on;
```

```
leftAngle(i) = 90+atand(leftCoefficients(1)); %% left contact angle

rightAngle(i) = 90-atand(rightCoefficients(1)); %% right contact angle

stats2 = regionprops(binaryImage,'Extrema');

Extrema1 = [stats2.Extrema];

bottomleft=Extrema1(6,1);

bottomright=Extrema1(5,1);


%% other impingement characteristics calculations

SpreadingDiameter(i)=(bottomright-bottomleft)*scale;

top=topEdge(find(topEdge>0));

h1(i)=BE-min(top);

HeightRatio(i)=(h1(i)*scale)/Dia(1,end);

ss=SD(i)*scale;

SpreadRatio(i)=1/(Dia(1,end)/SpreadingDiameter(i));

ht=h1(i)*scale;

Spreadingvelocity(i)=(SpreadingDiameter(i)-SpreadingDiameter(i-
1))/((time(i)-time(i-1)));


% displaying values

str=strcat('\bf sv=',num2str(Spreadingvelocity(i),'%.2f'),'m/s');

text(150,300,str,'HorizontalAlignment','center','VerticalAlignment',
'top','FontSize', fontSize+5,'Color','k');

str=strcat('\bf d=',num2str(ss,'%.2f'),'mm');

text(150,180,str,'HorizontalAlignment','center','VerticalAlignment',
'top','FontSize', fontSize+5,'Color','k');

str=strcat('\bf h=',num2str(ht,'%.2f'),'mm');

text(150,200,str,'HorizontalAlignment','center','VerticalAlignment',
'top','FontSize', fontSize+5,'Color','k');

str=strcat('\bf d/D=',num2str(SpreadRatio(i),'%.2f'));
```

```
text(150,220,str,'HorizontalAlignment','center','VerticalAlignment',
'top','FontSize', fontSize+5,'Color','k');

str=strcat('\bf h/D=',num2str(HeightRatio(i),'%.2f'));

text(150,240,str,'HorizontalAlignment','center','VerticalAlignment',
'top','FontSize', fontSize+5,'Color','k');

str=strcat('\bf Left \theta=',num2str(leftAngle(i),'%.2f'),'\circ');

text(150,260,str,'HorizontalAlignment','center','VerticalAlignment',
'top','FontSize', fontSize+5,'Color','k');

str=strcat('\bf Right \theta =',num2str(rightAngle(i),'%.2f'),'\circ');

text(150,280,str,'HorizontalAlignment','center','VerticalAlignment',
'top','FontSize', fontSize+5,'Color','k');

end



% defining axis

axis on

ax = gca;

ax.LineWidth = 1.5;

ax.FontSize = 13;

xticks([0:192:768]);

xticklabels({'0.00','3.46','6.92','10.38','13.84'});

yticks([0:100:400]);

yticklabels({'7.2','5.4','3.6','1.8','0.0'});

ylabel('Vertical Direction (mm)');

xlabel('Horizontal Direction (mm) ');



% displaying time

str=strcat('\bf T=',num2str(time(i),'%.2f'),' ms');

text(150,1,str,'HorizontalAlignment','center','VerticalAlignment',
'top','FontSize', fontSize+8,'Color','k');
```

```
if Impingingtime(i)>=0

str=strcat('\bf TAI=',num2str(Impingingtime(i),'%.2f'),' ms');

text(150,28,str,'HorizontalAlignment','center','VerticalAlignment',
'top','FontSize', fontSize+8,'Color','k');

else

end



str=strcat('\bf HOI=',num2str(Height,'%.2f'),'mm');

text(150,80,str,'HorizontalAlignment','center','VerticalAlignment',
'top','FontSize', fontSize+5,'Color','k');

%%%------------------

str=strcat('\bf',Fluid);

text(150,60,str,'HorizontalAlignment','center','VerticalAlignment',
'top','FontSize', fontSize+5,'Color','k');



str=strcat('\bf Re=',num2str(Re(1,end),'%.2f'));

text(150,100,str,'HorizontalAlignment','center','VerticalAlignment',
'top','FontSize', fontSize+5,'Color','k');



str=strcat('\bf We=',num2str(We(1,end),'%.2f'));

text(150,120,str,'HorizontalAlignment','center','VerticalAlignment',
'top','FontSize', fontSize+5,'Color','k');



str=strcat('\bf U=',num2str(closest(end) ,'%.2f'),'m/s');

text(150,140,str,'HorizontalAlignment','center','VerticalAlignment',
'top','FontSize', fontSize+5,'Color','k');



str=strcat('\bf D=',num2str(Diameter(1,end),'%.2f'),'mm');
```

```
text(150,160,str,'HorizontalAlignment','center','VerticalAlignment',
'top','FontSize', fontSize+5,'Color','k');


drawnow;

frame = getframe(figure(1));

writeVideo(writerObj,frame);


end


close(writerObj);


Impingingtime=Impingingtime';

time=time';

leftAngle=leftAngle';

rightAngle=rightAngle';

Spreadfactor=SpreadRatio';

SpreadingDiameter=SpreadingDiameter';

HeightRatio=HeightRatio';

Diameter=Diameter';


% writing in excel file

col_header={'Time (ms)', 'Impingingtime','Left Collision angle
(deg)','Right Collision Angle(deg)','Spread factor', 'Spread diameter',
'Height Ratio','Diametr before Impinegement'};

xlswrite(strcat(HHMM,'.xlsx'),time,1,'A2');

xlswrite(strcat(HHMM,'.xlsx'),Impingingtime,1,'B2');

xlswrite(strcat(HHMM,'.xlsx'),leftAngle,1,'C2');

xlswrite(strcat(HHMM,'.xlsx'),rightAngle,1,'D2');
```

```
xlswrite(strcat(HHMM,'.xlsx'),Spreadfactor,1,'E2');

xlswrite(strcat(HHMM,'.xlsx'),SpreadingDiameter,1,'F2');

xlswrite(strcat(HHMM,'.xlsx'),HeightRatio,1,'G2');

xlswrite(strcat(HHMM,'.xlsx'),Diameter,1,'H2');
```

10.2.4 Image processing for spray-wall impingement test images

```
% Spray-wall impingement (Single-hole Injector Test)

% Modified on Nov 8th, 2016

% Side View (Schlieren images)

% Scale 0.19 mm/pixel


%% Setup workspace

clear all;

close all;

clc;



workspace; % Make sure the workspace panel with all the variables is
showing.

format longg;

format compact;

fontSize = 12;

% Check that user has the Image Processing Toolbox installed.

hasIPT = license('test', 'image_toolbox');

if ~hasIPT

    % User does not have the toolbox installed.
```

```
    message = sprintf('Sorry, but you do not seem to have the Image
Processing Toolbox.\nDo you want to try to continue anyway?');

    reply = questdlg(message, 'Toolbox missing', 'Yes', 'No', 'Yes');

    if strcmpi(reply, 'No')

        % User said No, so exit.

        return;

    end

end

%=========================================================================
=========

%=========================================================================
=========

dir_raw = 'D:';

YYYYMMDD = 'DOE impinging plate window project\DOE 2016
NOV\20161129_sideview_hybrid';

HHMM = '2425';

Density='22.8 kg/m^3';

IP='1500bar';

soiframe=13;

actualSOI=10;

framelag=soiframe-actualSOI;



nfiles=200; % Tota no. of image files to be read. Determine this based
on number of file available within the time for complete evaporation or
wall hitting of spray

frame_speed=36000;

timelag=1000*(framelag/frame_speed);

scale=0.1465; % mm/pixel

SprFrac = 60; % percentage of maximum spray for spray angle

xInj =504; yInj = 10; % injector nozzle tip locations
```

```
incAngle = 30; % inclinded angle of 120 deg

%


cd([dir_raw '/' YYYYMMDD '/' HHMM]) % Change the working directory to
the desired folder

%

% Create movie.

%

writerObj = VideoWriter('Spray propeties.avi');

writerObj.FrameRate = 1;

open(writerObj);


bgfile = [dir_raw '/' YYYYMMDD '/' HHMM '/' HHMM '000007.bmp'];

Background = (imread(bgfile));

% Background1=imrotate(Background1,30);

[rows, columns, numberOfColorBands] = size(Background);

imq = zeros(rows,columns);




 % Read files after start of injection

for i=soiframe:2:135 % Read files after start of injection

if i < 10

     fullFileName = [dir_raw '/' YYYYMMDD '/' HHMM '/' HHMM '00000'
num2str(i) '.bmp'];

    elseif i < 100

     fullFileName = [dir_raw '/' YYYYMMDD '/' HHMM '/' HHMM '0000'
num2str(i) '.bmp'];

    elseif i < 1000
```

```
    fullFileName = [dir_raw '/' YYYYMMDD '/' HHMM '/' HHMM '000'
num2str(i) '.bmp'];

end

if i < 11

     fullFileName1 = [dir_raw '/' YYYYMMDD '/' HHMM '/' HHMM '00000'
num2str(i-1) '.bmp'];

    elseif i < 100

     fullFileName1 = [dir_raw '/' YYYYMMDD '/' HHMM '/' HHMM '0000'
num2str(i-1) '.bmp'];

    elseif i < 1000

    fullFileName1 = [dir_raw '/' YYYYMMDD '/' HHMM '/' HHMM '000'
num2str(i-1) '.bmp'];

end

% bgfile = [dir_raw '/' YYYYMMDD '/' HHMM '/' HHMM '000001.bmp'];

% Background = imread(fullFileName1);

grayImagea = imread(fullFileName); % Original image is read as gray
image

% imshow(grayImagea);

grayImage1 = (grayImagea - Background)+(Background-grayImagea); % After
subtraction



    ShadowSubtracted(:,:,i) = (grayImagea-Background)+(Background-
grayImagea);

%     imshow(ShadowSubtracted(:,:,j));

    ShadowS(:,:,i) = ShadowSubtracted(:,:,i);

    if i>10

        ShadowSub = (ShadowSubtracted(:,:,i)-ShadowSubtracted(:,:,i-
1))+(ShadowSubtracted(:,:,i-1)-ShadowSubtracted(:,:,i));

        ShadowS(:,:,i) = ShadowSub;

%         imshow(ShadowS(:,:,j));

        if i>11
```

```
        ShadowT = (ShadowS(:,:,i)-ShadowS(:,:,i-1))+(ShadowS(:,:,i-1)-
ShadowS(:,:,i));

        ShadowS(:,:,i) = ShadowT;


    end

    end

    ShadowS(:,:,i)=ShadowS(:,:,i);

Shadow=imadjust(ShadowS(:,:,i),stretchlim(ShadowS(:,:,i)));

S=imcomplement(grayImagea);

B=imcomplement(Background);

S=S-B;

%  imshow(S);



 Shadow= wiener2(S, [15 15]);

level=graythresh(Shadow);

 ShadowBW = im2bw(Shadow, level);

%   imshow(ShadowBW)

% % %  image dilation

    se = strel('disk', 1);

    ShadowImDilate = imdilate(ShadowBW, se);


    ShadowImFill = imfill(ShadowImDilate, 'holes');

%    imshow(ShadowImFill);

    ShadowClose = imclose(ShadowImFill, se);

    ShadowSmooth = imerode(ShadowClose,se);

    binaryImage= ExtractNLargestBlobs(ShadowSmooth, 1);
```

```
%
figure(1);


subplot(2, 2, 1);
imshow(grayImagea); grid on; axis on;hold on;
plot(xInj,yInj,'+b'); hold on;
title('Original image', 'FontSize', fontSize);
% Enlarge figure to full screen.
set(gcf, 'Units', 'Normalized', 'Outerposition', [0, 0, 1, 1]);
set(gca,'FontSize',fontSize,'FontWeight', 'bold');
%
axis on;
set(gca,'FontSize',fontSize,'FontWeight', 'bold')
set(gca,'xtick',[0:69:512])
set(gca,'XMinorTick','on');
xticklabels({'0','10','20','30','40','50','60','70'});
% Get the dimensions of the image.  numberOfColorBands should be = 3.
this
% step for test images is not necessary
[rows, columns, numberOfColorBands] = size(grayImagea);
org=grayImagea;
if numberOfColorBands > 1   % If it's really color, then convert to
gray scale.
    grayImage = grayImagea(:,:,2);
end
%
```

```
%------------------------------------------------------------------------


%

[L,num]=bwlabel(binaryImage,4);

stats2 = regionprops(L, 'orientation','area','Extrema','centroid');

BW=edge(binaryImage,'sobel');

area2=[stats2.Area]; %Spray area in pixel^2

 P(i)=max(area2)*scale*scale; % P is the array containing spray area
from each image

% disp(P(i));

%

% Display the binary image.

subplot(2, 2, 2);

imshow(binaryImage);hold on;

plot(xInj,yInj,'+b'); hold on;

grid on;

axis on;title('Biggest blob area after conversion to binary',
'FontSize', fontSize);

set(gca,'FontSize',fontSize,'FontWeight', 'bold');drawnow;

%

% Scan from left to right of the image to find out spray width in each
column

%

widths = zeros(1, rows);

leftEdge = zeros(1, rows);

rightEdge = zeros(1, rows);

%

for row = 1:rows
```

```
    thisRow = binaryImage(row,:);
    topIndex = find(thisRow, 1, 'first');
    if ~isempty(topIndex)
        leftEdge(row) = topIndex;
        rightEdge(row) = find(thisRow, 1, 'last');
        widths(row) = rightEdge(row) - leftEdge(row);
    end
end
%
% Scan from top to bottom of the image to find out spray height in each
row
%
heights = zeros(1, columns);
topEdge = zeros(1, columns);
bottomEdge = zeros(1, columns);
%
for col = 1:columns
    thisCol = binaryImage(:,col);
    topIndex = find(thisCol, 1, 'first');
    if ~isempty(topIndex)
        topEdge(col) = topIndex;
        bottomEdge(col) = find(thisCol, 1, 'last');
        heights(col) = bottomEdge(col) - yInj;
        lowest=max(bottomEdge(col));
    end
end
%
```

```
penet(i)=max(heights);

plim = max(heights);

nSprayAngle=round(penet(i)*SprFrac/100.) + yInj; % 100% of spray
penetration is considered while checking the angle



%

middleEdge = leftEdge + widths/2; % spray middle

ix=find(widths>1); % Find columns with spray width more than 1 pixel

%

il = 1; ir = 1; im = 1;

for ii = 1:nSprayAngle

    if leftEdge (ii) > 0

        xl(il) = leftEdge(ii);

        yl(il) = ii;

        il = il + 1;

    end

    if rightEdge (ii) > 0

        xr(ir) = rightEdge(ii);

        yr(ir) = ii;

        ir = ir + 1;

    end

    if middleEdge (ii) > 0

        xm(im) = middleEdge(ii);

        ym(im) = ii;

        im = im + 1;

    end
```

```
end
%
subplot(2, 2, 3);
imshow((org));% Original images positioned
hold on;
%
boundaries = bwboundaries(binaryImage);


for k=1:1
   b = boundaries{k};
   plot(b(:,2),b(:,1),'b','LineWidth',2);
end
%
plot(xl,yl,xr,yr,xm,ym,'b-', 'LineWidth', 2);hold on;
plot(xInj,yInj,'+b'); hold on;
% Lines for cone angle
%
leftCoefficients = polyfit(yl,xl,1);
rightCoefficients = polyfit(yr,xr,1);
centreline = polyfit(ym,xm,1);
%
% Plot the fitted lines
yleftFit = polyval(leftCoefficients, yl);
plot(yleftFit, yl,'g-', 'LineWidth', 2);hold on
yrightFit = polyval(rightCoefficients, yr);
plot(yrightFit, yr, 'r-', 'LineWidth', 2); hold on;
centreFit=polyval(centreline,ym);
```

```
plot(centreFit, ym, 'b-', 'LineWidth', 2);

% h_legend=legend('Top', 'Bottom','Centreline', 'Location',
'southwest');

% set(h_legend,'FontSize',fontSize-2);

title('Original image and spray boundary ','FontSize', fontSize );

axis on; set(gca,'FontSize',fontSize,'FontWeight', 'bold')

%

% Angle Measurement

c=1;% -1 for both spray edges on one side, + on either side axis

leftAngle = atand(leftCoefficients(1));

rightAngle = atand(rightCoefficients(1));

centreAngle(i)=abs(atand(centreline(1)));

coneAngle(i) = abs(leftAngle)-abs(rightAngle);

ca2(i)=coneAngle(i)/2;

if abs(leftAngle)< abs(rightAngle)

    ca2(i)=(abs(leftAngle))-c*ca2(i);

elseif abs(leftAngle)>= abs(rightAngle)

     ca2(i)=-ca2(i)+abs(rightAngle);

end

time(i-soiframe+1)=((1/frame_speed)*1000*(i-soiframe)) +timelag;

tms=time(i-soiframe+1);

penetration=penet(i);

CA12=coneAngle(i);

timeinms(i,1)=tms;

%

% cla_m=mean(coneAngle(i:i(1)));

cla_m = abs(centreAngle(i) - leftAngle) + abs(centreAngle(i) -
rightAngle);
```

```
penet(i)=(max(heights)*scale)/cos(incAngle*pi/180);

subplot(2,2,4);

C3=[1 250 250 1];

R3=[1 1 rows rows];

BW90=(roipoly(imq,C3,R3));

% subplot(3,3,6);

C4=[1 columns columns 1];

R4=[1 1 282 282];

BW80=(roipoly(imq,C4,R4));

maskedimage=(binaryImage.*BW90).*BW80;

maskedimage = ExtractNLargestBlobs(maskedimage, 1);

ms(:,:,i)=maskedimage;

 imshow(maskedimage);

 title('Masked Image for rebound characteristics ','FontSize',
fontSize );

axis on; set(gca,'FontSize',fontSize,'FontWeight', 'bold')

Stats = regionprops(maskedimage,'extrema');

Extrema = [Stats.Extrema];


  if Extrema~=0;


    [row, column, numberOfColorBand] = size(maskedimage);

    height = zeros(1, column);

topEdge1 = zeros(1, column);

bottomEdge1 = zeros(1, column);

    for col1 = 1:column

    thisCol = maskedimage(:,col1);
```

```
    topIndex = find(thisCol, 1, 'first');
    if ~isempty(topIndex)
        topEdge1(col1) = topIndex;
        bottomEdge1(col1) = find(thisCol, 1, 'last');
        height1(col1) = bottomEdge1(col1) - topEdge1(col1);
    end
    end
      Rebound_ht(i)=(max(height1)*scale);
    top_righty(i)=Extrema(2,2);
 top_lefty(i)=Extrema(1,2);
 ht=min(top_righty(i),top_lefty(i));
 %Rebound_ht(i)=(283-ht)*scale;
left_topx=Extrema(8,1);
          left_bottomx=Extrema(7,1);
          Bottom_leftx=Extrema(6,1);
                           radiuswallleftx(i)=scale*(350-
Bottom_leftx);
                    min2=min(left_topx,left_bottomx);
                    extremeleftpt=min(min2,Bottom_leftx);
                    reboundradiusleftx(i)=scale*(350-extremeleftpt);



 end


text(-100, -470,'\bf Spray wall Impingement Measurement-Side
View','HorizontalAlignment','center','VerticalAlignment',
'top','FontSize', fontSize+6);

str=strcat('\bf Time:',num2str(round(tms,2)),'ms');
```

```
str1=strcat('\bf Test:',HHMM);

 text(-850,-470,str,'HorizontalAlignment','center','VerticalAlignment',
'top','FontSize', fontSize+6);

str2=strcat('\bf Inj. Pressure :',IP);

str3=strcat('\bf Density:', Density);

% text(01,0.3,str2,'HorizontalAlignment','center','VerticalAlignment',
'top','FontSize', fontSize+6);

% text(1,0.4,str3,'HorizontalAlignment','center','VerticalAlignment',
'top','FontSize', fontSize+6);



drawnow;

frame = getframe(figure(1));

writeVideo(writerObj,frame);

%

end

%

%%



close(writerObj);

col_header={'Sl. No.','Time (ms)', 'Post Coll angle (deg)','Final angle
(deg)','centreAngle(deg)','Area (mm^2)','Penetration (mm)','Axial
Rebound Height','Axial Rebound Radius', ' Axial Rebound radius on
wall'};

xlswrite(strcat(HHMM,'.xlsx'),col_header,1,'A1');

xlswrite(strcat(HHMM,'.xlsx'),timeinms,1,'B2');

xlswrite(strcat(HHMM,'.xlsx'),coneAngle',1,'C2');

xlswrite(strcat(HHMM,'.xlsx'),cla_m,1,'D2');

xlswrite(strcat(HHMM,'.xlsx'),centreAngle',1,'E2');

xlswrite(strcat(HHMM,'.xlsx'),P',1,'F2');

xlswrite(strcat(HHMM,'.xlsx'),penet',1,'G2');
```

```
xlswrite(strcat(HHMM,'.xlsx'),Rebound_ht',1,'H2');
xlswrite(strcat(HHMM,'.xlsx'),reboundradiusleftx',1,'I2');
xlswrite(strcat(HHMM,'.xlsx'),radiuswallleftx',1,'J2');
%%

figure(2);

yyaxis right;
plot(timeinms,penet,'rd','linewidth',2);
hold on
ylabel('Penetration (mm)');
ax = gca;
ax.YColor = 'black';
yyaxis left;

plot(timeinms,Rebound_ht,'gd','linewidth',2); hold on;
plot(timeinms,reboundradiusleftx,'kd','linewidth',2); hold on;
plot(timeinms,radiuswallleftx,'bd','linewidth',2); hold on;

xlabel('Time (ms)');
ylabel('Length (mm)');
set(gca,'FontSize',fontSize,'FontWeight', 'bold')
ax = gca;
ax.YColor = 'black';

grid on;
```

```
% h_legend=legend('Penetration', 'Rebound Height', 'Axial rebound
radius','Axial Radius on wall', 'Location', 'E', 'FontSize',fontSize-
3);



%%%%%%%%%%%%%%%%%%%%%%%%%%%%%%%%%%%%%%%%%%%%%%%%%%%%%%%%%%%%%%%%%%%%%%%%%%%%%%%
%%%%

% Spray-wall impingement (Single-hole Injector Test)

% Modified on Nov 8th, 2016

% Front View (Mie)

%%%%%%%%%%%%%%%%%%%%%%%%%%%%%%%%%%%%%%%%%%%%%%%%%%%%%%%%%%%%%%%%%%%%%%%%%%%%%%%
%%%%

function  test

%% Setup workspace

clear all;

close all;

clc;

fontSize = 12;

%% Check that user has the Image Processing Toolbox installed.

hasIPT = license('test', 'image_toolbox');

if ~hasIPT

    % User does not have the toolbox installed.

    message = sprintf('Sorry, but you do not seem to have the Image
Processing Toolbox.\nDo you want to try to continue anyway?');

    reply = questdlg(message, 'Toolbox missing', 'Yes', 'No', 'Yes');

    if strcmpi(reply, 'No')

        % User said No, so exit.

        return;

    end

end
```

```
%% Import the file and define input parameter such as density, scale,
SOI, actual soi time

dir_raw = 'D:\DOE impinging plate window project\DOE 2016 NOV\';

YYYYMMDD = '20161129_frontview_Mie';

HHMM = '2358';

Density='22.8 kg/m^3';

IP='1500 bar';

nfiles=200; % Total no. of image files to be read. Determine this based
on number of file available within the time for complete evaporation or
wall hitting of spray

frame_speed=36000;

scale=0.2727; % mm/pixel

incAngle = 30;

soiframe=13; % this is the point where Matlab can read/recognize

actualSOI=10;% the actual soi, ASOI=0 ms

framelag=soiframe-actualSOI;

timelag=1000*(framelag/frame_speed); % ms

ximp=128; % Impinging point read from PFV

SprFrac = 60; % percentage of maximum spray for spray angle

xInj = 130; yInj = 24; % injector nozzle tip locations from PFV

%% Create movie.

cd([dir_raw '\' YYYYMMDD '\' HHMM]) % Change the working directory to
the desired folder

writerObj = VideoWriter('Spray propeties.avi');

writerObj.FrameRate = 1;

open(writerObj);

%% image directory

bgfile = [dir_raw '/' YYYYMMDD '/' HHMM '/' HHMM '000005.bmp']; % pick
up any frame before start of injection
```

```
Background = imread(bgfile);

[rows, columns] = size(Background);

imq = zeros(rows,columns); % creat the domain which is the same size
with background image and later use for creation of mask for rebound
region

C4=[1 columns columns 1]; % column = 256

R4=[1 1 174 174]; % 174 is the vertical/y direction for plate position

BW80=(roipoly(imq,C4,R4)); % mask used to remove the near wall region
which includes brigt reflection

C4=[1 columns columns 1];

R4=[130 130 190 190];



C4=[90 170  170 90];

R4=[1 1 155 155];

BW70=imcomplement(roipoly(imq,C4,R4));



figure(1);

for i=soiframe:100 % Read files after start of injection

if i < 10

     fullFileName = [dir_raw '/' YYYYMMDD '/' HHMM '/' HHMM '00000'
num2str(i) '.bmp'];

    elseif i < 100

     fullFileName = [dir_raw '/' YYYYMMDD '/' HHMM '/' HHMM '0000'
num2str(i) '.bmp'];

    elseif i < 1000

    fullFileName = [dir_raw '/' YYYYMMDD '/' HHMM '/' HHMM '000'
num2str(i) '.bmp'];

end

%
```

```
grayImage =(imread(fullFileName)); % Original image is read as gray
image

grayImage =(grayImage) -(Background); % After subtraction

org=grayImage;

% grayImage=imadjust(grayImage);% increase contrast of image

subplot(2, 3, 1);

imshow(grayImage);% Display the contrastd/original image.

grid on; axis on;

hold on;

plot(xInj,yInj,'+b');

title('Original image', 'FontSize', fontSize);

% Enlarge figure to full screen.

set(gcf, 'Units', 'Normalized', 'Outerposition', [0, 0, 1, 1]);

set(gca,'FontSize',fontSize,'FontWeight', 'bold');

set(gca,'xtick',[0:36:252])

set(gca,'XMinorTick','on');

xticklabels({'0','10','20','30','40','50','60','70'});

%% Get the dimensions of the image.  numberOfColorBands should be = 3.
this step for test images is not necessary

[rows, columns, numberOfColorBands] = size(grayImage);

if numberOfColorBands > 1   % If it's really color, then convert to
gray scale.

   grayImage = grayImage(:,:,2);

end

%% Threshold the image

level=graythresh(grayImage); % default threshold value based on Ostu's,
e.g. 0.1882, 0.1882*255=47 is used to find the final threshold value
based on sensitivity analysis

thresholdValue =45;% Use a higher value, say 50, for vapor boundary; +-
20% of 47
```

```
binaryImage = grayImage > thresholdValue;

binaryImage=BW80.*binaryImage;% to get rid of unidentified luminicence
due to the plate reflection like the lower region

%% Extract the largest area using our custom function
ExtractNLargestBlobs().

numberToExtract = 1; % to creat only one largest area

binaryImage = ExtractNLargestBlobs(binaryImage, numberToExtract);

%% Fill any holes that might be present and % Do an opening to smooth
out the edges.

binaryImage = imfill(binaryImage, 'holes');

se = strel('disk', 3, 0);

binaryImage = imopen(binaryImage, se);

%% for area calculation, but we may not use it for single hole
properties calculations

[L,num]=bwlabel(binaryImage,4);% labelling the area in the binary image
using for regionprops, num=1 is actually already defined in line
"numberToExtract = 1"

stats2 = regionprops(L, 'orientation','area','Extrema','centroid');%
the data of properties stored

area2=[stats2.Area]; %call for area, spray area in pixel^2

P(i)=max(area2)*scale*scale; % P is the array containing spray area
from each image

%% Display the binary image.

subplot(2, 3, 2);

imshow(binaryImage);

hold on;

plot(xInj,yInj,'+b')

grid on;

axis on;

title('  Biggest blob area ', 'FontSize', fontSize);

set(gca,'FontSize',fontSize,'FontWeight', 'bold');
```

```
set(gca,'xtick',[0:36:252])

set(gca,'XMinorTick','on');

xticklabels({'0','10','20','30','40','50','60','70'});

%% Scan from left to right of the image to find out spray width in each
column


widths = zeros(1, rows);

leftEdge = zeros(1, rows);

rightEdge = zeros(1, rows); % initialize the variables


for row = 1:rows

    thisRow = binaryImage(row,:);

    topIndex = find(thisRow, 1, 'first');

    if ~isempty(topIndex)

        leftEdge(row) = topIndex;

        rightEdge(row) = find(thisRow, 1, 'last');

        widths(row) = rightEdge(row) - leftEdge(row);

    end

end


% Scan from top to bottom of the image to find out spray height in each
row

%

heights = zeros(1, columns);

topEdge = zeros(1, columns);

bottomEdge = zeros(1, columns);

%

for col = 1:columns
```

```
    thisCol = binaryImage(:,col);

    topIndex = find(thisCol, 1, 'first');

    if ~isempty(topIndex)

        topEdge(col) = topIndex; % it is not necessary since yInj is
fixed

        bottomEdge(col) = find(thisCol, 1, 'last');

        heights(col) = bottomEdge(col) - yInj;

    end

end

%

penet(i)=max(heights);

sprayfrcpixel=round(penet(i)*SprFrac/100) + yInj; % find the pixel
point based on 60% of penetration

penet(i)=max(heights)*scale/cos(incAngle*pi/180);


middleEdge = leftEdge + widths/2; % spray middle

il = 1; ir = 1; im = 1;

for ii = 1:sprayfrcpixel

    if leftEdge (ii) > 0

        xl(il) = leftEdge(ii);

        yl(il) = ii;

        il = il + 1;

    end

    if rightEdge (ii) > 0

        xr(ir) = rightEdge(ii);

        yr(ir) = ii;

        ir = ir + 1;

    end
```

```
    if middleEdge (ii) > 0
        xm(im) = middleEdge(ii);
        ym(im) = ii;
        im = im + 1;
    end
end


subplot(2, 3, 3);
imshow(org);% Original images positioned
hold on;
boundaries = bwboundaries(binaryImage);
for k=1:1
   b = boundaries{k};
   plot(b(:,2),b(:,1),'b','LineWidth',1);% for the whole boundary of
spray image
end
% plot(xl,yl,xr,yr,xm,ym,'b-', 'LineWidth', 2); % for 60% of
penetration raw boundary
hold on;
plot(xInj,yInj,'+b');
hold on;
%% Lines for cone angle
leftCoefficients = polyfit(yl,xl,1);
rightCoefficients = polyfit(yr,xr,1);
centreline = polyfit(ym,xm,1);
% Plot the fitted lines
yleftFit = polyval(leftCoefficients, yl);
% plot(yleftFit, yl,'r-', 'LineWidth', 2);hold on
```

```
yrightFit = polyval(rightCoefficients, yr);

% plot(yrightFit, yr, 'g-', 'LineWidth', 2); hold on;

centreFit=polyval(centreline,ym);

% plot(centreFit, ym, 'b-', 'LineWidth', 2);

% h_legend=legend('Top', 'Bottom','Centreline', 'Location',
'southwest');

% set(h_legend,'FontSize',fontSize-2);

title('Original image and spray boundary ','FontSize', fontSize );

axis on;

set(gca,'FontSize',fontSize,'FontWeight', 'bold')

set(gca,'xtick',[0:36:252])

set(gca,'XMinorTick','on');

xticklabels({'0','10','20','30','40','50','60','70'});

%% Angle Measurement

c=1;% -1 for both spray edges on one side, + on either side axis

leftAngle = atand(leftCoefficients(1));

rightAngle = atand(rightCoefficients(1));

centreAngle(i)=abs(atand(centreline(1))); % it did not use

coneAngle(i) = c*abs(leftAngle)+abs(rightAngle);

ca2(i)=coneAngle(i)/2;

if abs(leftAngle)< abs(rightAngle)

    ca2(i)=(abs(leftAngle))-c*ca2(i);

elseif abs(leftAngle)>= abs(rightAngle)

     ca2(i)=-ca2(i)+abs(rightAngle);

end

timeinms(i,1)=((1/frame_speed)*1000*(i-soiframe))+timelag ;

% cla_m = abs(centreAngle(i) - leftAngle) + abs(centreAngle(i) -
rightAngle);
```

```
%% rebound properties calculations

 subplot(2, 3, 4);

maskedimage=imq;

maskangle=10; % change based on case

dividenumber = round(1/tan(maskangle*pi/180));

inumber1 = round((208- yInj)/dividenumber) - 1; % to get the horizontal
length (for pixel, so need integer)

for p = 0:inumber1;

    for l = xInj-p:xInj+p;

        for k = 0:dividenumber-1;

       maskedimage(yInj+dividenumber*p+k-3,l) = 1; %??

        end

    end

end

maskedimage=ExtractNLargestBlobs(maskedimage, 1);

reboundchar=binaryImage-maskedimage;


C3=[1 118 118 1];

R3=[1 1 rows rows];

BW90=roipoly(imq,C3,R3);

BW10=imcomplement(BW90);

reboundcharleft=(BW90.*reboundchar).*BW70;%

imshow(reboundcharleft);

grid on;

axis on;

title('Masked Image left-side', 'FontSize', fontSize);

set(gca,'FontSize',fontSize,'FontWeight', 'bold');
```

```
subplot(2,3,5)

reboundcharright=(BW10.*reboundchar).*BW70;

imshow(reboundcharright);

grid on;

axis on;

title('Masked Image right-side ', 'FontSize', fontSize);

set(gca,'FontSize',fontSize,'FontWeight', 'bold');


%%reading rebound characteristics


if penet(i)==penet(i-1) % find impinging point

            Statsleft = regionprops(reboundcharleft,'extrema');

            Extremaleft = [Statsleft.Extrema];

                if Extremaleft~=0

                    top_leftlefty(i)=Extremaleft(1,2);

                    leftht(i)=scale*(180-top_leftlefty(i));% 180 is y-
direction at the plate, read from PFV, it may be changed by case

                    left_topx=Extremaleft(8,1); % for radius

                    left_bottomx=Extremaleft(7,1);% for radius, but
will compare with left top and pick up the max.

                    Bottom_leftx=Extremaleft(6,1); % for radius on wall

                     radiuswallleftx(i)=scale*(ximp-Bottom_leftx);

                     min1=min(left_topx,left_bottomx);% in left side,
find the min point which will be the max.radius with respect to
impinging point

                     extremeleftpt=min(min1,Bottom_leftx);

                     reboundradiusleftx(i)=scale*(ximp-extremeleftpt);
```

```
                    Statsright= regionprops(reboundcharright,'extrema');

                   Extremaright = [Statsright.Extrema];

                       if Extremaright~=0

                    top_rightrighty(i)=Extremaright(2,2);

                    rightht(i)=scale*(180-top_rightrighty(i));

                      right_bottomx=Extremaright(4,1);

                         right_topx=Extremaright(3,1);

                    Bottom_rightx=Extremaright(5,1);

                     radiuswallrightx(i)=scale*(Bottom_rightx-ximp);% for
radius on wall in right side

                                    max1=max(right_topx,Bottom_rightx);

                     extremerightpoint=max(max1,right_bottomx);

                     reboundradiusright(i)=scale*(extremerightpoint-ximp);

                       end

                   end

else

end



text(100,-335,'\bf Spray wall Impingement Measurement- Front
View','HorizontalAlignment','center','VerticalAlignment',
'top','FontSize', fontSize+6);

str=strcat('\bf Time:',num2str(round(timeinms(i,1),2)),'ms');

text(450,0,str,'HorizontalAlignment','center','VerticalAlignment',
'top','FontSize', fontSize+6);

str2=strcat('\bf Injection Pressure :',IP);

str3=strcat('\bf Density:', Density);

text(450,50,str2,'HorizontalAlignment','center','VerticalAlignment',
'top','FontSize', fontSize+6);

text(450,100,str3,'HorizontalAlignment','center','VerticalAlignment',
'top','FontSize', fontSize+6);
```

```
drawnow;

frame = getframe(figure(1));

writeVideo(writerObj,frame);

end



close(writerObj);

col_header={'Time (ms)', 'Post Coll angle (deg)','Penetration
(mm)','left rebound ht', 'right rebound ht', 'left radius on
wall','right radius on wall', 'left rebound radius',' right rebound
radius' };

xlswrite(strcat(HHMM,'.xlsx'),col_header,1,'A1');

xlswrite(strcat(HHMM,'.xlsx'),timeinms,1,'A2');

xlswrite(strcat(HHMM,'.xlsx'),coneAngle',1,'B2');

xlswrite(strcat(HHMM,'.xlsx'),penet','C2');

xlswrite(strcat(HHMM,'.xlsx'),leftht',1,'E2');

xlswrite(strcat(HHMM,'.xlsx'),rightht',1,'F2');

xlswrite(strcat(HHMM,'.xlsx'),radiuswallleftx',1,'G2');

xlswrite(strcat(HHMM,'.xlsx'),radiuswallrightx',1,'H2');

xlswrite(strcat(HHMM,'.xlsx'),reboundradiusleftx',1,'I2');

xlswrite(strcat(HHMM,'.xlsx'),reboundradiusright',1,'J2');



figure(2);

plot(timeinms,penet,'-bo'); hold on; grid on;

plot(timeinms,leftht,'-ko'); hold on;

plot(timeinms,rightht,'-k+');

grid on;

plot(timeinms,radiuswallleftx,'-ro'); hold on;

plot(timeinms,radiuswallrightx,'-r+')
```

```
grid on;

plot(timeinms,reboundradiusleftx,'-go'); hold on;

plot(timeinms,reboundradiusright,'-g+')

grid on;

%

%=========================================================================
=======================

% Function to return the specified number of largest or smallest blobs
in a binary image.

% If numberToExtract > 0 it returns the numberToExtract largest blobs.

% If numberToExtract < 0 it returns the numberToExtract smallest blobs.

% Example: return a binary image with only the largest blob:

%   binaryImage = ExtractNLargestBlobs(binaryImage, 1);

% Example: return a binary image with the 3 smallest blobs:

%   binaryImage = ExtractNLargestBlobs(binaryImage, -3);



function binaryImage = ExtractNLargestBlobs(binaryImage,
numberToExtract)

try

    % Get all the blob properties.  Can only pass in originalImage in
version R2008a and later.

    [labeledImage, numberOfBlobs] = bwlabel(binaryImage);

    blobMeasurements = regionprops(labeledImage, 'area');

    % Get all the areas

    allAreas = [blobMeasurements.Area];

    if numberToExtract > length(allAreas);

        % Limit the number they can get to the number that are
there/available.

        numberToExtract = length(allAreas);
```

```
    end
    if numberToExtract > 0
        % For positive numbers, sort in order of largest to smallest.
        % Sort them.
        [sortedAreas, sortIndexes] = sort(allAreas, 'descend');
    elseif numberToExtract < 0
        % For negative numbers, sort in order of smallest to largest.
        % Sort them.
        [sortedAreas, sortIndexes] = sort(allAreas, 'ascend');
        % Need to negate numberToExtract so we can use it in
sortIndexes later.
        numberToExtract = -numberToExtract;
    else
        % numberToExtract = 0.  Shouldn't happen.  Return no blobs.
        binaryImage = false(size(binaryImage));
        return;
    end
    % Extract the "numberToExtract" largest blob(a)s using ismember().
    biggestBlob = ismember(labeledImage,
sortIndexes(1:numberToExtract));
    % Convert from integer labeled image into binary (logical) image.
    binaryImage = biggestBlob > 0;
catch ME
    errorMessage = sprintf('Error in function
ExtractNLargestBlobs().\n\nError Message:\n%s', ME.message);
    fprintf(1, '%s\n', errorMessage);
    uiwait(warndlg(errorMessage));
end
```

10.2.5 Heat flux calculation during spray-wall impingement

```
%% this code is for heat flux calculation during spray impinging on hot
surface

%%%%%%%%%%%%%%%%%%%%%%%%%%%%%%%%%%%%%%%%%%%%%%%%%%%%%%%%%%%%%%%%%%%%%%%%%%

close all

clear all

%% Reading data from excel file

dir_raw = 'D:\CV\DOE\2017 Dec DOE heatflux\20171230';

cd(dir_raw);

%% Extract the raw data

start = 1;

Injection_start = 10000;

ending = 40000;

Repeat_1 = 1751;

Repeat_2 = 1752;

Repeat_3 = 1753;

Repeat_4 = 1754;

Repeat_5 = 1755;

% Repeat 1

LA_e_1 = xlsread([num2str(Repeat_1) '.xlsx'],1,'A1:A60001');

LA_s_1 = xlsread([num2str(Repeat_1) '.xlsx'],1,'B1:B60001');

LB_e_1 = xlsread([num2str(Repeat_1) '.xlsx'],1,'C1:C60001');

LB_s_1 = xlsread([num2str(Repeat_1) '.xlsx'],1,'D1:D60001');

LC_e_1 = xlsread([num2str(Repeat_1) '.xlsx'],1,'E1:E60001');

LC_s_1 = xlsread([num2str(Repeat_1) '.xlsx'],1,'F1:F60001');
```

```
LA_e_1 = LA_e_1(start:ending);

LA_s_1 = LA_s_1(start:ending);

LB_e_1 = LB_e_1(start:ending);

LB_s_1 = LB_s_1(start:ending);

LC_e_1 = LC_e_1(start:ending);

LC_s_1 = LC_s_1(start:ending);

% Repeat 2

LA_e_2 = xlsread([num2str(Repeat_2) '.xlsx'],1,'A1:A60001');

LA_s_2 = xlsread([num2str(Repeat_2) '.xlsx'],1,'B1:B60001');

LB_e_2 = xlsread([num2str(Repeat_2) '.xlsx'],1,'C1:C60001');

LB_s_2 = xlsread([num2str(Repeat_2) '.xlsx'],1,'D1:D60001');

LC_e_2 = xlsread([num2str(Repeat_2) '.xlsx'],1,'E1:E60001');

LC_s_2 = xlsread([num2str(Repeat_2) '.xlsx'],1,'F1:F60001');

LA_e_2 = LA_e_2(start:ending);

LA_s_2 = LA_s_2(start:ending);

LB_e_2 = LB_e_2(start:ending);

LB_s_2 = LB_s_2(start:ending);

LC_e_2 = LC_e_2(start:ending);

LC_s_2 = LC_s_2(start:ending);

% Repeat 3

LA_e_3 = xlsread([num2str(Repeat_3) '.xlsx'],1,'A1:A60001');

LA_s_3 = xlsread([num2str(Repeat_3) '.xlsx'],1,'B1:B60001');

LB_e_3 = xlsread([num2str(Repeat_3) '.xlsx'],1,'C1:C60001');

LB_s_3 = xlsread([num2str(Repeat_3) '.xlsx'],1,'D1:D60001');

LC_e_3 = xlsread([num2str(Repeat_3) '.xlsx'],1,'E1:E60001');

LC_s_3 = xlsread([num2str(Repeat_3) '.xlsx'],1,'F1:F60001');

LA_e_3 = LA_e_3(start:ending);
```

```
LA_s_3 = LA_s_3(start:ending);

LB_e_3 = LB_e_3(start:ending);

LB_s_3 = LB_s_3(start:ending);

LC_e_3 = LC_e_3(start:ending);

LC_s_3 = LC_s_3(start:ending);

% Repeat 4

LA_e_4 = xlsread([num2str(Repeat_4) '.xlsx'],1,'A1:A60001');

LA_s_4 = xlsread([num2str(Repeat_4) '.xlsx'],1,'B1:B60001');

LB_e_4 = xlsread([num2str(Repeat_4) '.xlsx'],1,'C1:C60001');

LB_s_4 = xlsread([num2str(Repeat_4) '.xlsx'],1,'D1:D60001');

LC_e_4 = xlsread([num2str(Repeat_4) '.xlsx'],1,'E1:E60001');

LC_s_4 = xlsread([num2str(Repeat_4) '.xlsx'],1,'F1:F60001');

LA_e_4 = LA_e_4(start:ending);

LA_s_4 = LA_s_4(start:ending);

LB_e_4 = LB_e_4(start:ending);

LB_s_4 = LB_s_4(start:ending);

LC_e_4 = LC_e_4(start:ending);

LC_s_4 = LC_s_4(start:ending);

% Repeat 5

LA_e_5 = xlsread([num2str(Repeat_5) '.xlsx'],1,'A1:A60001');

LA_s_5 = xlsread([num2str(Repeat_5) '.xlsx'],1,'B1:B60001');

LB_e_5 = xlsread([num2str(Repeat_5) '.xlsx'],1,'C1:C60001');

LB_s_5 = xlsread([num2str(Repeat_5) '.xlsx'],1,'D1:D60001');

LC_e_5 = xlsread([num2str(Repeat_5) '.xlsx'],1,'E1:E60001');

LC_s_5 = xlsread([num2str(Repeat_5) '.xlsx'],1,'F1:F60001');

LA_e_5 = LA_e_5(start:ending);

LA_s_5 = LA_s_5(start:ending);
```

```
LB_e_5 = LB_e_5(start:ending);

LB_s_5 = LB_s_5(start:ending);

LC_e_5 = LC_e_5(start:ending);

LC_s_5 = LC_s_5(start:ending);

%% Plot raw data

L = length(LA_e_1);

K = 44.5; % W/mK

dx = 2; % mm

Fs = 100000;

T = 1/Fs;

t = (0:L-1)*T*1000;

Comb_start = 10000;

Comb_end = 10200;

t = t - Comb_start*T*1000;

%% FFT Filter % Frequency resolution is 2.5 Hz

Cut_off = 100;

Cut_off_2 = 20;

% Repeat 1

LA_fft_e_1 = fft(LA_e_1);

LA_fft_s_1 = fft(LA_s_1);

LB_fft_e_1 = fft(LB_e_1);

LB_fft_s_1 = fft(LB_s_1);

LC_fft_e_1 = fft(LC_e_1);

LC_fft_s_1 = fft(LC_s_1);

% Repeat 2

LA_fft_e_2 = fft(LA_e_2);

LA_fft_s_2 = fft(LA_s_2);
```

```
LB_fft_e_2 = fft(LB_e_2);

LB_fft_s_2 = fft(LB_s_2);

LC_fft_e_2 = fft(LC_e_2);

LC_fft_s_2 = fft(LC_s_2);

% Repeat 3

LA_fft_e_3 = fft(LA_e_3);

LA_fft_s_3 = fft(LA_s_3);

LB_fft_e_3 = fft(LB_e_3);

LB_fft_s_3 = fft(LB_s_3);

LC_fft_e_3 = fft(LC_e_3);

LC_fft_s_3 = fft(LC_s_3);

% Repeat 4

LA_fft_e_4 = fft(LA_e_4);

LA_fft_s_4 = fft(LA_s_4);

LB_fft_e_4 = fft(LB_e_4);

LB_fft_s_4 = fft(LB_s_4);

LC_fft_e_4 = fft(LC_e_4);

LC_fft_s_4 = fft(LC_s_4);

% Repeat 5

LA_fft_e_5 = fft(LA_e_5);

LA_fft_s_5 = fft(LA_s_5);

LB_fft_e_5 = fft(LB_e_5);

LB_fft_s_5 = fft(LB_s_5);

LC_fft_e_5 = fft(LC_e_5);

LC_fft_s_5 = fft(LC_s_5);

% Frequency plot

f = Fs*(0:(L/2))/L;
```

```
% Location A

P2_e_1_A = abs(LA_fft_e_1);

P2_s_1_A = abs(LA_fft_s_1);

P1_e_1_A = P2_e_1_A(1:L/2+1);

P1_s_1_A = P2_s_1_A(1:L/2+1);

P2_e_2_A = abs(LA_fft_e_2);

P2_s_2_A = abs(LA_fft_s_2);

P1_e_2_A = P2_e_2_A(1:L/2+1);

P1_s_2_A = P2_s_2_A(1:L/2+1);

P2_e_3_A = abs(LA_fft_e_3);

P2_s_3_A = abs(LA_fft_s_3);

P1_e_3_A = P2_e_3_A(1:L/2+1);

P1_s_3_A = P2_s_3_A(1:L/2+1);

P2_e_4_A = abs(LA_fft_e_4);

P2_s_4_A = abs(LA_fft_s_4);

P1_e_4_A = P2_e_4_A(1:L/2+1);

P1_s_4_A = P2_s_4_A(1:L/2+1);

P2_e_5_A = abs(LA_fft_e_5);

P2_s_5_A = abs(LA_fft_s_5);

P1_e_5_A = P2_e_5_A(1:L/2+1);

P1_s_5_A = P2_s_5_A(1:L/2+1);

figure(2);

plot(f,P1_e_1_A/max(P1_e_1_A),f,P1_e_2_A/max(P1_e_2_A),f,P1_e_3_A/max(P
1_e_3_A),f,P1_e_4_A/max(P1_e_4_A),f,P1_e_5_A/max(P1_e_5_A));

ylim([0 0.001]);

% figure();

% plot(f,P1_s_1_A,f,P1_s_2_A,f,P1_s_3_A,f,P1_s_4_A,f,P1_s_5_A);
```

```
% ylim([0 10000]);
% Location B
P2_e_1_B = abs(LB_fft_e_1);
P2_s_1_B = abs(LB_fft_s_1);
P1_e_1_B = P2_e_1_B(1:L/2+1);
P1_s_1_B = P2_s_1_B(1:L/2+1);
P2_e_2_B = abs(LB_fft_e_2);
P2_s_2_B = abs(LB_fft_s_2);
P1_e_2_B = P2_e_2_B(1:L/2+1);
P1_s_2_B = P2_s_2_B(1:L/2+1);
P2_e_3_B = abs(LB_fft_e_3);
P2_s_3_B = abs(LB_fft_s_3);
P1_e_3_B = P2_e_3_B(1:L/2+1);
P1_s_3_B = P2_s_3_B(1:L/2+1);
P2_e_4_B = abs(LB_fft_e_4);
P2_s_4_B = abs(LB_fft_s_4);
P1_e_4_B = P2_e_4_B(1:L/2+1);
P1_s_4_B = P2_s_4_B(1:L/2+1);
P2_e_5_B = abs(LB_fft_e_5);
P2_s_5_B = abs(LB_fft_s_5);
P1_e_5_B = P2_e_5_B(1:L/2+1);
P1_s_5_B = P2_s_5_B(1:L/2+1);
% figure();
% plot(f,P1_e_1_B,f,P1_e_2_B,f,P1_e_3_B,f,P1_e_4_B,f,P1_e_5_B);
% ylim([0 10000]);
% figure();
% plot(f,P1_s_1_B,f,P1_s_2_B,f,P1_s_3_B,f,P1_s_4_B,f,P1_s_5_B);
```

```
% ylim([0 10000]);
% Location C
P2_e_1_C = abs(LC_fft_e_1);
P2_s_1_C = abs(LC_fft_s_1);
P1_e_1_C = P2_e_1_C(1:L/2+1);
P1_s_1_C = P2_s_1_C(1:L/2+1);
P2_e_2_C = abs(LC_fft_e_2);
P2_s_2_C = abs(LC_fft_s_2);
P1_e_2_C = P2_e_2_C(1:L/2+1);
P1_s_2_C = P2_s_2_C(1:L/2+1);
P2_e_3_C = abs(LC_fft_e_3);
P2_s_3_C = abs(LC_fft_s_3);
P1_e_3_C = P2_e_3_C(1:L/2+1);
P1_s_3_C = P2_s_3_C(1:L/2+1);
P2_e_4_C = abs(LC_fft_e_4);
P2_s_4_C = abs(LC_fft_s_4);
P1_e_4_C = P2_e_4_C(1:L/2+1);
P1_s_4_C = P2_s_4_C(1:L/2+1);
P2_e_5_C = abs(LC_fft_e_5);
P2_s_5_C = abs(LC_fft_s_5);
P1_e_5_C = P2_e_5_C(1:L/2+1);
P1_s_5_C = P2_s_5_C(1:L/2+1);
% figure();
% plot(f,P1_e_1_C,f,P1_e_2_C,f,P1_e_3_C,f,P1_e_4_C,f,P1_e_5_C);
% ylim([0 10000]);
% figure();
% plot(f,P1_s_1_C,f,P1_s_2_C,f,P1_s_3_C,f,P1_s_4_C,f,P1_s_5_C);
```

```
% ylim([0 10000]);
% Filtered data
% Repeat 1
LA_fft_e_1(Cut_off_2:L-Cut_off_2) = 0;
LA_fft_s_1(Cut_off:L-Cut_off) = 0;
LB_fft_e_1(Cut_off_2:L-Cut_off_2) = 0;
LB_fft_s_1(Cut_off:L-Cut_off) = 0;
LC_fft_e_1(Cut_off_2:L-Cut_off_2) = 0;
LC_fft_s_1(Cut_off:L-Cut_off) = 0;
LA_filter_e_1 = ifft(LA_fft_e_1);
LA_filter_s_1 = ifft(LA_fft_s_1);
LB_filter_e_1 = ifft(LB_fft_e_1);
LB_filter_s_1 = ifft(LB_fft_s_1);
LC_filter_e_1 = ifft(LC_fft_e_1);
LC_filter_s_1 = ifft(LC_fft_s_1);
LA_filter_e_1 = abs(LA_filter_e_1);
LA_filter_s_1 = abs(LA_filter_s_1);
LB_filter_e_1 = abs(LB_filter_e_1);
LB_filter_s_1 = abs(LB_filter_s_1);
LC_filter_e_1 = abs(LC_filter_e_1);
LC_filter_s_1 = abs(LC_filter_s_1);
% Repeat 2
LA_fft_e_2(Cut_off_2:L-Cut_off_2) = 0;
LA_fft_s_2(Cut_off:L-Cut_off) = 0;
LB_fft_e_2(Cut_off_2:L-Cut_off_2) = 0;
LB_fft_s_2(Cut_off:L-Cut_off) = 0;
LC_fft_e_2(Cut_off_2:L-Cut_off_2) = 0;
```

```
LC_fft_s_2(Cut_off:L-Cut_off) = 0;

LA_filter_e_2 = ifft(LA_fft_e_2);

LA_filter_s_2 = ifft(LA_fft_s_2);

LB_filter_e_2 = ifft(LB_fft_e_2);

LB_filter_s_2 = ifft(LB_fft_s_2);

LC_filter_e_2 = ifft(LC_fft_e_2);

LC_filter_s_2 = ifft(LC_fft_s_2);

LA_filter_e_2 = abs(LA_filter_e_2);

LA_filter_s_2 = abs(LA_filter_s_2);

LB_filter_e_2 = abs(LB_filter_e_2);

LB_filter_s_2 = abs(LB_filter_s_2);

LC_filter_e_2 = abs(LC_filter_e_2);

LC_filter_s_2 = abs(LC_filter_s_2);

% Repeat 3

LA_fft_e_3(Cut_off_2:L-Cut_off_2) = 0;

LA_fft_s_3(Cut_off:L-Cut_off) = 0;

LB_fft_e_3(Cut_off_2:L-Cut_off_2) = 0;

LB_fft_s_3(Cut_off:L-Cut_off) = 0;

LC_fft_e_3(Cut_off_2:L-Cut_off_2) = 0;

LC_fft_s_3(Cut_off:L-Cut_off) = 0;

LA_filter_e_3 = ifft(LA_fft_e_3);

LA_filter_s_3 = ifft(LA_fft_s_3);

LB_filter_e_3 = ifft(LB_fft_e_3);

LB_filter_s_3 = ifft(LB_fft_s_3);

LC_filter_e_3 = ifft(LC_fft_e_3);

LC_filter_s_3 = ifft(LC_fft_s_3);

LA_filter_e_3 = abs(LA_filter_e_3);
```

```
LA_filter_s_3 = abs(LA_filter_s_3);

LB_filter_e_3 = abs(LB_filter_e_3);

LB_filter_s_3 = abs(LB_filter_s_3);

LC_filter_e_3 = abs(LC_filter_e_3);

LC_filter_s_3 = abs(LC_filter_s_3);

% Repeat 4

LA_fft_e_4(Cut_off_2:L-Cut_off_2) = 0;

LA_fft_s_4(Cut_off:L-Cut_off) = 0;

LB_fft_e_4(Cut_off_2:L-Cut_off_2) = 0;

LB_fft_s_4(Cut_off:L-Cut_off) = 0;

LC_fft_e_4(Cut_off_2:L-Cut_off_2) = 0;

LC_fft_s_4(Cut_off:L-Cut_off) = 0;

LA_filter_e_4 = ifft(LA_fft_e_4);

LA_filter_s_4 = ifft(LA_fft_s_4);

LB_filter_e_4 = ifft(LB_fft_e_4);

LB_filter_s_4 = ifft(LB_fft_s_4);

LC_filter_e_4 = ifft(LC_fft_e_4);

LC_filter_s_4 = ifft(LC_fft_s_4);

LA_filter_e_4 = abs(LA_filter_e_4);

LA_filter_s_4 = abs(LA_filter_s_4);

LB_filter_e_4 = abs(LB_filter_e_4);

LB_filter_s_4 = abs(LB_filter_s_4);

LC_filter_e_4 = abs(LC_filter_e_4);

LC_filter_s_4 = abs(LC_filter_s_4);

% Repeat 5

LA_fft_e_5(Cut_off_2:L-Cut_off_2) = 0;

LA_fft_s_5(Cut_off:L-Cut_off) = 0;
```

```
LB_fft_e_5(Cut_off_2:L-Cut_off_2) = 0;

LB_fft_s_5(Cut_off:L-Cut_off) = 0;

LC_fft_e_5(Cut_off_2:L-Cut_off_2) = 0;

LC_fft_s_5(Cut_off:L-Cut_off) = 0;

LA_filter_e_5 = ifft(LA_fft_e_5);

LA_filter_s_5 = ifft(LA_fft_s_5);

LB_filter_e_5 = ifft(LB_fft_e_5);

LB_filter_s_5 = ifft(LB_fft_s_5);

LC_filter_e_5 = ifft(LC_fft_e_5);

LC_filter_s_5 = ifft(LC_fft_s_5);

LA_filter_e_5 = abs(LA_filter_e_5);

LA_filter_s_5 = abs(LA_filter_s_5);

LB_filter_e_5 = abs(LB_filter_e_5);

LB_filter_s_5 = abs(LB_filter_s_5);

LC_filter_e_5 = abs(LC_filter_e_5);

LC_filter_s_5 = abs(LC_filter_s_5);

%% Median Filter

order = 100;

% Repeat 1

LA_median_e_1 = medfilt1(LA_e_1,order);

LA_median_s_1 = medfilt1(LA_s_1,order);

LB_median_e_1 = medfilt1(LB_e_1,order);

LB_median_s_1 = medfilt1(LB_s_1,order);

LC_median_e_1 = medfilt1(LC_e_1,order);

LC_median_s_1 = medfilt1(LC_s_1,order);

% Repeat 2

LA_median_e_2 = medfilt1(LA_e_2,order);
```

```
LA_median_s_2 = medfilt1(LA_s_2,order);

LB_median_e_2 = medfilt1(LB_e_2,order);

LB_median_s_2 = medfilt1(LB_s_2,order);

LC_median_e_2 = medfilt1(LC_e_2,order);

LC_median_s_2 = medfilt1(LC_s_2,order);

% Repeat 3

LA_median_e_3 = medfilt1(LA_e_3,order);

LA_median_s_3 = medfilt1(LA_s_3,order);

LB_median_e_3 = medfilt1(LB_e_3,order);

LB_median_s_3 = medfilt1(LB_s_3,order);

LC_median_e_3 = medfilt1(LC_e_3,order);

LC_median_s_3 = medfilt1(LC_s_3,order);

% Repeat 4

LA_median_e_4 = medfilt1(LA_e_4,order);

LA_median_s_4 = medfilt1(LA_s_4,order);

LB_median_e_4 = medfilt1(LB_e_4,order);

LB_median_s_4 = medfilt1(LB_s_4,order);

LC_median_e_4 = medfilt1(LC_e_4,order);

LC_median_s_4 = medfilt1(LC_s_4,order);

% Repeat 5

LA_median_e_5 = medfilt1(LA_e_5,order);

LA_median_s_5 = medfilt1(LA_s_5,order);

LB_median_e_5 = medfilt1(LB_e_5,order);

LB_median_s_5 = medfilt1(LB_s_5,order);

LC_median_e_5 = medfilt1(LC_e_5,order);

LC_median_s_5 = medfilt1(LC_s_5,order);

%% Combination with FFT filter and Median filter
```

```
% Repeat 1

LA_comb_e_1(1:Comb_start) = LA_median_e_1(1:Comb_start);

LA_comb_e_1(Comb_start + 1:Comb_end) = LA_filter_e_1(Comb_start +
1:Comb_end);

LA_comb_e_1(Comb_end + 1:L) = LA_median_e_1(Comb_end + 1:L);



LA_comb_s_1(1:Comb_start) = LA_median_s_1(1:Comb_start);

LA_comb_s_1(Comb_start + 1:Comb_end) = LA_filter_s_1(Comb_start +
1:Comb_end);

LA_comb_s_1(Comb_end + 1:L) = LA_median_s_1(Comb_end + 1:L);



LB_comb_e_1(1:Comb_start) = LB_median_e_1(1:Comb_start);

LB_comb_e_1(Comb_start + 1:Comb_end) = LB_filter_e_1(Comb_start +
1:Comb_end);

LB_comb_e_1(Comb_end + 1:L) = LB_median_e_1(Comb_end + 1:L);



LB_comb_s_1(1:Comb_start) = LB_median_s_1(1:Comb_start);

LB_comb_s_1(Comb_start + 1:Comb_end) = LB_filter_s_1(Comb_start +
1:Comb_end);

LB_comb_s_1(Comb_end + 1:L) = LB_median_s_1(Comb_end + 1:L);



LC_comb_e_1(1:Comb_start) = LC_median_e_1(1:Comb_start);

LC_comb_e_1(Comb_start + 1:Comb_end) = LC_filter_e_1(Comb_start +
1:Comb_end);

LC_comb_e_1(Comb_end + 1:L) = LC_median_e_1(Comb_end + 1:L);



LC_comb_s_1(1:Comb_start) = LC_median_s_1(1:Comb_start);

LC_comb_s_1(Comb_start + 1:Comb_end) = LC_filter_s_1(Comb_start +
1:Comb_end);
```

```
LC_comb_s_1(Comb_end + 1:L) = LC_median_s_1(Comb_end + 1:L);

% Repeat 2

LA_comb_e_2(1:Comb_start) = LA_median_e_2(1:Comb_start);

LA_comb_e_2(Comb_start + 1:Comb_end) = LA_filter_e_2(Comb_start +
1:Comb_end);

LA_comb_e_2(Comb_end + 1:L) = LA_median_e_2(Comb_end + 1:L);



LA_comb_s_2(1:Comb_start) = LA_median_s_2(1:Comb_start);

LA_comb_s_2(Comb_start + 1:Comb_end) = LA_filter_s_2(Comb_start +
1:Comb_end);

LA_comb_s_2(Comb_end + 1:L) = LA_median_s_2(Comb_end + 1:L);



LB_comb_e_2(1:Comb_start) = LB_median_e_2(1:Comb_start);

LB_comb_e_2(Comb_start + 1:Comb_end) = LB_filter_e_2(Comb_start +
1:Comb_end);

LB_comb_e_2(Comb_end + 1:L) = LB_median_e_2(Comb_end + 1:L);



LB_comb_s_2(1:Comb_start) = LB_median_s_2(1:Comb_start);

LB_comb_s_2(Comb_start + 1:Comb_end) = LB_filter_s_2(Comb_start +
1:Comb_end);

LB_comb_s_2(Comb_end + 1:L) = LB_median_s_2(Comb_end + 1:L);



LC_comb_e_2(1:Comb_start) = LC_median_e_2(1:Comb_start);

LC_comb_e_2(Comb_start + 1:Comb_end) = LC_filter_e_2(Comb_start +
1:Comb_end);

LC_comb_e_2(Comb_end + 1:L) = LC_median_e_2(Comb_end + 1:L);



LC_comb_s_2(1:Comb_start) = LC_median_s_2(1:Comb_start);
```

```
LC_comb_s_2(Comb_start + 1:Comb_end) = LC_filter_s_2(Comb_start +
1:Comb_end);

LC_comb_s_2(Comb_end + 1:L) = LC_median_s_2(Comb_end + 1:L);

% Repeat 3

LA_comb_e_3(1:Comb_start) = LA_median_e_3(1:Comb_start);

LA_comb_e_3(Comb_start + 1:Comb_end) = LA_filter_e_3(Comb_start +
1:Comb_end);

LA_comb_e_3(Comb_end + 1:L) = LA_median_e_3(Comb_end + 1:L);



LA_comb_s_3(1:Comb_start) = LA_median_s_3(1:Comb_start);

LA_comb_s_3(Comb_start + 1:Comb_end) = LA_filter_s_3(Comb_start +
1:Comb_end);

LA_comb_s_3(Comb_end + 1:L) = LA_median_s_3(Comb_end + 1:L);



LB_comb_e_3(1:Comb_start) = LB_median_e_3(1:Comb_start);

LB_comb_e_3(Comb_start + 1:Comb_end) = LB_filter_e_3(Comb_start +
1:Comb_end);

LB_comb_e_3(Comb_end + 1:L) = LB_median_e_3(Comb_end + 1:L);



LB_comb_s_3(1:Comb_start) = LB_median_s_3(1:Comb_start);

LB_comb_s_3(Comb_start + 1:Comb_end) = LB_filter_s_3(Comb_start +
1:Comb_end);

LB_comb_s_3(Comb_end + 1:L) = LB_median_s_3(Comb_end + 1:L);



LC_comb_e_3(1:Comb_start) = LC_median_e_3(1:Comb_start);

LC_comb_e_3(Comb_start + 1:Comb_end) = LC_filter_e_3(Comb_start +
1:Comb_end);

LC_comb_e_3(Comb_end + 1:L) = LC_median_e_3(Comb_end + 1:L);
```

```
LC_comb_s_3(1:Comb_start) = LC_median_s_3(1:Comb_start);

LC_comb_s_3(Comb_start + 1:Comb_end) = LC_filter_s_3(Comb_start +
1:Comb_end);

LC_comb_s_3(Comb_end + 1:L) = LC_median_s_3(Comb_end + 1:L);

% Repeat 4

LA_comb_e_4(1:Comb_start) = LA_median_e_4(1:Comb_start);

LA_comb_e_4(Comb_start + 1:Comb_end) = LA_filter_e_4(Comb_start +
1:Comb_end);

LA_comb_e_4(Comb_end + 1:L) = LA_median_e_4(Comb_end + 1:L);



LA_comb_s_4(1:Comb_start) = LA_median_s_4(1:Comb_start);

LA_comb_s_4(Comb_start + 1:Comb_end) = LA_filter_s_4(Comb_start +
1:Comb_end);

LA_comb_s_4(Comb_end + 1:L) = LA_median_s_4(Comb_end + 1:L);



LB_comb_e_4(1:Comb_start) = LB_median_e_4(1:Comb_start);

LB_comb_e_4(Comb_start + 1:Comb_end) = LB_filter_e_4(Comb_start +
1:Comb_end);

LB_comb_e_4(Comb_end + 1:L) = LB_median_e_4(Comb_end + 1:L);



LB_comb_s_4(1:Comb_start) = LB_median_s_4(1:Comb_start);

LB_comb_s_4(Comb_start + 1:Comb_end) = LB_filter_s_4(Comb_start +
1:Comb_end);

LB_comb_s_4(Comb_end + 1:L) = LB_median_s_4(Comb_end + 1:L);



LC_comb_e_4(1:Comb_start) = LC_median_e_4(1:Comb_start);

LC_comb_e_4(Comb_start + 1:Comb_end) = LC_filter_e_4(Comb_start +
1:Comb_end);

LC_comb_e_4(Comb_end + 1:L) = LC_median_e_4(Comb_end + 1:L);
```

```
LC_comb_s_4(1:Comb_start) = LC_median_s_4(1:Comb_start);

LC_comb_s_4(Comb_start + 1:Comb_end) = LC_filter_s_4(Comb_start +
1:Comb_end);

LC_comb_s_4(Comb_end + 1:L) = LC_median_s_4(Comb_end + 1:L);

% Repeat 5

LA_comb_e_5(1:Comb_start) = LA_median_e_5(1:Comb_start);

LA_comb_e_5(Comb_start + 1:Comb_end) = LA_filter_e_5(Comb_start +
1:Comb_end);

LA_comb_e_5(Comb_end + 1:L) = LA_median_e_5(Comb_end + 1:L);



LA_comb_s_5(1:Comb_start) = LA_median_s_5(1:Comb_start);

LA_comb_s_5(Comb_start + 1:Comb_end) = LA_filter_s_5(Comb_start +
1:Comb_end);

LA_comb_s_5(Comb_end + 1:L) = LA_median_s_5(Comb_end + 1:L);



LB_comb_e_5(1:Comb_start) = LB_median_e_5(1:Comb_start);

LB_comb_e_5(Comb_start + 1:Comb_end) = LB_filter_e_5(Comb_start +
1:Comb_end);

LB_comb_e_5(Comb_end + 1:L) = LB_median_e_5(Comb_end + 1:L);



LB_comb_s_5(1:Comb_start) = LB_median_s_5(1:Comb_start);

LB_comb_s_5(Comb_start + 1:Comb_end) = LB_filter_s_5(Comb_start +
1:Comb_end);

LB_comb_s_5(Comb_end + 1:L) = LB_median_s_5(Comb_end + 1:L);



LC_comb_e_5(1:Comb_start) = LC_median_e_5(1:Comb_start);

LC_comb_e_5(Comb_start + 1:Comb_end) = LC_filter_e_5(Comb_start +
1:Comb_end);
```

```
LC_comb_e_5(Comb_end + 1:L) = LC_median_e_5(Comb_end + 1:L);


LC_comb_s_5(1:Comb_start) = LC_median_s_5(1:Comb_start);

LC_comb_s_5(Comb_start + 1:Comb_end) = LC_filter_s_5(Comb_start +
1:Comb_end);

LC_comb_s_5(Comb_end + 1:L) = LC_median_s_5(Comb_end + 1:L);

%% Surface temperature profile plot

T_AVE_A_E = (LA_comb_e_1 + LA_comb_e_2 + LA_comb_e_3 + LA_comb_e_4 +
LA_comb_e_5)/5;

T_AVE_A_S = (LA_comb_s_1 + LA_comb_s_2 + LA_comb_s_3 + LA_comb_s_4 +
LA_comb_s_5)/5;

T_AVE_B_E = (LB_comb_e_1 + LB_comb_e_2 + LB_comb_e_3 + LB_comb_e_4 +
LB_comb_e_5)/5;

T_AVE_B_S = (LB_comb_s_1 + LB_comb_s_2 + LB_comb_s_3 + LB_comb_s_4 +
LB_comb_s_5)/5;

T_AVE_C_E = (LC_comb_e_1 + LC_comb_e_2 + LC_comb_e_3 + LC_comb_e_4 +
LC_comb_e_5)/5;

T_AVE_C_S = (LC_comb_s_1 + LC_comb_s_2 + LC_comb_s_3 + LC_comb_s_4 +
LC_comb_s_5)/5;

T_A_E(:,1) = LA_comb_e_1;

T_A_E(:,2) = LA_comb_e_2;

T_A_E(:,3) = LA_comb_e_3;

T_A_E(:,4) = LA_comb_e_4;

T_A_E(:,5) = LA_comb_e_5;

T_STD_A_E = std(T_A_E,0,2);


T_A_S(:,1) = LA_comb_s_1;

T_A_S(:,2) = LA_comb_s_2;

T_A_S(:,3) = LA_comb_s_3;

T_A_S(:,4) = LA_comb_s_4;
```

```
T_A_S(:,5) = LA_comb_s_5;
T_STD_A_S = std(T_A_S,0,2);


T_B_E(:,1) = LB_comb_e_1;
T_B_E(:,2) = LB_comb_e_2;
T_B_E(:,3) = LB_comb_e_3;
T_B_E(:,4) = LB_comb_e_4;
T_B_E(:,5) = LB_comb_e_5;
T_STD_B_E = std(T_B_E,0,2);


T_B_S(:,1) = LB_comb_s_1;
T_B_S(:,2) = LB_comb_s_2;
T_B_S(:,3) = LB_comb_s_3;
T_B_S(:,4) = LB_comb_s_4;
T_B_S(:,5) = LB_comb_s_5;
T_STD_B_S = std(T_B_S,0,2);


T_C_E(:,1) = LC_comb_e_1;
T_C_E(:,2) = LC_comb_e_2;
T_C_E(:,3) = LC_comb_e_3;
T_C_E(:,4) = LC_comb_e_4;
T_C_E(:,5) = LC_comb_e_5;
T_STD_C_E = std(T_C_E,0,2);


T_C_S(:,1) = LC_comb_s_1;
T_C_S(:,2) = LC_comb_s_2;
```

```
T_C_S(:,3) = LC_comb_s_3;

T_C_S(:,4) = LC_comb_s_4;

T_C_S(:,5) = LC_comb_s_5;

T_STD_C_S = std(T_C_S,0,2);

figure(1);

% plot(t,T_AVE_A_E,'r',t,T_AVE_B_E,'b',t,T_AVE_C_E,'k');

% hold on

plot(t,T_AVE_A_S,'-r','LineWidth',1.5);

hold on

plot(t,T_AVE_B_S,'-b','LineWidth',1.5);

hold on

plot(t,T_AVE_C_S,'-k','LineWidth',1.5);

hold on

% T_STD_A_EE =
shadedErrorBar(t(Comb_start+1:Comb_start+3000+1),T_AVE_A_E(Comb_start+1
:Comb_start+3000+1),T_STD_A_E(Comb_start+1:Comb_start+3000+1),'lineProp
s','-r','transparent',1,'patchSaturation',0.2);

T_STD_A_SS =
shadedErrorBar(t(Comb_start+1:Comb_start+3000+1),T_AVE_A_S(Comb_start+1
:Comb_start+3000+1),T_STD_A_S(Comb_start+1:Comb_start+3000+1),'lineProp
s','-r','transparent',1,'patchSaturation',0.2);

% T_STD_B_EE =
shadedErrorBar(t(Comb_start+1:Comb_start+3000+1),T_AVE_B_E(Comb_start+1
:Comb_start+3000+1),T_STD_B_E(Comb_start+1:Comb_start+3000+1),'lineProp
s','--r','transparent',1,'patchSaturation',0.2);

T_STD_B_SS =
shadedErrorBar(t(Comb_start+1:Comb_start+3000+1),T_AVE_B_S(Comb_start+1
:Comb_start+3000+1),T_STD_B_S(Comb_start+1:Comb_start+3000+1),'lineProp
s','-b','transparent',1,'patchSaturation',0.2);

% T_STD_C_EE =
shadedErrorBar(t(Comb_start+1:Comb_start+3000+1),T_AVE_C_E(Comb_start+1
:Comb_start+3000+1),T_STD_C_E(Comb_start+1:Comb_start+3000+1),'lineProp
s','-.r','transparent',1,'patchSaturation',0.2);

T_STD_C_SS =
shadedErrorBar(t(Comb_start+1:Comb_start+3000+1),T_AVE_C_S(Comb_start+1
```

```
:Comb_start+3000+1),T_STD_C_S(Comb_start+1:Comb_start+3000+1),'lineProp
s','-k','transparent',1,'patchSaturation',0.2);

legend({'Location A','Location B','Location
C'},'FontSize',20,'location','southeast');

xlim([-5 50]);

ylim([200 260]);

hold on

xlabel('TAI (ms)','FontSize',15);

ylabel('Temperature (^oC)','FontSize',15);

axes = gca(figure(1));

axes.FontSize = 20;

figure(8);

plot(t,LA_s_4,'r');

hold on

plot(t,LA_comb_s_4,'b');

xlim([-5 95]);

ylim([200 260]);

hold on

plot(t,LA_comb_e_1,'r',t,LA_comb_e_2,'g',t,LA_comb_e_3,'b',t,LA_comb_e_
4,'y',t,LA_comb_e_5,'k');

xlim([-5 95]);

ylim([200 260]);

hold on

% % plot(t,LA_comb_s_1,'r');

% % hold on

% % plot(t,LA_comb_e_1,'b');

% % hold on

%
```

```
% figure(2);

% plot(t,LB_s_1,'r');

% xlim([-5 95]);

% ylim([200 260]);

% hold on

%
plot(t,LB_comb_s_1,'r',t,LB_comb_s_2,'g',t,LB_comb_s_3,'b',t,LB_comb_s_
4,'y',t,LB_comb_s_5,'k');

% xlim([-5 95]);

% ylim([200 260]);

% hold on

% figure(3);

%
plot(t,LC_s_1,'r',t,LC_s_2,'g',t,LC_s_3,'b',t,LC_s_4,'y',t,LC_s_5,'k');

% hold on

%
plot(t,LC_comb_s_1,'r',t,LC_comb_s_2,'g',t,LC_comb_s_3,'b',t,LC_comb_s_
4,'y',t,LC_comb_s_5,'k');

% xlim([-5 95]);

% ylim([200 260]);

% hold on

%% Heat Flux calculation by using FFT filter

Shift_num = 10000 - start;

S_N_1 = 10000;

S_N_2 = 13000;

% Repeat 1

HF_A_1 = K * (LA_comb_e_1 - LA_comb_s_1) / dx;

HF_A_1_shift = mean(HF_A_1(1:Shift_num));

% HF_A_1(1:S_N_1) = HF_A_1(1:S_N_1) - HF_A_1_shift;
```

```
% HF_A_1(S_N_2:L) = HF_A_1(S_N_2:L) - HF_A_1_shift;
HF_B_1 = K * (LB_comb_e_1 - LB_comb_s_1) / dx;
HF_B_1_shift = mean(HF_B_1(1:Shift_num));
% HF_B_1(1:S_N_1) = HF_B_1(1:S_N_1) - HF_B_1_shift;
% HF_B_1(S_N_2:L) = HF_B_1(S_N_2:L) - HF_A_1_shift;
HF_C_1 = K * (LC_comb_e_1 - LC_comb_s_1) / dx;
HF_C_1_shift = mean(HF_C_1(1:Shift_num));
% HF_C_1(1:S_N_1) = HF_C_1(1:S_N_1) - HF_C_1_shift;
% HF_C_1(S_N_2:L) = HF_C_1(S_N_2:L) - HF_A_1_shift;
% Repeat 2
HF_A_2 = K * (LA_comb_e_2 - LA_comb_s_2) / dx;
HF_A_2_shift = mean(HF_A_2(1:Shift_num));
% HF_A_2(1:S_N_1) = HF_A_2(1:S_N_1) - HF_A_2_shift;
% HF_A_2(S_N_2:L) = HF_A_2(S_N_2:L) - HF_A_2_shift;
HF_B_2 = K * (LB_comb_e_2 - LB_comb_s_2) / dx;
HF_B_2_shift = mean(HF_B_2(1:Shift_num));
% HF_B_2(1:S_N_1) = HF_B_2(1:S_N_1) - HF_B_2_shift;
% HF_B_2(S_N_2:L) = HF_B_2(S_N_2:L) - HF_B_2_shift;
HF_C_2 = K * (LC_comb_e_2 - LC_comb_s_2) / dx;
HF_C_2_shift = mean(HF_C_2(1:Shift_num));
% HF_C_2(1:S_N_1) = HF_C_2(1:S_N_1) - HF_C_2_shift;
% HF_C_2(S_N_2:L) = HF_C_2(S_N_2:L) - HF_C_2_shift;
% Repeat 3
HF_A_3 = K * (LA_comb_e_3 - LA_comb_s_3) / dx;
HF_A_3_shift = mean(HF_A_3(1:Shift_num));
% HF_A_3(1:S_N_1) = HF_A_3(1:S_N_1) - HF_A_3_shift;
% HF_A_3(S_N_2:L) = HF_A_3(S_N_2:L) - HF_A_3_shift;
```

```
HF_B_3 = K * (LB_comb_e_3 - LB_comb_s_3) / dx;
HF_B_3_shift = mean(HF_B_3(1:Shift_num));
% HF_B_3(1:S_N_1) = HF_B_3(1:S_N_1) - HF_B_3_shift;
% HF_B_3(S_N_2:L) = HF_B_3(S_N_2:L) - HF_B_3_shift;
HF_C_3 = K * (LC_comb_e_3 - LC_comb_s_3) / dx;
HF_C_3_shift = mean(HF_C_3(1:Shift_num));
% HF_C_3(1:S_N_1) = HF_C_3(1:S_N_1) - HF_C_3_shift;
% HF_C_3(S_N_2:L) = HF_C_3(S_N_2:L) - HF_C_3_shift;
% Repeat 4
HF_A_4 = K * (LA_comb_e_4 - LA_comb_s_4) / dx;
HF_A_4_shift = mean(HF_A_4(1:Shift_num));
% HF_A_4(1:S_N_1) = HF_A_4(1:S_N_1) - HF_A_4_shift;
% HF_A_4(S_N_2:L) = HF_A_4(S_N_2:L) - HF_A_4_shift;
HF_B_4 = K * (LB_comb_e_4 - LB_comb_s_4) / dx;
HF_B_4_shift = mean(HF_B_4(1:Shift_num));
% HF_B_4(1:S_N_1) = HF_B_4(1:S_N_1) - HF_B_4_shift;
% HF_B_4(S_N_2:L) = HF_B_4(S_N_2:L) - HF_B_4_shift;
HF_C_4 = K * (LC_comb_e_4 - LC_comb_s_4) / dx;
HF_C_4_shift = mean(HF_C_4(1:Shift_num));
% HF_C_4(1:S_N_1) = HF_C_4(1:S_N_1) - HF_C_4_shift;
% HF_C_4(S_N_2:L) = HF_C_4(S_N_2:L) - HF_C_4_shift;
% Repeat 5
HF_A_5 = K * (LA_comb_e_5 - LA_comb_s_5) / dx;
HF_A_5_shift = mean(HF_A_5(1:Shift_num));
% HF_A_5(1:S_N_1) = HF_A_5(1:S_N_1) - HF_A_5_shift;
% HF_A_5(S_N_2:L) = HF_A_5(S_N_2:L) - HF_A_5_shift;
HF_B_5 = K * (LB_comb_e_5 - LB_comb_s_5) / dx;
```

```
HF_B_5_shift = mean(HF_B_5(1:Shift_num));
% HF_B_5(1:S_N_1) = HF_B_5(1:S_N_1) - HF_B_5_shift;
% HF_B_5(S_N_2:L) = HF_B_5(S_N_2:L) - HF_B_5_shift;
HF_C_5 = K * (LC_comb_e_5 - LC_comb_s_5) / dx;
HF_C_5_shift = mean(HF_C_5(1:Shift_num));
% HF_C_5(1:S_N_1) = HF_C_5(1:S_N_1) - HF_C_5_shift;
% HF_C_5(S_N_2:L) = HF_C_5(S_N_2:L) - HF_C_5_shift;
% Average heat flux and standard deviation;
% Location A
HF_AVE_A = (HF_A_1 + HF_A_2 + HF_A_3 + HF_A_4 + HF_A_5)/5;
HF_A(:,1) = HF_A_1;
HF_A(:,2) = HF_A_2;
HF_A(:,3) = HF_A_3;
HF_A(:,4) = HF_A_4;
HF_A(:,5) = HF_A_5;
HF_STD_A = std(HF_A,0,2);
% Location B
HF_AVE_B = (HF_B_1 + HF_B_2 + HF_B_3 + HF_B_4 + HF_B_5)/5;
HF_B(:,1) = HF_B_1;
HF_B(:,2) = HF_B_2;
HF_B(:,3) = HF_B_3;
HF_B(:,4) = HF_B_4;
HF_B(:,5) = HF_B_5;
HF_STD_B = std(HF_B,0,2);
% Location C
HF_AVE_C = (HF_C_1 + HF_C_2 + HF_C_3 + HF_C_4 + HF_C_5)/5;
HF_C(:,1) = HF_C_1;
```

```
HF_C(:,2) = HF_C_2;

HF_C(:,3) = HF_C_3;

HF_C(:,4) = HF_C_4;

HF_C(:,5) = HF_C_5;

HF_STD_C = std(HF_C,0,2);


Accu_A_1(Comb_start) = 0;

Accu_B_1(Comb_start) = 0;

Accu_C_1(Comb_start) = 0;

Accu_A_2(Comb_start) = 0;

Accu_B_2(Comb_start) = 0;

Accu_C_2(Comb_start) = 0;

Accu_A_3(Comb_start) = 0;

Accu_B_3(Comb_start) = 0;

Accu_C_3(Comb_start) = 0;

Accu_A_4(Comb_start) = 0;

Accu_B_4(Comb_start) = 0;

Accu_C_4(Comb_start) = 0;

Accu_A_5(Comb_start) = 0;

Accu_B_5(Comb_start) = 0;

Accu_C_5(Comb_start) = 0;

for i = Comb_start+1:Comb_start+30000;

Accu_A_1(i) = Accu_A_1(i-1) + HF_A_1(i)*T;

Accu_B_1(i) = Accu_B_1(i-1) + HF_B_1(i)*T;

Accu_C_1(i) = Accu_C_1(i-1) + HF_C_1(i)*T;

Accu_A_2(i) = Accu_A_2(i-1) + HF_A_2(i)*T;

Accu_B_2(i) = Accu_B_2(i-1) + HF_B_2(i)*T;
```

```
Accu_C_2(i) = Accu_C_2(i-1) + HF_C_2(i)*T;

Accu_A_3(i) = Accu_A_3(i-1) + HF_A_3(i)*T;

Accu_B_3(i) = Accu_B_3(i-1) + HF_B_3(i)*T;

Accu_C_3(i) = Accu_C_3(i-1) + HF_C_3(i)*T;

Accu_A_4(i) = Accu_A_4(i-1) + HF_A_4(i)*T;

Accu_B_4(i) = Accu_B_4(i-1) + HF_B_4(i)*T;

Accu_C_4(i) = Accu_C_4(i-1) + HF_C_4(i)*T;

Accu_A_5(i) = Accu_A_5(i-1) + HF_A_5(i)*T;

Accu_B_5(i) = Accu_B_5(i-1) + HF_B_5(i)*T;

Accu_C_5(i) = Accu_C_5(i-1) + HF_C_5(i)*T;

end


Accu_AVE_A = (Accu_A_1 + Accu_A_2 + Accu_A_3 + Accu_A_4 + Accu_A_5)/5;

Accu_AVE_B = (Accu_B_1 + Accu_B_2 + Accu_B_3 + Accu_B_4 + Accu_B_5)/5;

Accu_AVE_C = (Accu_C_1 + Accu_C_2 + Accu_C_3 + Accu_C_4 + Accu_C_5)/5;


Accu_A(:,1) = Accu_A_1;

Accu_A(:,2) = Accu_A_2;

Accu_A(:,3) = Accu_A_3;

Accu_A(:,4) = Accu_A_4;

Accu_A(:,5) = Accu_A_5;


Accu_STD_A = std(Accu_A,0,2);


Accu_B(:,1) = Accu_B_1;

Accu_B(:,2) = Accu_B_2;
```

```
Accu_B(:,3) = Accu_B_3;

Accu_B(:,4) = Accu_B_4;

Accu_B(:,5) = Accu_B_5;


Accu_STD_B = std(Accu_B,0,2);


Accu_C(:,1) = Accu_C_1;

Accu_C(:,2) = Accu_C_2;

Accu_C(:,3) = Accu_C_3;

Accu_C(:,4) = Accu_C_4;

Accu_C(:,5) = Accu_C_5;


Accu_STD_C = std(Accu_C,0,2);
% figure(4);
% plot(t,HF_AVE_A,'r',t,HF_AVE_B,'g',t,HF_AVE_C,'b');
% ylim([-100 400]);
figure(5);
plot(t(1:20:L),HF_AVE_A(1:20:L),'r','LineWidth',1.5);
xlim([-5 50]);
ylim([-100 800]);
hold on
plot(t(1:20:L),HF_AVE_B(1:20:L),'b','LineWidth',1.5);
xlim([-5 50]);
ylim([-100 800]);
hold on
plot(t(1:20:L),HF_AVE_C(1:20:L),'k','LineWidth',1.5);
xlim([-5 50]);
```

```
ylim([-100 800]);

hold on

ylabel('Heat flux (kW/m^2)','FontSize',15);

xlabel('TAI (ms)','FontSize',15);

STD_A =
shadedErrorBar(t(Comb_start+1:Comb_start+3000+1),HF_AVE_A(Comb_start+1:
Comb_start+3000+1),HF_STD_A(Comb_start+1:Comb_start+3000+1),'lineProps'
,'r','transparent',1,'patchSaturation',0.2);

STD_B =
shadedErrorBar(t(Comb_start+1:Comb_start+3000+1),HF_AVE_B(Comb_start+1:
Comb_start+3000+1),HF_STD_B(Comb_start+1:Comb_start+3000+1),'lineProps'
,'b','transparent',1,'patchSaturation',0.2);

STD_C =
shadedErrorBar(t(Comb_start+1:Comb_start+3000+1),HF_AVE_C(Comb_start+1:
Comb_start+3000+1),HF_STD_C(Comb_start+1:Comb_start+3000+1),'lineProps'
,'k','transparent',1,'patchSaturation',0.2);

axes = gca(figure(5));

axes.FontSize = 20;

legend({'Location A','Location B','Location C'},'FontSize',20);

figure(6);

plot(t(Comb_start+1:Comb_start+30000),Accu_AVE_A(Comb_start+1:Comb_star
t+30000),'r','LineWidth',1.5);

hold on

plot(t(Comb_start+1:Comb_start+30000),Accu_AVE_B(Comb_start+1:Comb_star
t+30000),'b','LineWidth',1.5);

hold on

plot(t(Comb_start+1:Comb_start+30000),Accu_AVE_C(Comb_start+1:Comb_star
t+30000),'k','LineWidth',1.5);

hold on

Accu_A_STD =
shadedErrorBar(t(Comb_start+1:Comb_start+3000+1),Accu_AVE_A(Comb_start+
1:Comb_start+3000+1),Accu_STD_A(Comb_start+1:Comb_start+3000+1),'linePr
ops','r','transparent',1,'patchSaturation',0.2);

Accu_B_STD =
shadedErrorBar(t(Comb_start+1:Comb_start+3000+1),Accu_AVE_B(Comb_start+
```

```
1:Comb_start+3000+1),Accu_STD_B(Comb_start+1:Comb_start+3000+1),'linePr
ops','b','transparent',1,'patchSaturation',0.2);

Accu_C_STD =
shadedErrorBar(t(Comb_start+1:Comb_start+3000+1),Accu_AVE_C(Comb_start+
1:Comb_start+3000+1),Accu_STD_C(Comb_start+1:Comb_start+3000+1),'linePr
ops','k','transparent',1,'patchSaturation',0.2);

xlim([0 50]);

legend({'Location A','Location B','Location
C'},'FontSize',20,'location','northwest');

ylabel('Cumulative Heat Release (kJ/m^2)','FontSize',15);

xlabel('TAI (ms)','FontSize',15);

axes = gca(figure(6));

axes.FontSize = 20;
```

10.2.6 Heat flux measurement results

This section provides the effects of ambient density and injection pressure on heat flux at different orientations (90° and 180°) during spray impinging on a hot surface (250 °C).

10.2.5.1 Heat flux measurement results at 90°

Figure 10.1 shows the effect of ambient density on the heat flux at three different locations at 90°. The injection pressure during the test remains the same for all conditions, 150 MPa.

In general, at 90°, due to the impinged spray location, the heat flux is lower than that at 90°. In Figure 10.1, at the same ambient density, the heat flux at Location A is always larger than other two locations at any given time since Location A is closer to the impinging point as the spray interacting with the hot surface compared with other two locations, this results in the relatively large amount of liquid film deposited near this location and the temperature difference between the liquid and surface is larger. By comparing the heat flux from Location B with that from Location C, Location B gives more heat flux because Location C nearly resides in the edge of the impinged spray, resulting in less liquid spray cross it. Further, ambient density shows insignificant effect on the heat flux at any locations.

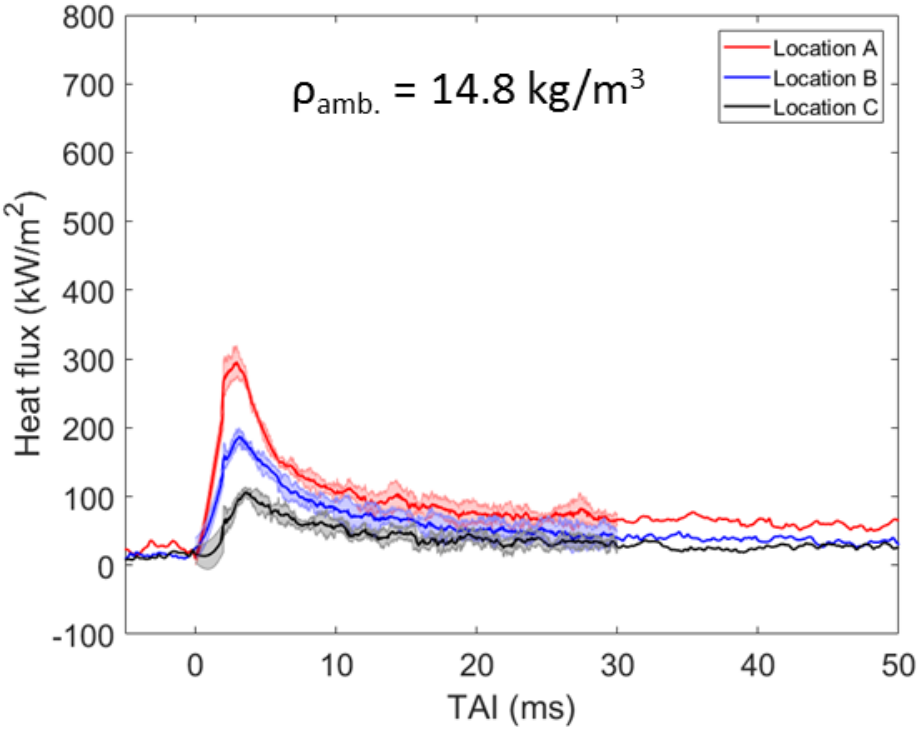

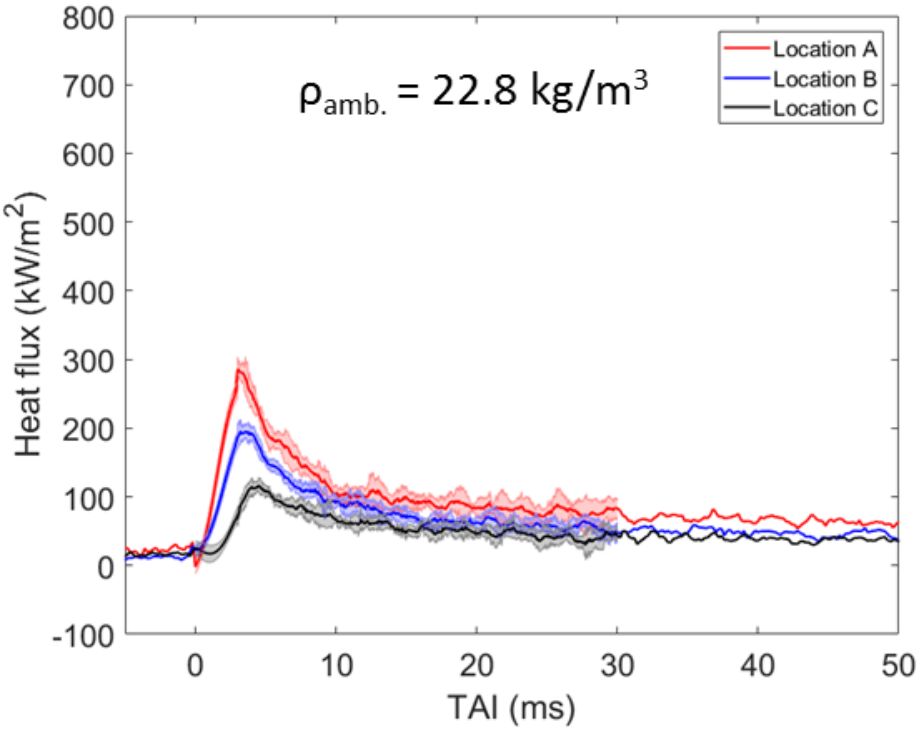

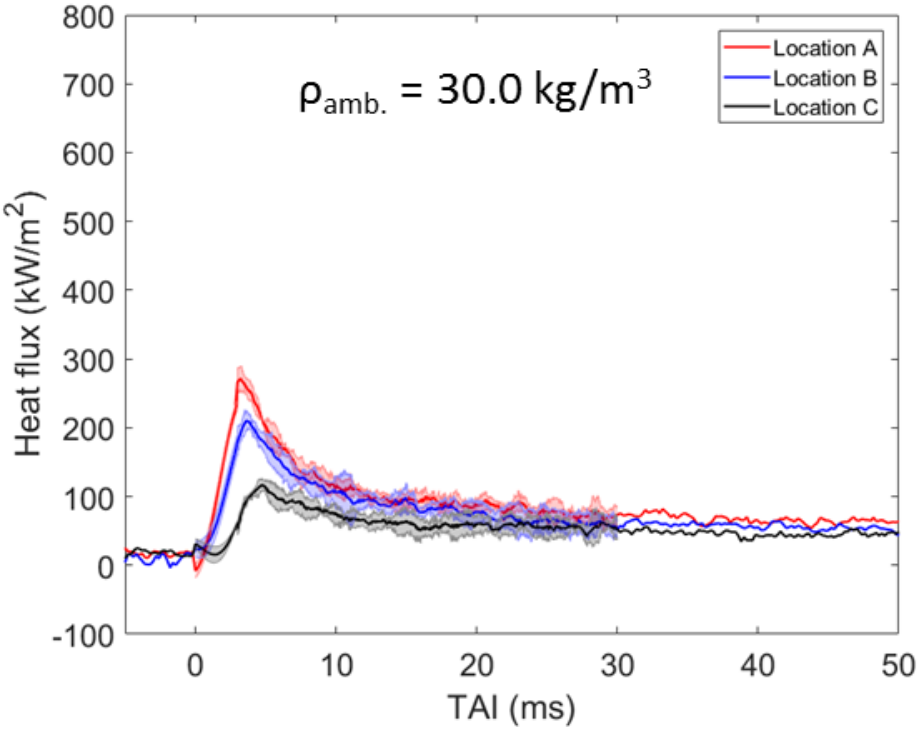

Figure 10.1: Ambient density effect on the heat flux at three different locations at 90°.

Figure 10.2 shows the effect of injection pressure on the heat flux at three different locations at 90°. The ambient density during the test remains the same for all conditions, 22.8 kg/m^3. The heat flux at various injection pressures is generally lower at 90° than that.at 0° due to the impinged spray location. With the same injection pressure, at any given time, the heat flux curve at Location A is always above ones in other two locations due to its closer distances from the impinging point, followed by the heat flux at Location B, finally the heat flux at Location C. At any fixed location, the heat flux overall slightly increases with the injection pressure, however, there is no a substantial monotone trend of heat flux as the injection pressure increases or decreases.

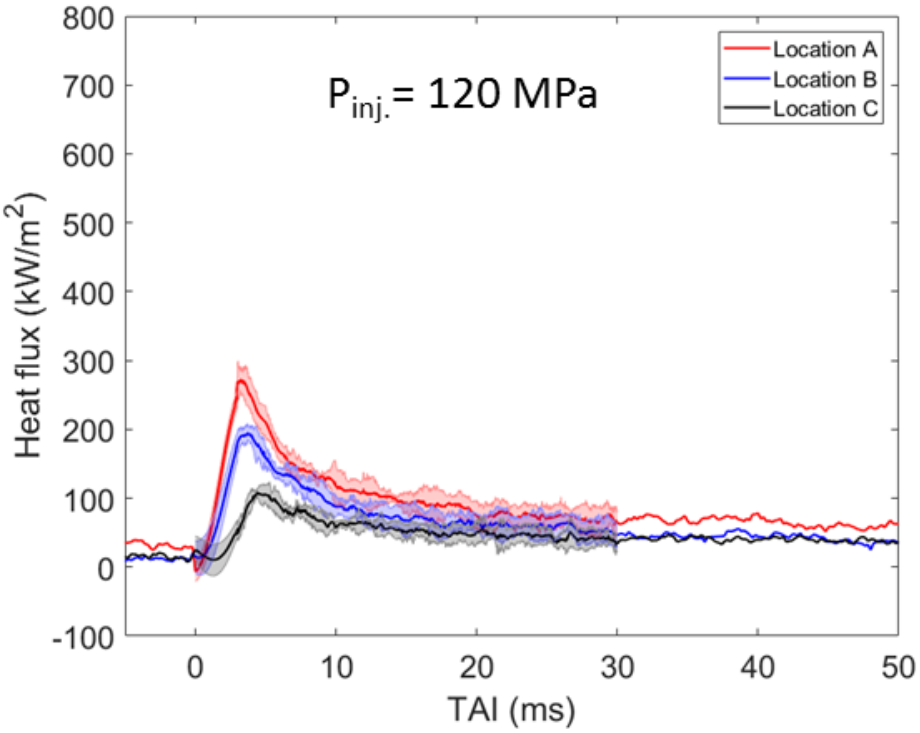

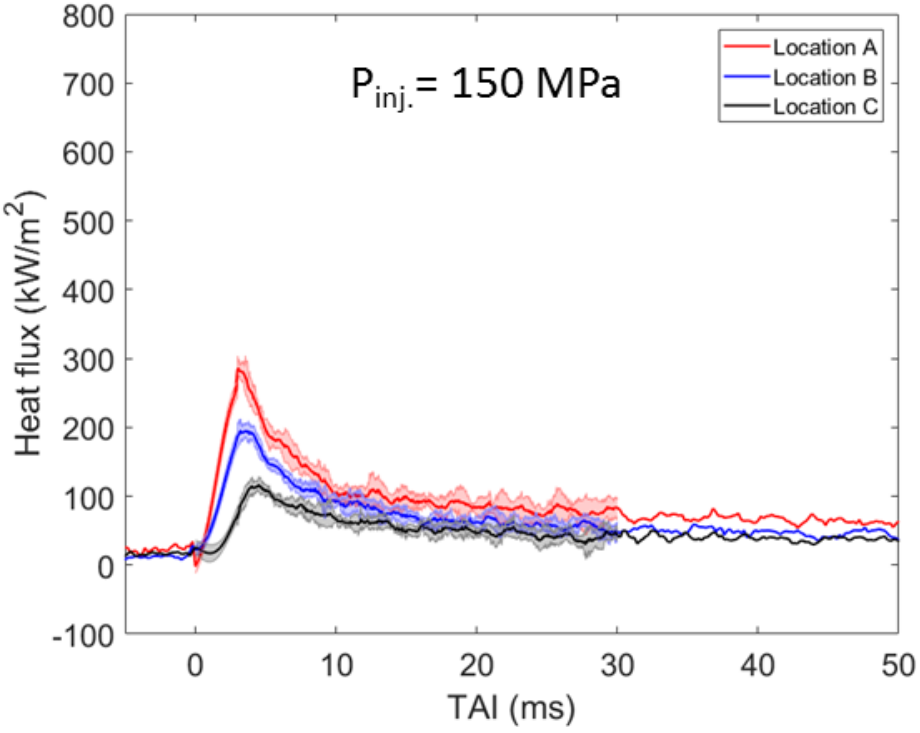

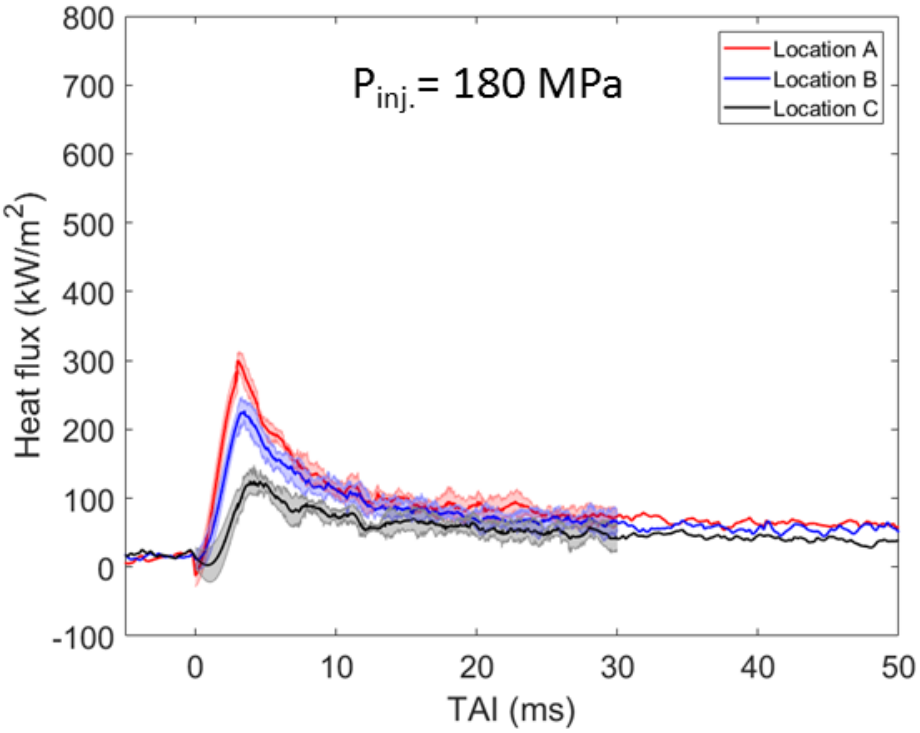

Figure 10.2: Injection pressure effect on the heat flux at three different locations at 90º.

10.2.5.2 Heat flux measurement results at 180º

Overall, the heat flux at 180º with different ambient densities is smallest compared with other two orientation since the locations at 180º are the farthest away from the impinging point. In Figure 10.3, as the same reason mentioned in the 90º cases, at the same ambient density, the heat flux at Location A is always larger than other two locations at any given time. By comparing the heat flux from Location B with that from Location C, Location B gives more heat flux. Further, ambient density shows insignificant effect on the heat flux at any locations.

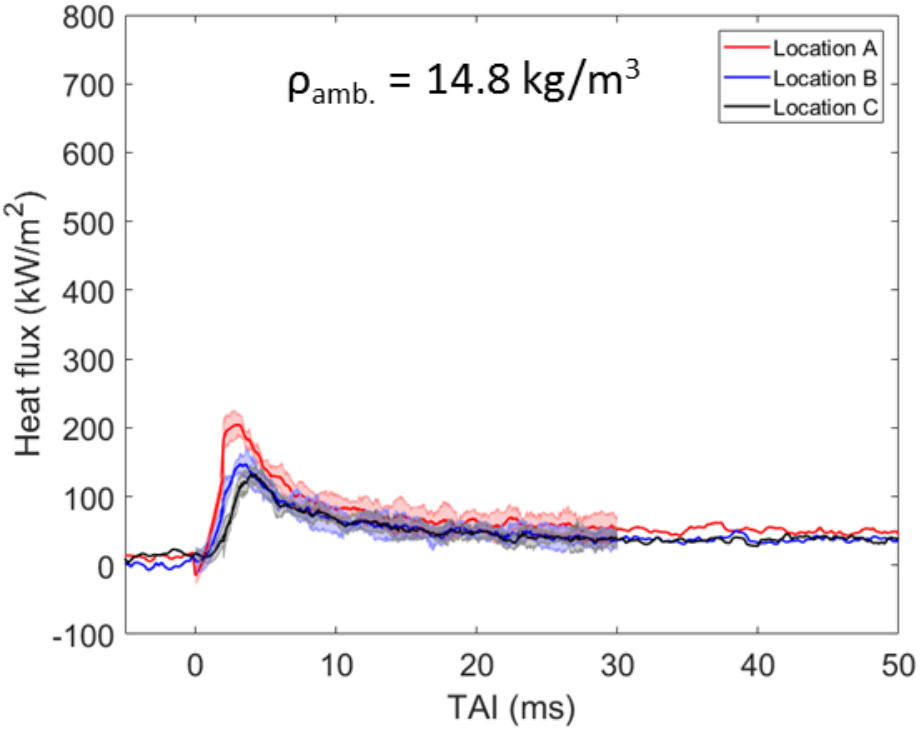

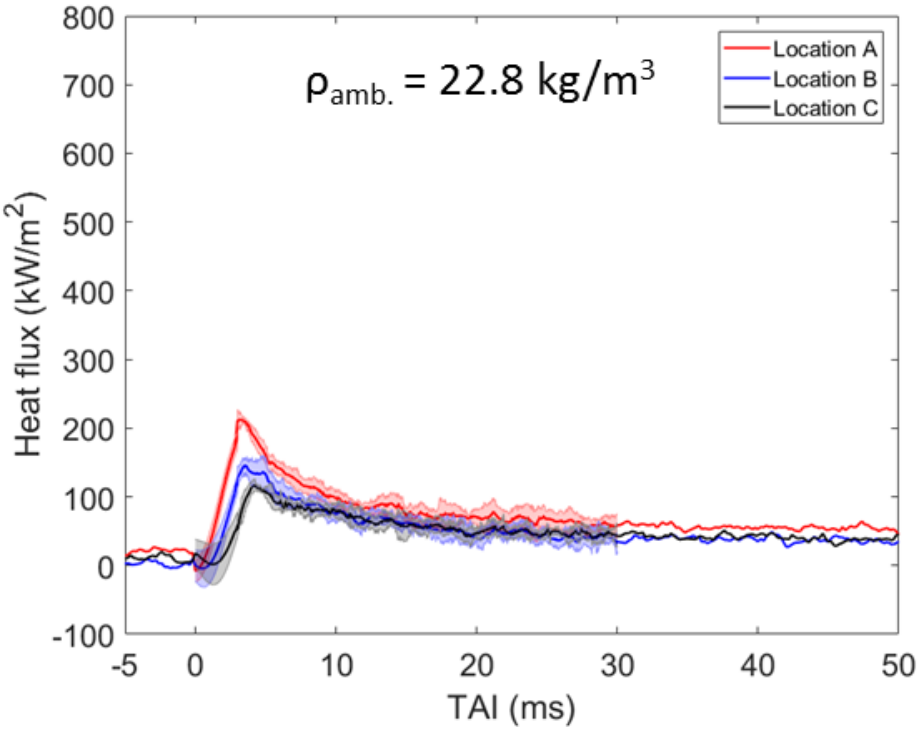

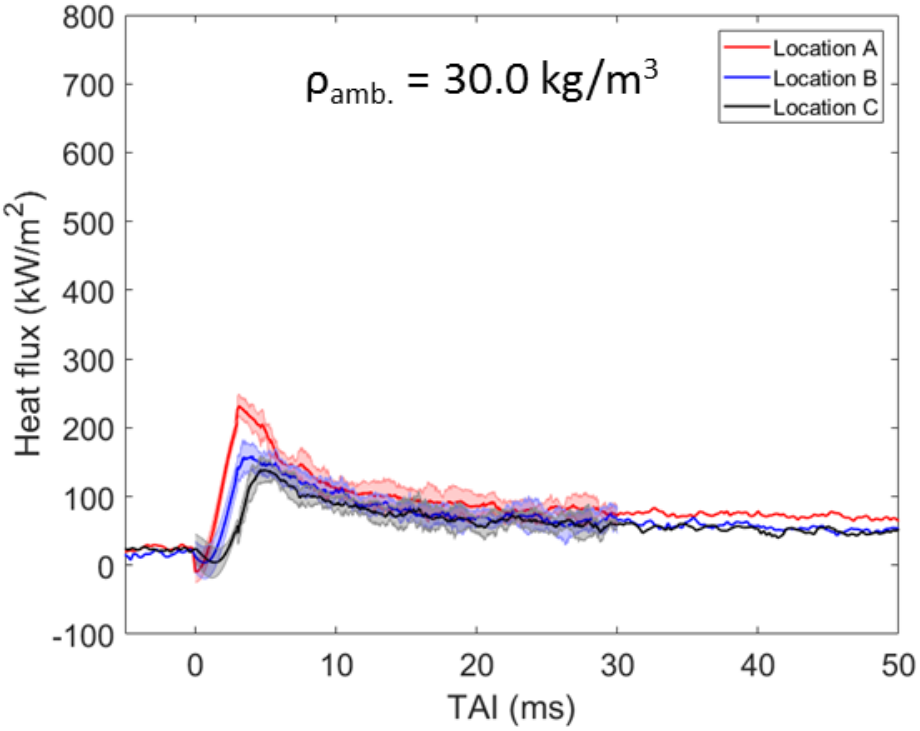

Figure 10.3: Ambient density effect on the heat flux at three different locations at 180°.

Figure 10.4 shows the effect of injection pressure on the heat flux at three different locations at 180°. The ambient density during the test remains the same for all conditions, 22.8 kg/m^3. The heat flux at 180° with various injection pressures is smallest compared with other two orientations. With the same injection pressure, at any given time, the heat flux curve at Location A is always above ones in other two locations as it is closer to the impinging point, followed by the heat flux at Location B, finally the heat flux at Location C. At any fixed location, the heat flux overall slightly increases with the injection pressure, however, there is no a substantial monotone trend of heat flux as the injection pressure increases or decreases.

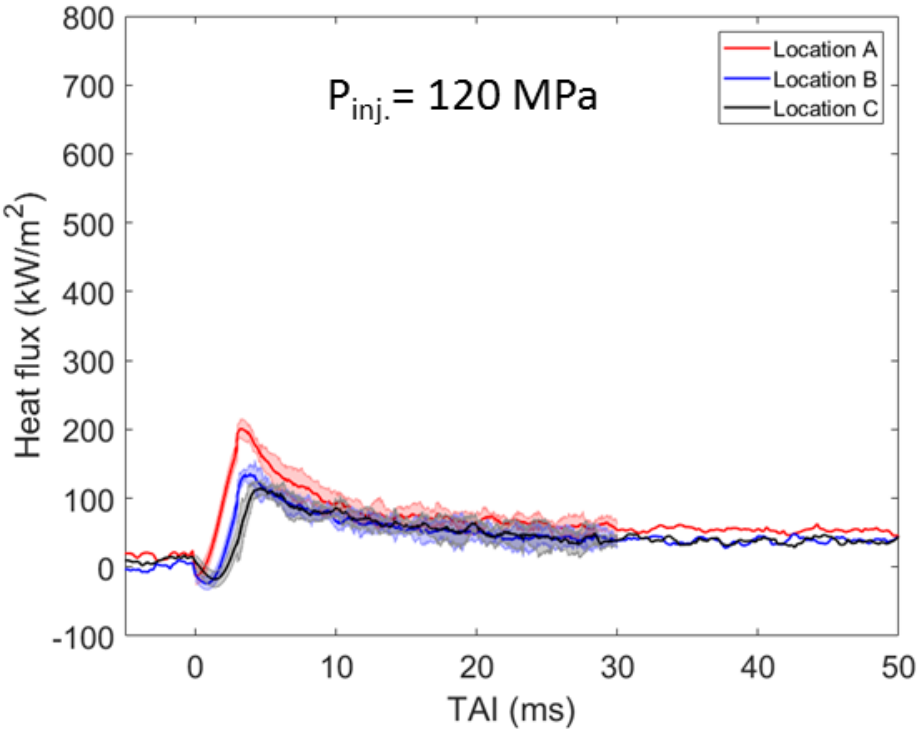

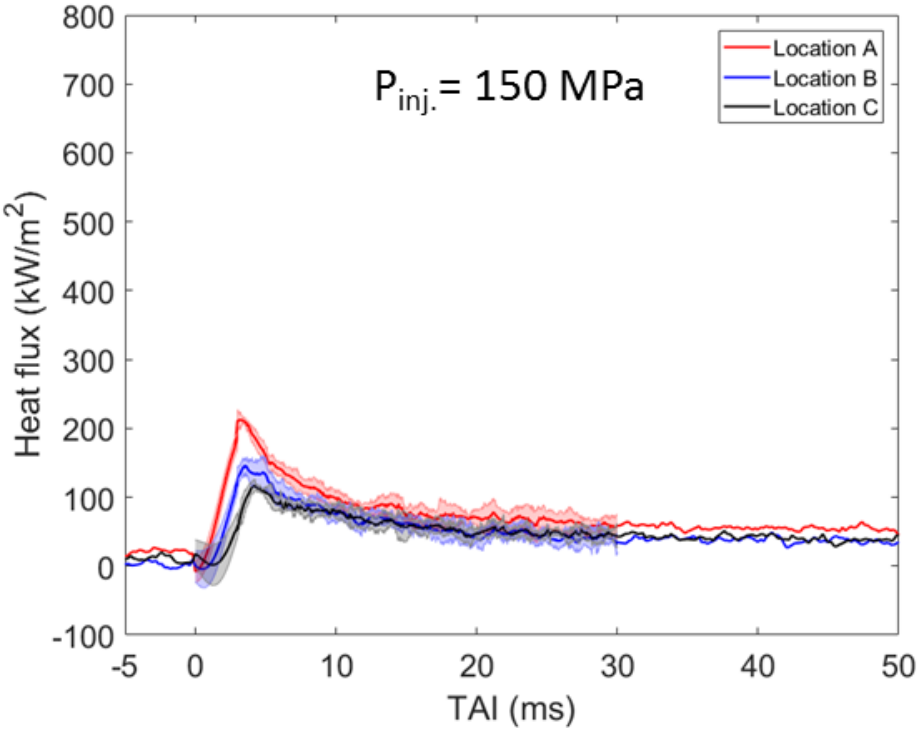

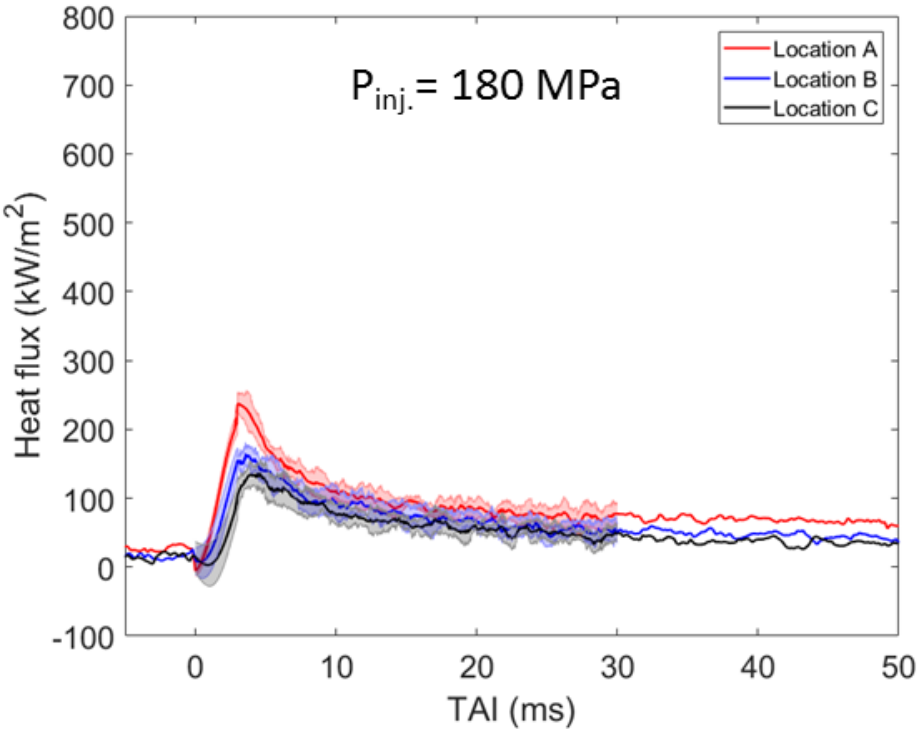

Figure 10.4: Injection pressure effect on the heat flux at three different locations at 180°.

CHAPTER 11 REFERENCE LIST

1 Sperling, D. and Gordon, D., *Two Billion Cars: Driving toward Sustainability*. 2010:Oxford University Press.

2 "Https://Www.Eia.Gov/Energyexplained/Index.Cfm?Page=Oil_Use".

3 Burtscher, H., "Physical Characterization of Particulate Emissions from Diesel Engines: A Review," *Journal of Aerosol Science* 36(7):896-932, 2005, doi:https://doi.org/10.1016/j.jaerosci.2004.12.001.

4 Yusri, I.M., Mamat, R., Najafi, G., Razman, A., et al., "Alcohol Based Automotive Fuels from First Four Alcohol Family in Compression and Spark Ignition Engine: A Review on Engine Performance and Exhaust Emissions," *Renewable and Sustainable Energy Reviews* 77(169-181, 2017, doi:https://doi.org/10.1016/j.rser.2017.03.080.

5 Elliott, M.A., Nebel, G.J., and Rounds, F.G., "The Composition of Exhaust Gases from Diesel, Gasoline and Propane Powered Motor Coaches," *Journal of the Air Pollution Control Association* 5(2):103-108, 1955, doi:10.1080/00966665.1955.10467686.

6 Parent, M.-É., Rousseau, M.-C., Boffetta, P., Cohen, A., et al., "Exposure to Diesel and Gasoline Engine Emissions and the Risk of Lung Cancer," *American Journal of Epidemiology* 165(1):53-62, 2007, doi:10.1093/aje/kwj343.

7 Zhang, J., McCreanor, J., Cullinan, P., Chung, K., et al., "Health Effects of Real-World Exposure to Diesel Exhaust in Persons with Asthma," *Research report (Health Effects Institute)* 138):5-109; discussion 111-123, 2009,

8 Pope, C.A., Thun, M.J., Namboodiri, M.M., Dockery, D.W., et al., "Particulate Air Pollution as a Predictor of Mortality in a Prospective Study of Us Adults," *American journal of respiratory and critical care medicine* 151(3):669-674, 1995,

9 Attfield, M.D., Schleiff, P.L., Lubin, J.H., Blair, A., et al., "The Diesel Exhaust in Miners Study: A Cohort Mortality Study with Emphasis on Lung Cancer," *JNCI: Journal of the National Cancer Institute* 104(11):869-883, 2012, doi:10.1093/jnci/djs035.

10 Katsouyanni, K., Schwartz, J., Spix, C., Touloumi, G., et al., "Short Term Effects of Air Pollution on Health: A European Approach Using Epidemiologic Time Series Data: The Aphea Protocol," *Journal of Epidemiology and Community Health* 50(Suppl 1):S12-S18, 1996, doi:10.1136/jech.50.Suppl_1.S12.

11 Li, N., Hao, M., Phalen, R.F., Hinds, W.C., et al., "Particulate Air Pollutants and Asthma: A Paradigm for the Role of Oxidative Stress in Pm-Induced Adverse

Health Effects," *Clinical Immunology* 109(3):250-265, 2003, doi:https://doi.org/10.1016/j.clim.2003.08.006.

12 "Emission Standards: Europe: Cars and Light Trucks - Dieselnet". https://www.dieselnet.com/standards/eu/ld.php.

13 "Emission Standards Reference Guide for on-Road and Nonroad Vehicles and Engines". U.S. Environmental Protection Agency https://www.epa.gov/emission-standards-reference-guide.

14 Bai, C. and Gosman, A.D., "Development of Methodology for Spray Impingement Simulation," SAE Technical Paper 1995, doi:https://doi.org/10.4271/950283.

15 Matsui, Y. and Sugihara, K., "Sources of Hydrocarbon Emissions from a Small Direct Injection Diesel Engine," SAE Technical Paper 1987, doi:https://doi.org/10.4271/871613.

16 Lefebvre, A.H. and McDonell, V.G., *Atomization and Sprays*. 2017: CRC press

17 Bush, J.W.M. and Hasha, A.E., "On the Collision of Laminar Jets: Fluid Chains and Fishbones," *Journal of Fluid Mechanics* 511(285-310, 2004, doi:10.1017/S002211200400967X.

18 Sutton, G.P. and Biblarz, O., *Rocket Propulsion Elements*. 2017: John Wiley & Sons

19 Chen, X., Ma, D., Yang, V., and Popinet, S., "High-Fidelity Simulations of Impinging Jet Atomization," 23(12):1079-1101, 2013, doi:10.1615/AtomizSpr.2013007619.

20 Kim, S.C. and Ryou, H.S., "An Experimental and Numerical Study on Fire Suppression Using a Water Mist in an Enclosure," *Building and Environment* 38(11):1309-1316, 2003, doi:https://doi.org/10.1016/S0360-1323(03)00134-3.

21 Moreira, A.L.N., Moita, A.S., and Panão, M.R., "Advances and Challenges in Explaining Fuel Spray Impingement: How Much of Single Droplet Impact Research Is Useful?," *Progress in Energy and Combustion Science* 36(5):554-580, 2010, doi:https://doi.org/10.1016/j.pecs.2010.01.002.

22 Young, V., *Liquid Rocket Engine Combustion Instability*. Vol. 169. 1995: Aiaa

23 Potham, S.P., Zhao, L., and Lee, S.-Y., "Numerical Study on Evaporation of Spherical Droplets Impinging on the Wall Using Volume of Fluid (Vof) Model," SAE Technical Paper 2017, doi:https://doi.org/10.4271/2017-01-0852.

24 Bai, C.X., Rusche, H., and Gosman, A.D., "Modeling of Gasoline Spray Impingement," *Atomization and Sprays* 12(1-3):1-27, 2002, doi:10.1615/AtomizSpr.v12.i123.10.

25 Habchi, C., Foucart, H., and Baritaud, T., "Influence of the Wall Temperature on the Mixture Preparation in Di Gasoline Engines," *Oil & Gas Science and Technology - Rev. IFP* 54(2):211-222, 1999,

26 Stow C.D. , H.M.G., "An Experimental Investigation of Fluid Flow Resulting from the Impact of a Water Drop with an Unyielding Dry Surface," *Proceedings of the Royal Society of London. A. Mathematical and Physical Sciences* 373(1755):419, 1981,

27 Lindagren, R. and Denbratt, I., "Influence of Wall Properties on the Characteristics of a Gasoline Spray after Wall Impingement," SAE Technical Paper 2004-01-1951, 2004, doi:10.4271/2004-01-1951.

28 Yarin, A.L. and Weiss, D.A., "Impact of Drops on Solid Surfaces: Self-Similar Capillary Waves, and Splashing as a New Type of Kinematic Discontinuity," *Journal of Fluid Mechanics* 283(141-173, 1995, doi:10.1017/S0022112095002266.

29 Mundo, C., Sommerfeld, M., and Tropea, C., "Droplet-Wall Collisions: Experimental Studies of the Deformation and Breakup Process," *International journal of multiphase flow* 21(2):151-173, 1995, doi:10.1016/0301-9322(94)00069-V.

30 Rioboo, R., Tropea, C., and Marengo, M., "Outcomes from a Drop Impact on Solid Surfaces," 11(2):12, 2001, doi:10.1615/AtomizSpr.v11.i2.40.

31 Brant Foote, G., "A Numerical Method for Studying Liquid Drop Behavior: Simple Oscillation," *Journal of Computational Physics* 11(4):507-530, 1973, doi:https://doi.org/10.1016/0021-9991(73)90135-6.

32 Trapaga, G. and Szekely, J., "Mathematical Modeling of the Isothermal Impingement of Liquid Droplets in Spraying Processes," *Metallurgical and Materials Transactions B* 22(6):901-914, 1991, doi:10.1007/bf02651166.

33 Fukai, J., Zhao, Z., Poulikakos, D., Megaridis, C.M., et al., "Modeling of the Deformation of a Liquid Droplet Impinging Upon a Flat Surface," *Physics of Fluids A: Fluid Dynamics* 5(11):2588-2599, 1993, doi:10.1063/1.858724.

34 Bussmann, M., Mostaghimi, J., and Chandra, S., "On a Three-Dimensional Volume Tracking Model of Droplet Impact," *Physics of Fluids* 11(6):1406-1417, 1999, doi:10.1063/1.870005.

35 Nikolopoulos, N., Theodorakakos, A., and Bergeles, G., "Three-Dimensional Numerical Investigation of a Droplet Impinging Normally onto a Wall Film," *Journal of Computational Physics* 225(1):322-341, 2007, doi:https://doi.org/10.1016/j.jcp.2006.12.002.

36 Tamura, Z. and Tanasawa, Y., "Evaporation and Combustion of a Drop Contacting with a Hot Surface," *Symposium (International) on Combustion* 7(1):509-522, 1958, doi:https://doi.org/10.1016/S0082-0784(58)80086-7.

37 Kang, B.S. and Lee, D.H., "On the Dynamic Behavior of a Liquid Droplet Impacting Upon an Inclined Heated Surface," *Experiments in Fluids* 29(4):380-387, 2000, doi:10.1007/s003489900104.

38 Manzello, S. and C Yang, J., *An Experimental Study of High Weber Number Impact of Methoxy-Nonafluorobutane C4f9och3 (Hfe-7100) and N-Heptane Droplets on a Heated Solid Surface* 1*. Vol. 45. 2002.10.1016/S0017-9310(02)00103-5

39 Nukiyama, S., "The Maximum and Minimum Values of the Heat Q Transmitted from Metal to Boiling Water under Atmospheric Pressure," *International Journal of Heat and Mass Transfer* 9(12):1419-1433, 1966, doi:https://doi.org/10.1016/0017-9310(66)90138-4.

40 Leidenfrost, J.G., "On the Fixation of Water in Diverse Fire," *International Journal of Heat and Mass Transfer* 9(11):1153-1166, 1966, doi:https://doi.org/10.1016/0017-9310(66)90111-6.

41 Nguyen, T.K. and Avedisian, C.T., "Numerical Solution for Film Evaporation of a Spherical Liquid Droplet on an Isothermal and Adiabatic Surface," *International Journal of Heat and Mass Transfer* 30(7):1497-1509, 1987, doi:https://doi.org/10.1016/0017-9310(87)90181-5.

42 Pasandideh-Fard, M., Bhola, R., Chandra, S., and Mostaghimi, J., "Deposition of Tin Droplets on a Steel Plate: Simulations and Experiments," *International Journal of Heat and Mass Transfer* 41(19):2929-2945, 1998, doi:https://doi.org/10.1016/S0017-9310(98)00023-4.

43 Harvie, D.J.E. and Fletcher, D.F., "A Hydrodynamic and Thermodynamic Simulation of Droplet Impacts on Hot Surfaces, Part I: Theoretical Model," *International Journal of Heat and Mass Transfer* 44(14):2633-2642, 2001, doi:https://doi.org/10.1016/S0017-9310(00)00303-3.

44 Nikolopoulos, N., Theodorakakos, A., and Bergeles, G., "A Numerical Investigation of the Evaporation Process of a Liquid Droplet Impinging onto a Hot Substrate," *International Journal of Heat and Mass Transfer* 50(1):303-319, 2007, doi:https://doi.org/10.1016/j.ijheatmasstransfer.2006.06.012.

45 Mahulkar, A.V., Marin, G.B., and Heynderickx, G.J., "Droplet–Wall Interaction Upon Impingement of Heavy Hydrocarbon Droplets on a Heated Wall," *Chemical Engineering Science* 130(275-289, 2015, doi:https://doi.org/10.1016/j.ces.2015.03.012.

46 Hu, J., Xiong, X., Xiao, H., and Wan, K.-t., "Effects of Contact Angle on the Dynamics of Water Droplet Impingement," presented at COMSOL, Boston, 2015.

47 Vadillo, D.C., Soucemarianadin, A., Delattre, C., and Roux, D.C.D., "Dynamic Contact Angle Effects onto the Maximum Drop Impact Spreading on Solid Surfaces," *Physics of Fluids* 21(12):122002, 2009, doi:10.1063/1.3276259.

48 Šikalo, Š., Wilhelm, H.-D., Roisman, I.V., Jakirlić, S., et al., "Dynamic Contact Angle of Spreading Droplets: Experiments and Simulations," *Physics of Fluids* 17(6):062103, 2005, doi:10.1063/1.1928828.

49 Schrader, M.E., "Young-Dupre Revisited," *Langmuir* 11(9):3585-3589, 1995, doi:10.1021/la00009a049.

50 Malgarinos, I., Nikolopoulos, N., Marengo, M., Antonini, C., et al., "Vof Simulations of the Contact Angle Dynamics During the Drop Spreading: Standard Models and a New Wetting Force Model," *Advances in Colloid and Interface Science* 212(1-20, 2014, doi:https://doi.org/10.1016/j.cis.2014.07.004.

51 Roisman, I.V., Opfer, L., Tropea, C., Raessi, M., et al., "Drop Impact onto a Dry Surface: Role of the Dynamic Contact Angle," *Colloids and Surfaces A: Physicochemical and Engineering Aspects* 322(1–3):183-191, 2008, doi:https://doi.org/10.1016/j.colsurfa.2008.03.005.

52 Schiaffino, S. and Sonin, A.A., "Molten Droplet Deposition and Solidification at Low Weber Numbers," *Physics of Fluids* 9(11):3172-3187, 1997, doi:10.1063/1.869434.

53 Rayleigh, J.W.S.B., *The Theory of Sound*. Vol. 2. 1896: Macmillan

54 Schotland, R.M., "Experimental Results Relating to the Coalescence of Water Drops with Water Surfaces," *Discussions of the Faraday Society* 30(0):72-77, 1960, doi:10.1039/DF9603000072.

55 O. W. Jayaratne, B.J.M., "The Coalescence and Bouncing of Water Drops at an Air/Water Interface," *Proceedings of the Royal Society of London. Series A. Mathematical and Physical Sciences* 280(1383):545-565, 1964, doi:10.1098/rspa.1964.0161.

56 List, R. and Whelpdale, D.M., "A Preliminary Investigation of Factors Affecting the Coalescence of Colliding Water Drops," *Journal of the Atmospheric Sciences* 26(2):305-308, 1969, doi:10.1175/1520-0469(1969)026<0305:apiofa>2.0.co;2.

57 Qian, J. and Law, C.K., "Regimes of Coalescence and Separation in Droplet Collision," *Journal of Fluid Mechanics* 331(59-80, 2009, doi:10.1017/S0022112096003722.

58 Ko, G.H. and Ryou, H.S., "Droplet Collision Processes in an Inter-Spray Impingement System," *Journal of Aerosol Science* 36(11):1300-1321, 2005, doi:https://doi.org/10.1016/j.jaerosci.2005.02.005.

59 Low, T.B. and List, R., "Collision, Coalescence and Breakup of Raindrops. Part I: Experimentally Established Coalescence Efficiencies and Fragment Size Distributions in Breakup," *Journal of the Atmospheric Sciences* 39(7):1591-1606, 1982, doi:10.1175/1520-0469(1982)039<1591:ccabor>2.0.co;2.

60 Ashgriz, N. and Givi, P., "Binary Collision Dynamics of Fuel Droplets," *International Journal of Heat and Fluid Flow* 8(3):205-210, 1987, doi:https://doi.org/10.1016/0142-727X(87)90029-4.

61 Jiang, Y.J., Umemura, A., and Law, C.K., "An Experimental Investigation on the Collision Behaviour of Hydrocarbon Droplets," *Journal of Fluid Mechanics* 234(171-190, 2006, doi:10.1017/S0022112092000740.

62 Pan, Y. and Suga, K., "Numerical Simulation of Binary Liquid Droplet Collision," *Physics of Fluids* 17(8):082105, 2005, doi:10.1063/1.2009527.

63 Ashgriz, N. and Poo, J.Y., "Coalescence and Separation in Binary Collisions of Liquid Drops," *Journal of Fluid Mechanics* 221(183-204, 2006, doi:10.1017/S0022112090003536.

64 Xing Gang, L. and Udo, F., "Numerical Investigation of Binary Droplet Collisions in All Relevant Collision Regimes," *The Journal of Computational Multiphase Flows* 3(4):207-224, 2011, doi:10.1260/1757-482X.3.4.207.

65 Saroka, M., Ashgriz, N., and Movassat, M., "Numerical Investigation of Head-on Binary Drop Collisions in a Dynamically Inert Environment," *Journal of Applied Fluid Mechanics* 5(1):2012,

66 Soriano, G., Alvarado, J.L., and Lin, Y.P., "Experimental Characterization of Single and Multiple Droplet Impingement on Surfaces Subject to Constant Heat Flux Conditions," 49415):707-715, 2010, doi:10.1115/IHTC14-22515.

67 Lewis, S.R., Anumolu, L., and Trujillo, M.F., "Numerical Simulations of Droplet Train and Free Surface Jet Impingement," *International Journal of Heat and Fluid Flow* 44(610-623, 2013, doi:https://doi.org/10.1016/j.ijheatfluidflow.2013.09.001.

68 Zhao, L., Moiz, A.A., Lee, S.-Y., Naber, J., et al., "Investigation of Multi-Hole Impinging Jet High Pressure Spray Characteristics under Gasoline Engine-Like Conditions," SAE Technical Paper 2016-01-0847, 2016, doi:10.4271/2016-01-0847.

69 Zhao, L., Torelli, R., Zhu, X., Scarcelli, R., et al., "An Experimental and Numerical Study of Diesel Spray Impingement on a Flat Plate," *SAE Int. J. Fuels Lubr.* 10(2):407-422, 2017, doi:10.4271/2017-01-0854.

70 Stanglmaier, R.H., Li, J., and Matthews, R.D., "The Effect of in-Cylinder Wall Wetting Location on the Hc Emissions from Si Engines," SAE Technical Paper 1999-01-0502, 1999, doi:10.4271/1999-01-0502.

71 Stanton, D.W. and Rutland, C.J., "Modeling Fuel Film Formation and Wall Interaction in Diesel Engines," SAE Technical Paper 960628, 1996, doi:10.4271/960628.

72 Drake, M.C., Fansler, T.D., Solomon, A.S., and Szekely, G.A., "Piston Fuel Films as a Source of Smoke and Hydrocarbon Emissions from a Wall-Controlled Spark-Ignited Direct-Injection Engine," SAE Technical Paper 2003-01-0547, 2003, doi:10.4271/2003-01-0547.

73 Behnia, M. and Milton, B.E., "Fundamentals of Fuel Film Formation and Motion in Si Engine Induction Systems," *Energy Conversion and Management* 42(15–17):1751-1768, 2001, doi:https://doi.org/10.1016/S0196-8904(01)00041-3.

74 Reitz, R.D. and Duraisamy, G., "Review of High Efficiency and Clean Reactivity Controlled Compression Ignition (Rcci) Combustion in Internal Combustion Engines," *Progress in Energy and Combustion Science* 46(12-71, 2015, doi:http://dx.doi.org/10.1016/j.pecs.2014.05.003.

75 Akop, M.Z., Zama, Y., Furuhata, T., and Arai, M., "Experimental Investigations on Adhered Fuel and Impinging Diesel Spray Normal to a Wall," *Atomization and Sprays* 23(3):211-231, 2013, doi:10.1615/AtomizSpr.2013007447.

76 Akop, M.Z., Zama, Y., Furuhata, T., and Arai, M., "Characteristics of Adhesion of Diesel Fuel on Impingement Disk Wall. Part 1: Effect of Impingement Area and Inclination Angle of Disk," *Atomization and Sprays* 23(8):725-744, 2013, doi:10.1615/AtomizSpr.2013008113.

77 Akop, M.Z., Zama, Y., Furuhata, T., and Arai, M., "Characteristics of Adhesion Diesel Fuel on an Impingement Disk Wall Part 2: Droplet Weber Number and Adhered Fuel Mass," *Atomization and Sprays* 24(8):651-671, 2014, doi:10.1615/AtomizSpr.2014008445.

78 Sandia National Laboratory ECN website. "Engine Combustion Network". http://www.sandia.gov/ecn, accessed 2016;

79 Pope, S., "An Explanation of the Turbulent Round-Jet/Plane-Jet Anomaly," *AIAA journal* 16(3):279-281, 1978, doi:http://dx.doi.org/10.2514/3.7521.

80 Montanaro, A., Allocca, L., Meccariello, G., and Lazzaro, M., "Schlieren and Mie Scattering Imaging System to Evaluate Liquid and Vapor Contours of a Gasoline Spray Impacting on a Heated Wall," SAE Technical Paper 2015-24-2473, 2015, doi:10.4271/2015-24-2473.

81 Yu, H., Liang, X., Shu, G., Wang, Y., et al., "Experimental Investigation on Spray-Wall Impingement Characteristics of N-Butanol/Diesel Blended Fuels," *Fuel* 182(Supplement C):248-258, 2016, doi:https://doi.org/10.1016/j.fuel.2016.05.115.

82 Yu, H., Liang, X., Shu, G., Sun, X., et al., "Experimental Investigation on Wall Film Ratio of Diesel, Butanol/Diesel, Dme/Diesel and Gasoline/Diesel Blended Fuels During the Spray Wall Impingement Process," *Fuel Processing Technology* 156(Supplement C):9-18, 2017, doi:https://doi.org/10.1016/j.fuproc.2016.09.029.

83 Li, K., Ido, M., Ogata, Y., Nishida, K., et al., "Effect of Spray/Wall Interaction on Diesel Combustion and Soot Formation in Two-Dimensional Piston Cavity," *SAE International Journal of Engines* 6(4):2061-2071, 2013, doi:https://doi.org/10.4271/2013-32-9021.

84 Kuichun, L., Keiya, N., Youichi, O., and Baolu, S., "Effect of Flat-Wall Impingement on Diesel Spray Combustion," *Proceedings of the Institution of Mechanical Engineers, Part D: Journal of Automobile Engineering* 229(5):535-549, 2014, doi:10.1177/0954407014547242.

85 Borthwick, R.P. and Farrell, P.V., "Fuel Injection Spray and Combustion Chamber Wall Impingement in Large Bore Diesel Engines," SAE Technical Paper 2002, doi:https://doi.org/10.4271/2002-01-0496.

86 Saito, A. and Kawamura, K., "Behavior of Fuel Film on a Wall at Fuel Spray Impinging," 24(4-6):707-715, 1997, doi:10.1615/InterJFluidMechRes.v24.i4-6.260.

87 Senda, J., Ohnishi, M., Takahashi, T., Fujimoto, H., et al., "Measurement and Modeling on Wall Wetted Fuel Film Profile and Mixture Preparation in Intake Port of Si Engine," SAE Technical Paper 1999-01-0798, 1999, doi:10.4271/1999-01-0798.

88 Lindgren, R., Block, R., and Denbratt, I., "Development of a Wall Film Thickness Measuring Device," presented at Optical and Laser Diagnostics: Proceedings of the First International Conference London, 16-20 December 2002, 2003.

89 Panão, M.R. and Moreira, A.L.N., "Visualization and Analysis of Spray Impingement under Cross-Flow Conditions," SAE Technical Paper 2002-01-2664, 2002, doi:10.4271/2002-01-2664.

90 Cheng, Y.-s., Deng, K., and Li, T., "Measurement and Simulation of Wall-Wetted Fuel Film Thickness," *International Journal of Thermal Sciences* 49(4):733-739, 2010, doi:https://doi.org/10.1016/j.ijthermalsci.2009.10.006.

91 Ko, K. and Arai, M., "Diesel Spray Impinging on a Flat Wall, Part I: Characteristics of Adhered Fuel Film in an Impingement Diesel Spray," 12(5&6):737-751, 2002, doi:10.1615/AtomizSpr.v12.i56.120.

92 Mathews, W.S., Lee, C.F., and Peters, J.E., "Experimental Investigations of Spray/Wall Impingement," 13(2&3):20, 2003, doi:10.1615/AtomizSpr.v13.i23.40.

93 Yang, B. and Ghandhi, J., "Measurement of Diesel Spray Impingement and Fuel Film Characteristics Using Refractive Index Matching Method," SAE Technical Paper 2007-01-0485, 2007, doi:10.4271/2007-01-0485.

94 Maligne, D. and Bruneaux, G., "Time-Resolved Fuel Film Thickness Measurement for Direct Injection Si Engines Using Refractive Index Matching," SAE Technical Paper 2011-01-1215, 2011, doi:10.4271/2011-01-1215.

95 Zheng, Y., Xie, X., Lai, M.-C., and VanDerWege, B., "Measurement and Simulation of Di Spray Impingements and Film Characteristics," presented at 12th Triennial International Conference on Liquid Atomization and Spray Systems, Heidelberg, Germany, 2012.

96 O'Rourke, P.J. and Amsden, A.A., "A Particle Numerical Model for Wall Film Dynamics in Port-Injected Engines," SAE Technical Paper 961961, 1996, doi:10.4271/961961.

97 Naber, J.D. and Reitz, R.D., "Modeling Engine Spray/Wall Impingement," SAE Technical Paper 880107, 1988, doi:10.4271/880107.

98 Han, Z., Xu, Z., and Trigui, N., "Spray/Wall Interaction Models for Multidimensional Engine Simulation," *International Journal of Engine Research* 1(1):127-146, 2000, doi:10.1243/1468087001545308.

99 O'Rourke, P.J. and Amsden, A.A., "A Spray/Wall Interaction Submodel for the Kiva-3 Wall Film Model," SAE Technical Paper 2000-01-0271, 2000, doi:10.4271/2000-01-0271.

100 Han, Z. and Xu, Z., "Wall Film Dynamics Modeling for Impinging Sprays in Engines," SAE Technical Paper 2004-01-0099, 2004, doi:10.4271/2004-01-0099.

101 Ma, T., Feng, L., Wang, H., Liu, H., et al., "A Numerical Study of Spray/Wall Impingement Based on Droplet Impact Phenomenon," *International Journal of Heat and Mass Transfer* 112(401-412, 2017, doi:https://doi.org/10.1016/j.ijheatmasstransfer.2017.04.110.

102 Palacios, J., Hernández, J., Gómez, P., Zanzi, C., et al., "Experimental Study of Splashing Patterns and the Splashing/Deposition Threshold in Drop Impacts onto Dry Smooth Solid Surfaces," *Experimental Thermal and Fluid Science* 44(571-582, 2013, doi:https://doi.org/10.1016/j.expthermflusci.2012.08.020.

103 Wal, R.L.V., Berger, G.M., and Mozes, S.D., "The Splash/Non-Splash Boundary Upon a Dry Surface and Thin Fluid Film," *Experiments in Fluids* 40(1):53-59, 2006, doi:10.1007/s00348-005-0045-1.

104 James, C.B., Scott, S.H.T., and Howard, A.S., "Inclined to Splash: Triggering and Inhibiting a Splash with Tangential Velocity," *New Journal of Physics* 11(6):063017, 2009.

105 Pan, K.-L., Tseng, K.-C., and Wang, C.-H., "Breakup of a Droplet at High Velocity Impacting a Solid Surface," *Experiments in Fluids* 48(1):143-156, 2010, doi:10.1007/s00348-009-0697-3.

106 Stanton, D.W. and Rutland, C.J., "Multi-Dimensional Modeling of Thin Liquid Films and Spray-Wall Interactions Resulting from Impinging Sprays," *International Journal of Heat and Mass Transfer* 41(20):3037-3054, 1998, doi:https://doi.org/10.1016/S0017-9310(98)00054-4.

107 Montorsi, L., Magnusson, A., and Andersson, S., "A Numerical and Experimental Study of Diesel Fuel Sprays Impinging on a Temperature Controlled Wall," SAE Technical Paper 2006-01-3333, 2006, doi:10.4271/2006-01-3333.

108 Montorsi, L., Magnusson, A., Andersson, S., and Jedrzejowski, S., "Numerical and Experimental Analysis of the Wall Film Thickness for Diesel Fuel Sprays Impinging on a Temperature-Controlled Wall," SAE Technical Paper 2007-01-0486, 2007, doi:10.4271/2007-01-0486.

109 Habchi, C., Foucart, H., and Baritaud, T., "Influence De La Température De Paroi Sur La Préparation Du Mélange Dans Les Moteurs À Essence À Injection Directe," *Oil & Gas Science and Technology - Rev. IFP* 54(2):211-222, 1999, doi:http://dx.doi.org/10.2516/ogst:1999017.

110 Zhang, Y., Jia, M., Liu, H., and Xie, M., "Development of an Improved Liquid Film Model for Spray/Wall Interaction under Engine-Relevant Conditions," *International Journal of Multiphase Flow* 79(74-87, 2016, doi:https://doi.org/10.1016/j.ijmultiphaseflow.2015.10.002.

111 Zhao, L., Torelli, R., Zhu, X., Naber, J., et al., "Evaluation of Diesel Spray-Wall Interaction and Morphology around Impingement Location," SAE Technical Paper 2018-01-0276, 2018.

112 Lippert, A.M., Stanton, D.W., Reitz, R.D., Rutland, C.J., et al., "Investigating the Effect of Spray Targeting and Impingement on Diesel Engine Cold Start," SAE Technical Paper 2000-01-0269, 2000, doi:10.4271/2000-01-0269.

113 Cole, V., Mehra, D., Lowry, S., and Gray, D., "A Numerical Spray Impingement Model Coupled with a Free Surface Film Model," presented at The Fifth International Symposium on Diagonstics and Modeling of Combustion in Internal Combustion Engines, Nayoga, July 1-4, 2001.

114 Bayvel, L., *Liquid Atomization*. Vol. 1040. 1993: CRC Press

115 Chen, X., Ma, D., and Yang, V., "Dynamics and Stability of Impinging Jets," presented at ILASS Americas, 24th annual conference on liquid atomization and spray systems, San Antonio (TX), 2012.

116 Ghasemi, A., Barron, R., and Balachandar, R., "Spray-to-Spray Collision Breakup of Ultra High Injection Pressure Diesel Fuel," presented at 20th Annual Conference of the CFD Society of Canada, Canmore, 2012.

117 Tsuru, D., Tajima, H., Ishibashi, R., and Kawauchi, S., "Droplet Collision Modelling between Merging Immiscible Sprays in Direct Water Injection System," presented at ILASS Europe, 23rd annual conference on liquid atomization and spray systems, Brno, Czech Republic, 2010.

118 Bravo, L., Ivey, C., Kim, D., and Bose, S., "High Fidelity Simulation of Atomization in Diesel Engine Sprays″. 2015, ARMY RESEARCH LAB ABERDEEN PROVING GROUND MD VEHICLE TECHNOLOGY DIRECTORATE.

119 Morgan, C.J., "Spray Characterization of Eoo E85 Direct Injection in an Optical Combustion Vessel under Starting Conditions″. 2011, Michigan Technological University.

120 "Https://Carbonzapp.Com/Products/Diesel/Crdi/Cru-4r".

121 "Https://Www.Cmt.Upv.Es/Ecn03.Aspx".

122 Bower, G.R. and Foster, D.E., "A Comparison of the Bosch and Zuech Rate of Injection Meters," SAE Technical Paper 910724, 1991, doi:10.4271/910724.

123 Moiz, A.A., "Low Temperature Split Injection Spray Combustion: Ignition, Flame Stabilization and Soot Formation Characteristics in Diesel Engine Conditions″. 2016, Michigan Technological University.

124 Cung, K.D., "Spray and Combustion Characteristics of Dimethyl Ether under Various Ambient Conditions: An Experimental and Modeling Study″. 2015, Michigan Technological University.

125 Nesbitt, J.E., *Diesel Spray Mixing Limited Vaporization with Non-Ideal and Multi-Component Fuel Thermophysical Property Effects*. 2011: Michigan Technological University

126 Otsu, N., "A Threshold Selection Method from Gray-Level Histograms," *IEEE transactions on systems, man, and cybernetics* 9(1):62-66, 1979,

127 Zhang, A., Montanaro, A., Allocca, L., Naber, J., et al., "Measurement of Diesel Spray Formation and Combustion Upon Different Nozzle Geometry Using Hybrid Imaging Technique," *SAE Int. J. Engines* 7(2):1034-1043, 2014, doi:10.4271/2014-01-1410.

128 Otsu, N., "A Threshold Selection Method from Gray-Level Histograms," *Automatica* 11(285-296):23-27, 1975,

129 Gonzalez, W. and Woods, R.E., *Eddins, Digital Image Processing Using Matlab*. Third New Jersey: Prentice Hall. 2004

130 Zhu, X., Zhao, L., Zhao, Z., Ahuja, N., et al., "An Experimental Study of Diesel Spray Impingement on a Flat Plate: Effects of Injection Conditions," presented at ILASS–Europe 2017, 28th Conference on Liquid Atomization and Spray Systems, 2017.

131 Potham, S., Zhao, L., and Lee, S., "Numerical Study on Evaporation of Spherical Droplets Impinging on the Wall Using Volume of Fluid (Vof) Model," SAE Technical Paper 2017, doi:10.4271/2017-01-0852.

132 Richards, K.J., Senecal, P. K., and Pomraning, E., "Converge Manual (Version 2.3)", Convergent Science Inc., Madison, WI – USA, 2016.

133 Schlottke, J. and Weigand, B., "Direct Numerical Simulation of Evaporating Droplets," *Journal of Computational Physics* 227(10):5215-5237, 2008.

134 Tonini, S. and Cossali, G.E., "An Analytical Model of Liquid Drop Evaporation in Gaseous Environment," *International Journal of Thermal Sciences* 57(45-53, 2012, doi:https://doi.org/10.1016/j.ijthermalsci.2012.01.017.

135 Dukowicz, J.K., "A Particle-Fluid Numerical Model for Liquid Sprays," *Journal of Computational Physics* 35(2):229-253, 1980, doi:10.1016/0021-9991(80)90087-X.

136 Reitz, R.D., "Modeling Atomization Processes in High-Pressure Vaporizing Sprays," *Atomisation and Spray Technology* 3(4):309-337, 1987,

137 Patterson, M.A. and Reitz, R.D., "Modeling the Effects of Fuel Spray Characteristics on Diesel Engine Combustion and Emission," SAE Technical Paper 980131, 1998, doi:10.4271/980131.

138 Taylor, G., "The Instability of Liquid Surfaces When Accelerated in a Direction Perpendicular to Their Planes. I," presented at Proceedings of the Royal Society of London A: Mathematical, Physical and Engineering Sciences, 1950.

139 Schmidt, D.P. and Rutland, C., "A New Droplet Collision Algorithm," *Journal of Computational Physics* 164(1):62-80, 2000, doi:10.1006/jcph.2000.6568.

140 Post, S.L. and Abraham, J., "Modeling the Outcome of Drop–Drop Collisions in Diesel Sprays," *International Journal of Multiphase Flow* 28(6):997-1019, 2002, doi:http://dx.doi.org/10.1016/S0301-9322(02)00007-1.

141 Amsden, A.A., O'rourke, P., and Butler, T., "Kiva-Ii: A Computer Program for Chemically Reactive Flows with Sprays". 1989, Los Alamos National Lab., NM (USA).

142 Liu, A.B., Mather, D., and Reitz, R.D., "Modeling the Effects of Drop Drag and Breakup on Fuel Sprays". 1993, DTIC Document.

143 Williams, G., "Combustion Theory," 1985.

144 Speziale, C., "Turbulence Modeling for Time-Dependent Rans and Vles: A Review," *AIAA Journal* 36(2):173-184, 1998, doi:10.2514/2.7499.

145 Chen, Q., "Comparison of Different K-E Models for Indoor Air Flow Computations," *Numerical Heat Transfer, Part B: Fundamentals* 28(3):353-369, 1995, doi:10.1080/10407799508928838.

146 Yakhot, V. and Orszag, S.A., "Renormalization Group Analysis of Turbulence. I. Basic Theory," *Journal of Scientific Computing* 1(1):3-51, 1986, doi:10.1007/bf01061452.

147 Launder, B. and Sharma, B., "Application of the Energy-Dissipation Model of Turbulence to the Calculation of Flow near a Spinning Disc," *Letters in heat and mass transfer* 1(2):131-137, 1974, doi:10.1016/0094-4548(74)90150-7.

148 Senecal, P.K., Pomraning, E., Richards, K.J., and Som, S., "An Investigation of Grid Convergence for Spray Simulations Using an Les Turbulence Model," SAE Technical Paper 2013, doi:https://doi.org/10.4271/2013-01-1083.

149 Roohi, E., Zahiri, A.P., and Passandideh-Fard, M., "Numerical Simulation of Cavitation around a Two-Dimensional Hydrofoil Using Vof Method and Les Turbulence Model," *Applied Mathematical Modelling* 37(9):6469-6488, 2013, doi:https://doi.org/10.1016/j.apm.2012.09.002.

150 Senecal, P.K., Pomraning, E., Richards, K.J., Briggs, T.E., et al., "Multi-Dimensional Modeling of Direct-Injection Diesel Spray Liquid Length and Flame Lift-Off

Length Using Cfd and Parallel Detailed Chemistry," SAE Technical Paper 2003, doi:https://doi.org/10.4271/2003-01-1043.

151 Xin, J., Montgomery, D., Han, Z., and Reitz, R.D., "Multidimensional Modeling of Combustion for a Six-Mode Emissions Test Cycle on a Di Diesel Engine," *Journal of Engineering for Gas Turbines and Power* 119(3):683-691, 1997, doi:10.1115/1.2817041.

152 Peters, N., "Laminar Diffusion Flamelet Models in Non-Premixed Turbulent Combustion," *Progress in Energy and Combustion Science* 10(3):319-339, 1984, doi:https://doi.org/10.1016/0360-1285(84)90114-X.

153 Pitsch, H., Chen, M., and Peters, N., "Unsteady Flamelet Modeling of Turbulent Hydrogen-Air Diffusion Flames," *Symposium (International) on Combustion* 27(1):1057-1064, 1998, doi:https://doi.org/10.1016/S0082-0784(98)80506-7.

154 Halstead, M.P., Kirsch, L.J., and Quinn, C.P., "The Autoignition of Hydrocarbon Fuels at High Temperatures and Pressures—Fitting of a Mathematical Model," *Combustion and Flame* 30(45-60, 1977, doi:https://doi.org/10.1016/0010-2180(77)90050-5.

155 Colin, O., Benkenida, A., and Angelberger, C., "3d Modeling of Mixing, Ignition and Combustion Phenomena in Highly Stratified Gasoline Engines," *Oil & gas science and technology* 58(1):47-62, 2003,

156 Lafossas, F.-A., Castagne, M., Dumas, J.P., and Henriot, S., "Development and Validation of a Knock Model in Spark Ignition Engines Using a Cfd Code," SAE Technical Paper 2002, doi:https://doi.org/10.4271/2002-01-2701.

157 Henriot, S., Bouyssounnouse, D., and Baritaud, T., "Port Fuel Injection and Combustion Simulation of a Racing Engine," SAE Technical Paper 2003, doi:https://doi.org/10.4271/2003-01-1845.

158 Kleemann, A.P., Menegazzi, P., Henriot, S., and Marchal, A., "Numerical Study on Knock for an Si Engine by Thermally Coupling Combustion Chamber and Cooling Circuit Simulations," SAE Technical Paper 2003, doi:https://doi.org/10.4271/2003-01-0563.

159 Geppert, A., Chatzianagnostou, D., Meister, C., Gomaa, H., et al., "Classification of Impact Morphology and Splashing/Deposition Limit for N-Hexadecane," 26(10):983-1007, 2016, doi:10.1615/AtomizSpr.2015013352.

160 Cossali, G.E., Coghe, A., and Marengo, M., "The Impact of a Single Drop on a Wetted Solid Surface," *Experiments in Fluids* 22(6):463-472, 1997, doi:10.1007/s003480050073.

161 Bernard, R., Foltyn, P., Geppert, A., Lamanna, G., et al., *Generalized Analysis of the Deposition/Splashing Limit for One- and Two-Component Droplet Impacts Upon Thin Films*. 2017.10.4995/ILASS2017.2017.4810

162 Maitra, T., Tiwari, M.K., Antonini, C., Schoch, P., et al., "On the Nanoengineering of Superhydrophobic and Impalement Resistant Surface Textures Below the Freezing Temperature," *Nano Letters* 14(1):172-182, 2014, doi:10.1021/nl4037092.

163 Matlab Version 9.0.0. (R2016a), Computer Software, The MathWorks Inc., Natick, MA - USA, 2016.

164 Cung, K., Moiz, A., Johnson, J., Lee, S.-Y., et al., "Spray–Combustion Interaction Mechanism of Multiple-Injection under Diesel Engine Conditions," *Proceedings of the Combustion Institute* 35(3):3061-3068, 2015, doi:http://dx.doi.org/10.1016/j.proci.2014.07.054.

165 Andrew. Miers, S., *Identification and Characterization of Impingement Signatures in a High Speed Diesel Engine Using Piston Surface Temperature Measurements*. 2017.

166 Naber, J.D. and Siebers, D.L., "Effects of Gas Density and Vaporization on Penetration and Dispersion of Diesel Sprays," SAE Technical Paper 960034, 1996, doi:10.4271/960034.

167 Senecal, P.K., Pomraning, E., Richards, K.J., and Som, S., "Grid-Convergent Spray Models for Internal Combustion Engine Computational Fluid Dynamics Simulations," *Journal of Energy Resources Technology* 136(1):012204-012204, 2013, doi:10.1115/1.4024861.

168 Pei, Y., Torelli, R., Tzanetakis, T., Zhang, Y., et al., "Modeling the Fuel Spray of a High Reactivity Gasoline under Heavy-Duty Diesel Engine Conditions," 58325):V002T006A002, 2017, doi:10.1115/ICEF2017-3530.

169 Markt, D.P., Torelli, R., Pathak, A., Som, S., Scarcelli, R., Naber, J., Lee, S.-Y., and Raessi, M., "Using a Dns Framework to Test a Splashed Mass Sub-Model for Lagrangian Spray Simulations," SAE Technical Paper 2018-01-0297, 2018.

170 "Http://Www.Epa.Gov/Ttnchie1/Ap42/Ch07/Final/C07s01.Pdf,"

171 Aleiferis, P.G. and van Romunde, Z.R., "An Analysis of Spray Development with Iso-Octane, N-Pentane, Gasoline, Ethanol and N-Butanol from a Multi-Hole Injector under Hot Fuel Conditions," *Fuel* 105(143-168, 2013, doi:https://doi.org/10.1016/j.fuel.2012.07.044.

172 Kim, H.J., Park, S.H., and Lee, C.S., "Influence of the Fuel Spray Angle and the Injection Strategy on the Emissions Reduction Characteristics in a Diesel Engine," *Proceedings of the Institution of Mechanical Engineers, Part D: Journal of Automobile Engineering* 229(5):563-573, 2015.